UNIVERSITÉ PARIS DESCARTES

Ecole Doctorale n○158 : Cerveau, Cognition, Comportement

Laboratoire: INSERM U1129, CEA/Neurospin/UNIACT

Integration of multimodal imaging data for investigation of brain development.

Par Sofya KULIKOVA

Thèse de doctorat de Neurosciences

Dirigée par Lucie HERTZ-PANNIER

Co-dirigée par Cyril POUPON

et Co-encadrée par Jessica DUBOIS

Soutenance publique prévue le 6 juillet 2015

Devant un jury composé de :

Pr. François LAZEYRAS, PhD	Rapporteur - Université de Genève
Pr. François ROUSSEAU, PhD	Rapporteur - Université de Bretagne
Pr. Catherine ADAMSBAUM, MD, PhD	Examinateur - Université Paris-Saclay
Pr. Odile BOESPFLUG-TANGUY, MD, PhD	Examinateur - Université Paris-Diderot
Dr. Boris ZALC, MD, PhD	Examinateur - Université Pierre et Marie Curie
Dr. Lucie HERTZ-PANNIER, MD, PhD	Directeur de thèse - Université Paris Descartes
Dr. Jessica DUBOIS, PhD	Membre invité - Université Paris-Saclay
Dr. Cyril POUPON, PhD	Membre invité - Université Paris-Saclay

To my son Vladimir
To all infants and children who participated in this work
To all children of all researches

Acknowledgements

First of all, I would like to thank the people who were supervising and guiding my work during my PhD studies: Dr. Lucie Hertz-Pannier, Dr. Cyril Poupon and Dr. Jessica Dubois. Without their attentive guidance, precious advices, critics and comments it would have never been possible to accomplish this work.

I also thank all french neuropediatricians who have recuited children considered in this study and in particular, Dr.Chiron, Dr.Nabbout, and Dr.Chemaly from Hôpital Necker; Dr.Sevin and Dr.Aubourg from Hôpital Kremlin-Bicêtre, Dr.Auvin from Hôpital Robert-Debré Paris; Dr.Napuri from CHU de Rennes; Dr.Caubel from Lorient). I also thank Dr. Ghislaine Dehaene-Lambertz and Jessica Dubois for MRI acquisitions in healthy infants.

I would like also to thank administration of CEA and in particularly, of NeuroSpin, of INSERM U1129, of ED3C, and of Université PARIS DESCARTES for the smooth organization of my work and ELA foundation and PHRC for financial support of this work.

I thank jury members for accepting to review my work and for their comments.

I also thank Pamela Guevara for her presious help and comments on the creation of the children connectivity atlas and Sean Deoni who accepted to discuss with me some questions on MWF quantification during the 22nd ISMRM meeting in Milan.

I would like also to thank my Neurospin colleagues who helped me during my stay here. Delphine Duclap for developing clustering tools and making me understand them, Veronique Brion for our discussions on noise correction, David Germanaud for his comments and a nice palette for MWF maps, Fawzi Boumerzbeur for introducing to me MRI spectroscopy, Marion Noulhiane, Victor Delattre, Gael Varoquaux, Elodie Dogerdespeville, Parvaneh Adibpour, Yann Leprince, Alfredo Lopez Kolkovsky and all other people who were ready to help me with any types of questions and problems.

Finally, I would like to thank my relatives and friends who supported me during these 3 years and throughout the life, and especially to my mother and my mother-in-law. I thank my husband for his patience, support and his eagerness to debug my code or check my manuscripts even at midnight. I also thankfull to my son who provided me the most evident proof that brain development is too complex and amazing to be described with univariate approaches and thus, we need multiparametric MRI studies.

Contents

Publications

1. Multi-Parametric Evaluation of the White Matter Maturation. Kulikova S, Hertz-Pannier L, Dehaene-Lambertz G, Buzmakov A, Poupon C, and Dubois J, 2014. Brain Structure & Function, doi:10.1007/s00429-014-0881-y;

2. The Early Development of Brain White Matter: A Review of Imaging Studies in Fetuses, Newborns and Infants. Dubois J, Dehaene-Lambertz G, Kulikova S, Poupon C, Huppi PS, Hertz-Pannier L, 2014. Neuroscience;

3. Correction Strategy for Diffusion-Weighted Images Corrupted with Motion: Application to the DTI Evaluation of Infants' White Matter. Dubois J, Kulikova S, Hertz-Pannier L, Mangin JF, Dehaene-Lambertz G, Poupon C, 2014. Magnetic Resonance Imaging, doi:10.1016/j.mri.2014.05.007;

4. A new strategy for fast MWF quantification in children, Kulikova S, Hertz-Pannier L, Dehaene-Lambertz G, Poupon C, Dubois J. (submitted to Human Brain Mapping);

5. Exploring the early organization and maturation of linguistic pathways in the human infant brain, Dubois J, Poupon C, Thirion B, Simonnet H, Kulikova S, Leroy F, Lucie Hertz-Pannier L, Dehaene-Lambertz G. (accepted to Cerebral Cortex).

Oral Communications

1. 4-5th December 2014, NeWS Workshop (Gif-sur-Yvette, France). Creating an atlas of children brain connectivity;

2. 7-9th April 2014, Colloque de Roscoff de la 3ème année (Roscoff, France). A new strategy for fast quantification of the Myelin Water Fraction (MWF) in infants and children;

3. 3-5th October 2013, ESMRMB Congres (Toulouse, France). #476 Multi-parametric evaluation of the white matter maturation;

4. 20th June 2013, internal meeting of the PhD students of the Institute for Biomedical Imaging (CEA/I2BM). Integration of multimodal imaging data for the study of normal and pathological brain development;

5. 13th May 2013, Journée scientifique des 2ème année (Paris, France). Integration of multimodal imaging data for the study of normal and pathological brain development.

Poster Communications

1. 30th May - 5th June 2015, ISMRM Congress (Toronto, Canada). #2494 Creating a child brain connectivity atlas for reliable bundle identification in developmental studies;
2. 4-5th December 2014, NeWS Workshop (Gif-sur-Yvette, France). Multiparametric MRI to study brain development: Two novel promising approaches;
3. 10-16th May 2014, joint ISMRM-ESMRMB meeting (Milan, Italiy). #3147 A Novel Approach for Fast MWF Quantification;
4. 10-16th May 2014, joint ISMRM-ESMRMB meeting (Milan, Italiy). #1743 What New Do We Learn with Myelin Water Fraction in Infant White Matter Bundles in Comparison with Other MRI Parameters?;
5. 29th January - 1st February 2014, 24th Congress of the SFNP (Reims, France). #1072 La fraction d'eau liée à la myéline: un nouveau biomarqueur en imagerie de la myélinisation et de la démyélinisation?;
6. 3-5th October 2013, ESMRMB Congres (Toulouse, France). #600 Comparison of quantitative MRI parameters in the developing white matter bundles;
7. 3-5th October 2013, ESMRMB Congres (Toulouse, France). #655 3T multimodal quantitative longitudinal MRI study in metachromatic leukodystrophy: preliminary study;
8. 23-26th January 2013, 23rd Congress of the SFNP (Nancy, France). IRM multimodal quantitative à 3T dans la leukodystrophy métachromatique: données préliminaires;
9. 26th June 2012, internal meeting of the PhD students of the Institute for Biomedical Imaging (CEA/I2BM). Integration of multimodal imaging data for the study of normal and pathological brain development;
10. 15th Mars 2012, Journée scientifique des 1ère année (Paris, France). Integration of multimodal imaging data for the study of normal and pathological brain development.

List of used abbreviations

AC - Anterior commissure
AF - Arcuate Fasciculus
ALIC - Anterior Limb of Internal Capsule
ARSA - ARylSulfatase-A
ATP - Adenosine TriPhosphate
BECTS - Benign Childhood Epilepsy with CentroTemporal Spikes
CAM - Cell Adhesion Molecule
CC - Corpus Callosum
CG - CinGulum
CHARMED - Composite Hindered And Restricted Model of Diffusion
CNS - Central Nervous System
CS - Centrum Semiovale
CSF - CerebroSpinal Fluid
CSI - Chemical Shift Imaging
CST - CorticoSpinal Tract
CT - CorticoThalamic
dODF - diffusion Orientation Density Function
DTI - Diffusion Tensor Imaging
DWI - Diffusion Weighted Imaging
EC -External Capsule
EEG - ElectroEncephaloGraphy
EPI - Echo Planar Imaging
FA - Fractional Anisotropy
FCD - Focal Cortical Dysplasia
FLAIR - Fluid-Attenuated Inversion Recovery
fODF - fiber Orientation Density Function
FOF - Fronto-Occipital Fasciculus
FOV - Field Of View
FX - Fornix
GABA - Gamma-AminoButyric Acid
GI - Gyrification Index
GM- Grey Matter
HARDI - High Angular Resolution Diffusion Imaging
ICM - IntraCranial Matter
ILAE - International League Against Epilepsy

ILF - Inferior Longitudinal Fasciculus
IR - Inversion Recovery
IZ - Intermediate Zone
MBP - Myelin Basic Protein
MCD - Malformations of Cortical Development
MLD - Metachromatic LeukoDystrophy
MRI - Magnetic Resonance Imaging
msDESPOT - multicomponent Driven Equilibrium Single Pulse Observation of T1/T2
MTR - Magnetization Transfer Ratio
MWF - Myelin Water Fraction
MZ - Marginal Zone
NAA - N-Acetyl Aspartate
NCx - NeoCortex
NNLS - Non-Negative Least-Square
NODDI - Neurite Orientation Dispersion and Density Imaging
OR - Optic Radiations
PC - Posterior Commissure
PET - Positron Emission Tomography
PLIC - Posterior Limb of the Internal Capsule
PLP - ProteoLipid Protein
qT1 - quantitative longitudinal relaxation time
qT2 - quantitative transverse relaxation time
ROI - Regions Of Interest
SE - Spin-Echo
SLF- Superior Longitudinal Fasciculus
SNR - Signal-to-Noise Ratio
SP - SubPlate
STT - SpinoThalamic Tract
SVZ - SubVentricular Zone
TC - ThalamoCortical
TE - Echo Time
TI - Inversion Time
TIR - Turbo Inversion Recovery
TR - Repetition Time
UF - Uncinate Fasciculus
VZ - Ventricular Zone
WM - White Matter
$\langle D \rangle$ - mean diffusivity
$\lambda_{\parallel}$ - longitudinal diffusivity
$\lambda_{\perp}$ - transverse diffusivity

Introduction

Maturation of brain white matter is accompanied by a complex ensemble of different processes, including myelination, that leads to dramatic changes in microstructural properties. Across different regions, these changes proceed in a particular spatio-temporal order and can be investigated *in vivo* using Magnetic Resonance Imaging (MRI).

However, using MRI for investigating developing white matter still raises many questions. On the one hand, none of the existing MRI parameters can describe the whole complexity of the undergoing maturational changes; while, on the other hand, neither of them is specific of any particular developmental process or tissue property. Thus, reliable description of developing white matter requires specially-adapted multiparametric approaches that take into account complementary information from different parameters.

In this work, we will show some examples of how multimodal MRI may be used to describe normal white matter maturation and to identify biomarkers of pathological development.

In part I, we will first give a short overview of brain development, with a focus on white matter maturation. Then existing MRI techniques and previous imaging studies of developing white matter will be described.

In part II, we will present some new multiparametric approaches to describe global white matter maturation and myelination in a population of healthy infants. There we will also introduce a preliminary atlas of white matter structural connectivity in children that can be used for analysis of white matter microstructural properties across different bundles.

In the last part of this work, we will show how the multiparametric approaches and the connectivity atlas, described in part II, can be applied to investigate white matter pathologies and provide some preliminary observations in focal epilepsy and metachromatic leukodystrophy (MLD).

Part I

Development of the brain white matter in infants and children

This part of the manuscript contains two chapters. The first chapter provides an overview of normal brain development starting from the embryonic stage. It describes major developmental processes, including neurogenesis, neuronal migration, glial proliferation and differentiation, synaptogenesis, establishment of brain structural connectivity, and maturation of the white matter bundles through myelination. The second chapter focuses on the study of brain development with Magnetic Resonance Imaging (MRI). It first describes different imaging modalities, including T1 and T2 relaxation, diffusion tensor imaging (DTI) indices and some more complex metrics, like NODDI (neurite orientation dispersion and density imaging), MTR (magnetization transfer) and MWF (Myelin Water Fraction). For each modality, first, a brief explanation of the physical principles is provided, followed by description and interpretation of age-related changes. The principles of 3D fiber reconstruction and bundle identification are also given. Then a brief overview of imaging findings in the developing brain white matter is provided. Finally, some technical aspects of pediatric imaging are considered.

Chapter 1

Normal brain development

Brain development is a complex sequence of numerous processes, including neural induction, neurulation, neuronal proliferation and migration, apoptosis, synaptogenesis and myelination. It spans through entire childhood till adulthood. This chapter provides a short overview of these developmental processes, with a particular focus on white matter development, i.e. establishment of the neural connectivity and white matter myelination, which represents an important step in the maturation of the white matter that is protracted into the postnatal life until late adolescence.

1.1 Embryonic development

Human brain development starts at the 2nd - 3rd post-conceptional week with differentiation of the neural progenitor cells, a process initiated by inductive signaling molecules coming from mesodermic cells of the dorsal marginal zone [1]. From the end of the 3rd week and until approximately embryonic day 42 (∼E42) neural progenitor cells undergo several turns of "symmetrical" cell division to increase the size of the neural progenitor pool [1–4]. The first distinct neural structure, the neural tube, is formed by folding and fusion of the neuroectoderm. This process occurs between embryonic days 20-27 (E20-27) [3] and starts with the appearance of two ridges on the sides of the neural plate at ∼E21. These ridges rise, fold and then fuse, forming the neural tube. The fusion starts from the center and proceeds both rostrally and caudally [5]. The anterior and the posterior neuropores close at ∼E25 and E27 respectively. At the end of the 4th week, just before the closure of the posterior neuropore, the anterior portion of the neural tube forms the three primary brain vesicles: the prosencephalon that will evolve into the forebrain, the mesencephalon that will give rise to the midbrain structures and the rhombencephalon that will become the hindbrain (Fig. 1.1) [1, 3, 4, 6]. The prosencephalon will further divide into the telencephalon and the diencephalon, and the rhombencephalon will be splitted into the metencephalon and the myelencephalon. The resulting five secondary brain vesicles present the primary organization of the central nervous system.

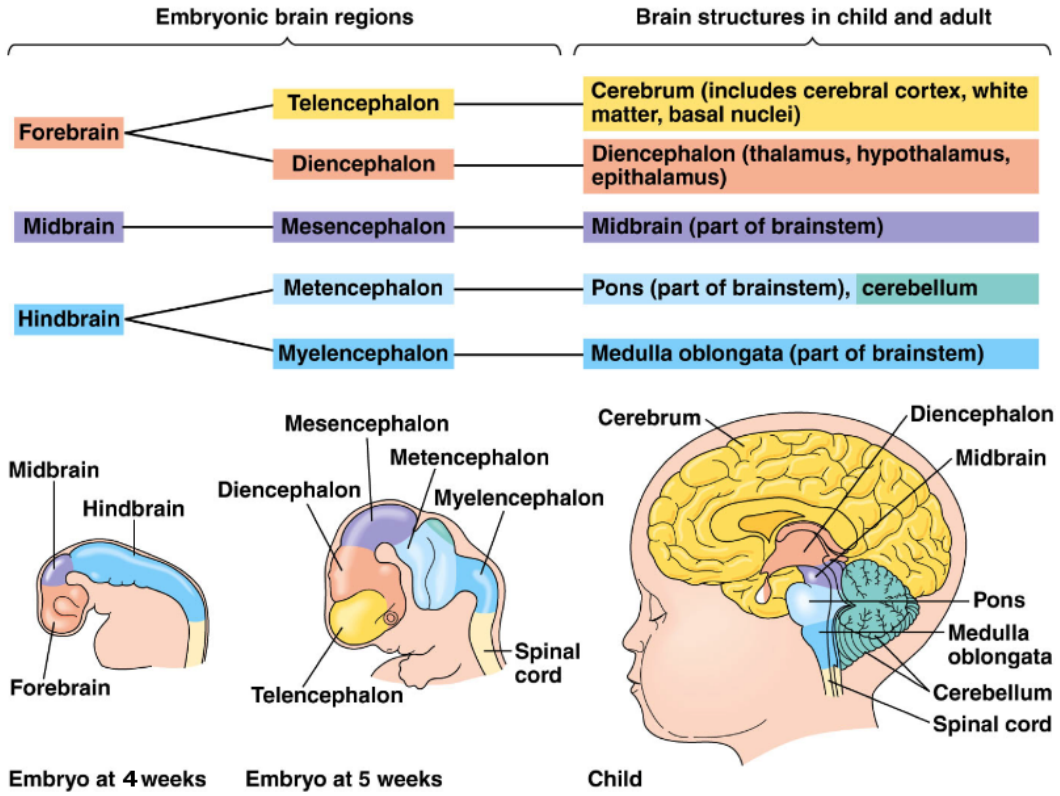

Figure 1.1: Correspondance between embryonic brain regions and mature brain structures. Adapted from http://howtoimprovemybrain.info/key-brain-development-stages/

1.2 Corticogenesis

During the fetal period, which spans from the 9th week till the end of pregnancy, the developping brain undergoes dramatic morphological changes that are accompanied by numerous complex events at the cellular level. Starting from ∼E42 cell division in the proliferative ventricular zone (VZ, Fig. **??**) gradually becomes asymmetrical [7]: each cell produces one neuron and one neural progenitor. The new neural progenitor cell remains in the proliferative zone and continues to divide. The first generated neurons form the preplate, which later splits into the marginal zone (layer I) and the subplate [8]. All subsequently generated neurons migrate in an "inside–out" manner to form cortical laminae: the deeper cortical layers are formed earlier than the superficial layers [3, 4, 9–11]. Different neuronal types are produced in sequential waves depending on their location relative to the molecular gradients in the ventricular zone [4, 8, 9, 12–18].

Most neurons migrate along radial glial cells; however, an important portion of neurons, originating from the ganglionic eminences of the ventral telencephalon (a transitory brain structure that disappears by the end of midgestation, 30-35 weeks [19, 20]) migrates tangentially (parallel to the outer cortical surface) and

becomes the inhibitory cortical interneurons [3, 4, 21–25]. This migration mostly occurs between 12th and 20th weeks and results in a 6-layered neocortex with distinctions between the layers based on the cell types and connections that predominate in each layer [26, 27]. Disruption of neuronal migration can lead to severe neurodevelopmental disorders, like lissencephaly [28]. Such disturbances can also result in local foci of ectopic cortical tissue in the white matter that can induce seizures [29, 30].

1.3 Glial proliferation and differentiation

There are three types of glial (non-neuronal) cells: astrocytes, oligodendrocytes and microglia (brain macrophages). Unlike neurons, their proliferation, migration and differentiation are protracted long into the postnatal period [3, 31]. Glial progenitors migrate from the forebrain subventricular zone into neighboring structures, including the overlying white matter, neocortex, striatum, and hippocampus, where they differentiate into astrocytes and oligodendrocytes [31–34]. Microglial cells are believed to be of mesodermal origin and probably to enter the developing central nervous system (CNS) from the blood stream, the ventricles or the meninges [35, 36].

Astrocytic proliferation in human neocortex starts at ∼24th week and peaks around 26-28th weeks [37, 38]. Astrocytes play multiple important roles during brain development and later on, including axonal guidance, stimulation of neuritic growth and synaptic formation, production of trophic factors and extracellular matrix components, neuronal survival, myelination, establishment of the blood-brain-barrier [37–42]. Astrocytes have also various nutritive roles, participate in osmoregulation and help to support neuronal metabolic homeostasis [37–39, 43].

Oligodendrocytes are responsible for myelin production and myelination of the white matter, which will be further detailed in section 1.6. Recent studies suggest that oligodendrocytes also produce trophic factors contributing to the maintenance of axonal integrity and neuronal survival, they influence neuronal size and axon diameter, and may possibly contribute actively and directly to neural signaling [3, 44, 45]. According to their maturation stage, oligodendrocytes can be divided into four types: oligodendrocyte progenitors, preoligodendrocytes, immature oligodendrocytes and mature myelinating oligodendrocytes. Oligodendrocyte progenitors are produced in the proliferative subventricular zone during the last months of gestation and in the early postnatal period. These bipolar, mitotically active cells differentiate into preoligodendrocytes, multipolar cells with retained proliferative capacity, during their migration into the white matter. In the third trimester immature oligodendrocytes progressively start to form membrane wraps around nearby axons. Finally, mature myelinating highly multipolar oligodendrocytes tightly wrap nearby axons with multi-layered membrane sheaths from which most of the cytoplasm has been extruded. This process, called myelination, follows a particular spatiotemporal order, described in section 1.6.

The peak of microglia in the developing brain coincides with apoptosis [36].

This phenomenon can be explained by microglia's role in phagocytosis of cellular fragments and elimination of redundant axons and dendrites [36, 46]. In addition, microglia may have more active roles, for example by inducing degeneration of some cells [36]. Microglial cells produce trophic factors crucial for normal development and function of neurons and glia [36, 47–49]. They participate in the growth and guidance of neurites, increase myelinogenesis and stimulate the vascularization of the CNS [36, 50].

1.4 Brain growth and gyrification

Brain development is marked by dramatic increase in brain size: between the 16th gestational week and birth, brain volume increases almost 10-folds [51–54]. Brain growth continues in the postnatal life with an increase of ∼88% during the 1st year and of ∼15% during the 2nd year [55, 56] (Fig. 1.2).

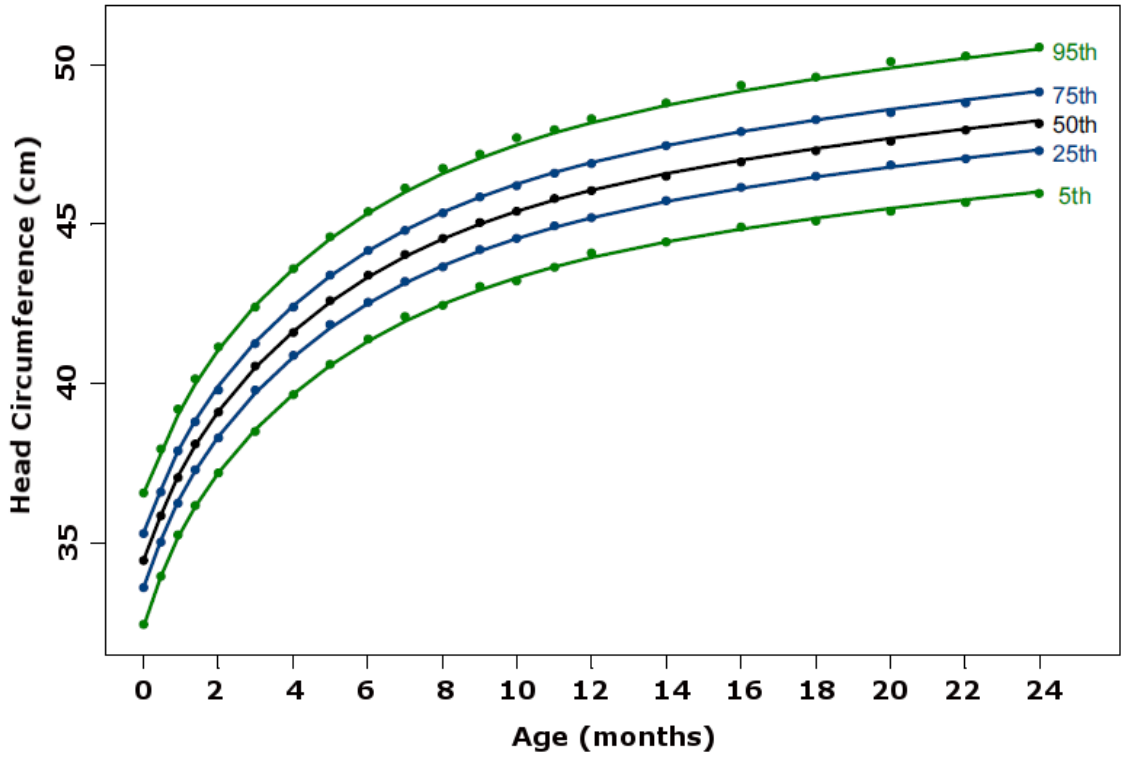

Figure 1.2: Changes in head circumference for boys from birth to 24 months. The 5th, 25th, 50th, 75th and 95th centile curves and shown. Adapted from [57].

Although neurogenesis and neural migration continue in the postnatal period both in the subgranular zone of the hippocampus and in the subventricular zone lining the lateral ventricles [58, 59], it is thought that the main contribution to the observed brain growth in the postnatal period arises from glial proliferation and myelination of the white matter [55].

To accomodate the growing cortex volume and surface within a limited space, brain undergoes changes in surface morphology through gyrification: the brain surface progressively folds to create a complex pattern of sulcal and gyral regions. Gyrification starts between the 10-15th postconceptional weeks [60, 61], peaks during the third trimester of pregnancy, when brain undergoes considerable growth and reaches its relatively stable stage between the 66-80th postconceptional weeks [62]. Although gyrification patterns of human individuals are highly variable [62], they do reveal a common spatiotemporal gyrification order [62, 63]. The Sylvian fissure and the callosal sulcus are the first to appear during the 13-14th gestational weeks (Fig. 1.3) [60, 61, 63, 64]. They are followed by the olfactory, calcarine and parieto-occipital sulci in the 15-19th weeks [62, 63]. The cingulate sulcus and the circular sulcus of the insular cortex appear at ∼18th gestational week. The central sulcus can be clearly observed from the 20th week, the superior temporal and collateral sulci - from the 23rd week, the precentral sulcus - from the 24th week, the post-central and superior frontal sulci - from the 25th week, and the intraparietal and middle temporal sulci - from the 26th week [62, 63]. The lateral occipital sulcus appears at the 27th week and the inferior frontal sulcus - at the 28th week [62, 63]. The most secondary sulci and gyri start to appear from the 32nd-34th weeks, while tertiary sulci develop in the post-natal life [60, 62, 63].

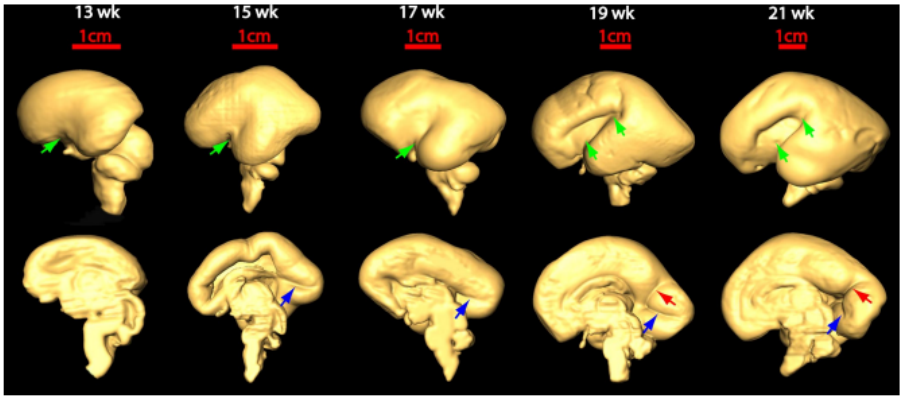

Figure 1.3: The Sylvian fissure (green arrow), the calcarine fissure (blue arrow), and the parieto-occipital sulcus (red arrow) are among the first to appear during brain gyrification as revealed by 3-dimensional reconstruction of the lateral (top row) and medial (bottom row) surface of 13–21 week brains. Adapted from [61].

1.5 Synaptogenesis and development of neural circuits

Development of neural circuits starts during the early fetal period (9-15 postconceptional weeks) with most major axonal pathways being established in the preterm

period. When neurons reach their target regions in the cortex, they start to make connections (synapses) with other neurons by extending their axons and dendrites. This process strongly depends on interaction with scaffolding cells (radial glial cells and tangentially migrating neurons named 'corridor' cells) and on gradients of guidance molecules [4, 65–67]. The first growing axons, so-called pioneering axons, lay down the path for the following axons that tend to fasciculate with them [68, 69]. The first temporary synaptic connections can be found as early as at the 5th week in the preplate (the primordial plexiform layer) [4, 70–72]. These temporary connections play an essential role in establishing important white matter pathways, including the thalamocortical (TC) and corticothalamic (CT) pathways [3, 4, 73–77].

In the early fetal period, the internal capsule already contains thalamocortical fibres radiating towards the lateral cerebral wall. At this stage these fibers do not penetrate into the cortical plate to establish synaptic connections in it. Additionally, internal capsule also has growing efferent (motor) corticosubcortical projection pathways. The modulatory brain-stem afferent fibres are also present above and below the cortical plate [78–81]. Several limbic bundles, including fornix, stria terminalis and cingulum, can be already identified on histological and MRI/DTI images [82].

Midfetal period (15-23 postconceptional weeks) is characterized by transient connectivity networks. Thalamocortical and basal forebrain afferent fibres establish numerous synaptic connections with subplate neurons. Subplate neurons not only guide ingrowing afferent fibres and early efferent projections but also form active endogenous cortical network and serve as an associative cortico-cortical system for medial cortex [83–85]: the subplate receives massive fibre projections from precingulate area and the anterior cingulate cortex that connect these areas with intermediate and posterior cingulate areas. At this stage most cortical efferent pathways already penetrate their targets in striatum, pons and the spinal cord. The cortico-pontine pathway can be easily visualized using imaging techniques [82]. Although still growing, the corpus callosum can also be already identified [86–88].

During cortical development there is an overproduction of neurons and synaptic connections and by the end of adolescence, almost 50% of them are eliminated by synaptic pruning (synapse elimination) and apoptosis (programmed cell death) that explodes around 19–23rd gestational weeks [4, 89–93]. These processes are regulated by synaptic activity and various trophic factors produced by neurons and glia cells.

The major event in the neural circuits development during early preterm period (24-28 postconceptional weeks) is the beginning of synaptogenesis within the cortical plate [70, 94] and establishment of first permanent connections with future cortical layer IV neurons, i.e. projection pathways that connect the cerebral cortex with lower brain parts, brainstem and the spinal cord. This occurs by relocation of the thalamocortical and basal forebrain afferent fibres from the subplate into the cortical plate [70, 95]. At the same time other afferent and efferent pathways also establish permanent connections with their target areas, including limbic cortico-

cortical connections in the cingulate, entorhinal and hippocampal cortex. Although most cortico-cortical connections are still poorly defined [96, 97], three neocortical associative pathways are already present, namely the fronto-occipital fascicle, the uncinate fascicle and the deep portion of the external capsule [20, 98].

Late preterm period (29-34 postconceptional weeks) is characterized by rapid development of neural networks. After the 28th week, the declining subplate mainly contains neurons predetermined for commissural (interconnecting the corresponding regions of the two brain hemispheres) and association (connecting different regions within the same brain hemisphere) pathways, which are among the last to develop [4, 70]. The short range cortico-cortical connections, originating from layer II, develop earlier than longer-range connections between distant cortical regions, originating from layer III [99]. At this stage both *in vivo* and *in vitro* imaging studies are able to identify the following associative pathways: fronto-occipital and uncinate fascicles (already present at earlier stages), the inferior fronto-occipital fasciculus, and the superior longitudinal fasciculus [20, 82, 100]. At the end of the late fetal period, cerebral white matter networks become quite similar to those of the newborn brain. Since this time and later on after birth, the established neuronal networks continue to refine and to mature through myelination until the end of adolescence.

1.6 Myelination of the brain white matter

1.6.1 Role of myelin

Myelination of the white matter results in dramatic increase of axonal conduction and velocity of the information transmission between neurons [101]. In the central nervous system, myelin sheaths present extended membranes of oligodendrocytes that wrap around neural axons (Fig.1.4). Periodic uncovered short portions of axons between the segments, called the nodes of Ranvier, are crucial for impulse propagation along the axons: unlike unmyelinated fibers, when a membrane of a myelinated axon is excited at the node of Ranvier, local circuits of ion currents cannot flow out through the insulating myelin sheath but flow out and depolarize the next node. This form of axon excitation jumping from one node to another is called saltatory conduction and allows both increasing propagation velocity and saving energy required for membrane excitation.

1.6.2 Myelin biochemical composition

Insulating properties of myelin stem from its biochemical composition [102, 103]. In comparison with other biological membranes, myelin is characterized by a very high lipid content, with lipids making up to 70-80% of the total dry weight. On the contrary, the protein content of 15-30% is rather low. The water content of myelin is about 40%. Although there is no 'myelin-specific' lipid, cerebroside (galactosyl ceramide) is the most typical for myelin, with its concentration being

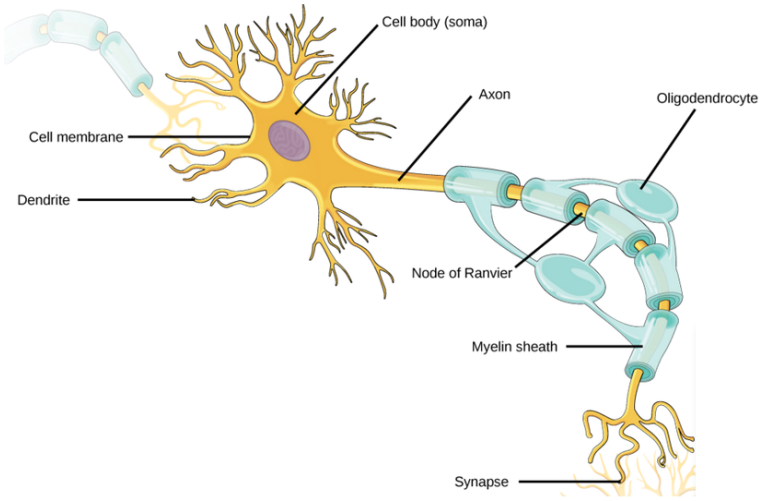

Figure 1.4: Myelin sheaths are formed by extended processes of olygodendrocytes that wrap around neural axons with periodic uncovered portions (nodes of Ranvier). Adapted from www.boundless.com.

directly proportional to the brain myelin content. Myelin lipids contain 25–28% of cholesterol, 27–30% of galactolipids, and 40–45% phospholipids when expressed as percentages of total lipid weight. The myelin protein composition is simpler than in other membranes, with most proteins being unique to myelin. ProteoLipid Protein (PLP) and Myelin Basic Protein (MBP) constitute 60–80% of the total protein content.

1.6.3 Myelin structure

Myelin structure presents a double lipid bilayer with proteins fully or partially embedded in both sides of the bilayer, or attached to it by weaker linkages (Fig. 1.5). Lipids and proteins can easily diffuse in the plane of the membrane (lateral diffusion), unless they are anchored by specific interactions. On the contrary, transverse diffusion (transition from one membrane surface to the other) is limited and the distribution of lipids and proteins across bilayer's sides is asymmetric: galactolipids, cholesterol, phosphatidylcholine, and sphingomyelin are situated mainly on the extracellular side, while ethanolamine plasmalogen and myelin basic protein are mainly found on the cytoplasmic side of the bilayer. Different myelin components are synthesized by different cellular compartments, they are transported to the myelin sheaths by different mechanisms and at different rates.

1.6.4 Myelinogenesis

Myelinogenesis, starting from initial axon ensheathment up to formation of mature multilayer myelin sheath, is regulated by precise sequence of gene expression in the

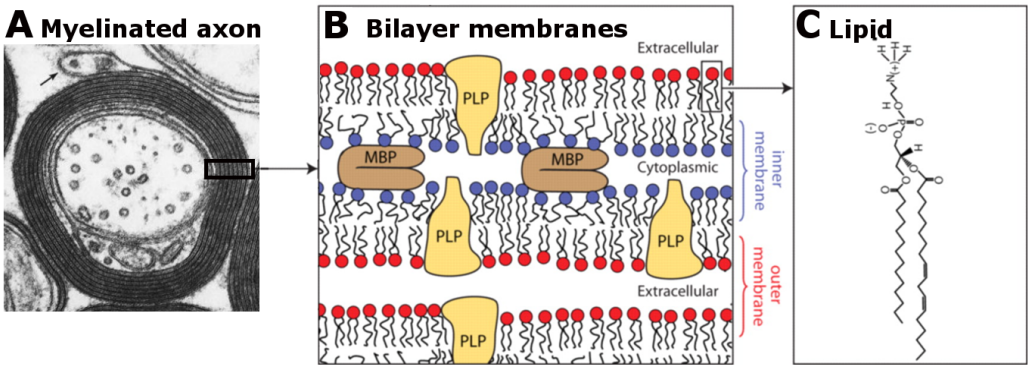

Figure 1.5: A. A typical CNS myelinated fiber; B. Myelin sheaths present repeating lipid bilayer membranes with embedded or attached proteins. ProteoLipid Protein (PLP) and Myelin Basic Protein (MBP) constitue around 60–80% of the total protein content; C. Phospholipids are major myelin lipid components, making up to 45% of lipid content [104]. The figure shows the structure of phosphatidylethanolamine. Adapted from [103, 105].

oligodendrocytes. In the central nervous system myelin genes are expressed only in oligodendrocytes and their expression is significantly up-regulated just before the onset of rapid myelination. This period is the most vulnerable and crucial in the myelination process. There is evidence that expression of these genes is controlled by both tissue-specific and stage-specific mechanisms. Successful myelination strongly depends on efficient interactions between oligodendrocytes, neurons and astrocytes [102, 106]. During pre-myelination stage, proliferation of oligodendrocyte precursor cells, differentiation of oligodendroglia and expression of myelin genes are greatly influenced by the presence of axons and neural electrical activity (Fig.1.6) [107]. Action potential firing in axons results in nonsynaptic release of adenosine, which activates adenosine receptors on oligodendrocyte precursor cells, inhibiting their proliferation, stimulating both their differentiation and myelin formation [108]. Axonal diameter is another important factor for the initiation of myelination and it determines the final thickness of the myelin sheath. Astrocytes produce trophic factors essential for proliferation, migration and differentiation of oligodendrocyte progenitors, extension of oligodendrocyte processes and their adhesion to axons, myelin formation and maintenance (Fig.1.6). These factors can modulate hormones playing important roles in myelination, including growth hormone, thyroid hormone and steroids. Deficiency in these hormones during early development may cause hypomyelination [109, 110].

1.6.5 Spatiotemporal progression of brain myelination

Brain myelination starts from the 5th fetal month and continues until the end of adolescence, being most intensive during the first 2 post-natal years. Asynchronous

spatiotemporal progression of the white matter myelination in the child brain has been extensively documented by postmortem studies (Fig.1.7) [117–121] and it can be summarized by the following rules [102]:

- Myelination proceeds in the direction of the impulse conduction.
- Central sensory areas tend to myelinate before central motor areas.
- Motor and sensory pathways myelinate before association pathways.
- Myelination generally progresses in the caudo-rostral direction and from central to peripheral regions.
- As first suggested by Flechsig et al. [122], there is a link between structural and functional maturation: pathways that start functioning earlier have a tendency to myelinate first.

However, one should keep in mind that there are many exceptions to these rules and that there is a normal variability in the onset of myelination for different white matter bundles. Moreover, definition of myelination onset may also depend on the used methodology for myelin detection (light microscopy, immunological approaches, MRI).

At the 20th gestational week, myelin can be already detected in the spinocerebellar tract, lateral spinothalamic tract, in the statoacoustic tectum and tegmentum [118]. At the same time, cerebellar peduncles begin to myelinate, first in the inferior peduncles, then in the superior peduncles and later, at around 26 gestational weeks, in the middle peduncles [118, 121]. At the 22nd gestational week, myelin appears in the inferior olive [118]. Optic chiasm and optic tract start myelination at around the 25th gestational week, followed by optic radiations: rostral part at the 27-28th weeks and occipital part at the 29-30th weeks [118]. At the 27-28th weeks, myelin can be observed in the central part of the corona radiata [118]. During the 29-30th weeks, the first myelin signs successively appear in the corticospinal tract, cingulum, fornix, anterior limb of the internal capsule [118]. From the 32nd week, myelin can be found in the corpus callosum and from the 34th week - in the anterior commissure [118]. By the 40th gestational week, myelin can be detected in the acoustic radiations [123].

Despite early beginning of myelination, most brain structures and white matter bundles appear poorly myelinated at birth and their myelination is protracted in the postnatal period, being most intensive in the first two postnatal years. At birth, mature myelinated stage is reached only in the spinocerebellar tract, the

spinothalamic tract, the statoacoustic system, the cerebellar peduncles, optic chiasm and optic tract and the posterior limb of the internal capsule [118, 121]. In histological studies, mature myelinated stage in the optic radiations and partially in the corticospinal tract can be detected after the first 2-3 postnatal months (50-52 post-conceptional weeks) [119]. Starting from the 3rd postnatal month, myelination progressively spreads from the central sulcus area in the anterior direction, and in the temporal direction from the 4-5th postnatal months (Fig. 1.8). The body of the corpus callosum starts to show mature appearance at the 5th postnatal month (∼60 post-conceptional weeks) [119]. At the 6th postnatal month (∼65 post-conceptional weeks) mature myelinated appearance is seen in the splenium and the acoustic radiations [119]. The most frontal brain areas start to myelinate between the 7th and 11th months [124]. At around 9 months (∼80 post-conceptional weeks), mature myelinated stage is reached in the cingulum and in the posterior frontal areas [119]. At 11 months (∼87 post-conceptional weeks) mature myelinated stage is reached in the anterior limb of the internal capsule and the genu of the corpus callosum, at 15 months - in the external capsule [119]. Mature myelinated appearance is observed in frontal areas at ∼18 months (∼119 post-conceptional weeks), and in the temporal areas at ∼19 months (∼122 post-conceptional weeks). Although myelination rates are greatest during the first two postnatal years, the process continues, although at slower rates, during childhood, adolescence, and even adulthood [125–132]. Magnetic resonance imaging (MRI) provides important tools for the *in vivo* studing white matter maturation (for review see chapter II and [133]): being in agreement with histological studies, they are able to further detail the spatio-temporal pattern of myelination progression [134, 135].

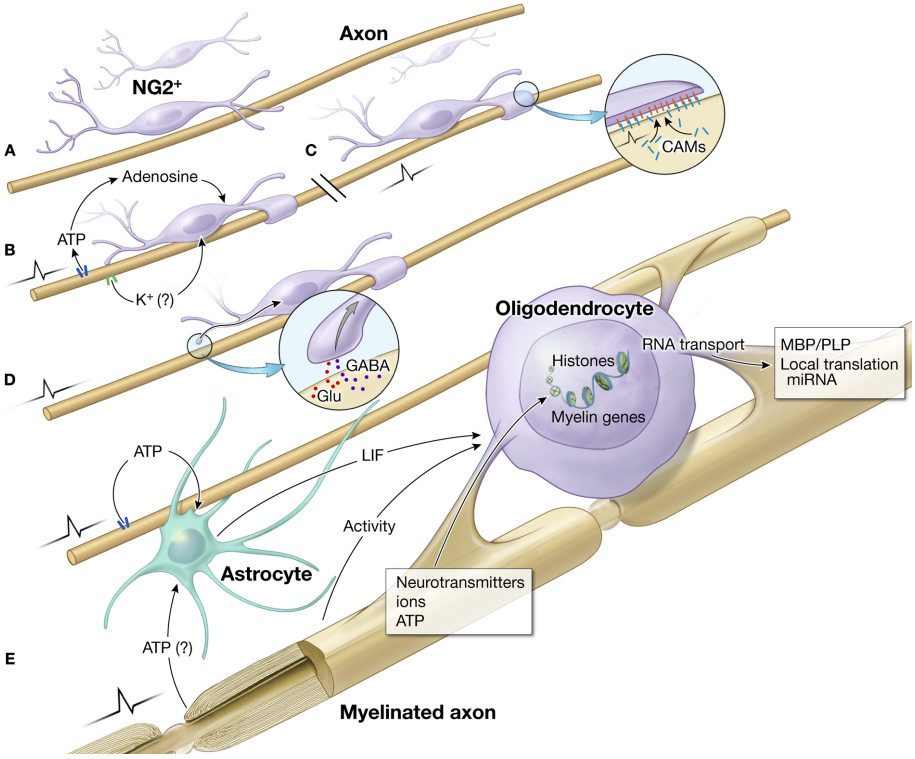

Figure 1.6: Myelination is regulated by complex interactions between oligodendrocytes, neurons and astrocytes. Adapted from [107] A. Before myelination starts, immature oligodendrocyte precursor cells ($NG2^+$) and silent, non-active axons can be seen. B. Propagation of action potentials along the axons results in ATP release and adenosine generation, which activates adenosine receptors on $NG2^+$ cells and promotes their differentiation and myelination [108]. Electrically active axons also release K^+ that blocks K^+-channels on in oligodendrocytes and may contribute to oligodendrocyte proliferation [111]. C. Electrical activity may also modulate expression of cell adhesion molecules (CAMs) that play role in initiation of myelination [112–114]. D. Glu (glutamate) or GABA release from synapses on $NG2^+$ cells may also participate in regulation of myelination [115]. E. Release of neurotransmitters, ions and ATP from electrically active axons may influence myelination by modifying gene expression in oligodendrocytes and release of the cytokine LIF from astrocytes [107, 116].

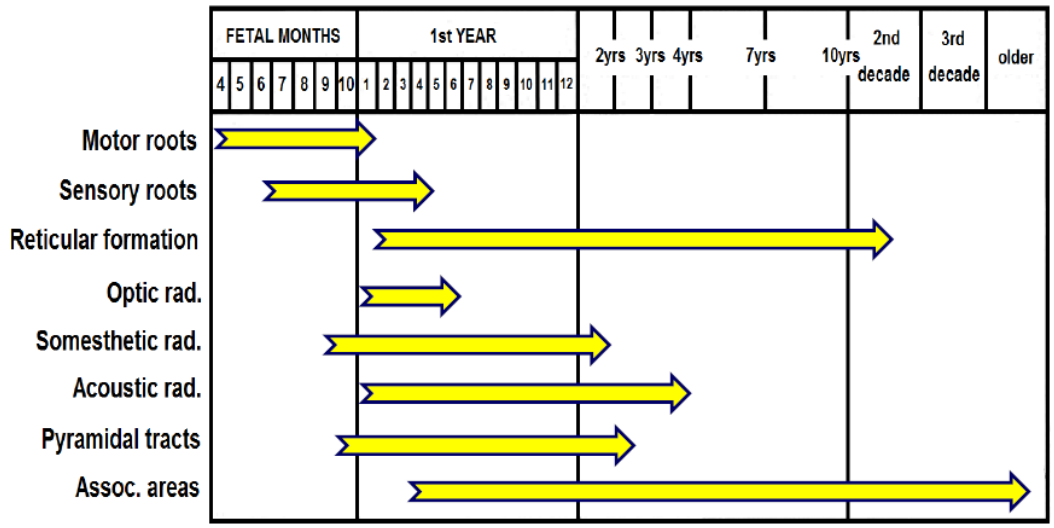

Figure 1.7: Asynchronous progression of myelination across different white matter pathways as revealed by histological studies of Yakovlev and Lecours. Adapted from [121].

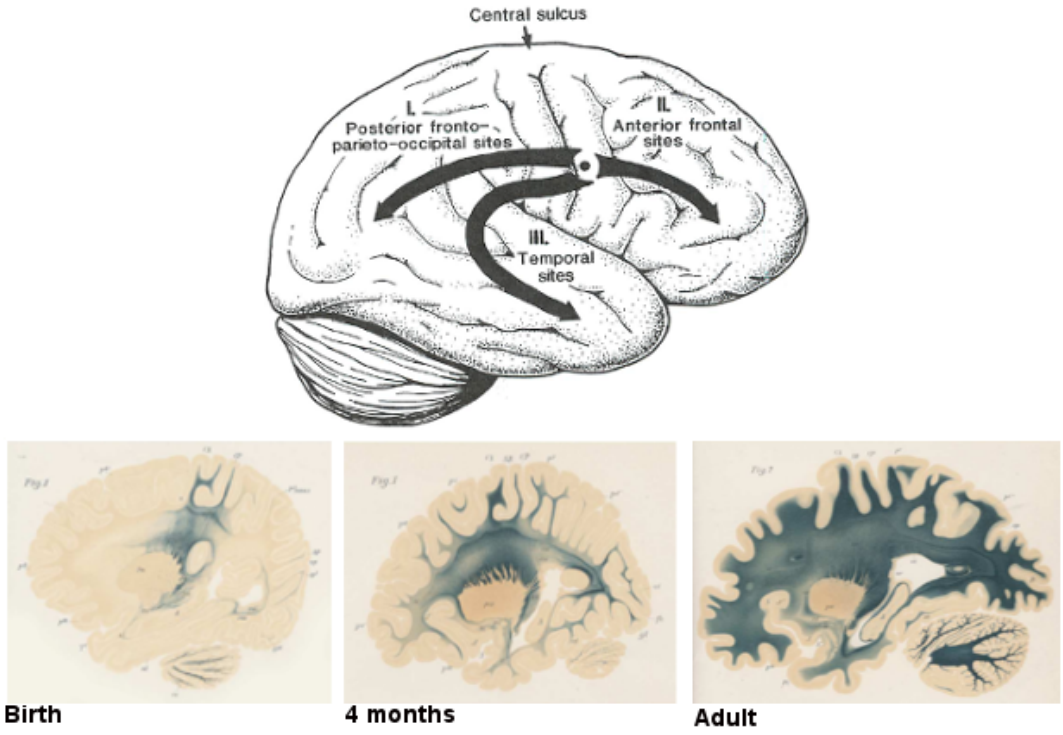

Figure 1.8: Myelination proceeds from the central sulcus area first in the posterior direction, then into anterior areas, and finally to the temporal sites. Adapted from [119, 122].

Chapter 2

Imaging studies of white matter development in infants and children

Magnetic Resonance Imaging (MRI) provides various contrasts and quantitative parameters reflecting different micro- and macroscopic tissue properties. As white matter properties dramatically change with age, these parameters can be used by both researchers and clinicians for evaluation of its development. In this chapter, I will first provide a brief overview of MRI parameters, explaining their physical principles, relating biological interpretations of their age-related changes and describing previous findings in imaging studies of normal white matter development. Next, 3D fiber reconstruction and identification of white matter bundles for studying principles of white matter connectivity will be described. Finally, some specific technical aspects of MRI in the pediatric populations, with a focus on correction of motion artifacts in DWI (Diffusion Weighted Imaging), will be discussed.

At the end of the chapter two articles are included. The first is a research paper describing a new correction strategy for diffusion-weighted images corrupted with motion artifacts, with my contribution to it consisting of 1) validation of the proposed strategy using data with simulated motion-related artifacts and 2) comparison of the proposed strategy with another widely-used correction strategy. The second article is a review article on imaging studies of early white matter maturation in fetuses, newborns and infants. Its content is largely covered in the present and partially in previous chapters and includes description of the basic concepts underlying white matter development, explications of main MRI techniques and desription of the main imaging findings in studies of white matter development in relation with different undergoing maturational processes.

2.1 T1 and T2 relaxation times

2.1.1 Physical principles of T1 and T2 imaging

Quantitative T1 and T2 relaxation times describe behavior of nuclear spins of the hydrogen atoms of water molecules after their excitation by application of a radio frequency (RF) pulse.

The recovery of the longitudinal magnetization component M_L towards its initial state (called longitudinal or spin-lattice relaxation) in inversion-recovery experiments is an exponential process described as:

$$M_L(t) \propto \rho(1 - 2e^{-TI/T1}) \tag{2.1}$$

where T1 is the longitudinal relaxation time, TI is the inversion time and ρ stands for proton density. T1 values are different within different tissues and are highly affected by tissue microenvironment [136–138]: for example, T1 values are smaller (fast recovery) in the presence of macromolecules and higher (slow recovery) in free liquids. At 3 Tesla, the typical T1 values measured in an adult brain in white matter, grey matter and cerebrospinal fluid (CSF) are in the ranges of 800-1100ms, 1300-1900ms and 3000-4000ms respectively [137–141].

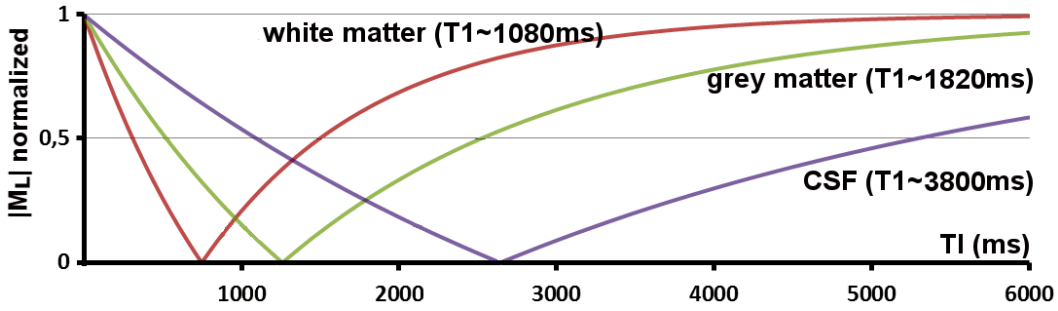

Figure 2.1: Recovery of normalized longitudinal magnetization for tissues with different T1 values in a 3 Tesla magnetic field. The graph shows absolute values of the normalized longitudinal magnetization, as it is measured from the acquired T1 relaxation signal. T1 values for different tissues at 3T were taken from [140].

Transverse (or spin-spin) relaxation describes the decrease of the transverse magnetization M_T due to the loss of coherence in a population of nuclear spins as a result of local magnetic field perturbation associated with the proximity of the excited spins to each other:

$$M_T(t) \propto \rho e^{-TE/T2} \tag{2.2}$$

where T2 is a transverse relaxation time and TE is an echo time. Similar to T1, T2 values depend on the tissue microstructural properties [136, 138, 141]. For example, in tissue microenvironments with strong spin-spin interactions (ordered

cell assemblies, microstructures, etc.) T2 values are shorter because of a rapid loss of coherence across the spin population. At 3 Tesla, typical T2 values measured in an adult brain are ∼70ms for white matter, ∼100ms for grey matter and ∼1440ms in the CSF [140, 141].

In this way, T1 and T2 values allow to distinguish different tissues: gray matter, white matter, cerebrospinal fluid (CSF), scalp fat, etc. Of importance, they also reflect pathological changes at a microscopic level. For example, in diseases leading to disruption of the tissue microenvironment (cell lysis, matrix breakdown, etc.) they are usually elevated relative to nonpathological conditions [136, 142–144].

Quantitative T1 and T2 maps should not be confused with commonly used in radiology T1-weighted (T1w) and T2-weighted (T2w) images [136]. T1w/T2w images that are acquired using single TI/TE value are not quantitative maps of T1 and T2 relaxation times, but are rather proton density images with pixel intensities weighted by local T1/T2 values. The degree of weighting depends on TI/TE and other acquisition parameters. On the contrary, quantitative T1 and T2 maps are computed from multiple measures with different TI/TE values, using, for example, EPI single-shot spin-echo (SE) sequences [145]. This makes acquisitions longer but the resulting maps reflect local quantitative T1 and T2 relaxation times measured in milliseconds.

Finally, it should also be mentioned that the measured T1 and T2 values depend on the strength of the magnetic field [137, 140, 146, 147]. T1 increases with the field strength (B_0) approximately as $B_0^{1/3}$, increasing by ∼25% when the field strength raises from 1.5 T to 3.0 T. T2 values are rather stable for field strengths between 0.2 and 3 Tesla and decrease at higher fields: when the field stregth raises from 1.5 to 7T, T2 values decrease by a factor of ∼1.6 [148, 149].

2.1.2 Changes during development

In the developing brain, T1w and T2w images show several changes depending on the maturational stage [150](Fig. 2.2). Before 6 months the infantile pattern is characterized by a reversal of the normal adult contrasts: on T1w images, signal intensity is lower in the white matter than in the grey matter; on T2w images, white matter intensity is higher than in the grey matter. Between 8 and 12 months a heterogeneous isointense pattern in observed, which is characterized by poor contrast between grey and white matters in maturing regions. The early-adult pattern is observed starting from 1 year. This pattern has higher signal intensity in the white matter than in the grey matter on T1w images and vice versa on the T2w images.

The times of the transitions between these patterns vary across different brain regions and depends on the acquisition sequence, with T1w images acquiring the "early-adult" pattern earlier than T2w images. At birth, on T1w images, the mature "myelinated" appearance can be observed in the pons and cerebellar peduncles; at 1-3 months, it is observed in the posterior limb of the internal capsule, optic radiations and the splenium of the corpus callosum. Then, at ∼6 months it

is seen in the anterior limb of the internal capsule and genu of the corpus callosum. Finally, at 8-12 months it is observed in the white matter of the frontal, parietal and occipital lobes. Although the observed changes on T1w and T2w images can be used to describe undergoing maturational processes, they cannot be used for quantitative evaluation of the maturation and can be compared across individuals only when using similar sequences.

Quantitative evaluation of the maturation can be approached by measuring T1 and T2 relaxation times. As it has been repeatedly shown in MRI studies, both T1 and T2 values decrease with age in both grey and white matter [151–156](Fig. 2.2). This decrease is rapid during the first decade of life and attenuated thereafter.

The mechanisms underlying the decreases of T1 and T2 relaxation times during brain maturation are still under discussion [153, 154, 157–159]. The shortenings of T1 and T2 can be largely explained by a drop of brain water content [154](Fig. 2.3). However, other processes may also contribute to these age-related changes. T1 values may be also affected by increasing concentrations of cholesterol and phospholipids during myelin synthesis (Fig. 2.3) as well as by changes in fiber organization [153, 154]. Changes in T2 values can be also explained by iron accumulation [160–162] and increasing lipid packing. Consequently, T1 and T2 decreases have different timecourses: decrease in T1 starts earlier than in T2, already during the "pre-myelinating" stage; while T2 decrease correlates with the maturation of the myelin sheath [106, 124, 163–165].

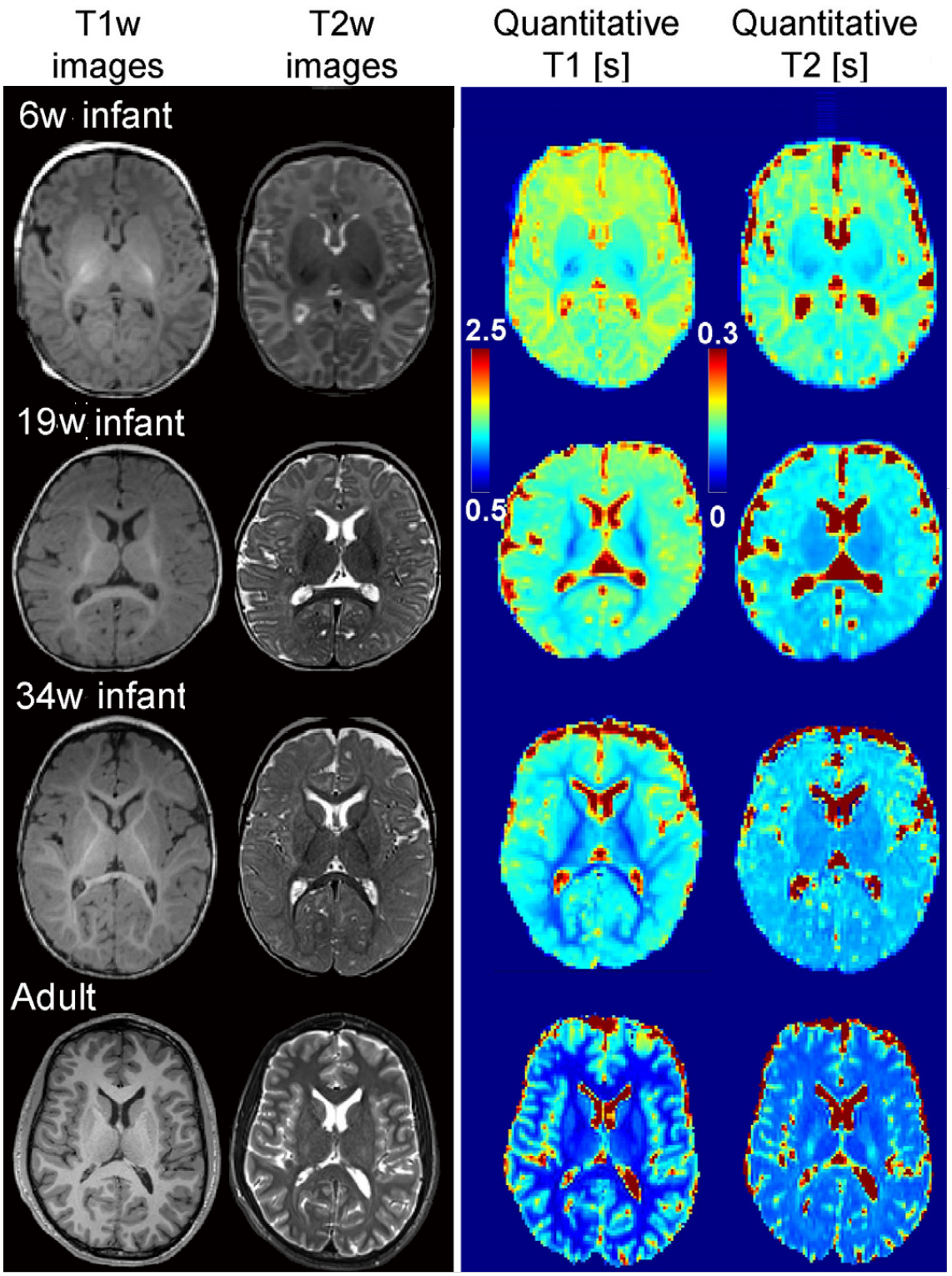

Figure 2.2: Changes in T1w and T2w images and in quantitative T1 and T2 maps during development. Images were acquired on a 3T MRI system in infants of different post-term ages (3, 19 and 34 weeks) and in a young adult. Adapted from [133].

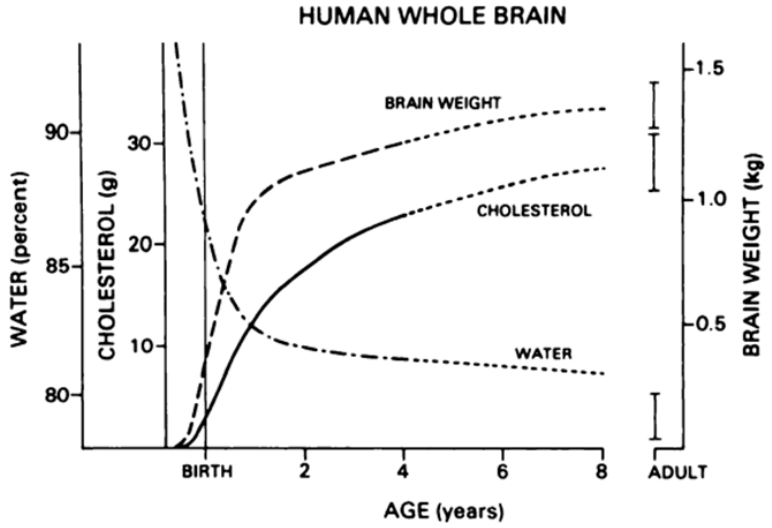

Figure 2.3: Age-related changes in brain weight, water and cholesterol content [154].

2.2 Diffusion Imaging

Since its first application for imaging the human brain in the mid-1980s [166, 167], diffusion imaging has become an important tool for investigating the brain structure. In particular, it has a considerable potential for explorating of normal and abnormal white matter maturation as diffusion parameters quantitatively reflect various maturation processes, while 3D-reconstruction (tractography) techniques enable studying the organization of white matter bundles.

2.2.1 Physical principles of diffusion imaging

Diffusion imaging allows investigating tissue microstructural properties through diffusion of water molecules within those tissues. Diffusion is a random motion of molecules, and in a free medium, the resulting molecular displacements can be described by a three-dimensional Gaussian distribution, with the mean-squared displacement of the molecules for a given time interval t equal to $6Dt$, where D is a constant called "diffusion coefficient", which depends only on the molecular size, temperature and viscosity of the medium. However, in biological tissues, molecular displacements are smaller, because moving water molecules interact with various tissue components, including cell membranes, fibers and macromolecules. Moreover, in the presence of aligned structures, molecular mobility can no longer be considered equal in all directions (anisotropic diffusion): e.g. within white matter, water molecules move more easily along fiber bundles than perpendicular to them because in this direction there are fewer obstacles restricting their diffusion (Fig.**??**) [168]. In this way, water molecules can be used to investigate tissue microstructure at a scale beyond the usual image resolution. Indeed, typical diffusion times are 10-50ms, corresponding to average displacements of water molecules of $\sim$10 μm, comparable to the size of a cell.

Diffusion images can be obtained by implementing the Stejskal-Tanner diffusion encoding [169], in which a pair of diffusion-sensitizing gradients (motion-probing gradients) is added to a T2-weighted spin-echo sequence before and after the 180° refocusing pulse (Fig.2.4A).

In this scheme, diffusion results in an incomplete rephasing of the spins that have diffused between the applications of the diffusion-sensitizing gradients and thus, in a loss of signal intensity (Fig.2.4B), described as follows:

$$S_i/S_0 = e^{-bD_i} \tag{2.3}$$

where S_i is the signal intensity observed in a given voxel for the diffusion-sensitizing gradients applied along direction i, S_0 is the signal intensity at the same location measured without diffusion-sensitizing gradients, D_i is the diffusion coefficient describing diffusion in the i direction, assuming it being Gaussian, and b is a diffusion weighting, which depends on the strength, duration, and temporal spacing of the diffusion-sensitizing gradients. For rectangular gradient pulses, b-values are expressed as:

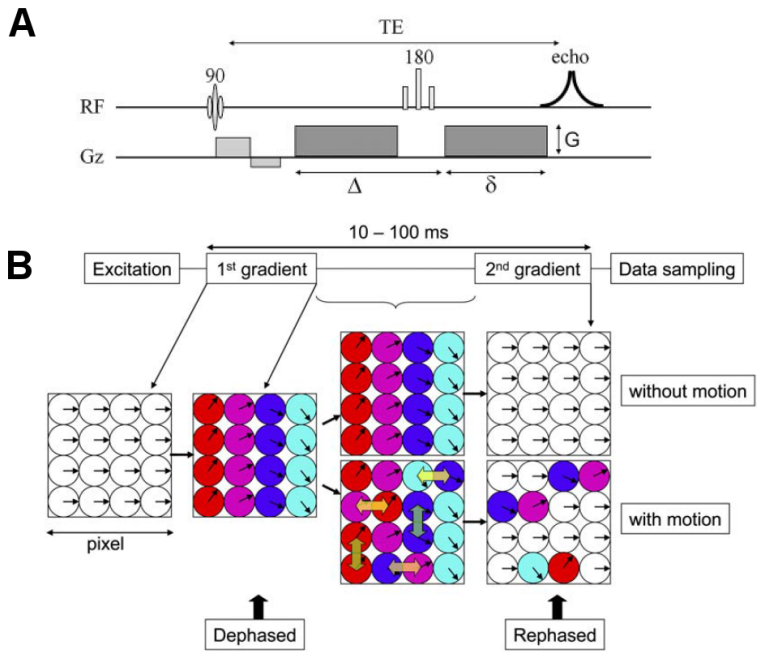

Figure 2.4: A. A diagram of a pulse sequence for diffusion-weighted acquisition [170]. Two diffusion-sensitizing gradients (G is amplitude and δ is duration of the gradients, Δ is the time interval between gradient onsets) are added to a spin-echo sequence before and after the 180° refocusing pulse. B. Circles with arrows represent nuclear spins of the water molecules. Because of water diffusion between the application of the diffusion-sensitizing gradients, the second gradient cannot completely refocus the spins leading to the signal loss. Adapted from [171].

$$b = \gamma^2 G^2 \delta^2 (\Delta - \delta/3) \tag{2.4}$$

where γ is the gyromagnetic ratio, G is the amplitude of the diffusion gradient, δ is the duration of the diffusion gradients, Δ is the time interval between the onsets of the diffusion gradients. Eq.2.3 can be directly used to calculate diffusion coefficient D_i for a given direction.

2.2.2 Diffusion tensor imaging (DTI)

To describe diffusion in a 3D medium, D_i in eq.2.3 can be replaced by a diffusion tensor D and the tensor diffusion model can be fitted by multilinear regression methods using at least 6 measurements with noncollinear diffusion gradients [172]. Geometrically, diffusion tensor can be represented by an ellipsoid whose shape is defined by its 6 independent components (Fig.2.5).

Several rotation invariant parameters can be used to characterize the size and shape of the diffusion ellipsoid: mean $\langle D \rangle$, longitudinal $\lambda_{\parallel}$ and transverse $\lambda_{\perp}$ diffusivities and fractional anisotropy FA. These parameters can be calculated from

the eigenvalues $\lambda_1, \lambda_2, \lambda_3$ of the diffusion tensor, that describe diffusion along the 3 diffusion ellipsoid axes:

$$< D >= (\lambda_1 + \lambda_2 + \lambda_3)/3 \tag{2.5}$$

$$\lambda_{\|} = \lambda_1 \tag{2.6}$$

$$\lambda_{\perp} = (\lambda_2 + \lambda_3)/2 \tag{2.7}$$

$$FA = \sqrt{\frac{3}{2}} \frac{\sqrt{\sum_{i=1}^{3} (\lambda_i - < D >)^2}}{\sqrt{\sum_{i=1}^{3} \lambda_i^2}} \tag{2.8}$$

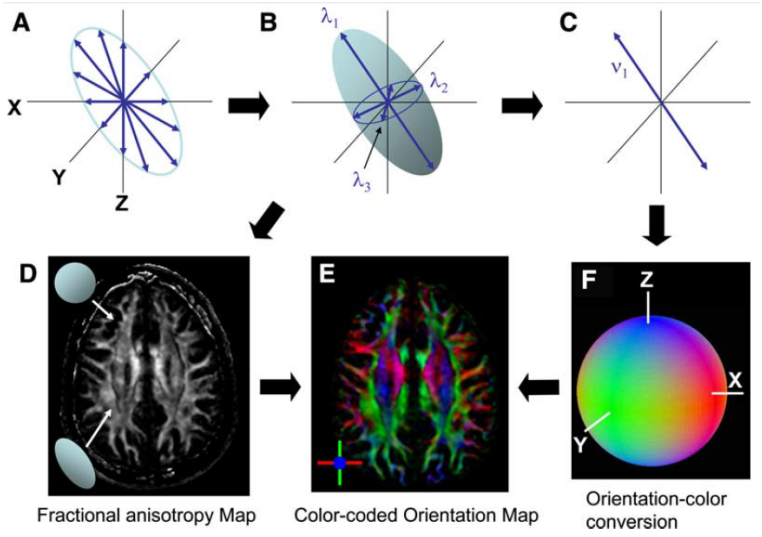

Figure 2.5: Principles of DTI. A. Diffusion is measured in at least 6 directions in order to estimate the diffusion tensor represented by diffusion ellipsiod. B. Estimated diffusion tensor is diagonalized to find its eigenvectors and corresponding eigenvalues. C. The principal direction of the diffusion ellipsoid is identified and color-coded (F). D. Eigenvalues of the diffusion tensor are used to create fractional anisotropy maps. E. Information about fractional anisotropy intensity (D) and local fiber orientation (C) can be combined to produce color-coded orientation maps [171].

2.2.3 DTI changes during development

During white matter maturation, changes in the DTI indices show complex dynamics according to the maturational stage (Fig.2.6). First, progressive organization of

the fibers into fascicles likely results in increased longitudinal diffusivity $\lambda_{\parallel}$ and decreased perpendicular diffusivity $\lambda_{\perp}$, thus leading to increased fractional anisotropy. This process is probably responsable for increased anisotropy that can be observed even in unmyelinated fibers [173–176]. At this stage mean diffusivity is likely to be unchanged. Next, at the "pre-myelination" stage, proliferation of oligodendrocytes, accompanied by water decrease, should result in the decrease of all 3 diffusivities [176, 177]. This process was initially considered spatially isotropic [106], however, recent evidence suggests that oligodendrocytes prefer to make initial extension of their processes in the axonal direction, leading to anisotropy increase [178, 179]. Finally, during "true" myelination, ensheathment of the axons by the oligodendroglial processes should lead to decreased transverse diffusivity due to decrease in both membranes permeability and extracellular distance between the axons in the perpendicular direction [180, 181]. In places with crossing fibers, this scheme may become more complex if crossing bundles have different maturational timelines: anisotropy first increases as the first bundle gets myelinated, but when the second crossing bundle gets myelinated it decreases, meanwhile diffusivities decrease in both cases.

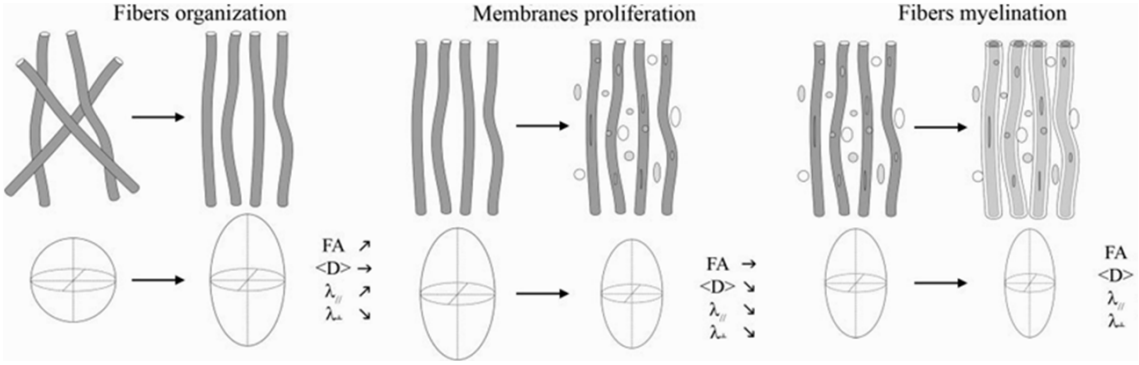

Figure 2.6: Theoretical relationships between maturational stages and DTI parameters in the white matter. Adapted from [182].

DTI studies *in utero* [86, 88, 183] and in preterm newborns [174, 184–189] confirmed age-related decrease in mean diffusivity and increase in anisotropy within different white matter regions, including pyramidal tract, corpus callosum, frontal and occipital regions. Decreases in diffusivities and increases in fractional anisotropy continue after birth (Fig. 2.7), being rapid in the first post-natal year and slower in the second year [126–128, 131, 132, 190–192].

Because of myelination asynchrony across bundles, age-related changes in DTI parameters show considerable regional variations both across and along white matter bundles [127, 133, 178]. These maturational differences between white matter regions can be identified as early as at 28-43 weeks of gestational age (Fig. 2.8.A), suggesting an early maturation of cerebral peduncles, internal capsule and commissural tracts of the corpus callosum [192]. To describe maturation asynchrony across white matter bundles in infants between 4 and 18 weeks (Fig. 2.8.B), Dubois

et al. [182] suggested a model based on different sensitivities of mean diffusivity $\langle D \rangle$ and fractional anisotropy FA to different maturational processes. This model classifies white matter bundles using information from both $\langle D \rangle$ and FA values normalized to the values from the corresponding bundles in the adult population, and the speed of their changes. The model was supported in 8 out of 11 considered bundles that were classified as follows. The cortico-spinal tract appeared to be the most mature bundle, followed by the spino-thalamic tract and the fornix. The optic radiations, the inferior longitudinal and arcuate fascicles appeared relatively immature at this age. The least mature bundles were the anterior limb of the internal capsule and the cingulum. Evaluations of the changes in DTI parameters over a larger age-range confirmed asynchronous maturation of white matter bundles [127, 193] (Fig. 2.8.C). A tract-based analysis of the DTI parameters during the first two postnatal years suggested that sensory and motor tracts show higher maturation degree at birth but slower maturation rates compared to others bundles [127]. On the contrary, association bundles, including arcuate, uncinate and inferior longitudinal fasciculus have lower maturation degree at birth, but mature at higher rates during the first year as compared to projection bundles. Similarly, comparison of the changes in mean diffusivity $\langle D \rangle$ and fractional anisotropy FA across almost the entire lifespan (5-83 years) suggested that frontal–temporal connections, including cingulum, uncinate fasciculus and superior longitudinal fasciculus, have a prolonged maturation, while the fornix, corpus callosum and inferior longitudinal fasciculus showed relatively fast maturational rates [193].

Finally, DTI allowed revealing differences in maturation progression within individual bundles [127, 192, 194–196]. For example, it was shown that during the late preterm period the cortico-thalamic tract starts to myelinate first at the level of the internal capsule [194]. It was also shown that in the optic radiations of infants (6-17 post-natal weeks) there are two maturational waves: an early wave in the anterior region, starting from the lateral geniculate nucleus, and a later catching-up wave in the posterior region, starting from the occipital cortex [196]. These waves may result from myelination of the geniculo-cortical and cortico-geniculate fibers respectively. Generally, during the first two post-natal years, maturational changes near cortical regions appear smaller than in the central regions [127].

2.2.4 Other diffusion models

Diffusion tensor model is based on the assumption that in each voxel diffusion process can be described by a Gaussian distribution. However, at higher b-values this assumption is no longer valid [197]. Furthermore, each voxel may contain several tissue compartments with different diffusion characteristics (grey matter, white matter, cerebrospinal fluid) that differently contribute to the total measured diffusion signal. Diffusion tensor model will also fail to adequatly describe diffusion in white matter regions containing fiber populations with different orientations, i.e. crossing or diverging fibers. To overcome these limitations several other diffusion models have been introduced. Here we will mention the most known models used

to characterize microstructural tissue properties, while those used for 3D fiber tractography to better characterize the spatial distribution of fiber orientations and resolve complex fiber configurations will be described later in the corresponding section in section 2.6.

Using High Angular Resolution Diffusion Imaging (HARDI) [198], it is possible to model diffusion signal as a mixture of diffusion signals from several tissue compartments and estimate their parameters and fractions.

The **bi-exponential** model describes two distinct diffusing pools (fast and slow) with different diffusion coefficients and volume fractions [199, 200]. However, these fast and slow components are not equivalent to the extra- and intracellular components as initially hypothesized since fitted and true volume fractions are significantly different [201, 202].

The **ball-and-stick** model accounts for an intra-axonal component modeled as a cylinder with zero radius ("stick") and an extra-axonal component with an isotropic diffusion ("ball") [203]. This model allows estimating fiber orientation, the relative volume fractions of the two components and their inherent diffusion coefficients.

The **CHARMED** (Composite Hindered And Restricted Model of Diffusion) model accounts for intra-axonal and extra-axonal compartments [204]. The intra-axonal compartment is characterized by a restricted model of diffusion within impermeable parallel cylinders of a given diameter. This model explains non-Gaussian diffusion with increasing diffusion time at high b-values. Hindered extra-axonal compartment is modeled by an effective diffusion tensor explaining anisotropic Gaussian diffusion observed at low b-values. Using diffusion data acquired at both high and low b-values along different directions, the CHARMED model allows to estimate various microstructural parameters, such as the diffusivity of the extra-axonal component, the axonal density (volume fraction of the intra-axonal component) and fiber orientations (3D probability distribution obtained from 3D Fourier transformation of the signal attenuation profile). This model is further extended in the AxCaliber model by introducing the distribution of axonal diameters as an unknown function to be estimated from diffusion data at both different degrees of diffusion weighting and different diffusion times [205].

NODDI (neurite orientation dispersion and density imaging) relies on a three-compartment model of the tissue microenvironement. It includes the intra-cellular compartment modeled as "sticks" (cylinders of zero radius) with orientation dispersion described by a Watson distribution, the extra-cellular compartment characterized by anisotropic Gaussian diffusion, and the CSF compartment with isotropic Gaussian diffusion [206]. This model allows to disentangle two key factors contributing to FA: neurite density and neurite orientation dispersion.

The main limitation of these models for studying brain development is that they require long acquisition times to provide the data necessary for reliable model fitting. This remains a critical constraint for their applications in healthy unsedated infants and children and so far, there were only a few studies applying these techniques to the developing brain [207–209].

It was shown that in newborns scanned at term, CHARMED and NODDI parameters were able to identify several microstructural components of the white matter: early maturing fibers (myelinated and tightly packed fibers in the posterior limb of the internal capsule), partially mature fibers (tightly packed but relatively unmyelinated fibers of long association and callosal cortico-cortical connections) and immature fibers (less tightly packed and incoherently oriented short cortico-cortical fibers and periventricular crossroad of pathways) [209]. In this study the early maturing bundles were clearly highlighted on the intra-axonal/neurite volume fraction maps derived from both CHARMED and NODDI, showing higher values as compared to other areas. Both methods also highlighted the compact and oriented structure of the corpus callosum with the highest intra-neurite volume fraction and the smallest neurite orientation dispersion index. With these parameters, it was also possible to differentiate between the posterior and anterior internal capsule that have similar cellular structure but different maturation stages (i.e. partially myelinated and non-myelinated stages respectively).

Another study addressed age-related changes in NODDI parameters within the posterior limb of the internal capsule (PLIC), the genu and splenium of the corpus callosum during the first 3 post-natal years [208]. The study revealed a non-linear increase in intra-axonal water fraction in all 3 regions. The most rapid increase was seen in PLIC, followed by splenium and then by genu. The fraction of the CSF compartment did not change with age in the splenium (11% on average) and in the genu (5% on average) but sligthly increased in PLIC (from 0 to 3%). Orientation dispersion index was rather stable across the age-range in all 3 regions and ranked splenium as the most aligned bundle, followed by genu and PLIC. Tortuosity of the extra-axonal space was found to increase exponentially with age in all three regions, with the most rapid changes observed in PLIC, followed by the splenium and genu. At the age of 3 years, the splenium was found to be the most tortuous tract, followed by genu and PLIC. The observed changes in intra-axonal water fraction and tortuosity are believed to result from active myelination, via the reduction of the extra-axonal space.

2.2.5 Conclusion

Although investigation of the age-related changes in diffusion parameters may provide insights on white matter maturation, none of these parameters is specific to any particular tissue property or maturational prossess but they are rather influenced by a complex ensemble of various maturational processes. At the same time, none of these parameters can reflect the whole complexity of the undergoing maturational changes. Thus, reliable description of white matter maturation may require development of more sophisticated multiparametric approaches that integrate complementary information from several parameters. Examples of such approaches will be presented in the experimental part of this work.

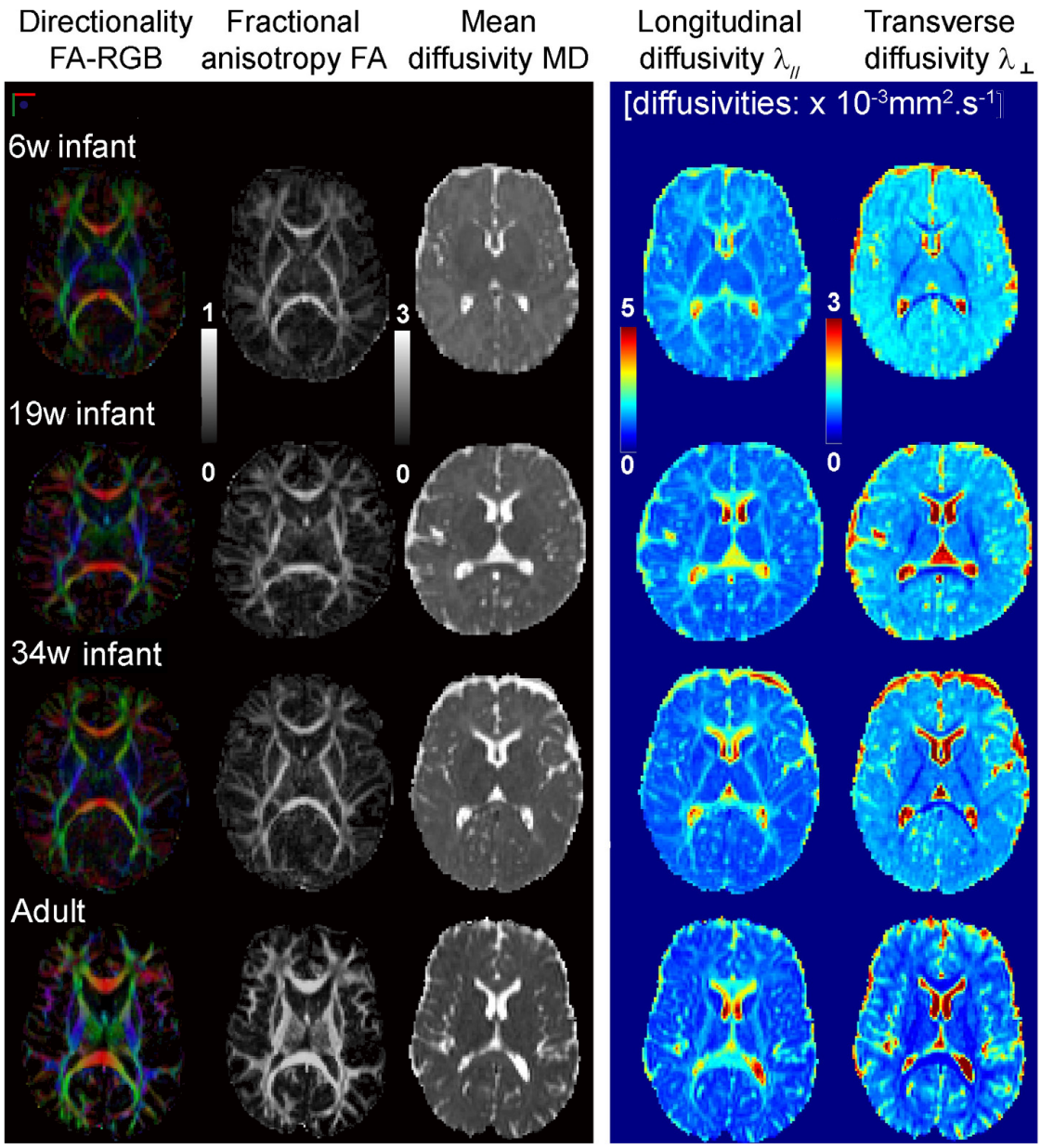

Figure 2.7: Changes in the DTI maps during development. The maps are presented for the same subjects as in Fig. 2.2. FA-RGB maps are color-coded directionality maps. In the white matter, FA increases with age, while $\langle D \rangle$, $\lambda_{\parallel}$ and $\lambda_{\perp}$ decrease. Adapted from [133].

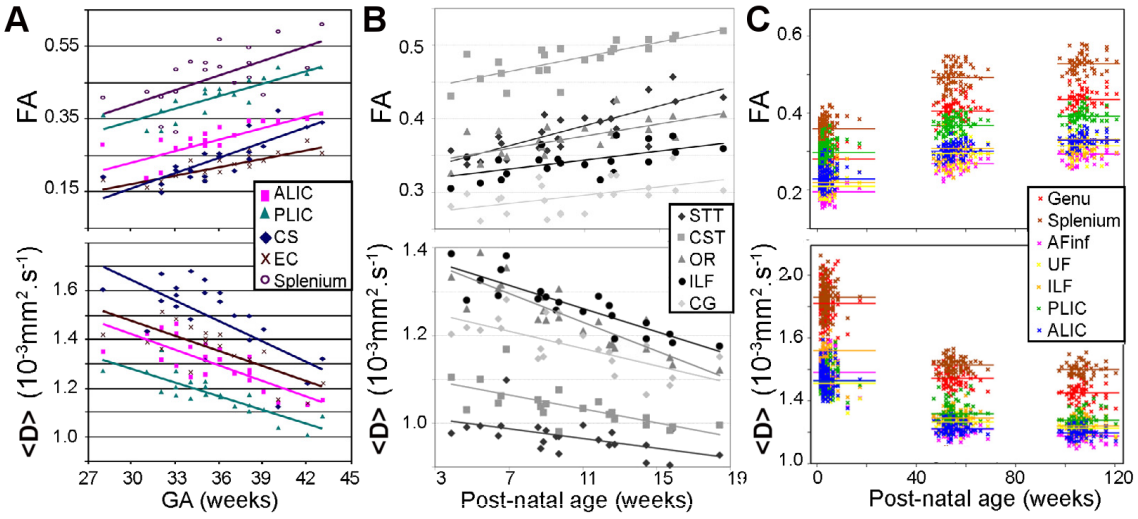

Figure 2.8: Age-related changes in FA and $\langle D \rangle$ across different white matter bundles (A) in preterm newborns imaged at 1.5T (adapted from [192]); (B) in infants imaged at 1.5T (adapted from [182]); (C) in infants at birth, at 1 year and 2 years of age imaged at 3T (adapted from [127]). Abbreviations: AFinf, inferior branch of the arcuate fasciculus; ALIC, anterior limb of the internal capsule; CG, cingulum; CS, centrum semiovale; CST, cortico-spinal tract; EC, external capsule; ILF, inferior longitudinal fasciculus; OR, optic radiations; PLIC, posterior limb of the internal capsule; STT, spino-thalamic tract; UF, uncinate fasciculus.

2.3 Other myelin-related imaging parameters

2.3.1 Magnetization transfer ratio (MTR)

2.3.1.1 Physical principles of MTR

MTR evaluates the ratio between free protons with unrestricted motion and protons bounded to macromolecules, such as lipids and proteins, that are characterized by restricted motion [163, 210–213]. It relies on transfer of magnetization between the protons of these two pools and produces a contrast that allows tissue differentiation: tissues with higher number of protons with restricted motion have higher MTR values [210]. Thus, myelinated white matter, containing a large number of bound protons, has higher MTR values than gray matter [214]. MTR contrast is achieved by saturating macromolecule protons using an off-resonance radio frequency (RF) pulse [210, 215]. The saturated bound protons then interact with free protons, leading to magnetization transfer to the free protons and reducing the measured MRI signal. This transfer can occur both through dipolar coupling or through direct chemical exchange [210]. Thus, MTR can be calculated as follows:

$$MTR = (1 - \frac{M_S}{M_0}) * 100 \tag{2.9}$$

where M_0 is MRI signal intensity without the saturation pulse and M_S is signal intensity after the saturation pulse.

2.3.1.2 Changes during development

MTR is thought to provide a measure of myelin amount. During the first 2 postnatal years, myelination of the white matter is accompanied by an increase in MTR values from 13-19% in unmyelinated white matter to 34-37% after myelination [153, 216]. This increase likely results from increasing concentrations of macromolecules in the myelinating white matter, with the main contribution ascribed to increasing concentrations of galactocerebrosides [152, 153, 163]. In gray matter, MTR values at birth are similar to those of unmyelinated white matter and during maturation, MTR values in gray matter gradually increase to 25-26% [153].

Evaluation of MTR within individual white matter bundles was in agreement with the known posterior-anterior progression of brain myelination [217]. MTR values were found to be higher in projection and commissural bundles compared to association bundles, with this difference being already detectable at 1 month of age, reflecting early myelination of the former bundles [217]. MTR values reach a relatively mature stage in the occipital and frontal white matter at ∼13 and ∼16 months respectively, and at ∼18 and ∼19 months in the splenium and genu of the corpus callosum [218]. In adulthood, MTR is relatively stable with a slight tendency to increase in occipital and temporal white matter regions [214, 219]

Nevertheless, MTR interpretation is not straightforward because the technique is likely to be sensitive not only to myelin-associated macromolecules, but also to

other factors, including the macromolecular density of axonal cytoskeleton components such as microtubules and neurofilaments [178]. Furthermore, MTR relies on a simple two-pool model ("free" and "bound" proton pools), while the actual resulting MTR reflects more complex combination of various relaxation and exchange processes [220]. It was also suggested that MTR values strongly depend on specific pulse sequence characteristics and thus, may be difficult to compare across studies [220].

2.3.2 Myelin Water Fraction (MWF)

2.3.2.1 Physical principles of MWF

MWF corresponds to the fraction of water trapped by the myelin sheaths relative to the total water volume within an imaging voxel [135, 221–223]. MWF mapping assumes multicomponent origin of T1 and/or T2 relaxation signals and can be derived from a multicomponent analysis of these signals. Whereas the exact number of components is still under discussion, the shortest T2 component (below 40-50ms) is consistently attributed to myelin-related water [135, 221–223] and thus, is thought to faithfully reflect the amount of true myelin in the tissue (myelin sheaths). Unlike relaxation times, MWF is *a priori* independent from the magnetic field but its computation is highly sensitive to both the acquisition and computational settings, making direct comparisons across studies hardly achievable.

The most conventional strategies for MWF quantification do not make any assumptions on the number of components and are based on the calculation of the T2-spectrum (Fig. 2.9A). In these approaches, MWF is computed in each voxel as the ratio between the signal with T2 below 40-50ms and the total water signal in the T2 distribution [223–229]. Similar strategies have been also proposed for T2* [230] and T1 spectra [231]. However, reliable estimation of a spectrum requires acquisition of the relaxation signal with a large number of time-points (N>32) [222, 223], making the acquisition protocol impractically long for infants and children.

An alternative strategy is to make a multicomponent model of the relaxation signals that takes into account the relative contributions of the different components, and to fit this model with the acquired data in order to estimate the fractions of the components (Fig. 2.9B) [221, 232, 233]. These models will differ depending on the acquisition sequences, on the number of modelled components, which usually varies from 2 to 4, including myelin-related component, intra/extra-cellular water and free water of the cerebro-spinal fluid (CSF), and on the presence or absence of exchange between these components. Unless some *a priori* assumptions are made on the components relaxation characteristics [233], such models are described by non-linear equations, and their robustness relies on the sampling strategy and the number of measurements. Although with mcDESPOT sequences, it is possible to make acquisition time as short as 18min 22sec [135], it remains nevertheless rather long for pediatric applications where acquisition times should be kept as short as possible. Furthermore, such approaches typically require long post-processing times due to sophisticated stochastic model fitting [221]. An alternative strategy

for fast MWF quantification that overcomes these limitations will be introduced in the experimental part of this PhD work (see chapter 5).

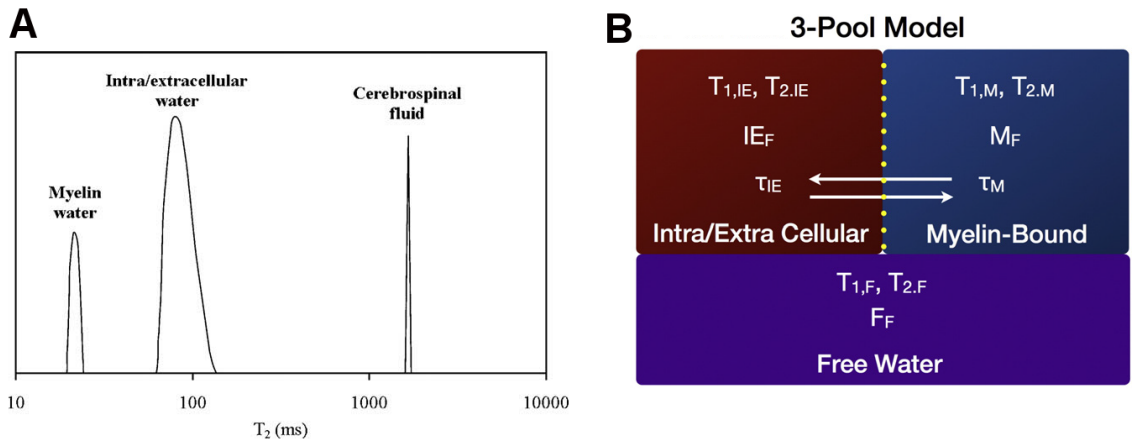

Figure 2.9: A. Example of a T2 spectrum from *in vivo* human white matter, showing multiple peaks corresponding to different compartments of the white matter. B. Graphical representation of a three-compartement relaxation model used to fit the mcDESPOT data. The model includes two compartments with water exchange (intra/extra cellular water and myelin-bound water) and the third free water compartement (cerebral spinal fluid) without water exchange. Adapted from [135, 234].

2.3.2.2 MWF changes during development

MWF provides a more direct measure of the brain myelin content than any other MRI parameter. It has shown good correlation with myelin amount [226] and seems particularly relevant for quantifying progression of the white matter myelination [134, 135, 233]. MWF dramatically increases during white matter maturation and nicely demonstrates the spatiotemporal pattern of myelination progression (Fig. 2.10). In agreement with the known caudo-rostral myelination progression, increase in MWF values starts earlier in projection fibers (frontal–parietal region) and later in association fibers (frontal region) [233]. From the 3rd post-natal month, MWF increases in the cerebellum, pons, and internal capsule; then the increase in MWF values spreads from the splenium of the corpus callosum and the optic radiations (at 3–4 months) to the occipital and parietal lobes (at 4–6 months), followed by the genu of the corpus callosum and the frontal and temporal lobes (at 6–8 months) [134]. The spatio-temporal pattern over a larger age range (3–60 months) was consistent with histological findings on myelination [135].

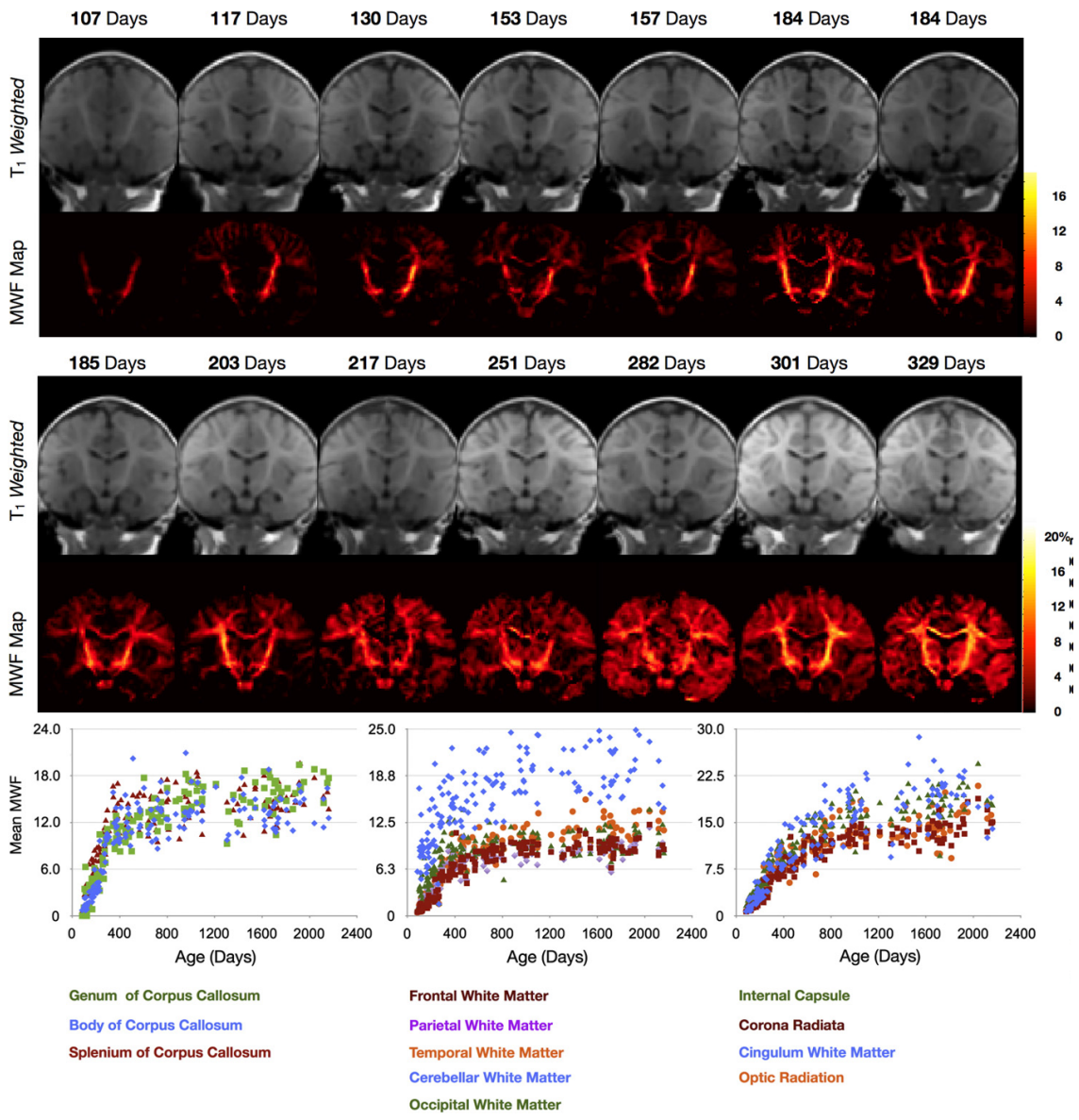

Figure 2.10: MWF maps demonstrate the spatiotemporal sequence of the increase in brain myelin content across the developmental period. Plots at the bottom depict myelination trajectories for different white matter regions and pathways from the 83rd to the 2040th post-natal days. Adapted from [134].

2.4 Multiparametric imaging

Multiparametric analysis of MRI data may open new perspectives for studies of white matter development. However, to our knowledge, there were only a few attempts to describe white matter maturation using multiparametric MRI data [132, 182, 235, 236]:

- In the work of Dubois et al. [182], a maturational model was based on the estimation of the global bundle maturation by progression through four stages, which took into account both the maturation state and speed of each bundle, calculated from DTI indices (FA and $\langle D \rangle$). This model suggested that the cortico-spinal tract appeared the most mature, followed by the spino-thalamic tract and the fornix, then the optic radiations, the arcuate and inferior longitudinal fasciculi, and the least mature were the anterior limb of the internal capsule and the cingulum.

- Prastawa et al. [235] introduced an absolute maturational measure from the total growth rate for a set of multimodal observations (longitudinal and transverse diffusivities, proton density and intensity of T1w and T2w images). The relative maturational measure was calculated as the time shift required to transform a maturational curve for a given bundle to a reference curve computed from the posterior limb of the internal capsule (because of its known early myelination). This model was in agreement with the known temporal order of the white matter maturation: (1) brain regions related to basic functions such as sensory and motor information processing are the most advanced in the maturation; (2) central regions of the white matter tracts mature before peripheral sub-cortical regions.

- Vardhan et al. [236] proposed using the Hellinger distance to measure age-related changes in the intensities of T1w and T2w images. This strategy also demonstrated that maturation begins in posterior regions and frontal regions mature later on. Finally, Sadeghi et al. [132] suggested using the Gompertz function to model age-related changes in both FA and the intensities of T1w and T2w images in order to provide landmarks on maturation asynchrony across bundles.

Despite their advantages, the above mentioned approaches had several strong limitations:

- The model of Dubois et al. [182] was not supported in three bundles (corpus callosum, external capsule, and uncinate fasciculus) and did not give quantitative assessment of the relative maturational delays between the bundles.

- Prastawa et al. [235] also did not report any quantitative results on the relative maturational delays between white matter regions, and this study was focused on different regions rather than on different bundles.

- The works of Vardhan et al. [236] and Sadeghi et al. [132] also provided region specific rather than tract-based information possibly mixing the information about different bundles passing at the same location.

- All these approaches, except the one from Dubois et al. [182], used the intensities of T1w and T2w images, which are hardly comparable across subjects because of signal inhomogeneities and of varying acquisition tunings.

- None of these approaches, except the one from Dubois et al. [182], takes into account the differences in the parameters and their variations at the mature adult stage, so that it was not possible to assess bundles maturational degrees relative to their mature stages.

Example of a novel multiparametric appraoch free from these drawbacks will be introduced in this work in chapters 3 and 4.

2.5 Functional correlates of MRI biomarkers of white matter maturation

The observed structural maturational changes accompany changes in the functional efficiency of brain networks and are correlated with behavioral indices [237–247]. Thus, analysis of the structural changes during development may help to understand the biological principles underlying cognitive development, by revealing the early structural features associated with certain functions such as language, and by investigating correlations between these structural features and cognitive performance. Below we will describe some examples of such correlations observed in language-related networks.

DTI studies in healthy infants (1-4 months old) have shown early asymmetries within language-related networks [248], including 1) the larger temporal part of the arcuate fasciculus in the left hemisphere; and 2) higher FA values in its left parietal part, suggesting either better microscopic organization or advanced myelination. At the functional level, specialization of the left hemisphere for language processing can be observed in preterm babies already at the 6th gestational month [249]. Such early asymmetries may point to the genetic constraints driving early development of lateralized functions in the human brain.

In the developing language network, language acquisition goes in parallel with white matter myelination [250, 251]. Expressive and receptive language abilities

show significant correlations with MWF values in frontal and temporal white matter, with the leftward asymmetry in frontal white matter and the rightward asymmetry in the external/extreme capsule [242].

Recently, using an original clustering approach based on DTI parameters, Dubois et al. [252] was able to further highlight the developmental tempos of the linguistic bundles. Maturation of the ventral pathway, which is assumed to support semantic processing was more advanced than maturation of the dorsal pathway, which is believed to support phonological processing. However, the latter catches up during the first post-natal months. Its fast development during this period might relate to the learning of speech cross-modal representations and to the first combinatorial analyses of the speech input.

It was also demonstrated that performance in word learning correlates with FA and $\lambda_\perp$ in the direct connections between Broca's and Wernicke's areas of the left hemisphere, suggesting that our ability to learn new words may rely on an efficient communications between temporal and frontal areas [253]. In eldery subjects, FA in these tracts was also correlated with performance in artificial grammar learning task [254], suggesting that the acquisition of syntactic knowledge in older adults relies on intact white matter microstructure in language-related areas as well as their interhemispheric functional coupling. Finally, adult dyslexic patients show specific correlations between performance on phoneme awareness and speech perception and the integrity of the left arcuate fasciculus evaluated by FA, and between orthographic processing and FA in left inferior fronto-occipital fasciculus [255].

2.6 Investigating white matter connectivity

2.6.1 3D fiber reconstruction (tractography)

Another important issue in studies of the developing white matter is investigation of white matter structural connectivity. Diffusion imaging allows reconstruction of the white matter fibers in 3D using various tractography algorithms based on different diffusion models [256].

2.6.1.1 Diffusion models

In **DTI model**, it is assumed that in each voxel the principal fiber direction is parallel to the main axis of the diffusion ellipsoid (primary eigenvector of the diffusion tensor). This information on fiber orientation can be visualized on 2D directional color-coded maps [257] (Fig.2.5). The fibers can be further reconstructed in 3D by algorithms following the primary eigenvector from one voxel to another [256]. The main limitation of this DTI-based approach is that it can reveal only one fiber direction per voxel and faces problems in regions of crossing fibers.

To overcome this limitation, alternative approaches that allow resolving multiple fiber orientations within a voxel, have been introduced [258, 259], with most of them being based on High Angular Resolution Diffusion Imaging (HARDI) [198].

In these approaches, estimation of fiber orientations are obtained either from the **diffusion orientation density function (dODF)** or from the **fiber orientation density function (fODF)** and the tractography algorithms then use peaks in these functions to reconstruct white matter fibers.

Approaches based on dODF estimate the diffusion propagator $p(\vec{r}, t)$ that gives the probability of certain molecular displacement $\vec{r}$ within the diffusion time t. The radial integral of the diffusion propagator gives the dODF:

$\Psi(\theta, \phi) = \int_0^\infty p\left(\vec{r}, \theta, \phi\right) r^2 dr, \theta \in [0, \pi], \phi \in [0, 2\pi]$,

which describes the relative number of particles that have diffused along the line connecting a given point on the sphere to the origin. In **q-ball imaging** dODF is estimated using the Funk–Radon transform [260, 261]. This approach can resolve multiple peaks in the dODF missed by the tensor model. In **analytical q-ball** imaging, dODF is just a linear transformation of the modified spherical harmonics coefficients, representing HARDI signal [260].

In contrast to dODF approaches, **fODF techniques** reveal the angular distribution of fiber orientations from the angular structure of either the signal [262, 263] or the dODF [264] by spherical deconvolution with a kernel. This kernel presents the simplest model of the diffusion properties of a single fiber and it is obtained either by assuming that white matter with the highest anisotropy contains coherent fibers with single orientation, or by simulating the response from an idealized fiber.

2.6.1.2 Tractography algorithms

Once the information on fiber orientations is known at every image voxel, it can be used to reconstruct white matter pathways in 3D using different fiber tracking algorithms that can be divided into deterministic and probabilistic [170, 265].

In deterministic approaches, fiber trajectories, also called “streamlines”, are reconstructed by connecting the neighboring image voxels that are thought to belong to the same white matter fiber. This can achieved by following the fiber direction (for example, principle eigen vector in DTI) from one voxel to another. Constraints on the maximum turning angle of the fiber trajectory between voxels and propagation masks with defined minimum FA values can be applied to make reconstruction more realistic and, in analogy to curve fitting, some regularization may also be introduced [266–268]. Tractography can be initiated from user-defined voxels ("seeds") placed in certain regions of interest to identify white matter tracts passing through them. Alternatively, in the "brute force" approach, the seed voxels can be placed within the entire brain volume [269].

In contrast to deterministic tractography, probabilistic approaches incorporate the expected uncertainty of fiber orientations. This can be done, for example, by interpreting the local ODF as a probability density distribution of the local fiber orientation, then sampling randomly this distribution many times, and performing streamline tractography with each sample from the same starting point. In this way, such approaches can produce connectivity maps, showing probabilities of connections between different brain regions and the starting point.

2.6.2 Identification of white matter bundles

Once 3D tractography is performed over the entire brain volume, individual white matter bundles can be identified and extracted from tractography datasets using various approaches. For example, this can be done in each individual subject using manually defined regions of interest (ROI) that should be passed through or avoided by the fibers (Fig. 2.11) [269–272]. This approach is very time-consuming, it imposes *a priori* assumptions on bundle locations and depends on the expert experience. Alternatively, ROI atlases could be applied using affine or non-linear transformations [273–275]. However, in this case results strongly depend on normalization quality and do not take into account variability of fiber shapes.

Recently, more sophisticated approaches using fiber-clustering techniques have been proposed for automatic bundles segmentation [276–284]. In such approaches, organization of the brain white matter is represented by an atlas that is generated over a group of subjects and that contains bundles present in most subjects of the considered population (Fig. 2.12) [277, 281, 285, 286]. Then bundles' identification in individual subjects can be performed by comparing fiber clusters from the considered individuals to the labeled bundles from the atlas (Fig. 2.12J). Such approaches are more efficient because they take into account fiber shapes and localization variabilities. Being fully automatic, they save time and increase reproducibility of the reconstructed bundles. Furthermore, such atlases can be also used to analyse tissue microstructural properties, even when its not possible to perform reliable tractography (for example, in myelin-related diseases), by projecting atlas bundles to the subject data. However, existing atlases were generated from adult data and projection of their bundles to pediatric patients (for example, to children with metachromatic leukodystrophy, see chapter 8) may not be adequate since fiber shapes and lengths change during development and those in young children differ from those in adults. Thus, studies in pediatric patients require creating age-specific atlases. Example of such a preliminary atlas will be described in the experimental part of this work (see chapter 6).

2.6.3 Imaging development of the white matter connectivity

Diffusion imaging and tractography techniques are very useful to investigate the developing organization of the white matter. *Post-mortem* imaging studies in fetuses have shown that tracts in the brainstem and limbic tracts are among the first to develop, beeing already detectable before the second trimester [61, 100]. At the 13th gestational week, the pontine crossing tract and the corticospinal tract can be already identified. At the 15th week, the pontine crossing tract increases in size and gets the configuration similar to the adult state, completely surrounding the corticospinal tract. Between the 15th and 20th weeks, the corticospinal tract increases its size. At the same time, the middle and inferior cerebellar peduncles and the medial lemniscus become distinguishable. Limbic tracts, including fornix and the stria terminalis, can also be easily detected at the age of 13 weeks, while

cingulum can be detected only after 17 weeks. At the age of 13 weeks, among the commissural tracts, one can observe the middle cerebellar peduncle, optic chiasm and anterior commissure. The corpus callosum appears only at the 15th week. At the 20th gestational week, corpus callosum is more advanced in the frontal regions (genu and forceps minor) than in other areas (splenium and forceps major, body). The internal capsule can also be detected at the 13th week and during development it extends from its core to anterior and posterior regions. Starting from the 19th week the uncinate fasciculus, the inferior frontooccipital fasciculus and the inferior longitudinal fasciculus can be observed. The superior longitudinal fasciculus could not be reliably traced (though it is not absent), even at birth, likely due to its slow maturation [287].

In vivo investigations in fetuses and preterm babies are in global agreement with findings in post-mortem studies [86, 88, 288, 289]. Using fetal MRI *in utero* it is possible to reconstruct certain fiber tracts, like corpus callosum, thalamo-cortical and corticospinal tracts as early as at the 18th gestational week [86, 88, 289]. In cases of the corpus callosum agenesis, it is possible to detect the Probst bundles (longitudinal callosal fascicles) [290]. The uncinate fasciculus and the inferior fronto-occipital fasciculus can be revealed as early as at the 20th gestational week [288]. Identification of the cingulum and the fornix was possible only starting from the 27th week [288]. The inferior longitudinal fasciculus could be revealed from the 30th week, however in some cases it was possible to identify it as early as in the 23rd week [288].

After term birth, despite low anisotropy values, almost all main white matter tracts can be reliably reconstructed, including commissural bundles (genu, body and splenium of the corpus callosum), projection bundles (corticospinal tract, spino-thalamic tract, optic radiations, anterior limb of the internal capsule), limbic bundles (fornix and cingulum) and associative bundles (external capsule, uncinate, arcuate, superior and inferior longitudinal fascicles) (Fig. 2.13) [128, 182, 291]. A similar organization of the major bundles has been demonstrated between newborns and toddlers of 1 and 2 years of age [127]. However, certain associative bundles, like the superior longitudinal fasciculus, remain difficult to reconstruct at birth and show large reorganization in the fiber orientations during the first post-natal months [287].

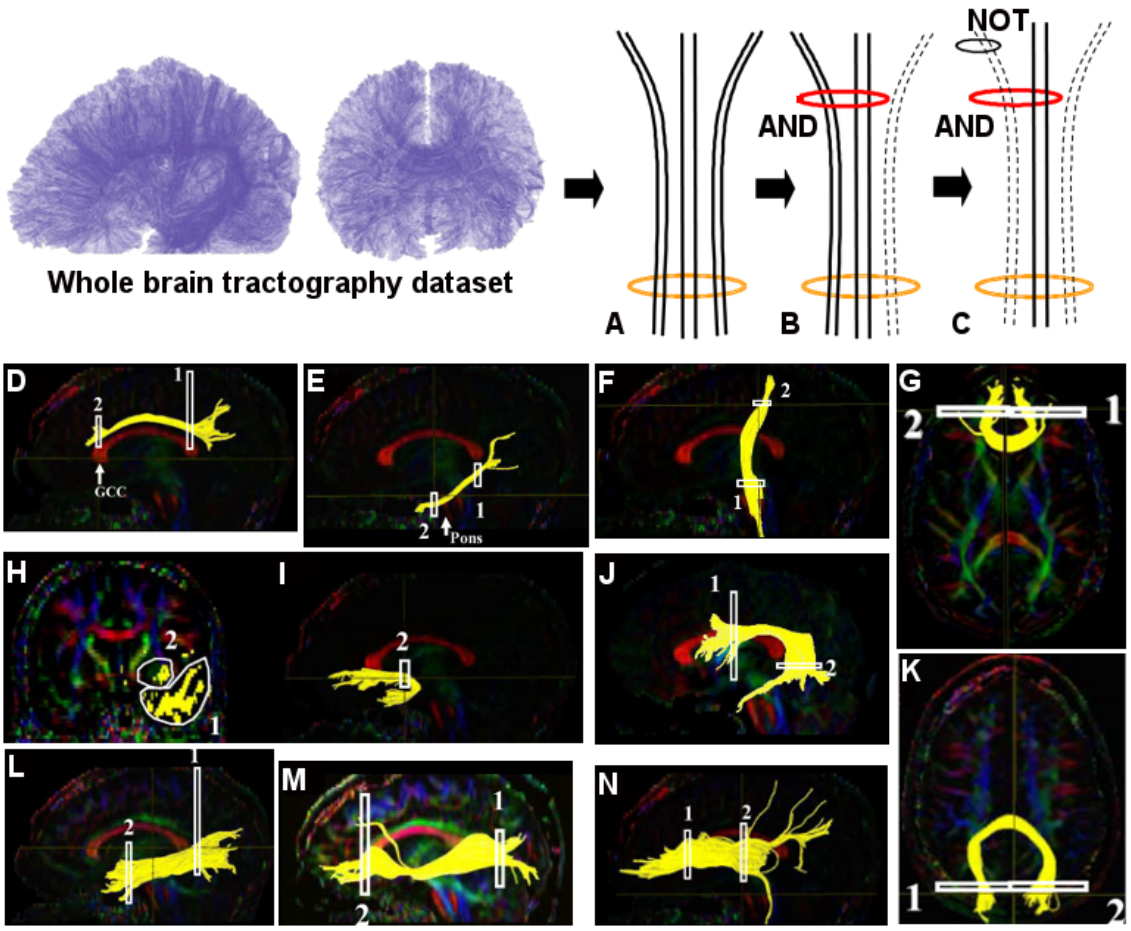

Figure 2.11: Principles of bundles' identification using ROIs and examples of identified bundles in adult subjects scanned at 1.5T. Individual bundles are extracted from whole brain tractography datasets using AND and NOT ROI operations. For example, first all tracts that penetrate the 1st ROI (orange circle) are selected (A). When the 2nd "AND" ROI (red circle) is applied, only the fibers that go through both ROIs are kept (B). Finally, "NOT" ROI (black circle) is used to remove undesired fibers (C). D-N Examples of identified bundles: D - cingulum in the cingulate gyrus part. GCC indicates the splenium of corpus callosum; E - cingulum in the hippocampal part; F - corticospinal tract; G - forceps minor; H and I - ROIs for uncinate and identified uncinate respectively; J - superior longitudinal fasciculus; K - forceps major; L - inferior longitudinal fasciculus; M - fronto-occipital fasciculus; N - anterior thalamic radiation. Adapted from [272].

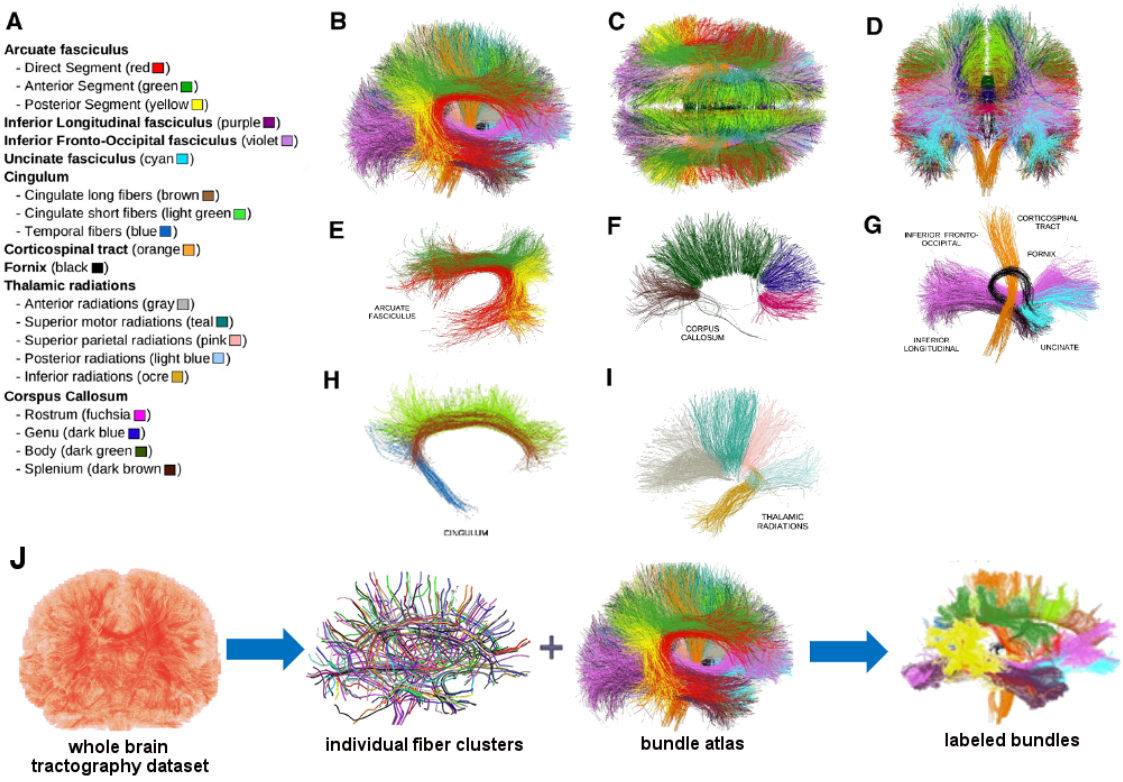

Figure 2.12: Multi-subject atlas of white matter bundles in adults and principles of its application for automatic bundles identification in whole brain tractography datasets as suggested by Guevara et al [277]. (A) List of atlas bundles and corresponding colors. (B–D) All bundles as seen from right (B), top (C) and front (D) sides. (E–I): Detailed view of the bundles: (E) Exterior view of the left arcuate fasciculus; (F) Exterior view of the corpus callosum tracts; (G) Interior view of left fornix, uncinate, inferior fronto-occipital, inferior longitudinal and corticospinal tracts; (H) Interior view of the left cingulum fascicles; (I) Exterior view of the left thalamic radiations. J. To identify bundles in a new tractography dataset, the fibers should be clustered and the resulting clusters should be compared to the atlas bundles to label them with the closest bundle from the atlas. Adapted from [277].

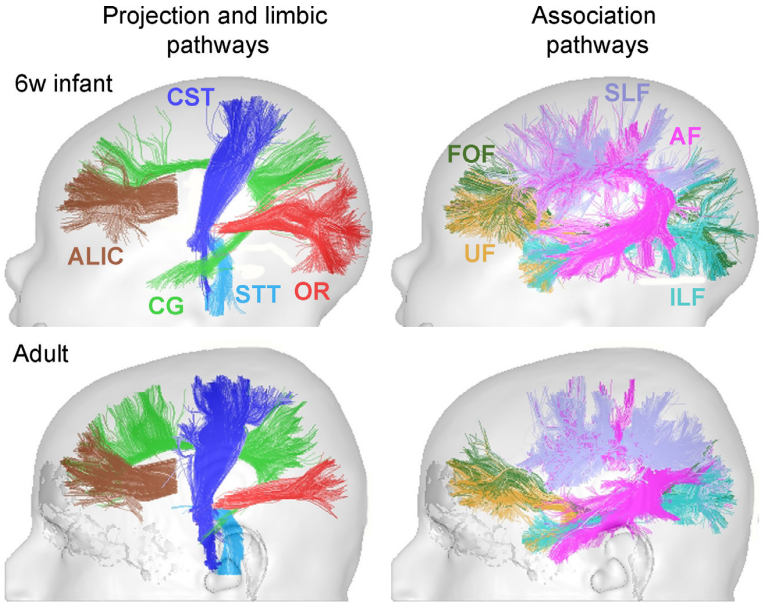

Figure 2.13: Similar organization of the major white matter bundles reconstructed in a 6-week-old infant and in an adult. Abbreviations: AF, arcuate fasciculus; ALIC, anterior limb of the internal capsule; CG, cingulum; CST, cortico-spinal tract; FOF, fronto-occipital fasciculus; ILF, inferior longitudinal fasciculus; OR, optic radiations; SLF, superior longitudinal fasciculus; STT, spino-thalamic tract; UF, uncinate fasciculus. From [133].

2.7 Technical aspects of imaging in infants and children

Imaging of the developing brain in infants and children presents additional technical challenges during both data acquisition and analysis [133, 139, 292]. Some of them are described below.

2.7.1 Data acquisition

Rapid brain growth may require using specially-designed coils adapted to the size of the subject head [293]. Smaller sizes of the cerebral structures require higher spatial resolution, however the acquisition time should be kept as short as possible to reduce exposure to acoustic noise and to avoid as much as possible motion artifacts. In clinical practice, some of these difficulties can be avoided by sedating pediatric patients and acoustic noise can be reduced by using foam earplugs or industrial-grade earmuffs. However, in the absence of strong clinical arguments, healthy infants and children cannot be sedated and it is extremely difficult to make them stay motionless during acquisition, unless they are naturally asleep. Furthermore, even in clinics it is highly desired to reduce the overall need for sedation in order to prevent any potential negative side effects. However, for some MRI techniques, including MWF mapping and HARDI imaging, that naturally require acquisition of a large amount of data, long acquisition time is a main limitation for their applications in pediatric imaging. Thus, for these techniques specially adapted protocols should be developed, like the one proposed by Poupon et al. for T1, T2 and T2* mapping [145]. Recently, using the Kalman filtering framework, it became possible to speed up the q-ball imaging, making it a useful tool to 3D white matter tractography [294, 295]. A specially designed approach for fast MWF quantification from infant data acquired with a short acquisition protocol will be described later on in the experimental part of this work (chapter 5).

2.7.2 Tissue segmentation and image alignement

Another source of difficulties in pediatric imaging arises from the rapid developmental changes. In conventional imaging, this leads to rapid changes in T1w and T2w contrasts with brain tissue maturation (see chapter 2.1.2). Thus, to assure good contrast between different tissues, different MRI sequences are often used depending on the developmental period. To differentiate myelinated from unmyelinated white matter regions, T1w contrast is generally preferred during the first 6–8 post-natal months, and T2w contrast between 6 and 14 months [296, 297]. This makes comparison across ages difficult, possibly leading to misclassification of cerebral tissues [298, 299] and thus, dedicated post-processing tools for tissue segmentation are required for different developmental periods. Changes in brain size, its underlying organization and in imaging contrasts impose additional difficulties

for image alignement and comparison across ages and subjects. To overcome these difficulties a number of pediatric brain templates have been proposed [300–303].

2.7.3 Estimation of DTI parameters

Reliable estimation of the DTI parameters depends on the signal-to-noise ratio (SNR) of the diffusion-weighted images and on the number of diffusion directions. During the first post-natal months the SNR decreases because of the decrease in both T2 relaxation time and diffusivities [304]. Thus, to make data comparable across subjects with different ages it is important to adapt the number of diffusion directions according to age, acquiring data with more directions in older subjects. One should also keep in mind that DTI is very sensitive to motions artifacts that should be reduced or corrected during acquisition [295, 305–308] or post-processing [309–314]. Motion can occur during slice or volume acquisition ("intra-slice"/"intra-volume" motion) or between acquisitions corresponding to different orientations of diffusion-sensitizing gradients ("intervolume" motion). This results in two types of motion-related artifacts:

1. artifacts within a volume (signal irregularities and outliers with alomost complete signal dropout;

2. misregistration between the volumes acquired before and after a movement.

To deal with these artifacts, we recently proposed a fully automated correction strategy [310] (Fig. 2.14), which has the 2 following steps:

1. **detection and resampling of slices corrupted by motion or technical problems (mechanical vibrations, spike noise).** Detection of the corrupted slices is based on their comparison with the volume acquired at b=0s/mm^2, using mutual information, and reampling of the detected outliers is based on spherical-harmonics decomposition of the diffusion signal and takes advantage of high number of diffusion gradients orientations.

2. **realignment of orientation volumes misregistered due to inter-volume motion and distortions stemming from eddy currents.** At this step, all orientation volumes are first registered to the first DW orientation volume, using affine transformation with shearing that maximizes mutual information. Then the geometric mean product of all DW volumes is computed and realigned to the volume acquired at b=0s/mm^2. Next, all initial orientation volumes are registered to this realigned product and resampled. Finally, a optional 3D rigid transformation can be applied to put the corrected data into the Talairach space by aligning the anterior and posterior commissures (AC-PC).

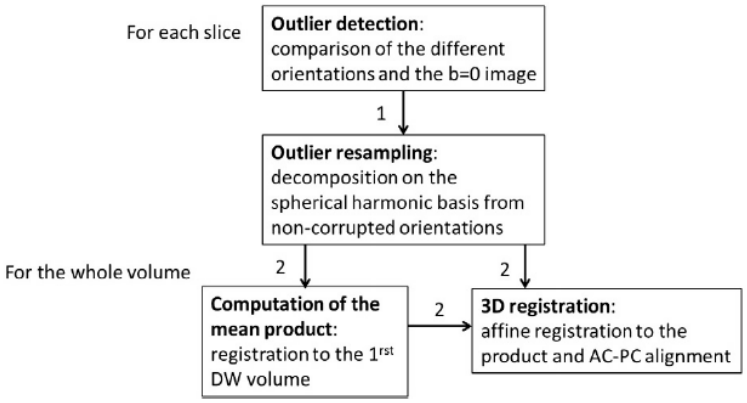

Figure 2.14: Schematic representation of the 2-step correction strategy from [310].

The proposed strategy was tested in real data acquired in healthy unsedated infants (6-22 weeks old) and it was shown to improve DTI maps and increase the reliability of DTI quantification. My personal contribution to this work consisted of further validation of the proposed strategy using data with simulated artifacts arising from different possible types of motion (translational and rotational motion, vibration along a given axis). The quality of the correction strategy was evaluated for artifacts of various strengths in terms of deviations from the reference diffusion-weighted signal, differences in the tensor main direction and in the resulting FA values. Finally, I also compared the proposed strategy with another widely-used correction approach, named RESTORE [309].

Magnetic Resonance Imaging 32 (2014) 981–992

Contents lists available at ScienceDirect

Magnetic Resonance Imaging

journal homepage: www.mrijournal.com

Correction strategy for diffusion-weighted images corrupted with motion: application to the DTI evaluation of infants' white matter

Jessica Dubois [a,b,c,*], Sofya Kulikova [d,e,f], Lucie Hertz-Pannier [d,e,f], Jean-François Mangin [c,g], Ghislaine Dehaene-Lambertz [a,b,c], Cyril Poupon [c,h]

[a] INSERM, U992, Cognitive Neuroimaging Unit, Gif-sur-Yvette, France
[b] CEA, NeuroSpin Center, UNICOG, Gif-sur-Yvette, France
[c] University Paris Sud, Orsay, France
[d] CEA, NeuroSpin Center, UNIACT, Gif-sur-Yvette, France
[e] INSERM, U663, Paris, France
[f] University Paris Descartes, Paris, France
[g] CEA, NeuroSpin Center, UNATI, Gif-sur-Yvette, France
[h] CEA, NeuroSpin Center, UNIRS, Gif-sur-Yvette, France

ARTICLE INFO

Article history:
Received 31 January 2013
Revised 24 April 2014
Accepted 26 May 2014

Keywords:
MRI
Diffusion imaging
Artifact
Motion
Vibration
Brain

ABSTRACT

Objective: Diffusion imaging techniques such as DTI and HARDI are difficult to implement in infants because of their sensitivity to subject motion. A short acquisition time is generally preferred, at the expense of spatial resolution and signal-to-noise ratio. Before estimating the local diffusion model, most pre-processing techniques only register diffusion-weighted volumes, without correcting for intra-slice artifacts due to motion or technical problems. Here, we propose a fully automated strategy, which takes advantage of a high orientation number and is based on spherical-harmonics decomposition of the diffusion signal.
Material and methods: The correction strategy is based on two successive steps: 1) automated detection and resampling of corrupted slices; 2) correction for eddy current distortions and realignment of misregistered volumes. It was tested on DTI data from adults and non-sedated healthy infants.
Results: The methodology was validated through simulated motions applied to an uncorrupted dataset and through comparisons with an unmoved reference. Second, we showed that the correction applied to an infant group enabled to improve DTI maps and to increase the reliability of DTI quantification in the immature cortico-spinal tract.
Conclusion: This automated strategy performed reliably on DTI datasets and can be applied to spherical single- and multiple-shell diffusion imaging.

1. Introduction

Imaging the diffusion of water molecules by MRI enables the non-invasive exploration of the tissues' microstructure. This is done by making the MR signal sensitive to spin motion through the application of diffusion gradients during acquisition [1]. To explore the anisotropic structure of tissues, such as the fiber organization of white matter, diffusion-weighted (DW) images are currently acquired along several orientations of the diffusion gradients taken on a single shell in the Q-space, for a fixed b-value, with models like diffusion tensor imaging (DTI) and high angular resolution diffusion imaging (HARDI). In DTI, MR measurements are performed along at least 6 orientations of the diffusion gradients. In comparison with data averaging, increasing the number of orientations also improves the signal-to-noise ratio (SNR) of the resulting diffusion maps. On condition that orientations are uniformly distributed over the space [2,3], it further enables a more precise spatial and angular estimation of the diffusion model, thus improving the local estimation of the spatial organization of tissues. But it also increases the acquisition time and thus the risk of motion artifacts. Increasing the b-value improves the reliability of diffusion models, but decreases the SNR. HARDI models, such as Q-ball imaging (QBI), better explore the tissue microstructure and anisotropy, but the acquisition of a high number of diffusion gradient orientations is required. Therefore, a compromise between image quality and acquisition time must be found.

Diffusion techniques are based on 2-dimensional (2D) acquisitions with echo planar imaging (EPI), and slices are generally acquired in an interleaved order. Because of diffusion gradients, the acquisition time of a slice is of the order of 200 ms, which

* Corresponding author at: CEA/SAC/DSV/I2BM/NeuroSpin/Cognitive Neuroimaging Unit U992, Bât 145, point courrier 156, 91191 Gif-sur-Yvette, France. Tel.: +33 1 69 08 81 72; fax: +33 1 69 08 79 73.
E-mail address: jessica.dubois@centraliens.net (J. Dubois).

http://dx.doi.org/10.1016/j.mri.2014.05.007
0730-725X/

corresponds to a 10 s scan duration to cover the whole brain with 50 slices. If for instance 30 different orientations of the diffusion gradients are acquired, the total acquisition time is at least 5 min (plus the acquisition time for b = 0 images and calibration scans required for parallel imaging). Consequently, motion can occur during the acquisition of a slice ("intra-slice" motion) or a volume ("intra-volume" motion), or between the acquisitions corresponding to different orientations of diffusion sensitization ("inter-volume" motion). It results in two kinds of motion-related errors: 1) artifacts within a volume (signal irregularities and potential outliers with near-complete signal dropout that generate "black stripes" artifacts along the slice direction, when images are viewed from the side, or signal loss in a region of the brain, due to repeated excitation of spins during slice selection); and 2) 3D misregistration between the volumes acquired before and after the movement. Other artifacts are also frequently observed in DW images, independently of subject's motion, because of hardware problems during acquisition like mechanical vibrations [4] or spike noise [5]. The impact of such corrupted data on DTI and QBI metrics has recently been highlighted with simulations [6].

MR diffusion techniques are particularly informative to explore the developing brain [7,8], but they are challenging in non-sedated infants [9,10] because of their sensitivity to subject's motion. To improve data quality, the first step is to optimize data acquisition. Short acquisition times, relying on low orientation number, are generally used, but at the expense of accuracy. DWI and DTI sequences performed within a breath-hold of the mother have been devised for fetal brain imaging [11]. Continuous scanning has also been performed in order to acquire repeated series, whose volumes have to be registered a posteriori [12]. Alternatively, DTI acquisitions may be adapted in real time according to patient motion, by continuously adjusting all applied gradients to compensate for changes in head position [13], by identifying corrupted data according to the position and the magnitude of the largest echo-peak in the k-space [14], or by directly evaluating the quality of DTI maps, which are estimated on-line [15]. The implementation of a self-navigation scheme with variable density spiral acquisition gradients has also enabled to remove both eddy current distortions and motion artifacts in the adult brain [16]. To deal with mechanical vibrations, Gallichan and colleagues [4] recommended a full Fourier k-space sampling, but this increases the minimum echo time and decreases the slice number available per repetition time. In infants, specific spatial distributions of diffusion orientations, which take into account their temporal order during acquisition, have enabled to reliably estimate the diffusion tensor even if the acquisition is interrupted due to motion [3,17].

Another direction to deal with motion in DW images is to apply post-processing correction strategies, which definitely help improve the precision and accuracy of the metrics estimation in DTI [18] and HARDI imaging [19]. The most common registration technique corrects for eddy current distortions and 3D motion [20], and is based on mutual information between diffusion orientation volumes and a reference volume, with a subsequent rotation of the B-matrix before analysis of DW images [20,21]. Integrating motion in the signal model used for the tensor estimation seems to perform superiorly compared with the conventional method [22]. In pediatric patients, an automated reconstruction software has recently been implemented [10], but it requires a dedicated acquisition for Nyquist ghost calibration and parallel imaging GRAPPA weight. These post-processing strategies hardly correct for within-slice artifacts, which are frequently observed in rapidly moving subjects like infants or due to mechanical vibrations or spike noise. The easiest solution to deal with these artifacts is to exclude the whole corrupted volumes on a simple visual basis, but it is time consuming, dependent on the experimenter and it also potentially removes uncorrupted slices. Automatic detection of outliers has previously been performed through linear correlation coefficients between DW volumes [10], during a robust estimation of the diffusion tensor [23], or by finding the local maxima on the Laplacian of DW signals across diffusion orientations [24]. For the correction of detected outliers, methods include removing such voxels [23] or volumes [10], fitting the signal using linear regression methods [4], or interpolating the Q-space signal directly on the spherical shell [6]. Recently, an algorithm which detects and removes outliers prior to 3D resampling, while taking misalignment into account, has been proposed [9]. Despite their respective advantages, all these approaches also present some drawbacks: rejecting instead of correcting the corrupted data, making hypothesis on the diffusion model, etc.

Alternatively we here propose a global post-processing methodology for automatically correcting all motion-related artifacts in DW images before computing the diffusion model. It is based on two successive steps: 1) automated detection and 2D resampling of slices corrupted by motion or technical problems (mechanical vibrations, spike noise); 2) 3D realignment of orientation volumes misregistered due to inter-volume motion and distortions stemming from eddy current. This correction strategy was applied on DTI data from 20 non-sedated infants, aged from 6 to 22 weeks. First, the two steps of the methodology were validated by simulating motion in an uncorrupted dataset. Second, we applied this strategy to all infants, and we studied quantitatively the immature cortico-spinal tract, because its development has already been detailed over this age range.

2. Materials and methods

2.1. Description of the correction method

Our post-processing strategy takes advantage of a high diffusion orientation number to correct for corrupted (also called outlier) images. It relies on two successive steps: 2D resampling of the outlier individual slices, followed by 3D registration and correction of the eddy current distortions in the resulting volumes (Fig. 1). It is implemented within BrainVISA [25] in the Connectomist toolbox [26].

2.1.1. Detection of outlier slices

To detect corrupted slices, the basic concept is to compare the DW image for the i^{th} orientation O_i to all the other orientations (O_j, $j \neq i$), for each slice independently. To do so, the b = 0 image is used as a reference and, a distance between it and each DW O_i image is computed. The mutual information (MI) coefficient [27,28] was chosen because it does not impose any particular relationship between images (except sharing some information), which makes the measurement independent of the grey level intensity that is variable across diffusion orientations, and it is a reliable and robust criterion to compare b = 0 and DW images and correct eddy current distortions [29]. The outlier detection in a given slice s is done with a simple criterion: slice s for the orientation O_i is considered as an outlier if its MI coefficient is not in the range: mean $\pm$ f x StdDev, where the mean and standard-deviation (StdDev) of MI coefficients are computed over all orientations (the median values were systematically computed and found almost equal to the means). The f factor is the only parameter to be tuned once for a specific protocol (see below). This strategy for outliers detection is fully automatic. Note that several DW images (for different orientations O_i) may be corrupted in the same slice. On the other hand, several slices may be corrupted at the same diffusion orientation, which may reveal a weakness of the gradient power amplifier or a vibration problem, in the absence of motion.

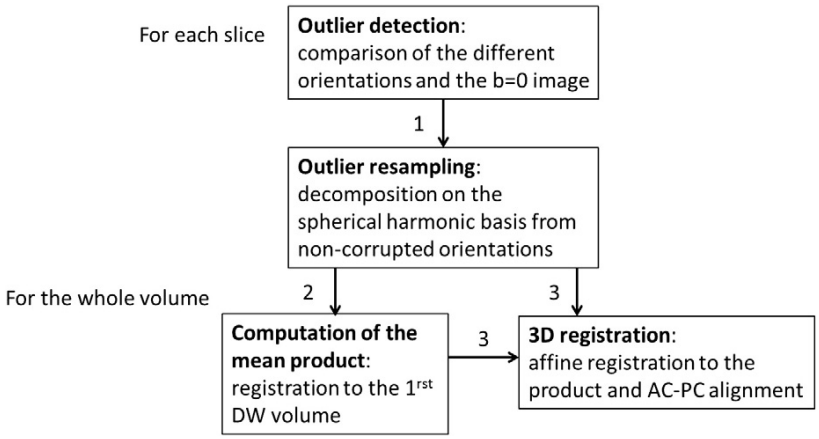

Fig. 1. Schematic summary of the 2-step correction strategy. The successive steps to correct motion artifacts are detailed schematically.

2.1.2. Resampling strategy of outlier slices

When an outlier is detected using the previous criterion, our strategy consists of resampling it instead of discarding the corresponding diffusion orientation from the set of available DW data. Corrections are performed through resampling from the non-outlier DW images in the Q-space. A decomposition of the DW signal is performed over the non-corrupted orientations, by using the modified spherical harmonics basis (SH) proposed by Frank [30]: for acquisitions performed on a single shell q, the signal of each voxel can be decomposed on this basis Ψ: $S\left(q\vec{u}\right) = S_0 \sum_j SH(q,j)\Psi_j\left(\vec{u}\right)$, where $\vec{u}$ represents a normed vector coding for the diffusion orientation. This decomposition is limited to the 6th order to avoid overfitting, and some regularization is introduced by Descoteaux and colleagues to improve its reliability [31]. The resulting SH coefficients are used to compute the "theoretical" signal values along the orientations corresponding to rejected outliers. Thus, in a given slice, corrupted DW images are replaced by these images interpolated onto the SH basis computed from the set of non-corrupted DW images. Such interpolation should be applied to images with relatively high signal-to-noise ratio (greater than ~4) as the Laplace–Beltrami regularization imposes a Gaussian noise model.

Note that the outlier detection and resampling are performed first, independently for each slice and before the 3D volume registration, because rapid-motion artifacts generally corrupt 2D slices. Consequently, we cannot exclude potential contributions from "inter-volume" motion. Nevertheless, these contributions are expected to be small in comparison with the potential impact of 2D outliers on the 3D registration, and not the whole volume is modified when only a single slice is corrupted (this hypothesis was tested by simulations in Section 2.2.4.5). Furthermore, this approach does not rely on strong hypothesis concerning the diffusion model, except that it can be decomposed onto an SH basis, contrarily to a previous approach which considered a diffusion tensor model [6].

2.1.3. 3D volumes registration of the different orientations

To correct both motion misregistration and eddy current distortions, the volumes corresponding to the different diffusion orientations are realigned according to an original strategy based on mutual information. In the conventional strategy [20], all orientation volumes are registered to the b = 0 volume, but registration may be impaired by the difference in signal intensity from the cortico-spinal fluid (CSF) between the b = 0 volume (high signal) and the DW volumes (null signal). To gain in robustness, the 3D registration was here performed in two consecutive steps. First, all orientation volumes were registered to the first DW orientation volume according to the maximization of 3D MI coefficients, based on an affine transformation with shearing. Then the geometric mean product of all DW volumes was computed: $\left(\prod_{i=1}^{N} V_{Oi}\right)^{1/N}$, where N represents the total number of orientations, and realigned to the volume acquired with b = 0 s.mm^{-2}. Second, all initial orientation volumes were registered to this realigned product and resampled. A further 3D rigid transformation can be optionally added to put the corrected data into Talairach space by aligning the anterior and posterior commissures (AC-PC) in a single axial slice (see the application Section 2.2.5). The assigned diffusion orientations are subsequently corrected by applying the rotation stemming from the resulting transformation [20,21]. Since registration is based on an affine transformation with scaling and shearing, it corrects for both 3D misregistration between volumes and eddy current distortions at the same time.

2.2. Method evaluation and validation

Correction strategies were evaluated on brain DTI images of adults and of non-sedated infants, as these subjects are particularly prone to motion during MR acquisitions. Five strategies were compared: #1 no correction, #2 visual rejection of corrupted volumes, #3 resampling of outlier slices alone, #4 3D motion registration alone and #5 2-step correction strategy (corresponding to strategy #3 followed by strategy #4). First, the outlier detection was evaluated in adults' data with vibration- or motion-related artifacts. Motion was also simulated to further validate the method with ground-truth knowledge stemming from an uncorrupted infant dataset: corrupted slices were introduced randomly (simulation of random "intra-slice" and "intra-volume" motion) or around a specific orientation (simulation of a systematic equipment vibration effect) to test the resampling of outlier slices (strategy #3); random translations and rotations were also introduced to test the 3D motion registration (strategy #4). Second, the two steps (strategy #5) were combined to correct real motion on an adult who moved on purpose. Third, the five strategies were applied to the whole infant group, and we focused on the cortico-spinal tract, as an example of a well-described fasciculus, relatively mature in the developing brain.

2.2.1. Subjects

The study was performed on two adults and 20 healthy infants born at term (details in Table 1). The MRI protocol was approved by the regional ethical committee for biomedical research, and all subjects or parents gave written informed consents. Infants were non-sedated and spontaneously asleep at the beginning of MR imaging, but some of them moved during acquisition (see the Results section for details). Particular precautions were taken to minimize noise exposure, by using customized headphones and covering the magnet tunnel with special noise protection foam.

2.2.2. Data acquisition

Acquisitions were performed on a Tim Trio 3 T MRI system (Siemens, Erlangen), equipped with a whole body gradient (40 mT/m, 200 T/m/s) and a 32-channel head coil. A DW spin-echo single-shot EPI sequence was used, with parallel imaging (GRAPPA reduction factor 2), partial Fourier sampling (factor 6/8) and monopolar gradients to minimize mechanical and acoustic vibrations. Interleaved axial slices covering the whole brain (50 for infants, 70 for adults) were imaged with a 1.8 mm isotropic spatial resolution (matrix = 128 × 128). After the acquisition of the b = 0 volume, diffusion gradients were applied along 30 orientations with b = 700 s. mm^{-2} (TE = 72 ms, TR = 10 s for infants, 14 s for adults). An adult moved on purpose in a first acquisition and remained motionless in a second scan to get a reference unbiased dataset. For another adult, because of technical problems, data were corrupted with vibration-related artifacts (located in the occipital lobe over 25 slices) for orientations of the diffusion gradients along the x-axis. From this dataset we selected 5 datasets of 25 orientations including 1 to 5 artifacted orientations.

Table 1
Summary of the numbers of corrected volumes for the different strategies.

For each infant, the age and the number of volumes corrected for the four applied strategies are specified in comparison with no correction. For all parameters, the mean and standard deviations over the 20 infants are detailed, as well as the minimum and maximum values.

Subjects		Mean count of subjects' corrected volumes						
#	Age	Manual	Outlier correction		3D registration		2-step correction	
	(Weeks)	Rejection	Dif >0%	Dif >1%	Dif >1%	Dif >5%	Dif >1%	Dif >5%
1	5.9	8	2.3	1.5	26.6	15.0	26.6	15.2
2	7.4	0	0.9	0.3	6.2	0.0	6.5	0.1
3	9.7	0	0.9	0.1	15.4	0.0	15.6	0.0
4	9.9	3	1.2	0.3	22.5	6.8	22.5	6.9
5	11.1	3	2.4	0.6	23.3	4.0	23.3	4.3
6	11.3	5	2.2	1.5	28.3	23.2	28.5	23.7
7	11.6	6	3.2	1.7	21.2	7.7	21.4	8.5
8	11.7	0	0.0	0.0	11.2	0.0	11.2	0.0
9	11.7	1	2.5	0.9	8.5	0.3	8.8	0.3
10	12.7	3	1.0	1.0	23.0	12.3	23.3	13.2
11	13.1	0	0.8	0.2	8.3	0.1	8.4	0.2
12	13.3	0	0.2	0.1	6.9	0.0	7.0	0.0
13	13.7	0	0.6	0.3	11.9	0.1	12.0	0.1
14	15.0	2	0.7	0.6	14.9	1.2	15.1	1.6
15	15.6	3	1.9	0.8	17.9	4.0	18.3	4.3
16	16.3	0	0.0	0.0	10.9	0.1	10.9	0.1
17	17.6	0	1.0	0.7	23.6	3.7	23.6	3.7
18	18.0	0	2.2	0.1	8.1	0.0	8.1	0.0
19	21.4	6	1.9	1.5	21.1	5.7	21.4	6.1
20	22.4	0	0.6	0.2	17.6	0.0	17.5	0.1
Mean	13.5	2.0	1.3	0.6	16.4	4.2	16.5	4.4
std-dev	4.2	2.5	0.9	0.6	7.1	6.2	7.1	6.4
min	6	0	0.0	0.0	6.2	0.0	6.5	0.0
max	22	8	3.2	1.7	28.3	23.2	28.5	23.7

2.2.3. DTI post-processing and tractography

For each set of DW images (corrected or not), the diffusion tensor parameters were estimated in each voxel using BrainVISA software [25]. DTI maps were generated (mean < D>, longitudinal $\lambda_{//}$ and transverse $\lambda_{\perp}$ diffusivities, fractional anisotropy FA and color-encoded directionality RGB). 3D tractography was performed using regularized particle trajectories [32], with an aperture angle of 45° and from a whole-brain mask excluding voxels with low FA (<0.15) or high < D > (>$2.10^{-3}mm^2.s^{-1}$), which may correspond to grey matter or CSF ([33]). Because its reconstruction requires an accurate matching of the slices, the cortico-spinal tract was selected with manual regions and split between the cerebral peduncles and low centrum semiovale for quantification of DTI parameters [33,34].

2.2.4. Validation of the correction strategies

2.2.4.1. Validation of the detection of outlier slices (strategy #3): adult dataset. For the adult datasets (motion on purpose and vibration-related artifacts), different detection factors f were tested, from f = 3 to f = 1. The slices automatically detected as outliers were compared with the slices visually labeled as outliers. We computed the percentage of false-negative detection, characterizing the outliers missed by the automatic method, and the percentage of false-positive detection, describing the over-detection errors.

2.2.4.2. Validation of the resampling of outlier slices (strategy #3): simulations of motion. We further selected the data from a single infant who had not moved at all during the acquisition (subject #8 from Table 1, middle age of 11.7w) and compared the corrected datasets (after simulating different kinds of motion) with the reference dataset (the real uncorrupted dataset). On the one hand, random intra-slice motion was simulated by introducing different numbers (from 1 to 5 over 30) of outlier orientations in a given slice (by making the DW signal aberrant). Ten random sets of corrupted orientations were tested for each number of outliers, and 3 random slices were independently corrected. On the other hand, vibrations and miscalibration of a gradient were simulated by corrupting gradient(s) around a specific diffusion orientation: the read axis (along which the echo-planar echo-train is collected) was considered because it is highly and frequently on demand in MR scanners, and it may induce mechanical vibrations due to the coupling of the gradient coil, the subject itself and the table [4]. All slices of the corresponding volumes were considered as outliers since such artifacts affect the whole volume. The strength of the vibrations was taken into account by increasing the conic angle of the corrupted DW orientations. For our specific set of 30 orientations (Siemens package VB15), it concerned 1 orientation (angle 0°), 2 orientations (up to 11.5° around x), 3 orientations (up to 23.5°), and 5 orientations (up to 31.5°).

For both the simulated random motion and the vibrations, the corrected datasets (with resampling of the outlier slices—strategy #3—or by exclusion—strategy #2) were compared with the acquired reference dataset. First, the resampled DW signal within each voxel of the outlier slices was compared with the reference signal in order to investigate the impact of the number of outliers and of the kind of motion (random or vibration) on the resampling performance. Mean normalized deviation was computed as $\frac{1}{N_{voxel}}\sum_{voxel}\left|\frac{S_{reference}-S_{resampled}}{S_{reference}}\right|$, where N is the number of voxels in the outlier slice excluding voxels in the surrounding noise. The percentages of voxels with signal values different for more than 5% or 10% of the reference were evaluated. Second, we assessed the errors in the estimation of the direction of the main tensor eigenvector $e\vec{v}$: the averaged angle between the reference and the corrected eigenvectors was computed

as $\frac{1}{N_{voxel}}\sum_{voxel}\arccos\left(\frac{e\vec{v}_{reference}\bullet e\vec{v}_{reference}}{|e\vec{v}_{reference}|\times|e\vec{v}_{reference}|}\right)$. Since these errors may depend on the local accuracy of the tensor model and on the ratio between the first, the second and the third eigenvalues, we segregated the voxels according to FA values: three independent classes of voxels were considered with FA in the range [0.1–0.3], [0.3–0.5] and [0.5–1]. Third, we focused on the corrected FA maps generated from the 30 diffusion orientations after resampling or exclusion of outliers, and we reported differences within slices relatively to the reference FA map in terms of mean normalized deviation and percentages of voxels with FA values differing by more than 5% and 10% as previously mentioned. For each measure, the average values and standard deviations were computed over all the considered slices and over all the corrupted sets of orientations within a given number of outliers.

2.2.4.3. Comparison of methods to correct outlier slices (strategy #3): adult dataset. Our method to correct outliers was qualitatively compared with a widely-used approach (RESTORE [23]). Because the steps for outlier detection and 3D motion registration are not applied in the same order in these two approaches (outliers are first corrected with our method, and secondly excluded with RESTORE), we focused on data without 3D motion by considering the adult dataset corrupted with vibration-related artifacts for 1 orientation.

2.2.4.4. Validation of the 3D motion registration (strategy #4): simulations of motion. First, we checked whether eddy current distortions were finely corrected by strategy #4 by registering in 3D the uncorrupted DW volumes to the product of DW images. MI coefficients were computed between the b = 0 and DW images, and were compared between the initial and the registered DW images using a paired t-test across all slices and all diffusion orientations.

Second, specific translations and rotations were introduced in the initial uncorrupted dataset for a given diffusion orientation in order to assess the strategy robustness in case of motion. Increasing shifts (from 1 to 5 mm) and angles (from 1 to 5°) were applied independently along the three spatial axes (x, y and z). According to strategy #4, the shifted volumes and the initial dataset were independently registered to the product of DW images based on mutual information, in such a way that eddy current distortions were corrected in the same way and that both datasets were resampled. As in the previous Section (2.2.4.2), the resulting registered datasets were compared in terms of DW signal (mean normalized deviation, percentages of voxels with values differing by more than 5% and 10%), direction of the main eigenvector (averaged angle errors for voxels with FA in the range [0.1–0.3], [0.3–0.5] and [0.5–1]), and FA within slices (mean normalized deviation, percentages of voxels with values differing by more than 5% and 10%).

2.2.4.5. Validation of the 2-step correction strategy (strategy #5): simulation of motion and adult dataset. First, we tested whether it is justified to perform first the outlier detection step, before the 3D volume registration. In the uncorrupted infant dataset, we introduced both an outlier volume for a specific orientation (as in Section 2.2.4.2) and a 3D motion for another volume (as in Section 2.2.4.4), because motion that corrupts 2D slices generally leads to the 3D misalignment of next DW volume.

Second, in the adult dataset with intentional movements, the two steps (strategy #5) were combined to correct motion artifacts. For both the corrected and the uncorrected datasets, errors in terms of DW signal, direction of the main eigenvector and FA were computed relatively to the reference dataset without motion and compared in order to evaluate the correction effects.

2.2.5. Evaluation of the correction strategies: optimization over the infant group

2.2.5.1. Implementation of motion correction strategies. For each infant, experimenter JD performed visual rejection of corrupted volumes (strategy #2): whole volumes were rejected if they presented typical signal dropout ("black stripes" when viewed from the side), while volumes with minor irregularities in the diffusion signal were kept (see Fig. 2 for examples).

For the automatic detection of outlier slices (strategies #3 and #5), the choice of the f factor was based on the distributions of MI coefficients (between the b = 0 image and the non-corrected DW images) across all diffusion orientations. Histograms computed for typical subjects and slices were screened to decide which criteria to use for the detection of corrupted data (factor f). Examples are presented in Fig. 3.1 for two specific infants. For the quiet infant (Fig. 3.1.a) all MI coefficients were always in the range mean ± f x StdDev for f = 3, but not for f = 2. For the moving infant (Fig. 3.1.b) the distributions were more spread because of a drifting effect of MI coefficients due to inter-volume motion (Fig. 3.2.): MI coefficients of corrupted DW data were far from the distribution peak, and the factor f = 3 enabled to detect these outliers. These observations were similar across all infants and slices, so a value f = 3 was applied to detect the most corrupted slices.

Besides, a resampling of DW images was performed for all strategies (even if no correction or registration was performed) in order to align the anterior and posterior commissures (AC-PC) in a single slice. This realignment aimed to provide a consistent color coding on directionality RGB maps across all infants, despite the variability in brain positions that resulted from how the infant fell asleep. For strategies #4 and #5, this resampling was applied jointly with the 3D-motion registration by composing the two transformations. After the AC-PC placement all orientation volumes resulted in 60 slices, the first and last of which being possibly cut or empty when the anterior and posterior commissures were already well-aligned in the initial brain orientation. Thus only the 40 central slices were considered when a global estimation of the corrections over the brain was required.

2.2.5.2. Comparison of motion correction strategies. In each infant we quantitatively evaluated and compared the correction strategies by computing the MI coefficients between b = 0 image and DW image for each slice and diffusion orientation. For each orientation the MI coefficients were also averaged over the 40 central slices. For each correction strategy, the MI coefficients were compared with the coefficients from the initial images. For strategy #2 we reported non-null or 1% larger differences. For strategies #4 and #5 we only reported differences larger than 1% or 5% because the 3D realignment always implied small corrections for eddy current distortions (differences between 0 and 1%). For strategies #3, #4 and #5, we also computed an apparent number of corrected volumes (by dividing by 40 the number of corrected slices within the 40 central slices) in order to facilitate the comparison with strategy #2 which excluded whole volumes. Besides, our 2-step approach was qualitatively compared with RESTORE method in terms of RGB maps.

2.2.5.3. DTI quantification over the infants group. Because the range of ages was restricted to a short developmental period, linear models between DTI parameters in the cortico-spinal tract and age provided the best fits across the infants group as compared with quadratic models. For each correction strategy, we computed correlation coefficients R, as well as mean, minimal and maximal values over the group, and standard deviations after taking into account the significant linear age-related effects. For the strategies comparison, note that lower standard deviations mean better registration across

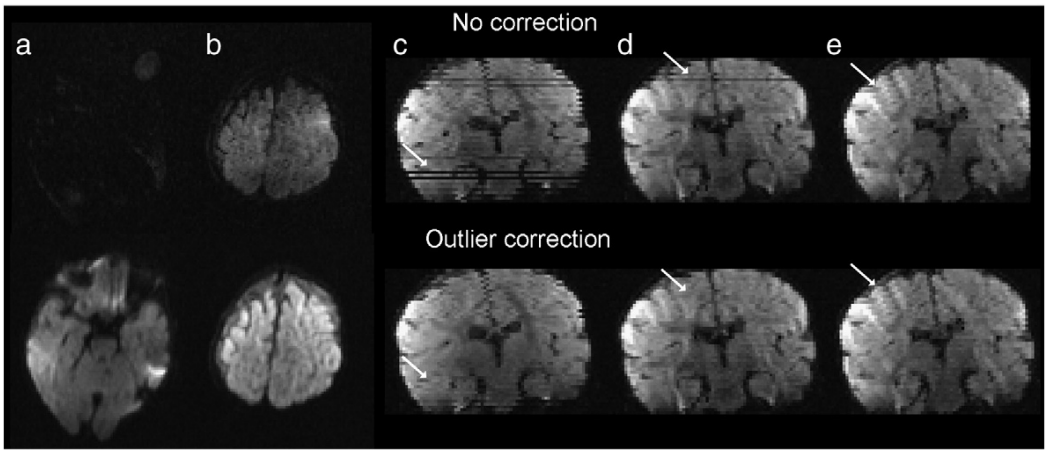

Fig. 2. Automated resampling of corrupted slices. DW images of a 21.4 week-old infant are presented for different slices and different orientations of the diffusion gradients without any correction (first row) and after resampling for the detected outlier slices with f = 3 (second row). Slices are presented in axial (a, b) or coronal views (c–e: arrows in c and d respectively correspond to slices in a and b). Corrupted slices resulting from fast motion during the volume acquisition (a–d) were finely resampled whereas minor irregularities in the diffusion signal (arrow in e) were not corrected. Strategy #2 performed in the same way (visual rejection of volumes a–d, but not of volume e).

babies, and thus better motion correction. Higher FA values also mean better delineation of the fasciculus according to surrounding tissue and less partial volume effect.

3. Results

3.1. Validation of the correction strategies

3.1.1. Validation of the detection of outlier slices (strategy #3): adult datasets

In the dataset from the adult who moved on purpose, no more than 4 orientations per slice were corrupted. For detection factors f higher than 2.4, the percentage of false-negatives was around 60%, and no false-positive was detected. Then the false-negative percentage decreases and the false-positive percentage increases with decreasing factor, and both percentages were balanced at 40% for f = 1.2. The false-negative percentage did not pass the 10% threshold for reasonable f factors (f > 1). For this dataset, the false-negative percentage was quite high in comparison with the false-positive percentage.

In the adult dataset corrupted with vibration-related artifacts, similar patterns were observed. The false-negative percentage was below 10% for false-positive percentage equal to 15% for 1 corrupted orientation (f = 3), and around 50% for 2 to 5 corrupted orientations (f = 1.8 to 1.2). Furthermore, the values for balanced false-negative and false-positive percentages increased with the number of corrupted orientations, from 30% to 42% for 2 to 5 orientations (f = 2.1 to 1.6). Consequently, the performances of the detection approach were reasonable but decreased with the degree of data corruption.

3.1.2. Validation of the resampling of outlier slices (strategy #3): simulations of motion

Considering the infant dataset where motion-related artifacts were introduced, the slices that were corrected for random outliers presented a mean normalized deviation in DW signal of 5.1% ± 0.6% in comparison with the reference and on average over the different outlier numbers. 34% ± 4% (resp. 11% ± 3%) of voxels within the corrected slices showed signal differences higher than 5% (resp. 10%). The number of random outliers had no influence on these deviations (Fig. 4.a). Concerning the resampling of outliers stemming from vibration-related artifacts, the mean normalized deviations and the percentages of voxels with differing signals were higher and increased with the number of outliers (Fig. 4.a).

In terms of angular errors in the main eigenvector direction (Fig. 4.b), the strategy of outliers resampling performed better than the strategy of outliers exclusion, both for randomly distributed outliers and for outliers along a specific orientation in the case of vibrations. Errors were particularly small when resampling the random outliers (for instance, for 5 outliers: 5.0° ± 0.5° for voxels with FA in [0.1–0.3]; 2.7° ± 0.6° for voxels with FA in [0.3–0.5]; 1.9° ± 1.1° for voxels with FA in [0.5–1]). On the contrary, errors were quite large when excluding the outliers along the x-direction (up to 18.9° ± 0.6° for 5 outliers for voxels with FA in [0.1–0.3]), suggesting that the exclusion strategy was not appropriate to correct important vibrational artifacts. Because the tensor estimation is based on the whole set of 30 orientations, errors increased with the number of outliers. Larger errors were observed when resampling the vibration outliers in comparison with the random outliers, highlighting the impact of orientation distribution over the space. Finally, angular errors differed according to FA ranges, with higher errors in low-FA voxels where the tensor model estimation was less reliable (for instance, for the resampling of 5 vibration outliers: 7.6° ± 0.7° for voxels with FA in [0.1–0.3]; 4.1° ± 0.9° for voxels with FA in [0.3–0.5]; 2.8° ± 1.0° for voxels with FA in [0.5–1]).

For both the random motion and vibration outliers, errors in FA estimation were of the same order of magnitude as errors in DW signal (Fig. 4.c). No significant difference was observed between the strategies of outliers resampling and exclusion in terms of mean normalized deviations to the reference (up to 8% ± 0.3%) and percentages of voxels with differing FA values (5%: up to 51% ± 1%; 10%: up to 27% ± 1%). As for angular errors in the main eigenvector direction, these deviations increased drastically when the outlier number increased from 1 to 5 (Fig. 4.c). This reflects the high dependence of the tensor estimation on the acquired number of orientations. For an equivalent number of outliers, the mean normalized deviations and the voxel percentages were again higher for outliers along a specific orientation (vibrations) than for outliers along orientations randomly distributed over the whole space (random motion) (Fig. 4.c).

All these results together suggest that artifacts due to technical problems (vibrations) may impair the robustness of DTI quantification more than a reasonable random motion. Even if the strategy of exclusion is less sensitive than the signal geodesic interpolation on

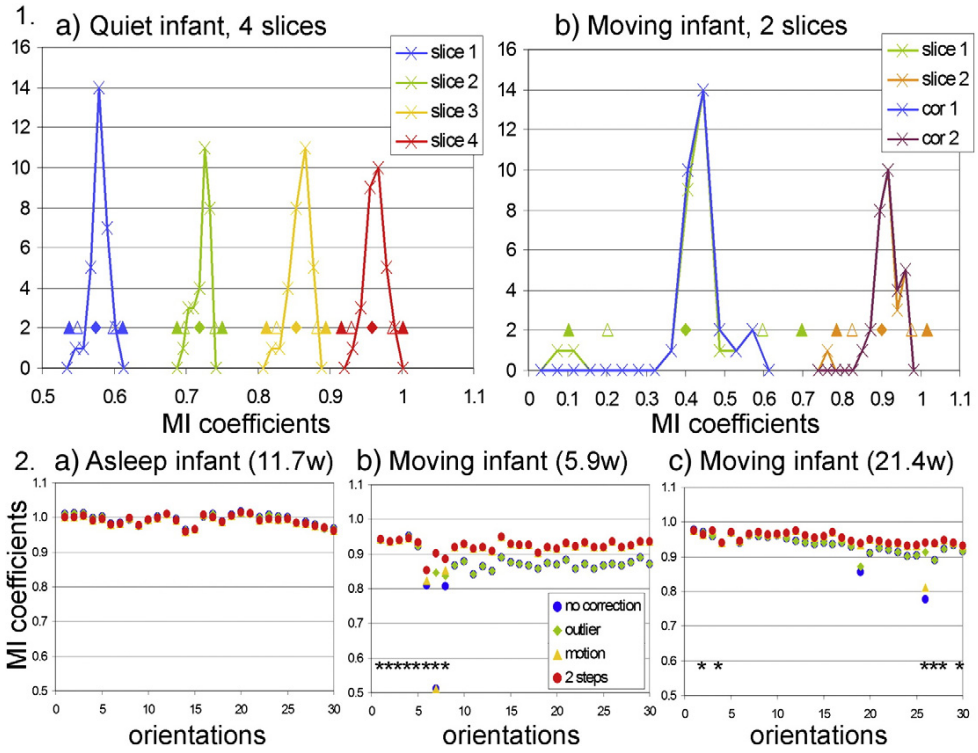

Fig. 3. Variations of MI coefficients across the diffusion orientations. 3.1. Examples of MI distributions are presented for different slices of two infants (quiet infant in Figure 3.1.a, moving infant in Figure 3.1.b), with the mean (diamond signs) and the intervals mean ± f × StdDev for f = 2 (empty triangle signs) and f = 3 (filled triangle signs). 3.2. For three infants, averaged MI coefficients are plotted over the 30 orientations for the strategy without correction (blue dots, strategy #1) and for the strategies with resampling of outlier slices (green diamonds, strategy #3), with 3D registration (yellow triangles, strategy #4), and with the 2-step correction (red dots, strategy #5). The first infant (a: #8 from Table 1) was quietly asleep whereas the two others (b, c: #1 and 19 from Table 1) moved a little during acquisition (the orientations rejected with strategy #2 are highlighted with stars). In comparison with the other corrections, the 2-step strategy enabled to drastically homogenize the MI coefficients over the 30 orientations.

the diffusion shell, errors cannot be avoided when the signal sampling is missing around a specific orientation. In our analyses, resampling outliers according to the spherical harmonics basis appeared as the most reliable strategy.

3.1.3. Comparison of methods to correct outlier slices (strategy #3): adult dataset

For the adult dataset with vibration-related artifacts for 1 orientation over 25, our approach could provide correct RGB maps contrarily to RESTORE (Supplementary Fig. 1).

3.1.4. Validation of the 3D motion registration (strategy #4): simulations of motion

Eddy current distortions were finely corrected when the initial dataset was registered to the product of DW images, as assessed visually and by the increase in MI coefficients between b = 0 images and DW images (paired t-test across slices and orientations: $t = 14$ $p < 0.001$).

Correcting the 3D-motion after introducing translations or rotations on purpose to the uncorrupted dataset triggered relatively small errors in comparison with the reference, and there were no influence of the motion kind or amplitude (for up to 5 mm and 5°). These errors were smaller in comparison with the outlier resampling, in terms of DW signal (on average over all translations and rotations, mean normalized deviations: 2.7% ± 0.5; percentage of voxels with differences >5%: 14% ± 4%; percentage of voxels with differences >10%: 5% ± 2%), tensor main eigenvector direction (angle errors: 0.18° ± 0.01° for voxels with FA [0.1–0.3]; 0.09° ± 0.01° for voxels with FA [0.3–0.5]; 0.09° ± 0.08° for voxels with FA [0.5–1]) and FA estimation (mean normalized deviations: 2.1% ± 0.2%; percentage of voxels with differences >5%: 14% ± 2%; percentage of voxels with differences >10%: 5% ± 1%). On the contrary, translating a single volume by 5 mm and not correcting it can lead to large angle errors in the tensor main direction (FA [0.1–0.3]: 9.1° ± 1.2°; FA [0.3–0.5]: 4.8° ± 1.9°; FA [0.5–1]: 6.7° ± 11.6°). Consequently, correcting such 3D motion with our approach appeared to be worthwhile and efficient.

3.1.5. Validation of the 2-step correction strategy (strategy #5): simulation of motion and adult dataset

When both a corrupted volume and a 3D-moved volume were simultaneously introduced in the uncorrupted infant dataset, the outlier detection step finely detected the corrupted volume, whereas the 3D-moved volume was not detected for translations up to 5 mm. Less than 3 peripheral slices were detected for rotations up to 5° (1 slice for 1° and 2° rotations, 2 slices for 3° rotations), except for 5° rotation along z (14 slices detected). Since smaller amplitudes of 3D motion are generally observed in infants, this simulation justified to perform the outlier detection step before the 3D volume registration.

For the adult dataset moved on purpose, the deviation errors computed according to the reference unmoved dataset were relatively high in terms of DW signal (mean normalized deviation: 18%; percentage of voxels with differences >5%: 73%; percentage of voxels with differences >10%: 51%), tensor main eigenvector

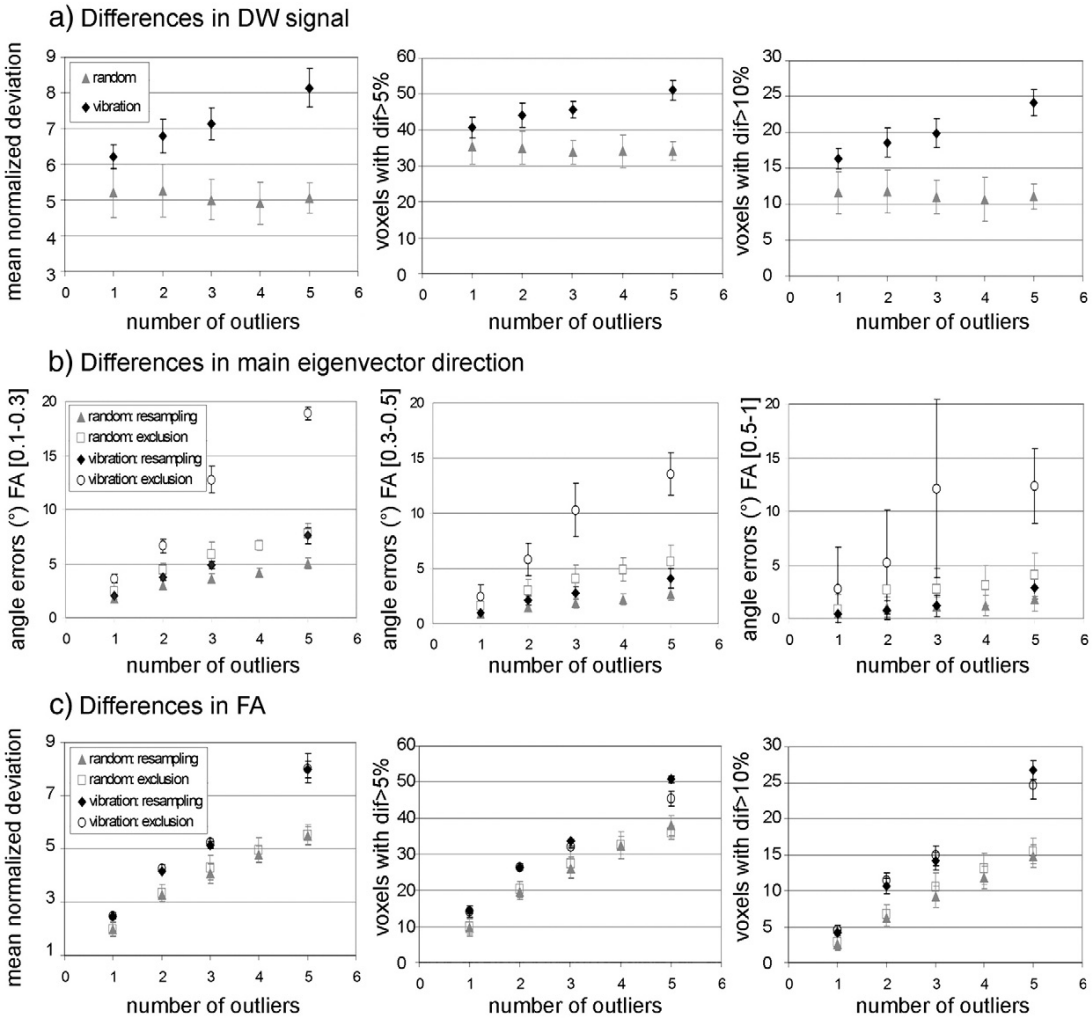

Fig. 4. Validation of the outliers resampling strategy. Deviations from the reference are presented after resampling or excluding 1 to 5 random or vibration-related outliers introduced in an uncorrupted dataset. For deviations in DW signal (Figure 4.a) and in FA (Figure 4.c), mean normalized deviations are presented (left column in %), as well as the percentages of voxels presenting differences larger than 5% (middle column) and 10% (right column). For angle errors in the tensor main direction (Figure 4.b), three classes of voxels are considered according to FA (left column [0.1–0.3], middle column [0.3–0.5], right column [0.5–1]).

direction (angle errors: 38° for voxels with FA [0.1–0.3]; 41° for voxels with FA [0.3–0.5]; 43° for voxels with FA [0.5–1]) and FA estimation (mean normalized deviations: 38%; percentage of voxels with differences >5%: 90%; percentage of voxels with differences >10%: 80%). The 2-step correction strategy enabled to significantly reduce these errors for DW signal (mean normalized deviation: 10%; percentage of voxels with differences >5%: 62%; percentage of voxels with differences >10%: 35%) and tensor main eigenvector direction (angle errors: 31° for voxels with FA [0.1–0.3]; 32° for voxels with FA [0.3–0.5]; 33° for voxels with FA [0.5–1]). For FA estimation, the errors remained high (mean normalized deviations: 32%; percentage of voxels with differences >5%: 89%; percentage of voxels with differences >10%: 80%), probably because the corrected dataset did not match entirely the reference dataset, which was not corrected for 3D motion and eddy current distortions. These results highlighted the correct performances of our correction approach but also the difficulty to compare successive acquisitions that present intrinsic variability: spatial variability due to varying head position, and signal variability caused by different technical tuning.

3.2. Comparison of the correction strategies over the infant group

High-quality DW images were acquired in all infants (mean SNR measured on b = 0 image in frontal white matter: 184 ± 32). Because of small movements during sleep, we visually detected some motion artifacts in 10/20 infants, concerning 1 to 8/30 orientations (see Fig. 2). For strategy #2, it led to a mean visual rejection of 2 ± 2.5 orientations over all infants (range: 0–8, Table 1).

3.2.1. Evaluation of the correction of outlier slices (strategy #3)

The detection of outlier slices performed finely with a factor f = 3 and detected all visually corrupted slices (Fig. 2). In all infants, no more than 5 orientations per slice were resampled by this strategy, which means that the SH decomposition was

performed over at least 25 orientations according to our acquisition sampling scheme. Over all orientations and in all infants, strategy #3 modified 1.3 ± 0.9 volumes (range: 0–3.2 volumes) (Table 1, strategy #3), which was less than the visual rejection. The corrections were small since only 0.6 ± 0.6 volumes on average showed differences in MI coefficients higher than 1%.

The number of automatically resampled volumes was highly correlated with the number of visually rejected volumes across infants (correlation coefficient for non-null differences R = 0.68; for differences higher than 1% R = 0.89), showing that both methods did perform comparably, but the slices visually rejected and those automatically resampled were not exactly the same. Indeed, the visual method rejects the whole volume when it appears visually corrupted, whereas the automated method only resamples part of the volume, i.e., the corrupted slices. Conversely, the latter method also corrects for small flaws detected in slices of non-rejected volumes, which are wrongly not taken into account by the experimenter in the visual exclusion step, e.g. at the bottom of the brainstem or at the top of the brain. Altogether, the automated resampling of outlier slices modified on average a smaller number of volumes, and has the advantages to be automated and independent from the experimenter, therefore fully reproducible. In addition, it allows us both to keep uncorrupted data within each volume, and to detect and correct subtle artifacts that are not readily visible on visual inspection.

3.2.2. Evaluation of the 3D motion registration (strategy #4)

To correct for 3D motion and eddy current distortions, the registration to the mean geometric product outperformed the conventional registration to b = 0 image in all infants except 3. It corrected 16.4 ± 7.1 volumes on average over all infants when considering MI differences larger than 1% (range: 6.2–28.3) (Table 1). This expected large number of corrected volumes is due to the correction of eddy current distortions, performed even when the infant did not move at all. But those corrections were actually small, since this number fell to 4.2 ± 6.2 volumes (range: 0–23.2) when considering MI differences larger than 5%.

3.2.3. Evaluation of the 2-step correction strategy (strategy #5)

Combining the resampling of outlier slices and the registration for 3D motion and eddy current distortions (strategy #5) modified a similar volume number than the 3D registration alone (strategy #4): 16.5 ± 7.1 volumes on average over infants for differences larger than 1% (range: 6.5–28.5); 4.4 ± 6.4 for differences larger than 5% (range: 0–23.7) (Table 1). In comparison with the other approaches, this strategy enabled to drastically homogenize the MI coefficients over the 30 orientations in moving babies, while it implied no changes in quiet babies (Fig. 3.2): the standard deviation over the 30 orientations (normalized by the mean) was the smallest with strategy #5 for most infants (except for 2 for whom differences were less than 0.2%).

This strategy further improved the quality of resulting DTI maps, as outlined by RGB maps (Fig. 5). When outlier slices were either not rejected or resampled (strategies #1 and #4), remaining artifacts were seen with a color-code corresponding to corrupted orientations (see arrows in Fig. 5b). The red color (right/left orientation) corresponds to the read echo-train axis that often shows artifacts because it is highly solicited when the DW orientation is along the x-gradient axis. When 3D motion registration was not performed (strategies #1, #2 and #3), the bundles' delineation was blurred and questionable (see arrows in Fig. 5c), particularly in the sub-cortical white matter and the corpus callosum. In quiet infants, all RGB maps were relatively similar, except that the correction of eddy current distortions (strategies #4 and #5) enabled to reduce artifacts over the whole brain and obvious discrepancies at the frontal and occipital borders (see arrows in Fig. 5a). Finally, the 2-step strategy provided the maps with the highest quality (Fig. 5.5), appearing more reliable and less artifacted than maps obtained after correction with RESTORE (Fig. 5.6).

3.2.4. Impact of the correction strategies: focus on the developing cortico-spinal tract

In all infants, the cortico-spinal tract was finely reconstructed by tractography, similarly with all five correction strategies. All strategies also globally provided equivalent quantification of mean

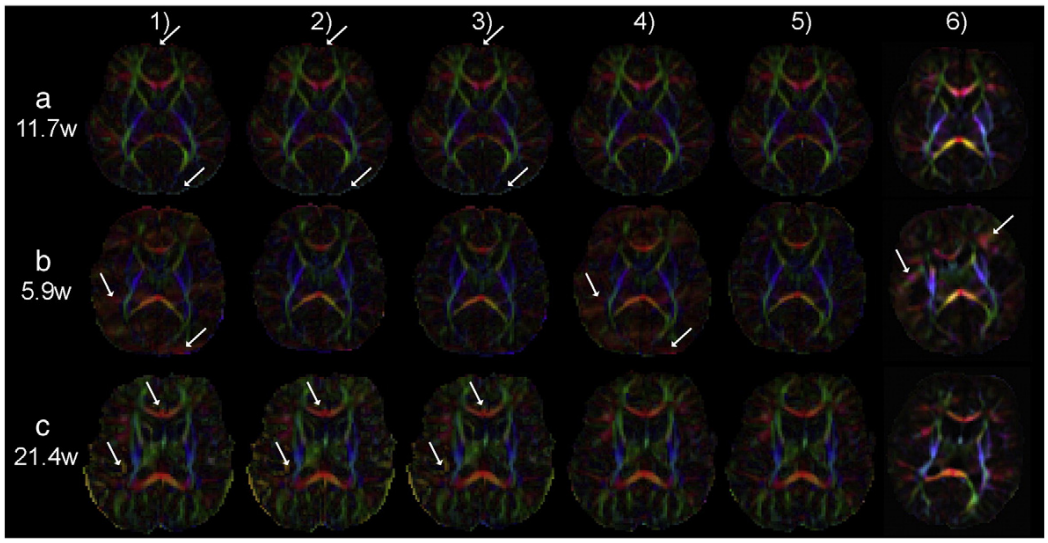

Fig. 5. Evaluation of RGB maps quality in infants. RGB maps are presented for the same three infants as in Fig. 3.2 (a: quiet infant; b, c: moving infants), and were computed according to DW images obtained 1) without correction, 2) with visual rejection of corrupted volumes, 3) with resampling of outlier slices, 4) with 3D registration of motion, 5) with our 2-step correction strategy and 6) with RESTORE approach. The 2-step strategy (5) corrected most artifacts (arrows) and provided the best RGB maps on visual assessment. With RESTORE (6), images appeared smoother, but the comparison remained difficult because of differences in orientations (images were not resampled to AC-PC referential). Some motion artifacts remained, particularly in b (arrows).

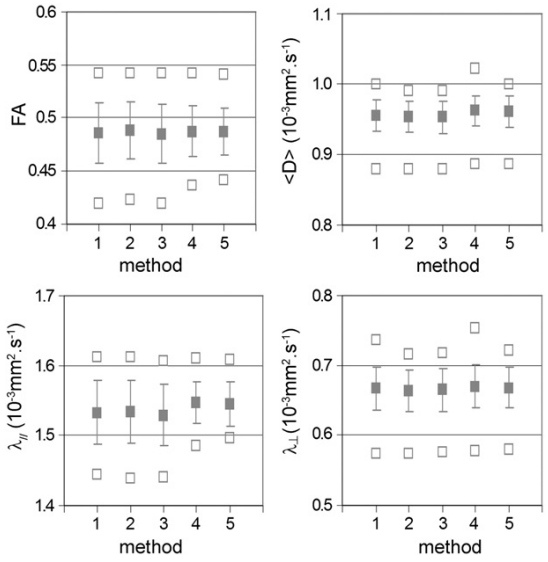

Fig. 6. Comparison of correction strategies through DTI parameter quantification. DTI parameters (fractional anisotropy FA, mean < D>, longitudinal $\lambda_{//}$ and transverse diffusivities $\lambda_{\perp}$) were computed in the cortico-spinal tract, reconstructed according to DW images obtained as in Fig. 5. For each strategy, the mean values are presented over the infant group (filled symbols, with standard deviations corrected for significant age-related effects in plot bars), as well as the minimal and maximal values (empty symbols).

and maximal parameters over the infant group, on average in the tract section, but standard deviations were the smallest with the 2-step correction strategy because of higher minimal values (Fig. 6). Furthermore, the age-related increase in FA was more accurate when motion registration was performed (strategies #4 and #5: R = 0.62; strategies #1/2/3: R = 0.53/0.48/0.48). The detected increase in anisotropy (+0.004/week of age), and the decreases in mean diffusivity (-4.10^{-6}mm^2.s^{-1}/week of age) and transverse diffusivity (-6.10^{-6} mm^2.s^{-1}/week of age) were in good agreement with previous studies [33]. Altogether this suggests that the 2-step strategy (strategy #5) was the most reliable approach to reconstruct the immature cortico-spinal tract and to quantify DTI parameters on average over the tract.

4. Discussion

DTI and HARDI techniques are sensitive to motion in two ways. First, because they are based on 2D acquisition, motion artifacts may be observed on isolated slices. In addition, misregistration can occur between DTI volumes because of the successive acquisition of several diffusion orientations, and because of eddy current distortions in EPI images. It seems intuitively important to correct images corrupted by such motion-related artifacts before estimating the diffusion models. Actually, it has been shown that the contributions of motion and noise are of the same order of magnitude at 3T, and that both are influenced by the choice of sampling scheme [18]. Motion is generally due to the subject, some of which being more susceptible to move than others, like infants, children and patients. But artifacts can also result from technical problems: in many MRI systems, instabilities of the gradients can lead to spikes [5], and the table may vibrate due to low-frequency mechanical resonances, which are stimulated by the low-frequency gradient switching associated with the diffusion-weighting [4]. This leads to corrupted data along specific gradient orientations.

We proposed in this study a post-processing approach relying on two successive and uncorrelated steps, which were first validated by introducing selected motion artifacts or discrepancies on different datasets, and comparing the corrected datasets with reference ones. It was further tested on DW data obtained in non-sedated infants, who frequently move during MRI acquisition: it successfully corrected sets corrupted by motion, while it had lower influence on uncorrupted data.

For intra-slice motion, we implemented an original method to detect and resample corrupted slices. For the outlier detection, a distance measure was defined to compare any DW slice and the corresponding b = 0 slice. A natural distance could be a correlation coefficient, but no linear relationship exists between the b = 0 and the DW signals which are variable across diffusion orientations [35]. Since mutual information (MI) does not rely on any relationship on the grey level intensity [29], it was a more reliable criterion in order to detect putative outliers for each slice independently. Furthermore, b = 0 image was selected as a reference to compute MI coefficients. If it is corrupted, this step would fail: using a DW image (for a specific orientation) would bias the detection for closed orientations, and the product of all DW volumes may be corrupted if a single DW image is artifacted. Nevertheless, this may not be a limiting issue: in the context of single-shell diffusion imaging, b = 0 image is required anyway to compute the diffusion model, and in multi-shell imaging it is unlikely that all b = 0 images would be corrupted.

With this setting-up, the detection was fully automated and reproducible, and the factor f was the only parameter to be tuned once for a specific protocol. The detection was performed on a slice-by-slice basis. Given the acquisition time of a slice (200 ms), intra-slice motion generally corrupts the whole slice: artifacts may not be visible in some regions of the brain; nevertheless it does not imply that the signal sampling is reliable in such regions. Besides, vibration-related artifacts corrupt clusters of voxels within a slice, but it remains difficult to limit the borders of the regions with impaired signal. Consequently methods which correct the artifacts locally (either on a voxel-by-voxel basis [9,23] or with a moving average window) may fail to correct the wholeness of such artifacts, and rejecting the whole slice may be more reliable. In this study, only a qualitative comparison between our method and RESTORE was performed, but it appeared that using the diffusion tensor model was quite unsuccessful to detect outliers in both infants and an adult dataset locally corrupted for a specific orientation of the diffusion gradients. Combining the two approaches (MI criteria on the whole slice and local constraint on signal intensity) would be a perspective to improve the outlier detection.

Resampling of the detected outliers can be performed from the non-outlier DW images, either in the image space, or in the Q-space. The former strategy is not adequate because the tissue local microstructure can change significantly between neighboring slices: interpolating the signal can introduce incoherence, partial voluming effects, and consequently lead to the mixture of heterogeneous populations of fibers. Resampling the corrupted data in the Q-space is more robust. In a recent study Sharman and collaborators [6] also considered this correction strategy after manual detection of the outliers. Two smoothing steps were used: a first spatial smoothing in the image space, using a Gaussian filter, which can only be applied to low b-values acquisitions and a second Q-space smoothing applied to the five closest neighbors using a weighted mean, which restricted the smoothed estimates to a very small quantity of DW data and imposed that they remain of good quality. Following smoothing, Q-space interpolation was performed directly on the spherical shell in the native DW signal space [6]. In our approach, the resampling of outlier slices relied on the decomposition of the DW signal on the modified spherical harmonics basis [36], which is a natural basis on the sphere. Contrarily to the geodesic resampling approach [6], it made use of all non-corrupted data, rather than on a restricted neighborhood. Thus, it required a smaller number of valid data to

compute a robust diffusion model estimation, and increased robustness to local corruption on the spherical shell, for instance when DW data contained artifacts around a specific orientation because of gradient system instabilities. Since using a non-parametric model may lead to overfitting of the signal, the spherical harmonics decomposition was limited to the 6^{th} order. In addition, a Laplace–Beltrami regularization term was used to better deal with noise removal and avoid any kind of overfitting with spurious spikes that may be present in the signal acquired on a shell of the Q-space. The resampling was validated for 1 to 5 outlier orientations over 30, leading to small errors in diffusion signal (~5%, Fig. 4a) in comparison with acquired images. But it may fail in case of severe motion when most orientations are corrupted, and then prospective strategies that adapt the acquisition according to the subject's motion should be preferred [13].

This correction approach is well indicated for any DW acquisition involving spherical samplings. It can be applied not only to the tensor model, but to most HARDI and multiple shell models since the spherical harmonics decomposition can be generalized to acquisitions with multiple q samplings [36,37]. For such protocols, our method would be particularly useful because the long acquisition times lead to more probable motion. Besides, the regularization relying on the Laplace–Beltrami operator makes the decomposition implicitly robust to noise, and the novel implementation using a modified LMMSE approach [38] also makes it robust to Rician and non-central Chi noise, which is observed in high b-values acquisitions.

In comparison with the strategy based on visual rejection of whole corrupted volumes, our method presents several advantages. It is fully automated and quick, independent from the experimenter, and is performed slice-by-slice rather than volume-by-volume, which is a particularly suitable when a single slice is corrupted. By introducing outliers on purpose in a set initially not corrupted by motion, we observed that filling in the missing data was equivalent to rejecting these data in terms of FA estimation, but it performed better when considering the estimation of the main eigenvector direction, particularly for outliers along a specific orientation (vibration). Furthermore, over the whole infant group, the final numbers of corrected volumes were smaller, and the resulting DTI maps were equivalent for both strategies. The main advantage of filling in the missing data was to make the number of DW measurements constant from voxel-to-voxel before the computation of the DTI model. Nevertheless it remained that the number of recovered orientations differed across slices. Besides, as the accuracy of the SH decomposition estimation increases with the spatial distribution of the diffusion orientations, it is important to combine our correction method with DW acquisition strategies that optimize the spatial orientation distribution according to the acquisition time and the motion hypotheses [3,17].

Our 2-step correction strategy also included a 3D realignment of orientation volumes, misregistered by inter-volume motion and eddy current distortions. The implemented registration was based on mutual information with the mean product of DW images, which appeared to be more robust in comparison with the conventional registration based on $b = 0$ image, and gave reliable results for simulated translations and rotations along the three axis and on real data.

The combination of both the resampling of outlier slices and the registration between orientation volumes was critical [9]. However one may wonder which step should be performed first. On the one hand, if an orientation volume still presents irregularities in the diffusion signal, it will be difficult to realign it in 3D. On the other hand, the resampling of corrupted slices may be wrong if the volume is spatially shifted in comparison with the reference. We performed the outlier resampling first, because this step is made slice-by-slice, and would thus be wrong anyhow should the slices be tilted previously by the 3D registration. Moreover, the initial 3D misregistration that we observed between volumes in all infants was verified to be small enough to guarantee the reliability of the outlier slice resampling.

5. Conclusion

The 2-step correction strategy was validated on datasets with various motion- and vibration-related artifacts, and it was successfully applied to DTI data of the infant brain. Since no hypothesis on the diffusion model is made, it can be used to correct any dataset acquired over a single shell in the Q-space (e.g., DTI and HARDI local models) and could be easily extended to multiple-shell acquisitions. So it is worth applying this correction in all DW data with potential sources of artifacts. As an example, it here enabled to reliably study the developing cortico-spinal tract, in agreement with previous studies of unmoved datasets [33].

Supplementary data to this article can be found online at http://dx.doi.org/10.1016/j.mri.2014.05.007.

Acknowledgments

This work was supported by the Fyssen Foundation (for JD), the Fondation de France (for JD), the Ecole des Neurosciences de Paris (for JD and CP), the Association France Parkinson and the DHOS Inserm-APHP (for CP), the McDonnell Foundation and the Fondation Motrice (for GDL), and the French National Agency for Research (ANR NIBB for GDL, LHP, JFM; ANR Maladies Neurodégénératives et Psychiatriques for CP).

References

[1] Le Bihan D, et al. MR imaging of intravoxel incoherent motions: application to diffusion and perfusion in neurologic disorders. Radiology 1986;161(2):401–7.
[2] Jones DK, Horsfield MA, Simmons A. Optimal strategies for measuring diffusion in anisotropic systems by magnetic resonance imaging. Magn Reson Med 1999;42(3):515–25.
[3] Dubois J, et al. Optimized diffusion gradient orientation schemes for corrupted clinical DTI data sets. MAGMA 2006;19(3):134–43.
[4] Gallichan D, et al. Addressing a systematic vibration artifact in diffusion-weighted MRI. Hum Brain Mapp 2010;31(2):193–202.
[5] Chavez S, Storey P, Graham SJ. Robust correction of spike noise: application to diffusion tensor imaging. Magn Reson Med 2009;62(2):510–9.
[6] Sharman MA, et al. Impact of outliers on diffusion tensor and Q-ball imaging: clinical implications and correction strategies. J Magn Reson Imaging 2011;33(6):1491–502.
[7] Dubois J, et al. The early development of brain white matter: a review of imaging studies in fetuses, newborns and infants. Neuroscience 2014. http://dx.doi.org/10.1016/j.neuroscience.2013.12.044.
[8] Huppi PS, Dubois J. Diffusion tensor imaging of brain development. Semin Fetal Neonatal Med 2006;11(6):489–97.
[9] Morris D, et al. Preterm neonatal diffusion processing using detection and replacement of outliers prior to resampling. Magn Reson Med 2011;66(1):92–101.
[10] Holdsworth SJ, et al. Diffusion tensor imaging (DTI) with retrospective motion correction for large-scale pediatric imaging. J Magn Reson Imaging 2012;36(4):961–71.
[11] Kim DH, et al. Diffusion-weighted imaging of the fetal brain in vivo. Magn Reson Med 2008;59(1):216–20.
[12] Jiang S, et al. Diffusion tensor imaging (DTI) of the brain in moving subjects: application to in-utero fetal and ex-utero studies. Magn Reson Med 2009;62(3):645–55.
[13] Herbst M, et al. Prospective motion correction with continuous gradient updates in diffusion weighted imaging. Magn Reson Med 2012;67(2):326–38.
[14] Shi X, et al. Improvement of accuracy of diffusion MRI using real-time self-gated data acquisition. NMR Biomed 2009;22(5):545–50.
[15] Poupon C, et al. Real-time MR diffusion tensor and Q-ball imaging using Kalman filtering. Med Image Anal 2008;12(5):527–34.
[16] Frank LR, et al. High efficiency, low distortion 3D diffusion tensor imaging with variable density spiral fast spin echoes (3D DW VDS RARE). Neuroimage 2010;49(2):1510–23.
[17] Cook PA, et al. Optimal acquisition orders of diffusion-weighted MRI measurements. J Magn Reson Imaging 2007;25(5):1051–8.
[18] Tijssen RH, Jansen JF, Backes WH. Assessing and minimizing the effects of noise and motion in clinical DTI at 3 T. Hum Brain Mapp 2009;30(8):2641–55.
[19] Sakaie KE, Lowe MJ. Quantitative assessment of motion correction for high angular resolution diffusion imaging. Magn Reson Imaging 2010;28(2):290–6.
[20] Rohde GK, et al. Comprehensive approach for correction of motion and distortion in diffusion-weighted MRI. Magn Reson Med 2004;51(1):103–14.
[21] Leemans A, Jones DK. The B-matrix must be rotated when correcting for subject motion in DTI data. Magn Reson Med 2009;61(6):1336–49.

[22] Aksoy M, et al. Single-step nonlinear diffusion tensor estimation in the presence of microscopic and macroscopic motion. Magn Reson Med 2008;59(5):1138–50.
[23] Chang LC, Jones DK, Pierpaoli C. RESTORE: robust estimation of tensors by outlier rejection. Magn Reson Med 2005;53(5):1088–95.
[24] Niethammer M, et al. Outlier rejection for diffusion weighted imaging. Med Image Comput Comput Assist Interv 2007;10(Pt. 1):161–8.
[25] Cointepas Y, et al. A freely available Anatomist/BrainVISA package for analysis of diffusion MR data. Proceedings of the 9th HBM Scientific Meeting, New York, USA, 19. , NeuroImage; 2003. p. S810.
[26] Duclap D, et al. Connectomist-2.0: a novel diffusion analysis toolbox for BrainVISA. Proceedings of the 29th ESMRMB meeting; 2012. p. 842.
[27] Wells III WM, et al. Multi-modal volume registration by maximization of mutual information. Med Image Anal 1996;1(1):35–51.
[28] Maes F, et al. Multimodality image registration by maximization of mutual information. IEEE Trans Med Imaging 1997;16(2):187–98.
[29] Mangin JF, et al. Distortion correction and robust tensor estimation for MR diffusion imaging. Med Image Anal 2002;6(3):191–8.
[30] Frank LR. Characterization of anisotropy in high angular resolution diffusion-weighted MRI. Magn Reson Med 2002;47(6):1083–99.
[31] Descoteaux M, et al. Regularized, fast, and robust analytical Q-ball imaging. Magn Reson Med 2007;58(3):497–510.
[32] Perrin M, et al. Fiber tracking in q-ball fields using regularized particle trajectories. Inf Process Med Imaging 2005;19:52–63.
[33] Dubois J, et al. Asynchrony of the early maturation of white matter bundles in healthy infants: quantitative landmarks revealed noninvasively by diffusion tensor imaging. Hum Brain Mapp 2008;29(1):14–27.
[34] Dubois J, et al. Assessment of the early organization and maturation of infants' cerebral white matter fiber bundles: a feasibility study using quantitative diffusion tensor imaging and tractography. Neuroimage 2006;30(4):1121–32.
[35] Mangin JF. Entropy minimization for automatic correction of intensity nonuniformity. IEEE Work, MMBIA, Hilton Head Island, South Carolina; 2000. p. 162–9.
[36] Descoteaux M, et al. Diffusion propagator imaging: using Laplace's equation and multiple shell acquisitions to reconstruct the diffusion propagator. Inf Process Med Imaging 2009;21:1–13.
[37] Assemlal HE, Tschumperle D, Brun L. Efficient and robust computation of PDF features from diffusion MR signal. Med Image Anal 2009;13(5):715–29.
[38] Brion V, et al. Parallel MRI noise correction: an extension of the LMMSE to non central chi distributions. Med Image Comput Comput Assist Interv 2011;14(Pt. 2):226–33.

Neuroscience 276 (2014) 48–71

REVIEW

THE EARLY DEVELOPMENT OF BRAIN WHITE MATTER: A REVIEW OF IMAGING STUDIES IN FETUSES, NEWBORNS AND INFANTS

J. DUBOIS, [a,b,c*] **G. DEHAENE-LAMBERTZ,** [a,b,c] **S. KULIKOVA,** [d,e,f] **C. POUPON,** [g] **P. S. HÜPPI** [h,i] **AND L. HERTZ-PANNIER** [d,e,f]

[a] *INSERM, U992, Cognitive Neuroimaging Unit, Gif-sur-Yvette, France*

[b] *CEA, NeuroSpin Center, UNICOG, Gif-sur-Yvette, France*

[c] *University Paris Sud, Orsay, France*

[d] *CEA, NeuroSpin Center, UNIACT, Gif-sur-Yvette, France*

[e] *INSERM, U663, Child epilepsies and brain plasticity, Paris, France*

[f] *University Paris Descartes, Paris, France*

[g] *CEA, NeuroSpin Center, UNIRS, Gif-sur-Yvette, France*

[h] *Geneva University Hospitals, Department of Pediatrics, Division of Development and Growth, Geneva, Switzerland*

[i] *Harvard Medical School, Children's Hospital, Department of Neurology, Boston, MA, USA*

Abstract—Studying how the healthy human brain develops is important to understand early pathological mechanisms and to assess the influence of fetal or perinatal events on later life. Brain development relies on complex and intermingled mechanisms especially during gestation and first postnatal months, with intense interactions between genetic, epigenetic and environmental factors. Although the baby's brain is organized early on, it is not a miniature adult brain: regional brain changes are asynchronous and protracted, i.e. sensory-motor regions develop early and quickly, whereas associative regions develop later and slowly over decades. Concurrently, the infant/child gradually achieves new performances, but how brain maturation relates to changes in behavior is poorly understood, requiring non-invasive *in vivo* imaging studies such as magnetic resonance imaging (MRI). Two main processes of early white matter development are reviewed: (1) establishment of connections between brain regions within functional networks, leading to adult-like organization during the last trimester of gestation, (2) maturation (myelination) of these connections during infancy to provide efficient transfers of information. Current knowledge from post-mortem descriptions and *in vivo* MRI studies is summed up, focusing on T1- and T2-weighted imaging, diffusion tensor imaging, and quantitative mapping of T1/T2 relaxation times, myelin water fraction and magnetization transfer ratio.

This article is part of a Special Issue entitled: The CNS White Matter.

Key words: brain development, white matter bundles, myelination, magnetic resonance imaging, diffusion tensor imaging, fetus and infant.

Contents

*Correspondence to: J. Dubois, CEA/SAC/DSV/I2BM/NeuroSpin/Cognitive Neuroimaging Unit U992, Bât 145, point courrier 156, 91191 Gif-sur-Yvette, France. Tel: +33-1-69-08-81-72; fax: +33-1-69-08-79-73.

E-mail address: jessica.dubois@centraliens.net (J. Dubois).

Abbreviations: AF, arcuate fasciculus; ALIC, anterior limb of the internal capsule; CC, corpus callosum; CG, cingulum; Cl, linear diffusion anisotropy; CNS, central nervous system; Cp, planar diffusion anisotropy; CS, centrum semiovale; CST, cortico-spinal tract; DEHSI, diffuse excessive high signal intensity; DTI, diffusion tensor imaging; DWI, diffusion-weighted imaging; EC, external capsule; FA, fractional anisotropy; GA, gestational age; GM, gray matter; HARDI, high-angular resolution diffusion imaging; ILF, inferior longitudinal fasciculus; MD, mean diffusivity; MRI, magnetic resonance imaging; MTR, magnetization transfer ratio; MWF, myelin water fraction; OR, optic radiations; PD, proton density; PLIC, posterior limb of the internal capsule; PTA, post-term age: post-natal age corrected for gestational age at birth considering a term age of 40 weeks; PVWM, peri-ventricular white matter; R1, relaxation rate associated with T1 relaxation time (R1 = 1/T1); R2, relaxation rate associated with T2 relaxation time (R2 = 1/T2); SNR, signal-to-noise ratio; STT, spino-thalamic tract; TBSS, tract-based spatial statistics; TE, echo time; TI, inversion time; TR, repetition time; T1, longitudinal relaxation time; T1w, T1-weighted; T2, transverse relaxation time; T2w, T2-weighted; UF, uncinate fasciculus; VLBW, very low birth weight; WM, white matter; 2D, 2 dimensions; 3D, 3 dimensions; $\lambda_{//}$, longitudinal diffusivity; $\lambda_{\perp}$, transverse diffusivity.

0306-4522/13 $36.00
http://dx.doi.org/10.1016/j.neuroscience.2013.12.044

INTRODUCTION

Brain development relies on several complex and intermingled mechanisms, such as the maturation and functional specialization of gray matter (GM) regions (cerebral cortex and central gray nuclei) and the establishment and myelination of white matter (WM) connections between the different neural regions. Typical development is the global consequence of interactions between genetic programming, epigenetic and environmental factors (e.g. external stimulations, maternal, nutritional or medical factors). Cerebral changes are particularly intense during the last weeks of gestation and the first post-natal months, as indirectly highlighted by the non-linear increase of the cranial perimeter (by about 14 cm during the two first post-natal years, followed by only 7 cm until adulthood). Although the baby's brain is organized early on into functional networks, it is not an adult brain in miniature: growth and maturation are asynchronous, some regions, like the sensory ones, develop early on and quickly, whereas associative regions, like frontal ones, develop later on and slowly until the end of adolescence (Paus et al., 2001).

Concurrently with this anatomical evolution of the brain, the infant gradually achieves new psycho-motor and cognitive skills, but how brain maturation explains the often abrupt changes of behavior observed during development is poorly understood. Before the development of non-invasive brain imaging methods, our knowledge on human brain development was relying on (fortunately) rare post-mortem investigations, which are intrinsically limited by the lack of anatomo-functional correlations and by the uncertainty on brain normality. Using myelin staining, most of these studies described whether myelin is present or not in a given WM region at a given age: this information is however not bundle-specific and thus might be misleading at bundles crossings. Advanced post-mortem dissection techniques now enable to follow the trajectory of long-distance bundles (Martino et al., 2010; Maldonado et al., 2013). But absolute measurements of myelin amount are still missing, which prevents the quantitative comparison across WM regions.

Another approach to understand brain development is to study animals, but if such studies enable to test particular hypotheses, they remain largely inadequate because of the specificity of human cognitive functioning and brain development. Mammals are generally classified according to their developmental stage at birth, belonging either to species with early development or to species with immature development. Humans have a special position since brain responses are already observed *in utero* (Draganova et al., 2007), while some high-level functions have a protracted development over two decades. For instance, the fiber myelination in the somatosensory, motor, frontopolar and visual neocortices is delayed in humans compared with chimpanzees, with slower myelination during childhood extending beyond late adolescence (Miller et al., 2012).

The recent development of non-invasive techniques (magnetic resonance imaging (MRI), electroencephalography (EEG), magnetoencephalography (MEG)) has further enabled to relate maturation of cerebral structures to infants' neurodevelopment and behavior. In particular, several MRI techniques available on clinical scanners (section 'Structural MRI techniques and developmental specificities') enable to investigate and follow longitudinally the brain development and plasticity of healthy and at-risk children (Barkovich, 2000; Paus et al., 2001; Neil et al., 2002; Prayer and Prayer, 2003; Huppi and Dubois, 2006; Yoshida et al., 2013). But when these imaging techniques are applied to babies, many difficulties arise and require adapting data acquisition and post-processing to different developmental periods (fetus, preterm or at-term newborn, infant, toddler, etc.).

With these constraints in mind, we here review the main insights revealed by recent MRI studies on the early development of WM, which is a complex and long-lasting process that plays a crucial role during the human motor and cognitive development (section 'The basic concepts of white matter development'). Two main stages can be delineated: (1) the establishment of long and short

connections between brain regions during the last trimester of human gestation, leading to an early adult-like organization of neural networks, (2) the maturation of these fibers during infancy and toddlerhood to provide an efficient transfer of information between functional regions. These two processes are consecutively described in the healthy brain by summarizing current knowledge obtained from post-mortem and *in vivo* imaging studies (sections 'Imaging the early organization of white matter' and 'Imaging the maturation of white matter'). Finally, the functional significance of early structural biomarkers of the developing WM is discussed based on studies with behavioral and neurophysiologic evaluations of infants, with a specific focus on preterms without overt brain lesions (section 'Functional correlates of MRI biomarkers of WM maturation').

THE BASIC CONCEPTS OF WM DEVELOPMENT

The early organization of WM

WM organization in adults. WM contains a large amount of glial cells (astrocytes, oligodendrocytes and microglia, which account for around 50% of the total brain volume and nearly 90% of brain cells), but it is mainly studied as the brain compartment of crossing paths that connect different functional regions. Long-distance fibers, generally gathered into bundles, can be classified according to their connection patterns. Commissural fibers connect the two cerebral hemispheres, mostly between homotopic regions (e.g. the corpus callosum (CC)). Projection fibers are bi-directional fibers between the thalamus and the cortex, between the cortex and the brainstem and spinal cord (e.g. the cortico-spinal tract (CST), the optic radiations (OR)). Associative fibers regroup cortico-cortical fibers between intra-hemispheric regions (e.g. the arcuate fasciculus (AF)) and fibers of the limbic system (e.g. the fornix).

Growth of fiber connections during the last trimester of gestation. The progressive organization of WM connections has been established with post-mortem studies. Once the neuron has migrated to its final localization, it develops connections with other neurons at both ends: a dendritic tree within the GM, and the formation of an axon running through the WM. At the macroscopic level, the axons formation leads to the formation of long-distance bundles. This wiring occurs mostly during the second part of pregnancy, but its exact temporal progression is still poorly described in humans. It includes processes of neuronal and synaptic overproduction, followed by cellular apoptosis, axonal retraction and synaptic pruning. All these processes of overproduction/elimination are essential to sustain the functional networks plasticity (Stiles and Jernigan, 2010). The early wave of migrating neurons remains in the subplate (underneath the future cortex) and is crucial to establish a first rough blueprint of the cerebral organization, both for the cortex and the WM. On the one hand, they relay thalamo-cortical projections in the late fetal and preterm brain, amplifying sensory signals (Kanold and Luhmann, 2010; Kostovic and Judas, 2010), and on the other hand they send pioneering axons toward the internal capsule to guide axons from the later migrating neurons (McConnell et al., 1989). They also guide inter-hemispheric connections through the CC between 25 and 32 weeks of gestational age (w GA) (deAzevedo et al., 1997).

To reach their target structure, axons grow and are guided by their extremity growth cones, which are attracted or repulsed by positive or negative signals (e.g. contact signals, chemical signals, neuro-transmitters, growth factors). They follow ''pioneering'' axons (process of ''fasciculation''). The initial connection production stage is followed by a pruning stage that aims at suppressing redundant or aberrant circuits and is dramatically sensitive to the environment (Huttenlocher and Bonnier, 1991). This process may be influenced by several factors: e.g. neuron survival, competition for trophic factors, electrical activity of axons, afferent inputs. In particular, in the CC, pruning is a major morphogenetic process between the end of gestation and the first and second postnatal months (Innocenti and Price, 2005). In the rhesus monkey, up to 70% of callosal axons are eliminated in the four first post-natal months (LaMantia and Rakic, 1990). In humans, the number of axons in the CC may be close to a maximum in the newborn brain (with no new axons being formed to cross the midline), and the process of axonal pruning is supposed to occur after birth (Kostovic and Jovanov-Milosevic, 2006).

The maturation of WM

Concurrently and subsequently to the organization of WM networks, fiber connections become progressively mature and functionally efficient through the myelination process that favors the conduction of the nervous impulse (Baumann and Pham-Dinh, 2001; Van der Knaap and Valk, 1995a,b).

Myelin description. In the adult brain, the WM white color is due to the high myelin content (40–50% of dry weight). The myelin sheaths enwrapped around axons are complex bilamellar membranes constituted by lipoproteins (myelin basic proteins (MBP), proteo-lipid proteins (PLP), myelin associated glycoproteins (MAG), 2′,3′-Cyclic nucleotide-3′-phosphohydrolase (CNP), etc.) and lipids (cholesterol, phospholipids, glycolipids, galactocerebrosides, etc.). This ''roll-cake like'' structure is formed by the membrane prolongations of oligodendrocytes in the central nervous system (CNS) (Barkovich, 2000).

The myelin role is to allow a fast conduction of the nerve impulse. Indeed, the action potential propagates along the axon by electrical depolarization of the nervous membrane, continuously when no myelin sheath enwraps the axon, or via saltatory conduction from a Ranvier node to the next (Ranvier nodes are the fiber places between myelin sheath segments). The conduction speed depends on the distance between nodes, on axonal diameter and on the myelin sheath

thickness: from 2 m s^{-1} in unmyelinated CNS fibers to 120 m s^{-1} in myelinated fibers of the peripheral nervous system.

Myelination of WM fibers. Myelination (i.e. myelin formation around axons) is the last stage of WM development, that begins after the process of axonal overproduction-pruning and follows premyelinating stages including the formation and maturation of oligodendrocytes (Thomas et al., 2000). This process includes several steps (Hardy and Friedrich, 1996; Butt and Berry, 2000; Prayer and Prayer, 2003). Oligodendrocyte precursors proliferate, migrate and form ''initiator'' processes, which align along axons (predominant radial orientation) and identify targeting axons (Volpe, 2008). Spiral ensheathment around the axon starts with an extension of such a process that elongates and wraps around the axon. Afterward, the myelin sheath becomes more compact, through an increasing number of spiral turns that is determined by the axonal diameter (Baumann and Pham-Dinh, 2001).

A single oligodendrocyte myelinates several axons (even of different diameters), suggesting that each axon participates to the regulation of its myelination (Friede, 1972). In the human brain, four stages of oligodendrocyte maturation have been described: early and late progenitor cells, immature and mature oligodendrocytes. The immature oligodendrocytes (which are multipolar cells rich in a lipid called galactocerebroside) account for 30–40% of the entire oligodendroglia population in the preterm period (~28–37 w GA).

The ''pre-myelinating'' state generally refers to the initial period when pre-oligodendroglial cells increase and settle along the axons (Baumann and Pham-Dinh, 2001), and when the cholesterol and glycolipids concentration starts to increase (Poduslo and Jang, 1984; Barkovich et al., 1988). The following ''true'' myelination process corresponds to the ensheathment of oligodendroglial processes around the axons, and to the chemical maturation of the myelin sheath with rising amount of macromolecules (Poduslo and Jang, 1984; Barkovich et al., 1988). At the microscopic level, the myelination induces major changes in water molecules content and compartmentalization (Matsumae et al., 2001) and in protein and lipid contents (Barkovich et al., 1988; Kucharczyk et al., 1994). Notably, a strong correlation exists between myelination and the concentration of galactocerebroside in immature and mature oligodendrocytes (Matthieu, 1993).

Regional asynchrony of WM myelination. Myelination occurs in the human brain from the second part of pregnancy to the end of adolescence. A peak is observed during the first post-natal year. Its progression varies across cerebral regions: it follows a caudo-rostral gradient and progresses from the center to the periphery. Post-mortem studies have detailed this sequence (Flechsig, 1920; Yakovlev, 1962; Yakovlev and Lecours, 1967; Gilles et al., 1983; Brody et al., 1987; Kinney et al., 1988), using a visual ordering from stages 0 to 4 according to staining with hematoxylin and eosin-luxol fast (''mature myelin'' refers to stages 3 and 4). Some myelin is observed microscopically from 20 w GA on at the level of the bulb and pons, which are myelinated at birth. Mature myelin is detected from 37 to 40 w GA in the cerebellum and internal capsule. Between the first and third post-natal months, the posterior limb of the internal capsule (PLIC), the OR and the CC splenium become myelinated. Mature myelin can be found from the 6th month in the anterior limb of the internal capsule (ALIC) and in the CC genu, from the 15th month in the occipital pole, and from the 23rd month in the frontal and temporal lobes (for review (Baumann and Pham-Dinh, 2001).

From these post-mortem studies, several rules can be outlined on the myelination progression in the brain (Kinney et al., 1988): it occurs earlier and faster (1) in proximal pathways than in distal ones; (2) in sensory pathways (somatosensory, vision, audition) than in motor ones; (3) in projection fibers than in associative ones; (4) in central regions than in polar ones; (5) in the occipital pole than in the posterior parietal WM and in the temporal and frontal poles. These global schemes cannot be dissociated from one another, and suggest eight sub-groups of maturation, depending on the presence/absence of myelin at birth (sub-groups A/B) and the time periods at which mature myelin is observed (sub-groups 1–4) (Kinney et al., 1988). For example, the middle cerebellar peduncles, the optic tract and chiasm, the PLIC, the CST in the midbrain and pons and the central corona radiata belong to sub-group A1; OR (proximal and mid-distal), auditory radiations (proximal), the CC body and splenium belong to sub-group B1; cingulum (CG), external capsule (EC), the ALIC, the CC rostrum and Heschl's gyrus belong to sub-group B2; fornix and extreme capsule belong to sub-group B4. This asynchrony in the maturation sequence is supposed to depend on the hierarchy of connections between cortical areas (Guillery, 2005): the early maturation of receptive sensory areas (responsible for low-level processing) would enable a stabilization of the information used by integrative areas (involved in high-level processing) which develop later on.

Functional correlates of WM myelination. Beside glial factors, neuronal maturation and electrical activity might control myelination induction (Kinney et al., 1988). Blocking this activity *in vitro* inhibits myelination (Demerens et al., 1996), and the proliferation of oligodendrocytes precursors is influenced by neighboring axonal activity (Barres and Raff, 1993). Electrical activity in the mouse optic nerve influences the triggering of myelination over a short time period (Demerens et al., 1996). This nerve myelination is further delayed in mice kept in a dark environment after birth (Gyllensten and Malmfors, 1963) and accelerated in rabbits whose eyelids have been opened prematurely (Tauber et al., 1980). Astrocytes may act as an intermediary between myelination and electrical impulse activity, through the mediation of a cytokine leukemia inhibitory factor (Ishibashi et al., 2006). Nowadays, the

inhibitory role of oligodendrocytes and myelin on neuritic growth is also considered, which may partly explain the weak plasticity of the adult brain (Ng et al., 1996).

Since myelination leads to a spectacular increase in the conduction speed of the nerve impulse (Baumann and Pham-Dinh, 2001), it is assumed to improve the functional efficiency of brain networks (van der Knaap et al., 1991). Myelination of the midbrain and spinal cord is actually coupled with behavioral improvement (Langworthy, 1928a,b), but fiber myelination and functional maturation are uncorrelated in different cerebral systems. For instance, the myelination of the CST occurs before birth in several regions (midbrain, internal capsule, central corona radiata) while the newborn motor capacities are weak. On the other hand, the acoustic radiations have an extended myelination until 3 years of age while the infant auditory system is efficient early on.

Such discrepancy may rely on the fact that extending myelination may be necessary in a second step to compensate for brain growth and maintain similar latencies between brain regions across ages (Salami et al., 2003). In the visual system for example, the latency of the first positive wave of response to a stimulus (P1) reaches the adult latency (~100 ms) at around four post-natal months, whereas the distance between the retina and the calcarine fissures still increases by around 6 cm until adulthood. Whereas the transfer of visual information may be efficient early on in 4-month-old infants, an extending myelination may enable to further increase the conduction speed by around 0.6 m s^{-1} in relation with brain growth.

STRUCTURAL MRI TECHNIQUES AND DEVELOPMENTAL SPECIFICITIES

Several complementary MRI techniques can be used to image brain development in healthy infants. Since signal comes from the hydrogen nuclei (the ''protons'') of water molecules, cerebral tissues with different water concentrations and environments demonstrate on MR images different contrasts that change with brain maturation.

Conventional MR imaging and relaxometry

Physical basics. ''Conventional'' MRI generally refers to images whose signal is weighted (noted ''w'') by proton density (PD) or by relaxation times, which characterize how fast the water magnetization returns to equilibrium after the perturbation induced by electromagnetic waves. The longitudinal relaxation time (T1) characterizes the proton interactions with its environment (''spin–lattice'' interactions), while the transverse relaxation time (T2) characterizes the interactions between protons (''spin–spin'' interactions). In the developing brain, T1 weighting is generally obtained with short TR and short TE, or using inversion recovery sequences with long inversion times (TI), while T2 weighting is obtained with long repetition times (TR) and long echo times (TE). Since relaxation times depend on tissue characteristics, T1w and T2w images demonstrate high contrast between cerebral tissues in the adult brain (Fig. 1).

Developmental specificities of T1w and T2w contrasts. Because of brain tissues immaturity and high water content, T1w and T2w contrasts are very different in the infant brain from what is described in the adult brain, and contrasts evolve with brain maturation (Fig. 1). Considering the brain as a whole, successive maturational stages are described (Paus et al., 2001): (1) the infantile pattern (0–6 months), showing a reversal of the normal adult contrasts (T1w: lower WM intensity than GM intensity; T2w: higher WM intensity than GM intensity); (2) the iso-intense pattern (8–12 months), characterized by a poor contrast between GM and WM; and (3) the early-adult pattern (> 12 months) (T1w: higher WM intensity than GM intensity; T2w: lower WM intensity than GM intensity). Actually, the specific time-course of these patterns depends on brain regions because of maturation asynchrony (see Section 'Imaging the maturation of white matter').

As a consequence, the delineation between the GM and WM is often not obvious on infant images, contrarily to the clear border observed on adult T1w images. T1 weighting is mostly used during the preterm and perinatal periods, but the contrast becomes poorer with age until it recovers during the second post-natal year. T2 weighting transitorily enables a better contrast between term and 4–6 months post-term (Leroy et al., 2011b). The second post-natal semester is actually the most difficult period to image, with a weak delineation of the GM/WM border.

To identify myelinated WM regions from unmyelinated regions, T1w contrast is generally preferred during the first 6–8 post-natal months, and T2w contrast between 6 and 14 months because changes in WM contrasts are observed on T1w images before T2w images (van der Knaap and Valk, 1990; Barkovich et al., 1992).

Mapping T1 and T2 relaxation times during WM maturation. The changes observed on T1w and T2w contrasts can be used to understand maturation processes, but T1w and T2w signals cannot be directly compared across individuals because of the variability between exams related to technical tunings. To provide such inter-individual comparisons, either signals may be normalized for each subject in reference to a given tissue (e.g. the cerebro-spinal fluid) (Leroy et al., 2011a), or T1 and T2 relaxation times may be quantitatively measured (Fig. 1) by recording signals from dedicated MRI acquisitions with different sequence parameters (e.g. different inversion times TI to compute T1, different echo times TE to compute T2).

In the developing brain, T1 and T2 decrease more strongly in WM than in GM because of myelination processes (Fig. 4a) (Barkovich, 2000; Prayer and Prayer, 2003). At least two distinct pools of water molecules are supposed to contribute to MR signal in the WM: water located within the myelin sheath (with relatively short T1 and T2 relaxation times) and

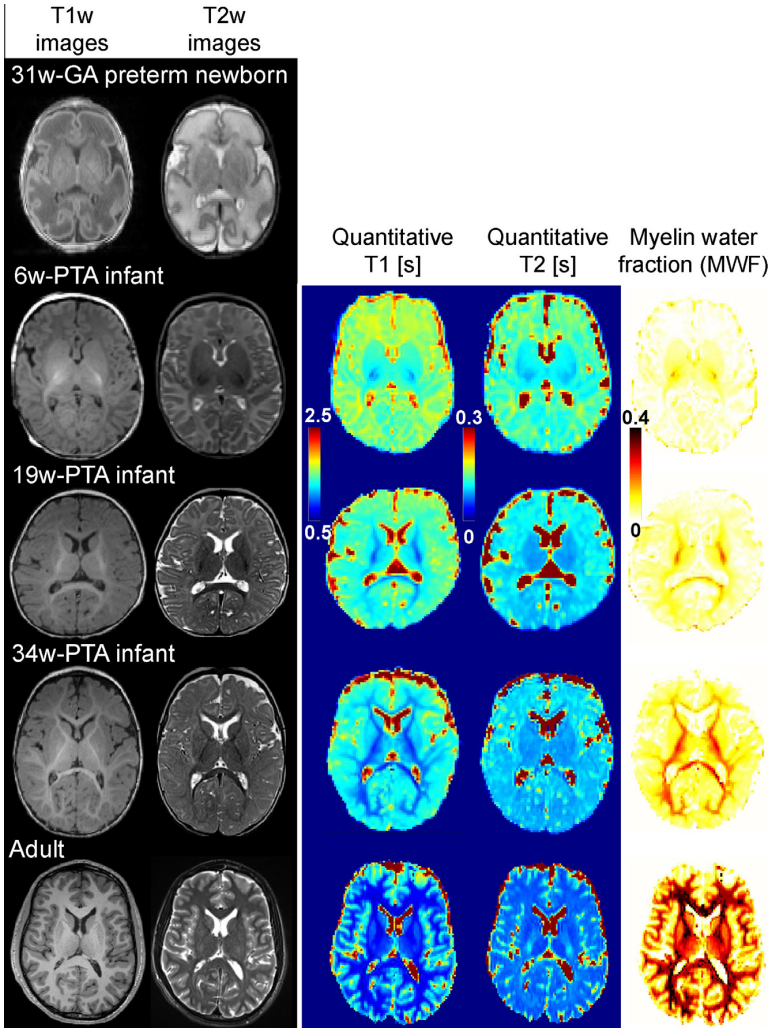

Fig. 1. Anatomical images of the developing brain. T1w and T2w images are presented for subjects of different ages: a preterm newborn of 31 weeks of gestational age (GA), term-born infants at a post-term age (PTA) of 6 weeks, 19 weeks and 34 weeks (PTA: post-natal age corrected for gestational age at birth, considering a term age of 40 weeks), and a young adult. Note the contrast inversion between GM and WM during the first post-natal year. For the infants and adults, quantitative maps of T1 and T2 relaxation times (in seconds), and of myelin water fraction (MWF) are also presented. Within the white matter, T1 and T2 decrease with age, while MWF increases. Preterm images were acquired on a 1.5-T MRI system, the other images on a 3-T system.

intra-axonal, intra-cellular and interstitial water (i.e. water outside of the myelin sheath, with longer T1 and T2). Both T1 and T2 decreases parallel the decrease in water concentration, nevertheless their time courses are different, and two distinct mechanisms can be distinguished: the change in water molecules compartmentalization (Matsumae et al., 2001), and the increase of protein and lipid contents (Barkovich et al., 1988; Kucharczyk et al., 1994). T1 shortening starts already during the "pre-myelinating" state, while T2 shortening correlates temporally with the chemical maturation of the myelin sheath (Poduslo and Jang, 1984; Barkovich et al., 1988; Baumann and Pham-Dinh, 2001) (Fig. 4c).

Diffusion imaging

Physical basics and post-processing strategies. Another recent approach to assess WM maturation is diffusion-weighted imaging (DWI) which measures the natural motion of water molecules. The diffusion in cerebral tissues is not "free" (Le Bihan, 2003). Microscopic displacements may be restricted within multiple physical compartments, or hindered by cell and organelle membranes: this results in tortuous pathways around these obstacles. Imaging diffusion at the macroscopic scale thus enables to explore the tissue microstructure non-invasively (Le Bihan et al.,

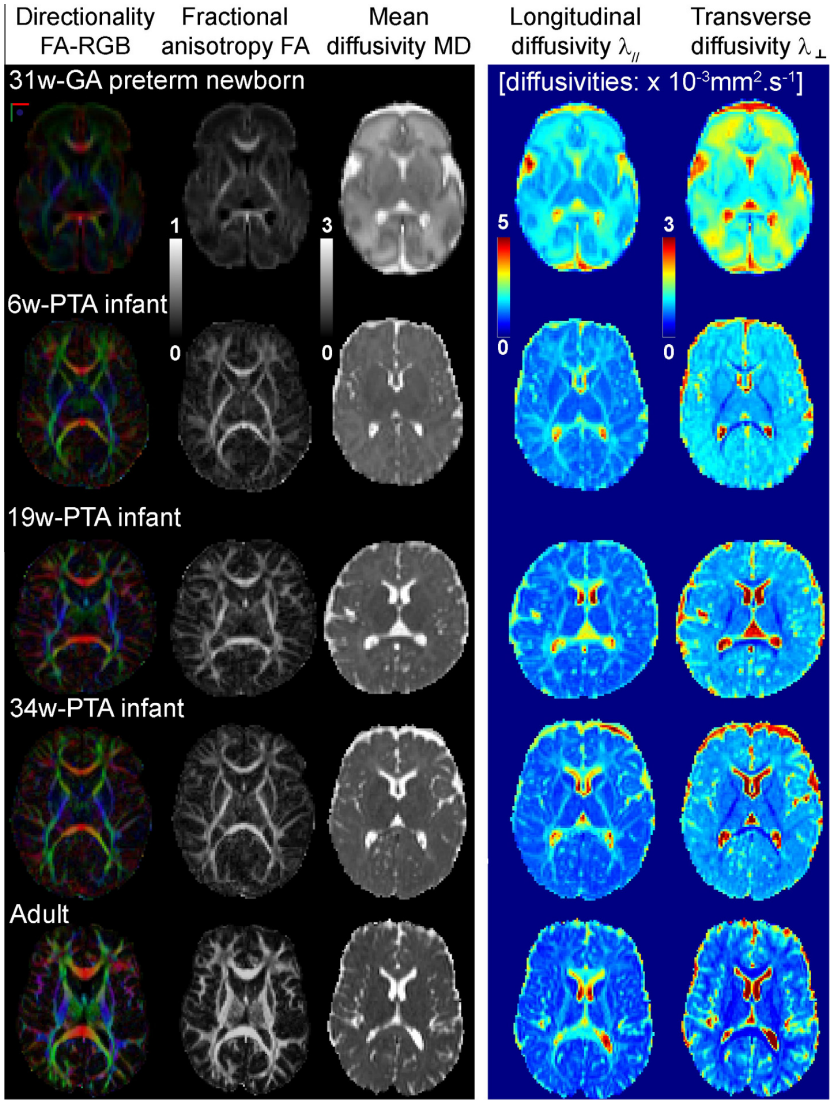

Fig. 2. DTI images of the developing brain. DTI maps are presented for the same subjects as in Fig. 1. Color-coded directionality maps (FA-RGB, where color informs on the direction of the tensor main eigenvector) nicely highlight early WM organization, and immature bundles already demonstrate high fractional anisotropy (FA). The different DTI parameters provide different contrasts between brain tissues. Within WM, FA increases with age, while mean (MD), longitudinal ($\lambda_{//}$) and transverse ($\lambda_{\perp}$) diffusivities (in 10^{-3} mm^2 s^{-1}) decrease.

2001). To take into account the spatial heterogeneity of the diffusion process, the diffusion information is generally encoded in different spatial directions, and the diffusion tensor (DT) formalism is used with the assumption that a single fiber orientation is present in each voxel of the image and that the diffusion process can be represented by an ellipsoid that encodes the tensor eigenvectors and eigenvalues. The diffusion tensor imaging (DTI) technique provides maps of quantitative and complementary parameters (Fig. 2): diffusion anisotropy (e.g. fractional anisotropy (FA)) (Beaulieu, 2002), mean diffusivity (MD = one third of the tensor trace), longitudinal diffusivity ($\lambda_{//}$ = diffusivity along the main tensor axis) and transverse diffusivity ($\lambda_{\perp}$ = diffusivity perpendicular to the main axis).

The trajectory of WM fibers can be further reconstructed virtually in 3 dimensions (3D) using tractography algorithms that follow the direction of the main DT eigenvector from a voxel to a neighboring voxel (Le Bihan and Johansen-Berg, 2012) (Fig. 3). The dissection of major WM bundles is then based either on the individual definition of regions crossed by the fibers, or through automatic classifications recently proposed for the adult brain, such as clustering (Guevara et al., 2011, 2012) and probabilistic methods (Yendiki et al., 2011). Recently, some alternatives to the tensor model have been proposed, such as Q-ball imaging, diffusion spectrum imaging (DSI) and high-angular resolution diffusion imaging (HARDI). These techniques enable to resolve multiple fiber orientations within a voxel, but

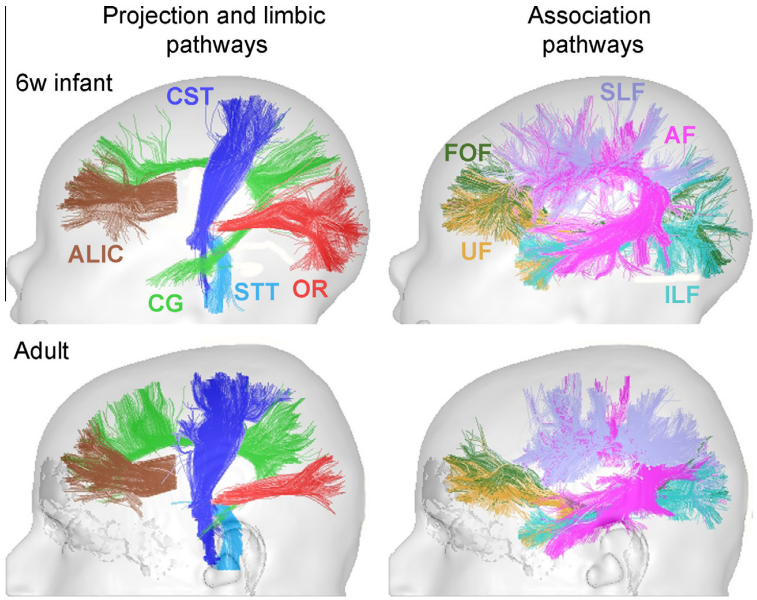

Fig. 3. Tractography of the developing WM bundles. Examples of major WM bundles, reconstructed with regularized tractography using Connectomist software (Duclap et al., 2012), are presented for the 6-week-old infant and the adult of Figs. 1 and 2: projection and limbic pathways (left column), and associative pathways (right column). Note the similar organization between the infant and adult brains. Abbreviations: AF, arcuate fasciculus; ALIC, anterior limb of the internal capsule; CG, cingulum; CST, cortico-spinal tract; FOF, fronto-occipital fasciculus; ILF, inferior longitudinal fasciculus; OR, optic radiations; SLF, superior longitudinal fasciculus; STT, spino-thalamic tract; UF, uncinate fasciculus.

they require long acquisition times hardly achievable *in vivo* in healthy unsedated infants.

DTI correlates of WM maturation. DTI parameters are well suited to reveal information that is not apparent on T1w and T2w images during brain development (Fig. 2) (Neil et al., 2002; Huppi and Dubois, 2006). It is generally assumed that diffusivities decrease with maturation, while anisotropy increases in the developing WM (Neil et al., 1998; Huppi et al., 1998a) and decreases in the cortex during the preterm period (McKinstry et al., 2002; Ball et al., 2013). Transverse diffusivity decreases more in WM than in GM (Mukherjee et al., 2002), leading to a reversed contrast between newborns and adults on transverse diffusivity maps (Fig. 2). In WM bundles, changes are more intense for transverse than for longitudinal diffusivity (Mukherjee et al., 2002; Dubois et al., 2008b; Geng et al., 2012), with even no change in longitudinal diffusivity detected after 1 year of age (Gao et al., 2009). These parameter dynamics in WM bundles are consistent with the assumption of a cylindrically symmetric decrease in diffusion due to myelination process (Mukherjee et al., 2002).

Fifteen years ago, it had been suggested that the age-related decrease in mean diffusivity in both GM and WM would reflect the overall decrease in brain water content, while the increase in anisotropy in the WM would rather rely on its microstructure (e.g. packing and myelination) (Neil et al., 1998). Nowadays the current hypotheses on the relationships between these parameters and the maturational mechanisms are recognized as more complex in the WM (Fig. 4b).

Even in the absence of myelin, the tight organization of WM fibers inside a bundle lead to intrinsic anisotropy related to high longitudinal diffusivity contrasting with low transverse diffusivity (Beaulieu, 2002). Studies in rat pups have shown that the first evidence of anisotropy precedes initial myelin (Wimberger et al., 1995), and that this early anisotropy may be related to sodium-channel activity (Prayer et al., 2001).

During the first stage of myelination (“pre-myelination”), when glial cell bodies and membranes proliferate, both a decrease in brain water content and an increase in membrane density are observed, which imply decreases in mean, longitudinal and transverse diffusivities. Whereas this mechanism had initially been assumed spatially isotropic (Dubois et al., 2008b), recent evidence rather suggests that the initial extension of oligodendroglial processes is anisotropic in favor of the axonal direction (Zanin et al., 2011; Nossin-Manor et al., 2012). This anisotropy increase has been related to the maturation of the compound action potential and the development of immature oligodendrocytes in the rabbit developing WM (Drobyshevsky et al., 2005).

The following “true” myelination process (with the ensheathment of oligodendroglial processes around the axons) is further accompanied by a decrease in both membranes permeability and extracellular distance between membranes, implying an increase in anisotropy, a decrease in transverse diffusivity, but no change in longitudinal diffusivity. At crossing fibers places, the situation may appear puzzling when crossing

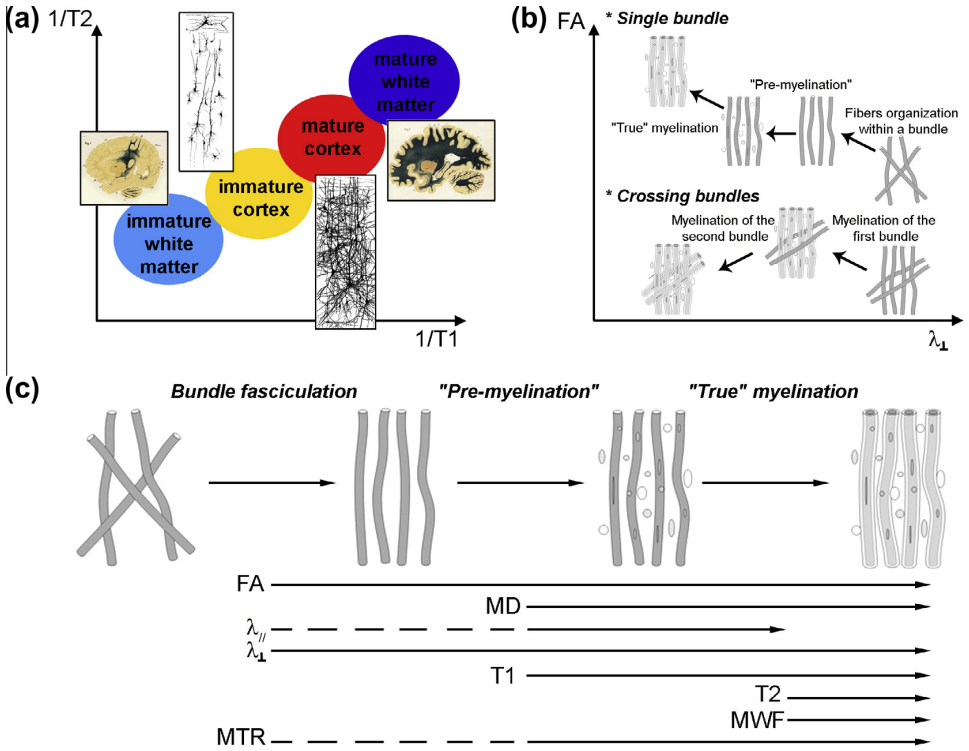

Fig. 4. Illustrations of maturation-related changes in MRI parameters. (a) The decreases in T1 and T2 relaxation times (increases in relaxation rates R1 = 1/T1 and R2 = 1/T2) are more intense in the developing WM than in the developing GM, which leads to contrast inversions on T1w and T2w images during the first post-natal year (Fig. 1). Post-mortem images of WM myelin staining were reproduced from (Flechsig, 1920). (b) During the myelination of WM fibers, two successive processes occur: ''pre-myelination'' with oligodendrocytes and membranes proliferation, and ''true'' myelination. Both lead to changes in DTI parameters: e.g. increase in fractional anisotropy (FA) and decrease in transverse diffusivity ($\lambda_\perp$) in the case of a single maturing bundle (upper row) (Dubois et al., 2008b). But changes are more complex in other configurations, for instance when crossing bundles are maturing at different times (lower row). (c) In summary, quantitative parameters are expected to change at different times depending on the major steps of WM maturation (bundles fasciculation, ''pre-myelination'', ''true'' myelination), suggesting strong parameters complementarity. In a single-bundle configuration, anisotropy (FA) increases, mean (MD) and transverse ($\lambda_\perp$) diffusivities decrease, while longitudinal diffusivity first increases (dashed line) then decreases (Dubois et al., 2008b). T1 and T2 relaxation times decrease, whereas myelin water fraction (MWF) and magnetization transfer ratio (MTR) increase (the dashed line corresponds to MTR observations in preterm corpus callosum (Nossin-Manor et al., 2012)).

bundles follow different maturational calendars: when the first bundle gets myelinated, anisotropy first increases, but it subsequently decreases when the second crossing bundle gets mature (the reverse argument has been detailed for neurodegenerative disorders (Douaud et al., 2011)); at the same time, diffusivities are decreasing (Fig. 4b).

Therefore anisotropy and longitudinal diffusivity are rather good markers of tissue macrostructure and organization, finely characterizing compactness, crossing fibers, etc. but the interpretation of their changes may remain difficult during WM maturation. On the contrary, transverse diffusivity consistently decreases with all maturational processes (Fig. 4c).

Recently, other geometrical diffusion measures (linear and planar diffusion anisotropies Cl and Cp) have been considered to model more accurately different WM microstructures in comparison with the classical cylindrical shape of a fiber bundle (Chen et al., 2011). During maturation, these parameters may be sensitive to changing compactness since after birth Cl growth velocities are highest in central WM while Cp growth velocities are highest in peripheral WM.

Finally, let us keep in mind that DTI parameters vary across bundles in the adult brain, in relation with their macroscopic geometry and compactness. Highlighting maturational effects in the developing brain thus requires either considering the developmental trajectories toward adulthood to evaluate the asymptotes of maturation, or normalizing infant measurements by the adult references (Dubois et al., 2008a).

Myelin-related imaging parameters

Other quantitative parameters relying on the myelin amount have been proposed to evaluate the maturation of WM.

Magnetization transfer ratio. The ''magnetization transfer ratio'' (MTR) informs about the ratio between free water and water with restricted motion, bound to

macromolecules such as proteins and lipids (McGowan, 1999). Thus it is thought to reflect the myelin amount and increase during WM maturation (Kucharczyk et al., 1994). Nevertheless, during the preterm period (26–34 w GA), MTR values have been found higher in the genu and splenium of the CC than in the PLIC and the periventricular white matter (PVWM) (Nossin-Manor et al., 2012). Since at this stage callosal fibers are highly organized, closely packed, but non-myelinated fibers, this technique appears to be sensitive not only to myelin-associated macromolecules, but also to the macromolecular density of axonal cytoskeleton components such as microtubules and neurofilaments (Nossin-Manor et al., 2012) (Fig. 4c).

Myelin water fraction. As for approaches based on ''multi-component relaxation'' (MCR) analyses, different pools of water molecules are modeled in each voxel (Spader et al., 2013). These pools can be distinguished from measured MR signals, on the basis of different relaxometry properties (T1 and/or T2) and of specific exchange relationships (Menon et al., 1991; Whittall et al., 1997; Beaulieu et al., 1998). Such decomposition is supposed to provide valuable information on the tissue microstructure. Whereas the exact number of pools to be modeled is still debated (Deoni et al., 2012b), a consistent pool of water related to myelin is always considered, and studies generally describe maps of ''myelin water fraction'' (MWF) (Fig. 1). This fraction drastically increases during WM maturation (Deoni et al., 2012a) (Fig. 4c). Contrarily to relaxation times, the definition of MWF is *a priori* independent from the magnetic field. But its computation is highly sensitive to both the acquisition protocol and the post-processing modeling, making direct comparisons across studies hardly achievable.

Practical considerations for imaging the developing brain

In vivo *imaging of the baby brain.* The pre- and post-term periods are radically different, not only in terms of brain organization (see next section) but also in terms of practical possibilities to obtain MR images. Because infants after term are generally healthy, ethical and practical issues are similar to older ages. On the contrary, the main difficulty in imaging the pre-term period is to obtain images of healthy (or at least not neurologically ill) brains. Imaging fetuses *in utero* is not commonly done without strong medical arguments. Similarly, preterm newborns are at high-risk of neurological lesions, and their physiological stage is very unstable making them difficult to move to MRI center without good reasons.

In all cases, imaging fetuses and infants is a challenge. Data are difficult to acquire first because of the techniques' sensitivity to motion. Without clinical indication, healthy babies cannot be sedated, then one cannot prevent a fetus to move within the womb, and quietness is difficult to obtain in infants during a long time. Thus, data acquisition should remain short, especially in preterms in whom it is difficult to maintain a stable thermal state inside the MR scanner. Acoustic noise should also remain reasonable, in order to avoid any acoustic trauma and discomfort, and to assure baby's sleep or quiet cooperation. Second, despite short acquisition time, image spatial resolution should be higher than in adults because cerebral structures are smaller. That is why the scarce images obtained at early ages (i.e. before 5 months of gestation) have been obtained in post-mortem fetuses with very long acquisition times.

Technical constraints of conventional imaging. The developing brain is changing every day, much more rapidly than the adult brain between 20 and 50 years of age, and T1w and T2w contrasts change with the brain tissues maturation. This contrast variability and the use of different MR sequences along the first post-natal year require dedicated post-processing tools for different developmental periods to segment unmyelinated and myelinated WM from other cerebral tissues (GM, cerebro-spinal fluid). However it may lead to misclassification of cerebral tissues (Matsuzawa et al., 2001; Choe et al., 2012), and the comparison across ages remains difficult.

Technical constraints of DTI. The signal-to-noise ratio (SNR) of DW images decreases with infants' age because both T2 relaxation times and diffusivities decline during the first post-natal months (Mukherjee et al., 2002). Actually the reliability of DTI estimation is influenced by SNR and by the number of diffusion directions. To a certain extent, acquiring more directions is equivalent to averaging (Dubois et al., 2006a). Adapting the number of diffusion directions according to the infants' age (with more numerous directions in older infants) is worth considering to make the data reproducible across subjects. Furthermore, DTI quantification is particularly sensitive to motion artifacts, and several strategies have been proposed to reduce or correct them during the acquisition (Dubois et al., 2006b) or in post-processing (Dubois et al., in revision).

IMAGING THE EARLY ORGANIZATION OF WM

Imaging the WM growth

Increase in WM volume. With all these difficulties in mind, we can try to appreciate the WM growth by estimating its volume from T1w and T2w images acquired before and after term (Fig. 5a). In normally developing fetuses *in utero*, the global volume of the intermediate zone and subplate (whose frontier remains difficult to delineate) increases from around 15 to 90 cm^3 between 21 w and 31 w GA, i.e. 15% per week (Scott et al., 2011). In premature neonates, the WM volume increases from around 50 cm^3 at 29 w GA to 170 cm^3 at 44 w GA, as reported in age-specific atlases (Kuklisova-Murgasova et al., 2011). Afterward, a longitudinal follow-up study in infants has demonstrated that WM volume increases from around 164 cm^3 at term

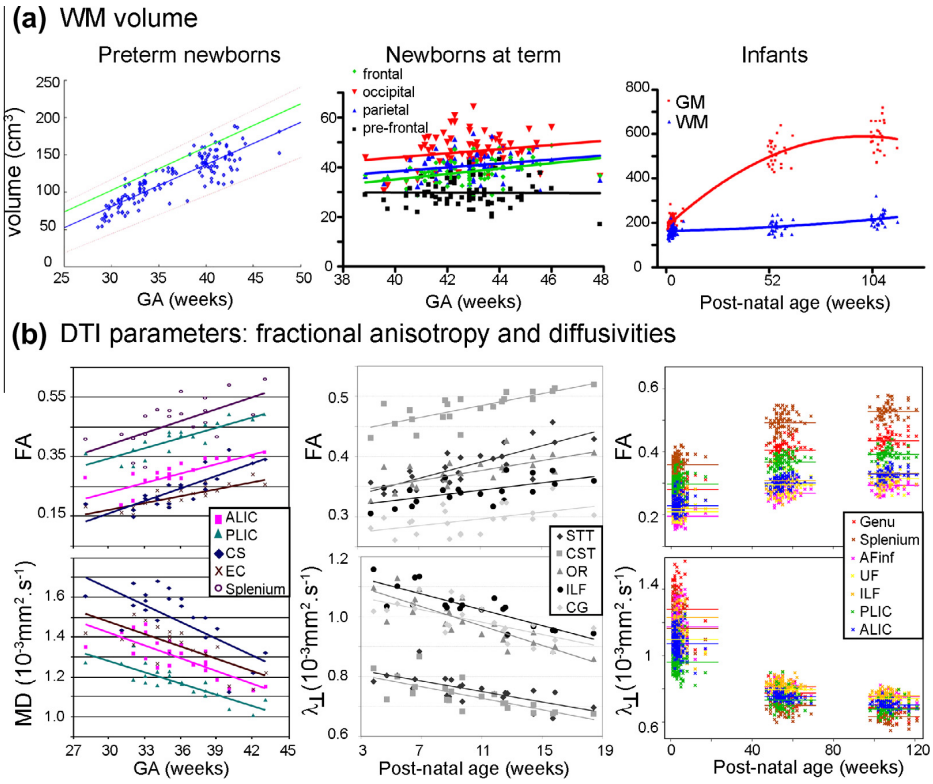

Fig. 5. Age-related changes in WM volume and DTI parameters. Age-related changes in WM volume (a) and in DTI parameters (b) are highlighted in different populations: preterm newborns (left column), at term-born newborns or infants (middle column) and during the first two post-natal years (right column). Note that WM volume increases more slowly than GM volume. Fractional anisotropy (FA) increases in major WM bundles, while mean (MD) and transverse ($\lambda_{\perp}$) diffusivities decrease. DTI parameters strongly differ among WM bundles. Figures were adapted with permission from different studies: WM volumes in preterm newborns imaged at 3 T (Kuklisova-Murgasova et al., 2011), in newborns at term imaged at 3 T (Gilmore et al., 2007), in infants at 0, 1 year and 2 years of age imaged at 3 T (Knickmeyer et al., 2008); DTI parameters in preterm newborns imaged at 1.5 T (Partridge et al., 2004), in infants imaged at 1.5 T (Dubois et al., 2008b), in infants at 0, 1 year and 2 year of age imaged at 3 T (Geng et al., 2012). Abbreviations: AFinf, inferior branch of the arcuate fasciculus; ALIC, anterior limb of the internal capsule; CG, cingulum; CS, centrum semiovale; CST, cortico-spinal tract; EC, external capsule; ILF, inferior longitudinal fasciculus; OR, optic radiations; PLIC, posterior limb of the internal capsule; STT, spino-thalamic tract; UF, uncinate fasciculus.

birth to 183 cm^3 at 1 year of age (i.e. increase by 11% per year), to 218 cm^3 at 2 years of age (i.e. increase by 19% per year).

Thus at these ages WM growth is relatively slow in comparison with the rapid GM growth (by 149% in the first year and 14% in the second year), leading to a decrease in the percentage of WM when normalized for the total brain volume (Gilmore et al., 2007; Knickmeyer et al., 2008). Subsequently the WM volume increases at a higher rate than GM volume throughout childhood (Matsuzawa et al., 2001), and the ratio between WM and GM volumes dramatically increases during childhood and adolescence (Groeschel et al., 2010).

Imaging a mix of several processes. While WM tissue is imaged as a whole on T1w and T2w images, its volume increase actually reflects several processes that occur successively or concomitantly during development, but whose contributions are hard to separate. WM composition is changing dramatically, especially during the mid-gestation period which is marked by neuronal migration: pyramidal neurons follow radial patterns along glial fibers, from the central periventricular region to the cortical periphery, while interneurons follow tangential patterns from the ganglionic eminence. Axonal connections are also growing from central gray nuclei and from cortical regions. Besides, the vascularity is developing according to a radial organization. These coherent structural patterns are mixing, making the dissection of growing fascicles difficult. Concurrently, glial cells proliferate: oligodendrocytes play a crucial role to myelinate axonal fibers during the late pre-term and post-term periods, while the contribution of developing astrocytes and microglia is still poorly understood, notably in terms of metabolism. Overall, several mechanisms contribute to the global increase in WM volume, and more subtle MRI techniques are thus required to detail the axonal organization in the growing WM.

Before term: imaging the growth of fiber connections

Post-mortem investigations with conventional MRI. Correlation studies between histology and

conventional MRI with high spatial resolution in post-mortem fetuses (Judas et al., 2005; Rados et al., 2006) have shown that three fiber systems are recognizable as early as 12 w GA: the CC, the fornix and the hemispheric stalk, which represents a massive connection between the telencephalon and the diencephalon and contains all the projection fibers of the developing internal capsule, including the thalamo-cortical fibers. During the mid-fetal period (17–24 w GA), a substantial elaboration of major cerebral fiber systems is observed in the ''intermediate zone'' (the fetal ''WM''). In the fronto-polar and occipito-polar regions, the fiber architectonics of the fetal cerebrum displays a tangential axon strata. Below the CC, the fornix is well developed. The CC, the internal and ECs are growing. In the central WM, the ''periventricular crossroads'' are the intersections between these major fiber systems: callosal fibers (transverse direction), associative fibers (sagittal direction), thalamo-cortical/cortico-fugal fibers (radial direction).

Between 24 and 32 w GA, the major events are the development of the corona radiata, from the transformation of the tangential fetal fiber-architectonic stratification. All major segments of the cerebral WM can be recognized: CC, corona radiata, centrum semiovale (CS), gyral WM (which is not yet fully developed because the subplate zone remains interposed between the corona radiata and the cortex). Fibers continue to grow at the levels of the periventricular crossroads and of the ventricular part of the CC, which leads to a blurring on post-mortem images. By term birth, all major fiber systems are to be in place.

Post-mortem investigations with diffusion imaging. DTI imaging is an exquisite technique to detail the developing organization of WM and precise the developmental calendar observed on conventional images. Imaging fetuses post-mortem at 19–20 w GA confirmed that limbic fibers (CG, fornix) develop first (entire trajectories visible at 19 w GA) and association fibers last (Huang et al., 2006). The CC, the UF and inferior longitudinal fasciculus (ILF) become apparent between 13 and 22 w GA (Huang et al., 2009). At 20 w GA, the CC formation is more advanced in the frontal lobe (genu and forceps minor) than in other regions (splenium and forceps major, body). The core regions of projection fibers are well-developed early on, but not the peripheral regions (i.e. the corona radiata), and the ALIC develops before the posterior limb.

The more elaborated technique of HARDI tractography applied to post-mortem fetuses between 19 w to 42 w GA (Takahashi et al., 2012) has clarified the calendar of tract development. A few immature long-range association pathways are visible early on in the WM (e.g. the uncinate and fronto-occipital fascicles), and short-range cortico-cortical tracts emerge prior to gyrification in regions where sulci will later develop. An early dominant radial organization of WM that gradually diminishes by term age is observed. This feature disappears first in dorsal parieto-occipital regions, second in ventral fronto-temporal regions; earlier at the depths of sulci than in the crests of gyri. At 19 w GA, the ganglionic eminence presents a dominant tangential organization which gradually disappears by term. These radial and tangential patterns are related to neuronal migration as confirmed by the combination of HARDI technique with the structural analysis of conventional images in post-mortem fetuses between 21 w and 24 w GA (Kolasinski et al., 2013). The radial pattern originates in dorsopallial ventricular/subventricular zone, while the tangentio-radial patterns originate in subpallial ganglionic eminence. These patterns regress in a caudo-rostral and lateral–ventral to medial–dorsal direction across this short developmental period. The post-mortem application of immunomarkers to radial glial fibers, axons, and blood vessels has enabled to decipher the histological origins of the HARDI-defined coherence (Xu et al., 2012), suggesting that the radial coherence in the fetal WM likely reflects a mixture of radial glial fibers (at mid-gestation), penetrating blood vessels (that are consistently radial), and radial axons (among radial, tangential and oblique axons).

In vivo investigations. Data acquired *in vivo* in preterms and fetuses have confirmed post-mortem studies. Using diffusion imaging, the early laminar organization of the cerebrum (cortical plate, subplate zone, intermediate zone, subventricular and periventricular zones, germinal matrix) has been delineated in 25–27 w GA preterm newborns (Maas et al., 2004). Imaging studies of *in utero* fetuses have described that the pyramidal tract and the splenium and genu of the CC are depicted early on and may be reconstructed in 3D using tractography algorithms between 18 and 37 w GA (Bui et al., 2006; Kasprian et al., 2008; Pontabry et al., 2013), as well as the Probst bundles in cases of CC agenesis (Kasprian et al., 2013). In preterms, association tracts and subcortical projection tracts are also identified (Partridge et al., 2004; Dudink et al., 2007).

After term: imaging the WM bundles and developing connectivity

Imaging the WM bundles. After term birth, almost all prominent WM tracts are identified despite low anisotropy values (Hermoye et al., 2006). This early organization has been further mapped in 3D in infants between 1 and 4 months of age, using a dedicated protocol for acquisition and post-processing (Dubois et al., 2006a, 2008b). Most commissural bundles (genu, body and splenium of the CC), projection bundles (CST, spino-thalamic tract (STT), OR, ALIC), limbic bundles (fornix and CG) and associative bundles (EC, uncinate, arcuate, superior and inferior longitudinal fascicles) can be detected and tracked (Fig. 3). In a longitudinal study using a dedicated DTI atlas, a similar organization of the major bundles has been shown between newborns and toddlers of 1 and 2 years of age (Geng et al., 2012).

However, some associative bundles that mature later on (see section 'Imaging the maturation of white matter'), such as the superior longitudinal fasciculus, demonstrate large changes in fiber orientations during the first

post-natal months (Zhang et al., 2007). High-field imaging at 3 T may enable the precise exploration of subtle connections within specific developing networks (e.g. the language network (Dubois et al., in preparation)). Actually one should keep in mind that DTI methodology does not enable to decipher between exact fiber directions in the place of crossing fibers, particularly when crossing bundles are maturing at different rates and over different time periods. This leads to erroneous interpretation on the presence/absence of a bundle in the developing brain. Accordingly, the dorsal pathway of the developing language network (the AF) may not seem to fully connect temporal and frontal regions in newborns (Perani et al., 2011; Brauer et al., 2013), but this might be artifactually related to its low maturation in comparison with the crossing CST (Dubois et al., in preparation).

Developing WM connectivity. Recently, the wiring pattern of cerebral connections and the maturational calendar have been reinterpreted in the framework of small-world topology (Hagmann et al., 2010). The principal characteristics observed in adults have been found in infants demonstrating that the infant brain is neither fully connected, nor only locally connected (Fan et al., 2011; Yap et al., 2011; Pandit et al., 2013). This result might appear trivial, given the anatomical results reviewed above showing that the short and main long-distance connections are already observed before term, but this approach has the advantage to have no *a priori* and to place the brain within a mathematical formalism. Longitudinal studies performed from birth to two years of age and based on regional GM volumes (Fan et al., 2011) and on the number of fibers passing through pairs of regions (Yap et al., 2011) have been interpreted as showing an increase in integration and a decrease in functional segregation.

Behavioral and functional studies certainly support such hypotheses, but structural studies are confronted with several unsolved drawbacks. For example, the difficulties in GM/WM segmentation vary with age due to changes in T1w and T2w contrasts; weakly myelinated fibers may appear shorter because of lower anisotropy that impacts tractography reconstructions; smaller head size creates partial volume effects that might blur connectivity results in younger infants. Finally, network efficiency is sometimes indirectly inferred from diffusion metrics (Hagmann et al., 2010), and not directly from the transfer times of the neural information, whereas the information propagation at the same latency in the infant and adults brains may not require a similar tract myelination because of the different brain sizes (Salami et al., 2003). Fortunately, combining these structural measures with electrophysiological and/or resting-state fMRI has indeed shown a strengthening of the correlations between structural and functional connectivities (Hagmann et al., 2010).

IMAGING THE MATURATION OF WM

When the bundles are in place, a slow process of maturation begins, following a different calendar in different bundles.

Different periods of WM maturation

Before term: localized myelination. Before 36 w GA, unmyelinated WM is the most prominent brain tissue according to T1w and T2w images, and an abrupt increase in myelinated WM is detected between 35 and 41 w GA (Huppi et al., 1998b). However, there is earlier evidence of myelination in specific WM regions (Counsell et al., 2002) such as the inferior and superior cerebellar peduncles before 28 w GA, the PLIC, the CST around the central sulcus and the corona radiata from 36 w GA on.

DTI studies of *in utero* fetuses (Righini et al., 2003; Bui et al., 2006; Kasprian et al., 2008; Jiang et al., 2009) and ex utero preterm newborns as young as 26 w GA (Huppi et al., 1998a,b; Neil et al., 1998; Miller et al., 2002; Dudink et al., 2007; Aeby et al., 2009, 2012) have found the general pattern of age-related decrease in mean diffusivity and increase in anisotropy in different WM regions (pyramidal tract, CC, frontal and occipital regions). In longitudinal imaging between 28 and 43 w GA (Partridge et al., 2004), early differences have been further identified between several projection and association pathways, with low mean diffusivity and high FA in cerebral peduncles, internal capsule and commissural tracts of the CC, suggesting an early maturation of these tracts (Fig. 5b) and confirming the analyses done on T1w/T2w images.

After term: major changes related to myelination. After term, WM myelination is intense in the developing brain, and quantitative MRI parameters have underlined successive maturational periods: acute changes during the first post-natal months, less rapid modifications during toddlerhood, and slower changes thereafter until young adulthood. It is particularly obvious for DTI parameters (Fig. 5b): decrease in MD and increase in FA are rapid during the first post-natal year and slower during the second year (Mukherjee et al., 2001; Forbes et al., 2002; Hermoye et al., 2006; Geng et al., 2012; Sadeghi et al., 2013). Age-related decreases in diffusivities have been modeled through exponential decays from birth to childhood (Mukherjee et al., 2001), or by a sigmoid function (Gompertz growth function, based on intuitive variables related to delay, speed, and expected asymptotic value) longitudinally from birth to 2 years of age (Sadeghi et al., 2013).

In the same way, T1 and T2 decreases are particularly rapid over the two first years (Engelbrecht et al., 1998; Haselgrove et al., 2000), yielding to exponential decays with age (Fig. 6a) (Leppert et al., 2009). Conversely, the MTR increases exponentially (Engelbrecht et al., 1998; van Buchem et al., 2001) (Fig. 6b). Between 3 and 60 months, the increase in MWF is best modeled by a modified Gompertz function which is characterized by four distinct parameters: the developmental lag, the transitionary period and two growth rates (Fig. 6c) (Dean et al., 2014).

To summarize, for all MRI and DTI parameters, the dynamic of changes is intense between birth and 2 years of age, which does not match the relatively slow

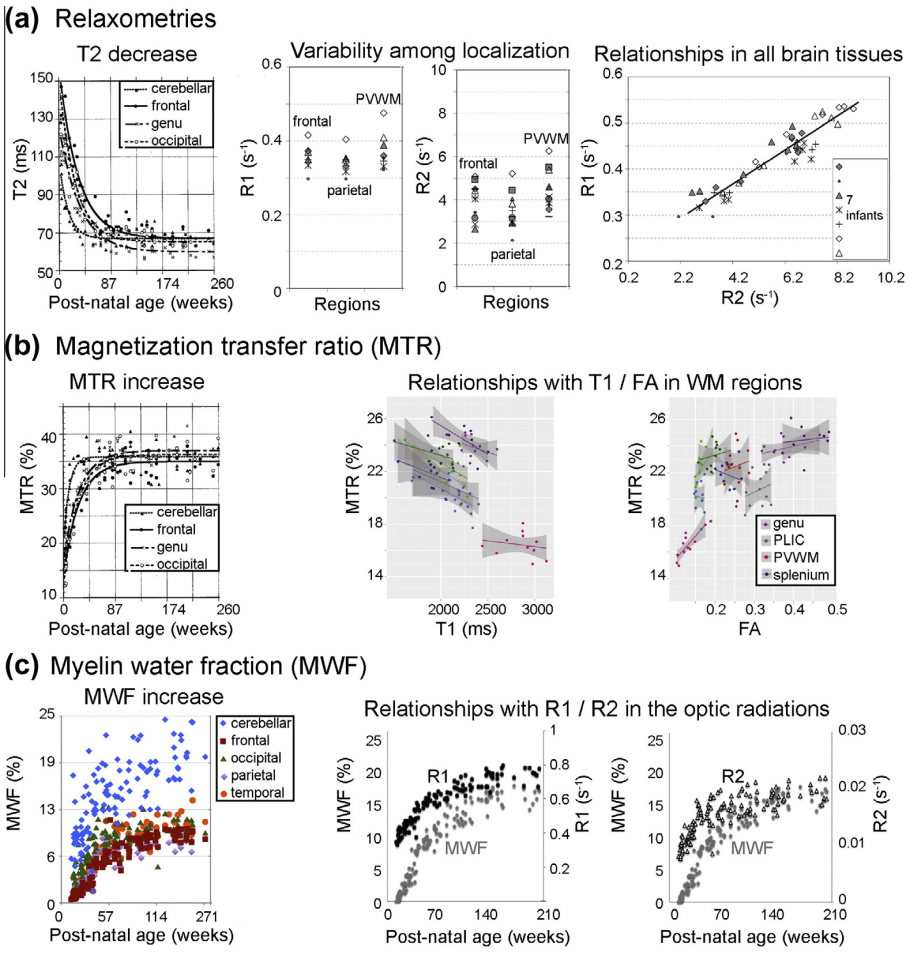

Fig. 6. Age-related changes in quantitative parameters related to myelin. Relaxation times T1 and T2 (a), magnetization transfer ratio (MTR) (b) and myelin water fraction (MWF) (c) are shown during infancy and toddlerhood. T1 and T2 decrease exponentially with age while relaxation rates (Ri = 1/Ti), MTR and MWF increase (left column). Note parameters variability across WM regions, which demonstrate different temporal maturation courses (left and middle columns). Some correlations between the parameters have been shown (right and middle columns), but these correlations mainly rely on co-variations with the infants age. Figures were adapted with permission from different studies: age-related changes in T2 and MTR at 1.5 T in infants (Engelbrecht et al., 1998), variability in relaxation rates at 3 T in newborns at term (Williams et al., 2005), correlations between MTR, T1 and FA at 1.5 T in preterm newborns (Nossin-Manor et al., 2012), MWF increase at 3 T in infants (Deoni et al., 2012a). Abbreviations: PLIC, posterior limb of the internal capsule; PVWM, peri-ventricular white matter.

increase in WM volume during this developmental period. Furthermore these non-linear patterns of changes reveal considerable regional variations across and along WM bundles because of myelination asynchrony.

Spatio-temporal sequence of WM maturation

Maturation asynchrony across WM bundles. The interest of DTI studies rests in the quantification of differences across WM bundles, detailing a progression of maturation from a central-to-peripheral and a posterior-to-anterior direction (Oishi et al., 2011). For instance, the increase in anisotropy appears greater in non-compact ones (corona radiata and peripheral WM) than in compact WM structures (CC, internal capsule, cerebral peduncle) across the first three post-natal years (McGraw et al., 2002). Diffusivities and anisotropy show different evolutive patterns across brain regions of the preterm brain (Nossin-Manor et al., 2012) and of the infant brain during the first two post-natal years (Geng et al., 2012), with highest FA in the CC and lowest mean diffusivity in the PLIC.

By taking advantage of the different sensitivities of diffusivity and anisotropy to maturational processes, a model based on the parameter changes during the ''pre-myelination'' and the ''true'' myelination periods was build to describe the bundles maturational stages in infants between 4 and 18 weeks of post-natal age in comparison with an adult group (Dubois et al., 2008b). This model enabled to detect early spatio-temporal differences in the maturation progression of a set of

bundles, from the more to the less mature bundles: (1) the CST, (2) the STT and the fornix, (3) the OR, the arcuate and inferior longitudinal fascicles, (4) the ALIC and the CG. In a similar way, three distinct phases of maturation, with specific dynamics for each bundle type, have been modeled and identified in the fetal WM between 23 and 38 w GA: (i) the axonal organization, (ii) the myelination gliosis, and (iii) the myelination, which appears early in the CST, followed by the OR and the CC (Zanin et al., 2011).

Regional asynchrony in WM maturation is also observed by MTR, showing a relatively mature stage at 12.9 and 15.6 m in the occipital and frontal WM respectively, and at 17.7 and 18.7 m in the splenium and genu of CC (Xydis et al., 2006). The spatio-temporal pattern of myelination progression is also nicely demonstrated through MWF (Deoni et al., 2011, 2012a). It rises earlier in a frontal–parietal region (projection fibers) than in an frontal region (association fibers) during childhood, following the standard caudal-to-rostral trend (Lancaster et al., 2003). In infants between 3 and 11 months of age, MWF increases in the cerebellum, pons, and internal capsule; it further increases caudo-cranially from the splenium of the CC and OR (at 3–4 months); to the occipital and parietal lobes (at 4–6 months); and then to the genu of the CC and frontal and temporal lobes (at 6–8 months) (Deoni et al., 2011). The spatio-temporal pattern provided over a larger age range (3–60 months) is coherent with histological studies of myelination (Deoni et al., 2012a).

Maturation progression within a WM bundle. The spatial resolution of DTI also allows to studying maturation along a WM tract: maturation does not evolve at the same time and speed in different spatial locations within a bundle (Partridge et al., 2005; Colby et al., 2012). During the first two post-natal years, changes near cortical regions generally appear smaller than in brain central regions (Geng et al., 2012). In preterm newborns between 28 and 43 w GA, the motor tract and the somatosensory radiations of the CST begin to myelinate during the late preterm period first at the level of the internal capsule (Berman et al., 2005). Maturation further seems to proceed earlier in the motor pathway than in the sensory one at the vertex where motor fibers initiate from the cortex. From term-equivalent age (Berman et al., 2005; Geng et al., 2012), the anisotropy profile presents a local dip at the level of the corona radiata, which suggests the beginning and ongoing maturation of crossing pathways (fibers of the CC and superior longitudinal fasciculus).

The myelination progression in the visual pathways of infants between 6 and 17 weeks of post-natal age has also been studied, showing two asynchronous fronts of maturation in the OR: an early wave in the anterior region, initiating from the lateral geniculate nucleus, and a later catching-up wave in the posterior region, initiating from the occipital cortex (Dubois et al., 2008c). According to the assumption that myelination proceeds from the neuron body to the periphery (McCart and Henry, 1994), this pattern may result from the respective myelination of the geniculo-cortical (projection) fibers and cortico-geniculate (feedback) fibers, with a delayed maturation of the cortical retrocontrol to the thalamus relative to bottom-up fibers.

Sophisticated approaches to map WM maturation asynchrony

Recently, original approaches that combine MRI parameters have been proposed to measure even more precisely the maturation across WM regions.

Correlations between MRI parameters. The different parameters (T1, T2, DTI, MTR, MWF) capture different properties of WM maturation (Fig. 4c). Some studies have described specific correlations between them, but most have missed to take into account their major age-related dependencies.

In neonates, a strong correlation has been detected between relaxation rates R1 (1/T1) and R2 (1/T2) among different WM regions (Williams et al., 2005) (Fig. 6a). In the kitten WM, DTI mean diffusivity seems to correlate more with R2 than with R1 (Baratti et al., 1999), whereas maps of mean diffusivity demonstrate a pattern of regional variations similar to T1 maps in preterm newborns between 26 and 45 w GA (Nossin-Manor et al., 2012).

According to the inverse correlation between MTR increase and T2 decrease in WM after term birth, it has been assumed that both changes rely on fast proton relaxation within macromolecules in myelinated tissue (Engelbrecht et al., 1998). An inverse correlation between MTR and T1 is observed in preterm newborns near term (Nossin-Manor et al., 2012) (Fig. 6b). MTR is also positively correlated with FA in WM during the preterm period, suggesting a coupling between the increase in concentration of pre-myelination-associated macromolecules and the increase in axonal alignment and axonal density (Nossin-Manor et al., 2012) (Fig. 6b). The comparison of MWF measurements with age-related dynamics of T1 (R1) and T2 (R2) relaxation times (rates) has shown that all parameters are sensitive to WM maturation in infants, but in different ways suggesting that they provide complementary information on maturation processes (Lancaster et al., 2003; Deoni et al., 2012a) (Fig. 6c).

Since T1, T2, DTI, MTR and MWF maps show regional variations following different evolutions with age, these parameters are to be sensitive to multiple and complementary mechanisms of WM development. It is only by combining and comparing these parameters that one can hope to outline comprehensive patterns of the tissue macro- and microstructures. For instance, in preterm infants the CC displays high values of MTR, T1, FA and longitudinal diffusivity and low transverse diffusivity values, because callosal fibers are highly organized, closely packed, with high axonal density of microstructural components (e.g. microtubules, neurofilaments), leading to high directionality, coherence and restriction, but the fibers are not myelinated and the water content is high (Nossin-Manor et al., 2012). On the other hand, the PLIC shows in the preterm period

(pre-myelinating stage) low values of MTR, FA and diffusivities and high T1 values, resulting from a lower fiber packing density than in the CC, a lower macromolecular density, along with lower directionality and coherence but higher restriction; at term, the increase in MTR values, along with lower transverse diffusivity, are markers of the myelination process (Nossin-Manor et al., 2012). Thus a clever use of these different parameters, informed by a better understanding of the mechanisms they are sensitive to, do provide more precise *in vivo* maps of the WM maturation.

Multi-parametric imaging. Dealing with multi-parametric data will open new perspectives in the study of WM development. Combining the time trajectories of anisotropy, longitudinal and transverse diffusivities may definitely provide accurate landmarks on maturation asynchrony across bundles (Sadeghi et al., 2013). Modeling the information from structural (T1w, T2w, PD images) and DTI data (longitudinal and transverse diffusivities) with modified Legendre polynomials has also provided an absolute measure of maturation (rate of change) and a relative measure (time shift) (Prastawa et al., 2010). Maps of growth rates demonstrate slow regions (e.g. internal capsule) and rapidly growing regions (e.g. deep WM in anterior and posterior regions, temporal lobe). Maps of time shifts based on structural data demonstrate gradual changes in regions that undergo myelination, while surprisingly those based on DTI data mostly highlight differences between central and peripheral regions (Prastawa et al., 2010).

DTI parameters may also be combined with quantitative relaxation times T1 and T2. Because of the complex relations between these parameters in developing bundles (Kulikova et al., 2013a), an original measure of maturation has been defined in infants between 3 and 21 weeks of post-natal age to summarize the changes in all parameters while taking into account their possible correlations. This measure, based on the computation of the Mahalanobis distance in comparison with a group of adults, confirms the evidence of WM maturation asynchrony over a short developmental period and outperforms univariate approaches (Kulikova et al., 2013b). It further provides a quantitative evaluation in weeks of the developmental delays between WM bundles. The maturation order provided by this multi-parametric approach during the first post-natal year is congruent with the, from the most to the least mature bundle: the STT; the OR; 6 weeks later: the middle portion of the CST and the fornix; 12 weeks later: the inferior portion of the CST; 7 weeks later: the genu and splenium of the CC and the superior portion of the CST; 6 weeks later: the inferior CG; 3 weeks later: the CC body and the superior CG; 3 weeks later: the inferior longitudinal, fronto-occipital and uncinate fascicles; 2 weeks later: the EC; 3 weeks later: the ALIC; 4 weeks later: the superior longitudinal and arcuate fascicles literature (Kulikova et al., in preparation).

FUNCTIONAL CORRELATES OF MRI BIOMARKERS OF WM MATURATION

In healthy infants, WM maturation correlates with psychomotor acquisitions (Prayer and Prayer, 2003) but the exact relationships between cerebral structure and function remain difficult to grasp. Brain anatomical analyses might help to understand the biological bases of cognitive development, by revealing the early structural specificities that may underlie human complex functions such as language, and by mapping correlations between structural indices and functional efficiency. WM studies are also crucial to understand early functional impairments such as the ones triggered by preterm birth.

Early WM asymmetries in highly lateralized functional networks

Finding which hemisphere is the left one on an axial image of an adult human brain is usually relatively easy thanks to the Yakovlev torque creating right frontal and left occipital petalias, and a steeper and shorter right sylvian fissure (Toga and Thompson, 2003). Some of the structural asymmetries observed in the peri-sylvian regions (Heschl gyrus, *planum temporale*, superior temporal sulcus (STS)) have been described during the early brain development of fetuses and preterm newborns (Chi et al., 1977; Feess-Higgins and Laroche, 1987; Dubois et al., 2008a, 2010a). Other asymmetries evolve later on during development: for instance the posterior extension of the sylvian fissure progresses until adolescence and adulthood (Sowell et al., 2002). At the functional level, the left-hemisphere specialization for language processing is observed early on in infants (Dehaene-Lambertz et al., 2002, 2006) and already at 6 months of gestation (Mahmoudzadeh et al., 2013), and the lateralization of the somato-sensory response is also detected at birth (Erberich et al., 2006). The origins and relationships between these early anatomical and functional asymmetries are still debated.

Using DTI in healthy infants, three WM regions have been shown asymmetric early on (Dubois et al., 2009): (1) the temporal part of the AF is larger on the left; (2) its left parietal part shows a better microscopic organization than the right; (3) the CST is more mature in the left hemisphere between the cerebral peduncles and the PLIC. These two bundles have also been shown asymmetric in preterm infants at term-equivalent age (Liu et al., 2010) and in adults (Buchel et al., 2004; Parker et al., 2005). Since these WM pathways are related to language and motor networks, such early structural asymmetries might be biomarkers of the genetic constraints driving development of lateralized functions in the human brain, although no strict correlation has been found between asymmetries of the motor pathways and later handedness.

Myelin content is also asymmetrical in multiple WM regions, with no significant change over time during infancy (O'Muircheartaigh et al., 2013): toward the left hemisphere in the temporal/occipital lobe on the trajectory of the arcuate and inferior longitudinal

fascicles, in the medial frontal and posterior parietal lobes; toward the right hemisphere in the dorsal external/extreme capsule and in central WM. Furthermore, language ability correlates with MWF rightward asymmetry in the external/extreme capsule and with MWF leftward asymmetry in frontal WM, and such relationships seem to stabilize around 4 years of age (O'Muircheartaigh et al., 2013).

Correlations between DTI parameters and functional measurements

The key question that encourages further *in vivo* MRI studies of the developing brain is to which extent advanced structural imaging provides biomarkers of the sensori-motor and cognitive development of infants. In the developing language network, the time course of WM myelination parallels language acquisition, with lexical explosion after 18 months of age (Pujol et al., 2006; Su et al., 2008). Similar relationships have been highlighted in 12-month-old infants, where visuospatial working memory performance correlated with DTI microstructural characteristics of WM tracts connecting brain regions known to be involved in working memory (genu of the CC, anterior and superior thalamic radiations, anterior CG, AF), beyond individual variations in age and developmental level (Short et al., 2013).

Structure–function correlations can also be highlighted by comparing MRI parameters with neurophysiological measures. In the visual system during the first post-natal months, several maturation processes (e.g. fiber myelination, retina and cortex development) lead to a dramatic decrease of the latency of the first response wave to a visual stimulus (P1) as measured by event-related potentials, from about 260 ms at birth to about 120 ms at 4 months of age (McCulloch et al., 1999). This decrease is related to an increase in the conduction speed of the neural impulse, which is correlated to the OR microstructure and maturation (FA and transverse diffusivity) beyond the effect of age (Dubois et al., 2008c). This correlation study of EEG and DTI measurements (obtained in the same infants) outlines the functional significance of structural markers during WM maturation. The ability to characterize individual anatomical and functional differences across infants is very promising for the understanding of normal development with special focus on experience-dependent mechanisms and critical periods of plasticity. It is also crucial for the definition of biomarkers that will characterize and detect early perturbations of developmental trajectories.

Functional correlates of MRI biomarkers in preterm newborns

Based on the results obtained in healthy infants, early biomarkers of neurological deficits are searched for, especially in the case of premature birth. The early organization and maturation of axonal pathways is a highly vulnerable process during the second half of pregnancy (Kostovic and Jovanov-Milosevic, 2006). In infants born prematurely, brain growth is disturbed by the change from *in utero* to ex utero environment, and the difficulties to maintain a stable homeostasis. But whereas the neurodevelopmental disabilities of children born prematurely are now rather well described, the underlying alterations of brain development (that lead to disabilities) remain poorly understood (Ment et al., 2009).

Early impairments in WM development. MRI studies might provide early biomarkers of functional outcome and of specific disturbances of cognitive development. While several reviews have detailed WM abnormalities related to prematurity (periventricular leucomalacia, punctate lesions, diffuse excessive high signal intensity (DEHSI)) and their long-term effects on the child brain (for example (Ment et al., 2009; Rutherford et al., 2010), we here summarize only major findings observed in preterm infants without gross brain lesions and imaged below 2 years of age.

The impact of prematurity on WM development has been mainly evaluated by comparing preterms at term-equivalent age with full-term infants. Preterm infants present with less GM/WM differentiation and myelination in comparison with full-term newborns (Huppi et al., 1996; Mewes et al., 2006). The macrostructure of the CC is impaired, with reduced volume correlating with lower GA at birth (Thompson et al., 2012). Using voxel-based analyses (Rose et al., 2008) or tract-based spatial statistics (TBSS) (Anjari et al., 2007), FA reductions were found in several WM regions (CS, frontal WM, CC, internal and ECs), but higher FA associated with lower T2 values were also observed in cortico-spinal projections, suggesting a decreased number of crossing inter-hemispheric fibers associated with a decreased water concentration (Rose et al., 2008).

Beside WM, thalamic development is also dramatically disrupted by prematurity, with reduced volume related to abnormalities in ''allied'' WM structures (CSTs and CC) at term-equivalent age (Ball et al., 2012b). The thalamo-cortical loop seems highly vulnerable, with diminished connections between the thalamus and frontal cortices, supplementary motor areas, occipital lobe and temporal gyri in preterm infants (Ball et al., 2012a). Prematurity is also related to widespread reductions in the connection strength of WM tracts involving all cortical lobes and several subcortical structures during the second post-natal year (Pandit et al., 2013).

Correlations with behavioral measures. Local reductions in WM volumes at term-equivalent age in the sensorimotor and mid-temporal regions are strongly correlated with measures of cognitive and motor development between 18 and 20 months of corrected age (Peterson et al., 2003). In the absence of apparent WM lesions, higher mean diffusivity values at the level of the CS at term-equivalent age have been associated with poorer developmental quotient on the Griffiths Mental Development Scales at 2 years of corrected age (Krishnan et al., 2007). Similarly, a TBSS analysis has shown that developmental quotient at 2 years corrected age is related to FA in subparts of the CC at

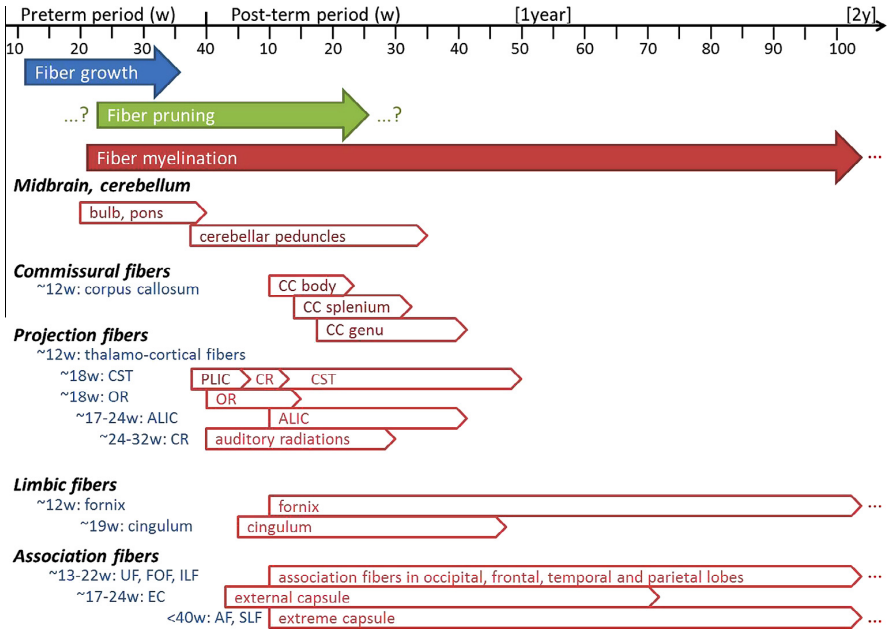

Fig. 7. General time-line of WM development. The time-courses of developmental mechanisms are tentatively summarized across WM bundles, according to post-mortem investigations and MRI studies. These mechanisms include the growth, pruning and myelination of axonal fibers, during the pre-term and post-term periods (fetal and post-natal ages in weeks). For each mechanism, approximate time periods are indicated. To our knowledge, information on the beginning and ending of axonal pruning are missing in the human brain. Purple-bordered arrows refer to the myelination process. Abbreviations: AF, arcuate fasciculus; ALIC, anterior limb of the internal capsule; CC, corpus callosum; CG, cingulum; CR, corona radiate; CST, cortico-spinal tract; EC, external capsule; FOF, fronto-occipital fasciculus; ILF, inferior longitudinal fasciculus; PLIC, posterior limb of the internal capsule; OR, optic radiations; SLF, superior longitudinal fasciculus; STT, spino-thalamic tract; UF, uncinate fasciculus. (For interpretation of the references to color in this figure legend, the reader is referred to the web version of this article.)

term-equivalent age; performance sub-scores to FA in the CC and right CG; and eye-hand coordination sub-scores to FA in the CG, fornix, anterior commissure, CC and right uncinate fasciculus (UF) (Counsell et al., 2008).

Focus on the developing visual system. Three studies have focused on the early development of the visual system in preterm infants, because this function matures early on and is frequently impaired by premature birth. Between 29 and 41 w GA, the microstructural development (FA) of the OR has been correlated with the newborn visual maturity (scores from a visual fixation tracking assessment) independently of GA (Berman et al., 2009). This has been confirmed at term-equivalent age, with a specific correlation between the visual assessment score and the FA in the OR, independently from GA at birth, GA at scan or presence of lesions on conventional MRI (Bassi et al., 2008). A recent study has further evidenced an effect of the period of premature extra-uterine life in addition to the degree of prematurity: indeed, visual function around term-equivalent age seems related to FA in the OR at that age, but also to FA evolution pattern, as characterized by the rate of increase between two successive scans (the first between 30 and 36 w GA, the second at term-equivalent age between 39 and 46 w GA) (Groppo et al., 2012). The alteration of WM pathways microstructural maturation during the late preterm period thus impacts the visual function at birth.

CONCLUSION

Characterizing the dynamics of human brain development and the structural bases of functional maturation requires *in vivo* studies of the healthy newborn and infant. These studies are challenging and require dedicated methodologies for image acquisition and post-processing. But it is worth the effort since new quantitative markers of maturation have been recently validated, also providing a better understanding of the deleterious effects of early disturbances such as prematurity.

Mechanisms of WM development are complex and intermingled. In terms of early WM organization, the growth and wiring of axonal fibers occur mostly during the preterm period, whereas the pruning of aberrant or useless connections rather starts during the first post-natal weeks along with external stimulations. Afterward, fibers get myelinated and progressively functionally mature, which may result from neuronal activity and also reinforce it. WM maturation further impacts on the functional efficiency of brain networks, which correlates with the infant acquisitions. All these mechanisms occur at different times and speeds according to cerebral

regions and involved functions, with maturation proceeding until adulthood in some associative frontal and temporal regions. A tentative summary of the timeline of WM development during the preterm period and the first post-natal months can be provided from post-mortem investigations and *in vivo* MRI studies (Fig. 7). Although relatively coherent, some variations in the time courses are observed because the techniques are differently sensitive to mechanisms of WM organization and maturation. Let us keep in mind that MRI techniques remain indirect and macroscopic approaches to explore the developing microstructure. They can hardly investigate some mechanisms (e.g. fiber pruning), but their main advantage is to be non-invasive techniques that can be applied *in vivo* in healthy fetuses and infants. For instance, they are the only conceivable approach to investigate how brain maturation is influenced early on by environmental factors and nutrition (e.g. boosting of WM myelination by breastfeeding (Deoni et al., 2013)).

Other emerging MRI techniques, such as magnetic susceptibility mapping and phase imaging, are promising to help characterize the microstructural properties of the developing WM (Zhong et al., 2011; Lodygensky et al., 2012; Chen et al., 2013). Of course, WM changes are not completed by 2 years of age, but are protracted in some brain regions until the end of adolescence; however it is beyond the scope of the current article to review all existing studies based on structural MRI (Paus et al., 1999, 2001; Paus, 2005, 2010; Giedd and Rapoport, 2010) and DTI (Barnea-Goraly et al., 2005; Eluvathingal et al., 2007; Lebel et al., 2008; Faria et al., 2010; Lebel and Beaulieu, 2011). Finally, the interactions between the developing WM connectivity and the development of cortical regions will probably take a place of honor soon, since an increasing number of studies have recently provided early quantitative markers of cortical maturation (Leroy et al., 2011a), that may also correlate with the development of infant cognitive abilities (Aeby et al., 2013; Travis et al., 2013).

To sum, correlation approaches based on complementary imaging approaches (including anatomical and functional imaging and behavioral assessments) enable to explore the developing brain at several levels, from brain structure development to the infant motor and cognitive acquisitions. Beyond normal development, these studies are crucial to understand the mechanisms of pathologies that result from early cerebral anomalies (e.g. genetic diseases, epilepsies, mental retardation, learning disorders), to assess the influence of early disturbances related to fetal conditions (e.g. intra-uterine growth restriction, teratogen exposures) or perinatal events (e.g. premature birth, neonatal stroke), and to follow the efficiency and robustness of medical interventions.

Acknowledgments—The author research is supported by the Fyssen Foundation, the McDonnell Foundation, the "Ecole des Neurosciences de Paris", the "Fondation Motrice", the "Fondation de France", the French National Agency for Research (ANR), the CIBM imaging center from Geneva and Lausanne, the Swiss National Science Foundation, the Leenards Foundation and the European consortium NEOBRAIN.

REFERENCES

Aeby A, De Tiege X, Creuzil M, David P, Baleriaux D, Van Overmeire B, Metens T, Van Bogaert P (2013) Language development at 2 years is correlated to brain microstructure in the left superior temporal gyrus at term equivalent age: a diffusion tensor imaging study. Neuroimage 78(C):145–151.

Aeby A, Liu Y, De Tiege X, Denolin V, David P, Baleriaux D, Kavec M, Metens T, Van Bogaert P (2009) Maturation of thalamic radiations between 34 and 41 weeks' gestation: a combined voxel-based study and probabilistic tractography with diffusion tensor imaging. AJNR Am J Neuroradiol 30(9):1780–1786.

Aeby A, Van Bogaert P, David P, Baleriaux D, Vermeylen D, Metens T, De Tiege X (2012) Nonlinear microstructural changes in the right superior temporal sulcus and lateral occipitotemporal gyrus between 35 and 43 weeks in the preterm brain. Neuroimage 63(1):104–110.

Anjari M, Srinivasan L, Allsop JM, Hajnal JV, Rutherford MA, Edwards AD, Counsell SJ (2007) Diffusion tensor imaging with tract-based spatial statistics reveals local white matter abnormalities in preterm infants. Neuroimage 35(3):1021–1027.

Ball G, Boardman JP, Aljabar P, Pandit A, Arichi T, Merchant N, Rueckert D, Edwards AD, Counsell SJ (2012a) The influence of preterm birth on the developing thalamocortical connectome. Cortex 49(6):1711–1721.

Ball G, Boardman JP, Rueckert D, Aljabar P, Arichi T, Merchant N, Gousias IS, Edwards AD, Counsell SJ (2012b) The effect of preterm birth on thalamic and cortical development. Cereb Cortex 22(5):1016–1024.

Ball G, Srinivasan L, Aljabar P, Counsell SJ, Durighel G, Hajnal JV, Rutherford MA, Edwards AD (2013) Development of cortical microstructure in the preterm human brain. Proc Natl Acad Sci U S A 110(23):9541–9546.

Baratti C, Barnett AS, Pierpaoli C (1999) Comparative MR imaging study of brain maturation in kittens with T1, T2, and the trace of the diffusion tensor. Radiology 210(1):133–142.

Barkovich AJ (2000) Concepts of myelin and myelination in neuroradiology. AJNR Am J Neuroradiol 21(6):1099–1109.

Barkovich AJ, Kjos BO, Jackson Jr DE, Norman D (1988) Normal maturation of the neonatal and infant brain MR imaging at 15 T. Radiology 166(1 Pt 1):173–180.

Barkovich AJ, Lyon G, Evrard P (1992) Formation, maturation, and disorders of white matter. AJNR Am J Neuroradiol 13(2):447–461.

Barnea-Goraly N, Menon V, Eckert M, Tamm L, Bammer R, Karchemskiy A, Dant CC, Reiss AL (2005) White matter development during childhood and adolescence: a cross-sectional diffusion tensor imaging study. Cereb Cortex 15(12):1848–1854.

Barres BA, Raff MC (1993) Proliferation of oligodendrocyte precursor cells depends on electrical activity in axons. Nature 361(6409):258–260.

Bassi L, Ricci D, Volzone A, Allsop JM, Srinivasan L, Pai A, Ribes C, Ramenghi LA, Mercuri E, Mosca F, et al (2008) Probabilistic diffusion tractography of the optic radiations and visual function in preterm infants at term equivalent age. Brain 131(2):573–582.

Baumann N, Pham-Dinh D (2001) Biology of oligodendrocyte and myelin in the mammalian central nervous system. Physiol Rev 81(2):871–927.

Beaulieu C (2002) The basis of anisotropic water diffusion in the nervous system – a technical review. NMR Biomed 15(7–8):435–455.

Beaulieu C, Fenrich FR, Allen PS (1998) Multicomponent water proton transverse relaxation and T2-discriminated water diffusion in myelinated and nonmyelinated nerve. Magn Reson Imaging 16(10):1201–1210.

Berman JI, Glass HC, Miller SP, Mukherjee P, Ferriero DM, Barkovich AJ, Vigneron DB, Henry RG (2009) Quantitative fiber tracking analysis of the optic radiation correlated with visual performance in premature newborns. AJNR Am J Neuroradiol 30(1):120–124.

Berman JI, Mukherjee P, Partridge SC, Miller SP, Ferriero DM, Barkovich AJ, Vigneron DB, Henry RG (2005) Quantitative diffusion tensor MRI fiber tractography of sensorimotor white matter development in premature infants. Neuroimage 27(4):862–871.

Brauer J, Anwander A, Perani D, Friederici AD (2013) Dorsal and ventral pathways in language development. Brain Lang 127(2):289–295.

Brody BA, Kinney HC, Kloman AS, Gilles FH (1987) Sequence of central nervous system myelination in human infancy. I. An autopsy study of myelination. J Neuropathol Exp Neurol 46(3):283–301.

Buchel C, Raedler T, Sommer M, Sach M, Weiller C, Koch MA (2004) White matter asymmetry in the human brain: a diffusion tensor MRI study. Cereb Cortex 14(9):945–951.

Bui T, Daire JL, Chalard F, Zaccaria I, Alberti C, Elmaleh M, Garel C, Luton D, Blanc N, Sebag G (2006) Microstructural development of human brain assessed in utero by diffusion tensor imaging. Pediatr Radiol 36(11):1133–1140.

Butt AM, Berry M (2000) Oligodendrocytes and the control of myelination in vivo: new insights from the rat anterior medullary velum. J Neurosci Res 59(4):477–488.

Chen WC, Foxley S, Miller KL (2013) Detecting microstructural properties of white matter based on compartmentalization of magnetic susceptibility. Neuroimage 70:1–9.

Chen Y, An H, Zhu H, Jewells V, Armao D, Shen D, Gilmore JH, Lin W (2011) Longitudinal regression analysis of spatial–temporal growth patterns of geometrical diffusion measures in early postnatal brain development with diffusion tensor imaging. Neuroimage 58(4):993–1005.

Chi JG, Dooling EC, Gilles FH (1977) Left–right asymmetries of the temporal speech areas of the human fetus. Arch Neurol 34(6):346–348.

Choe MS, Ortiz-Mantilla S, Makris N, Gregas M, Bacic J, Haehn D, Kennedy D, Pienaar R, Caviness Jr VS, Benasich AA, et al (2012) Regional infant brain development: an MRI-based morphometric analysis in 3 to 13 month olds. Cereb Cortex 23(9):2100–2117.

Colby JB, Soderberg L, Lebel C, Dinov ID, Thompson PM, Sowell ER (2012) Along-tract statistics allow for enhanced tractography analysis. Neuroimage 59(4):3227–3242.

Counsell SJ, Edwards AD, Chew AT, Anjari M, Dyet LE, Srinivasan L, Boardman JP, Allsop JM, Hajnal JV, Rutherford MA, et al (2008) Specific relations between neurodevelopmental abilities and white matter microstructure in children born preterm. Brain 131(Pt 12):3201–3208.

Counsell SJ, Maalouf EF, Fletcher AM, Duggan P, Battin M, Lewis HJ, Herlihy AH, Edwards AD, Bydder GM, Rutherford MA (2002) MR imaging assessment of myelination in the very preterm brain. AJNR Am J Neuroradiol 23(5):872–881.

Dean 3rd DC, O'Muircheartaigh J, Dirks H, Waskiewicz N, Lehman K, Walker L, Han M, Deoni SC (2014) Modeling healthy male white matter and myelin development: 3 through 60 months of age. Neuroimage 84:742–752.

deAzevedo LC, Hedin-Pereira C, Lent R (1997) Callosal neurons in the cingulate cortical plate and subplate of human fetuses. J Comp Neurol 386(1):60–70.

Dehaene-Lambertz G, Dehaene S, Hertz-Pannier L (2002) Functional neuroimaging of speech perception in infants. Science 298(5600):2013–2015.

Dehaene-Lambertz G, Hertz-Pannier L, Dubois J (2006) Nature and nurture in language acquisition: anatomical and functional brain-imaging studies in infants. Trends Neurosci 29(7):367–373.

Demerens C, Stankoff B, Logak M, Anglade P, Allinquant B, Couraud F, Zalc B, Lubetzki C (1996) Induction of myelination in the central nervous system by electrical activity. Proc Natl Acad Sci U S A 93(18):9887–9892.

Deoni SC, Dean 3rd DC, O'Muircheartaigh J, Dirks H, Jerskey BA (2012a) Investigating white matter development in infancy and early childhood using myelin water faction and relaxation time mapping. Neuroimage 63(3):1038–1053.

Deoni SC, Dean 3rd DC, Piryatinksy I, O'Muircheartaigh J, Waskiewicz N, Lehman K, Han M, Dirks H (2013) Breastfeeding and early white matter development: a cross-sectional study. Neuroimage 82:77–86.

Deoni SC, Matthews L, Kolind SH (2012b) One component? Two components? Three? The effect of including a nonexchanging "free" water component in multicomponent driven equilibrium single pulse observation of T1 and T2. Magn Reson Med 70(1):147–154.

Deoni SC, Mercure E, Blasi A, Gasston D, Thomson A, Johnson M, Williams SC, Murphy DG (2011) Mapping infant brain myelination with magnetic resonance imaging. J Neurosci 31(2):784–791.

Douaud G, Jbabdi S, Behrens TE, Menke RA, Gass A, Monsch AU, Rao A, Whitcher B, Kindlmann G, Matthews PM, et al (2011) DTI measures in crossing-fibre areas: increased diffusion anisotropy reveals early white matter alteration in MCI and mild Alzheimer's disease. Neuroimage 55(3):880–890.

Draganova R, Eswaran H, Murphy P, Lowery C, Preissl H (2007) Serial magnetoencephalographic study of fetal and newborn auditory discriminative evoked responses. Early Hum Dev 83(3):199–207.

Drobyshevsky A, Song SK, Gamkrelidze G, Wyrwicz AM, Derrick M, Meng F, Li L, Ji X, Trommer B, Beardsley DJ, et al (2005) Developmental changes in diffusion anisotropy coincide with immature oligodendrocyte progression and maturation of compound action potential. J Neurosci 25(25):5988–5997.

Dubois J, Benders M, Cachia A, Lazeyras F, Ha-Vinh Leuchter R, Sizonenko SV, Borradori-Tolsa C, Mangin JF, Huppi PS (2008a) Mapping the early cortical folding process in the preterm newborn brain. Cereb Cortex 18(6):1444–1454.

Dubois J, Benders M, Lazeyras F, Borradori-Tolsa C, Leuchter RH, Mangin JF, Huppi PS (2010a) Structural asymmetries of perisylvian regions in the preterm newborn. Neuroimage 52(1):32–42.

Dubois J, Dehaene-Lambertz G, Perrin M, Mangin JF, Cointepas Y, Duchesnay E, Le Bihan D, Hertz-Pannier L (2008b) Asynchrony of the early maturation of white matter bundles in healthy infants: quantitative landmarks revealed noninvasively by diffusion tensor imaging. Hum Brain Mapp 29(1):14–27.

Dubois J, Dehaene-Lambertz G, Soares C, Cointepas Y, Le Bihan D, Hertz-Pannier L (2008c) Microstructural correlates of infant functional development: example of the visual pathways. J Neurosci 28(8):1943–1948.

Dubois J, Hertz-Pannier L, Cachia A, Mangin JF, Le Bihan D, Dehaene-Lambertz G (2009) Structural asymmetries in the infant language and sensori-motor networks. Cereb Cortex 19(2):414–423.

Dubois J, Hertz-Pannier L, Dehaene-Lambertz G, Cointepas Y, Le Bihan D (2006a) Assessment of the early organization and maturation of infants' cerebral white matter fiber bundles: a feasibility study using quantitative diffusion tensor imaging and tractography. Neuroimage 30(4):1121–1132.

Dubois J, Kulikova S, Hertz-Pannier L, Mangin JF, Dehaene-Lambertz G, Poupon C (in revision) Correction strategy for diffusion-weighted images corrupted with motion: application to the DTI evaluation of infants' white matter. Magn Reson Imag.

Dubois J, Poupon C, Lethimonnier F, Le Bihan D (2006b) Optimized diffusion gradient orientation schemes for corrupted clinical DTI data sets. MAGMA 19(3):134–143.

Dubois J, Poupon C, Thirion B, Leroy F, Simonnet H, Hertz-Pannier L, Dehaene-Lambertz G (in preparation) Exploring the language networks in the human infant brain.

Duclap D, Schmitt B, Lebois A, Riff O, Guevara P, Marrakchi-Kacem L, Brion V, Poupon F, Mangin JF, Poupon C (2012) Connectomist-2.0: a novel diffusion analysis toolbox for BrainVISA. In: Proceedings of the 29th ESMRMB meeting, 842.

Dudink J, Lequin M, van Pul C, Buijs J, Conneman N, van Goudoever J, Govaert P (2007) Fractional anisotropy in white matter tracts of very-low-birth-weight infants. Pediatr Radiol 37(12):1216–1223.
Eluvathingal TJ, Hasan KM, Kramer L, Fletcher JM, Ewing-Cobbs L (2007) Quantitative diffusion tensor tractography of association and projection fibers in normally developing children and adolescents. Cereb Cortex 17(12):2760–2768.
Engelbrecht V, Rassek M, Preiss S, Wald C, Modder U (1998) Age-dependent changes in magnetization transfer contrast of white matter in the pediatric brain. AJNR Am J Neuroradiol 19(10):1923–1929.
Erberich SG, Panigrahy A, Friedlich P, Seri I, Nelson MD, Gilles F (2006) Somatosensory lateralization in the newborn brain. Neuroimage 29(1):155–161.
Fan Y, Shi F, Smith JK, Lin W, Gilmore JH, Shen D (2011) Brain anatomical networks in early human brain development. Neuroimage 54(3):1862–1871.
Faria AV, Zhang J, Oishi K, Li X, Jiang H, Akhter K, Hermoye L, Lee SK, Hoon A, Stashinko E, et al (2010) Atlas-based analysis of neurodevelopment from infancy to adulthood using diffusion tensor imaging and applications for automated abnormality detection. Neuroimage 52(2):415–428.
Feess-Higgins A, Laroche JC (1987) Development of the human foetal brain: an anatomical atlas. Inserm-CNRS; Masson.
Flechsig P (1920) Anatomie des Menschlichen Gehirn und Rückenmarks, auf myelogenetischer grundlage. G. Thieme.
Forbes KP, Pipe JG, Bird CR (2002) Changes in brain water diffusion during the 1st year of life. Radiology 222(2):405–409.
Friede RL (1972) Control of myelin formation by axon caliber (with a model of the control mechanism). J Comp Neurol 144(2):233–252.
Gao W, Lin W, Chen Y, Gerig G, Smith JK, Jewells V, Gilmore JH (2009) Temporal and spatial development of axonal maturation and myelination of white matter in the developing brain. AJNR Am J Neuroradiol 30(2):290–296.
Geng X, Gouttard S, Sharma A, Gu H, Styner M, Lin W, Gerig G, Gilmore JH (2012) Quantitative tract-based white matter development from birth to age 2 years. Neuroimage 61(3):542–557.
Giedd JN, Rapoport JL (2010) Structural MRI of pediatric brain development: what have we learned and where are we going? Neuron 67(5):728–734.
Gilles F, Shankle W, Dooling E (1983) Myelinated tracts: growth patterns. In: Gilles F, Leviton A, Dooling E, editors. Boston: John Wright PSG.
Gilmore JH, Lin W, Prastawa MW, Looney CB, Vetsa YS, Knickmeyer RC, Evans DD, Smith JK, Hamer RM, Lieberman JA, et al (2007) Regional gray matter growth, sexual dimorphism, and cerebral asymmetry in the neonatal brain. J Neurosci 27(6):1255–1260.
Groeschel S, Vollmer B, King MD, Connelly A (2010) Developmental changes in cerebral grey and white matter volume from infancy to adulthood. Int J Dev Neurosci 28(6):481–489.
Groppo M, Ricci D, Bassi L, Merchant N, Doria V, Arichi T, Allsop JM, Ramenghi L, Fox MJ, Cowan FM, et al (2012) Development of the optic radiations and visual function after premature birth. Cortex.
Guevara P, Duclap D, Poupon C, Marrakchi-Kacem L, Fillard P, Le Bihan D, Leboyer M, Houenou J, Mangin JF (2012) Automatic fiber bundle segmentation in massive tractography datasets using a multi-subject bundle atlas. Neuroimage 61(4):1083–1099.
Guevara P, Poupon C, Riviere D, Cointepas Y, Descoteaux M, Thirion B, Mangin JF (2011) Robust clustering of massive tractography datasets. Neuroimage 54(3):1975–1993.
Guillery RW (2005) Is postnatal neocortical maturation hierarchical? Trends Neurosci 28(10):512–517.
Gyllensten L, Malmfors T (1963) Myelinization of the optic nerve and its dependence on visual function – a quantitative investigation in mice. J Embryol Exp Morphol 11:255–266.
Hagmann P, Sporns O, Madan N, Cammoun L, Pienaar R, Wedeen VJ, Meuli R, Thiran JP, Grant PE (2010) White matter maturation reshapes structural connectivity in the late developing human brain. Proc Natl Acad Sci U S A 107(44):19067–19072.
Hardy RJ, Friedrich Jr VL (1996) Progressive remodeling of the oligodendrocyte process arbor during myelinogenesis. Dev Neurosci 18(4):243–254.
Haselgrove J, Moore J, Wang Z, Traipe E, Bilaniuk L (2000) A method for fast multislice T1 measurement: feasibility studies on phantoms, young children, and children with Canavan's disease. J Magn Reson Imaging 11(4):360–367.
Hermoye L, Saint-Martin C, Cosnard G, Lee SK, Kim J, Nassogne MC, Menten R, Clapuyt P, Donohue PK, Hua K, et al (2006) Pediatric diffusion tensor imaging: normal database and observation of the white matter maturation in early childhood. Neuroimage 29(2):493–504.
Huang H, Xue R, Zhang J, Ren T, Richards LJ, Yarowsky P, Miller MI, Mori S (2009) Anatomical characterization of human fetal brain development with diffusion tensor magnetic resonance imaging. J Neurosci 29(13):4263–4273.
Huang H, Zhang J, Wakana S, Zhang W, Ren T, Richards LJ, Yarowsky P, Donohue P, Graham E, van Zijl PC, et al (2006) White and gray matter development in human fetal, newborn and pediatric brains. Neuroimage 33(1):27–38.
Huppi PS, Dubois J (2006) Diffusion tensor imaging of brain development. Semin Fetal Neonatal Med 11(6):489–497.
Huppi PS, Maier SE, Peled S, Zientara GP, Barnes PD, Jolesz FA, Volpe JJ (1998a) Microstructural development of human newborn cerebral white matter assessed in vivo by diffusion tensor magnetic resonance imaging. Pediatr Res 44(4):584–590.
Huppi PS, Schuknecht B, Boesch C, Bossi E, Felblinger J, Fusch C, Herschkowitz N (1996) Structural and neurobehavioral delay in postnatal brain development of preterm infants. Pediatr Res 39(5):895–901.
Huppi PS, Warfield S, Kikinis R, Barnes PD, Zientara GP, Jolesz FA, Tsuji MK, Volpe JJ (1998b) Quantitative magnetic resonance imaging of brain development in premature and mature newborns. Ann Neurol 43(2):224–235.
Huttenlocher PR, Bonnier C (1991) Effects of changes in the periphery on development of the corticospinal motor system in the rat. Brain Res Dev Brain Res 60(2):253–260.
Innocenti GM, Price DJ (2005) Exuberance in the development of cortical networks. Nat Rev Neurosci 6(12):955–965.
Ishibashi T, Dakin KA, Stevens B, Lee PR, Kozlov SV, Stewart CL, Fields RD (2006) Astrocytes promote myelination in response to electrical impulses. Neuron 49(6):823–832.
Jiang S, Xue H, Counsell S, Anjari M, Allsop J, Rutherford M, Rueckert D, Hajnal JV (2009) Diffusion tensor imaging (DTI) of the brain in moving subjects: application to in-utero fetal and ex-utero studies. Magn Reson Med 62(3):645–655.
Judas M, Rados M, Jovanov-Milosevic N, Hrabac P, Stern-Padovan R, Kostovic I (2005) Structural, immunocytochemical, and mr imaging properties of periventricular crossroads of growing cortical pathways in preterm infants. AJNR Am J Neuroradiol 26(10):2671–2684.
Kanold PO, Luhmann HJ (2010) The subplate and early cortical circuits. Annu Rev Neurosci 33:23–48.
Kasprian G, Brugger PC, Schopf V, Mitter C, Weber M, Hainfellner JA, Prayer D (2013) Assessing prenatal white matter connectivity in commissural agenesis. Brain 136(Pt 1):168–179.
Kasprian G, Brugger PC, Weber M, Krssak M, Krampl E, Herold C, Prayer D (2008) In utero tractography of fetal white matter development. Neuroimage 43(2):213–224.
Kinney HC, Brody BA, Kloman AS, Gilles FH (1988) Sequence of central nervous system myelination in human infancy. II. Patterns of myelination in autopsied infants. J Neuropathol Exp Neurol 47(3):217–234.
Knickmeyer RC, Gouttard S, Kang C, Evans D, Wilber K, Smith JK, Hamer RM, Lin W, Gerig G, Gilmore JH (2008) A structural MRI study of human brain development from birth to 2 years. J Neurosci 28(47):12176–12182.
Kolasinski J, Takahashi E, Stevens AA, Benner T, Fischl B, Zollei L, Grant PE (2013) Radial and tangential neuronal migration pathways in the human fetal brain: anatomically distinct patterns of diffusion MRI coherence. Neuroimage 79:412–422.

Kostovic I, Jovanov-Milosevic N (2006) The development of cerebral connections during the first 20–45 weeks' gestation. Semin Fetal Neonatal Med 11(6):415–422.
Kostovic I, Judas M (2010) The development of the subplate and thalamocortical connections in the human foetal brain. Acta Paediatr 99(8):1119–1127.
Krishnan ML, Dyet LE, Boardman JP, Kapellou O, Allsop JM, Cowan F, Edwards AD, Rutherford MA, Counsell SJ (2007) Relationship between white matter apparent diffusion coefficients in preterm infants at term-equivalent age and developmental outcome at 2 years. Pediatrics 120(3):e604–e609.
Kucharczyk W, Macdonald PM, Stanisz GJ, Henkelman RM (1994) Relaxivity and magnetization transfer of white matter lipids at MR imaging: importance of cerebrosides and pH. Radiology 192(2):521–529.
Kuklisova-Murgasova M, Aljabar P, Srinivasan L, Counsell SJ, Doria V, Serag A, Gousias IS, Boardman JP, Rutherford MA, Edwards AD, et al (2011) A dynamic 4D probabilistic atlas of the developing brain. Neuroimage 54(4):2750–2763.
Kulikova S, Hertz-Pannier L, Dehaene-Lambertz G, Poupon C, Dubois J (2013a) Comparison of quantitative MRI parameters in the developing white matter bundles. In: Proceedings of the 30th ESMRMB meeting, 660.
Kulikova S, Hertz-Pannier L, Dehaene-Lambertz G, Poupon C, Dubois J (2013b) Multi-parametric evaluation of the white matter maturation. In: Proceedings of the 30th ESMRMB meeting, 476.
Kulikova S, Hertz-Pannier L, Dehaene-Lambertz G, Poupon C, Dubois J (in preparation) Multi-parametric evaluation of the white matter maturation.
LaMantia AS, Rakic P (1990) Axon overproduction and elimination in the corpus callosum of the developing rhesus monkey. J Neurosci 10(7):2156–2175.
Lancaster JL, Andrews T, Hardies LJ, Dodd S, Fox PT (2003) Three-pool model of white matter. J Magn Reson Imaging 17(1):1–10.
Langworthy OR (1928a) A correlated study of the development of reflex activity in fetal and young kittens and the myelinization of the tracts in the nervous system. Contrib Embryol 20:127–172.
Langworthy OR (1928b) The behaviour of pouch young opossums correlated with the myelinization of tracts in the central nervous system. J Comp Neurol 46:201–248.
Le Bihan D (2003) Looking into the functional architecture of the brain with diffusion MRI. Nat Rev Neurosci 4(6):469–480.
Le Bihan D, Johansen-Berg H (2012) Diffusion MRI at 25: exploring brain tissue structure and function. Neuroimage 61(2):324–341.
Le Bihan D, Mangin JF, Poupon C, Clark CA, Pappata S, Molko N, Chabriat H (2001) Diffusion tensor imaging: concepts and applications. J Magn Reson Imaging 13(4):534–546.
Lebel C, Beaulieu C (2011) Longitudinal development of human brain wiring continues from childhood into adulthood. J Neurosci 31(30):10937–10947.
Lebel C, Walker L, Leemans A, Phillips L, Beaulieu C (2008) Microstructural maturation of the human brain from childhood to adulthood. Neuroimage 40(3):1044–1055.
Leppert IR, Almli CR, McKinstry RC, Mulkern RV, Pierpaoli C, Rivkin MJ, Pike GB (2009) T(2) relaxometry of normal pediatric brain development. J Magn Reson Imaging 29(2):258–267.
Leroy F, Glasel H, Dubois J, Hertz-Pannier L, Thirion B, Mangin JF, Dehaene-Lambertz G (2011a) Early maturation of the linguistic dorsal pathway in human infants. J Neurosci 31(4):1500–1506.
Leroy F, Mangin JF, Rousseau F, Glasel H, Hertz-Pannier L, Dubois J, Dehaene-Lambertz G (2011b) Atlas-free surface reconstruction of the cortical grey–white interface in infants. PLoS One 6(11):e27128.
Liu Y, Baleriaux D, Kavec M, Metens T, Absil J, Denolin V, Pardou A, Avni F, Van Bogaert P, Aeby A (2010) Structural asymmetries in motor and language networks in a population of healthy preterm neonates at term equivalent age: a diffusion tensor imaging and probabilistic tractography study. Neuroimage 51(2):783–788.
Lodygensky GA, Marques JP, Maddage R, Perroud E, Sizonenko SV, Huppi PS, Gruetter R (2012) In vivo assessment of myelination by phase imaging at high magnetic field. Neuroimage 59(3):1979–1987.
Maas LC, Mukherjee P, Carballido-Gamio J, Veeraraghavan S, Miller SP, Partridge SC, Henry RG, Barkovich AJ, Vigneron DB (2004) Early laminar organization of the human cerebrum demonstrated with diffusion tensor imaging in extremely premature infants. Neuroimage 22(3):1134–1140.
Mahmoudzadeh M, Dehaene-Lambertz G, Fournier M, Kongolo G, Goudjil S, Dubois J, Grebe R, Wallois F (2013) Syllabic discrimination in premature human infants prior to complete formation of cortical layers. Proc Natl Acad Sci U S A 110(12):4846–4851.
Maldonado IL, de Champfleur NM, Velut S, Destrieux C, Zemmoura I, Duffau H (2013) Evidence of a middle longitudinal fasciculus in the human brain from fiber dissection. J Anat 223(1):38–45.
Martino J, Brogna C, Robles SG, Vergani F, Duffau H (2010) Anatomic dissection of the inferior fronto-occipital fasciculus revisited in the lights of brain stimulation data. Cortex 46(5):691–699.
Matsumae M, Kurita D, Atsumi H, Haida M, Sato O, Tsugane R (2001) Sequential changes in MR water proton relaxation time detect the process of rat brain myelination during maturation. Mech Ageing Dev 122(12):1281–1291.
Matsuzawa J, Matsui M, Konishi T, Noguchi K, Gur RC, Bilker W, Miyawaki T (2001) Age-related volumetric changes of brain gray and white matter in healthy infants and children. Cereb Cortex 11(4):335–342.
Matthieu JM (1993) An introduction to the molecular basis of inherited myelin diseases. J Inherit Metab Dis 16(4):724–732.
McCart RJ, Henry GH (1994) Visual corticogeniculate projections in the cat. Brain Res 653(1–2):351–356.
McConnell SK, Ghosh A, Shatz CJ (1989) Subplate neurons pioneer the first axon pathway from the cerebral cortex. Science 245(4921):978–982.
McCulloch DL, Orbach H, Skarf B (1999) Maturation of the pattern-reversal VEP in human infants: a theoretical framework. Vision Res 39(22):3673–3680.
McGowan JC (1999) The physical basis of magnetization transfer imaging. Neurology 53(5 Suppl 3):S3–S7.
McGraw P, Liang L, Provenzale JM (2002) Evaluation of normal age-related changes in anisotropy during infancy and childhood as shown by diffusion tensor imaging. AJR Am J Roentgenol 179(6):1515–1522.
McKinstry RC, Mathur A, Miller JH, Ozcan A, Snyder AZ, Schefft GL, Almli CR, Shiran SI, Conturo TE, Neil JJ (2002) Radial organization of developing preterm human cerebral cortex revealed by non-invasive water diffusion anisotropy MRI. Cereb Cortex 12(12):1237–1243.
Menon RS, Rusinko MS, Allen PS (1991) Multiexponential proton relaxation in model cellular systems. Magn Reson Med 20(2):196–213.
Ment LR, Hirtz D, Huppi PS (2009) Imaging biomarkers of outcome in the developing preterm brain. Lancet Neurol 8(11):1042–1055.
Mewes AU, Huppi PS, Als H, Rybicki FJ, Inder TE, McAnulty GB, Mulkern RV, Robertson RL, Rivkin MJ, Warfield SK (2006) Regional brain development in serial magnetic resonance imaging of low-risk preterm infants. Pediatrics 118(1):23–33.
Miller DJ, Duka T, Stimpson CD, Schapiro SJ, Baze WB, McArthur MJ, Fobbs AJ, Sousa AM, Sestan N, Wildman DE, et al (2012) Prolonged myelination in human neocortical evolution. Proc Natl Acad Sci U S A 109(41):16480–16485.
Miller SP, Vigneron DB, Henry RG, Bohland MA, Ceppi-Cozzio C, Hoffman C, Newton N, Partridge JC, Ferriero DM, Barkovich AJ (2002) Serial quantitative diffusion tensor MRI of the premature brain: development in newborns with and without injury. J Magn Reson Imaging 16(6):621–632.
Mukherjee P, Miller JH, Shimony JS, Conturo TE, Lee BC, Almli CR, McKinstry RC (2001) Normal brain maturation during childhood: developmental trends characterized with diffusion-tensor MR imaging. Radiology 221(2):349–358.

Mukherjee P, Miller JH, Shimony JS, Philip JV, Nehra D, Snyder AZ, Conturo TE, Neil JJ, McKinstry RC (2002) Diffusion-tensor MR imaging of gray and white matter development during normal human brain maturation. AJNR Am J Neuroradiol 23(9):1445–1456.

Neil J, Miller J, Mukherjee P, Huppi PS (2002) Diffusion tensor imaging of normal and injured developing human brain – a technical review. NMR Biomed 15(7–8):543–552.

Neil JJ, Shiran SI, McKinstry RC, Schefft GL, Snyder AZ, Almli CR, Akbudak E, Aronovitz JA, Miller JP, Lee BC, et al (1998) Normal brain in human newborns: apparent diffusion coefficient and diffusion anisotropy measured by using diffusion tensor MR imaging. Radiology 209(1):57–66.

Ng WP, Cartel N, Roder J, Roach A, Lozano A (1996) Human central nervous system myelin inhibits neurite outgrowth. Brain Res 720(1–2):17–24.

Nossin-Manor R, Card D, Morris D, Noormohamed S, Shroff MM, Whyte HE, Taylor MJ, Sled JG (2012) Quantitative MRI in the very preterm brain: assessing tissue organization and myelination using magnetization transfer, diffusion tensor and T(1) imaging. Neuroimage.

O'Muircheartaigh J, Dean 3rd DC, Dirks H, Waskiewicz N, Lehman K, Jerskey BA, Deoni SC (2013) Interactions between white matter asymmetry and language during neurodevelopment. J Neurosci 33(41):16170–16177.

Oishi K, Mori S, Donohue PK, Ernst T, Anderson L, Buchthal S, Faria A, Jiang H, Li X, Miller MI, et al (2011) Multi-contrast human neonatal brain atlas: application to normal neonate development analysis. Neuroimage 56(1):8–20.

Pandit AS, Robinson E, Aljabar P, Ball G, Gousias IS, Wang Z, Hajnal JV, Rueckert D, Counsell SJ, Montana G, et al (2013) Whole-brain mapping of structural connectivity in infants reveals altered connection strength associated with growth and preterm birth. Cereb Cortex.

Parker GJ, Luzzi S, Alexander DC, Wheeler-Kingshott CA, Ciccarelli O, Lambon Ralph MA (2005) Lateralization of ventral and dorsal auditory-language pathways in the human brain. Neuroimage 24(3):656–666.

Partridge SC, Mukherjee P, Berman JI, Henry RG, Miller SP, Lu Y, Glenn OA, Ferriero DM, Barkovich AJ, Vigneron DB (2005) Tractography-based quantitation of diffusion tensor imaging parameters in white matter tracts of preterm newborns. J Magn Reson Imaging 22(4):467–474.

Partridge SC, Mukherjee P, Henry RG, Miller SP, Berman JI, Jin H, Lu Y, Glenn OA, Ferriero DM, Barkovich AJ, et al (2004) Diffusion tensor imaging: serial quantitation of white matter tract maturity in premature newborns. Neuroimage 22(3):1302–1314.

Paus T (2005) Mapping brain maturation and cognitive development during adolescence. Trends Cogn Sci 9(2):60–68.

Paus T (2010) Growth of white matter in the adolescent brain: myelin or axon? Brain Cogn 72(1):26–35.

Paus T, Collins DL, Evans AC, Leonard G, Pike B, Zijdenbos A (2001) Maturation of white matter in the human brain: a review of magnetic resonance studies. Brain Res Bull 54(3):255–266.

Paus T, Zijdenbos A, Worsley K, Collins DL, Blumenthal J, Giedd JN, Rapoport JL, Evans AC (1999) Structural maturation of neural pathways in children and adolescents: in vivo study. Science 283(5409):1908–1911.

Perani D, Saccuman MC, Scifo P, Anwander A, Spada D, Baldoli C, Poloniato A, Lohmann G, Friederici AD (2011) Neural language networks at birth. Proc Natl Acad Sci U S A 108(38):16056–16061.

Peterson BS, Anderson AW, Ehrenkranz R, Staib LH, Tageldin M, Colson E, Gore JC, Duncan CC, Makuch R, Ment LR (2003) Regional brain volumes and their later neurodevelopmental correlates in term and preterm infants. Pediatrics 111(5 Pt 1):939–948.

Poduslo SE, Jang Y (1984) Myelin development in infant brain. Neurochem Res 9(11):1615–1626.

Pontabry J, Rousseau F, Oubel E, Studholme C, Koob M, Dietemann JL (2013) Probabilistic tractography using Q-ball imaging and particle filtering: application to adult and in-utero fetal brain studies. Med Image Anal 17(3):297–310.

Prastawa M, Sadeghi N, Gilmore J, Lin W, Gerig G (2010) A new framework for analyzing white matter maturation in early brain development. In: Proceedings of the 22nd IPMI meeting.

Prayer D, Barkovich AJ, Kirschner DA, Prayer LM, Roberts TP, Kucharczyk J, Moseley ME (2001) Visualization of nonstructural changes in early white matter development on diffusion-weighted MR images: evidence supporting premyelination anisotropy. AJNR Am J Neuroradiol 22(8):1572–1576.

Prayer D, Prayer L (2003) Diffusion-weighted magnetic resonance imaging of cerebral white matter development. Eur J Radiol 45(3):235–243.

Pujol J, Soriano-Mas C, Ortiz H, Sebastian-Galles N, Losilla JM, Deus J (2006) Myelination of language-related areas in the developing brain. Neurology 66(3):339–343.

Rados M, Judas M, Kostovic I (2006) In vitro MRI of brain development. Eur J Radiol 57(2):187–198.

Righini A, Bianchini E, Parazzini C, Gementi P, Ramenghi L, Baldoli C, Nicolini U, Mosca F, Triulzi F (2003) Apparent diffusion coefficient determination in normal fetal brain: a prenatal MR imaging study. AJNR Am J Neuroradiol 24(5):799–804.

Rose SE, Hatzigeorgiou X, Strudwick MW, Durbridge G, Davies PS, Colditz PB (2008) Altered white matter diffusion anisotropy in normal and preterm infants at term-equivalent age. Magn Reson Med 60(4):761–767.

Rutherford MA, Supramaniam V, Ederies A, Chew A, Bassi L, Groppo M, Anjari M, Counsell S, Ramenghi LA (2010) Magnetic resonance imaging of white matter diseases of prematurity. Neuroradiology 52(6):505–521.

Sadeghi N, Prastawa M, Fletcher PT, Wolff J, Gilmore JH, Gerig G (2013) Regional characterization of longitudinal DT-MRI to study white matter maturation of the early developing brain. Neuroimage 68:236–247.

Salami M, Itami C, Tsumoto T, Kimura F (2003) Change of conduction velocity by regional myelination yields constant latency irrespective of distance between thalamus and cortex. Proc Natl Acad Sci U S A 100(10):6174–6179.

Scott JA, Habas PA, Kim K, Rajagopalan V, Hamzelou KS, Corbett-Detig JM, Barkovich AJ, Glenn OA, Studholme C (2011) Growth trajectories of the human fetal brain tissues estimated from 3D reconstructed in utero MRI. Int J Dev Neurosci 29(5):529–536.

Short SJ, Elison JT, Goldman BD, Styner M, Gu H, Connelly M, Maltbie E, Woolson S, Lin W, Gerig G, et al (2013) Associations between white matter microstructure and infants' working memory. Neuroimage 64:156–166.

Sowell ER, Thompson PM, Rex D, Kornsand D, Tessner KD, Jernigan TL, Toga AW (2002) Mapping sulcal pattern asymmetry and local cortical surface gray matter distribution in vivo: maturation in perisylvian cortices. Cereb Cortex 12(1):17–26.

Spader HS, Ellermeier A, O'Muircheartaigh J, Dean 3rd DC, Dirks H, Boxerman JL, Cosgrove GR, Deoni SC (2013) Advances in myelin imaging with potential clinical application to pediatric imaging. Neurosurg Focus 34(4):E9.

Stiles J, Jernigan TL (2010) The basics of brain development. Neuropsychol Rev 20(4):327–348.

Su P, Kuan CC, Kaga K, Sano M, Mima K (2008) Myelination progression in language-correlated regions in brain of normal children determined by quantitative MRI assessment. Int J Pediatr Otorhinolaryngol 72(12):1751–1763.

Takahashi E, Folkerth RD, Galaburda AM, Grant PE (2012) Emerging cerebral connectivity in the human fetal brain: an MR tractography study. Cereb Cortex 22(2):455–464.

Tauber H, Waehneldt TV, Neuhoff V (1980) Myelination in rabbit optic nerves is accelerated by artificial eye opening. Neurosci Lett 16(3):235–238.

Thomas JL, Spassky N, Perez Villegas EM, Olivier C, Cobos I, Goujet-Zalc C, Martinez S, Zalc B (2000) Spatiotemporal development of oligodendrocytes in the embryonic brain. J Neurosci Res 59(4):471–476.

Thompson DK, Inder TE, Faggian N, Warfield SK, Anderson PJ, Doyle LW, Egan GF (2012) Corpus callosum alterations in very preterm infants: perinatal correlates and 2 year neurodevelopmental outcomes. Neuroimage 59(4):3571–3581.

Toga AW, Thompson PM (2003) Mapping brain asymmetry. Nat Rev Neurosci 4(1):37–48.

Travis KE, Curran MM, Torres C, Leonard MK, Brown TT, Dale AM, Elman JL, Halgren E (2013) Age-related changes in tissue signal properties within cortical areas important for word understanding in 12- to 19-month-old infants. Cereb Cortex.

van Buchem MA, Steens SC, Vrooman HA, Zwinderman AH, McGowan JC, Rassek M, Engelbrecht V (2001) Global estimation of myelination in the developing brain on the basis of magnetization transfer imaging: a preliminary study. AJNR Am J Neuroradiol 22(4):762–766.

van der Knaap MS, Valk J (1990) MR imaging of the various stages of normal myelination during the first year of life. Neuroradiology 31(6):459–470.

Van der Knaap MS, Valk J (1995a) Myelin and white matter. In: Van der Knaap MS, Valk J, editors. Magnetic resonance of myelin, myelination and myelin disorders. Berlin: Springer-Verlag. p. 1–17.

Van der Knaap MS, Valk J (1995b) Myelination and retarded myelination. In: Van der Knaap MS, Valk J, editors. Magnetic resonance of myelin, myelination and myelin disorders. Berlin: Springer-Verlag.

van der Knaap MS, Valk J, Bakker CJ, Schooneveld M, Faber JA, Willemse J, Gooskens RH (1991) Myelination as an expression of the functional maturity of the brain. Dev Med Child Neurol 33(10):849–857.

Volpe JJ (2008) Neuronal proliferation, migration, organization, and myelination. In: Neurology of the newborn. Philadelphia: Saunders Elsevier Inc. p. 51–118.

Whittall KP, MacKay AL, Graeb DA, Nugent RA, Li DK, Paty DW (1997) In vivo measurement of T2 distributions and water contents in normal human brain. Magn Reson Med 37(1):34–43.

Williams LA, Gelman N, Picot PA, Lee DS, Ewing JR, Han VK, Thompson RT (2005) Neonatal brain: regional variability of in vivo MR imaging relaxation rates at 3.0 T – initial experience. Radiology 235(2):595–603.

Wimberger DM, Roberts TP, Barkovich AJ, Prayer LM, Moseley ME, Kucharczyk J (1995) Identification of ‘‘premyelination’’ by diffusion-weighted MRI. J Comput Assist Tomogr 19(1):28–33.

Xu G, Takahashi E, Folkerth RD, Haynes RL, Volpe JJ, Grant PE, Kinney HC (2012) Radial coherence of diffusion tractography in the cerebral white matter of the human fetus: neuroanatomic insights. Cereb Cortex.

Xydis V, Astrakas L, Zikou A, Pantou K, Andronikou S, Argyropoulou MI (2006) Magnetization transfer ratio in the brain of preterm subjects: age-related changes during the first 2 years of life. Eur Radiol 16(1):215–220.

Yakovlev PI (1962) Morphological criteria of growth and maturation of the nervous system in man. Res Publ Assoc Res Nerv Ment Dis 39:3–46.

Yakovlev PI, Lecours AR (1967) The myelogenetic cycles of regional maturation in the brain. In: Minowski A, editor. Regional development of the brain in early life. Oxford: Blackwell. p. 3–69.

Yap PT, Fan Y, Chen Y, Gilmore JH, Lin W, Shen D (2011) Development trends of white matter connectivity in the first years of life. PLoS One 6(9):e24678.

Yendiki A, Panneck P, Srinivasan P, Stevens A, Zöllei L, Augustinack J, Wang R, Salat D, Ehrlich S, Behrens T, et al (2011) Automated probabilistic reconstruction of white-matter pathways in health and disease using an atlas of the underlying anatomy. Front Neuroinform 5:23.

Yoshida S, Oishi K, Faria AV, Mori S (2013) Diffusion tensor imaging of normal brain development. Pediatr Radiol 43(1):15–27.

Zanin E, Ranjeva JP, Confort-Gouny S, Guye M, Denis D, Cozzone PJ, Girard N (2011) White matter maturation of normal human fetal brain. An in vivo diffusion tensor tractography study. Brain Behav 1(2):95–108.

Zhang J, Evans A, Hermoye L, Lee SK, Wakana S, Zhang W, Donohue P, Miller MI, Huang H, Wang X, et al (2007) Evidence of slow maturation of the superior longitudinal fasciculus in early childhood by diffusion tensor imaging. Neuroimage 38(2):239–247.

Zhong K, Ernst T, Buchthal S, Speck O, Anderson L, Chang L (2011) Phase contrast imaging in neonates. Neuroimage 55(3):1068–1072.

(Accepted 16 December 2013)
(Available online 28 December 2013)

Part II

Experimental work

This part describes the experimental work conducted during my PhD studies. It is separated into 4 chapters.

The first chapter deals with the description of the variability of multiple MRI parameters during normal early post-natal development. In this chapter a clustering approach is applied to separate different white matter bundles according to differences in their maturation reflected by 6 MRI parameters: quantitative T1 and T2 relaxation times, fractional anisotropy FA, mean $\langle D \rangle$, longitudinal $\lambda_{\parallel}$ and transverse $\lambda_{\perp}$ diffusivities. The results of this chapter were presented at the 30th Annual Scientific ESMRMB Meeting in Toulouse (2013) and a copy of the presented poster is included at the end of the chapter. Although the applied approach allowed reasonable description of the white matter maturation that was globally in agreement with post-mortem studies, it could not be used neither for comparison of the maturational dynamics across the bundles, nor for quantitative measurements of the maturational stages. This required more sophisticated multiparametric approaches introduced in the following chapters.

The second chapter introduces a novel multiparametric index for quantitative evaluation of the white matter maturation. This index is based on Mahalanobis distance derived from 4 complementary MRI parameters: T1 and T2, $\lambda_{\parallel}$ and $\lambda_{\perp}$. This novel index is demonstrated to be more appropriate for investigating asynchrony of the white matter maturation than conventional univariate approaches. Furthermore, it provides a quantitative model that can be used to predict relative maturational delays between different white matter bundles. The results of this chapter were selected for an oral presentation at the 30th Annual Scientific ESMRMB Meeting (Toulouse, 2013) and were also recently published (the paper is attached at the end of the chapter [315]). As the developped approach provides a global maturational measure, it may not be optimal for evaluation of specific maturational processes, e.g. myelination, which would require using dedicated techniques, like the one described in the following chapter.

The third chapter deals with evaluation of white matter myelination. In that chapter, we present a novel approach for fast and reliable quantification of the Myelin Water Fraction (MWF) in infants using a 3-compartment model of T1 and T2 relaxation signals. The results were presented at the Joint Annual ISMRM-ESMRMB Meeting 2014 (Milan) and form the bases of a submitted article (2 posters and the manuscript are included at the end of the chapter).

Finally, the fourth chapter is focused on the study of white matter connectivity in the developing brain. This chapter describes creation of a preliminary child white matter connectivity atlas that can be used for automatic identification and extraction of the white matter bundles from child whole-brain tractography datasets. Results of this chapter will be presented at the ISMRM 23rd Annual Meeting (2015) and the abstract is attached at the end of the chapter.

Chapters 4 and 5 are based on a published and on a submitted papers, each attached at the end of the corresponding chapter. In these chapters, we highligh the most important points of the work, while all necessary details are available in the attached articles.

The first two works are based on infant and adult databases previously acquired and post-processed by Jessica Dubois and Ghislaine Dehaene. These databases are described in the first chapter of this part. MWF quantification also uses these databases but in addition 3 adult calibration subjects were acquired and post-processed. The white matter connectivity atlas is based on data that were acquired at Neurospin by Lucie Hertz-Pannier mostly during my PhD and they were post-processed by myself. The pulse sequences, used for data acquisition, and post-processing tools, implemented in Connectomist software and PTK toolbox [316], were developped by Cyril Poupon and the UNIRS team.

Children used for creation of the connectivity atlas were recruited in neuropediatric hospitals in Paris (Hôpital Necker: Dr.Chiron, Dr.Nabbout, Dr.Chemaly; Hôpital Kremlin-Bicêtre: Dr.Sevin, Dr.Aubourg; Hôpital Robert-Debré: Dr.Auvin) and throughout the France (CHU de Rennes: Dr.Napuri; Lorient: Dr.Caubel).

Chapter 3

Correlations of quantitative MRI parameters in the developing white matter bundles

As different MRI parameters are sensitive to different maturational processes (see Part I Chapter 2 and [133]), investigating brain maturation can greatly benefit from multimodal approaches that take into account complementary information from several parameters. Studying age-related correlations between MRI parameters may shed light on the undergoing maturational processes. In this chapter this approach is applied to describe the correlations of six MRI parameters: relaxation times qT1 and qT2, fractional anisotropy FA, mean $\langle D \rangle$, longitudinal $\lambda_{\parallel}$ and transverse $\lambda_{\perp}$ diffusivities, within white matter bundles of healthy infants born at term. This work was based on previously acquired and post-processed infant and adult data, which will be briefly described at the beginning of the chapter. Then description of the correlation analysis and corresponding results will be given, followed by results' interpretations. At the end of the chapter, a poster presented at the 30th Annual Scientific ESMRMB Meeting, which summarizes results of this chapter, is included [317].

3.1 Description of the infant and adult databases

3.1.1 Subjects

Infant MRI database included 17 healthy subjects born at term (3-21 weeks old, 7 girls, 10 boys). Adult MRI database, used as a reference group to assess white matter maturation, consisted of 13 healthy subjects (22.4 ± 1.6 years, 6 women, 7 men). None of the subjects had any neurodevelopmental problems or brain abnormalities detected on MR images. Data was obtained using the study protocol approved by the regional ethical committee for biomedical research and informed consents were obtained from parents and adult subjects.

3.1.2 Acquisition protocol

Data was acquired on a 3T MRI system (Tim Trio, Siemens Medical Systems, Erlangen, Germany), equipped with a whole body gradient (40 mT/m, 200 T/m/s) and a 32-channel head coil. Interleaved axial slices covering the whole brain (50/70 slices for infants/adults respectively) were acquired with a 1.8mm isotropic spatial resolution (FOV = $23\times23\text{cm}^2$, matrix = 128×128) using EPI single-shot spin-echo (SE) sequences:

- **For qT1 mapping**, an inversion recovery (IR) SE-EPI sequence with eight different values of inversion time (TI=250→1500ms, each step 250ms + TI=2000, 2500ms): TE = 38 ms, TR = TI+15s (TR = TI+21s for adults), partial Fourier sampling factor 5/8, leading to an acquisition time of 2min 11s (3min 03s for adults). This sequence was developped in house by Cyril Poupon [145];

- **For qT2 mapping**, a SE-EPI sequence with 8 different values of echo time (TE = 50→260ms, each step 30ms): TR = 15.5s (TR = 21.7 s for adults), parallel imaging GRAPPA factor 2, partial Fourier sampling factor 6/8, leading to an acquisition time of 2min 51 s (4min for adults). This sequence was developped in house by Cyril Poupon [145];

- **For DTI**, a DW-SE-EPI sequence with 30 orientations of diffusion gradients and $b = 700s/mm^2$ ($+b = 0$ volume): TE = 72ms, TR = 10s (TR = 14s for adults), parallel imaging GRAPPA factor 2, partial Fourier sampling factor 6/8, leading to an acquisition time of 5min 40s (7min 56s for adults).

3.1.3 Data post-processing

MRI data were post-processed beforehand using in-house developped Connectomist software [145, 316]. DWI data were corrected for motion and eddy currents-induced artifacts [310] and quantitative MRI and DTI maps were generated for 6 parameters: quantitative relaxation times qT1 and qT2, fractional anisotropy FA, mean $\langle D\rangle$, longitudinal $\lambda_{\parallel}$ and transverse $\lambda_{\perp}$ diffusivities (Fig. 3.1).

Whole brain tractography was performed according to a 4-order analytical Q-ball model with a regularized 3D tractography [294] and 18 white matter bundles that mature at different times and rates [248] were identified in each subject using manually delineated regions of selection and exclusion [269] (Fig. 3.2, 3.3, 3.4):

- **projection bundles**: cortico-spinal tract CST with three subdivisions (inferior, middle and superior portions); spino-thalamic tract STT; optic radiations OR; anterior limb of the internal capsule ALIC;

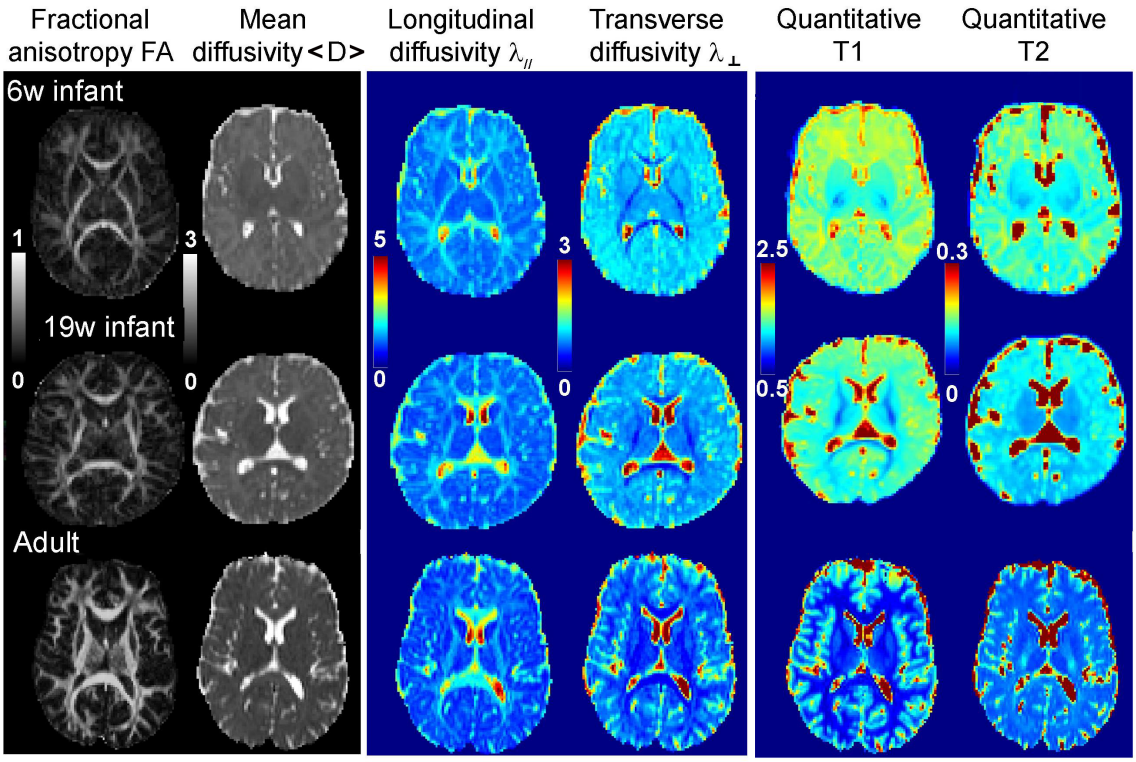

Figure 3.1: Quantitative MRI and DTI maps of 6 parameters (fractional anisotropy FA, mean $\langle D \rangle$, longitudinal $\lambda_{\parallel}$ and transverse $\lambda_{\perp}$ diffusivities, quantitative relaxation times qT1 and qT2) generated for subjects of different ages: infants at 6 and 19 weeks, and a young adult. Scale for diffusivities: $\times 10^{-3} mm^2/s$; relaxation times are given in seconds.

- **association bundles**: external capsule EC, arcuate fasciculus AF, superior SLF and inferior ILF longitudinal fascicles, uncinate fasciculus UF, fronto-occipital fasciculus FOF;

- **limbic bundles**: fornix FX; inferior CGinf and superior CGsup parts of the cingulum;

- **commissural bundles**: genu CCg, body CCb and splenium CCs of the corpus callosum.

In each subject, MRI parameters were quantified and averaged over the bundle length (Fig. 3.2, 3.3, 3.4), taking into account fiber density [291].

3.2 Correlation analysis

Since MRI parameters vary across different bundles in adults and since they have different scales, maturational changes of the MRI parameters in infants should be considered relative to the adult mature stage and thus, for further analysis MRI parameters in infants were normalized by the corresponding mean values from the adult reference group. Normalized MRI parameters in infants were plotted as a function of age for all bundles (Fig. 3.5). Correlations between each pair of MRI parameters were computed for each bundle in the adult group. For correlation analysis in infants, age-related effects were eliminated by linear regressions and correlations between MRI parameters residuals were computed for each bundle. The resulting correlation coefficients in infants (15=6*5/2 correlation coefficients per infant) were used for hierarchical clustering of the bundles based on squared Euclidean distance and centroid linkage (Fig. 3.6). This approach exploited the hypothesis that bundles clustered together should have similar maturational properties.

3.3 Results

Distributions of all parameters for all bundles were significantly different between infants and adults (ad-hoc t-tests, $p<0.05$, Fig. 3.2, 3.3, 3.4), showing lower FA values and higher values of other parameters in infants. In infants, FA increased with age in all bundles, while diffusivities and relaxation times decreased (Fig. 3.5). The mean infant parameters and the rates of their changes were different across bundles and parameters, reflecting differences in bundles maturational stages and suggesting that certain tracts (e.g. spino-thalamic and cortico-spinal tracts) matured faster than the others. However, it was hard to compare the maturational dynamics for the majority of the bundles using such representation.

Correlation analysis of the MRI parameters in the adult group revealed several strong correlations, including FA-$\lambda_\perp$, $\langle D\rangle$-$\lambda_\perp$, $\langle D\rangle$-$\lambda_\parallel$ (Tab. 3.1). In infants, correlation analysis also retrieved the above mentioned correlations, as well as additional correlations, namely, $\langle D\rangle$-qT2, $\lambda_\perp$-qT2, $\lambda_\parallel$-qT2, $\lambda_\perp$-$\lambda_\parallel$, FA-$\langle D\rangle$, FA-$\lambda_\parallel$ (Tab. 3.2).

Clustering analysis based on the infant correlation coefficients allowed to separate the bundles into 4 distinct groups (Fig. 3.6):

- **1st group**: arcuate fasciculus, inferior longitudinal fasciculus, fronto-occipital fasciculus, uncinate fasciculus, genu and body of the corpus callosum, superior parts of the cingulum;

- **2nd group**: superior portion of the cortico-spinal tract, external capsule, splenium of the corpus callosum, superior longitudinal fasciculus, optic radiations, anterior limb of the internal capsule;

- **3rd group**: fornix, inferior portion of the cortico-spinal tract, inferior portion of the cingulum;

- **4th group**: middle portion of the cortico-spinal tract, spino-thalamic tract;

Projection bundles															
bundle	**FA-$\langle D \rangle$**	**FA-$\lambda_\parallel$**	**FA-$\lambda_\perp$**	**FA-qT1**	**FA-qT2**	**$\langle D \rangle$-$\lambda_\parallel$**	**$\langle D \rangle$-$\lambda_\perp$**	**$\langle D \rangle$-qT1**	**$\langle D \rangle$-qT2**	**$\lambda_\parallel$-$\lambda_\perp$**	**$\lambda_\parallel$-qT1**	**$\lambda_\parallel$-qT2**	**$\lambda_\perp$-qT1**	**$\lambda_\perp$-qT2**	**qT1-qT2**
CSTinf	0,04	**0,57**	**-0,80**	0,26	0,31	**0,76**	0,40	0,17	-0,15	-0,16	0,24	-0,04	-0,17	-0,30	**0,54**
CSTmid	0,22	**0,87**	**-0,90**	0,14	0,42	**0,65**	0,18	0,08	0,07	**-0,61**	0,07	0,32	-0,04	-0,31	0,14
CSTsup	**-0,75**	**0,50**	**-0,97**	0,28	0,08	0,17	**0,88**	-0,27	-0,02	-0,30	0,14	0,09	-0,32	-0,03	0,17
STT	-0,37	0,18	**-0,76**	-0,46	-0,06	**0,83**	**0,87**	0,10	**0,66**	0,45	-0,12	**0,57**	0,25	**0,51**	0,01
OR	-0,44	0,08	**-0,81**	**-0,52**	-0,14	**0,82**	**0,86**	**0,51**	0,32	0,47	0,17	0,28	**0,56**	0,32	0,19
ALIC	**-0,67**	0,21	**-0,87**	0,29	0,20	**0,56**	**0,93**	-0,15	0,11	0,25	0,19	0,37	-0,21	-0,01	**0,51**
Association bundles															
bundle	**FA-$\langle D \rangle$**	**FA-$\lambda_\parallel$**	**FA-$\lambda_\perp$**	**FA-qT1**	**FA-qT2**	**$\langle D \rangle$-$\lambda_\parallel$**	**$\langle D \rangle$-$\lambda_\perp$**	**$\langle D \rangle$-qT1**	**$\langle D \rangle$-qT2**	**$\lambda_\parallel$-$\lambda_\perp$**	**$\lambda_\parallel$-qT1**	**$\lambda_\parallel$-qT2**	**$\lambda_\perp$-qT1**	**$\lambda_\perp$-qT2**	**qT1-qT2**
EC	**-0,75**	0,12	**-0,93**	0,35	0,01	0,47	**0,93**	-0,17	-0,13	0,19	0,15	-0,16	-0,26	-0,03	-0,07
AF	**-0,68**	0,14	**-0,91**	0,25	0,00	**0,60**	**0,91**	-0,24	0,00	0,24	-0,16	-0,12	-0,24	0,01	0,44
SLF	-0,44	0,18	**-0,82**	-0,12	0,29	**0,78**	**0,84**	0,02	0,13	0,33	-0,08	0,36	0,01	-0,11	0,25
ILF	**-0,82**	-0,22	**-0,94**	0,13	**-0,53**	**0,70**	**0,95**	0,19	0,46	**0,50**	0,49	-0,05	0,07	**0,51**	-0,10
FOF	**-0,56**	0,10	**-0,86**	0,11	-0,20	**0,75**	**0,90**	-0,23	0,24	0,40	-0,02	0,08	-0,18	0,24	-0,26
UF	**-0,69**	-0,09	**-0,92**	0,35	-0,12	**0,75**	**0,90**	-0,14	0,15	0,43	0,05	0,12	-0,29	0,13	-0,01
Limbic bundles															
bundle	**FA-$\langle D \rangle$**	**FA-$\lambda_\parallel$**	**FA-$\lambda_\perp$**	**FA-qT1**	**FA-qT2**	**$\langle D \rangle$-$\lambda_\parallel$**	**$\langle D \rangle$-$\lambda_\perp$**	**$\langle D \rangle$-qT1**	**$\langle D \rangle$-qT2**	**$\lambda_\parallel$-$\lambda_\perp$**	**$\lambda_\parallel$-qT1**	**$\lambda_\parallel$-qT2**	**$\lambda_\perp$-qT1**	**$\lambda_\perp$-qT2**	**qT1-qT2**
FX	-0,26	0,11	**-0,52**	0,22	0,25	**0,91**	**0,95**	-0,26	**0,79**	**0,75**	-0,26	**0,91**	-0,38	**0,61**	-0,27
CGinf	**-0,66**	0,30	**-0,90**	0,07	-0,13	0,47	**0,91**	-0,26	0,45	0,11	-0,09	0,37	-0,23	0,33	0,08
CGsup	-0,42	**0,54**	**-0,91**	**-0,74**	0,03	**0,52**	**0,76**	0,25	-0,07	-0,15	-0,44	0,01	**0,64**	-0,07	0,23
Commissural bundles															
bundle	**FA-$\langle D \rangle$**	**FA-$\lambda_\parallel$**	**FA-$\lambda_\perp$**	**FA-qT1**	**FA-qT2**	**$\langle D \rangle$-$\lambda_\parallel$**	**$\langle D \rangle$-$\lambda_\perp$**	**$\langle D \rangle$-qT1**	**$\langle D \rangle$-qT2**	**$\lambda_\parallel$-$\lambda_\perp$**	**$\lambda_\parallel$-qT1**	**$\lambda_\parallel$-qT2**	**$\lambda_\perp$-qT1**	**$\lambda_\perp$-qT2**	**qT1-qT2**
CCg	-0,31	0,02	**-0,69**	-0,08	**-0,64**	**0,92**	**0,52**	0,07	0,41	0,15	-0,02	0,10	0,28	**0,90**	0,30
CCb	-0,44	-0,29	**-0,50**	0,06	0,28	**0,93**	**0,89**	**0,58**	0,16	**0,67**	0,45	0,21	**0,58**	0,12	**0,58**
CCs	0,10	0,14	0,02	0,40	0,07	**0,99**	**0,89**	0,33	**0,58**	**0,83**	0,29	**0,56**	0,37	**0,54**	0,46

Table 3.1: Correlation coefficients for different MRI parameters across white matter bundles in the adult group. Coefficients with p<0.05 are given in bold.

Projection bundles															
bundle	**FA-$\langle D \rangle$**	**FA-$\lambda_\parallel$**	**FA-$\lambda_\perp$**	**FA-qT1**	**FA-qT2**	**$\langle D \rangle$-$\lambda_\parallel$**	**$\langle D \rangle$-$\lambda_\perp$**	**$\langle D \rangle$-qT1**	**$\langle D \rangle$-qT2**	**$\lambda_\parallel$-$\lambda_\perp$**	**$\lambda_\parallel$-qT1**	**$\lambda_\parallel$-qT2**	**$\lambda_\perp$-qT1**	**$\lambda_\perp$-qT2**	**qT1-qT2**
CSTinf	-0,28	0,41	**-0,79**	-0,39	-0,13	**0,64**	**0,64**	-0,14	**0,73**	-0,03	**-0,57**	0,42	0,45	**0,62**	0,12
CSTmid	**-0,58**	**0,61**	**-0,96**	**-0,66**	-0,38	0,16	**0,74**	**0,52**	**0,75**	-0,39	-0,43	0,15	**0,62**	**0,51**	0,42
CSTsup	-0,22	-0,01	-0,46	**-0,57**	-0,28	**0,93**	**0,94**	0,41	**0,79**	**0,8**	0,22	**0,76**	**0,57**	**0,57**	**0,65**
STT	-0,16	**0,83**	**-0,77**	0,16	-0,38	0,29	**0,71**	0,21	**0,54**	-0,4	0,18	0,09	0,01	**0,57**	-0,21
OR	**-0,64**	-0,29	**-0,79**	-0,22	-0,37	**0,9**	**0,96**	**0,57**	**0,8**	**0,76**	**0,53**	**0,73**	**0,59**	**0,78**	**0,83**
ALIC	**-0,66**	-0,25	**-0,83**	-0,33	-0,43	**0,79**	**0,95**	**0,6**	**0,8**	**0,65**	**0,58**	**0,75**	**0,51**	**0,73**	**0,53**
Association bundles															
bundle	**FA-$\langle D \rangle$**	**FA-$\lambda_\parallel$**	**FA-$\lambda_\perp$**	**FA-qT1**	**FA-qT2**	**$\langle D \rangle$-$\lambda_\parallel$**	**$\langle D \rangle$-$\lambda_\perp$**	**$\langle D \rangle$-qT1**	**$\langle D \rangle$-qT2**	**$\lambda_\parallel$-$\lambda_\perp$**	**$\lambda_\parallel$-qT1**	**$\lambda_\parallel$-qT2**	**$\lambda_\perp$-qT1**	**$\lambda_\perp$-qT2**	**qT1-qT2**
EC	-0,4	-0,26	**-0,5**	-0,19	-0,28	**0,97**	**0,98**	0,39	**0,87**	**0,92**	0,3	**0,86**	0,46	**0,88**	**0,59**
AF	**-0,66**	-0,09	**-0,51**	**-0,52**	**-0,52**	**0,78**	**0,52**	**0,55**	**0,84**	0,27	0,37	**0,84**	0,41	0,4	**0,51**
SLF	**-0,77**	-0,42	**-0,82**	-0,46	**-0,53**	**0,87**	**0,97**	**0,62**	**0,82**	**0,79**	0,47	**0,79**	**0,64**	**0,83**	**0,68**
ILF	**-0,59**	-0,24	**-0,74**	-0,3	-0,45	**0,89**	**0,94**	0,37	**0,83**	**0,71**	0,23	**0,68**	0,41	0,41	**0,52**
FOF	**-0,65**	-0,17	**-0,84**	-0,39	**-0,55**	**0,85**	**0,93**	0,36	**0,84**	**0,64**	0,28	**0,74**	0,41	**0,81**	0,38
UF	**-0,57**	0,08	**-0,77**	**-0,54**	-0,41	**0,73**	**0,96**	0,4	**0,92**	**0,55**	0,06	**0,75**	**0,53**	**0,84**	0,26
Limbic bundles															
bundle	**FA-$\langle D \rangle$**	**FA-$\lambda_\parallel$**	**FA-$\lambda_\perp$**	**FA-qT1**	**FA-qT2**	**$\langle D \rangle$-$\lambda_\parallel$**	**$\langle D \rangle$-$\lambda_\perp$**	**$\langle D \rangle$-qT1**	**$\langle D \rangle$-qT2**	**$\lambda_\parallel$-$\lambda_\perp$**	**$\lambda_\parallel$-qT1**	**$\lambda_\parallel$-qT2**	**$\lambda_\perp$-qT1**	**$\lambda_\perp$-qT2**	**qT1-qT2**
FX	0,01	0,38	-0,38	**-0,57**	-0,05	**0,87**	**0,9**	0,05	**0,79**	**0,61**	-0,23	**0,6**	0,37	**0,77**	-0,07
CGinf	-0,22	**0,5**	**-0,73**	-0,04	-0,21	**0,66**	**0,81**	-0,13	**0,75**	0,14	-0,13	**0,5**	-0,05	**0,66**	0,01
CGsup	**-0,76**	0,01	**-0,91**	**-0,56**	**-0,72**	**0,61**	**0,96**	0,49	**0,93**	0,37	0,14	**0,55**	**0,5**	**0,89**	0,46
Commissural bundles															
bundle	**FA-$\langle D \rangle$**	**FA-$\lambda_\parallel$**	**FA-$\lambda_\perp$**	**FA-qT1**	**FA-qT2**	**$\langle D \rangle$-$\lambda_\parallel$**	**$\langle D \rangle$-$\lambda_\perp$**	**$\langle D \rangle$-qT1**	**$\langle D \rangle$-qT2**	**$\lambda_\parallel$-$\lambda_\perp$**	**$\lambda_\parallel$-qT1**	**$\lambda_\parallel$-qT2**	**$\lambda_\perp$-qT1**	**$\lambda_\perp$-qT2**	**qT1-qT2**
CCg	**-0,76**	-0,37	**-0,97**	-0,3	**-0,7**	**0,65**	**0,82**	0,4	**0,7**	**0,56**	0,46	**0,62**	0,34	**0,77**	0,31
CCb	**-0,77**	-0,07	**-0,92**	-0,34	**-0,61**	**0,66**	**0,96**	0,45	**0,7**	0,43	0,2	0,42	0,43	**0,66**	0,28
CCs	**-0,91**	**-0,76**	**-0,96**	-0,45	**-0,66**	**0,93**	**0,98**	0,47	**0,75**	**0,87**	0,43	**0,67**	0,44	**0,75**	**0,55**

Table 3.2: Correlation coefficients for different MRI parameters across white matter bundles in the infant group. Coefficients with p<0.05 are given in bold.

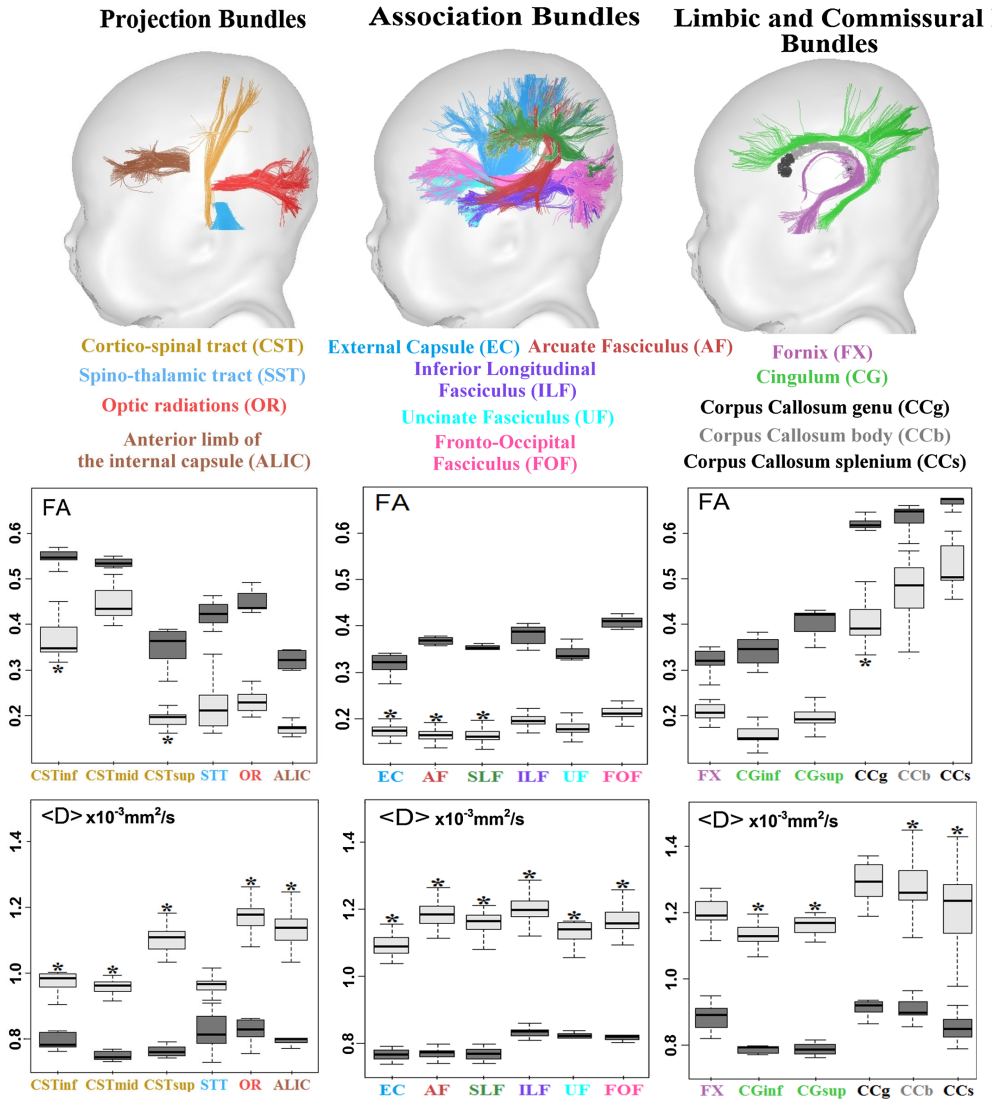

Figure 3.2: Mean and standard deviations of FA and $\langle D \rangle$ across different white matter bundles in the infant (light boxes) and adult groups (dark boxes). Asterisk indicates when variations in the infant group could be explained by the age-related changes using linear regressions with age ($R^2 > 0.46, p < 0.05$). Adapted from [315].

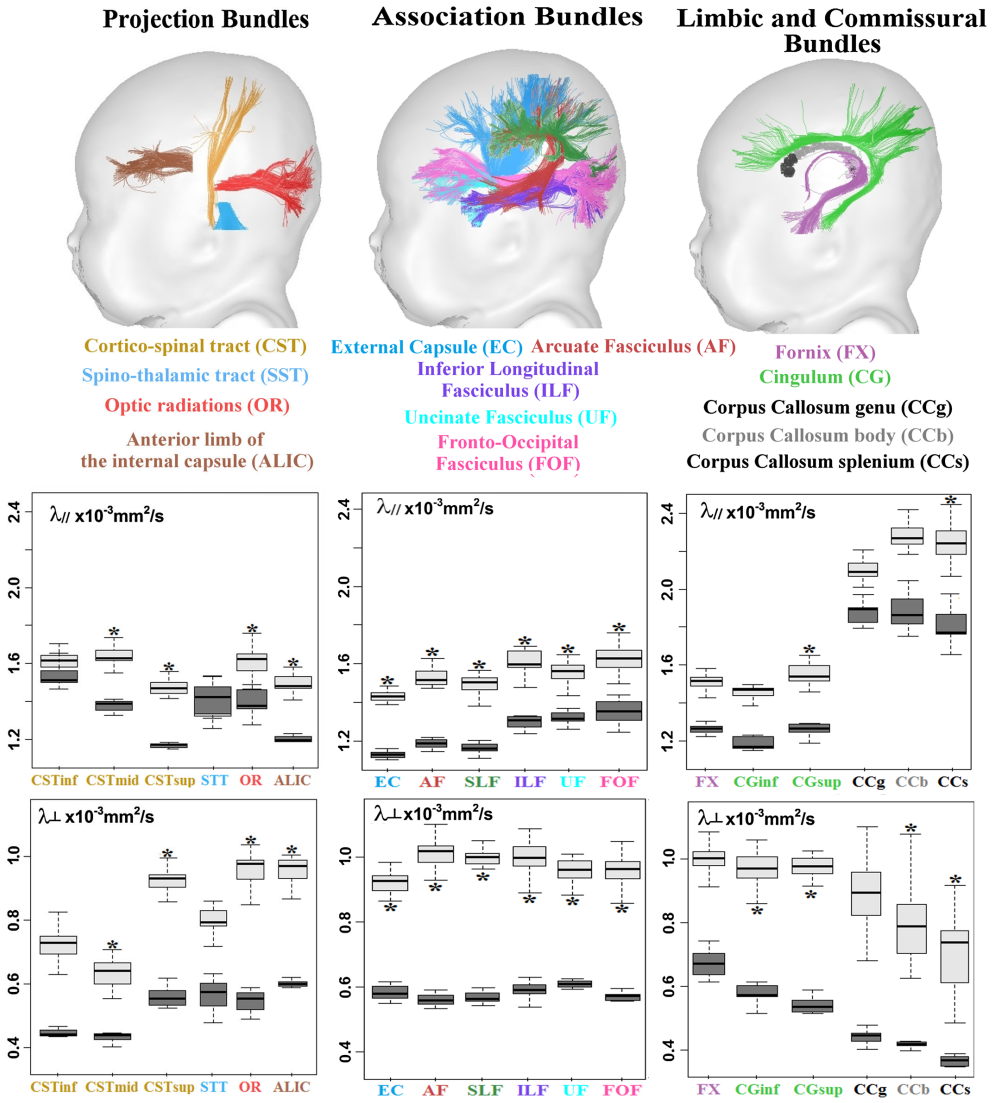

Figure 3.3: Mean and standard deviations of $\lambda_{\parallel}$ and $\lambda_{\perp}$ across different white matter bundles in the infant (light boxes) and adult groups (dark boxes). Asterisk indicates when variations in the infant group could be explained by the age-related changes using linear regressions with age ($R^2 > 0.46, p < 0.05$). Adapted from [315].

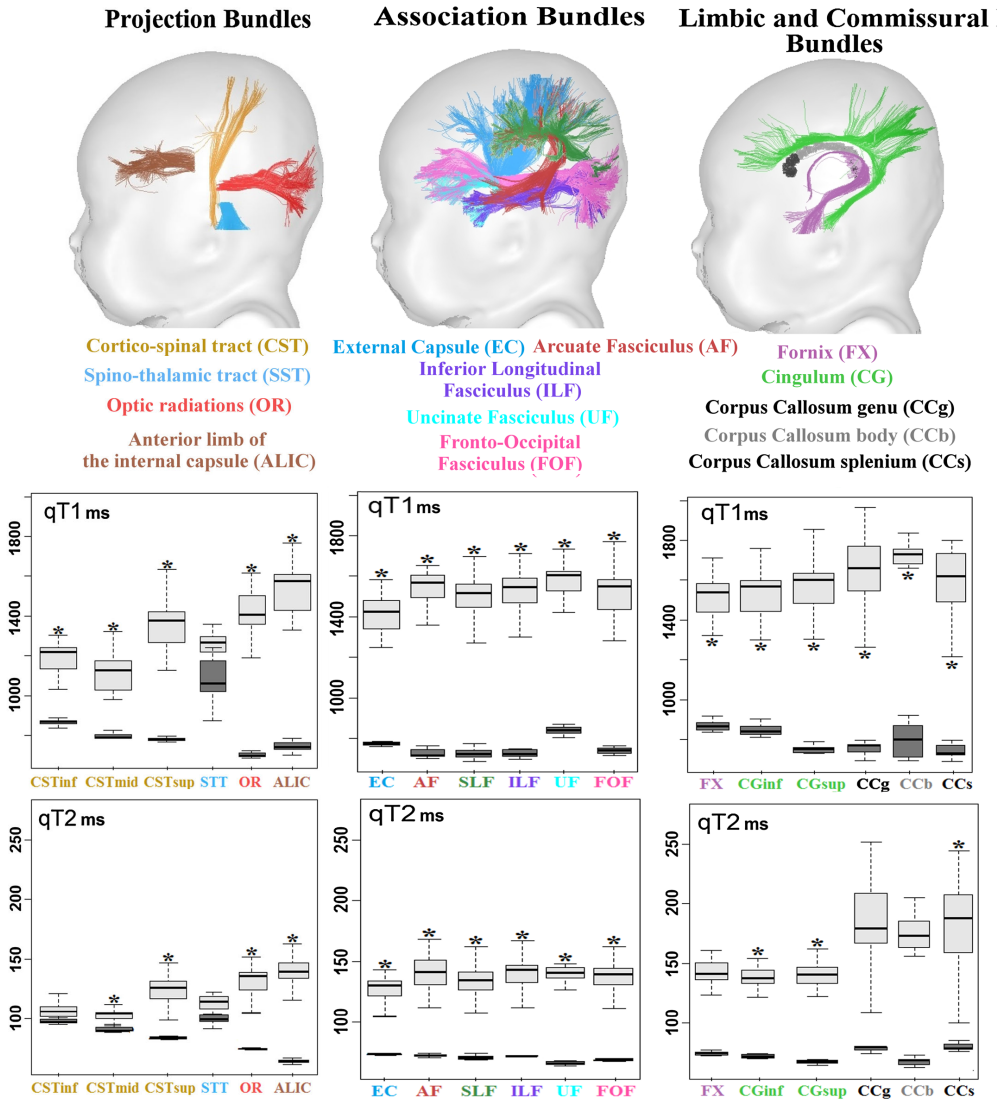

Figure 3.4: Mean and standard deviations of qT1 and qT2 across different white matter bundles in the infant (light boxes) and adult groups (dark boxes). Asterisk indicates when variations in the infant group could be explained by the age-related changes using linear regressions with age ($R^2 > 0.46, p < 0.05$). Adapted from [315].

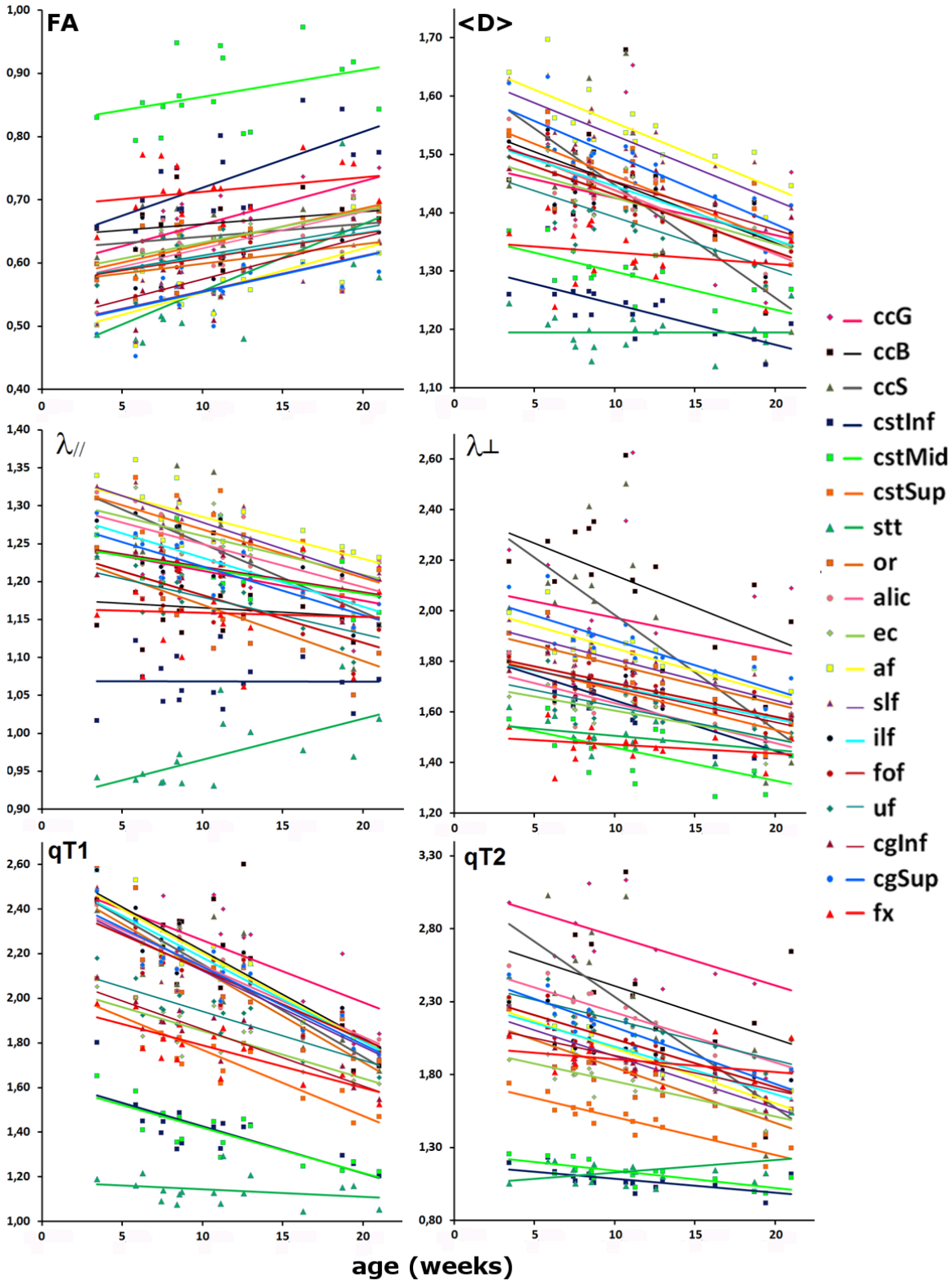

Figure 3.5: Changes of the normalized MRI parameters (i.e. MRI parameters divided by corresponding mean values from the adult group) in infants with age for different bundles.

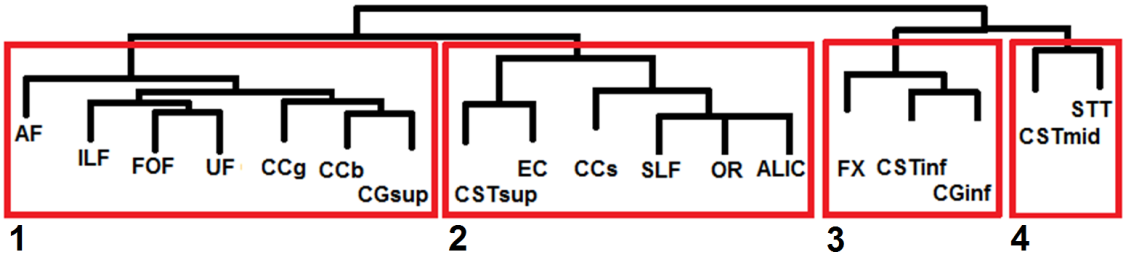

Figure 3.6: Bundle groups revealed by clustering analysis of the correlations coefficients between infant MRI parameters.

Some of the revealed correlations were shared by all clusters ($\langle D\rangle$-$\lambda_\perp$,$\langle D\rangle$-qT2), certain were bundle-specific (Tab. 3.3): cluster 1 was characterized by additional correlations $\langle D\rangle$-$\lambda_\parallel$, FA-$\lambda_\perp$, and FA-$\langle D\rangle$; cluster 2 was characterized by correlations $\langle D\rangle$-$\lambda_\parallel$, $\lambda_\perp$-qT2, $\lambda_\parallel$-qT2 and $\lambda_\perp$-$\lambda_\parallel$; cluster 3 was characterized by correlations $\langle D\rangle$-$\lambda_\parallel$ and $\lambda_\perp$-qT2; cluster 4 was characterized by correlations $\lambda_\perp$-qT2, FA-$\lambda_\perp$ and FA-$\lambda_\parallel$.

Correlations	Possible interpretation	cluster 1	cluster 2	cluster 3	cluster4
$\langle D\rangle$-$\lambda_\perp$ and $\langle D\rangle$-qT2	decrease of the water content (not specific to any maturational stage)	+	+	+	+
$\langle D\rangle$-$\lambda_\parallel$	pre-myelination processes	+	+	+	
$\lambda_\perp$-qT2	increasing fiber compactness		+	+	+
FA-$\lambda_\perp$	extreme maturational stages	+			+
FA-$\lambda_\parallel$	?				+
$\lambda_\parallel$-$\lambda_\perp$ and $\lambda_\parallel$-qT2	pre-myelination changes in the longitudinal diffusivity		+		
FA-$\langle D\rangle$	?	+			

Table 3.3: Correlations between MRI parameters revealed in four bundles clusters and their possible interpretations. "?" means that there was no obvious interpretation.

3.4 Interpretation of the results

The observed age-related changes of the normalized MRI parameters in infants confirmed asynchronous progression of the white matter maturation. In agreement with post-mortem studies [121, 122], projection bundles (e.g. spino-thalamic and cortico-spinal tracts) seemed to be among the fastest maturating bundles. However, in this representation maturation comparison between the rest of the bundles was not evident due to the fact that age-related changes of different MRI parameters showed different dynamics across the considered age-range.

As different MRI parameters reflect different maturational processes, different maturational stages are likely to show different correlations between MRI parameters. Indeed, correlation analysis of the infant MRI parameters revealed a number of correlations that might be used to differentiate between bundles' maturational stages. Correlation between $\langle D\rangle$ and qT2, which was present in all clusters, likely

accounts for general decrease of the water content that is not specific to any maturational stage. Correlation between $\langle D \rangle$ and $\lambda_{\parallel}$ may reflect pre-myelination processes and thus, bundles from the 4th cluster, which does not show this correlation, may be viewed as more mature than bundles from the 3 other clusters. Correlation between $\lambda_{\perp}$-qT2 may reflect increasing fiber compactness and thus, bundles from the 1st cluster that does not show this correlation may be considered as less mature than bundles from 2-4th clusters that have this correlation. Correlations $\lambda_{\parallel}$-qT2 and $\lambda_{\perp}$-$\lambda_{\parallel}$ that were specific to the 2nd cluster may reflect pre-myelination changes in the longitudinal diffusivity and suggest that bundles from this cluster are likely to be less mature than bundles from the 3rd cluster. Finally, correlation between FA and $\lambda_{\perp}$, which is one of the most difficult to interpret, may be observed during both fiber organization and myelination, and thus, reflect extreme maturational stages of 1st and 4th clusters. Other correlations, like FA-$\lambda_{\parallel}$ and FA-$\langle D \rangle$, do not have obvious interpretation.

To summarize, bundles from cluster 4 appeared as the most mature, followed by bundles from cluster 3, then by bundles from cluster 2, and finally, by the least mature bundles from cluster 1.

3.5 Limitations of the approach

Although the clustering results for clusters 1,3 and 4 were globally in agreement with post-mortem studies [121, 122], this approach has several severe drawbacks. First of all, grouping certain bundles together in cluster 2, i.e. optic radiations (quite mature) and anterior limb of the internal capsule (relatively immature), is not supported by the known progression of the white matter maturation and remains difficult to explain. Furthermore, this approach does not provide any comparison of the maturational dynamics across bundles, nor any quantitative measure of the maturational stages. Thus, reliable quantitative description of white matter maturation requires more sophisticated multiparametric models that will be introduced in the two following chapters.

660

Comparison of quantitative MRI parameters in the developing white matter bundles

S Kulikova [1]*, L Hertz-Pannier[1], G Dehaene-Lambertz[2], C Poupon[3], J Dubois[2]

1. CEA-Saclay, Neurospin/UNIACT/UMR663; 2. INSERM UMR992, CEA/Neurospin/UNICOG; 3. CEA-Saclay,Neurospin/UNIRS; *Sofya.KULIKOVA@cea.fr

Introduction

Maturation of the white matter is a complex process, which includes several stages: fiber organization into bundles, proliferation of cells and organites, and "true" axonal myelination. These processes have different impacts on quantitative MRI parameters, which thus show different dynamics at different maturational stages [1,2]. Maturation is also an asynchronous process [3,4,5], which occurs over different time periods and at different rates across different bundles. Here we describe this variability in terms of correlations between six MRI parameters: relaxation times (qT1, qT2); fractional anisotropy (FA), mean (MD), longitudinal ($\lambda_{//}$) and perpendicular ($\lambda_{\perp}$) diffusivities, computed from diffusion tensor imaging (DTI).

Data acquisition

- 17 healthy infants born at term (7 girls, 10 boys, maturational age between 3 and 21 weeks).
- 13 adult subjects used as reference (6 women, 7 men, mean age: 22.4±1.6 years).
- Data was acquired on a 3T MRI system (Tim Trio, Siemens Medical Systems, Germany), equipped with a whole body gradient (40mT/m, 200T/m/s) and a 32-channel head coil.
- Brains were imaged with a 1.8mm isotropic spatial resolution (FOV=23x23cm2, matrix=128x128, 50 / 70 slices for infants / adults) using EPI single-shot spin-echo (SE) sequences.
- ***For DTI:*** 30 orientations of diffusion gradients, b=700s.mm-2, TE=72ms, TR=10s / 14s, parallel imaging GRAPPA factor 2, partial Fourier sampling factor 6/8, acquisition time 5min40s / 7min56s.
- ***For qT1 mapping:*** an inversion recovery sequence with 8 different values of inversion time (TI=250->1500ms each step 250ms + TI=2000, 2500ms): TE=38ms, TR= TI+15s / 21s, partial Fourier sampling factor 5/8, acquisition time 2min11s / 3min03s.
- ***For qT2 mapping:*** 8 different values of echo time (TE=50->260ms each step 30ms): TR= 15.5s / 21.7s, parallel imaging GRAPPA factor 2, partial Fourier sampling factor 6/8, acquisition time 2min51s / 4min.

Data post-processing (Connectomist software [6])

• Correction of the artifacts from field inhomogeneities, eddy currents and movements.

• Calculation of the diffusion tensor and creation of parameter maps: fractional anisotropy (FA), mean (MD), longitudinal ($\lambda_{//}$) and transverse ($\lambda_{\perp}$) diffusivities. (**Fig.1**).

• Computation of the quantitative T1 and T2 maps (**Fig.1**).

• 18 white matter bundles were reconstructed using regularized 3D tractography [7] and manually delineated regions of interest [8]. (**Fig.2**).

Data analysis

- For all subjects and all bundles MRI parameters were quantified and averaged over the bundle length (**Fig.3**).
- MRI parameters were normalized by the corresponding mean values from the adult population. Normalized MRI parameters in infants were plotted as a function of age for all bundles (**Fig.4**):
- For correlation analysis in infants, age-related effects were eliminated by linear regressions. Correlations between MRI parameters were computed for each bundle in both groups and the resulting correlation coefficients were used for bundle clustering (**Fig.5**).

Results

- Distributions of all parameters across all bundles are significantly different between infants and adults (**Fig.3**) showing lower FA values and higher values of other parameters in infants.
- During maturation in infants, FA increases with age in all bundles, while other parameters decrease. The rates of these changes are different across the bundles and the parameters (**Fig.4**), suggesting that certain fibers (i.e. STT , CST) mature faster than the others.
- Correlation analysis of the MRI parameters over the adult group reveals strong correlations FA - $\lambda_{\perp}$, MD - $\lambda_{\perp}$ and MD - $\lambda_{//}$ for most bundles. No consistent correlations were found between any DTI indices and qT1/qT2.
- Similarly to adults, analysis over the infant group reveals correlations FA - $\lambda_{\perp}$, MD - $\lambda_{\perp}$, MD - $\lambda_{//}$. Additional correlations were found for MD - qT2, $\lambda_{//}$ - qT2, $\lambda_{\perp}$ - qT2, $\lambda_{//}$ - $\lambda_{\perp}$, FA - MD, FA - $\lambda_{//}$.
- Clustering of the correlation coefficients of the 6 parameters across the bundles in infants separated bundles into 4 groups (**Fig.5**). Certain correlations were shared by all clusters (MD - $\lambda_{\perp}$, MD - qT2), certain were bundle-specific (MD - $\lambda_{//}$ for clusters 1-3, $\lambda_{\perp}$ - qT2 for clusters 2-4, FA - $\lambda_{\perp}$ for clusters 1 and 4, FA - $\lambda_{//}$ for the 4th cluster; $\lambda_{//}$ - qT2 and $\lambda_{//}$ - $\lambda_{\perp}$ for the 2nd cluster; FA - MD for the 1st cluster) and others were not consistent in any of the clusters.

Discussion and Conclusions

- Different correlations between MRI parameters may reflect different maturational changes in the white matter:
  1. MD - qT2 (all clusters) - general decrease of the water content, not specific to any maturational stage;
  2. MD - $\lambda_{//}$ (clusters 1-3) - pre-myelination processes → cluster 4 should be more mature than the others;
  3. $\lambda_{\perp}$ - qT2 (clusters 2-4) - fiber compactness → cluster 1may be considered as the least mature;
  4. $\lambda_{//}$ - qT2 and $\lambda_{//}$ - $\lambda_{\perp}$ (cluster 2) - pre-myelination changes in $\lambda_{//}$ → cluster 2 is less mature than cluster 3;
  5. FA - $\lambda_{\perp}$ - only for fiber organization and myelination,not for pre-myelination, → extreme maturational stages for clusters 1 and 4.
- Correlation analysis of the MRI parameters can be used to describe maturational processes in white matter and group bundles according to their maturational stages. Being in agreement with post-mortem studies [4,5], this approach has nevertheless several drawbacks:
  1. certain correlations remain difficult to interprete, i.e. FA - $\lambda_{//}$ (cluster 4) and FA - MD (cluster 1);
  2. groupment of certain bundles, i.e. OR (quite mature) and ALIC (relatively immature), remains questionable;
  3. *a priori* assumption that during the considered time period all bundles don't change their maturational stage.

Thus, multiparametric evaluation of the white matter maturation requires more robust and reliable models [9].

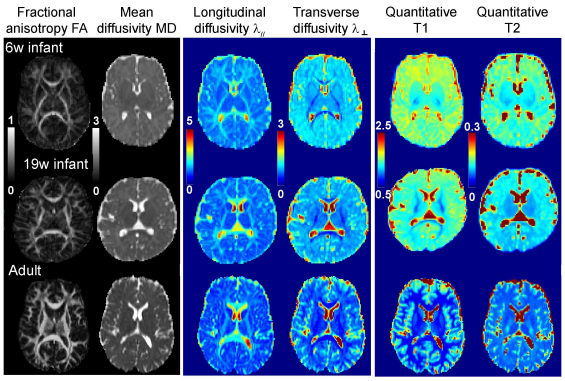

Fig.1 ***DTI maps (FA, MD, $\lambda_{//}$, $\lambda_{\perp}$) and quantitative maps for T1 and T2 relaxation times for subjects of different ages: infants at 6 and 19 weeks, and a young adult. Scale for diffusivities: x $10^{-3}mm^2.s^{-1}$; relaxation times are in seconds.***

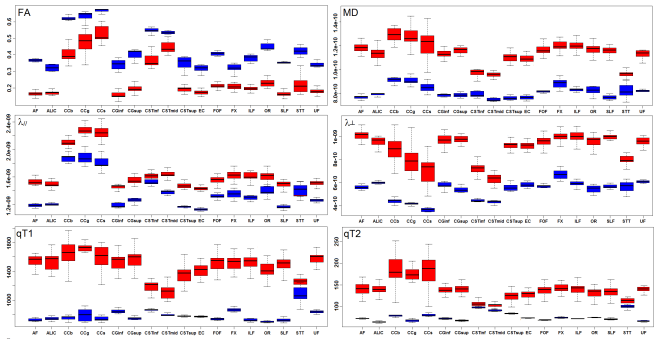

Fig.3 ***Distribution of the MRI parameters in infants and adults over different bundles.***

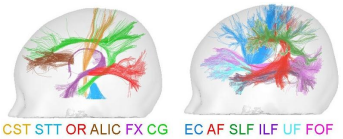

Fig.2 ***Example of the reconstructed bundles:***

- ***projection bundles:*** *cortico-spinal tract CST with three subdivisions (inferior, middle and superior portions) ; spino-thalamic tract STT; optic radiations OR; anterior limb of the internal capsule ALIC*
- ***association bundles:*** *external capsule EC, arcuate fasciculus AF, superior SLF and inferior ILF longitudinal fascicles, uncinate fasciculus UF, fronto-occipital fasciculus FOF.*
- ***limbic bundles:*** *fornix FX; inferior CGinf and superior CGsup parts of the cingulum.*
- ***commissural bundles:*** *genu CCg, body CCb and splenium CCs of the corpus callosum(not shown).*

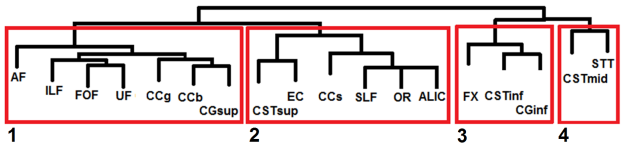

Fig.5 ***Bundle groups from clustering analysis of the correlations between the MRI parameters.***

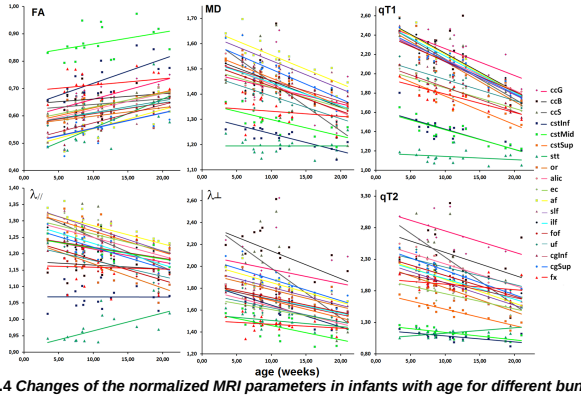

Fig.4 ***Changes of the normalized MRI parameters in infants with age for different bundles.***

Additional Information:

1 - Dubois et al. (Hum Brain Mapp, 2008); 2 - Deoni et al. (Magn Reson Med, 2005); 3 - Dubois et al. (ISMRM, 2010); 4 - Yakovlev, Lecours (Blackwell Scientific Publications, 1967); 5 - Flechsig (Leipzig, G Thieme, 1920);
6 - Duclap et al. (ESMRMB, 2012); 7 - Perrin et al. (Inf Process Med Imaging, 2005); 8 - Huang et al. (Magn Reson Med , 2004); 9 - Kulikova et al. (presentation #476, ESMRMB, 2013).

Chapter 4

Quantitative evaluation of white matter maturation using Mahalanobis distance

To quantitatively evaluate the maturational stage of a given white matter bundle in an infant at a certain age, the parameters characterizing that bundle should be compared with their typical "mature" values from the same bundle in an adult reference group using some "maturational distance". In this chapter, general considerations on choosing the "maturational distance" are first given. Then Mahalanobis distance is introduced. Finally, we present the application of this distance for the quantitative evaluation of the white matter maturation. The published paper is included [315].

4.1 Choosing "maturational distance"

A well-designed "maturational distance" should take into account both the inter-subject variability of the parameters and their correlations in the adult population. This is important because as soon as the difference between adult and infant values lays within the range of the normal parameters' variability in the adult population, infant values can no longer be considered as immature. On the contrary, even if infant values seem "very close" to the typical mature values but remain out of the range of the normal parameters' variability in the adult population, they should be regarded as immature. Ignoring that may lead to mistakes in comparing maturational stages across bundles. To illustrate this idea, let us consider a simplified example shown on Fig. 4.1. Let a given bundle of an adult population be described by only two parameters (Parameter 1 and Parameter 2), the mean adult parameters are marked as point C and the distribution of the parameters is described by covariation matrix Σ. Now let us compare the same bundle in two infants, having parameters marked by points A and B, to this adult population. When using Euclidean distance between these points (A and B) and the mean adult parameters (point C), it appears that infant B is closer to the adult stage C than infant A.

However, if we also consider the shape of the parameters distribution in the adult group, we can note that parameters in infant A are already in the range of normal parameters variability of the adult population, thus, they should be considered as already mature. On the contrary, parameters in infant B are still outside the normal parameters variability of the adult population and cannot yet be considered as mature, despite being "close" to adult mean values C.

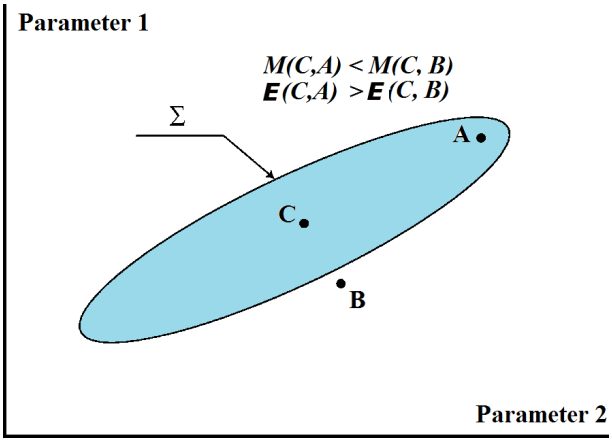

Figure 4.1: A simplified example showing why it is important to account for inter-subject variability of the parameters and their correlations in the adult population when comparing infant and adult parameters. Distributions of two parameters describing adult bundles are shown as a blue oval with mean parameters corresponding to point C and a covariation matrix Σ. Although according to the Euclidean distance E infant bundle B is closer to point C than another infant bundle A, it nevertheless cannot be considered as mature because it is outside the normal parameters variability of the adult population. On the contrary, bundle A is within the normal variability of adult parameters and can be considered as mature.

Taking into account these considerations and the fact that MRI parameters cannot be viewed as completely independent variables (see previous chapter), we proposed the Mahalanobis distance as a "maturational distance" between infant and adult bundles [315] (see article at the end of the chapter).

4.2 Mahalanobis distance

Mahalanobis distance M [318], which was initially introduced for multiparametric comparison of human skulls, is a unitless and scale-invariant measure of the distance between a multivariate vector $\vec{x}$ and a given multiparametric distribution with mean vector $\vec{\mu}$ and covariation matrix Σ:

$$M^2(\vec{x}) = (\vec{x} - \vec{\mu})^T \Sigma^{-1} (\vec{x} - \vec{\mu}) \tag{4.1}$$

When applied for comparison of infant and adult parameters, $\vec{x}$ corresponds to a multivariate vector describing a given infant bundle, $\vec{\mu}$ - to the vector with mean parameters from the corresponding bundle in the adult group ($\vec{\mu} = [1, 1, ..., 1]$ when all data are normalized by the corresponding mean adult values) and Σ is a covariance matrix of adult parameters for the same bundle. The smaller Mahalanobis distance is, the closer the infant bundle is to the mature stage.

Eq. 4.1 can be equally represented in the following way:

$$M^2(\vec{x}) = \sum_i^n ((\vec{x} - \vec{\mu})\vec{\nu_i})^2/\lambda_i \tag{4.2}$$

where $\vec{\nu_i}$ and λ_i are the n eigenvectors and eigenvalues of the covariance matrix Σ.

It should be noted here that the calculation accuracy for the Mahalanobis distance depends on the estimation accuracy of the covariance matrix Σ. When applied to small samples, Mahalanobis distance tends to be overestimated, mainly due to non-dominant components (components corresponding to smaller eigenvalues). In the simpliest way, this bias can be corrected by substituting the smaller eigenvalues with the maximal eigenvalue as suggested by Takeshita et al. [319]:

$$M^2(\vec{x}) = \sum_i^n ((\vec{x} - \vec{\mu})\vec{\nu_i})^2/\max\lambda_i \tag{4.3}$$

4.3 Applying Mahalanobis distance for evaluation of the white matter maturation

In this PhD work [315], we applied the Mahalanobis distance approach to evaluate and compare the maturation of 18 different white matter bundles in a population of 17 healthy infants, that were described in the previous chapter. The Mahalanobis distance was computed from four MRI parameters: quantitative qT1 and qT2 relaxation times, longitudinal $\lambda_\parallel$ and transverse $\lambda_\perp$ diffusivities. Fractional anisotropy and mean diffusivity $\langle D \rangle$ were not included as they are strongly correlated with $\lambda_\parallel$ and $\lambda_\perp$ (see previous chapter) and thus, may lead to singular covariance matrices. Possible bias from non-dominant components was corrected using Eq. 4.3 and the accuracy of Mahalanobis distance calculations was evaluated using simulated data, showing deviations not exceeding 6±1.8% [315].

Using Mahalanobis distance confirmed complex maturational relationships between bundles and allowed revealing the known spatiotemporal progression of the white matter maturation. As expected, bundles responsible for sensory and motor functions were the most mature: spino-thalamic tract was the most advanced followed by optic radiations and the cortico-spinal tract. The middle portion of the corticospinal tract was advanced relatively to its inferior and superior parts. As for limbic bundles, the fornix was more mature than the cingulum. The splenium of the corpus callosum were more mature than the body. The most delayed maturation was observed in the arcuate and superior longitudinal fasciculi and in the anterior limb of the internal capsule.

Compared to conventional univariate approaches, the Mahalanobis distance provided a more detailed description of the maturational asynchrony across bundles, revealing more maturational differences between them: Mahalanobis distance revealed 142 out of 153 $(18 * (18 - 1)/2)$ possible relationships between the considered 18 bundles, while this number did not exceed 90 for other parameters [315]. Furthermore, Mahalanobis distance approach made better predictions of the maturational ages than conventional univariate approaches and did not violate *a priori* known maturational relationships: spino-thalamic tract, cortico-spinal tract and optic radiations should be found among the most fast-maturing bundles, while anterior limb of the internal capsule and arcuate fasciculus should be classified as the most slowly maturing [121, 320].

Interestingly, age-related changes in the Mahalanobis distance across different bundles could be further modeled by exponential decays, which enabled computing the relative maturational delays between the bundles, providing a *quantitative* description of the bundles' maturational asynchrony. The total delay between the most and the least mature bundles was estimated to be 48–49 weeks, confirming that the most dramatic maturational changes occur during the first postnatal year.

It should be noted here that the Mahalanobis distance is not directly linked to brain myelination but is influenced by the whole ensemble of various maturational processes underlying age-related changes in the MRI parameters used for its calculation. Thus, although being relevant for *in vivo* evaluation of the white matter maturation, it may not be perfectly suited for evaluation of white matter myelination, which would require using more specific myelin-sensitive techniques, like the one described in the next chapter.

Brain Struct Funct
DOI 10.1007/s00429-014-0881-y

ORIGINAL ARTICLE

Multi-parametric evaluation of the white matter maturation

S. Kulikova · L. Hertz-Pannier · G. Dehaene-Lambertz · A. Buzmakov · C. Poupon · J. Dubois

Received: 4 April 2014 / Accepted: 18 August 2014

Abstract In vivo evaluation of the brain white matter maturation is still a challenging task with no existing gold standards. In this article we propose an original approach to evaluate the early maturation of the white matter bundles, which is based on comparison of infant and adult groups using the Mahalanobis distance computed from four complementary MRI parameters: quantitative qT1 and qT2 relaxation times, longitudinal $\lambda_{\parallel}$ and transverse $\lambda_{\perp}$ diffusivities from diffusion tensor imaging. Such multi-parametric approach is expected to better describe maturational asynchrony than conventional univariate approaches because it takes into account complementary dependencies of the parameters on different maturational processes, notably the decrease in water content and the myelination. Our approach was tested on 17 healthy infants (aged 3- to 21-week old) for 18 different bundles. It finely confirmed maturational asynchrony across the bundles: the spino-thalamic tract, the optic radiations, the cortico-spinal tract and the fornix have the most advanced maturation, while the superior longitudinal and arcuate fasciculi, the anterior limb of the internal capsule and the external capsule have the most delayed maturation. Furthermore, this approach was more reliable than univariate approaches as it revealed more maturational relationships between the bundles and did not violate a priori assumptions on the temporal order of the bundle maturation. Mahalanobis distances decreased exponentially with age in all bundles, with the only difference between them explained by different onsets of maturation. Estimation of these relative delays confirmed that the most dramatic changes occur during the first post-natal year.

Keywords Mahalanobis distance · White matter · Brain development · Bundles · Infants · T1 and T2 relaxometry · Diffusion tensor Imaging DTI

Electronic supplementary material The online version of this article (doi:10.1007/s00429-014-0881-y) contains supplementary material, which is available to authorized users.

S. Kulikova · L. Hertz-Pannier
UMR 1129 NeuroSpin/UNIACT, INSERM-CEA,
Gif-sur-Yvette, France

L. Hertz-Pannier (✉)
CEA/SAC/DSV/I2BM/NeuroSpin, Bât 145, point courrier 156,
91191 Gif-sur-Yvette, France
e-mail: lucie.hertz-pannier@cea.fr

G. Dehaene-Lambertz · J. Dubois
UMR 992 NeuroSpin/UNICOG INSERM-CEA,
Gif-sur-Yvette, France

A. Buzmakov
LORIA, CNRS-Inria Nancy Grand Est-Université de Lorraine,
Nancy, France

C. Poupon
NeuroSpin/UNIRS CEA-Saclay, Gif-sur-Yvette, France

Introduction

Maturation of the brain white matter is a complex process, which lasts from the third trimester of pregnancy until late adolescence, and proceeds in an asynchronous manner across cerebral regions (Yakovlev and Lecours 1967). Early *post-mortem* studies have shown that different white matter regions myelinate over different periods of time and at different rates, from the central regions to the periphery (Flechsig 1920). For instance, certain projection bundles (e.g. cortico-spinal and spino-thalamic tracts) mature before association bundles related to cognitive functions such as language (e.g. arcuate fasciculus) (Brody et al.

Published online: 03 September 2014

1987; Kinney et al. 1988). However, *post-mortem* studies have insurmountable limitations: they do not allow making correlations between anatomical and functional changes during maturation and provide "region-specific" rather than "bundle-specific" information. In vivo imaging is thus indispensable for understanding both normal and pathological brain development, but it remains a challenging task in unsedated infants.

Conventional Magnetic Resonance Imaging (MRI) studies, using T1- and/or T2-weighted images have confirmed that different white matter regions acquire "myelinated" appearance in a specific temporal order (Paus et al. 2001): first, in pons and cerebral peduncles, then in the optic radiations, the posterior limb of the internal capsule and the splenium of the corpus callosum, followed by the anterior limb of the internal capsule, the genu of the corpus callosum and finally, by the white matter of the occipital, frontal, parietal and temporal lobes. Whereas these studies provided only qualitative description of the white matter maturation, alternatives have been recently proposed with the quantitative mapping of the relaxation times qT1 and qT2 (Deoni et al. 2005) and with diffusion tensor imaging (DTI), which computes distinct parameters (mean <D>, longitudinal $\lambda_{\parallel}$ and transverse $\lambda_{\perp}$ diffusivities, fractional anisotropy FA (Le Bihan and Johansen-Berg 2012)) that can be quantified along the white matter bundles reconstructed using fiber tracking technics (Mori and van Zijl 2002).

All these parameters are known to change with age and are thought to reflect different maturational processes (Dubois et al. 2014a). qT1 mostly depends on the brain water and lipid contents (Steen et al. 1997), whereas qT2 mostly depends on water content and iron accumulation (Engelbrecht et al. 1998); both qT1 and qT2 decrease with age but changes in qT2 (associated with "true myelination") are known to start later than in qT1 (associated with "pre-myelination") (Barkovich et al. 1988).

Changes in the DTI parameters are more complex: they depend on the bundle maturational stage and are thought to reflect various processes such as organization of the nervous fibers into bundles, membrane proliferation in the intra- and extra-cellular space (''pre-myelination'') and myelination (Dubois et al. 2008, 2014a). Some fractional anisotropy can be observed even early on in poorly myelinated bundles of the premature newborns because of the tight organization of the fibers into bundles (Hüppi et al. 1998). With the decrease in water content and the increase in membrane density, all diffusivities decrease. During fiber myelination, fractional anisotropy increases due to a decrease in transverse diffusivity contrasting with constant longitudinal diffusivity.

Although it is possible to make inferences on bundles maturation on the basis of only one MRI or DTI parameter, the univariate approaches may not be efficient to discriminate bundles that are at different maturational stages. For example, the approach of Dubois et al. (2008), based on DTI indices, was supported in only 8 out of 11 bundles, facing problems in classification of the corpus callosum, external capsule and uncinate fasciculus. Thus, taking advantage of the complementary dependencies of the MRI parameters on maturational processes and considering multi-parametric maturational models should enable better characterization of the bundles maturation.

To evaluate a maturational stage of a given infant bundle at a certain age, one needs to compare the parameters characterizing that bundle with the typical values for the same bundle in an adult group, i.e. to compute the "maturational distance" between current and adult stages. Since MRI and DTI parameters are also known to vary across different bundles in the adult brain and to have different scales for different parameters (Dubois et al. 2008), their normalization is required before comparison. Furthermore, a well-designed "maturational distance" should take into account the inter-subject variability of the parameters in the adult population as well as their correlations: the difference between adult and infant values may be important or not, depending on whether it is or not within the range of the parameters variability in the adult population.

According to all these constraints, we introduce here a novel strategy to reliably describe and efficiently compare the bundles maturation in infants from 1 to 5 months of age. This strategy is based on estimation of the Mahalanobis distance between the multi-parametric vectors of four parameters (qT1, qT2, $\lambda_{\parallel}$, $\lambda_{\perp}$) describing bundles in infant and adult groups, and it is compared with univariate approaches. In addition to ordering the bundles according to their relative maturation, our approach suggests a general description of the maturation that allows estimating the relative maturational delays between the bundles.

Materials and methods

Subjects

This research study was performed on 17 healthy infants born at term (7 girls, 10 boys), with a maturational age (i.e. chronological age corrected for gestational age at birth) between 3 and 21 weeks. Infants were compared to an adult group of 13 healthy subjects (6 women, 7 men, mean age: 22.4 ± 1.6 years). Additionally, a 34-week-old girl (almost 8 months) was imaged for the model evaluation at an older age. None of the subjects displayed any neurodevelopmental problems or any brain abnormalities observed on MR images. The study protocol was approved

by the regional ethical committee for biomedical research; all parents and adult subjects gave written informed consents. Infants were spontaneously asleep during MR imaging. Particular precautions were taken to minimize noise exposure, by using customized headphones and covering the magnet tunnel with special noise protection foam.

MRI acquisitions

Data acquisition was performed on a 3T MRI system (Tim Trio, Siemens Medical Systems, Erlangen, Germany), equipped with a whole body gradient (40 mT/m, 200 T/m/s) and a 32-channel head coil. Interleaved axial slices covering the whole brain were imaged with a 1.8-mm isotropic spatial resolution (FOV = 23 × 23 cm^2, matrix = 128 × 128) using EPI single-shot spin-echo (SE) sequences (50 slices for infants; 70 for adults). For DTI, a DW-SE-EPI sequence was used with 30 orientations of diffusion gradients with $b = 700$ s mm^{-2} ($+b = 0$ volume): TE = 72 ms, TR = 10 s (TR = 14 s for adults), parallel imaging GRAPPA factor 2, partial Fourier sampling factor 6/8, leading to an acquisition time of 5 min 40 s (7 min 56 s for adults). For qT1 mapping, an inversion recovery (IR) SE-EPI sequence was used with eight different values of inversion time (TI = 250→1,500 ms each step 250 ms + TI = 2,000, 2,500 ms): TE = 38 ms, TR = TI + 15 s (TR = TI + 21 s for adults), partial Fourier sampling factor 5/8, leading to an acquisition time of 2 min 11 s (3 min 03 s for adults). For qT2 mapping, an SE-EPI sequence was used with 8 different values of echo time (TE = 50→260 ms each step 30 ms): TR = 15.5 s (TR = 21.7 s for adults), parallel imaging GRAPPA factor 2, partial Fourier sampling factor 6/8, leading to an acquisition time of 2 min 51 s (4 min for adults).

Data post-processing

After correction of artifacts from motion and eddy currents (Dubois et al. 2014b), quantitative MRI and DTI maps were generated for all parameters (qT1, qT2, FA, <D>, $\lambda_{\perp}$, $\lambda_{\parallel}$) using Connectomist software (Fig. 1) (Duclap et al. 2012; Poupon et al. 2010). Whole brain tractography was performed according to a 4-order analytical Q-ball model and using regularized 3D tractography (Perrin et al. 2005). White matter bundles were identified in each subject using manually delineated regions of selection and exclusion (Huang et al. 2004). We selected 18 bundles that mature at different times and rates (Fig. 2) (Dubois et al. 2008):

- projection bundles: cortico-spinal tract CST with three subdivisions (inferior portion below the internal capsule, middle portion below the low centrum semiovale and superior portion), spino-thalamic tract STT, optic radiations OR, anterior limb of the internal capsule ALIC;
- association bundles: external capsule EC, arcuate fasciculus AF, superior SLF and inferior ILF longitudinal fascicles, uncinate fasciculus UF, fronto-occipital fasciculus FOF;
- limbic bundles: fornix FX, inferior CGinf and superior CGsup parts of the cingulum;
- commissural bundles: genu CCg, body CCb and splenium CCs of the corpus callosum.

For each subject, MRI parameters were quantified and averaged over the bundle length, taking into account fiber

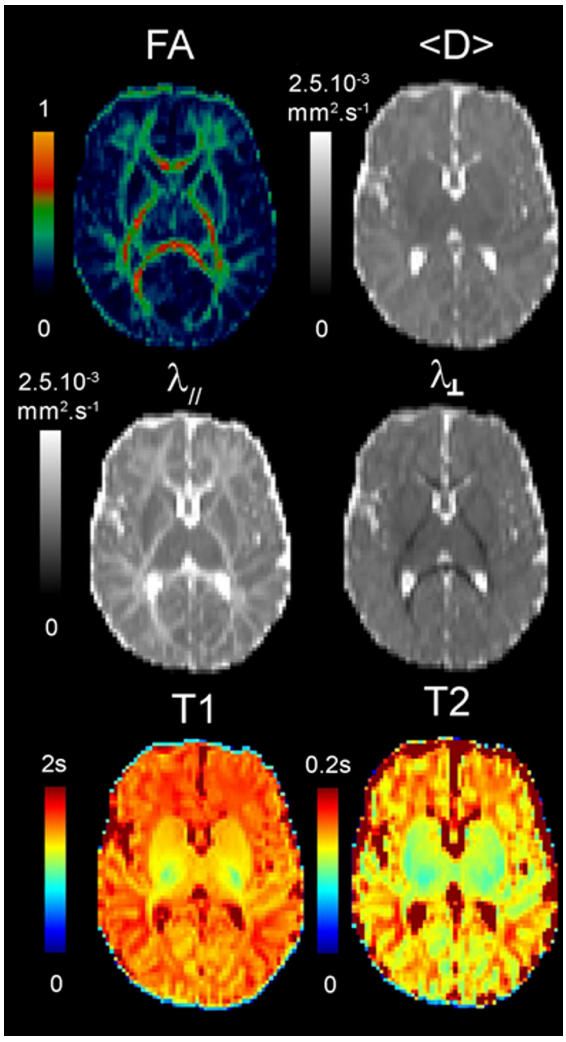

Fig. 1 Quantitative maps of MRI parameters. Maps of DTI parameters and relaxation times are presented for a 6-week-old infant

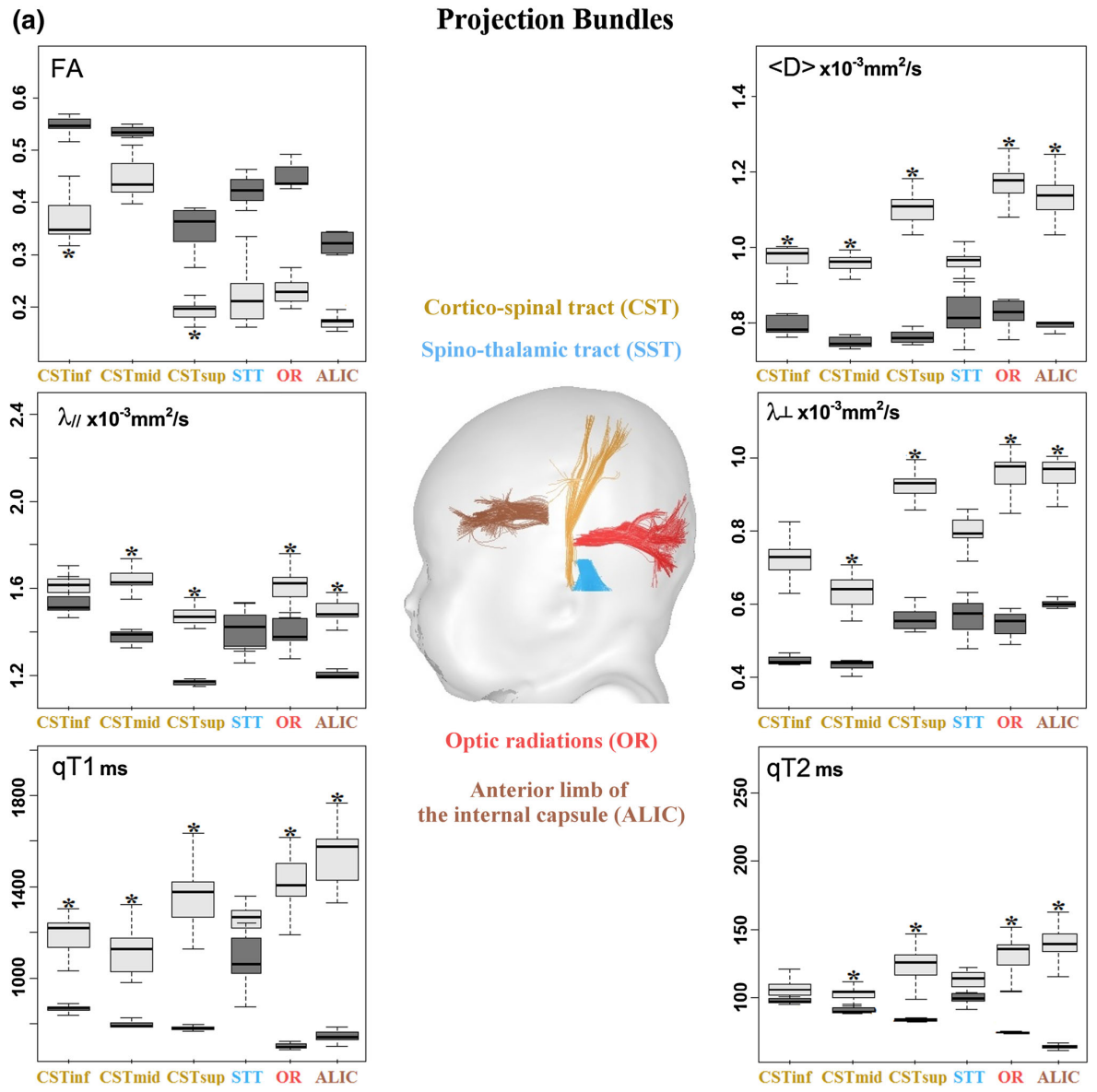

Fig. 2 Quantification of the MRI parameters over the infant and adult groups. Mean and standard deviations of the parameters are shown across the bundles in the infant (*light boxes*) and adult (*dark boxes*) groups. *Asterisk* indicates that variations in the infant group could be attributed to the age-related changes by performing linear regressions with age ($R^2 > 0.46$, $p < 0.05$)

density (Dubois et al. 2006). All infant and adult values were further normalized by the corresponding means from the adult group.

Implementation of the Mahalanobis approach

For all bundles, comparison of the normalized parameters in the infant and adult groups was performed using Mahalanobis distance M (Mahalanobis 1936) as it allows taking into account the inter-subject variability and the parameters correlations in the adult group as well as their variability across the bundles:

$$M^2(\vec{x}) = (\vec{x} - \vec{\mu})^T \sum^{-1} (\vec{x} - \vec{\mu}), \quad (1)$$

where $\vec{x}$ is a multivariate vector describing an infant bundle, $\vec{\mu} = [1, 1, \ldots, 1]$ is the mean vector for the

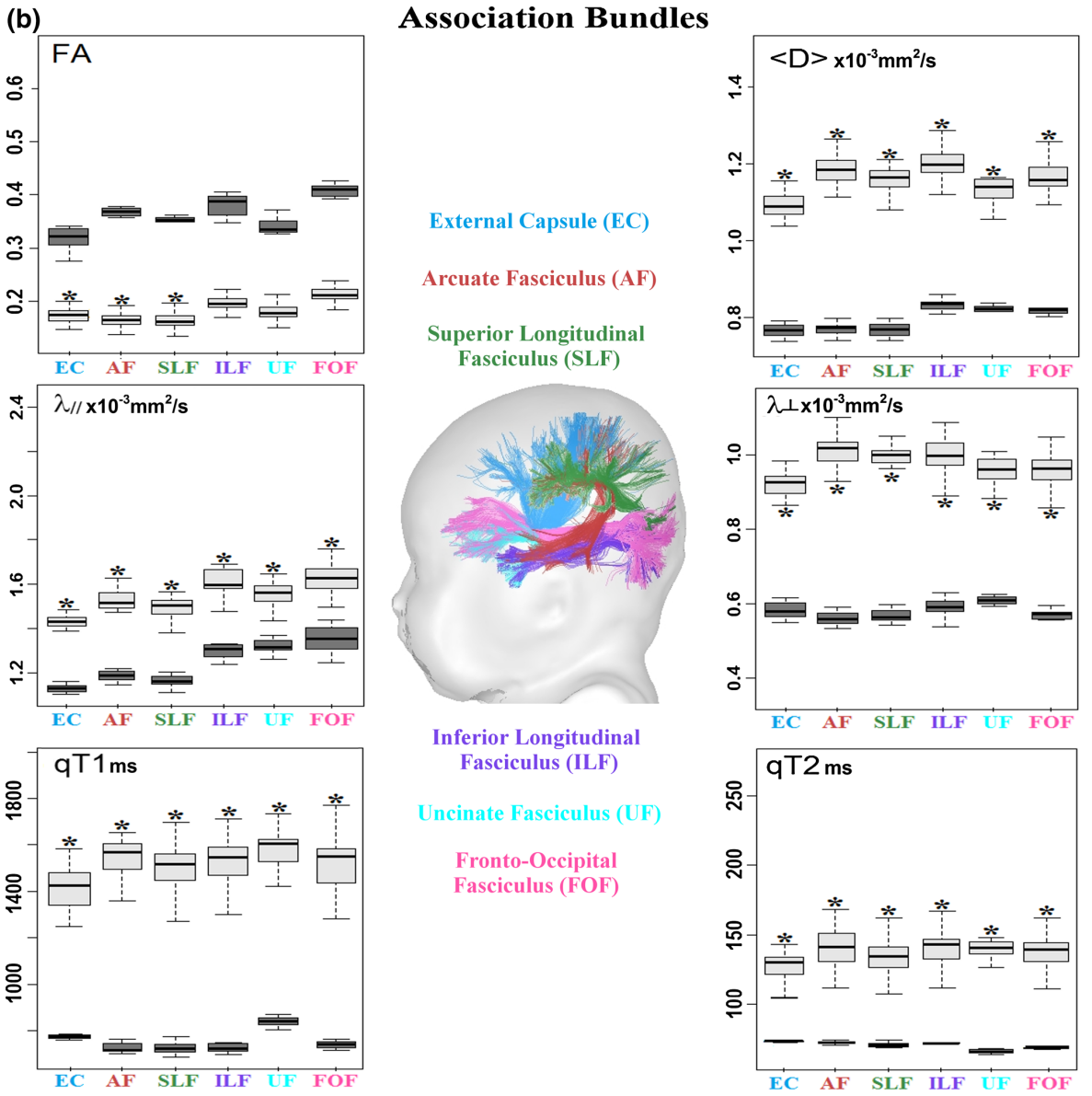

Fig. 2 continued

corresponding bundle in the adult group and $\sum$ is a covariation matrix for parameters in adults. The smaller this distance, the closer the infant bundle to its mature adult stage. Mahalanobis distance can be equally calculated using the eigen systems representation:

$$M^2(\vec{x}) = \sum_i^n \left((\vec{x} - \vec{\mu})\overrightarrow{v_i}\right)^2 / \lambda_i, \quad (2)$$

where $\overrightarrow{v_i}$ and λ_i are the n eigenvectors and eigenvalues of the covariation matrix $\sum$. In our study Mahalanobis distance was calculated using four "independent" parameters: qT1, qT2, $\lambda_\perp$, $\lambda_\parallel$ (FA and <D> were not included as they can be viewed as the functions of $\lambda_\perp$, $\lambda_\parallel$).

Possible bias from non-dominant components that appears in small samples was compensated by substituting the smaller eigenvalues with the maximal eigenvalue (Takeshita et al. 1993):

$$M^2(\vec{x}) = \sum_{i=1}^4 \left((\vec{x} - \vec{\mu})\overrightarrow{v_i}\right)^2 / \max(\lambda_1, \lambda_2, \lambda_3, \lambda_4) \quad (3)$$

The age-related decrease in Mahalanobis distance was assessed for each bundle using linear regressions.

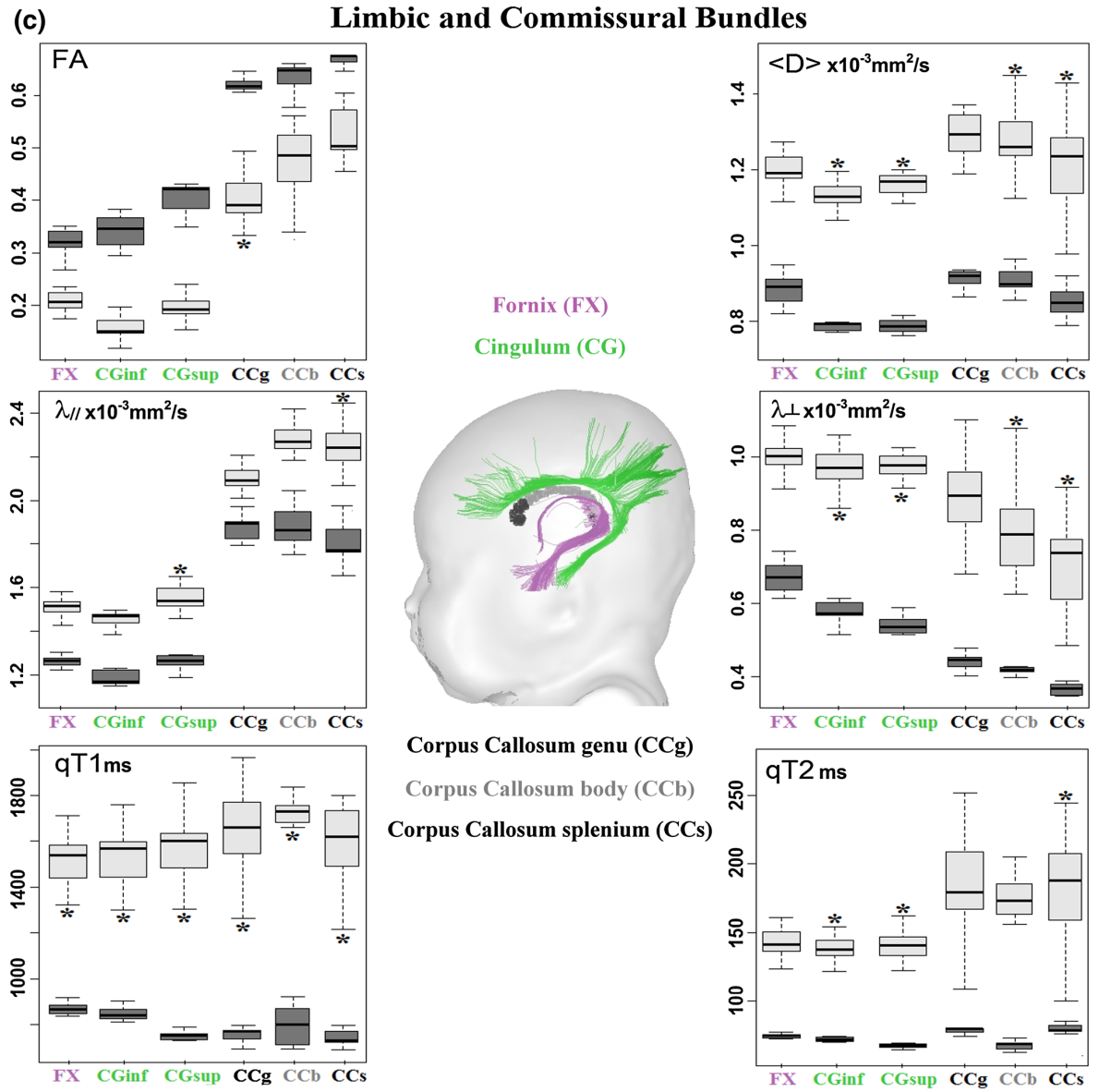

Fig. 2 continued

Estimation of the calculation errors

Using formula (3) may lead to underestimation of the Mahalanobis distance because (1) the smaller eigenvalues are replaced by the maximal eigenvalue and (2) in small samples dominant components (components corresponding to bigger eigenvalues) tend to be slightly smaller than their true values (Takeshita et al. 1993). To take this into account, we estimated, for each bundle independently, average calculation errors for Mahalanobis distances between infants and adults. This estimation was performed using a computer simulation that compared Mahalanobis distances, calculated using 13 multivariate vectors randomly selected from the "true" distribution of the adult parameters across all bundles, with the "true" distances. The "true" distribution of the parameters was a Gaussian mixture distribution with the mean vector $\vec{\mu}_{\text{sim}} = [1; 1; 1; 1]$ and the covariation matrix $\sum_{\text{sim}}$ determined from all 13

adults across all the bundles. A random sample of 13 vectors was taken from that distribution to estimate the Mahalanobis distance using (3) in each infant and for each bundle. These distances were compared with the "true" distances calculated using (1) and the "true" covariation matrix $\sum_{\text{sim}}$. The described procedure was repeated 1.000.000 times and the average positive σ_+^2 and negative σ_-^2 squared normalized deviations between estimated and "true" distances were computed for each bundle independently.

Comparison of the bundles maturation

In the group of infants with different ages, age-related changes of the Mahalanobis distance defined a maturational trajectory $M(b;\text{age})$ for each bundle$b$, and comparing the maturation of two bundles b_i and b_j was equivalent to comparing the trajectories $M(b_i;\text{age})$ and $M(b_j;\text{age})$ across ages. To compare these trajectories at a given age, we considered the overlap between the two intervals $[M(b_i;\text{age}) - \sigma_+(b_i;\text{age}); M(b_i;\text{age}) + \sigma_-(b_i;\text{age})]$ and $[M(b_j;\text{age}) - \sigma_+(b_j;\text{age}); M(b_j;\text{age}) + \sigma_-(b_j;\text{age})]$. If these intervals overlapped, then the difference between $M(b_i;\text{age})$ and $M(b_j;\text{age})$ was set to zero and the two bundles were not distinguished one from another at this age. If the intervals did not overlap, the difference between $M(b_i;\text{age})$ and $M(b_j;\text{age})$ was equal to the smallest distance between the points belonging to the intervals, taken with a positive sign if $M(b_i;\text{age}) < M(b_j;\text{age})$ (b_i was more mature than b_j at this age) and with a negative sign in the opposite case.

To compare two bundles across the whole age range, these differences were considered between the corresponding age-points on their maturational trajectories. If these differences were significantly different from zero (paired t test over the infant group) then the bundles were said to have different maturational trajectories. The result of the pair-wise comparisons between all bundles created a partial maturational order on the set of bundles that was presented as a graph, showing complex maturational relationships. Statistical tests were considered with a 0.95 significance level, corrected for multiple comparisons using FDR approach. Relationships that failed to reach the 0.95 significance level were also tested at the level of 0.9.

Comparison of the Mahalanobis approach with univariate approaches

As for univariate approaches, we evaluated the variations with age of each normalized MRI parameter, including FA and <D>, for each of the bundles. Similarly to the Mahalanobis distance approach, partial ordering of the bundles was performed using each MRI parameter independently. All partial orders (from Mahalanobis distance and from each parameter) were compared in terms of (1) the number of discriminated relationships between the bundles; (2) presence of violations in five a priori known maturational relationships: spino-thalamic tract, cortico-spinal tract and optic radiations should be among the most fast-maturing bundles, while anterior limb of the internal capsule and arcuate fasciculus should be among the most slowly maturing (Yakovlev and Lecours 1967; Paus et al. 1999; Zhang et al. 2007).

Additionally, we evaluated which strategy made better predictions on the maturational age using a "leave-one-out" approach. Because of the short age range, changes in the normalized MRI parameters and in the Mahalanobis distance with age were fitted with linear equations (where appropriate with $R^2 > 0.46$ corresponding to $p < 0.05$). To make predictions for each bundle, the fitting was done using all but one infant, and his/her age predicted by the fitting was then compared with the real age. The described procedure was repeated for all infants and the prediction errors were averaged.

Implementation of a general equation of the maturation

As detailed in the results section, the derivative $-\frac{dM(b;\text{age})}{d\text{age}}$ was found to linearly depend on the average (over the age range) Mahalanobis distance $\langle M(b)\rangle$, suggesting that the "general maturational equation" should take the exponential form:

$$M(b;\text{age}) = a(b) \times \exp(-c \times \text{age}) \tag{4}$$

$$\text{or}: M(b;\text{age}) = A_0 \times \exp(-c \times (\text{age} - \text{age}_0(b))), \tag{5}$$

where A_0, c are constants and $\text{age}_0(b)$ can be interpreted as the age of the maturation onset for a bundle b. This description further enabled to compute a relative maturational delay between two bundles b_i and b_j:

$$\text{age}_0(b_i) - \text{age}_0(b_j) = \frac{1}{c} \times \ln\left(a(b_i)/a(b_j)\right) \tag{6}$$

When bundle groups were defined in the Mahalanobis ordering, we indicated the minimal and maximal delays between bundles.

To investigate whether this exponential model remains adequate at older developmental stages, it was tested on a 34-week-old infant. For all bundles, the "true" Mahalanobis distances were calculated according to the infant's data and Eq. 3, and compared with the values predicted by the exponential Eq. 4.

Results

Changes in the normalized MRI parameters and Mahalanobis distance with age

Despite low brain maturation in infants, we obtained high-quality MRI maps in all subjects (Fig. 1), as well as reliable bundle reconstructions and parameter quantification for all bundles (Fig. 2). In all infant bundles, fractional anisotropy was lower than in adults, while other parameters (relaxation times and diffusivities) were higher. Besides, the means and the variabilities of the infant parameters were not the same across the bundles (Fig. 2), reflecting differences in the maturational stages and in the rates of the maturational changes over the age range. The global picture was even more complex because of unequal mean values and unequal variability of the parameters across the bundles in the adult group. This confirmed the need for normalization of the parameters by the corresponding means over the adult group in order to reliably compare the infant and adult groups and to highlight maturational differences across the bundles.

Over this short developmental period, normalized parameters changed with age (increase in fractional anisotropy, decrease in other parameters). For each parameter, the observed differences across the bundles suggested that certain bundles (e.g. spino-thalamic and cortico-spinal tracts) matured faster than the others; however, the majority of the bundles could not be differentiated one from another.

Besides, Mahalanobis distance was computed for each bundle in all infants: it decreased with age in all bundles, reflecting bundles' maturation (Fig. 3a). It seemed to provide better discrimination of the bundles than other MRI parameters, confirming the spino-thalamic and cortico-spinal tracts to be among the most mature bundles. Contrarily to univariate parameters (Fig. 2), age-related linear regressions were significant for all bundles (Fig. 3a). Despite the relatively small size of the adult group, simulations showed that Mahalanobis distance was calculated with an acceptable precision (Online Resource 1), with average (over all bundles) positive and negative deviations from the true values being equal to 1.0 ± 0.3 % and 6.0 ± 1.8 %, respectively.

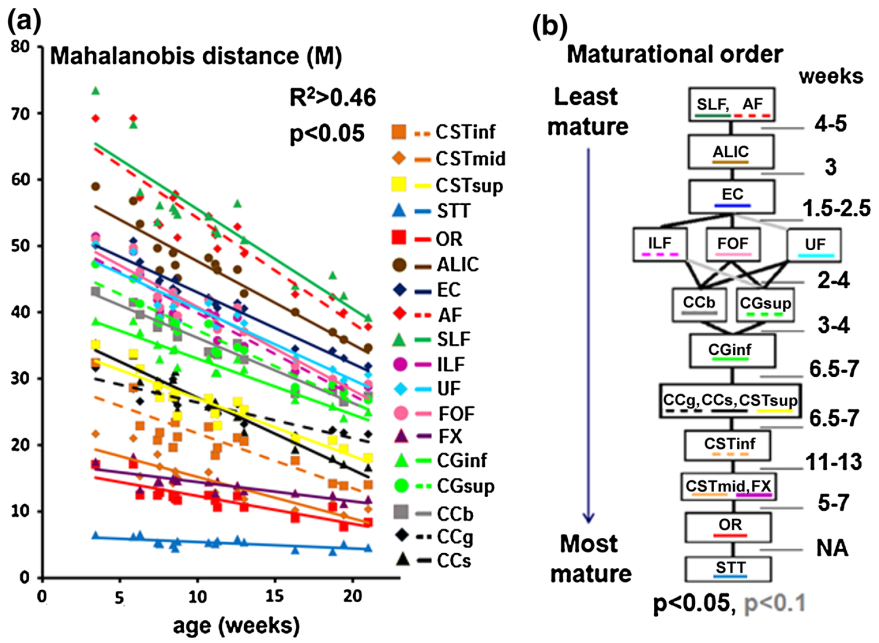

Fig. 3 Bundle maturational order revealed by the Mahalanobis distance. **a** Mahalanobis distances to the adult stage progressively decreased with the infants' age in all bundles and were modeled by linear fitting over this short developmental period. The rate of decrease was slower in the bundles already advanced in maturation (smaller distances) than in those showing higher distances to the adult bundles (see Fig. 4). **b** Maturational relationships between the bundles are represented as a graph. Bundles showing advanced maturation are close to the *bottom*; those with delayed maturation are on the *top*. *Gray lines* (between CGsup and ILF; UF and EC) mark relationships that failed to reach statistical significance ($0.05 < p < 0.1$). Relative maturational delays (in weeks) between the bundles or bundle groups are indicated on the *right side*. Delays between the spino-thalamic tract (STT) and other bundles were not considered (see text for explanations). See Fig. 2 for abbreviations

Ordering the bundles maturational trajectories with Mahalanobis approach

Pair-wise comparisons of Mahalanobis distances across the bundles created a partial maturational order represented as a graph (Fig. 3b). As expected, the most mature were the bundles responsible for sensory and motor functioning: spino-thalamic tract was the most advanced followed by optic radiations and the cortico-spinal tract; thus, most projection bundles (except the anterior limb of the internal capsule) appeared more mature than limbic, commissural and association bundles. The middle portion of the cortico-spinal tract was advanced relatively to its inferior and superior parts. As for limbic bundles, the fornix was more mature than the cingulum. The splenium and genu of the corpus callosum were more mature than the body. Concurrently and consistently with our expectations, the most delayed maturation was observed in the arcuate and superior longitudinal fasciculi and in the anterior limb of the internal capsule. Some bundles were grouped together when the comparison did not reveal any significant differences in their maturational trajectories: for example, the genu and splenium of the corpus callosum and the superior portion of the cortico-spinal tract. The obtained ordering did not violate the a priori known relationships and revealed 142 out of 153 (17 infants × 18 bundles divided by 2) maximal possible relationships.

Comparison of the Mahalanobis approach with univariate approaches

Maturational orderings were also obtained according to each normalized MRI parameter and compared with the Mahalanobis approach. For all univariate parameters, the number of discriminated relationships was below 90, and for all of them, except longitudinal diffusivity, maturational orders contained violations of the a priori known relationships (Table 1). The most common violation concerned the placement of the optic radiations relatively to other bundles in the maturational order: they were classified as relatively immature and placed at the same level as either the arcuate fasciculus (for qT2) or the anterior limb of the internal capsule (for qT1, <D>, FA, $\lambda_{\perp}$). Thus, according to our comparison criteria, Mahalanobis distance showed the best performance (Table 1). Note that none of the 11 relationships unrevealed by the Mahalanobis distance was discriminated by any of the univariate approaches.

Additionally, leave-one-out validations confirmed that linear models based on the Mahalanobis distance provided better predictions of the maturational age than univariate approaches in 14 out of 18 bundles (Table 1, Online Resource 2). Prediction errors for Mahalanobis distance were of 17 ± 8 % on average over all bundles. These errors were higher for all other parameters (Table 1, Online Resource 2).

Table 1 Comparison of the Mahalanobis distance approach (M) with other univariate approaches

	n	violations	Prediction errors (%)
M	142	–	17 ± 8
FA	74	1. Spino-thalamic tract was among the least mature bundles. 2. Optic radiations and anterior limb of the internal capsule were at the same immature level.	46 ± 20
<D>	72	Optic radiations and anterior limb of the internal capsule were placed at the same intermediate maturational level.	45 ± 24
$\lambda_{\parallel}$	76	–	54 ± 38
$\lambda_{\perp}$	70	1. Optic radiations were less advanced in maturation than anterior limb of the internal capsule. 2. Cortico-spinal tract and anterior limb of the internal capsule were at the same maturational level.	44 ± 21
qT1	90	Optic radiations were among the least mature bundles.	27 ± 20
qT2	89	Optic radiations and arcuate fasciculus were placed at the same intermediate maturational level	21 ± 10

Mahalanobis distance was able to discriminate more maturational relationships between the bundles (n out of 153) than other univariate approaches and it did not violate a priori known maturational relationships (violations). Additionally, prediction errors (in %) of the maturational age in the leave-one-out validation were smaller for Mahalanobis distance approach than for other univariate approaches (for details see Online Resource 2)

General equation of the maturation according to the Mahalanobis distance

Considering linear approximations of the maturational trajectories with age $M(b;\text{age}) = a_1(b) - a_2(b) * \text{age}$, we found that for all bundles, the slope $a_2(b)$ (or $-\frac{dM(b;\text{age})}{d\text{age}}$) linearly depended on the average Mahalanobis distance $\langle M(b) \rangle$ (over the age range) (Fig. 4, $R^2 = 0.89$). Thus, the maturational trajectories were further modeled by exponential decays (Eq. 4). Fitting our data with Eq. 4 resulted in constant $c = 0.03075$ and the bundle-related coefficients $a(b)$ detailed in Table 2.

The relative maturational delays between the bundles were further computed using Eq. 6 (see results in Fig. 4b). The minimal delay was 1.5 weeks between the fronto-occipital fasciculus and the external capsule, and the maximal delay was 13 weeks between the fornix and the

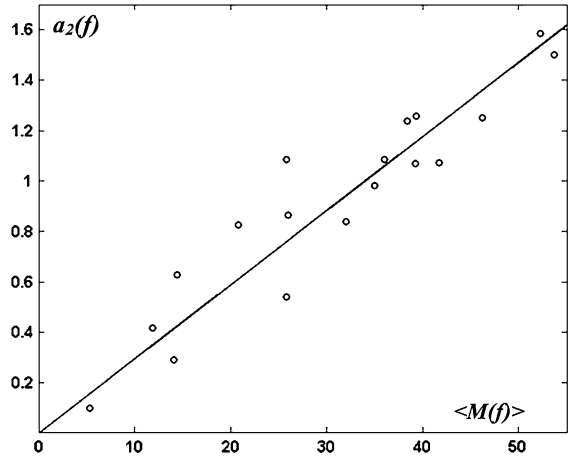

Fig. 4 Relationship between the speed of changes of the Mahalanobis distance and the maturational stage. For each bundle b, the age-related decrease in the Mahalanobis distance was modeled by a linear approximation: $M(b;age) = a_1(b) - a_2(b) * age$. Across the bundles, the corresponding slopes $(a_2(b))$ linearly increased with the mean Mahalanobis distances $\langle M(b) \rangle$ ($R^2 = 0.89$)

Table 2 Exponential fitting of the Mahalanobis distance (Eq. 4) for different bundles

	CSTinf	CSTmid	CSTsup	STT	OR	ALIC
$a(b)$	29.2	20.4	36.4	7.3	16.6	64.4
	EC	AF	SLF	ILF	UF	FOF
$a(b)$	58.1	73.1	74.9	53.7	54.7	55.0
	FX	CGinf	CGsup	CCg	CCb	CCs
$a(b)$	19.5	44.6	50.3	35.8	48.8	36.4

Bundle-related coefficients $a(b)$ are specified here: they were further used for calculation of the relative maturational delays between the bundles or bundle groups (Eq. 6). See Fig. 2 for abbreviations

inferior portion of the cortico-spinal tract. Delays between the spino-thalamic tract and other bundles were not considered because for this tract none of the individual parameters was able to reveal any significant age-related changes: thus, the Mahalanobis distance could not make use of any of them, having an artificially flat slope in the age-related changes, which resulted in overestimations of the relative maturational delays between the spino-thalamic tract and other bundles. The total delay between the optic radiations and the least mature group (arcuate and superior longitudinal fasciculi) was estimated to be 48–49 weeks.

Finally, this exponential model was tested on a 34-week-old infant to investigate its performance for older ages. Comparison of true and predicted values suggested a good agreement with an average prediction error of 13.5 % (Table 3). Prediction errors tended to be smaller for

Table 3 Evaluation of the maturational model in a 34-week-old infant

	CSTinf	CSTmid	CSTsup	STT	OR	ALIC
Predicted	10.3	7.2	12.8	2.6	5.8	22.6
True	9.8	5.4	11.6	3.9	5.7	24.8
Error (%)	5	33	11	33	1	9
	EC	AF	SLF	ILF	UF	FOF
Predicted	20.4	25.7	26.3	18.9	19.2	19.3
True	18.3	24.6	26.4	17.4	19.8	18.7
Error (%)	12	4	0.4	8.6	3	3
	FX	CGinf	CGsup	CCg	CCb	CCs
Predicted	6.9	15.7	17.7	12.6	17.1	12.8
True	7.6	15.3	17.7	11.8	14.5	11.6
Error (%)	9	2	0.2	7	18	10

For each bundle, the value of the Mahalanobis distance predicted by the maturational model (Eq. 4) and the true value calculated using Eq. 3, are detailed. The average prediction error across the bundles was 13.5 %. See Fig. 2 for abbreviations

bundles with delayed maturation (e.g. 3 and 4 % for uncinate and arcuate fasciculi, respectively) than for bundles with advanced maturation (e.g. up to 33 % for spino-thalamic tract and the middle portion of the cortico-spinal tract), presumably because greater changes in the Mahalanobis distance (corresponding to bundles with delayed maturation) could be better approximated over that age range than smaller changes (corresponding to bundles with advanced maturation). However, certain bundles did not follow this rule: although optic radiations were among the most advanced in maturation, the prediction error for them was surprisingly low (1 %).

Discussion

In this article we have proposed an original multi-parametric approach for quantitative in vivo evaluation of white matter maturation. This approach enabled demonstrating the asynchrony in the bundles' maturation more reliably than conventional univariate approaches within the period from 3 to 21 weeks of post-natal age. It further suggested a general quantitative description of the maturation that enabled estimating the relative maturational delays between the bundles.

Multi-parametric vs. univariate approaches

MRI and DTI parameters provide exquisite details on white matter maturation, and their age-related changes are known to reflect undergoing maturational processes. However,

none of these parameters alone can describe the complexity of white matter maturation because different MRI/DTI parameters are sensitive to different tissue properties and thus, to different stages of the maturational processes (Dubois et al. 2008; Steen et al. 1997; Engelbrecht et al. 1998; Barkovich et al. 1988; Dubois et al. 2014a). To overcome this difficulty, multi-parametric models that take advantage of the complementary dependencies of the MRI parameters on maturational processes should come on stage (Prastawa et al. 2010; Sadeghi et al. 2013; Vardhan et al. 2012). Such models should provide a measure of a maturational distance between infant and adult brains. They should also take into account variations and covariations of the parameters across different bundles in the adult group because a difference between infant and adult parameters is relevant only if it is superior to the normal variations within the adult group.

To our knowledge, there is only a couple of recent studies trying to combine both MRI and DTI parameters in a single maturational model (Sadeghi et al. 2013; Prastawa et al. 2010). Sadeghi et al. (2013) used Gompertz functions to model age-related changes in both FA and the intensities of T1- and T2-weighted images. Prastawa et al. (2010) suggested a non-linear growth model based on modified Legendre polynomial basis, that was used to create maturation maps, using five modalities: longitudinal and transverse diffusivities, proton density and intensity of T1- and T2-weighted images. Instead of quantitative T1 and T2 relaxation times, both of these studies used the intensities of T1- and T2-weighted images, which are hardly comparable across brain regions and across subjects because of signal inhomogeneities and of varying acquisition tunings. Furthermore, none of these models took into account the differences in the parameters and their variations at the mature adult stage. Finally, these studies provided region-specific rather than tract-based information possibly mixing the information about different bundles passing at the same location.

Our approach is free from these drawbacks, and to our knowledge, it is the first study using Mahalanobis distance to evaluate brain maturation. Mahalanobis, rather than Euclidean distance, was chosen because MRI parameters are correlated and cannot be viewed as completely independent variables. Moreover, their covariation matrices and thus, the eigensystems are different across bundles. In our study, Mahalanobis distance was calculated using four parameters: quantitative relaxation times (qT1, qT2), transverse ($\lambda_\perp$) and longitudinal ($\lambda_\parallel$) diffusivities. Fractional anisotropy (FA) and mean diffusivity (<D>) were not considered because they can be viewed as functions of $\lambda_\perp$ and $\lambda_\parallel$, and including them may result in a degenerate covariation matrix.

As for the approach validation, it outperformed univariate approaches in bundle discrimination at different maturational stages, and its discrimination capacity was extremely high. Our approach suggested a more reliable ordering of the bundles according to their relative maturation and showed smaller prediction errors of the maturational age.

Mapping the asynchrony of the white matter maturation

Although this study presents a preliminary investigation based on a small number of subjects, the proposed multi-parametric approach enabled precise and reliable demonstration of the asynchrony in the bundles maturation in the infant brain. The suggested maturational order was in good agreement with *post-mortem* studies (Yakovlev and Lecours 1967; Flechsig 1920), confirming maturation of the sensory and motor pathways before association bundles. The spino-thalamic tract was the most advanced in maturation, followed by the optic radiations, the middle portion of the cortico-spinal tract and the fornix. Most projection bundles (except the anterior limb of the internal capsule) thus appeared more mature than limbic, commissural and association bundles. As for limbic and commissural bundles, the fornix was more mature than the cingulum, and the splenium and genu of the corpus callosum were more mature than the body. The bundles with most delayed maturation included the arcuate and superior longitudinal fasciculi, the anterior limb of the internal capsule and the external capsule.

With this approach, the middle portion of the cortico-spinal tract was more advanced in maturation relatively to its inferior and superior parts, in agreement with previous in vivo imaging studies showing that central regions mature before peripheral regions (Prastawa et al. 2010; Gao et al. 2009). Nevertheless, earlier maturation of the middle portion in comparison with the inferior portion may seem to contradict the known rule of the caudo-cephalic direction of the myelin progression (Yakovlev and Lecours 1967; Flechsig 1920). However, one should keep in mind that the actual myelination sequence is very complex, being also governed by several other rules and showing multiple exceptions (van der Knaap et al. 1995; Kinney et al. 1988; Flechsig 1920). Here our observations in the cortico-spinal tract may have several explanations. First, this tract includes both sensory (thalamo-cortical) and motor (cortico-spinal) fibers, which are not supposed to myelinate with the same sequence and topography since most tracts become myelinated in the direction of the impulse conduction (van der Knaap et al. 1995). Furthermore, it may simply reflect the fact that the posterior limb of the internal capsule, which here corresponds to the

delimitation between the inferior and middle portions, already shows the presence of myelin at term and undergoes very rapid myelination (Kinney et al. 1988; Flechsig 1920), being one of the first to get the "myelinated" appearance on T1- and T2-weighted images in term newborns (Paus et al. 2001; Rutherford 2002), probably due to a high compactness of the fibers. Second, as remarked by Kinney et al. (1988), early myelination onset does not predict early myelin maturation. For example, optic radiations, unlike cortico-spinal tract, do not show evidence of myelin at term, but nevertheless get faster to the mature stage (Kinney et al. 1988). As myelination of the cortico-spinal tract is not restricted to the considered short developmental period (3–21 weeks) but continues up to 142 weeks (Kinney et al. 1988), it could have happened that the most dynamic changes during this period were in the middle portion, making our approach classify it as relatively more advanced. Similarly, although corpus callosum starts to myelinate after the cortico-spinal tract, it gets to the mature stage much faster than the superior portion of the cortico-spinal tract in the corona radiata (Kinney et al. 1988). As myelination of both of these bundles is not restricted to the first post-natal months, it is possible that during this period these bundles were at the same maturational stage, and thus grouped together.

Next, we should also highlight that the Mahalanobis distance is not directly linked to the myelin content but rather reflects the whole ensemble of various maturational processes underlying age-related changes in the MRI/DTI parameters used for its calculation (qT1, qT2, $\lambda_{\parallel}$ and $\lambda_{\perp}$). Besides, it might also be possible that co-registration of the different imaging modalities (qT1, qT2, DTI) in the lower parts of the brain was not as perfect as in the central regions (because geometric distortions related to EPI sequences are more prominent in the brainstem) and the relative maturational degree was slightly underestimated in the inferior portion of the cortico-spinal tract.

On the other hand, the bundles that were grouped together should not be considered as bundles with identical maturation, but rather as bundles for which maturational relationships could not be revealed using the proposed approach and the available data. Indeed, the middle portion of the cortico-spinal tract and the fornix were grouped together, whereas the fornix matures somewhat later than this projection tract (Yakovlev and Lecours 1967). Such unrevealed relationships may stem from a high inter-subject variability relatively to the age-related changes: for example, for the fornix, only Mahalanobis distance and qT1 showed significant age-related changes, nevertheless leading to high prediction errors in the leave-one-out validation after regressing out the age-related effects. Increasing the number of subjects may possibly help to further improve the discrimination capacity of our approach, as discussed below. Nevertheless, one should notice that none of such unrevealed relationships between the bundles could be discriminated by any of the univariate approaches. Another explanation could be that neither Mahalanobis distance nor individual MRI parameters directly reflect brain myelination, being influenced by all kinds of undergoing maturational processes that overlap in time (Dubois et al. 2014a). Thus, in future studies it will be of interest to compare our model to a novel MRI parameter, named myelin water fraction (MWF) (Deoni et al. 2012), which is supposed to be more directly linked to the myelin content (see discussion below) and may help to discriminate the unrevealed relationships between the bundles (Kulikova et al. 2014).

With all these considerations in mind, one should remember that there is still no gold standard for the in vivo evaluation of the white matter maturation and thus, direct comparison of our results and other studies should be made with caution. *Post-mortem* studies (Yakovlev and Lecours 1967; Flechsig 1920) provide region-specific but not bundle-specific information and thus, may mix up information about various bundles that pass at the same location. As for in vivo studies, there were only a few attempts to give a precise definition of a bundle maturational stage using multi-parametric MRI data. The model of Dubois et al. (2008) was based on the estimation of the global bundle maturation by progression through four stages, which took into account both the maturation state and speed of each bundle, calculated from DTI indices (mean diffusivity and fractional anisotropy), in comparison with the average over all bundles and according to age. This model suggested that the cortico-spinal tract appeared the most mature, followed by the spino-thalamic tract and the fornix, then the optic radiations, the arcuate and inferior longitudinal fasciculi, and the least mature were the anterior limb of the internal capsule and the cingulum. However, the model was not supported in three bundles (corpus callosum, external capsule, and uncinate fasciculus) and did not give quantitative assessment of the relative maturational delays between the bundles.

Prastawa et al. (2010) calculated an absolute maturational measure from the total growth rate for a set of multimodal observations (longitudinal and transverse diffusivities, proton density and intensity of T1- and T2-weighted images). The relative maturational measure was calculated as the time shift required to transform a maturational curve for a given bundle to a reference curve computed from the posterior limb of the internal capsule (because of its known early myelination). This model confirmed the known temporal order of the white matter maturation: (1) brain regions related to basic functions such as sensory and motor information processing are the most advanced in the maturation; (2) central regions of the white

matter tracts mature before peripheral sub-cortical regions. However, this study did not report any quantitative results on the relative maturational delays between white matter regions, and it was focused on different regions rather than on different bundles.

Vardhan et al. (2012) proposed using the Hellinger distance to measure age-related changes in the intensities of T1- and T2-weighted images. This strategy also demonstrated that maturation begins in posterior regions and that frontal regions mature later on. The authors further confirmed that T1 and T2 modalities are likely to reflect different maturational properties, as revealed by a time lag in the changes of T2-weighted contrast compared with T1-weigthed images. However, this study was again region- and not bundle-specific, and used weighted rather than quantitative images.

Other studies on white matter maturation used predominantly univariate approaches, trying to classify the bundles based on changes in a single modality: for example, fractional anisotropy (Imperati et al. 2011), quantitative qT1 (Steen et al. 1997) or qT2 (Engelbrecht et al. 1998) relaxation times, etc. Although these studies were able to capture the general pattern of white matter maturation, the exact placement of bundles in the maturational order may be biased because none of the MRI parameters alone can explain the whole ensemble of processes underlying maturation.

Fitting the data with our model further suggested that different white matter bundles follow a similar maturational trajectory but with different developmental onsets. This finding, being in agreement with (Prastawa et al. 2010), allowed us deriving a "general" maturational equation: similarly to univariate studies during childhood over a larger age range (Watanabe et al. 2013; Engelbrecht et al. 1998; van Buchem et al. 2001; Lebel et al. 2012), changes in the Mahalanobis distance with age in infants could be described by an exponential decay. This modeling allowed us to compute the relative maturational delays between the bundles, confirming that the most dramatic changes in the white matter occur during the first post-natal year, with a total relative maturational delay of 49 weeks between the most and the least mature bundles. That is why we tested our model on an older infant, with fair predictions for almost all bundles. The model tended to be less accurate for bundles with advanced maturation in which inter-subject variability was likely to become comparable with age-related changes. Nevertheless, further studies with larger sample sizes may enable to clarify this issue.

Technical considerations

When studying normal brain development, researchers always face the problem of data acquisition in healthy unsedated infants and children. To avoid devastating motion artifacts, data are usually acquired during natural sleep, trying to keep the acquisition sequences as short as possible. In our study we used EPI single-shot spin-echo sequences, which allowed us to acquire the whole multimodal dataset in less than 15 min. Although using these sequences may be complicated by image distortions, distortions for qT1, qT2 and DTI images were relatively coherent and did not pose problems for co-registration, except maybe in the brainstem as discussed above. Because the parameters were quantified over the bundles, our analysis was less affected than voxel-by-voxel analyses, and distortions were most prominent in the frontal regions, which lay apart from the majority of the bundles analyzed in our study.

Comparison of the parameters averaged over different bundles allowed us to capture the general picture of the maturational asynchrony. Although voxel-by-voxel analysis may potentially reveal more details on local maturational changes, it would require exact correspondence between cerebral structures among individuals and thus, precise co-registration between infant and adult images, which remains hardly achievable because babies' and adults' brains are not homothetic due to asynchronous growth of cerebral regions. Furthermore, as maturation is not homogeneous along axons and bundles (McArdle et al. 1987; McCart and Henry 1994), it would be interesting in future studies to split all bundles into several parts (as it was done here for the cortico-spinal tract, the cingulum and the corpus callosum) and to analyze them separately. In the same way, analyzing separately the left and right bundles would highlight inter-hemispherical asymmetries that may exist in bundles such as the arcuate fasciculus (Dubois et al. 2008; Lebel and Beaulieu 2009).

In our study the bundles were reconstructed using manually delineated regions of selection and exclusion. To avoid inter-subject variability, these regions were delineated according to predefined rules (Catani et al. 2002; Dubois et al. 2006). Although in adult subjects white matter bundles can be extracted using multiple automatically placed regions-of-interest (Suarez et al. 2012) or predefined bundle atlases and clustering techniques (Guevara et al. 2010), such approaches may fail to reliably extract the bundles in infant datasets. To our knowledge, so far there are no approaches designed specifically for the age ranges considered in our study. Thus, to be coherent in terms of bundles identification between infant and adult subjects, bundles were reconstructed in the same way in both groups.

The number of infants ($N = 17$) included in this work may seem relatively low to derive definite conclusions about white matter maturation, particularly for the white matter bundles showing higher prediction errors in the

leave-one-out validation (e.g. spino-thalamic tract, fornix), i.e. the bundles in which inter-subject variability in the MRI/DTI parameters or in the Mahalanobis distance was relatively high as compared to the age-related changes over the considered age period. Nevertheless, as most of the bundles indeed showed dramatic changes of both the Mahalanobis distance and the MRI/DTI parameters over this short developmental period (3–21 weeks), we were able to reveal a general scheme of the maturational asynchrony across the bundles, even in a cross-sectional analysis. However, the main goal of the present study was not to make definite conclusions about the exact bundle maturational order, but rather to introduce and explore the Mahalanobis distance approach and to demonstrate its advantages over conventional univariate approaches. Indeed, even in a small size group, Mahalanobis distance approach showed better performance than conventional approaches in bundle discrimination and suggested a more reliable bundle ordering with smaller prediction errors of the maturational age. Although the maturational order may be considered here as preliminary, requiring further validation in studies with larger sample sizes, notably to distinguish the bundles that were grouped together (see above), the obtained results suggest that our approach may be a promising candidate for the evaluation of pathological development or neuro-degeneration of the white matter when it is not possible to acquire large datasets. Similarly, interpolation of our model to older ages should be made with caution, since it was only tested in a single 34-week-old infant for demonstration purposes. Testing whether the exponential model and the Mahalanobis approach are indeed valid at older ages would require recruiting many healthy infants and toddlers during the second semester of the first post-natal year and the first semester of the second year (when, according to our model, the Mahalanobis distances in all bundles should decrease below the 10 % of their initial values). This is hardly achievable because it is exceptional to have healthy infants and toddlers spontaneously asleep (without sedation) during scanning at those ages.

The precision of our approach also depends on the size of the adult group, used to calculate covariation matrices of the MRI/DTI parameters. The exact relationship between the calculation errors of the Mahalanobis distance and the group size was described by Young (1978), and a number of strategies were introduced to compensate the bias in small samples (Iwamura et al. 2002; Jorgensen and Rothrock 2010; Omachi et al. 2000; Takeshita et al. 1993). In our study we applied the correction strategy suggested by Takeshita et al.(1993), and our computer simulations suggested that Mahalanobis distances were calculated with an acceptable precision that enabled to discriminate the maturational trajectories of different bundles.

Finally, another way to further improve the Mahalanobis approach may be to include other MRI-derived metrics, like myelin water fraction (MWF) (Deoni et al. 2012), magnetization transfer ratio (MTR)(van Buchem et al. 2001) or macromolecular tissue volume (MTV) (Mezer et al. 2013), that may yield additional information on maturational processes. MWF relies on the multi-compartment modeling of T1 and T2 relaxation signals and is thought to better correlate with the degree of bundle myelination than other MRI parameters. However, MWF calculation has still no gold standards and requires long acquisition and post-processing times (Deoni et al. 2013). MTR is another parameter sensitive to the myelin content, based on the exchange of magnetization between free protons and protons bounded to macromolecules, such as the cholesterol component of myelin, cerebrosides and phospholipids (Koenig 1991; Kucharczyk et al. 1994). Although MTR can be used to measure myelin content, it is also sensitive to multiple other factors (Nossin-Manor et al. 2013). Finally, MTV is a recent MRI parameter proposed by Mezer et al. (2013), which quantifies the non-water volume. Combining MTV with qT1 mapping may potentially provide new information about variations in local physico-chemical environments, while combining it with DTI imaging may help to distinguish between variations in tissue orientation and tissue density. Including these parameters into analysis will change the covariation matrices and likely result in different values of Mahalanobis distances, potentially increasing the discrimination capacity of the approach; however, we can expect the bundle maturational order to be preserved and the maturational model to remain exponential.

Conclusion

Using Mahalanobis distance, computed from relaxation times and DTI diffusivities, has been shown relevant for in vivo evaluation of the white matter maturation in infants. It confirmed the known spatio-temporal sequence of the white matter maturation, showing the spino-thalamic tract, the optic radiations, the cortico-spinal tract and the fornix to be among the most fast maturating bundles, while the superior longitudinal and arcuate fasciculi, the anterior limb of the internal capsule and the external capsule had the most delayed maturation. Of importance, Mahalanobis distance could reveal more details on the maturational differences between the bundles and enabled more precise predictions of the maturational ages than conventional univariate approaches. Additionally, our approach suggested a maturational model that enabled calculating the relative maturational delays between the bundles and confirmed that the most dramatic maturational changes

should occur during the first post-natal year. As the proposed approach is based on a short acquisition protocol and showed good performance even in a small-size group, it may be easily adapted to clinical studies when it is not possible to acquire large datasets (e.g. in rare diseases such as leukodystrophies) or when the patients cannot withstand long acquisitions (e.g. psychiatric patients).

Acknowledgements This work was supported by the Fyssen Foundation, the ELA Foundation, the "Fondation de France", the "Ecole des Neurosciences de Paris", and the French National Agency for Research (ANR). The finalization of this work received support from the European Union Seventh Framework Program (FP7/2007-2013, Grant agreement no 604102). We greatly appreciate the help of Mr. Brendan Adams, who kindly accepted to review the text of the manuscript.

References

Barkovich AJ, Kjos BO, Jackson DE Jr, Norman D (1988) Normal maturation of the neonatal and infant brain: MR imaging at 1.5 T. Radiology 166:173–180

Brody BA, Kinney HC, Kloman AS, Gilles FH (1987) Sequence of central nervous system myelination in human infancy. I An autopsy study of myelination. J Neuropathol Exp Neurol 46:283–301

Catani M, Howard RJ, Pajevic S, Jones DK (2002) Virtual in vivo interactive dissection of white matter fasciculi in the human brain. Neuroimage 17:77–94

Deoni SC, Peters TM, Rutt BK (2005) High-resolution T1 and T2 mapping of the brain in a clinically acceptable time with DESPOT1 and DESPOT2. Magn Reson Med 53:237–241

Deoni SC, Dean DC 3rd, O'Muircheartaigh J, Dirks H, Jerskey BA (2012) Investigating white matter development in infancy and early childhood using myelin water faction and relaxation time mapping. Neuroimage 63:1038–1053

Deoni SC, Matthews L, Kolind SH (2013) One component? Two components? Three? The effect of including a nonexchanging "free" water component in multicomponent driven equilibrium single pulse observation of T1 and T2. Magn Reson Med 70:147–154

Dubois J, Hertz-Pannier L, Dehaene-Lambertz G, Cointepas Y, Le Bihan D (2006) Assessment of the early organization and maturation of infants' cerebral white matter fiber bundles: a feasibility study using quantitative diffusion tensor imaging and tractography. Neuroimage 30:1121–1132

Dubois J, Dehaene-Lambertz G, Perrin M, Mangin J-F, Cointepas Y, Duchesnay E, Le Bihan D, Hertz-Pannier L (2008) Asynchrony of the early maturation of white matter bundles in healthy infants: quantitative landmarks revealed noninvasively by diffusion tensor imaging. Hum Brain Mapp 29:14–27

Dubois J, Dehaene-Lambertz G, Kulikova S, Poupon C, Huppi P, Hertz-Pannier L (2014a) The early development of brain white matter: a review of imaging studies in fetuses, newborns and infants. Neuroscience. doi:10.1016/j.neuroscience.2013.12.044

Dubois J, Kulikova S, Hertz-Pannier L, Mangin J-F, Dehaene-Lambertz G, Poupon C (2014b) Correction strategy for diffusion-weighted images corrupted with motion: application to the DTI evaluation of infants' white matter. Magn Reson Imaging. doi:10.1016/j.mri.2014.05.007

Duclap D, Schmitt A, Lebois B, Riff O, Guevara P, Marrakchi-Kacem L, Brion V, Poupon F, Poupon C (2012) Connectomist-2.0: a novel diffusion analysis toolbox for BrainVISA MAGMA. Springer, Lisbon

Engelbrecht V, Rassek M, Preiss S, Wald C, Mödder U (1998) Age-dependent changes in magnetization transfer contrast of white matter in the pediatric brain. AJNR 19:1923–1929

Flechsig P (1920) Anatomie des menschlichen Gehirns und Rückenmarks auf myelogenetischer Grundlage. G. Thieme, Leipzig

Gao W, Lin W, Chen Y, Gerig G, Smith JK, Jewells V, Gilmore JH (2009) Temporal and spatial development of axonal maturation and myelination of white matter in the developing brain. AJNR 30:290–296

Guevara P, Poupon C, Rivière D, Cointepas Y, Marrakchi L, Descoteaux M, Fillard P, Thirion B, Mangin J-F (2010) Inference of a HARDI fiber bundle atlas using a two-level clustering strategy. Med Image Comput Comput Assist Interv 13:550–557

Huang H, Zhang J, van Zijl PCM, Mori S (2004) Analysis of noise effects on DTI-based tractography using the brute-force and multi-ROI approach. Magn Reson Med 52:559–565

Hüppi PS, Maier SE, Peled S, Zientara GP, Barnes PD, Jolesz FA, Volpe JJ (1998) Microstructural development of human newborn cerebral white matter assessed in vivo by diffusion tensor magnetic resonance imaging. Pediatr Res 44:584–590

Imperati D, Colcombe S, Kelly C, Di Martino A, Zhou J, Castellanos FX, Milham MP (2011) Differential development of human brain white matter tracts. PLoS One 6:e23437. doi:10.1371/journal.pone.0023437

Iwamura M, Omachi S, Aso H (2002) A method to estimate the true Mahalanobis distance from eigenvectors of sample covariance matrix. In: Caelli T, Amin A, Duin RPW, de Ridder D, Kamel M (eds) Structural, syntactic, and statistical pattern recognition. Springer, Berlin, pp 498–507

Jorgensen T, Rothrock R (2010) Correcting for Bias in Mahalanobis and log-likelihood estimates. IEEE Trans Aerosp Electron Syst 46:2078–2089

Kinney HC, Brody BA, Kloman AS, Gilles FH (1988) Sequence of central nervous system myelination in human infancy. II Patterns of myelination in autopsied infants. J Neuropathol Exp Neurol 47:217–234

Koenig SH (1991) Cholesterol of myelin is the determinant of gray-white contrast in MRI of brain. Magn Reson Med 20:285–291

Kucharczyk W, Macdonald PM, Stanisz GJ, Henkelman RM (1994) Relaxivity and magnetization transfer of white matter lipids at MR imaging: importance of cerebrosides and pH. Radiology 192:521–529

Kulikova S, Hertz-Pannier L, Deahene-Lambertz G, Poupon C, Dubois J (2014) What new do we learn with Myelin water fraction in infant white matter bundles in comparison with other MRI parameters? In: Proceedings 23rd Annual ISMRM Meeting

le Bihan D, Johansen-Berg H (2012) Diffusion MRI at 25: exploring brain tissue structure and function. Neuroimage 61:324–341

Lebel C, Beaulieu C (2009) Lateralization of the arcuate fasciculus from childhood to adulthood and its relation to cognitive abilities in children. Hum Brain Mapp 30:3563–3573

Lebel C, Gee M, Camicioli R, Wieler M, Martin W, Beaulieu C (2012) Diffusion tensor imaging of white matter tract evolution over the lifespan. Neuroimage 60:340–352

Mahalanobis P (1936) On the generalised distance in statistics. In: Proceedings National Institute of Science, India, Vol 2, No 1

McArdle CB, Richardson CJ, Nicholas DA, Mirfakhraee M, Hayden CK, Amparo EG (1987) Developmental features of the neonatal brain: MR imaging. Part I gray-white matter differentiation and myelination. Radiology 162:223–229

McCart RJ, Henry GH (1994) Visual corticogeniculate projections in the cat. Brain Res 653:351–356

Mezer A, Yeatman JD, Stikov N, Kay KN, Cho N-J, Dougherty RF, Perry ML, Parvizi J, Hua LH, Butts-Pauly K, Wandell BA (2013) Quantifying the local tissue volume and composition in individual brains with magnetic resonance imaging. Nat Med 19:1667–1672

Mori S, van Zijl PCM (2002) Fiber tracking: principles and strategies-a technical review. NMR Biomed 15:468–480

Nossin-Manor R, Card D, Morris D, Noormohamed S, Shroff MM, Whyte HE, Taylor MJ, Sled JG (2013) Quantitative MRI in the very preterm brain: assessing tissue organization and myelination using magnetization transfer, diffusion tensor and T_1 imaging. Neuroimage 64:505–516

Omachi S, Sun F, Aso H (2000) A new approximation method of the quadratic discriminant function. In: Ferri FJ, Iñesta JM, Amin A, Pudil P (eds) Advances in pattern reco gnition. Springer, Berlin, pp 601–610

Paus T, Zijdenbos A, Worsley K, Collins D, Blumenthal J, Giedd J, Rapoport J, Evans A (1999) Structural maturation of neural pathways in children and adolescents: in vivo study. Science 283:1908–1911

Paus T, Collins DL, Evans AC, Leonard G, Pike B, Zijdenbos A (2001) Maturation of white matter in the human brain: a review of magnetic resonance studies. Brain Res Bull 54:255–266

Perrin M, Poupon C, Cointepas Y, Rieul B, Golestani N, Pallier C, Rivière D, Constantinesco A, le Bihan D, Mangin JF (2005) Fiber tracking in q-ball fields using regularized particle trajectories. Inf Process Med Imaging 19:52–63

Poupon C, Dubois J, Marrakchi L, Brion V, Mangin J-F, Poupon F (2010) Real-time EPI T1, T2 and T2* mapping at 3T. In: Proceedings 18th Annual ISMRM Meeting

Prastawa M, Sadeghi N, Gilmore JH, Lin W, Gerig G (2010) A new framework for analyzing white matter maturation in early brain development. In: Proceedings IEEE Int Symp Biomed Imaging, 97–100

Rutherford MA (2002) MRI of the Neonatal Brain. W. B Saunders, Philadelphia. ISBN 9780702025341

Sadeghi N, Prastawa M, Fletcher PT, Vachet C, Wang B, Gilmore J, Gerig G (2013) Multivariate modeling of longitudinal MRI in early brain development with confidence measures. In: Proceedings IEEE Int Symp Biomed Imaging, 1400–1403

Steen RG, Ogg RJ, Reddick WE, Kingsley PB (1997) Age-related changes in the pediatric brain: quantitative MR evidence of maturational changes during adolescence. AJNR 18:819–828

Suarez RO, Commowick O, Prabhu SP, Warfield SK (2012) Automated delineation of white matter fiber tracts with a multiple region-of-interest approach. Neuroimage 59:3690–3700

Takeshita T, Nozawa S, Kimura F (1993) On the bias of Mahalanobis distance due to limited sample size effect. In: Proceedings of the second international conference on document analysis and recognition, 171–174

van Buchem MA, Steens SC, Vrooman HA, Zwinderman AH, McGowan JC, Rassek M, Engelbrecht V (2001) Global estimation of myelination in the developing brain on the basis of magnetization transfer imaging: a preliminary study. AJNR 22:762–766

van der Knaap, Marjo S, Jacob Valk (1995) Myelin and white matter. Magnetic resonance of myelin, myelination, and myelin disorders. Springer, Berlin, pp 1–17

Vardhan A, Prastawa M, Gouttard S, Piven J, Gerig G (2012) Quantifying regional growth patterns through longitudinal analysis of distances between multimodal MR intensity distributions. In: Proceedings IEEE Int Symp Biomed Imaging, 1156–1159

Watanabe M, Liao JH, Jara H, Sakai O (2013) Multispectral quantitative MR imaging of the human brain: lifetime age-related effects. Radiographics 33:1305–1319

Yakovlev P, Lecours A (1967) The myelogenetic cycles of regional maturation of the brain. In: Minkowsky A (ed) Regional Development of the Brain in Early Life. Blackwell Scientific Publications, New Jersey, pp 3–70

Young I (1978) Further consideration of sample and feature size. IEEE Trans Inf Theory 24:773–775

Zhang J, Evans A, Hermoye L, Lee S-K, Wakana S, Zhang W, Donohue P, Miller MI, Huang H, Wang X, van Zijl PCM, Mori S (2007) Evidence of slow maturation of the superior longitudinal fasciculus in early childhood by diffusion tensor imaging. Neuroimage 38:239–247

Chapter 5

Quantitative assessment of the brain myelin content using Myelin Water Fraction

As mentioned in Part I, Myelin Water Fraction (MWF) is believed to be particularly relevant for quantitative *in vivo* evaluation of brain myelination [134, 233, 321]. By definition, it provides a more direct measure of brain myelin content than other MRI parameters and it has shown good correlation with the myelin amount revealed by histology [226]. However, existing MWF quantification strategies are rather difficult to implement both in research studies of normal development in infants and toddlers and in clinical practice due to very long acquisition and/or post-processing times.

In this chapter, a new MWF quantification approach overcoming these limitations is presented. This approach is based on a 3-compartment model of T1 and T2 relaxation signals adapted from [233]. The model takes into account 3 tissue compartments: myelin-related water, intra/extra-cellular water, and CSF. Each of these compartments has its own relaxation characteristics and the model explains the signals measured in different voxels by different relative proportions, i.e. fractions, of the compartments and thus, by their different contributions to the total measured relaxation signals. This model was chosen because it has been previously demonstrated to be applicable to a wide range of conditions, including developing white matter [134, 233, 321] and certain pathologies [322–326].

The proposed approach takes advantage of 1) pre-calibrated compartment $T1_c$ and $T2_c$ relaxation characteristics and 2) of a simplified linear model fitted with data acquired using a short acquisition protocol based on single-shot simple and inversion-recovery spin-echo EPI (SE-EPI and IR-SE-EPI) sequences adequate for the pediatric population. Below we will detail the main points of the proposed approach and its full description can be found in the article submitted to *Human Brain Mapping* (technical note), which is attached at the end of the chapter.

5.1 Modeling T1 and T2 relaxation signals

First, it worths explaining why unlike many other studies calculating MWF from multicomponent analysis of T2 relaxation alone [222–226, 229], it was necessary to consider in our experimental conditions both T1 and T2 relaxations signals.

In many conventional approaches, MWF quantification relies on calculation of the T2-spectrum and define MWF in each voxel as the ratio between the signal with T2 below 40-50ms and the total water signal in the T2 distribution (see also chapter 2). However, reliable spectrum estimation requires long acquisition protocols with a large number of time-points (N>32). Furthermore, as myelin-related compartment has rather fast relaxation characteristics (e.g. its T2 relaxation constant is ∼20ms), robust estimation of its fraction makes it necessary to start TE sampling with small values.

In this work, the acquisition protocol was based on single-shot SE-EPI and IR-SE-EPI sequences in order to keep the acquisition time as short as possible. However, with these sequences it was not possible to achieve TEs shorter than 33ms (mainly due to a long readout of the partial Fourier k-space [327]). Comparison of the theoretical T1/T2 relaxation signals from different compartments at the TIs/TEs used in the acquisition protocol (Fig. 5.1) suggests that even at the shortest TEs, T2 relaxation signal from myelin-related water is already strongly degraded, much more than T2 relaxation signals from the two other compartments. Thus, it is hardly possible to estimate MWF values based on T2 relaxation signals alone with SE-EPI sequences. However, information from T2 relaxation signals is useful to separate contributions of intra-/extracellular water and “free” water compartments. On the contrary, T1 relaxation signals allow revealing the contribution of the myelin-water compartment vs. the two other compartments, suggesting that in our experimental conditions it is necessary to consider information from both T1 and T2 relaxation signals.

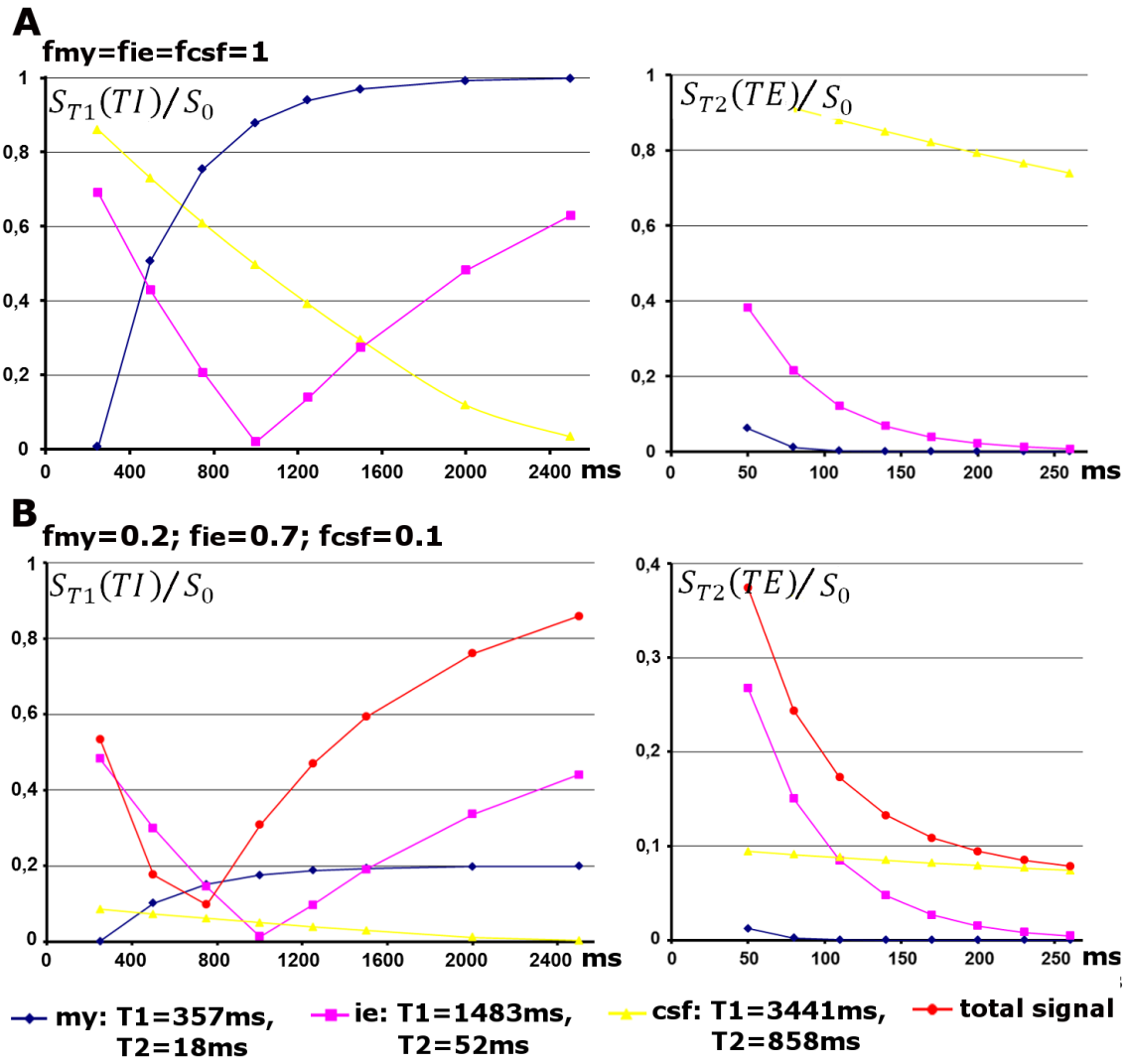

Figure 5.1: Comparison of theoretical values of normalized T1 and T2 relaxation signals ($S_{T1}(TI)/S_0$ and $S_{T2}(TE)/S_0$) computed for myelin-water (my), intra-/extracellular water (ie) and CSF (csf) compartements at different TIs/TEs used in the study. In A, normalized relaxation signals are shown in equal proportions (all fractions are equal to 1); in B, compartments fractions were taken according to their expected values within white matter and red lines show total relaxation signals measured at the voxel level. For this computation, compartments' relaxation characteristics were taken as identified in the calibration stage.

5.2 Calibration strategy

Calibration of the compartment $T1_c$ and $T2_c$ relaxation characteristics was performed on adult data (N=3, mean age: 23.2±2 years), acquired with a large number (N=30-60) of inversion times (TI) for T1 relaxometry and echo times (TE) for T2 relaxometry, using an original combination of a region contraction approach [322, 328] and a non-negative least-square (NNLS) algorithm. This calibration was performed to identify the $T1_c$ and $T2_c$ relaxation characteristics that provide the best fit of the 3-compartment relaxation model. To validate the calibration stage, we additionally verified that:

1. there was no particular spatial dependence for the compartments' relaxation characteristics $T1_c$ and $T2_c$ (Fig.3 on page 154);

2. we looked whether there was a possible effect of the choice of the MWF search interval on resulting $T1_c$ and $T2_c$ relaxation characteristics and on the generated MWF maps (Sup Fig.2 on page 173);

3. each of the calibration subjects had enough data points to perform stable calibration (Sup Fig.3 on page 174);

4. calibration could be performed in a reliable manner even in the presence of noise (tested in simulated data for various noise levels)(Fig.4 on page 156);

It should be noted that this calibration stage should be performed once for any given acquisition protocol (magnetic field, acquisition sequences, spatial resolution, etc.) and that the calibration results from this work may not be optimal for studies with other acquisition settings. However, there were no evident changes in MWF maps when spatial resolution in one of the calibration subjects was decreased from $1.8\times1.8\times1.8\text{mm}^3$ to $2\times2\times2\text{mm}^3$.

5.3 Application to testing datasets

After $T1_c$ and $T2_c$ values were identified in the calibration stage, we fixed these values and reduced the number of data points in the calibration dataset (similar to the infant data acquired with a short acquisition protocol) to test that under such conditions it was still possible to get reliable estimation of the MWF maps.

Then $T1_c$ and $T2_c$ values were fixed in a simplified linear relaxation model with 3 unknown compartments fractions to calculate MWF maps with NNLS algorithm in the testing datasets of infants (N=18, 3-34 weeks old) and adults (N=13, mean age: 22.4±1.6 years). The resulting MWF values were evaluated in 18 different

white matter bundles, and infant values were compared to the corresponding adult reference MWF values to access the bundle myelination relative to the mature stage.

The results showed that our strategy allows robust estimation of the compartments relaxation characteristics and enables fast MWF mapping in infants (acquisition <6 min, post-processing <5min)(Fig.5 on page 158).

5.4 Evaluation of white matter myelination in infants

The calculated infant MWF maps demonstrated asynchronous age-related increases in the MWF values across bundles, confirming the caudo-rostral progression of myelination (Fig. 5.2 and 5.3).

Although comparison of our results with other studies is complicated by the fact that MWF quantification is sensitive to acquisition and post-processing settings, the generated MWF maps showed good correlations with available MWF maps from another group [321]. Furthermore, comparing infant MWF values from different white matter bundles across the age range allowed more accurate description of the white matter myelination than approaches based on univariate MRI/DTI parameters (Tab. 5.1).

	n	violations
MWF	129	no
M	142	no
qT1	90	yes
qT2	89	yes
FA	74	yes
$\langle D \rangle$	72	yes
$\lambda_{\parallel}$	76	no
$\lambda_{\perp}$	70	yes

Table 5.1: Comparison of the bundle orderings based on normalized MWF values and on other MRI/DTI parameters. The ordering based on MWF values provided a more detailed description of the white matter maturation (higher number n of revealed differences between the bundles) and was more accurate with the reference to 5 *a priori* taken relationships: early maturation of spino-thalamic and corticospinal tracts and optic radiations; delayed maturation of anterior limb of the internal capsule and arcuate fasciculus.

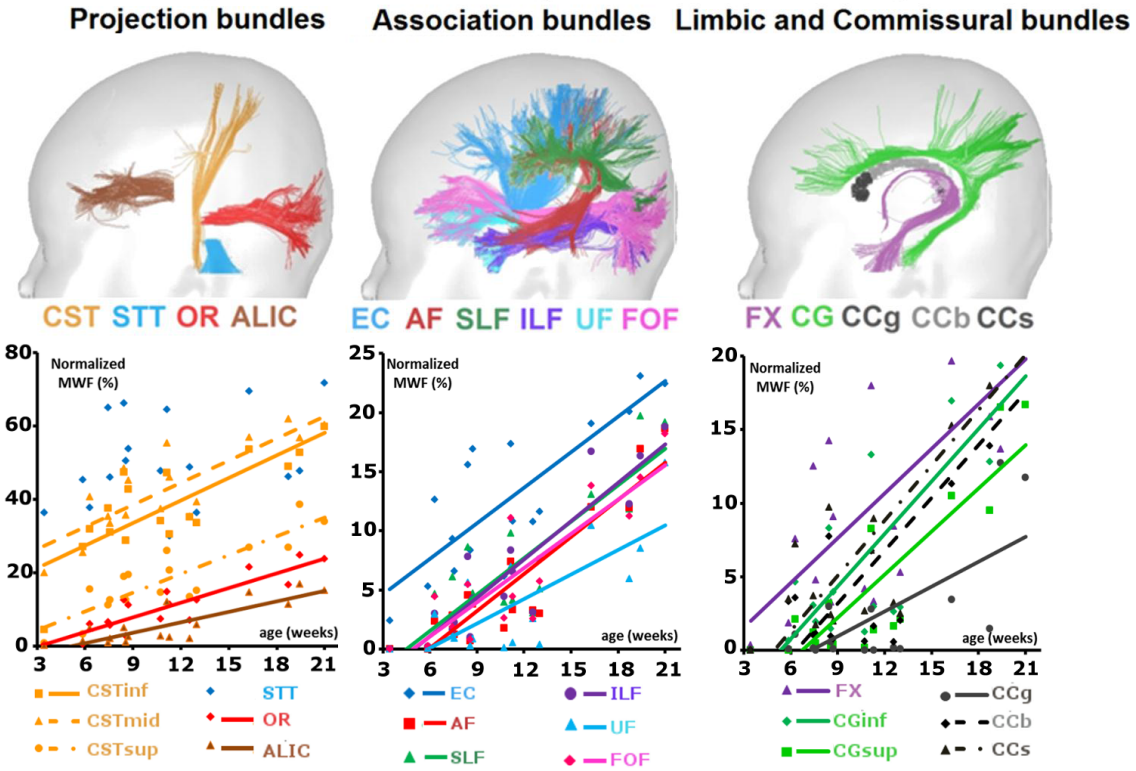

Figure 5.2: Age-related changes of the normalized infants MWF values (% of the mean adult values) for different white matter bundles. Lines show linear regressions (R^2>0.58, p<0.015). Abbreviations: cortico-spinal tract CST (inf – inferior, mid – middle, sup - superior portions), spino-thalamic tract STT, optic radiations OR, anterior limb of the internal capsule ALIC, external capsule EC, arcuate fasciculus AF, superior SLF and inferior ILF longitudinal fascicles, uncinate fasciculus UF, fronto-occipital fasciculus FOF, fornix FX, inferior CGinf and superior CGsup parts of the cingulum, genu CCg, body CCb and splenium CCs of the corpus callosum.

5.5 Comparison with Mahalanobis distance

Compared to Mahalanobis distance approach, MWF-based approach revealed less differences between bundles (129 vs. 142, Tab. 5.1). However, this was not surprising, since MWF is based on only two parameters (qT1 and qT2) and MWF changes across the age range should reflect only myelination, meanwhile Mahalanobis distance is influenced by all possible maturational processes reflected by 4 MRI parameters (qT1, qT2, $\lambda_{\parallel}$ and $\lambda_{\perp}$). This may also explain why the bundles orderings based on these two approaches were not identical (Fig. 5.3).

When comparing the bundle orderings based on MWF and on Mahalanobis distance, one can notice that the most mature bundles (spino-thalamic tract and 3 subdivision of the cortico-spinal tract) were similarly ordered by both approaches (Fig. 5.3). This observation may suggest that for these bundles at this age range

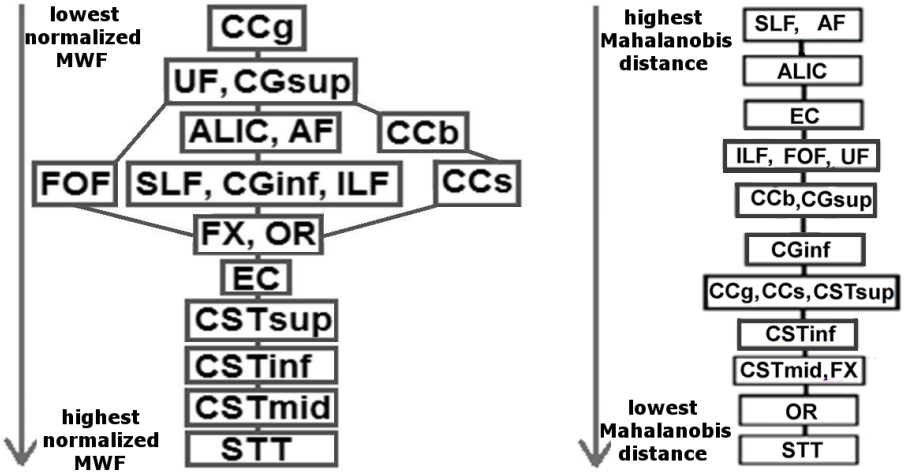

Figure 5.3: Orderings of the infant bundles based on paire-wise comparison of the normalized MWF values (on the left) and based on Mahalanobis distance (on the right, adapted from [315]). For abbreviations see Figure. 5.2.

myelination was the dominant maturational process. On the contrary, less mature bundles that were differently ordered in these approaches, may also be affected by other maturational processes (proliferation of oligodendrocytes, increase of bundle compactness, etc.) that do not have the same dynamics as myelination and that were captured by Mahalanobis distance, which provides a global maturational measure, but not by MWF. In future studies, it may be interesting to further investigate the relationship between Mahalanobis distance and MWF by applying a hybrid approach in which qT1 and qT2 are substituted by MWF for further calculation of the Mahalanobis distance. Alternatively, Mahalanobis distance may be calculated based only on qT1 and qT2 and compared to MWF. These approaches might help to better understand the contribution of bundles myelination, revealed by MWF values, to the ensemble of the maturational processes captured by Mahalanobis distance.

Because in this work we considered only a short age range of early post-natal development, the revealed bundles ordering based on MWF may not give adequate description of white matter myelination over larger age ranges. Indeed, it was previously suggested that the age-related increase in MWF can be efficiently described by a modified Gompertz function [321], which was not possible to estimate from the data available in our study and thus, unlike Mahalanois distance, it was not possible to estimate the relative myelination delays between the bundles. Furthermore, because within the considered age range most of the bundles still show low MWF values, bundles comparison may be strongly influenced by inter-subject variability of the calculated MWF values. Both of these issues should be addressed in future studies with larger number of subjects scanned over larger age ranges.

Nevertheless, MWF approach has several important advantages over Mahalanobis distance approach:

1. it has a more straightforward interpretation as it is supposed to reflect only one maturational process, i.e. myelination;

2. it provides information on tissue microstructural properties, i.e. compartments fractions and their associated relaxation characteristics;

3. unlike Mahalanobis distance, MWF can be analysed in a voxel-vise manner;

4. in studies when it is not necessary to compare MWF values in infants with those in adults (for example, when comparing healthy and sick infant groups), MWF does not require acquisition of a large adult reference group (though it will be necessary to acquire data in a couple of adults to perform the calibration stage);

5.6 Conclusion

The presented findings suggest that the proposed MWF quantification approach is relevant for evaluating brain myelination. It has reasonable acquisition and post-processing times and can be potentially used in practical application in unsedated infants and children, and in clinical patients. The proposed approach was presented at the Joint Annual ISMRM-ESMRMB Meeting (2014) and it is a subject of the submitted article (see below).

A new strategy for fast MWF quantification in infants

Sofya Kulikova (Buzmakova)[1], Lucie Hertz-Pannier[1], Ghislaine Dehaene-Lambertz[2],

Cyril Poupon[3*], Jessica Dubois[2*]

1. INSERM U1129, CEA/Neurospin/UNIACT, Gif-sur-Yvette, France; Paris Descartes University, Paris, France
2. INSERM U992, CEA/Neurospin/UNICOG, Gif-sur-Yvette, France; Paris Sud University, Orsay, France
3. CEA/Neurospin/UNIRS, Gif-sur-Yvette, France
* equal contribution

# of pages (including abstract, text, references, figure and table legends): 35
# of figures: 6 + 3 supplementary figures
# of tables: 1 + 1 supplementary table
# of words in abstract: 241 (<250 for HBM)

Corresponding author:

Jessica Dubois

CEA/SAC/DSV/I2BM/NeuroSpin/Cognitive Neuroimaging Unit U992

Bât 145, point courrier 156

91191 Gif-sur-Yvette, France

Email: jessica.dubois@centraliens.net

Phone: +33 1 69 08 81 72

Fax: +33 1 69 08 79 73

Short title:

Fast MWF quantification in infants

Technical report for Human Brain Mapping

May 11th, 2015

Abstract

Myelin Water Fraction (MWF) is a promising MRI index for *in vivo* assessment of brain myelination that can be derived from multicomponent analysis of T1 and T2 relaxometry signals. However, existing quantification methods require rather long acquisition and/or post-processing times, making implementation difficult both in research studies on healthy unsedated children and in clinical examinations. The goal of this work was to propose a novel strategy for MWF quantification within acceptable acquisition and post-processing times. Our approach is based on a 3-component model (myelin-related water, intra/extra-cellular water and cerebro-spinal fluid), and uses pre-calibrated inherent $T1_c$ and $T2_c$ relaxation characteristics for each compartment c. Calibration was performed on adult relaxometry data (N=3) acquired with large numbers of inversion times (TI) and echo times (TE), using an original combination of a region contraction approach and a non-negative least-square (NNLS) algorithm. This strategy was compared with voxel-wise fitting, and showed robust estimation of $T1_c$ and $T2_c$. The accuracy of MWF calculations depending on multiple factors was investigated using simulated data. In the testing stage, our strategy enabled fast MWF mapping, based on relaxometry data acquired with reduced TI and TE numbers (acquisition <6 min), and NNLS algorithm (post-processing <5min). In adults (N=13, mean age 22.4±1.6 years), MWF maps showed variability across white matter regions, in agreement with previously published studies. In healthy infants (N=18, aged 3 to 34 weeks), asynchronous changes in MWF values were demonstrated across bundles, confirming the well-known progression of maturation.

Keywords: Myelin Water Fraction (MWF); relaxometry; brain myelination; infant; calibration; white matter bundles; Magnetic Resonance Imaging (MRI)

Introduction

Myelination is a crucial process of the white matter maturation. Although there is a critical need for *in vivo* quantitative assessment of myelination in many clinical conditions that encompass most neurodevelopmental disorders, there is still no gold-standard for its evaluation. Whereas myelination can be assessed using conventional Magnetic Resonance Imaging (MRI) and Diffusion Tensor Imaging (DTI) parameters [Bird et al., 1989; Bosnell et al., 2008; Staudt et al., 1994], these methods provide only indirect and non-specific measures of the myelin content as they also reflect other tissue properties [Beaulieu, 2002; Dubois et al., 2014a]. Recent advances in relaxometry MRI have proposed a novel index, named Myelin Water Fraction (MWF), that has shown good correlation with the myelin amount [Laule et al., 2008] and seems relevant for quantifying the progression of white matter myelination [Deoni et al., 2011; Deoni et al., 2012; Lancaster et al., 2003].

MWF corresponds to the fraction of water volume trapped by the myelin sheaths relative to the total water volume within an imaging voxel, and can be derived from a multicomponent analysis of relaxometry signals [MacKay et al., 1994; Whittall et al., 1997]. The number of compartments, corresponding to different pools of water within a voxel, usually varies from 2 to 4 and includes myelin-related compartment, intra/extra-cellular water and free water of the cerebro-spinal fluid (CSF).

The most conventional approaches for MWF quantification rely on the calculation of T2 spectrum, and define MWF in each voxel as the ratio between the signal with T2 below 40-50ms, and the total water signal [Kolind et al., 2009; Laule et al., 2004; Laule et al., 2008; Levesque et al., 2010; Mädler et al., 2008; Oh et al., 2006; Whittall et al., 1997]. Similar strategies have been proposed for T2* [Hwang and Du, 2009] and T1 spectra [Labadie et al., 2013]. However, reliable estimation of a spectrum requires the acquisition of relaxometry signals for a large sampling number (N>32 for echo times TE or inversion times TI) [MacKay et al., 1994; Whittall et al., 1997], making the acquisition protocol impractically long for unsedated infants and children.

An alternative approach is based on a multicomponent model of MRI relaxometry signals that takes into account the relative contributions of different compartments: fitting this model with acquired data enables to estimate the compartment fractions [Deoni et al., 2008; Deoni et al., 2013; Lancaster et al., 2003]. In such models, differences in relaxometry signals across voxels may be explained either by different compartment fractions, or by variations in their relaxation

characteristics due to variations in their biophysical properties (axonal diameters, myelin thickness, myelin compactness, spacing between axons, etc.). Unless some *a priori* assumptions are made on the compartment relaxation characteristics[Lancaster et al., 2003], such models are described by non-linear equations, and their robustness relies on the sampling strategy and the number of measurements. In such approach, using mcDESPOT sequences allows to reduce the acquisition time: for instance, in infants aged between 3 and 9 months old, the total imaging time (including sequences for B_0 and B_1 corrections [Deoni, 2011]) is about 18min on a 3T scanner [Deoni et al., 2012], which is nevertheless rather long for unsedated pediatric subjects. In addition, long post-processing times (~14 hours per subject on an 8-core Intel I7 machine [Deoni et al., 2013]) are inevitable due to the sophisticated stochastic model fitting.

Thus, the goal of this study was to design and validate a novel strategy for fast MWF quantification in infants, with reasonable acquisition and post-processing times, and little assumptions on the compartment relaxation characteristics.

Description of the strategy for fast MWF quantification

A 3-component model

Our approach for MWF quantification is based on a 3-component model adapted from Lancaster et al. [Lancaster et al., 2003] (see below for the equations description). It considers 3 compartments with inherent relaxation characteristics: myelin-related water, intra/extra-cellular water, and CSF. Such a model can explain the variability in relaxometry signals across brain tissues and regions by differences in the compartment relative proportions, and thus by their different contributions to the total measured signal [Andrews et al., 2005; Deoni et al., 2013; Hwang et al., 2010; Kwon et al., 2013]. It further enables to efficiently describe changes in relaxometry signals related to brain maturation [Dean et al., 2014; Deoni et al., 2012; Lancaster et al., 2003].

This 3-component model (Eq. 1-4) links the compartment volume fractions (f_c) and their inherent relaxation times ($T1_c$ and $T2_c$), with the T1 relaxometry signals (S_{T1}) measured for N_{TI} inversion times (TI_m) and the T2 relaxometry signals (S_{T2}) measured for N_{TE} echo times (TE_k).

The first equation of this model merely states that there are only 3 compartments (my - myelin-related water, ie - intra/extra-cellular water, and CSF), and that MWF may vary from 0 to

$$\begin{cases} \sum_{c=1}^{3} f_c = 1,\ f_{my} \in [0,0.4],\ f_{ie,csf} \in [0,1] \ (1); \\ S_{T1}(TI_m) = S_0\left(1 - 2exp\left(-TI_m/T1\right)\right), m = 1..N_{TI} \ (2); \\ 1/T1 = \sum_{c=1}^{3} f_c/T1_c \ (3); \\ S_{T2}(TE_k) = S_0 \sum_{c=1}^{3} f_c exp\left(-TE_k/T2_c\right), k = 1..N_{TE} \ (4); \end{cases}$$

40% (see below for justification), while fractions for intra/extra-cellular water and CSF may vary from 0 to 100% [Akhondi-Asl et al., 2014; Deoni et al., 2013; Lancaster et al., 2003; Stikov et al., 2011; Warntjes et al., 2011]. Eq.2 describes the classical relationship between T1 relaxometry signal, inversion and relaxation times. Eq.3 comes from "fast exchange" modeling of T1 relaxometry signal: between-compartment water mixing times are assumed to be short compared with within-compartment T1 relaxation times. Eq.4 comes from "slow exchange" modeling of T2 relaxometry signal: T2 relaxation times are assumed to be short compared with the time it takes water molecules to exchange between compartments. The validity of this model assumptions was verified in [Lancaster et al., 2003].

Fitting such a non-linear model with a limited number of measurements is an ill-posed problem. However, if we pre-calculate $T1$ using Eq.2, and pre-calibrate and fix $T1_c$ and $T2_c$ values in Eq.3, the model becomes linear with respect to the 3 compartment fractions (Eq.5), and can be easily fitted using standard non-negative least-square (NNLS) algorithms [Lawson and Hanson, 1987]:

$$\begin{cases} \sum_{c=1}^{3} f_c = 1, \quad f_{my} \in [0,0.4], \; f_{ie,csf} \in [0,1]\,; \\ {}^{1}/_{T1} = \sum_{c=1}^{3} {}^{f_c}/_{T1_c}\,; \\ S_{T2}(TE_k) = S_0 \sum_{c=1}^{3} f_c exp\left({}^{-TE_k}/_{T2_c}\right), k = 1..N_{TE}\,; \end{cases} \quad (5)$$

A 2-step strategy

In this study, we implemented the following 2-step fitting strategy. First, calibration datasets, acquired in adults with a large number of measurements, were used to compute the most appropriate (providing the best fit of the model) inherent T1 and T2 characteristics for each compartment c, namely, $T1_c$ and $T2_c$. Second, the model complexity was reduced by fixing these $T1_c$ and $\mathrm{T2_c}$ characteristics: MWF maps were then computed for testing datasets of infants and adults, acquired with reduced number of measurements to preserve a short acquisition time. As detailed in the next sections, the calibration strategy was compared with voxel-wise model fitting, and we investigated the effects of f_{my} upper boundary and TI/TE numbers on the estimation of $T1_c$ and $\mathrm{T2_c}$ characteristics and MWF values. The accuracy of MWF calculation using this procedure was further evaluated on simulated data, and the impact of multiple factors was investigated (noise level, number of voxels simultaneously used to perform $T1_c$ and $T2_c$ calibration, MWF values).

Materials and Methods

Subjects

Calibration datasets were acquired on 3 healthy adult volunteers (1 female, 2 males, mean age: 23.2±2 years). Testing datasets included 2 groups. The first group consisted of 18 healthy infants born at term (8 girls, 10 boys), with a maturational age (i.e. chronological age corrected for gestational age at birth) between 3 and 21 weeks for 17 infants, and one infant of 34 weeks old. Infants were non-sedated and spontaneously asleep during MR imaging. The infant group was studied with respect to an adult group of 13 healthy subjects (6 females, 7 males, mean age:

22.4±1.6 years). The study protocol was approved by the regional ethical committee for biomedical research, all parents and adult subjects gave written informed consents. Particular precautions were taken to minimize noise exposure in infants, by using customized headphones and covering the magnet tunnel with special noise protection foam.

MRI acquisition

Data acquisition of both calibration and testing datasets was performed on a 3T MRI system (Tim Trio, Siemens Healthcare, Erlangen, Germany), equipped with a whole body gradient (40mT/m, 175T/m/s) and a 32-channel receive-only head coil. Interleaved axial slices covering the whole brain were acquired using single-shot spin-echo (SE) echo-planar-imaging (EPI) sequences, with a 1.8 mm isotropic spatial resolution. For T1 relaxometry signal, an inversion recovery (IR) SE-EPI sequence was used with different TI values and a partial Fourier sampling factor of 5/8. For T2 relaxometry signal, a SE-EPI sequence was used with different TE values, parallel imaging (GRAPPA factor 2), and a partial Fourier sampling factor of 6/8. Over the white matter, signal-to-noise ratio (SNR, estimated as the averaged local SNR over 2x2x2 sliding areas) was around 10% for T1 relaxometry data (from 5% at the shortest TI to 24% at the longest TI), and around 7% for T2 relaxometry data (from 3% at the shortest TE to 21% at the longest TE). These noise levels allowed us to consider the non-centered chi-noise present in GRAPPA-reconstructed images as a Gaussian noise, and thus to use NNLS estimators.

Adult calibration datasets

Seventy slices were acquired with a large number (N=30-60) of TI (sampled between 100ms and 3100ms) and TE (sampled between 30ms and 340ms) (for details see Tab.1). The TI and TE samplings were denser at the beginning of the sampling range to ensure good estimation of the parameters for the fast-relaxing myelin-related compartment. Acquisition parameters were: for T1 relaxometry signals - TE=38ms, TR=TI+21s; for T2 relaxometry signals - TR=21.7s. Additionally, anatomical T1-weighted (T1w) images were acquired with a 1mm isotropic spatial resolution using a 3D fast gradient inversion recovery sequence (MPRage).

Table 1 TI and TE sampling in the calibration datasets.

For each calibration subject, the sampling schemes of TI and TE points (values and numbers) are detailed, as well as the total acquisition time. For example, for Subject 1 acquisition time was 41min 30s with 3 sets of TI values and 3 sets of TE values, e.g., in the first TI set the values were distributed from 100ms to 1000ms with a step of 50ms, making in total 19 points for the first TI set and 30 points for all 3 sets. TE values should be read in the same way. Note that the number of sets may differ between TE and TI and across the subjects. Note also that in subject 3 the values in the 2 first sequences are distributed within overlapping ranges but with different steps.

Subject *(acq. time)*	*TI values*					*TE values*				
	low border (ms)	*upper border (ms)*	*step (ms)*	*Number of points*		*low border (ms)*	*upper border (ms)*	*step (ms)*	*Number of points*	
Subject 1 *(41min 30s)*	*100*	*1000*	*50*	*19*	*30*	*33*	*71*	*2*	*20*	*60*
	1100	*1500*	*100*	*5*		*65*	*160*	*5*	*20*	
	1750	*3000*	*250*	*6*		*150*	*340*	*10*	*20*	
Subject 2 *(34min 54s)*	*100*	*1000*	*50*	*19*	*30*	*33*	*51*	*2*	*10*	*47*
	1000	*3000*	*200*	*11*		*50*	*160*	*5*	*23*	
						170	*300*	*10*	*14*	
Subject 3 *(47min 11s)*	*100*	*1500*	*50*	*29*	*60*	*33*	*52*	*1*	*20*	*60*
	130	*980*	*50*	*18*		*55*	*131*	*4*	*20*	
	1630	*3130*	*250*	*7*		*140*	*311*	*9*	*20*	
	1750	*3000*	*250*	*6*						

Infant and adult testing datasets

Fifty/seventy slices were acquired in infants/adults respectively. For T1 relaxometry signals, 8 TI values were used (TI=250 to 1500ms, each step 250ms, + TI=2000 and 2500ms) and acquisition parameters were: TE=38ms, TR= TI+15s/21s (infants/adults), leading to an acquisition time of 2min11s/3min03s. For T2 relaxometry signals, 8 TE values were used

(TE=50 to 260ms, each step 30ms) and TR=15.5s/21.7s, leading to an acquisition time of 2min51s/4min. In order to identify different white matter bundles used as regions-of-interest for MWF quantification, diffusion-weighted (DW) images were also acquired with a DW-SE-EPI sequence with the following acquisition parameters: 30 orientations of diffusion gradients with b=700s/mm^2 (+b=0 volume), TE=72ms, TR=10s/14s, parallel imaging GRAPPA factor 2, partial Fourier sampling factor 6/8, leading to an acquisition time of 5min40s/7min56s. For anatomical image co-registration and comparison with MWF maps from other studies, T2-weighted (T2w) images were additionally acquired in infants using a 2D turbo spin echo sequence with spatial resolution of 1x1x1.1mm^3.

Data post-processing

In each subject, T1 and T2 relaxometry images (and DW images in the testing group) were co-registered with anatomical images (T1w for adults, T2w for infants) using affine transformations maximizing their mutual information. Quantitative T1 and T2 maps were then calculated for all subjects.

DW images in the testing datasets were corrected for motion and eddy current artifacts [Dubois et al., 2014b]. 18 projection, association, commissural and limbic bundles that mature at different times and rates were reconstructed in each subject according to a 4-order analytical Q-ball model [Descoteaux et al., 2007], regularized 3D tractography [Perrin et al., 2005], and manually delineated regions of interest [Kulikova et al., 2014].

All data were pre- and post-processed using PTK toolkit and Connectomist software both developed in-house at NeuroSpin [Duclap et al., 2012; Poupon et al., 2010].

MWF fitting strategy and validation

Calibration stage

In calibration datasets, the model was fitted using an original combination of a region contraction approach [Berger and Silverman, 1991; Deoni et al., 2013] and a standard NNLS algorithm [Lawson and Hanson, 1987] (Fig. 1). This procedure was programmed in Python using NumPy and SciPy libraries. The initial search intervals for the individual compartment $T1_c$ and $T2_c$ characteristics were set based on literature evidence [Deoni et al., 2013; Guo et al., 2012; Lancaster et al., 2003; MacKay et al., 2006] and to ensure the intervals contiguity:

- for myelin-related compartment: $T1_{my} \in [300; 570]$ms, $T2_{my} \in [1; 40]$ms
- for intra/extra-cellular water compartment: $T1_{ie} \in [570; 1600]$ms, $T2_{ie} \in [40; 200]$ms
- for CSF compartment: $T1_{csf} \in [1600; 4000]$ms, $T2_{csf} \in [200; 2000]$ms.

In each subject, we considered the 10 central slices (covering the ventricles, corpus callosum and basal ganglia) as they contain portions of all three compartments, and the following fitting procedure was applied for each slice independently. For each compartment, random $T1_c$ and $T2_c$ values were first selected within the corresponding search intervals, and the simplified model (Eq.5) was fitted in each voxel using a NNLS algorithm. Second, the total fitting error was calculated over all brain voxels of the slice (averaged number of voxels within a slice: 5718±406 across the 10 slices of the 3 calibration subjects). Similarly to [Deoni et al., 2013], these steps were repeated 10000 times for each slice, and the best 100 selections of $T1_c$ and $T2_c$ values (i.e. providing the smallest total fitting error) were used to contract the search intervals. After contraction, the whole procedure was re-started: 90% of random $T1_c$ and $T2_c$ values were chosen from the new search intervals, while the remaining 10% were selected from the initial intervals to avoid falling into a local minimum. This fitting procedure was executed until both the fitting errors and the difference between the interval boundaries became less than 1%.

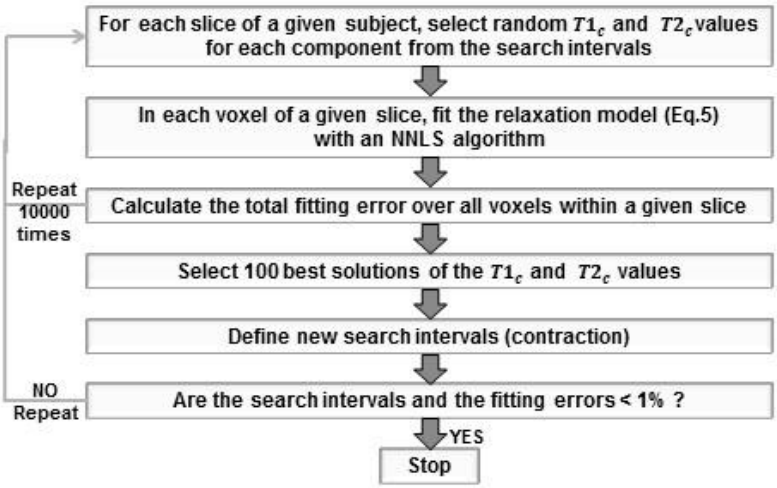

Figure 1. Schematic representation of the calibration algorithm.

The depicted fitting procedure was performed independently in each slice from all calibration subjects. The initial search intervals were selected based on the literature evidence. The fitting

steps were repeated until both the fitting error and the differences between the upper and lower borders of the search intervals became less than 1%.

Once the calibration was performed for each slice, $T1_c$ and $T2_c$ characteristics were set to the weighted averages (with inversed fitting errors) over all slices of all calibration subjects (10 slices x 3 subjects). These compartment relaxation characteristics were further used for MWF calculation in the testing datasets (see below).

Validation of the calibration strategy

First, we performed a voxel-wise model fitting in the 3 calibration datasets to assure that there was no particular regional dependence of $T1_c$ and $T2_c$ characteristics, and that calibrated values were adequate over whole brain volumes. The generated voxel-wise MWF maps were compared with MWF maps obtained at the calibration stage.

Second we explored the effect of f_{my} upper boundary at the calibration stage, since it was shown to have a considerable impact on MWF values derived from the relaxometry model based on mcDESPOT protocol [Zhang et al., 2014]. Because the quality of model fitting (sum-of-square of residuals) using stochastic region contraction approach is the best when the upper boundary is between 0.3 and 0.5 and is insensitive to changes within this range[Zhang et al., 2014], the search interval for f_{my} was initially set to [0;0.4]. We also considered two other upper boundaries (0.3 and 0.5), and compared $T1_c$ and $T2_c$ characteristics generated at the calibration stage, as well as MWF maps. Results (detailed below) suggested that fixing the upper boundary to 0.4 was a valid approach, so this value was considered in the following tests.

Third, we investigated the impact of TI and TE numbers on the resulting $T1_c$ and $T2_c$ characteristics, to make sure that each calibration dataset had enough sampling points for reliable calibration. To do so, we performed independent calibrations for the "largest" dataset (subject #3, Tab.1), after removing data points in a regular manner (from 60 down to 10 points).

Fourth, we checked using simulated data that the proposed calibration strategy applied to the 3 adult datasets provided reliable computation of MWF values. T1 and T2 relaxometry signals were simulated using Eq. 2-4 at all TI and TE sampling points (Tab.1), and fixing $T1_c$ and $T2_c$ values either equal to those identified at the calibration stage (see results) or as in previous studies [Deoni et al., 2013; Does and Gore, 2002; Lancaster et al., 2003; MacKay et al.,

2006]: $T1_{my}$=465ms, $T1_{ie}$=965ms, $T1_{csf}$=3500ms, $T2_{my}$=12ms, $T2_{ie}$=90ms, $T2_{csf}$=250ms. Relaxometry signals were simulated for different compartment fractions possibly observed in the white matter: $f_{my} = [5,10,15,20,25,30,40]\%$, $f_{csf} = [0,1,2,3,4,5]\%$ and $f_{ie} = (100 - f_{my} - f_{csf})\%$. Simulated signals were additionally corrupted with a Gaussian noise with a dispersion varying from 0 to 20% relative to signal values. Then our calibration procedure was applied to simulated datasets in order to identify the compartment fractions and relaxation characteristics $T1_c$ and $T2_c$. The error in MWF calculation was estimated as the averaged absolute percent difference between identified and simulated values. We also investigated how the number of voxels used for the model fitting impacted MWF errors. In theory, calculation errors are proportional to the inversed square root of the voxel number ($MWF\ error \sim 1/\sqrt{number\_of\_voxels}$) [Smith, 1997]. Thus, simulations were performed for voxel numbers equal to [1^2, 2^2,…,75^2=5625], and errors were fitted with the inverse square root function. Finally, we compared MWF calculation errors obtained in simulations using both T1 and T2 relaxometry signals together, vs. only T2 relaxometry signal.

Testing stage

Before considering the testing datasets, we applied the testing strategy to the calibration datasets in order to compare MWF maps: the simplified model was fitted according to Eq.5 and using a standard NNLS algorithm implemented in SciPy [Lawson and Hanson, 1987] and the compartment relaxation characteristics $T1_c$ and $T2_c$ computed during the calibration stage. We also checked that down-sampling the calibration datasets (to match TI and TE numbers and values of the testing datasets) had no significant impact on the generated MWF maps.

MWF maps were then calculated in the testing datasets of adults and infants. In adults, similarity between MWF distributions from calibration and testing maps was assessed by ad-hoc χ^2 test [Gagunashvili, 2006]. The infant MWF maps were compared with age-matched maps computed by another group using mcDESPOT sequences [Dean et al., 2014] (http://www.babyimaginglab.com/Research_files/meanMWFMaps.zip). For that, infants' anatomical T2w images were co-registered using affine transformations to the 3D Pediatric T1w template corresponding to age-matched MWF maps (http://www.babyimaginglab.com/Research_files/referenceMaps.zip). The resulting

transformations were applied to both infants' T2w images and MWF maps, and registered images were correlated voxel-wise with the aged-matched MWF maps.

For each adult and infant subject, MWF was further quantified and averaged over the 18 different white matter bundles. In the adult group, MWF values were compared with T1 and T2 relaxation times (computed at the voxel level). In the infant group, MWF age-related changes were assessed. Infant values were further normalized by the corresponding average from the adult group to address the degree of bundles myelination relatively to the adult mature stage [Dubois et al., 2008].

Results

Validation of the calibration strategy

Fitting the model with the adult calibration datasets resulted in the following $T1_c$ and $T2_c$ values (mean±SD over the 10 slices of the 3 subjects):

- for myelin-related compartment: $T1_{my} = 357 \pm 21$ms, $T2_{my} = 18 \pm 5$ms
- for intra/extra-cellular water compartment: $T1_{ie} = 1483 \pm 17$ms, $T2_{ie} = 52 \pm 6$ms
- for CSF compartment: $T1_{csf} = 3441 \pm 36$ms, $T2_{csf} = 858 \pm 47$ms.

The resulting MWF maps had similar visual appearances across the 3 subjects (Fig. 2I) and similar distributions of values as verified by ad-hoc χ^2 test ($p>0.95$). This calibration step took around 24 hours on Intel I3 machine without parallel computations.

Voxel-wise model fitting in the same calibration datasets suggested that $T1_c$ and $T2_c$ characteristics could be considered the same across brain regions (Fig. 3). Furthermore, the overall mean voxel-wise values (±SD) were very close to those obtained from the calibration stage:

- for myelin-related compartment: $T1_{my}$=360±39ms, $T2_{my}$=18±8ms
- for intra/extra-cellular water compartment: $T1_{ie}$=1482±29ms, $T2_{ie}$=53±12ms
- for CSF compartment: $T1_{csf}$=3431±78ms, $T2_{csf}$=852±79ms.

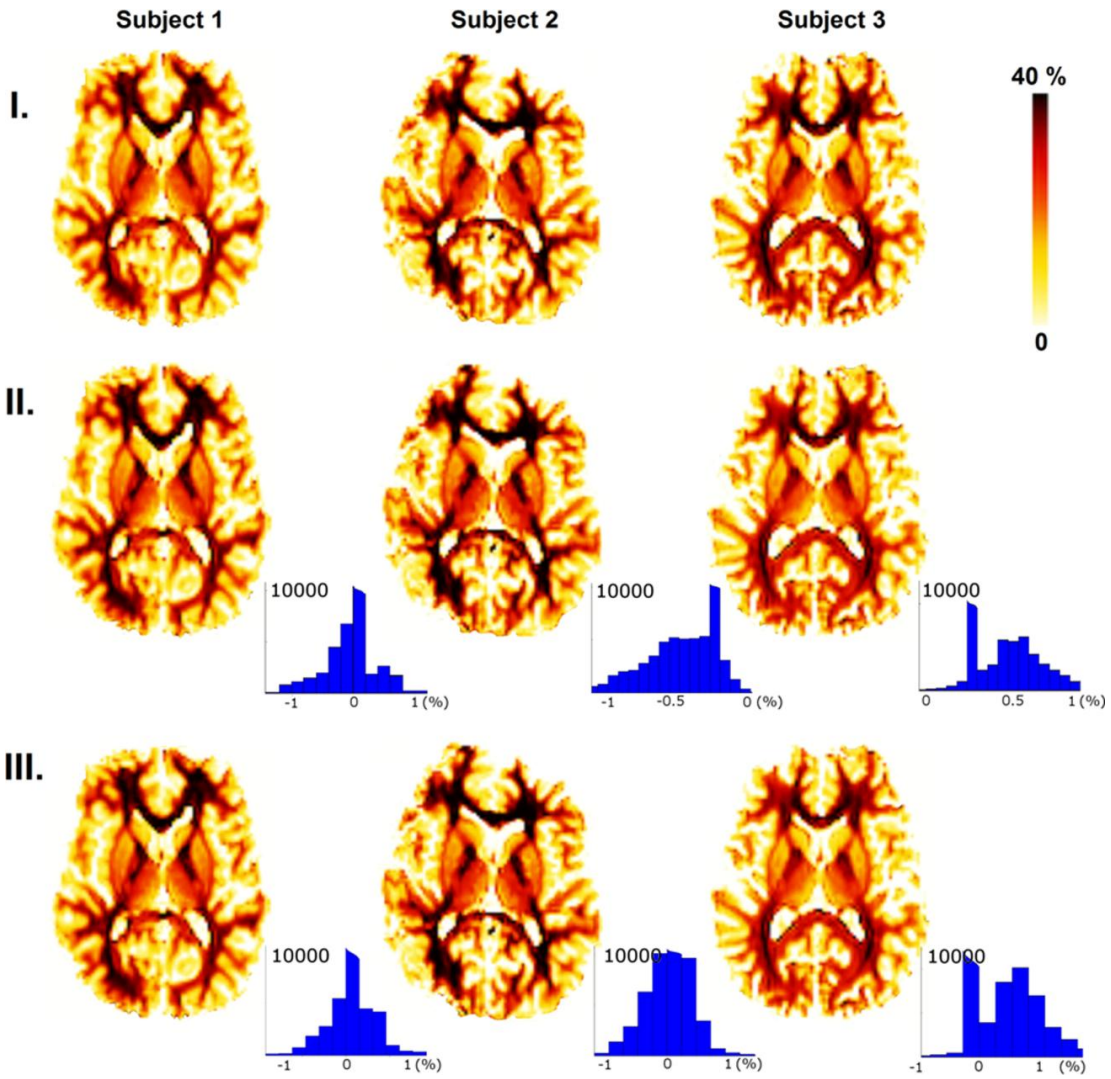

Figure 2. MWF maps in the 3 calibration adult subjects.

Maps were obtained using (I.) complete datasets, (II.) complete datasets and fixed $T1_c$ and $T2_c$ values, (III.) datasets with a reduced number of measurements and fixed $T1_c$ and $T2_c$ values. For each subject, histograms show the distribution of differences between the I^{st} and the II^{nd}/III^{rd} datasets correspondingly. Maps are displayed in radiological convention (left and right hemispheres are inversed).

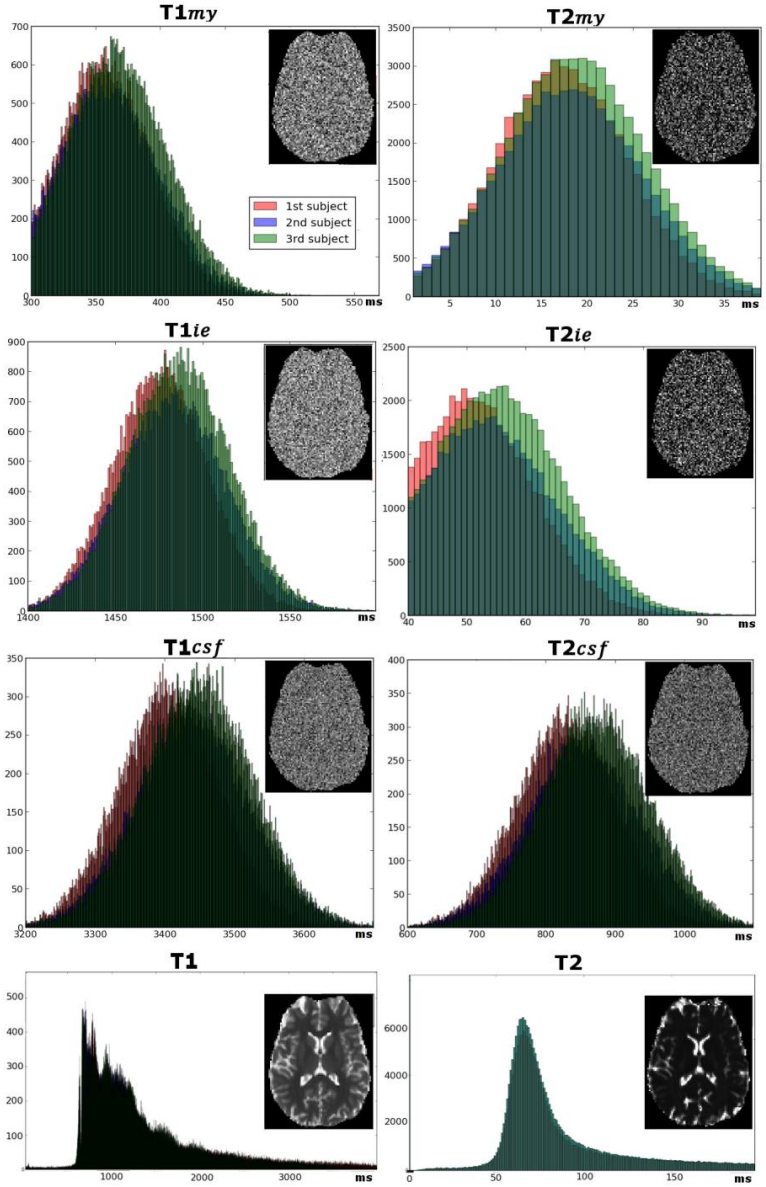

Figure 3. Variations of the compartment relaxation characteristics across voxels.

In the first three rows, histograms show distributions of $T1_c$ and $T2_c$ characteristics (for myelin-related water, intra/extra-cellular water, and CSF compartments) obtained from voxel-wise fitting within the search intervals, across all voxels in the 3 calibration adult subjects. The distribution peaks are close to $T1_c$ and $T2_c$ values identified at the calibration stage, although the distributions presented variances over the whole search intervals. $T1_c$ and $T2_c$ maps (presented for subject #3) did not reveal any regional dependence. In the bottom row, distributions of T1 and T2 values obtained from mono-exponential fittings at the voxel-level are shown, as well as quantitative T1 and T2 maps (subject #3).

Despite the high number of TI and TE sampling points, voxel-wise MWF maps had naturally noisier appearance. Nevertheless they were similar to MWF maps obtained at the calibration stage, with differences smaller than 3% (Sup. Fig. 1). These results suggested that our calibration strategy was reasonable in comparison with a voxel-wise strategy.

Besides, we investigated how the initial search interval for f_{my} (i.e. the upper boundary) impacted MWF values and the computation of $T1_c$ and $T2_c$ characteristics in the calibration stage. With a [0, 0.4] interval, quite high MWF values were observed in the adult white matter (Fig. 2I), in comparison with previous studies [Deoni et al., 2011; Lancaster et al., 2003]. When changing the upper boundary to 0.3 and 0.5 for the 3 calibration datasets, we observed a strong impact on MWF maps (Sup. Fig. 2): higher upper boundary resulted in higher values in all 3 subjects. However, the compartment relaxation characteristics were very close (Sup. Table 1). Of interest, when the upper boundary was set to 0.4, distributions of MWF values across the 3 subjects were the most similar (i.e. they had the biggest overlap, Sup. Fig. 2), and standard deviations for T1c and T2c estimations were globally the lowest (Sup. Table 1). These results suggested that fixing the upper boundary for f_{my} to 0.4 was valid despite it might provide high MWF values.

Sensitivity of the calibration strategy

We further assessed whether our calibration strategy was sensitive to different acquisition parameters (sampling points, noise level). First, reducing the number of calibration TI and TE points until N=25 for both T1 and T2 relaxometry signals, had no significant effect on $T1_c$ and $T2_c$ calibration in subject #3 (ad-hoc paired t-test between $T1_c$ or $T2_c$ values from individual slices: $p>0.06$, Sup Fig. 3). This suggested that our calibration stage was performed in a stable manner across all 3 subjects with different numbers of TI and TE points.

Application of the calibration strategy to simulated data showed that as the noise level increased, reliable calculation of MWF values required increasing the number of voxels used to estimate the compartment characteristics (Fig. 4a). In agreement with previously conducted simulations (19), even for a noise level of 20% of the signal values, the average estimation errors were less than 10% when using more than 2000 voxels (Fig. 4a). In simulations with a 20% noise level, with a number of voxels higher than 5000, and with $T1_c$ and $T2_c$ values fixed either according to the calibration stage or to values from previous studies [Deoni et al., 2013; Does and Gore, 2002; Lancaster et al., 2003; MacKay et al., 2006], we observed that estimation errors

decreased with increasing MWF values, and that maximal errors did not exceed 15% for MWF values of 5% (Fig. 4b). This suggested that the number of voxels considered in our calibration stage (~5718±406 voxels for each slice) was sufficient for reliable MWF estimation.

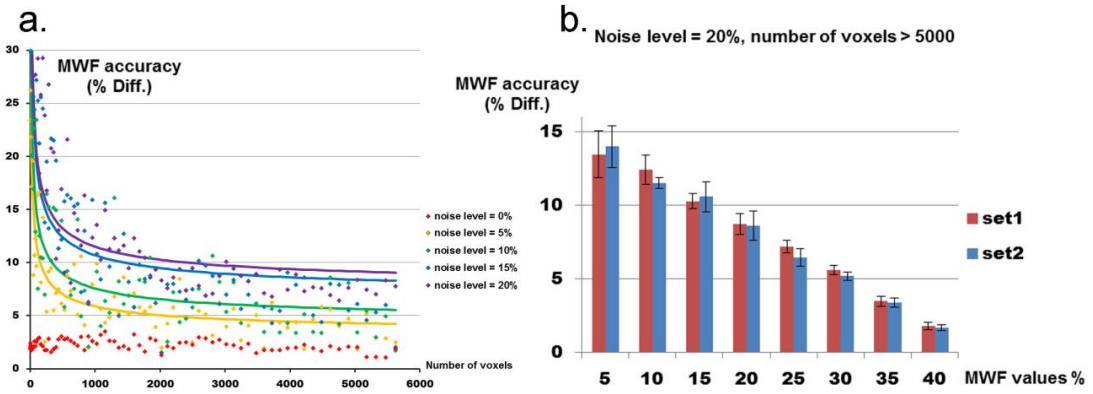

Figure 4. MWF calculation accuracy of the calibration strategy assessed in numerical simulations.

(a) The MWF calculation errors were calculated for $f_{my} = [5,10,15,20,25,30,40]\%$ and $f_{csf} = [0,1,2,3,4,5]\%$, and the resulting average values were represented as a function of the number of voxels used for the model fitting [1^2, 2^2,…,75^2=5625], for different noise levels (from 0 to 20%). As expected, relationship between the MWF calculation errors and the number of voxels could be described by inverse square root relationship (R^2>0.75).

(b) For a noise level of 20%, calculation errors for different simulated MWF values were averaged for voxel numbers higher than 5000 [71^2,.., 75^2] and $f_{csf} = [0,1,2,3,4,5]\%$, considering $T1_c$ and $T2_c$ characteristics fixed according to our calibration stage (set1) or to values of previous studies (set2).

Besides, in identical conditions (same noise level, number of voxels, compartment fractions and relaxation characteristics), removing T1 relaxation from the model (i.e. removing Eq.3) significantly reduced the accuracy of MWF calculations as compared to the full model (ad-hoc paired t-test, $p<10^{-6}$). This demonstrated that modelling T1 and T2 relaxometry signals together was more appropriate than considering T2 relaxation alone, probably because we could

not sample T2 signals for very short TE as compared with the very low $T2_{my}$ value (see Discussion below).

Validation of the testing strategy

Fitting MWF model in calibration datasets as in the testing stage, by fixing the identified $T1_c$ and $T2_c$ characteristics, had little effect on MWF maps, whether the number of data points was kept complete (Fig. 2II) or reduced to 8 TI and 8 TE values matching those of testing datasets (Fig. 2III): the average absolute differences between calibration maps and maps computed with fixed $T1_c$ and $T2_c$ characteristics were very low (e.g. 0.8±0.1%; Fig. 2). Furthermore, this stage took less than 5 min, suggesting that the testing strategy can be applied for fast and reliable computation of MWF maps in testing datasets.

MWF maps in testing datasets

In adults, MWF maps from testing datasets were very similar to maps from calibration datasets, in terms of visual appearance (Fig. 2 and 5) and distribution of MWF values (ad-hoc χ^2 test: $p>0.95$). In infants, MWF maps showed the myelination progression described by *post-mortem* studies [Flechsig, 1920]. Within white matter, the youngest infants had high MWF values only in the posterior limb of the internal capsule, and MWF values progressively increased with age in a caudo-rostral direction, from the center of the brain to the periphery (Fig. 5).

Moreover, age-matched MWF maps available from another group (36) were strongly correlated with our maps ($R^2>0.77$), significantly more ($p<0.001$, ad-hoc paired t-test) than with infants' anatomical T2w images ($R^2>0.67$), suggesting that correlations between MWF maps did not simply reflect the similarity in underlying anatomical structures.

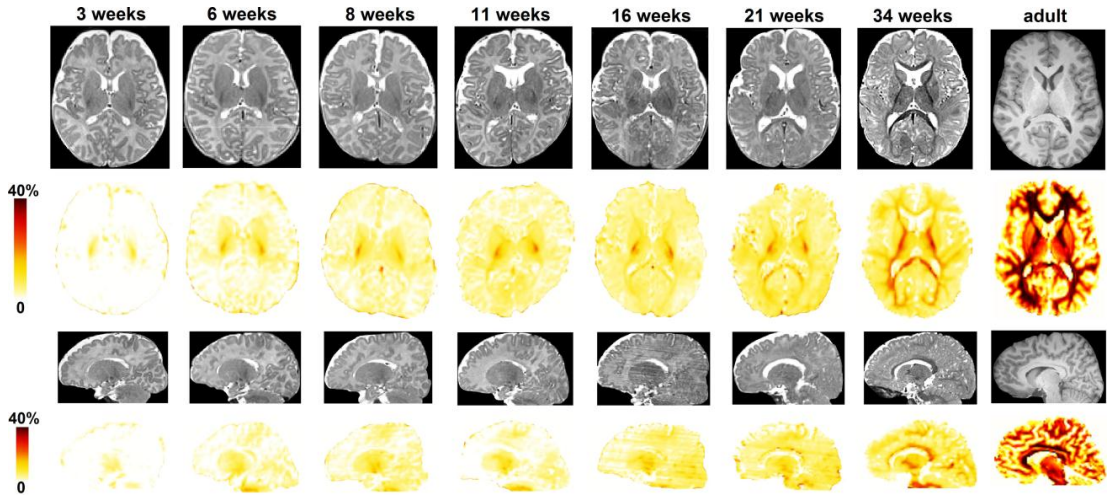

Figure 5. Infant MWF maps. Maps are presented in representative infants at different ages and in an adult subject, with corresponding anatomical images (T2w for infants / T1w for the adult). Axial slices are displayed in radiological convention.

MWF quantification in white matter bundles

In adults, MWF values were highly variable across bundles (Fig. 6a,b): from 0.14 in the spino-thalamic tract up to 0.36 in the optic radiations. In the spino-thalamic tract, surprisingly low values and high inter-individual variability were probably due to subtle misalignment between MWF and DW images in the brainstem of some adults. High variability in MWF values was also observed in the genu of corpus callosum, possibly due to partial volume effects with the ventricle CSF. In all bundles, MWF values were strongly correlated with T1 values across adult subjects (R^2>0.95), but not with T2 values.

In infants, MWF values were smaller than in adults and below 0.05 for most bundles (on average over the group) (Fig. 6b). Higher MWF values were observed in the cortico-spinal and spino-thalamic tracts and in the optic radiations, which are known to myelinate early on. By construction of the 3-component model, age-related changes, over the infant group, in T1 and T2 relaxation times (measured at the voxel level) were could explained by age-related changes in the compartment fractions, notably by changes in MWF values. For instance, in the middle cortico-spinal tract, we observed that MWF changed from 5% at 3w to 17% at 21w, in relation with changes in f_{ie} from 89% to 80%, and in f_{CSF} from 6% to 3%. According to Eq.3 and pre-calibrated $T1_c$ and $T2_c$ characteristics, T1 was expected to change from 1321 to 979, in agreement with experimental observations (the measured T1 changed from 1322 to 978 on average over the tract). These results were coherent with our initial hypothesis that age-related changes in

relaxometry signals and T1 / T2 relaxation times (measured at the voxel level), can be modeled by age-related changes in the compartment fractions, and do not require that $T1_c$ and $T2_c$ characteristics evolved with the tissues maturation.

In infants, MWF normalized by the mean values from the adult group, increased with age (from 3 to 21 weeks) in all bundles but in an asynchronous manner (Fig. 6c): in certain bundles (e.g. spino-thalamic tract, cortico-spinal tract, external capsule, fornix, optic radiations), normalized MWF values increased earlier than in other bundles (e.g. arcuate and uncinate fasciculi, anterior limb of the internal capsule, corpus callosum). In all bundles except the spino-thalamic tract, linear regressions could describe these age-related increases over this short developmental period. However, since certain bundles had zero MWF values in the youngest infants, non-linear fitting may be more pertinent for describing the earliest subtle changes in bundle myelination [Dean et al., 2014].

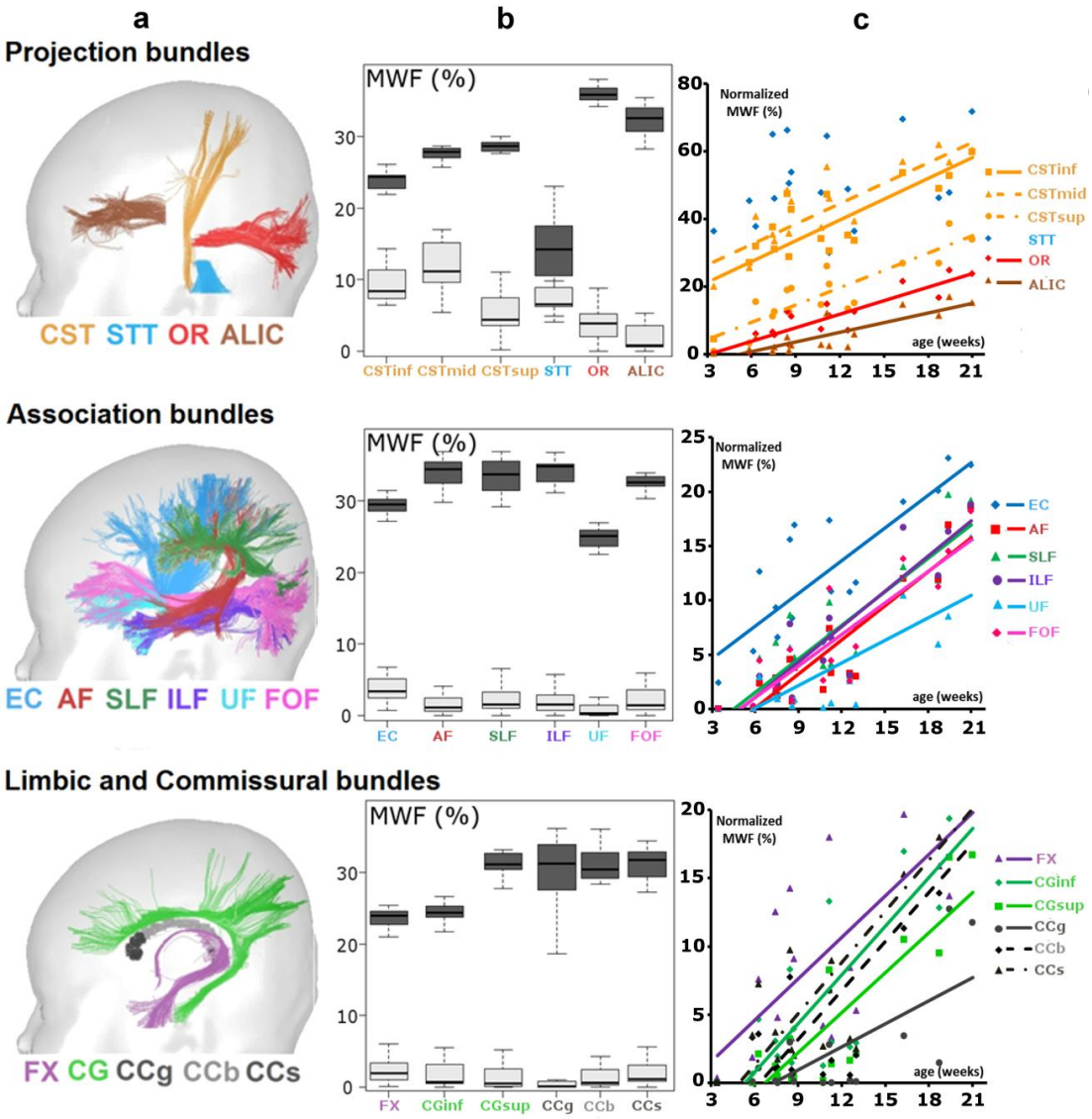

Figure 6. MWF quantification across white matter bundles in infants and adults.

(a): White matter bundles reconstructed with tractography.

(b): MWF values across bundles in infants (light) and adults (dark).

(c): Age-related changes in infants' normalized MWF values (in % of the mean adult values) for the same bundles. Lines show significant linear regressions with age (R^2>0.58, p<0.015), for all bundles except the spino-thalamic tract.

Abbreviations: *Projection bundles*: cortico-spinal tract CST (inf – inferior, mid – middle, sup - superior portions), spino-thalamic tract STT, optic radiations OR, anterior limb of the internal capsule ALIC; *Association bundles*: external capsule EC, arcuate fasciculus AF, superior SLF and inferior ILF longitudinal fascicles, uncinate fasciculus UF, fronto-occipital fasciculus FOF; *Limbic and Commissural bundles*: fornix FX, inferior CGinf and superior CGsup parts of the cingulum; corpus callosum: genu CCg, body CCb and splenium CCs.

Discussion

In this work we proposed an original 2-step approach for fast MWF quantification, based on a 3-component model (myelin-related water, intra/extra-cellular water, CSF) of T1 and T2 relaxometry signals. The first step consisted in the calibration of the compartment $T1_c$ and $T2_c$ relaxation characteristics using a long acquisition protocol, obtained in adult subjects, while the second step used a simplified linear model usable with a short acquisition protocol more adequate for the pediatric population.

Is this 2-step strategy valid for MWF quantification in the adult brain?

Validation of the calibration and 2-step strategy

One may first wonder whether our main hypothesis (i.e. fixing the compartment relaxation characteristics to identical values across all brain regions and tissues) is valid in the adult brain. Indeed, when we applied a voxel-wise fitting to calibrating datasets, $T1_c$ and $T2_c$ did not reveal any regional dependence across voxels, and their distributions showed mean values close to those identified with calibration. Furthermore differences in MWF values across methods were rather low (<3%). Thus local variations in $T1_c$ and $T2_c$ were not expected to dramatically vitiate our results in adults.

At the calibration stage, the initial search intervals for $T1_c$ and $T2_c$ were selected based on literature evidence [Deoni et al., 2013; Guo et al., 2012; Lancaster et al., 2003; MacKay et al., 2006], and identified values were in agreement with reported values [Does and Gore, 2002; Guo et al., 2012; Lancaster et al., 2003; Laule et al., 2008]. Before applying $T1_c$ and $T2_c$ characteristics to testing datasets, we checked that their calibration was stable by 1) showing that all calibration datasets had enough sampling points for robust estimation of the compartment characteristics; 2) verifying in simulations that the proposed calibration procedure resulted in reliable estimations of MWF values even in the presence of noise in relaxometry signals; 3) proving that fixing these characteristics and down-sampling the calibration datasets did not change the generated MWF maps. Experiments with simulated data further suggested that in the presence of noise, reliable calculation of MWF values was not possible on a voxel-wise level and required increased number of voxels used together to calibrate the compartment characteristics.

Comparison with other methods

With our approach, the calibration stage naturally required long acquisition (>35min) and post-processing times (up to 24 hours, without parallel computing). However, it should be performed only once for a given acquisition protocol (magnetic field, acquisition sequences, spatial resolution, etc.), and could be drastically accelerated using parallel computing. The main advantage of our approach is that, once the calibration is performed, MWF values can be computed over the whole brain within much shorter acquisition (~5 and 7min for fifty/seventy 1.8 mm slices in infants/adults correspondingly) and post-processing times (<5min) than in previous studies. Indeed, in conventional multicomponent relaxometry imaging studies [Whittall et al., 1997], acquisition time takes up to 15 min for 8–12 contiguous slices because estimation of the T2 spectrum requires acquisition of the relaxometry data with a large number of TE. Although alternative approaches using mcDESPOT protocol [Deoni et al., 2012] enable much shorter acquisition time (between 18 and 25 min for the age range between 3 and 67 postnatal months with a 1.8mm isotropic whole brain coverage on a 3T scanner, including B_0 and B_1 corrections [Deoni, 2011], or around 10-12 min without these corrections [Deoni et al., 2011]), these times remain longer than in our protocol and require rather long post-processing times (i.e. ~14 hours per subject [Deoni et al., 2013]).

Despite some exceptions [Akhondi-Asl et al., 2014;, Warntjes et al., 2011], our computed MWF values were generally higher than in previous studies of infants [Deoni et al., 2011; Lancaster et al., 2003] and adults [De Santis et al., 2014]. Simulations suggested that our strategy was reliable even in the presence of noise in relaxometry signals. Nevertheless, local variations in the biophysical tissue properties and hence, in $T1_c$ and $T2_c$ across voxels might have introduced some additional "physiological" noise, leading to slight overestimation of MWF values (indeed, MWF values from the calibration stage were slightly higher than voxel-wise MWF values). It should be noted that our model did not directly take into account the exchange between the different compartments: it only assumed that this exchange was fast relatively to T1 relaxation and slow relatively to T2 relaxation but it did not explicitly use exchange rate constants. Although these assumptions are generally true [Lancaster et al., 2003], ignoring exchange between compartments may also result in systematic bias [Deoni et al., 2013; Zhang et al., 2014]. However, including exchange through additional free parameters (exchange rate constants), would prevent the model to be linear, and our post-processing strategy would lose in reliability

and speed. B_0 and B_1 field inhomogeneities were also shown to lead to errors in MWF calculations when using mcDESPOT protocols [Deoni, 2011]. Here their effects were believed to be negligible [Zhang et al., 2014] since we used EPI sequences.

Besides, our potential bias in MWF values may arise from the stochastic fitting strategy that we used during calibration. Actually, in white matter structures, voxel-wise region contraction approach tend to assign MWF values to the upper part of the initial search interval, and the corresponding $T2_{my}$ values to the lower part of the initial search interval [Zhang et al., 2014]. Thus the initially selected search interval for f_{my} may have a considerable impact on MWF values derived from the relaxometry model based on mcDESPOT protocol. In our strategy, the upper boundary for f_{my} was set to 0.4, and we also observed a strong impact on MWF maps when this boundary was changed to 0.3 or 0.5: higher upper boundaries resulted in higher MWF values, and the 0.4 boundary provided the highest similarity in MWF distributions across the 3 subjects while the compartment relaxation characteristics were stable. These observations pointed out the main limitation of the present approach and possibly of other approaches using stochastic model fitting, meaning that MWF values are highly dependent on model fitting parameters. As a consequence, quantitative comparisons across studies remain difficult: MWF quantification strategies are very sensitive to acquisition and fitting settings, including field strength, phase rewinding, sampling schemes of the inversion- and echo-times, voxel size, repetition time of the acquisition protocol, regularization constants, etc. [Alonso-Ortiz et al., 2014; Guo et al., 2012; Kolind et al., 2009; Levesque et al., 2010].

Modeling both T1 and T2 relaxometry signals to measure MWF

As myelin-related compartment has rather fast relaxation characteristics (e.g. $T2_{my}$ ~ 20ms), robust estimation of its fraction from T2 spectrum requires to start TE sampling with small values [Kolind et al., 2009; MacKay et al., 1994; Whittall et al., 1997]. In this study, single-shot EPI sequences were used to keep the acquisition time as short as possible; then such short TE could not be achieved, mainly due to a long readout of the partial Fourier k-space (19). This means that even at the shortest TE, T2 relaxometry signal from myelin-related water was already strongly degraded. Consequently, estimating MWF values from T2 spectral analysis was not possible, and reliably fitting the 3-component model required to add information on T1 relaxation in order to reveal the contribution of myelin-water compartment. However, information from T2

relaxometry signal did help to separate intra-/extracellular water from CSF compartments. Thus in such experimental conditions, considering both T1 and T2 relaxometry signals was necessary. This may explain why MWF and T1 values were strongly correlated in all adult bundles, as in previous studies using mcDESPOT strategy [De Santis et al., 2014]. Note that this correlation may also be explained by the dramatic influence on T1 values of water compartmentalization and of macromolecules (large lipids and proteins) in the myelin sheath.

Is this approach valid for quantifying MWF in the developing or pathological brain?

Estimation of MWF in the infant brain through $T1_c$ and $T2_c$ calibration in the adult brain

In addition to hypothesis on $T1_c$ and $T2_c$ stability across brain tissues and regions, our testing stage in infants is based on the assumption that relaxation characteristics of the 3 compartments remain stable across different ages and that only compartment fractions are changing. Then compartment characteristics calibrated in adults can be applied to calculate MWF maps in infants and children. This assumption is implicitly used in MWF studies [Lancaster et al., 2003] as well as in multicomponent diffusion imaging studies [Kunz et al., 2014], but may not be strictly true as compartments may change their biophysical properties during development, thus probably affecting their relaxation characteristics. For example, increase in myelin compactness with maturation may shorten myelin-water relaxation characteristics; similarly, $T1_{ie}$ and $T2_{ie}$ values of the intra-/extra-cellular compartment may change with the development of intra-cellular cytoskeleton and microtubules.

However, investigating such age-related changes of the component relaxation characteristics in infants was beyond the scope of this study for several reasons. First, healthy infants cannot withstand long acquisition protocols without sedation, making voxel-wise MWF mapping and/or $T1_c$ and $T2_c$ calibration hardly achievable in infants. Second, even if calibration of these characteristics per age range was possible, it would not have much sense since maturation is not homogeneous across brain regions, i.e. certain regions will have more mature characteristics, while other regions will be less mature. Thus, such calibration will have the same drawbacks as calibration performed on adult subjects at the mature stage. The best approach would be to estimate $T1_c$ and $T2_c$ characteristics depending on the maturational stage. However, it's not achievable in practice as it would require defining maturational stages and making assumptions on region maturation, creating a vicious circle.

With our approach, we observed strong correlation between the infant MWF maps and those generated using an alternative approach based on age-range optimized mcDESPOT protocols [Dean et al., 2014; Deoni et al., 2012]. Nevertheless, differences in MWF values may come from the use of adult $T1_c$ and $T2_c$ characteristics to fit the model equations in infants. This limitation makes it difficult to compare our study with these previous studies that fit relaxometry signals voxel-wise to a 3-component model across all ages [Deoni et al., 2012]. Furthermore, the authors did not indicate whether $T1_c$ and $T2_c$ characteristics were stable across the life span. Finally, some correlations between MWF values, T1 and T2 (computed at the voxel level) were observed in infants. As both relaxation times do not exclusively reflect white matter myelination and change during different maturational processes [Dubois et al., 2014a], their correlations with MWF values are likely to be age-dependent [Deoni et al., 2012].

Modeling 3 compartments to measure MWF

In our model, the number of compartments was set to 3 because 3-component models were shown to be adequate under a wide range of different conditions, including developing white matter [Dean et al., 2014; Deoni et al., 2013; Deoni et al., 2015; Lancaster et al., 2003; Lancaster et al., 2005]. Although it is possible to quantify MWF using a 2-component model, 3-component models are thought to be more reliable, especially in regions of partial volume [Deoni et al., 2013]. Furthermore, consistent with a 3-pool model, T2 spectrum in both *in vitro* and *in vivo* experiments shows three major peaks [Andrews et al., 2005; Does and Gore, 2002; Menon and Allen, 1991; Vavasour, 1998; Wachowicz and Snyder, 2002]. If necessary, our model can be easily extended to a larger number of compartments at the expense of increased model fitting complexity due to additional free-parameters describing additional compartments. However, theoretical considerations suggest that there is no scope for deriving more than 2 or 3 components [Bertero et al., 1982] in healthy tissues.

The most reliable approach to estimate MWF without assumptions on the number of pools and their characteristics, is to calculate T2 spectrum [MacKay et al., 1994; Whittall et al., 1997]. However we could not apply this approach as reliable estimation requires acquisition of relaxometry signals for a large number of TE (making acquisition time unacceptably long for infants), including very short TE, which was not achievable with EPI sequences (see above). Simulations further suggested that in the presence of noise, using a 3-component model with

fixed $T1_c$ and $T2_c$ can significantly improve accuracy and reproducibility in determining the pool fractions as compared to T2 spectrum [Andrews et al., 2005].

Potential applications under pathological conditions

Although 3-component models have been previously applied to investigate pathologies [Deoni et al., 2013; Deoni et al., 2015; Du et al., 2007; Kwon et al., 2013; Lancaster et al., 2005; Raj et al., 2014], such as multiple sclerosis [Raj et al., 2014], autism [Deoni et al., 2015] and partial deletions of chromosome 18q [Lancaster et al., 2005], one should be careful when trying to apply the suggested approach to diseases. Indeed it may require including additional compartments (e.g., microvascular, tumor, inflammatory cells, gliosis, etc.) to account for pathological tissues [Guo et al., 2012]. Otherwise the results interpretation should be done cautiously. For example, in demyelinating diseases, gliotic tissue (tissue matrix that replaces myelin, being filled with water and macromolecules,) may be modeled as a separate compartment; if not it will likely contribute to the intra-/extracellular compartment which has the most similar properties to gliotic tissue among the 3 compartments. Consequently, applying the suggested approach to pathological conditions would require taking into account possible additional compartments specific to the pathology, and re-calibrating the model and the compartment relaxation characteristics in a few patients.

In conclusion, our MWF quantification strategy overcomes existing difficulties (long acquisition/post-processing times) that may limit its practical application in infants, children, and in clinical patients. Although reliable comparison with previous studies [Deoni et al., 2011; Deoni et al., 2012] is not achievable, our infant MWF maps were able to capture myelin-related changes across early development, suggesting that the proposed approach is relevant at least for evaluation of normal maturation.

Acknowledgements

The authors thank the UNIACT clinical team for precious help in scanning the infants, and especially Gaëlle Mediouni. This work was supported by the Fyssen Foundation, the ELA Foundation, the “Ecole des Neurosciences de Paris”, the “Fondation de France”, and the French National Agency for Research (ANR). The finalization of this work received support from the European Union Seventh Framework Program (FP7/2007-2013, grant agreement n°604102).

References

Akhondi-Asl A, Afacan O, Mulkern RV, Warfield SK (2014): T2-Relaxometry for Myelin Water Fraction Extraction Using Wald Distribution and Extended Phase Graph. Med Image Comput Comput-Assist Interv 17:145–152.

Alonso-Ortiz E, Levesque IR, Pike GB (2014): MRI-based myelin water imaging: A technical review. Magn Reson Med. 73(1):70-81

Andrews T, Lancaster JL, Dodd SJ, Contreras-Sesvold C, Fox PT (2005): Testing the three-pool white matter model adapted for use with T2 relaxometry. Magn Reson Med 54:449–454.

Beaulieu C (2002): The basis of anisotropic water diffusion in the nervous system - a technical review. NMR Biomed 15:435–455.

Berger MF, Silverman HF (1991): Microphone array optimization by stochastic region contraction. IEEE Trans Signal Process 39:2377–2386.

Bernstein MA, King KF, Zhou XJ (2004): Handbook of MRI Pulse Sequences. Elsevier.

Bertero M, Boccacci P, Pike ER (1982): On the Recovery and Resolution of Exponential Relaxation Rates from Experimental Data: A Singular-Value Analysis of the Laplace Transform Inversion in the Presence of Noise. Proc R Soc Lond 383:15–29.

Bird CR, Hedberg M, Drayer BP, Keller PJ, Flom RA, Hodak JA (1989): MR assessment of myelination in infants and children: usefulness of marker sites. AJNR 10:731–740.

Bosnell R, Giorgio A, Johansen-Berg H (2008): Imaging white matter diffusion changes with development and recovery from brain injury. Dev Neurorehabil 11:174–186.

Dean DC 3rd, O'Muircheartaigh J, Dirks H, Waskiewicz N, Lehman K, Walker L, Han M, Deoni SCL (2014): Modeling healthy male white matter and myelin development: 3 through 60months of age. NeuroImage 84:742–752.

Deoni SCL, Mercure E, Blasi A, Gasston D, Thomson A, Johnson M, Williams SCR, Murphy DGM (2011): Mapping Infant Brain Myelination with Magnetic Resonance Imaging. J Neurosci 31:784–791.

Deoni SCL, Zinkstok JR, Daly E, Ecker C, MRC AIMS Consortium, Williams SCR, Murphy DGM (2015): White-matter relaxation time and myelin water fraction differences in young adults with autism. Psychol Med 45:795–805.

Deoni SCL (2011): Correction of Main and Transmit Magnetic Field (B0 and B1) Inhomogeneity Effects in Multicomponent-Driven Equilibrium Single-Pulse Observation of T1 and T2. Magn Reson Med 65:1021–1035.

Deoni SCL, Dean DC, O'Muircheartaigh J, Dirks H, Jerskey BA (2012): Investigating white matter development in infancy and early childhood using myelin water faction and relaxation time mapping. NeuroImage 63:1038–1053.

Deoni SCL, Matthews L, Kolind SH (2013): One component? Two components? Three? The effect of including a nonexchanging "free" water component in multicomponent driven equilibrium single pulse observation of T1 and T2. Magn Reson Med 70:147–54.

Deoni SCL, Rutt BK, Arun T, Pierpaoli C, Jones DK (2008): Gleaning multicomponent T_1 and T_2 information from steady-state imaging data. Magn Reson Med 60:1372–1387.

Descoteaux M, Angelino E, Fitzgibbons S, Deriche R (2007): Regularized, fast, and robust analytical Q-ball imaging. Magn Reson Med 58:497–510.

Does MD, Gore JC (2002): Compartmental study of T(1) and T(2) in rat brain and trigeminal nerve in vivo. Magn Reson Med 47:274–283.

Dubois J, Dehaene-Lambertz G, Kulikova S, Poupon C, Huppi P, Hertz-Pannier L (2014a): The early development of brain white matter: a review of imaging studies in fetuses, newborns and infants. Neuroscience 276:48-71.

Dubois J, Dehaene-Lambertz G, Perrin M, Mangin J-F, Cointepas Y, Duchesnay E, Le Bihan D, Hertz-Pannier L (2008): Asynchrony of the early maturation of white matter bundles in healthy infants: quantitative landmarks revealed noninvasively by diffusion tensor imaging. Hum Brain Mapp 29:14–27.

Dubois J, Kulikova S, Hertz-Pannier L, Mangin J-F, Dehaene-Lambertz G, Poupon C (2014b): Correction strategy for diffusion-weighted images corrupted with motion: Application to the DTI evaluation of infants' white matter. Magn Reson Imaging 32(8):981-992.

Duclap, Schmitt, Lebois, Riff, Guevara, Marrakchi-Kacem, Brion, Poupon, Poupon (2012): Connectomist-2.0: a novel diffusion analysis toolbox for BrainVISA European Society for Magnetic Resonance in Medicine and Biology. Lisbon, Portugal: Springer.

Du YP, Chu R, Hwang D, Brown MS, Kleinschmidt-DeMasters BK, Singel D, Simon JH (2007): Fast multislice mapping of the myelin water fraction using multicompartment analysis ofT2* decay at 3T: A preliminary postmortem study. Magn Reson Med 58:865–870.

Flechsig P (1920): Anatomie des menschlichen Gehirns und Rückenmarks auf myelogenetischer Grundlage. Leipzig: G. Thieme.

Gagunashvili ND (2006): Comparison of weighted and unweighted histograms. arXiv:physics/0605123. http://arxiv.org/abs/physics/0605123.

Guo J, Ji Q, Reddick WE (2012): Multi-slice myelin water imaging for practical clinical applications at 3.0 T. Magn Reson Med 70(3):813-822.

Hwang D, Du YP (2009): Improved myelin water quantification using spatially regularized non-negative least squares algorithm. J Magn Reson Imaging 30:203–208.

Hwang D, Kim D-H, Du YP (2010): In vivo multi-slice mapping of myelin water content using T2* decay. NeuroImage 52:198–204.

Kolind SH, Mädler B, Fischer S, Li DKB, MacKay AL (2009): Myelin water imaging: Implementation and development at 3.0T and comparison to 1.5T measurements. Magn Reson Med 62:106–115.

Kulikova S, Hertz-Pannier L, Dehaene-Lambertz G, Buzmakov A, Poupon C, Dubois J (2014): Multi-parametric evaluation of the white matter maturation. Brain Struct Funct. doi: 10.1007/s00429-014-0881-y

Kunz N, Zhang H, Vasung L, O'Brien KR, Assaf Y, Lazeyras F, Alexander DC, Hüppi PS (2014): Assessing white matter microstructure of the newborn with multi-shell diffusion MRI and biophysical compartment models. NeuroImage 96:288–299.

Kwon OI, Woo EJ, Du YP, Hwang D (2013): A tissue-relaxation-dependent neighboring method for robust mapping of the myelin water fraction. NeuroImage 74:12–21.

Labadie C, Lee J-H, Rooney WD, Jarchow S, Aubert-Frécon M, Springer CS, Möller HE (2013): Myelin water mapping by spatially regularized longitudinal relaxographic imaging at high magnetic fields. Magn Reson Med 71(1):375-387.

Lancaster JL, Andrews T, Hardies LJ, Dodd S, Fox PT (2003): Three-pool model of white matter. J Magn Reson Imaging 17:1–10.

Lancaster JL, Cody JD, Andrews T, Hardies LJ, Hale DE, Fox PT (2005): Myelination in children with partial deletions of chromosome 18q. AJNR 26:447–454.

Laule C, Kozlowski P, Leung E, Li DKB, MacKay AL, Moore GRW (2008): Myelin water imaging of multiple sclerosis at 7 T: Correlations with histopathology. NeuroImage 40:1575–1580.

Laule C, Vavasour IM, Moore GRW, Oger J, Li DKB, Paty DW, MacKay AL (2004): Water content and myelin water fraction in multiple sclerosis. J Neurol 251:284–293.

Lawson CL, Hanson RJ (1987): Solving Least Squares Problems. Philadelphia, Pa.: Society for Industrial and Applied Mathematics.

Levesque IR, Chia CLL, Pike GB (2010): Reproducibility of in vivo magnetic resonance imaging-based measurement of myelin water. J Magn Reson Imaging 32:60–68.

MacKay A, Laule C, Vavasour I, Bjarnason T, Kolind S, Mädler B (2006): Insights into brain microstructure from the T2 distribution. Magn Reson Imaging 24:515–525.

MacKay A, Whittall K, Adler J, Li D, Paty D, Graeb D (1994): In vivo visualization of myelin water in brain by magnetic resonance. Magn Reson Med 31:673–677.

Mädler B, Drabycz SA, Kolind SH, Whittall KP, MacKay AL (2008): Is diffusion anisotropy an accurate monitor of myelination? Magn Reson Imaging 26:874–888.

Menon RS, Allen PS (1991): Application of continuous relaxation time distributions to the fitting of data from model systmes and excised tissue. Magn Reson Med 20:214–227.

Oh J, Han ET, Pelletier D, Nelson SJ (2006): Measurement of in vivo multi-component T2 relaxation times for brain tissue using multi-slice T2 prep at 1.5 and 3 T. Magn Reson Imaging 24:33–43.

Perrin M, Poupon C, Cointepas Y, Rieul B, Golestani N, Pallier C, Rivière D, Constantinesco A, Le Bihan D, Mangin JF (2005): Fiber tracking in q-ball fields using regularized particle trajectories. Inf Process Med Imaging 19:52–63.

Poupon C, Dubois J, Marrakchi L, Brion V, Mangin J-F, Poupon F (2010): Real-time EPI T1, T2 and T2* mapping at 3T. Proc 18th Annu ISMRM Meet.

Raj A, Pandya S, Shen X, LoCastro E, Nguyen TD, Gauthier SA (2014): Multi-Compartment T2 Relaxometry Using a Spatially Constrained Multi-Gaussian Model. PLoS ONE 9:e98391.

De Santis S, Drakesmith M, Bells S, Assaf Y, Jones DK (2014): Why diffusion tensor MRI does well only some of the time: variance and covariance of white matter tissue microstructure attributes in the living human brain. NeuroImage 89:35–44.

Smith SW (1997): The scientist and engineer's guide to digital signal processing 1st ed. San Diego, Calif: California Technical Pub.

Staudt M, Schropp C, Staudt F, Obletter N, Bise K, Breit A, Weinmann HM (1994): MRI assessment of myelination: an age standardization. Pediatr Radiol 24:122–127.

Stikov N, Perry LM, Mezer A, Rykhlevskaia E, Wandell BA, Pauly JM, Dougherty RF (2011): Bound pool fractions complement diffusion measures to describe white matter micro and macrostructure. NeuroImage 54:1112–1121.

Vavasour IM (1998): Magnetic resonance of human and bovine brain. Dissertation, Univ. of British Columbia

Wachowicz K, Snyder R (2002): A look at the transverse relaxation spectra of mammalian optic nerve at 3.0 T and 11.7 T. in Proc 10th Annu ISMRM Meet.

Warntjes J, West J, Dahlqvist-Leinhard O, Helms G, Landtblom A-M, Lundberg P (2011): Using multi-parametric quantitative MRI to model myelin in the brain. In: Proc 19th Annual ISMRM Meet., p 536.

Whittall KP, MacKay AL, Graeb DA, Nugent RA, Li DK, Paty DW (1997): In vivo measurement of T2 distributions and water contents in normal human brain. Magn Reson Med 37:34–43.

Zhang J, Kolind SH, Laule C, Mackay AL (2014): Comparison of myelin water fraction from multiecho T2 decay curve and steady-state methods. Magn Reson Med 73 (1):223-232.

Supplementary Figure 1. Comparison of MWF maps generated at the calibration stage and with voxel-wise model fitting.

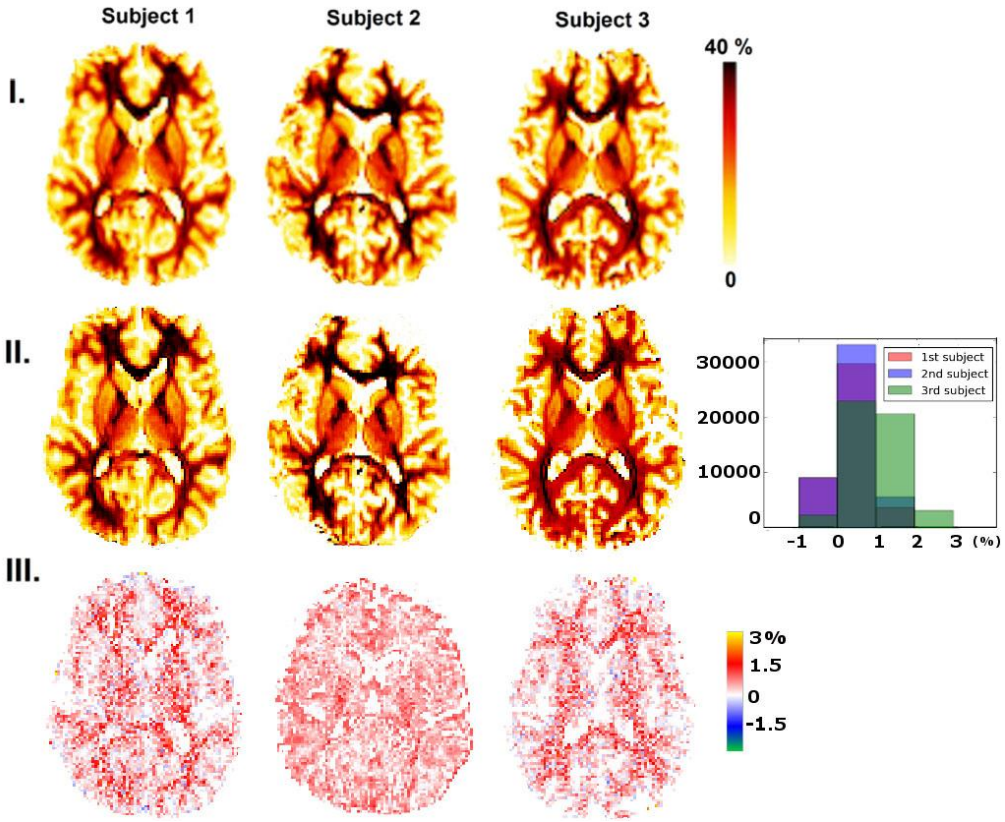

For the 3 calibration subjects, MWF maps generated using voxel-wise model fitting (II) were quite noisier than MWF maps generated at the calibration stage (I), despite the high number of TI and TE sampling points. MWF values from the calibration tended to be higher (see difference between these maps in III). Nevertheless, differences did not exceed 3% (histogram), and few regional dependence was observed on the difference maps (III).

Supplementary Figure 2. Impact of the upper search boundary for f_{my} on MWF values.

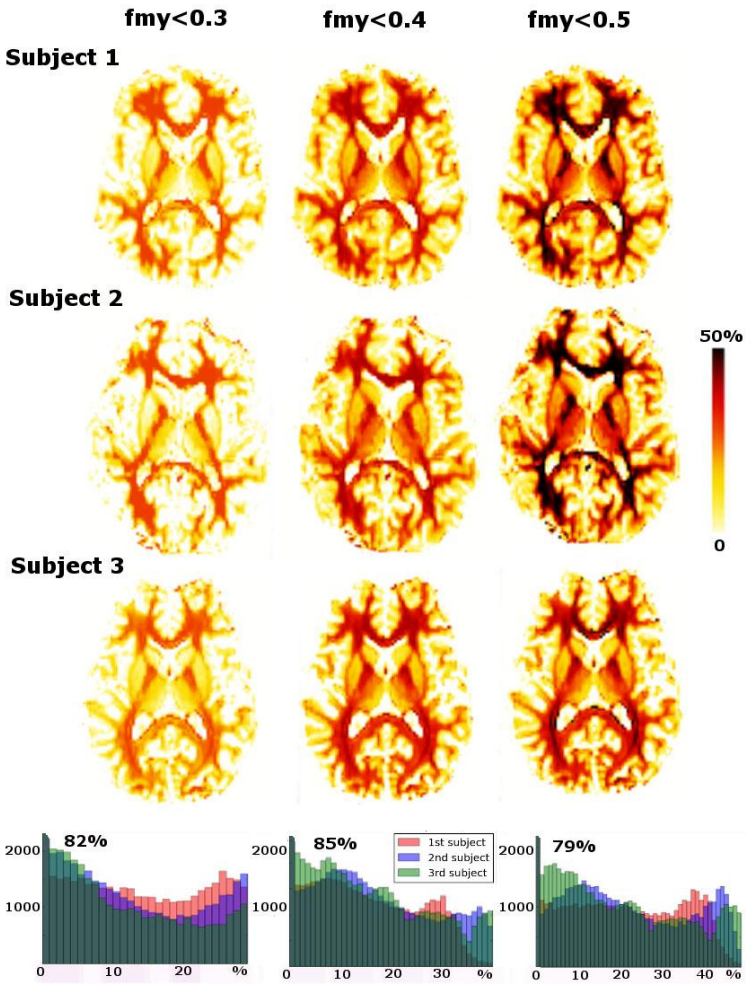

With the calibration strategy and for the 3 subjects, MWF maps were compared for independent calibrations performed with different upper boundary for f_{my} (0.3, 0.4 and 0.5). Although the compartment relaxation characteristics were similar (Supplementary Table 1), higher boundary for f_{my} led to higher MWF values, confirming a considerable impact on resulting MWF maps. In the bottom row, histograms show MWF distributions across all voxels for the 3 subjects. The percentages of common histogram area across the 3 subjects (82%, 85%, 79% for f_{my} equal to 0.3, 0.4 and 0.5 respectively) suggested that the upper boundary of 0.4 enabled the biggest overlap, and thus the highest reproducibility across subjects.

Supplementary Figure 3. Impact of the number of calibration data points on the resulting $T1_c$ and $T2_c$ characteristics.

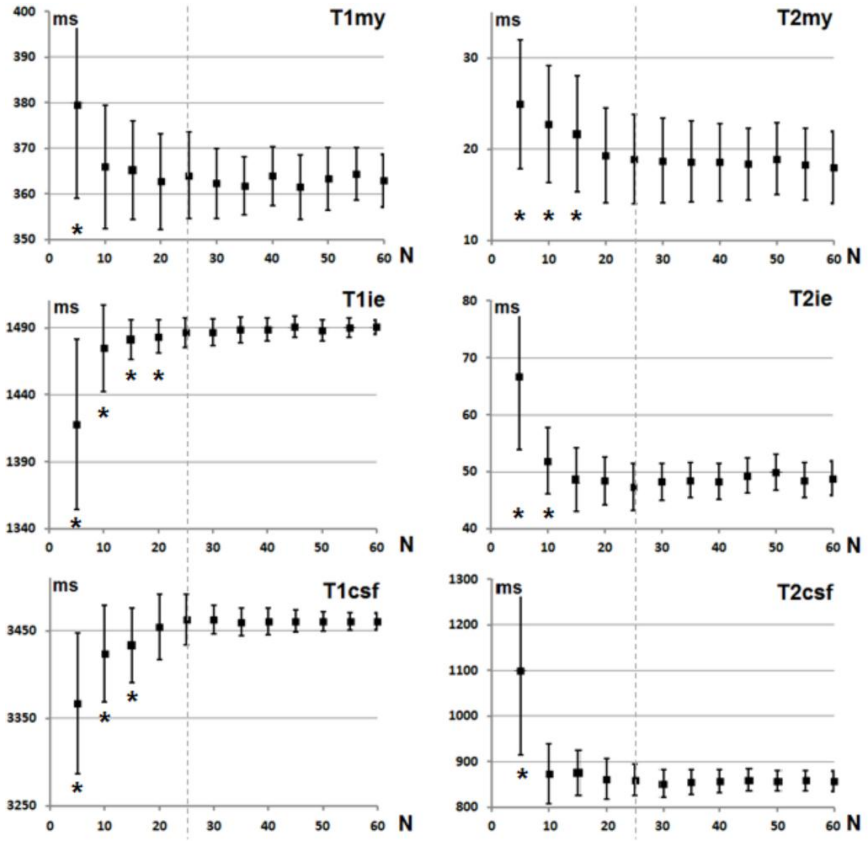

For subject #3, $T1_c$ and $T2_c$ values of the 3-component model were calculated with the calibration strategy using various numbers N of TI and TE sampling points (mean ± std over the 10 central slices). When this number was higher than 25, $T1_c$ and $T2_c$ values did not significantly differ from those calculated with N=60 (ad-hoc paired t-test between the values from individual slices, * indicates significant difference where $p<0.05$).

Supplementary Table 1

$T1_c$ and $T2_c$ compartment relaxation characteristics obtained with the calibration strategy for different upper search boundary for f_{my}.

Mean and standard deviations are computed over the 10 slices of the 3 subjects. Note that T1c and T2c values are roughly the same, while standard deviations tend to be the lowest for the 0.4 upper boundary.

	$f_{my} < 0.3$	$f_{my} < 0.4$	$f_{my} < 0.5$
$T2_{my}$(ms)	21±10	18±5	18±4
$T2_{ie}$(ms)	59±9	52±6	48±6
$T2_{csf}$(ms)	885±49	858±47	848±62
$T1_{my}$(ms)	359±16	357±21	321±21
$T1_{ie}$(ms)	1325±150	1481±17	1426±46
$T1_{csf}$(ms)	3203±210	3441±36	3403±75

A NOVEL APPROACH FOR FAST MWF QUANTIFICATION

Kulikova S[1], Hertz-Pannier L[1], Dehaene-Lambertz G[2], Poupon C[3], Dubois J[2].

1. INSERM UMR663, CEA/Neurospin/UNIACT; 2. INSERM UMR992, CEA/Neurospin/UNICOG; 3. CEA/Neurospin/UNIRS.

ELA RESEARCH FOUNDATION # 3147

INTRODUCTION & OBJECTIVES

Myelin Water Fraction (MWF) is a new promising candidate for *in vivo* evaluation of the brain myelin content: it shows strong correlation with the myelin amount[1-2] and is a more direct measure than conventional MRI indices. MWF is defined as the fraction of water trapped by myelin sheaths and is derived from multicomponent analysis of the relaxation signals[3-5]. However, existing strategies for its calculation require long acquisition and/or post-processing times[3-5], limiting their practical applications especially in pediatric patients.

Thus, the goal of our work was to design a novel strategy for MWF quantification with reasonable acquisition and post-processing times.

METHODS & MATERIALS

Model (adapted from Lancaster et al. [6]):

3 components: myelin-related water, intra/extra-cellular water, cerebro-spinal fluid

$$\begin{cases} \sum_{c=1}^{3} f_c = 1, \quad f_c \in [0,1]; \\ S_{T1}(TI_m) = S_0\left(1 - 2exp\left(-TI_m/T1\right)\right), m = 1..N_{TI}; \\ 1/T1 = \sum_{c=1}^{3} f_c/T1_c; \\ S_{T2}(TE_k) = S_0 \sum_{c=1}^{3} f_c exp\left(-TE_k/T2_c\right), k = 1..N_{TE}; \end{cases}$$

- f_c - component fractions;
- $T1_c$ and $T2_c$ - relaxation times associated with each component;
- S_{T1} - T1 relaxation signal measured for N_{TI} inversion times TI_m;
- S_{T2} - T2 relaxation signal measured for N_{TE} echo times TE_k.

Subjects and Data Acquisition:

3T MRI system , Siemens Trio
T1 and T2 relaxation signals:
EPI single-shot spin-echo sequences
1.8mm isotropic resolution

	Datasets	
	Calibration	*Testing*
Subjects	3 healthy adults 23.2 ± 2 years	18 healthy infants 3 - 34 weeks
T1	30-60 TI values 100 - 3100 ms	8 TI values 250 - 2500ms
T2	30-60 TE values 30 - 350 ms	8 TE values 50 - 260ms
Acq. Time	~ 1h	< 6 min

Calculation of the MWF maps using a 2-step approach:

1. Calibration of the $T1_c$ and $T2_c$ values for each model component (~24 h) was done using an original combination of a region contraction approach and a non-negative least-square (NNLS) algorithm (Fig.1).

2. Calculation of the MWF maps in testing datasets (<5 min) was done after fixing the calibrated $T1_c$ and $T2_c$ values (thus, reducing the task to solving a set of linear equations) by fitting the model using a standard NNLS algorithm.

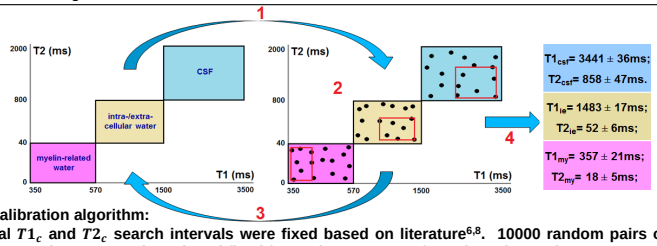

Fig.1 Calibration algorithm:

1. Initial $T1_c$ and $T2_c$ search intervals were fixed based on literature[6,8]. 10000 random pairs of $T1_c$ and $T2_c$ values were selected and fixed for each component from these intervals.
2. The model was fitted using an NNLS algorithm . 100 best solutions (with the smallest fitting errors) were used to define new search intervals (contraction).
3. Steps 1 and 2 were repeated until the search intervals and the fitting errors were not less than 1%.
4. Resulting values were weighted averages (with inversed fitting errors) from calibration datasets.

RESULTS & CONCLUSIONS

1) Fixing the calibrated $T1_c$ and $T2_c$ values and reducing the number of data points in the calibration datasets (TEs and TIs as in testing datasets) did not significantly change (average difference = 0.8 ± 0.2%) the corresponding MWF maps (Fig.2), showing that these values can be applied in testing datasets.

2) In infants, MWF maps showed progressive myelination of the white matter across early development (Fig.3)[7] and were in qualitative agreement with previous studies[8-9]. Quantitative comparison remains difficult because MWF quantification is very sensitive to acquisition and fitting parameters[10].

The suggested approach allows fast MWF mapping in datasets with a limited number of measurements, for instance in infants within 5 min acquisition and 6 min post-processing times.

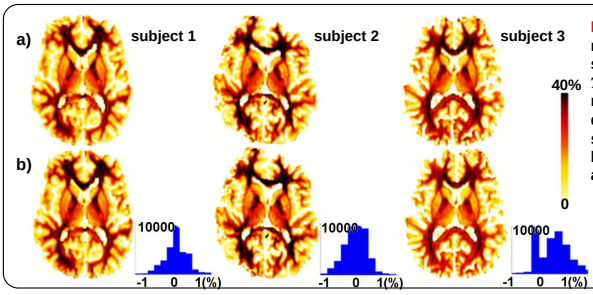

Fig.2 a) Calibration MWF maps b) MWF maps in the same subjects after fixing $T1_c$ and $T2_c$ values and reducing the number of data points. Histograms showing the difference between MWF maps in (a) and (b)

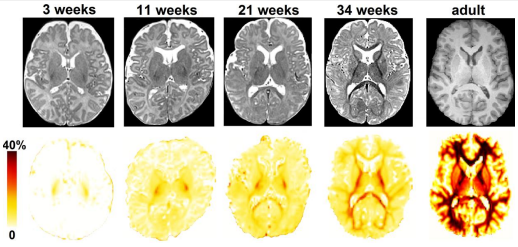

Fig.3 MWF maps and the corresponding anatomical images (T2w for infants; T1w for adult) in infants at different ages and in an adult.

References: 1. Laule et al. (Mult.Scler, 2006); 2 Webb et al. (Magn Reson Med, 2003); 3. Mackay et al. (Magn Reson Med, 1994); 4 Whittal et al (Magn Reson Med, 1997); 5. Deoni et al. (Magn Reson Med, 2012); 6. Lancaster et al. (JMRI, 2003); 6. Guo et al. (Magn Reson Med, 2012); 7. Kulikova et al. (ISMRM 2014, # 1743); 8. Deoni et al. (J Neurosci, 2011); 9. Deoni et al. (NeuroImage, 2012); 10. Levesque et al. (JMRI, 2010).

WHAT NEW DO WE LEARN WITH MYELIN WATER FRACTION IN INFANT WHITE MATTER BUNDLES IN COMPARISON WITH OTHER MRI PARAMETERS?

Kulikova S[1], Hertz-Pannier L[1], Dehaene-Lambertz G[2], Poupon C[3], Dubois J[2].

1. INSERM UMR663, CEA/Neurospin/UNIACT; 2. INSERM UMR992, CEA/Neurospin/UNICOG; 3. CEA/Neurospin/UNIRS.

INTRODUCTION & OBJECTIVES

Myelination is a crucial process for maturation and maintenance of the brain white matter. It starts late in the fetal development and continues until adolescence in an asynchronous manner across different cerebral regions[1]. *In vivo* myelination can be accessed using conventional MRI and DTI parameters[2-5]; however, they provide only indirect measures of the myelin content and are influenced by other tissue properties. The goal of this study was to describe myelination asynchrony in infants across different white matter bundles using Myelin Water Fraction (MWF), a novel MRI parameter for quantifying brain myelin content, and compare it with other MRI parameters (quantitative relaxation times and DTI parameters).

METHODS & MATERIALS

Subjects and Data Acquisition:

- 17 healthy infants (age: 3 - 21 weeks)
- 13 adults (mean age: 22.4 ± 1.6 years)
- 3T MRI system , Siemens Trio
- EPI single-shot spin-echo (SE) sequences (1.8mm isotropic resolution):

  qT1: 6 TI values = 250→1500ms, each step 250ms + TI=2000; 2500ms,

  qT2: 8 TE values = 50 → 260ms, each step 30ms ,

  DTI: 30 orientations of diffusion gradients, b=700s/mm ^{2}.

Post-treatment of the data:

- Quantitative maps for qT1, qT2 and DTI parameters (FA, <D>, $\lambda_{\parallel}$ and $\lambda_{\perp}$) were generated using Connectomist software[6].
- MWF maps were computed using multicomponent analysis of T1 and T2 relaxation signals adapted for infants[7].
- 18 different white matter bundles were reconstructed in each subject using 3D tractography[8] and manually delineated regions of interest[9].
- All parameters were quantified, averaged over the bundle length and normalized by the corresponding mean values from the adult group.

Comparison of the bundle maturation:

For each normalized parameter, bundles were pairwise compared over the infants group using paired t-test (significance level 0.95) and ordered according to their relative degree of maturation. The resulting orders were compared across the parameters in terms of:

1) number of discriminated relationships between the bundles;
2) agreement with 5 *a priori* known relationships[1,10-11] :
   - early maturation of STT, CST and OR;
   - delayed maturation of ALIC and AF.

Abbreviations:

Projection bundles: cortico-spinal tract CST (inf – inferior, mid – middle, sup - superior portions), spino-thalamic tract STT, optic radiations OR, anterior limb of the internal capsule ALIC;

Association bundles: external capsule EC, arcuate fasciculus AF, superior SLF and inferior ILF longitudinal fascicles, uncinate fasciculus UF, fronto-occipital fasciculus FOF;

Limbic and Commissural bundles: fornix FX, inferior CGinf and superior CGsup parts of the cingulum;bundles: genu CCg, body CCb and splenium CCs of the corpus callosum.

References: 1. Yakovlev, Lecours (1967); 2. Dubois et al. (HBM, 2008) ; 3. Deoni et al. (NeuroImage, 2013); 4. Nossin-Manor et al. (NeuroImage, 2012); 5. Dubois et al. (Neurosci, 2014); 6. Duclap et al. (ESMRMB 2012, #842); 7. Kulikova et al. (ISMRM 2014, #3147); 8. Perrin et al. (Inf. Process Med Imaging ProcConf, 2005); 9. Huang et al. (MagnReson Med, 2004); 10. Paus et al. (Science, 1999); 11. Zhang et al. (NeuroImage, 2007); 12. De Santis et al. (NeuroImage, 2014).

RESULTS & CONCLUSIONS

1) In adults, MWF values were highly variable across the bundles (Fig.1b) and negatively correlated with qT1 (R^2 > 0.94) coherently with the literature[12].

2) In infants, normalized MWF increased with age in all bundles in an asynchronous manner (Fig.1c): certain bundles (STT, CST, EC, FX, OR) showed higher ratios and faster increase than others (ALIC, AF, UF, CC).

3) Bundle ordering was more accurate for MWF than for other parameters, revealing more maturational relationships and not violating *a priori* relationships (Fig.2, Tab.1).

MWF seems to be more accurate than conventional MRI/DTI parameters for describing maturation of the white matter bundles in infants. Further comparisons with multiparametric models still need to be done.

Fig.1

a) Reconstructed white matter bundles

b) Distribution of the MWF values across the bundles in infants (light) and adults (dark)

c) Age-related changes of the infant MWF values for different bundles (in % of the mean adult values). Lines show significant linear regressions with age (R^2>0.58, p<0.015).

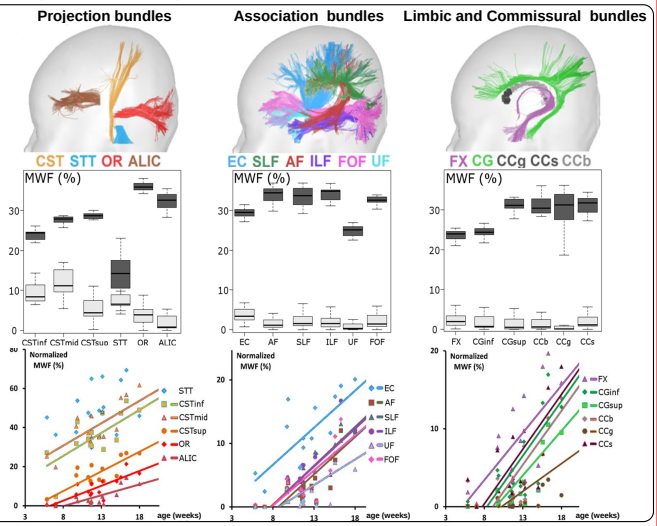

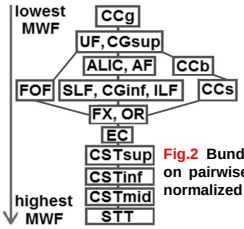

Fig.2 Bundle ordering based on pairwise comparisons of normalized MWF values.

	n	violations
MWF	129	no
qT1	90	yes
qT2	89	yes
FA	74	yes
$\langle D \rangle$	72	yes
$\lambda_{\parallel}$	76	no
$\lambda_{\perp}$	70	yes

Tab.1 Bundle ordering for different parameters: n - number of revealed relationships (out of 153), yes/no - violations of the known relationships.

Chapter 6

Investigating cerebral connectivity

In previous chapters, investigation of white matter regional maturation was performed in bundles reconstructed by tractography based on regions of interest (ROI) to select or to exclude certain fibers. However, as it was mentioned in chapter 2 of the part I, this approach is very time-consuming, imposes *a priori* assumptions on bundle locations and depends on the expert experience. Furthermore, this approach cannot be applied when it is not possible to perform reliable tractography, for example, in case of a severe demyelination, like the one observed in metachromatic leukodystrophy (see chapter 8). In such cases, analysis of tissue microstructure can be performed by projecting atlases of white matter bundles constructed from non-pathological brains to the subject data. However it is not adequate to project atlases generated from adult data to pediatric subjects due to non-homothetic brain growth and changes in fiber shapes and lengths during development. Thus, such analysis in pediatric patients should benefit from creation of dedicated bundle atlases from age-matched control groups.

In this chapter, we describe a preliminary age-specific bundle atlas for children aged 1 to 6 years, which was created in the frame of the study of children with metachromatic leukodystrophy (chapter 8), using a previously validated strategy [277]. This atlas was tested in children to demonstrate its potential for identifying bundles and studying white matter regional maturation. The chapter is organized as follows. First, description of the subjects and data acquisition will be given. Then, each step of the atlas creation will be described. Finally, the resulting atlas and evaluation age-related changes in MRI parameters across the reconstructed bundles will be presented. The results of this chapter were accepted for the ISMRM 23rd Annual Meeting (2015) [329] and the abstract is attached at the end of the chapter.

6.1 Subjects

Seventeen children (aged 47±20 months, min 17 months, max 81 months) with well-characterized focal epilepsy and fair psychomotor development have been considered for atlas creation (see Tab. 6.1 for details). These subjects were recruited

by french neuropediatricians (Hôpital Necker, Hôpital Robert-Debré Paris, CHU de Rennes, Lorient) as a control group for the study of children suffering from metachromatic leukodystrophy (promoted by Assistance Publique - Hôpitaux de Paris, protocol HCIT-MLD-P071232-IDRCB-2009-A00094-5, see chapter 8). In this study, it was not possible to include healthy children as it is exceptional to have them spontaneously asleep (without sedation) at the considered age range during a long MRI examination. Among considered subjects, 9 children were classified by a clinical expert (Lucie Hertz-Pannier) as having cryptogenic epilepsy. Eight other subjects had only tiny focal epileptogenic lesions at different locations (Tab. 6.1 and Fig. 6.1). Thus, under hypothesis that there are no (or only very subtle) pathological changes in the contra-lesional hemispheres, MRI parameters measured in these hemispheres may be viewed as "normal".

subject ID	age (months)	onset (months)	clinical EEG indications	MRI observations
ml130473	17	14	Right frontal	Right frontal, subcortical hypersignal on FLAIR image
mj110195*	18	1	Right temporal	Right superior temporal, visible on a T2w image
hm110219	25	15	Right temporal	Normal
lb110346	29	3	Left frontal	Left inferior frontal and insular (abnormal focal gyration)
kf110345	32	5	Right parieto-occipital	Normal
js110041	33	3	Right temporo-occipital	Right temporo-occipital, FCD, submitted to surgery
eg120436*	34	5	Right frontal	Right frontal, FCD, blurring on FLAIR image
tf140269	38	NA	Left temporo-occipital	Normal
am120196	47	Birth	Right fronto-central	Normal
cj140072*	48	NA	Left fronto-temporal	Left frontal opercular, abnormal focal gyration
lg130529	50	6	Left Occipital	Normal
em130462	64	30	Right frontal	Right frontal medial, FCD visible on FLAIR
nh140021	65	24	Right temporal	Normal
np140050	68	6	Right tempo-parietal	Normal
mh140270	70	9	Right frontal	Normal
eh120378	72	7	Left frontal	Left inferior frontal, focal abnormal gyration
am130535*	81	12	Right tempo-parietal	Normal appearance

Table 6.1: Subject details. FCD - focal cortical dysplasia. * - delay in language acquisition.

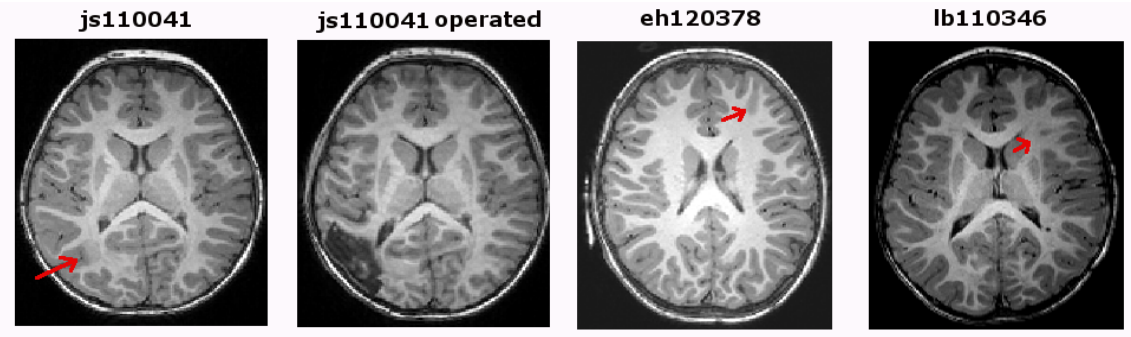

Figure 6.1: Examples of focal epileptogenic lesions (red arrows) localized on T1w images. For subject js110041 a post-surgery image is also given.

6.2 Data acquisition

MRI data was acquired on a 3T system (Tim Trio, Siemens Medical Systems, Erlangen, Germany), equipped with a whole body gradient (40mT/m, 175T/m/s) and a 32-channel head coil. During 1 hour scanning, all children were sedated with chloral hydrate. The whole study acquisition protocol included:

- anatomical T1-weighted image, acquired using a 3-D fast gradient recovery sequence (MPRage, TE/TI/TR = 4.18/900/2300 ms, parallel imaging GRAPPA reduction factor 2, partial Fourier sampling factor 7/8). Sagittal slices were acquired with a 1mm isotropic resolution (FOV = 256 mm; acquisition matrix = 256×256, no interpolation at reconstruction; 176 slices). For lesion localization, conventional anatomical images were also acquired using TIR and FLAIR sequences.

- diffusion-weighted images, acquired with a 2mm isotropic resolution using a single shot DW-SE-EPI sequence: 60 orientations of diffusion gradients, b = $1500 s/mm^2$ (+3b = 0), TE = 92ms, TR = 11s, parallel imaging GRAPPA reduction factor 2, partial Fourier sampling factor 6/8.

- T1 relaxometry data, acquired using an inversion recovery (IR) SE-EPI sequence at 8 different inversion times (TI=250->1500ms, each step=250ms, +TI=2000,2500ms): TE=35ms, TR=16s, 2mm isotropic resolution.

- T2 relaxometry data, acquired using a SE-EPI sequence at 8 different echo times (TE=35->280ms, each step=35ms): TR=19s, parallel factor 2, 2mm isotropic resolution.

- spectroscopy data, acquired with CSI-SE sequence: 16x16 voxels, TE = 100ms (analyzed as a part of another work).

The study protocol was approved by the regional ethical committee for biomedical research and all parents gave written informed consents.

6.3 Data post-processing

DW images were corrected for motion and eddy currents artifacts [310] and co-registered with the anatomical T1w images using affine transformations. In each subject, a regularized 3D tractography [294] was performed according to a 6-order analytical Q-ball model [260]. All data pre- and post-processings were done using in-house developed PTK toolkit and Connectomist software [145, 316].

6.4 Atlas creation

Bundle atlas was created using a strategy similar to the one suggested by Guevara et al. [277]. This strategy includes several steps:

1. Creation of an age-specific anatomical T1-weighted template for subsequent image co-registration.

2. Hierarchical intra-subject fiber clustering in each individual subject.

3. Inter-subject clustering of the clusters obtained in all individual subjects at the previous stage.

4. Manual selection and labelling of the inter-subject clusters.

5. Adapting classification thresholds for automatic bundle labeling when the atlas is applied to new subjects.

Each of these steps is detailed below.

6.4.1 Age-specific anatomical template

As both inter-subject clustering during bundle creation and bundle labeling in new subjects should be performed in a common space, all tractography datasets should be transformed to a common reference frame. In the work of Guevara et al. [277] tractography datasets were transformed to the Talairach space using affine transformations estimated from the T1-weighted (T1w) images with anterior and posterior commissures landmarks. This step assumes that the distance between the commissures is proportional to the brain size and thus, such transformation would provide sufficient image co-registration across adult brains. However, in the developing brain, this hypothesis cannot stand due to non-homothetic growth of different brain regions. Thus, to ensure good co-registration of the DTI datasets from all subjects, we created a dedicated age-specific T1w anatomical template (Fig. 6.2) to base co-registration across subjects on information from the whole brain image. To create such an anatomical template, we took the 9 T1w anatomical images from the children classified as "cryptogenic epilepsy" and non-linearly normalized them using SPM8 to the T1-weighted template for 48-months children available from another group [321]. This template was selected because it was the closest to our population (mean age 47 months). After normalization, the T1w images were averaged to create the final template, which was later used as a reference.

6.4.2 Intra-subject fiber clustering

At this step, a robust hierarchical intra-subject fiber clustering was performed [276]. This clustering allows reducing the complexity of the tractography dataset from more than a million of fibers to a few thousands of fascicles composed of fibers having similar shapes and lengths. This procedure allows performing further processing steps that are not possible over the complete tractography datasets. Each of the generated fascicles is represented by a single fiber, called the centroid, which reflects the global geometry of the fascicle: each centroid is located in the center of the fascicle and minimizes the sum of the symmetrized mean closest point distances [277, 280, 330] to the fibers of that fascicle.

6.4.3 Inter-subject clustering

For this step, all clusters from all subjects were transformed to the template space using the affine transformations calculated between the T1w images of the individual subjects and the T1w age-specific anatomical template. Then, all centroids, generated at the previous step, from all 17 subjects, were pairwise compared using the maximum of the Euclidean distances between the corresponding points and were further hierarchically clustered [277]. Among the resulting clusters only those were kept that contained centroids from at least half of the subjects (9 subjects out of 17). Taking this into consideration and the fact that 9 children in our database had normal-appearing MRI images, while the others 8 children showed only tiny lesions differently spatially distributed across subjects, it seems rather unlikely that spurious or lesion-affected fibers were to be included in the atlas.

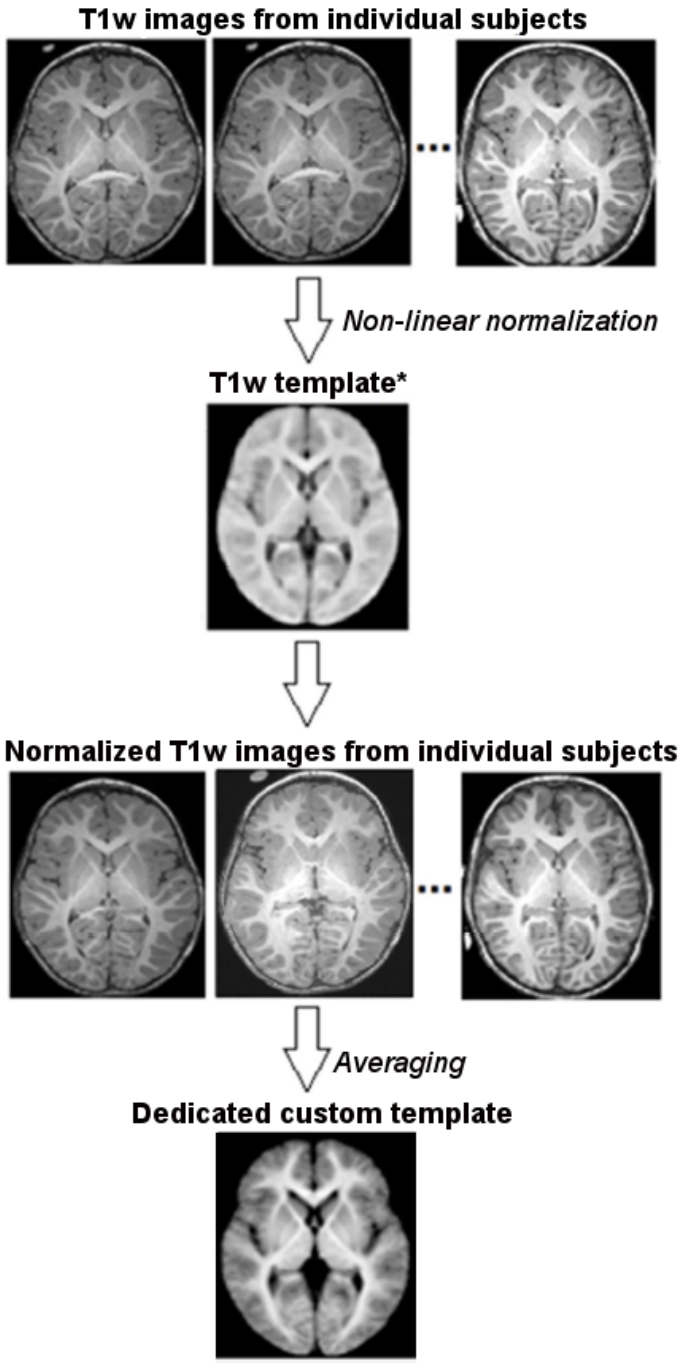

Figure 6.2: Creation of an age-specific anatomical template for children. T1-weighted template for non-linear normalization (*) was taken from [321] for 48-months children.

6.4.4 Clusters selection and labeling

Clusters generated at the previous stage were selected and labeled using manually delineated regions of selection and exclusion in the template space [269]. Alternatively, one can analyze each resulting cluster individually and assign it a particular label, but considering manually several thousands of clusters would be extremely time-consuming.

As a first step, we labeled the following 9 white matter bundles (Fig. 6.3):

- **projection bundles**: cortico-spinal tract CST;
- **association bundles**: arcuate fasciculus AF, superior SLF and inferior ILF longitudinal fascicles, uncinate fasciculus UF, fronto-occipital fasciculus FOF;
- **limbic bundles**: fornix FX, inferior CGinf and superior CGsup parts of the cingulum.

After clusters' selection was done, the extracted bundles were symmetrized, i.e. left and right parts of the bundles were flipped with respect to the brain midsagital plane and added to the atlas.

6.4.5 Adapting classification thresholds

The goal of the atlas is to be applied to analyze white matter microstructural properties within distinct bundles in various individuals. This can be done either by projecting the atlas to the subjects data when it is not possible to perform reliable tractography (see chapter 8) or by automatic bundle labeling based on tractography datasets. In a new subject, bundle labeling is performed following several steps:

1. intra-subject fiber clustering (see section 6.4.2);
2. calculation of cluster centroids and their transformation to the template space using affine transformations;
3. calculation of pairwise distances between each centroid from the new subject and each centroid of the atlas;
4. labelling each centroid of the new subject using a supervised classification based on the atlas labels, i.e. each centroid is labeled by the closest atlas centroid, assuming that the distance between them does not exceed a given threshold.

The thresholds, used at the last step, should be adapted for each bundle label independently because the variabilities of the bundles locations and compactness differ across different bundles. If for a given bundle this threshold is too small, that bundle will appear thinner than it should be or, in an extreme case, it will not be detected at all. On the contrary, if the threshold is too big, spurious fibers will be included.

Similar to Guevara et al. [277], these thresholds were adapted for each of the 9 bundles using a leave-5-out strategy. For that we considered 10 selections of 5 subjects and 10 corresponding atlases from the remaining 12 subjects, generated in the same manner as the atlas from all 17 subjects. These selections were made so that the mean age of the 12 subjects used for atlas creation was equal to the mean age of the complete dataset (47±20 months) (Tab. 6.4.5).

	atlas 1	atlas 2	atlas 3	atlas 4	atlas 5	atlas 6	atlas 7	atlas 8	atlas 9	atlas 10
am120196		+	+	+		+	+		+	+
am130535		+		+	+	+	+	+	+	
cj140072	+	+			+			+	+	+
eg120436	+		+	+	+	+	+	+		+
eh120378	+	+			+	+		+	+	+
em130462	+	+	+	+		+	+	+		+
hm110219	+	+	+	+		+	+	+	+	
js110041	+		+	+	+			+	+	+
kf110345				+	+		+		+	+
lb110346	+		+		+		+			
lg130529	+	+	+	+	+	+	+			+
mh140270	+	+	+		+	+	+		+	
mj110195	+	+	+		+	+		+	+	+
ml130473	+			+			+	+	+	+
nh140021		+	+	+	+	+	+	+		
np140050		+	+	+	+	+		+	+	+
tf140269	+	+	+	+		+	+	+	+	+

Table 6.2: Ten selections of 12 subjects that were used to create 10 testing atlases for adapting classification thresholds using a leave-5-out strategy.

Each of the 10 created testing atlases was used to perform bundles labeling in the corresponding 5 excluded subjects, using different classification thresholds. These thresholds were tested between 4mm (no clusters selected for any of the bundles) and 30mm (all bundles strongly contaminated by spurious fibers) with 1mm steps. For each threshold level and each bundle, we calculated the total number of correctly selected clusters in all 50 subjects (5 testing subjects x 10 selections) and the total number of false positives. For each of the 9 bundles, the final threshold was selected as the threshold maximizing the ratio between the total number of correctly selected clusters for that bundle and the corresponding total number of false positives (Tab. 6.3).

6.5 Resulting atlas and demonstration of its application for bundles identification

The generated atlas included 9 white matter bundles as shown in Fig. 6.3.

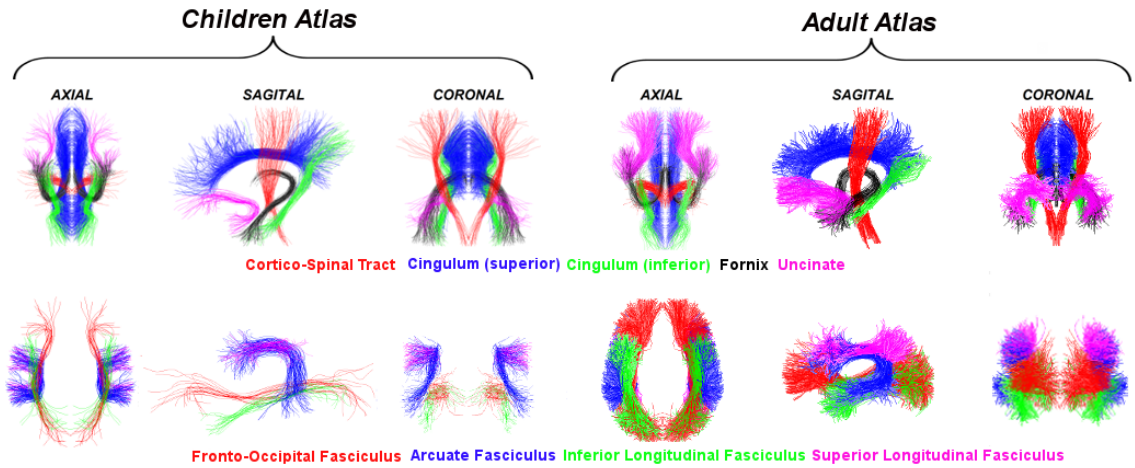

Figure 6.3: Comparison of white matter bundles (3 views) from the children atlas created in this study (left) and from the adult atlas taken from [277] (right).

Although looking similar, bundles in the children atlas appeared thinner than those of the adult atlas, probably due to higher variability of the bundle shapes in the children group resulting in fewer clusters consistent across the subjects. Thus, in cases when it is not possible to perform reliable tractography, projecting adult atlas to children data may include areas outside the bundles and thus, lead to bias in the analysis of bundles microstructural properties.

In half of the bundles, classification thresholds were close to those reported in the adult atlas [277] (Tab. 6.3). Identified thresholds higher than in the adult atlas, (e.g. for fronto-occipital fasciculus and inferior longitudinal fasciculus) may point to higher variability of the bundles' shapes in the children group (consequently, higher thresholds are required to detect bundles in all subjects during labelling), while smaller identified thresholds, (e.g. fornix) may be due to thinner bundles in children, which did not require the high thresholds necessary in adults.

bundle	CST	AF	SLF	ILF	UF	FOF	FX	CGsup	CGinf
current children atlas	**15**	**19**	16	**23**	17	**23**	15	**21**	**16**
adult atlas	14	18	17	18	17	20	20	17	14

Table 6.3: Classification thresholds (mm) identified for each bundle. For comparison, corresponding classification thresholds are given from the adult atlas [277]. Thresholds that were higher in children atlas are shown in bold.

Once this preliminary children atlas was created, it was applied to the 17 children for individual automatic labeling of the white matter bundles. In all subjects,

it allowed identification of all considered white matter bundles (Fig. 6.4 and 6.5), except for cingulum (inferior part missing in a subject of 50 months, superior part missing in a subject of 65 months), and fronto-occipital fasciculus (not detected in a subject of 48 months). The shapes of the reconstructed bundles were highly variable across the subjects, without any obvious relationship between shape and age. Nevertheless some artefacts were observed in individual reconstructions: reconstructed cortico-spinal tract also included fibers from spino-thalamic tract and reconstructed arcuate fasciculus included fibers from the extreme capsule. This suggests that using more shape-sensitive distance measures for fiber clustering may further improve the quality of bundle reconstruction.

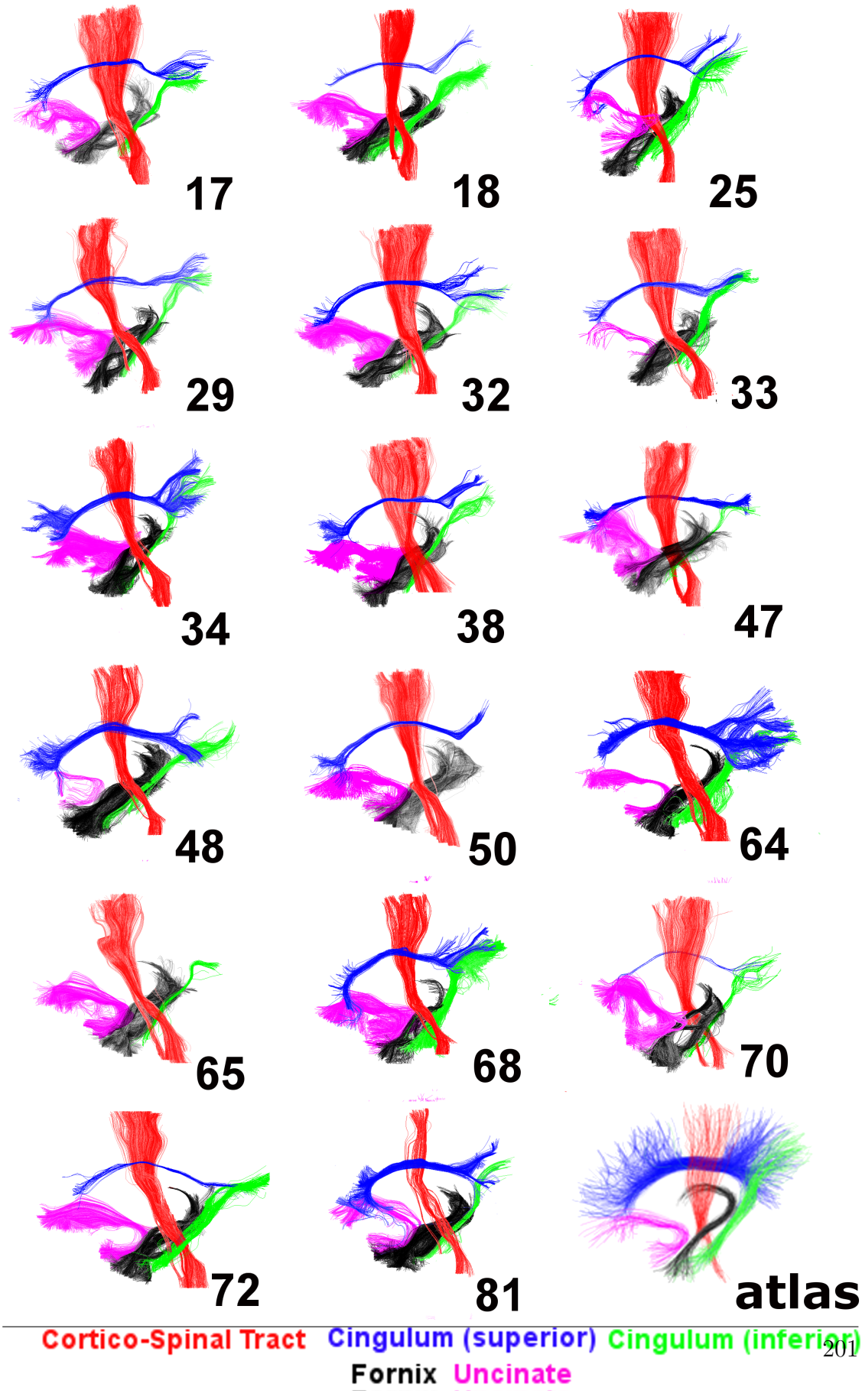

Figure 6.4: Bundles identified in all 17 children using the created atlas (bottom right). Numbers indicate children age in months.

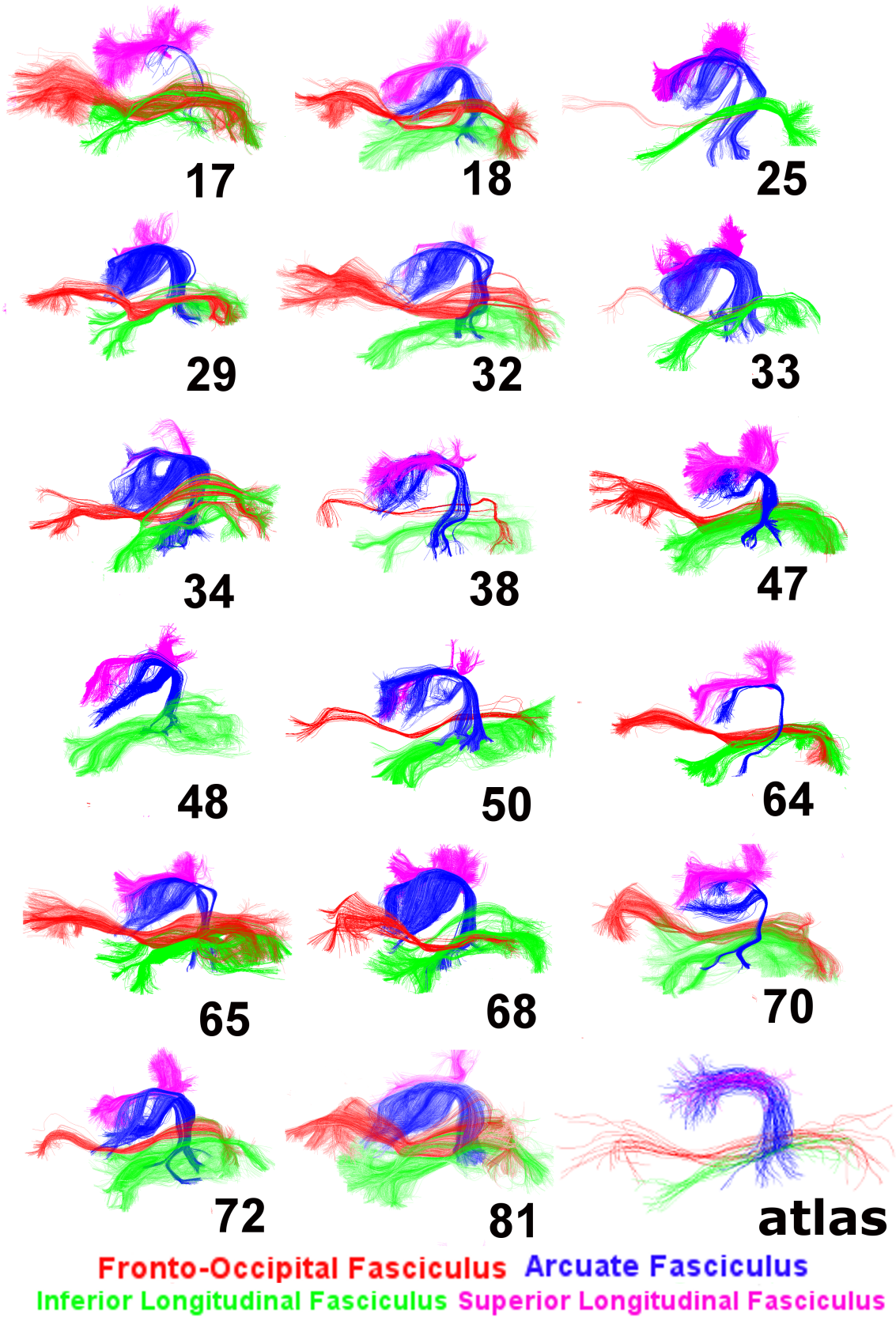

Figure 6.5: Bundles identified in all 17 children using the created atlas (bottom right). Numbers indicate children age in months.

6.6 Atlas application for evaluation of white matter maturation

At the current stage, this preliminary generated atlas could be already tested in children to investigate age-related changes in MRI parameters. This can be done either by projecting bundles of the atlas directly to the subjects data or by analyzing MRI parameters over the reconstructed bundles. It should be noted here that these two approaches are not identical. Results obtained using atlas projection will depend on normalization quality and if projected bundles pass outside the regions of subject bundles, the results will be biased: FA and MWF values will be underestimated, while diffusivities and relaxation times will be overestimated.

Here I used the reconstructed bundles from non-affected hemispheres to evaluate age-related changes in 6 MRI parameters described in previous chapters: quantitative qT1 and qT2 relaxation times; fractional anisotropy FA, mean $\langle D \rangle$, longitudinal $\lambda_{\parallel}$ and transverse $\lambda_{\perp}$ diffusivities computed from DTI.

Distributions of these parameters across the reconstructed bundles were in the range of previously reported values (Fig. 6.6) [127, 129, 135, 193].

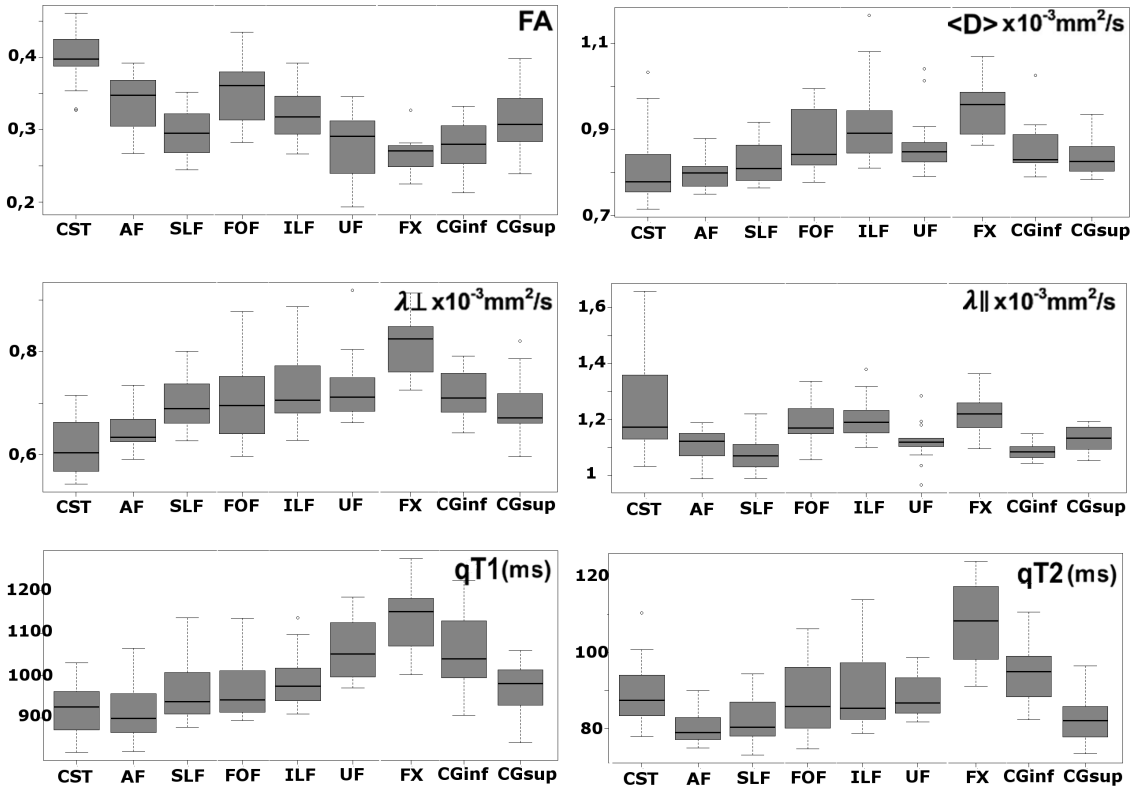

Figure 6.6: Distributions of MRI/DTI parameters across the reconstructed bundles.

As in this age range, MRI parameters show rapid exponential age-related changes [131, 193], they were further plotted as a function of age and fitted with exponents

(Fig. 6.7). Although the revealed changes showed rapid dynamics, none of the fits reached significance probably due to high intersubject variability.

To further test whether the parameters were increasing or decreasing with age, we considered the differences between children having the closest ages and tested (t-test) whether these differences were consistently positive or negative. With this strategy it was possible to confirm the following changes:

- qT2: decrease in arcuate and cingulum superior;
- qT1: decrease in arcuate, cingulum superior and superior longitudinal fasciculus;
- $\langle D \rangle$: decrease in arcuate and cingulum superior;
- $\lambda_{\parallel}$: decrease in arcuate and inferior longitudinal fasciculus;
- $\lambda_{\perp}$: decrease in all bundles.

Similar results could be obtained by comparing parameters from children younger than 47 months (the mean children age) with older children:

- qT2: lower in older children in arcuate and cingulum superior;
- qT1: lower in older children in cingulum superior;
- $\langle D \rangle$: lower in older children in arcuate and cingulum superior;
- $\lambda_{\parallel}$: lower in older children in arcuate and inferior longitudinal fasciculus;
- $\lambda_{\perp}$: lower in older children in arcuate, cingulum, cortico-spinal tract, and inferior longitudinal fasciculus.

These observations may point to late maturation of the arcuate fasciculus and superior cingulum.

Additionally, Myelin Water Fraction (MWF) was computed according to chapter 5 and evaluated in the reconstructed bundles. In agreement with previous studies [233, 321], MWF values increased non-linearly with age, reaching a plateau at the age of 3-5 years (Fig. 6.8). Between 3 and 60 months, the increase in MWF

could be modeled by the Gompertz function [321], which at high ages, near its plateau behaves as $a * (1 - b * e^{-c*age})$ (a,b,c are constants). Thus, the age-related changes in MWF values were further fitted with this function, which unlike conventional MRI parameters, provided very good fittings ($p<0.001$), suggesting that in this age range MWF was a more reliable measure of white matter maturation than diffusion and relaxometry MRI parameters.

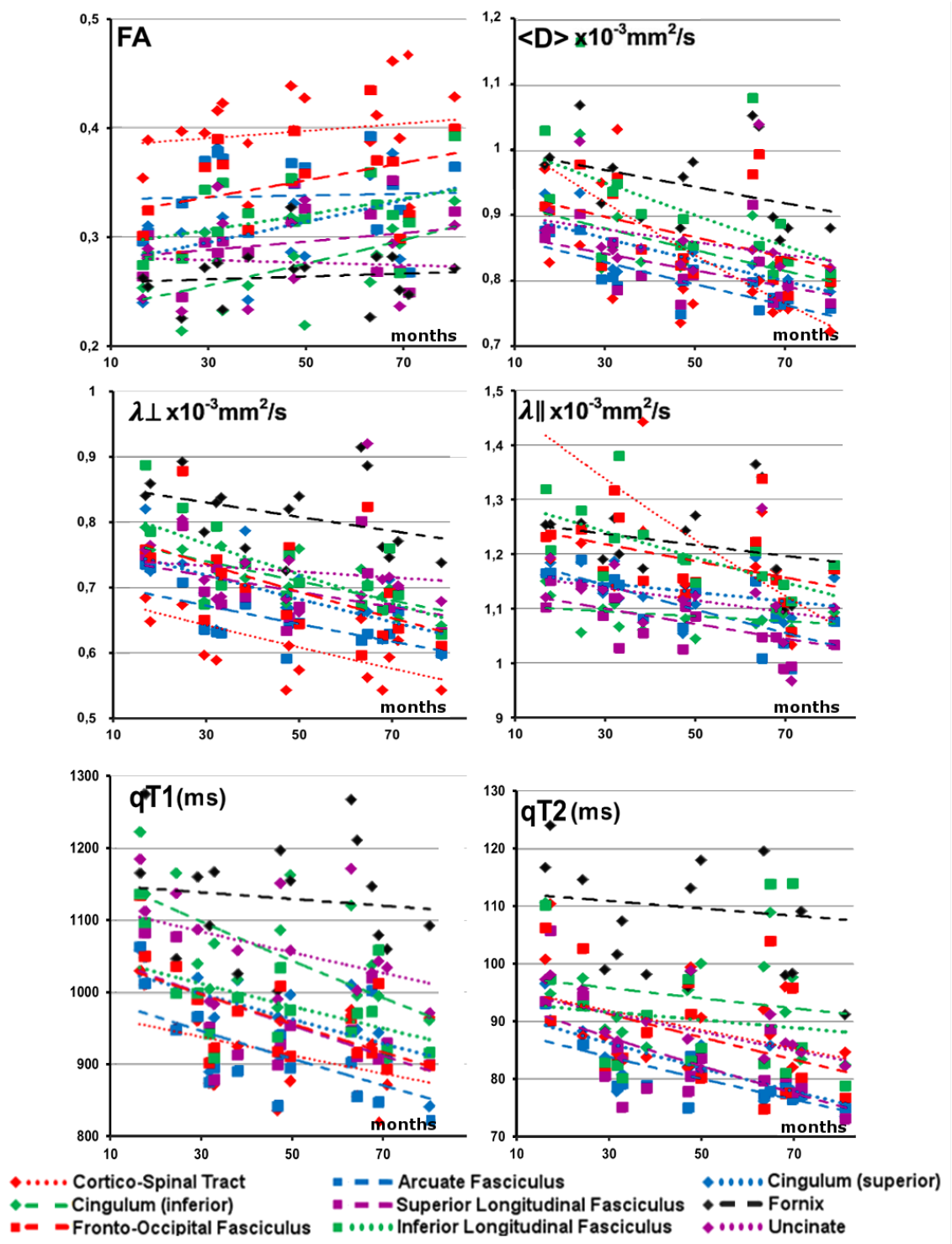

Figure 6.7: Age-related changes in MRI parameters across the identified bundles. Lines show exponential fits. FA increased with age, while other parameters decreased.

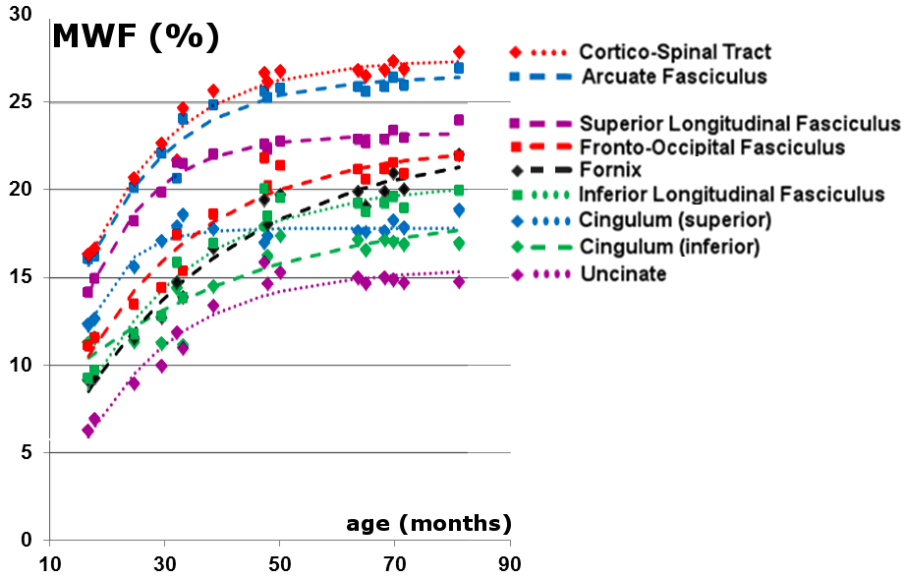

Figure 6.8: Non-linear age-related increases in MWF across the identified bundles: asymptotes are reached between 50 and 70 months. Lines show data fits ($p<0.001$) with the function $a * (1 - b * e^{-c*age})$, a,b,c - constants.

6.7 Conclusions and Future Work

In conclusion, the created atlas, even at its preliminary stage, demonstrated its potential for automatic bundles identification in preschool children and relevance for analyzing white matter microstructural properties. Thus, it opens a way to further studies of both normal and pathological brain regional development.

In the future, this atlas should be improved in several ways:

- it should be completed with other bundles, including at least the spinothalamic tract, the optic radiations, the anterior limb of the internal capsule, the external capsule, and the corpus callosum. In order to have good clustering and labelling results for bundles connecting thalamus and the cortex, it will be also necessary to add a mask of the thalamus to cut the fibers passing through it before clustering and labelling steps and avoid later extracting spurious fibers [277]. Alternatively, one may try to remove spurious fibers during labelling step by extracting only subparts of fibers that match bundles of the atlas.

- to better understand the developmental changes in bundles shapes, bundles identified using the created atlas should be compared with those that would be obtained by application of the adult atlas to the same data.

- the created atlas should be also tested for other age ranges (for example, in the infant population described in chapters 3-5) to understand the age limits within which the created atlas can provide reliable bundle labelling. Outside these limits, other age-specific atlases should be created.

- finally, it would be also interesting to test other distance measures for bundles comparison, for example, that would allow high variability at the bundles extremities but require high similarity in the central regions. Such distances may further improve the quality of bundles identification.

2494

Creating a child brain connectivity atlas for reliable bundle identification in developmental studies

Sofya Kulikova[1], Jessica Dubois[2], Pamela Guevara[3], Jean-François Mangin[4], Catherine Chiron[5], Nicole Chemaly[5], Silvia Napuri[6], Cyril Poupon[7], and Lucie Hertz-Pannier[1]

[1]*INSERM UMR1129, CEA/Neurospin/UNIACT, Université Paris Descartes, Sorbonne Paris Cité, Paris, France,* [2]*INSERM UMR992, CEA/Neurospin/UNICOG, Université Paris Sud, Paris, France,* [3]*University of Concepción/Departamento de Ingeniería Eléctrica, Chile,* [4]*CEA/Neurospin/UNATI, Gif-sur-Yvette, France,* [5]*INSERM UMR1129, Université Paris Descartes, Sorbonne Paris Cité, Paris, France,* [6]*Pediatric Department, CHU Hôpital Sud, Rennes, France,* [7]*CEA/Neurospin/UNIRS, Gif-sur-Yvette, France*

Target audience: This work would be of interest to neuroscientists and clinicians interested in brain development, for example in studies of normal or pathological maturation of the brain white matter within distinct bundles.

Introduction: Diffusion imaging offers a unique tool for *in vivo* visualization of the white matter bundles using 3D tractography techniques. Normal and abnormal brain regional maturation can be studied in reconstructed bundles using different MRI parameters that quantitatively reflect various maturation processes[1]. However, tractography datasets are extremely complex and extracting individual bundles from such datasets is still a challenging task. To reliably extract bundles and overcome drawbacks of using regions of interest (ROI), either defined manually in individual subjects or based on atlases, fiber-clustering techniques, that take into account fiber shape and localization variabilities, have been recently proposed for automatic bundles identification[2], based on an atlas of main bundles. However, this atlas was generated for adults hindering its application to children as fiber shapes and lengths change during development.

Purpose: Because reliable bundle identification in children requires dedicated atlases, we describe here the creation of the first atlas of this kind in preschool children.

Methods: *Subjects and Data Acquisition:* Seventeen children (47±20 months, 17 to 81 months) with unilateral focal epilepsy were considered: 9 subjects with normal MRI (cryptogenic epilepsy) and 8 with tiny focal lesions at different locations. It was not possible to include healthy children, as it is exceptional to have them spontaneously asleep for the whole acquisition time (50min) at the considered age range. Diffusion data was acquired under sedation on a 3T system with a 32-channel head coil using a DW-SE-EPI sequence: 2mm isotropic resolution, 60 orientations of diffusion gradients, b = 1500s/mm^2 (+ 3b = 0), TE = 92ms, TR = 11s, GRAPPA reduction factor 2. Anatomical T1w images were acquired using a 3-D MP RAGE sequence with 1mm isotropic resolution. *Post-treatment of the data*: Diffusion-weighted images were corrected for motion and eddy currents artifacts[3] and co-registered with the T1w images using affine transformations. Streamline-based regularized 3D tractography[4] was performed according to a 6-order analytical Q-ball model[5]. All data was pre- and post-processed using Connectomist software[6]. *Atlas creation*: Atlas was created using a strategy similar to Guevara et al.[2], with the following steps: a) creation of an age-specific anatomical T1 template (**Fig.1**). T1w images from the cryptogenic children were non-linearly registered to a T1w template for 48-month children[7] and averaged; b) hierarchical intra-subject fiber clustering in each individual subject[8]. Each cluster centroid minimizes the sum of the symmetrized mean closest point distances[2,8] to the fibers within that cluster; c) inter-subject clustering of the clusters obtained in all subjects. Among the resulting clusters only those were kept that included centroids from at least half of the subjects; d) manual selection and labeling of the inter-subject clusters (**Fig.2**); e) adapting classification thresholds for bundle labeling in new subjects using a leave-5-out strategy. The thresholds were selected as the values giving the maximum ratio between correctly selected clusters and false positives. *Atlas application*: Bundle identification in a new subject starts with an intra-subject fiber clustering and the calculated cluster centroids are transformed to the template space using affine transformations. Each centroid of the new subject is then labeled by the closest centroid of the atlas, assuming that the distance between them does not exceed the classification threshold.

Results and Discussion: The generated atlas included 8 white matter bundles, each containing several cluster centroids, as shown in **Fig.2**. As 9 out of 17 children (53%) had normal-appearing MRI images, and the rest 8 subjects had only tiny lesions differently distributed over the brain, it is unlikely that lesion-affected clusters were included in the atlas. Classification thresholds identified for these bundles were close to those reported in the adult atlas[2]; however, applying adult atlas to the same children data failed to detect any of the bundles, stressing out that it was important to create atlas and its anatomical template from children data. Indeed, our children atlas allowed automatic identification of all considered white matter bundles in all subjects (**Fig.3A**), except for arcuate fasciculus (missing in one subject), and fronto-occipital fasciculus (not detected in 2 subjects). The shapes of the reconstructed bundles were highly variable across the subjects, but not depending on age. Nevertheless artefacts were observed in some individual reconstructions: in certain subjects, reconstructed cortico-spinal tract also included fibers from spino-thalamic tract and reconstructed arcuate fasciculus included fibers from the extreme capsule. This suggests that using more shape-sensitive distance measures for fiber clustering may further improve the quality of bundle reconstruction. Nevertheless, even at the current stage evaluation of the fractional anisotropy (FA) across the reconstructed bundles was able to capture age-related increases with different slopes across the bundles (**Fig.3B**), showing the relevance of this approach for studies on white matter regional maturation.

Conclusions: Although still in progress, this atlas demonstrated its potentials for automatic bundles identification in preschool children. It thus opens the way to studies of normal and abnormal brain regional development. Furthermore, it may be also used to analyze white matter microstructural properties when it is not possible to perform reliable tractography (e.g. in case of white matter diseases, like demyelination) by projecting the atlas to the subject data.

References: 1. Kulikova et al. (Brain Struct Funct, 2014); 2. Guevara et al. (NeuroImage, 2012); 3. Dubois et al. (Magn Reson Imaging, 2014); 4. Perrin et al. (Inf Process Med Imaging Proc Conf, 2005); 5. Descoteaux et al. (Magn Reson Med, 2007); 6. Duclap et al. (ESMRMB 2012, #842); 7. Dean et al. (NeuroImage, 2014); 8. Guevara et al. (NeuroImage, 2011).

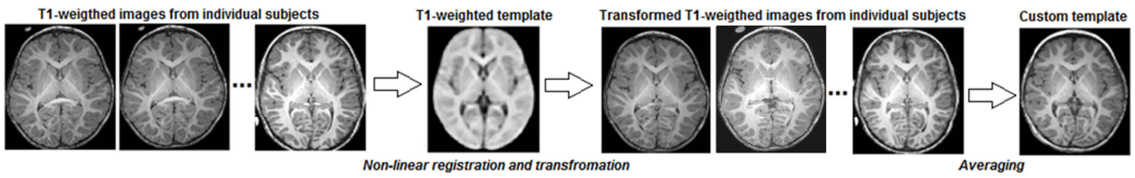

Fig.1 Creation of an age-specific anatomical template

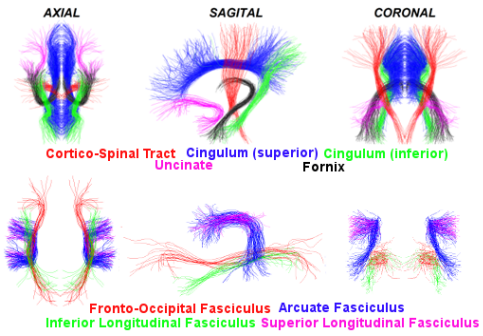

Fig.2 White matter bundles of the atlas

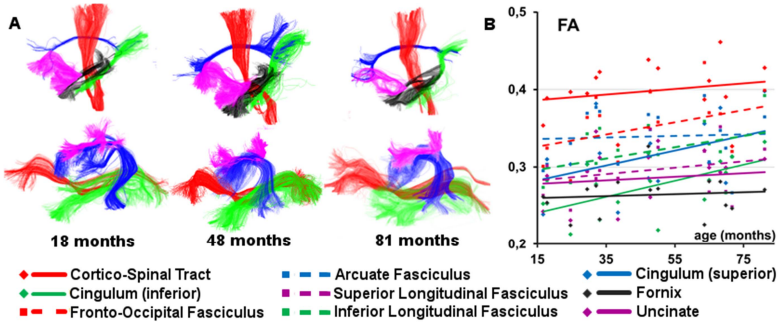

Fig.3 A) Identified bundles in selected subjects. B) Age-related changes in FA across the identified bundles.

Part III

Possible future clinical applications

The last part of this manuscript presents future clinical research applications of the tools described in the previous part. Indeed, those tools were developed on a population of healthy infants, with the intention of translating them to older children for specific questions on white matter pathology.

Specifically, in focal epilepsy, the main issue here concerns the integrity of epileptic networks, i.e. whether advanced techniques of fiber tracking and quantitative evaluation of MRI parameters in bundles can unravel microstructural changes in networks supporting propagation of the epileptic discharges.

The focus on metachromatic leukodystrophy (MLD) is also major in this work (my PhD was fully supported by ELA foundation and a PHRC funding to a project on MLD) with the aim of finding new subtle biomarkers of disease progression to assess future innovative therapies, such a gene therapy currently developed by Pr.P Aubourg, Hôpital Bicêtre (Le Kremlin-Bicêtre).

Each pathology is described in a separate chapter, which starts with a general biological background, followed by a summary of previous findings in imaging studies using different MRI modalities and finally, by our preliminary observations in a small group of pediatric patients.

Chapter 7

Focal Epilepsy

7.1 Definitions

Epilepsy is the most common neurological disorder, affecting ∼1% of the world population. Epilepsy does not correspond to one specific disease entity and according to the International League Against Epilepsy (ILAE) 6 etiological categories are distinguished: genetic, structural, metabolic, immune, infectious and unknown. From an electro-clinical point of view, epilepsies can be divided into generalized and focal. Focal epilepsies are defined as repeated seizures originating within networks limited to one hemisphere, which may be discretely localized or more widely distributed [331]. For each type of seizure, ictal onset is consistent from one seizure to another with preferential propagation patterns, which may involve the contralesional hemisphere [331]. When lesion is visible, epilepsy is called "symptomatic"; when it is nonvisible, epilepsy is called "cryptogenic". Almost 30% of focal epilepsies are drug-resistant, meaning that patients are likely to undergo surgical treatment, when epilepsy is due to the underlying lesion.

7.2 Epileptogenic lesions

7.2.1 Focal Cortical Dysplasia (FCD)

7.2.1.1 Pathology description

Malformations of cortical development (MCD) are largely associated with drug-resistant focal epilepsies and are thought to account for 25-40% of drug-resistant epilepsies in children. Among all MCD, focal cortical dysplasia (FCD) constitutes ∼75% of the cases. FCD are localized areas of malformed cerebral cortex with variable sizes and locations. Since its first description by Taylor et al. in 1971 [332], a large spectrum of FCD have been documented [333], which can be divided in 3 types:

- FCD Type I is characterized by abnormal radial and/or tangential cortical lamination.

- FCD Type II in addition to disrupted cortical lamination has specific cytological hallmarks: dysmorphic neurons (Fig. 7.1) without balloon cells for FCD Type IIa, and dysmorphic neurons with eosinophilic balloon cells for FCD Type IIb (Fig. 7.2) [334].

- FCD Type III refers to cortical lamination abnormalities associated with another principal lesion.

FCD Type I is more often located in the temporal lobe, while FCD Type II has a predisposition for the frontal lobe [335]. FCD is often accompanied by excessive heterotopic neurons within subcortical white matter leading to the blurring of the grey-white matter border. This blurring may also arrive from the reduction of the myelin content within subcortical white matter, however, the possible origin of this reduction still remains unclear.

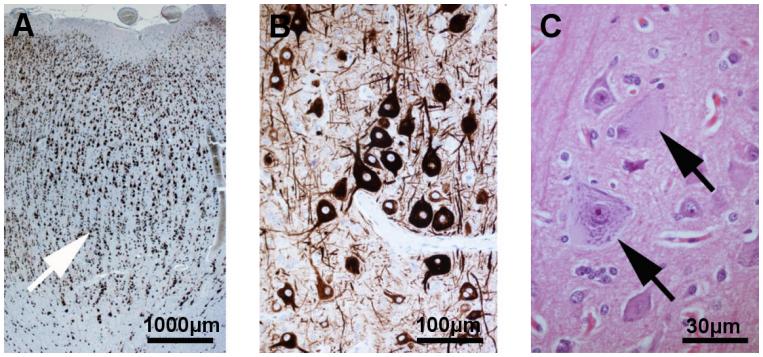

Figure 7.1: Histopathological findings in FCD Type IIa reveal severe cortical dyslamination (A) and abundant dysmorphic neurons (B and C) in the absence of the balloon cells. Adapted from [333].

Patients with FCD do not commonly have severe neurological deficits and the main clinical manifestation is epilepsy with seizure semiology depending on lesion location. In FCD patients, scalp EEG is characterized by rythmic, focal epileptiform discharges that are correlated with the lesion location [336]. Both electrocorticography (ECoG) and intracerebral recordings demonstrate intrinsic epileptogenicity of the affected tissues with a particular interictal activity [337, 338].

FCD patients may be relieved from seizures by focal cortical resections, and the extent of the dysplastic cortex removal is a crucial factor for a favourable outcome [338–343]. However, it remains often difficult to define the borders of the FCD.

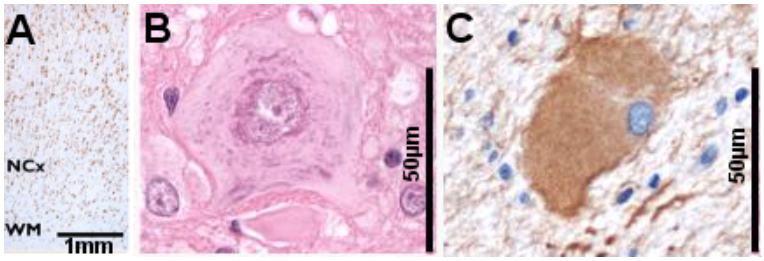

Figure 7.2: Histopathological findings in FCD Type IIb reveal severe cortical dyslamination without clear border between the neocortex (NCx) and white matter (WM)(A), dysmorphic neurons (B) and balloon cells detected by antivimentin immunohistochemistry (C). Adapted from [333].

7.2.1.2 Developmental origins

Although it is commonly accepted that FCD results from abnormal cortical development [344], the probable timing of its pathogenesis and its relation to seizures generation remain unclear. Histological findings suggest that excessive subcortical heterotopic neurons may result from abnormal neuronal migration and the presence of dysmorphic neurons and balloon cells may be explained by deficits in periventricular neuroglial differentiation [342, 345, 346]. Thus, FCD pathogenesis may stem from abnormalities happening during the *early phases* of cortical development [347].

On the contrary, a recent "dysmature cerebral developmental hypothesis" suggests that FCD pathogenesis may result from partial failure in the *later phases* of corticogenesis, and the timing of this failure may explain different forms and severity of the cortical dysplasia [348]: abnormalities occuring during the late second or early third gestational trimester are likely to be responsible for severe forms of cortical dysplasia, like hemimegalencephaly, while abnormalities happening later on would account for milder forms of cortical dysplasia. According to this hypothesis, FCD tissues contain neurons with immature cellular and synaptic properties [349, 350] and seizures may be evoked by local interactions of normal neurons with dysmature cells.

7.2.1.3 Imaging findings

MRI examination of patients with intractable focal epilepsy of structural origin is indispensable in surgical planning to identify exact lesion size and location and the extent of possible surgical resection. While favorable outcome is strongly correlated with successful lesion identification using MRI [351], imaging findings in FCD are not fully consistent, thus further improvement of MRI sensitivity for FCD identification is necessary. Below are summarized previous findings in FCD.

T1w and T2w images:

- Hyperintensity of adjacent subcortical white matter on T2-weighted images and hypointensity on T1-weighted images [332, 352–354], which is hypothe-

sized to be due to increased cellularity, the presence of balloon cells, proliferation of glial cell or insufficient myelination [354, 355].

- In FCD Type II, increased cortical thickness and blurring of the grey-white matter boundary [353] (Fig.7.3A,D)

- Abnormal cortical gyrification and focal enlargements of the subarachnoid space [333, 353]

- Radially-oriented linear or conical transmantle stripe (Fig.7.3E and F) in FCD Type IIb, indicating involvement of radial glio-neuronal units [356, 357].

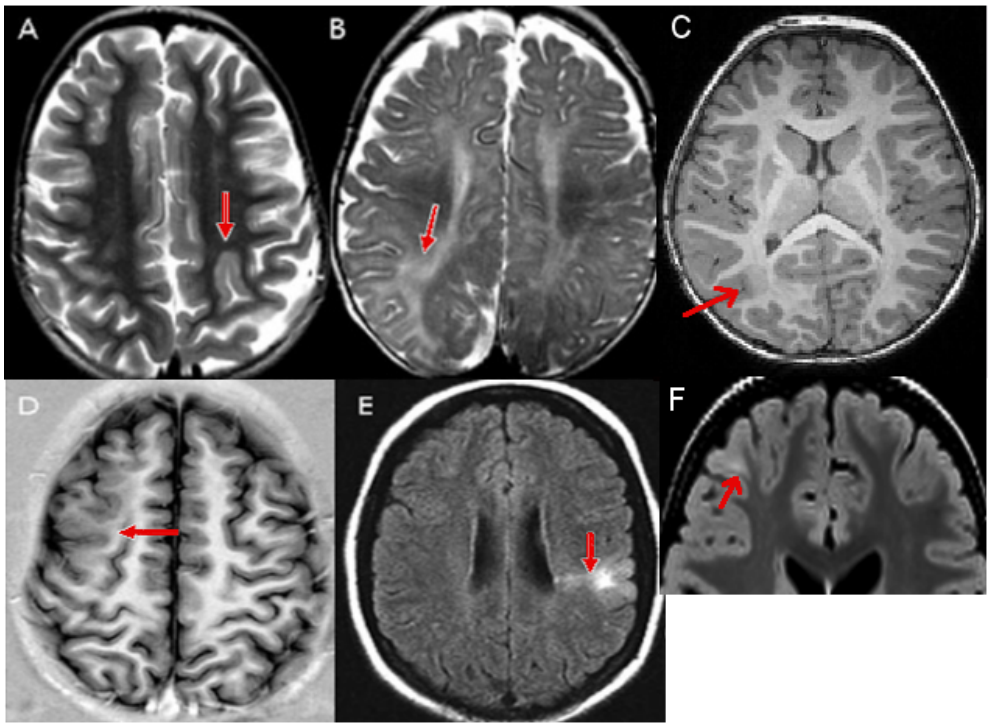

Figure 7.3: Common imaging findings in FCD include increased cortical thickness (A), T2 hyperintensity of the subcortical white matter (B), blurring of the grey-white matter boundary (C and D) and "transmantle sign" (E and F). C and F show two cases from this work. Adapted from [358].

Positron emission tomography (PET):

- On PET images, FCD areas usually appear hypometabolic inter-ictally, however (Fig. 7.4), sometimes they have normal or even hypermetabolic appear-

ance, especially during seizures [353].

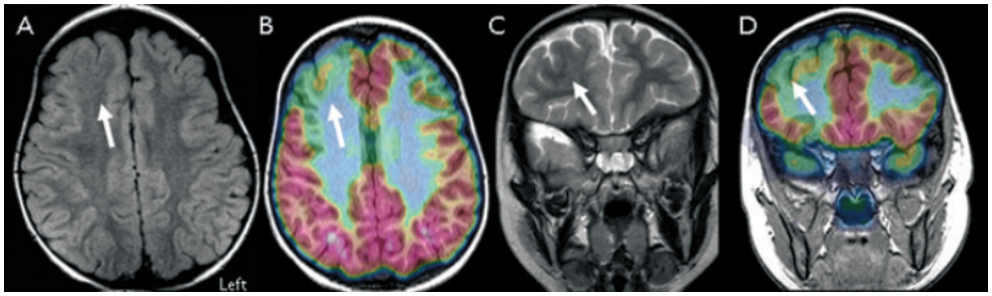

Figure 7.4: PET images superimposed on T1-weighted scans reveal hypometabolism associated with FCD in areas that are slightly larger than abnormalities detected on T2-weighted images. Adapted from [358].

Diffusion MRI:

- Reduced fractional anisotropy FA and increased mean $\langle D \rangle$ and transverse $\lambda_\perp$ diffusivities in the subcortical white matter underlying FCD regions [359–362]. Reduced FA is thought to result from abnormally located grey matter, presence of ectopic neurons, or abnormal myelination of the white matter, while increased $\langle D \rangle$ may result from increased extracellular space due to demyelination (in the white matter) or deficits during neurogenesis and cell loss (in the grey matter) [363].

- NODDI (neurite orientation dispersion and density imaging) in adult patients shows local reductions in neurite density within FCD areas identified on T1-weighted images (Fig. 7.5) [364].

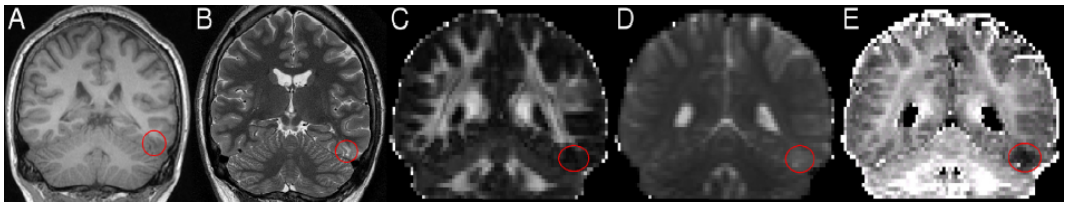

Figure 7.5: NODDI can help in FCD localization (E, red circle showing decreased neurite density) even when the dysplastic region is almost invisible on conventional MRI (A - T1-weigthed, B - T2-weigthed) and DTI images (C - FA, D - $\langle D \rangle$). Adapted from [364].

7.2.2 Other focal epileptogenic lesions

Other focal epileptogenic lesions may arise from several origins [365], including:

- ischemic-hypoxic injuries (global hypoxia due to perinatal asphyxia or large middle cerebral artery infarcts), characterized by variable degrees of encephalomalacia and gliosis;

- head trauma (penetrating brain injuries, focal contusions, hemorrhages, etc.)

- infections (meningitis, encephalitis)

In our population (see Tab. 6.1 and Fig. 6.1):

- 7 children had evidence of FCD, either with typical MRI imaging or proven later after surgery;

- 2 children had non-specific MRI abnormalities such as T2 and FLAIR hyperintensities likely corresponding to gliosis, thus ischemic lesions cannot be ruled out at this stage;

- 9 children had normal MRI, which may corrspond to either subtle MCD or to faint gliosis of various origin.

7.3 Diffusion imaging of epileptic white matter networks

Epileptogenic areas likely show both abnormal organization and microstructural properties of the white matter fibers passing through them [353] and through epileptic networks that sustain seizure propagation. Diffusion imaging may help to unravel these abnormalities within individual white matter bundles using tract-based analysis [366].

Previously, tract-based analysis in benign childhood epilepsy with centrotemporal spikes (BECTS) revealed higher $\lambda_{\parallel}$ and $\langle D \rangle$ compared to healthy subjects in the left superior longitudinal fasciculus, the retrolenticular part of the internal capsule, posterior thalamic radiation, sagittal stratum and the body of the corpus callosum [366]. Increased $\lambda_{\parallel}$ might result from changes of microtubules and neurofilaments or reduced axonal diameter. In the left superior longitudinal fasciculus,

it was correlated with low verbal IQ scores, being in agreement with hypothesis that BECTS predominantly affects the left hemisphere, related with language dysfunction [366–369].

In adults, evaluation of FA in temporal lobe epilepsy suggested decreased FA in a widespread white matter network, including limbic bundles (fornix), association bundles (uncinate, arcuate and inferior longitudinal fasciculi), motor projection tracts, and cerebellar white matter. Within the temporal lobe, the observed changes were correlated with memory performance [370].

It is believed that white matter tracts on the ipsilesional side are more affected than those from the contralesional side [371, 372]. However, evaluation of FA in different white matter tracts has shown that pathological changes may spread diffusely to white matter tracts in both hemispheres [372–374] and bilateral FA reductions may be observed outside epileptogenic zones [363, 370, 372–375]. In a group of pediatric patients (4-18 years), ROI analysis in white matter tracts revealed bilaterally lower FA as compared to healthy age-paired subjects in the genu and splenium of corpus callosum, in the fronto-occipital fasciculus, and in the inferior longitudinal fasciculus [372]. In adult patients, both ROI and tract-based analysis also showed bilaterally decreased FA values in forceps minor, anterior thalamic radiation, corticospinal tract, and uncinate fasciculus [373, 374]. Such widespread anormalities may be related to frequent seizures, hidden FCD areas unrevealed by conventional MRI examinations or more complex epileptogenesis processes [376–378].

7.4 Preliminary experimental observations

7.4.1 Objectives and Methods

As white matter bundles in the ipsilesional hemisphere are expected to be more affected than those from the contralesional hemisphere [371, 372] and as our young patients had relatively short epilesy duration (Tab. 6.1), we explored whether there were any global differences in the microstructural properties of the bundles from "affected" and "non-affected" hemispheres.

For that, we compared 7 MRI parameters (qT1 and qT2; FA, $\langle D \rangle$, $\lambda_{\parallel}$ and $\lambda_{\perp}$ from DTI, and MWF) across ipsilesional and contralesional bundles in the group of epileptic children previously described in chapter 6. The bundles were automatically extracted from the corresponding whole-brain tractography datasets using the approach and the white matter connectivity atlas described in chapter 6.

7.4.2 Results

We were able to detect differences between ipsilesional and contralesional parts in some of the bundles (Fig. 7.6). In agreement with previous findings [372], both the inferior longitudinal fasciculus and the fronto-occipital fasciculus showed reduced FA in the ipsilesional parts across the age range (paired t-test, $p<0.01$)

(Fig. 7.6). This supports the idea that contralesional hemispheres in our sample can be considered close or comparable to a normal population. The ipsilesional inferior longitudinal fasciculus also had reduced $\langle D \rangle$ values (paired t-test, $p<0.01$). Surprisingly, we found slightly increased MWF values in the inferior longitudinal fasciculus, the fronto-occipital fasciculus and the superior longitudinal fasciculus (paired t-test, $p<0.01$). For all other MRI parameters no global differences between ipsilesional and contralesional bundles were found.

Among all considered parameters, MWF revealed differences in 3 bundles (the inferior longitudinal fasciculus, the fronto-occipital fasciculus and the superior longitudinal fasciculus), followed by FA, which was assymetric in 2 bundles (the inferior longitudinal fasciculus and the fronto-occipital fasciculus), and finally, $\langle D \rangle$ in only in the inferior longitudinal fasciculus.

7.4.3 Discussion and perspectives

These preliminary findings are difficult to interprete: although FA decreased in the inferior longitudinal fasciculus and the fronto-occipital fasciculus, it could not be interpeted simply by demyelination as these changes were accompanied by elevated MWF values.

To elucidate these controversial observations, further investigation of the white matter microstructure should be improved in the several ways. First, the whole-tract approach applied here may have missed focal abnormalities, occuring in small fractions of the bundles. Thus, in future analysis bundles should be segmented and analyzed along the tracts taking into account the distance between their segments and lesion location. Such analysis should also take into account duration of the epilepsy, age of onset, lesion localization and asymmetry between hemispheres. Finally, comparing ipsilesional and contralesional sides may fail to detect pathological changes due to widespead white matter abnormalities, requiring acquisition of a healthy control group, whenever possible.

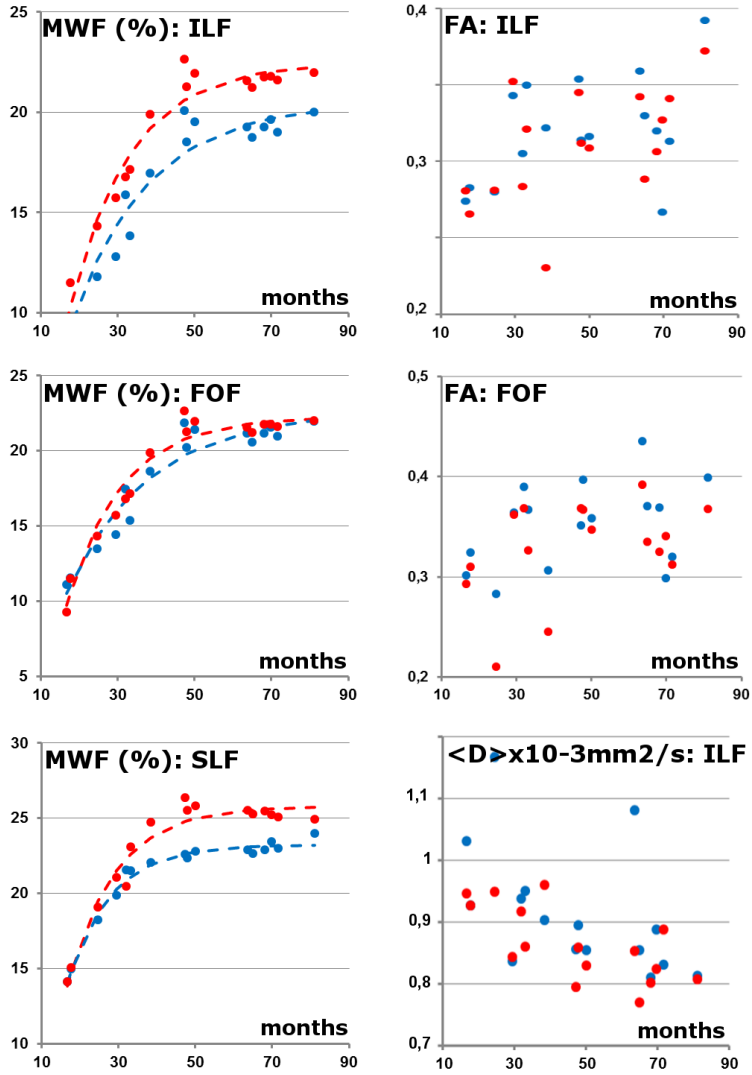

Figure 7.6: Differences in MRI parameters between ipsilesional (red dots) and contralesional (blue dots) bundles. **MWF:** non-linearly increased with age in both ipsilesional and contralesional parts of the inferior longitudinal fasciculus (ILF), the fronto-occipital fasciculus (FOF) and the superior longitudinal fasciculus (SLF). Similar to chapter 6, age-related increase in MWF values was fitted with the function $a * (1 - b * e^{-c*age})$, p<0.001. Across the age range, MWF values on the ipsilesional side were consistently higher than on the contralesional side (paired t-test, p<0.001). **FA:** increased with age in both ipsilesional and contralesional parts of both the inferior longitudinal fasciculus and the fronto-occipital fasciculus, however FA values were consistently lower in the ipsilesional side across the age range (paired t-test, p<0.05). **Mean diffusivity $\langle D \rangle$:** decreased with age in both ipsilesional and contralesional parts of the inferior longitudinal fasciculus, however across the age range, it was consistently lower on the ipsilesional side (paired t-test, p<0.05). According to literature [131, 193], age-related changes in FA and $\langle D \rangle$ are exponential; however, in our case exponential fittings (not shown) were not significant probably due to a large inter-subject variability.

Chapter 8

Metachromatic leukodystrophy

8.1 Introduction

Metachromatic leukodystrophy (MLD) is a rare recessive autosomal disease, with an estimated prevalence of 1 per 100,000 live births [379–382]. MLD is caused by the deficiency of the lysosomal catabolic enzyme arylsulfatase-A (ARSA) (more rarely, of its activator protein saposin-B) [383–385], which results in accumulation of the 3-O-sulfogalactosylceramide (sulfatide) in the central and peripheral nervous systems [382, 386–389], leading to progressive demyelination and consequent neurological deterioration. Another substance reported to accumulate in MLD patients is lysosulfatide (the deacylated form of sulfatide) [390, 391], which was shown to be cytotoxic and is thought to be also involved in MLD pathology.

8.2 Clinical presentation

Three major clinical forms (a late-infantile, a juvenile and an adult form) of MLD are distinguished by the age of onset [379]. The most frequent ($\sim$80% of cases) and fatal form is the late-infantile form, which starts by the ages of $1.5 - 2$ years. It manifests with gait abnormalities with hypotonic diplegia and ataxia, accompanied by speech disturbances and cognitive impairment at the later stages [382, 392]. The disease rapidly progresses within 6 months to 4 years following the onset of symptoms [382] and death usually occurs by the age of 5 years. The juvenile form usually has an onset between 4 and 16 years, when a previously well-developing child starts to manifest a spastic gait, ataxia, and intellectual deterioration. MLD in the juvenile form progresses more slowly than the late infantile MLD [389, 393–395]. The adult form of MLD usually manifests between the third and the fourth decades of life. It is characterized by disturbed visual-spatial discrimination, memory loss, disorganized thinking, and decreased mental alertness. The survival period after the onset of symptoms is usually within 5 to 10 years.

So far, no causal therapy for MLD is available. However, as new therapeutic approaches are currently emerging, it is important to deepen our understanding of the natural course of MLD and develop quantitative tools for evaluating of the

therapeutic options such as enzyme replacement therapy, hematopoietic stem cell transplantation and gene therapy [379, 396–399].

8.3 Imaging findings in the late-infantile MLD

8.3.1 Proton density, T1w and T2w images

MRI studies in MLD commonly report bilateral symmetric abnormal hyperintensities in the periventricular white matter, with extensive frontal, parietal, occipital and semiovale center involvement [382, 400–403]. A thin layer (1 to 3 mm) of the periventricular white matter wrapping around the lateral ventricles seems to be spared from demyelination [404]. The subcortical white matter is initially preserved; however, at later stages, the subcortical U-fibers may be affected [181, 400–402, 405].

Demyelination is thought to progress in the occipito-frontal direction [181, 401, 402, 406]. The first changes can be seen in the parieto-occipital central white matter, followed by changes in the fronto-central regions, in the commissural fibres of the corpus callosum (first splenium, then genu) and in the periventricular white matter (first parieto-occipital, then frontal and then temporal regions) [406]. Within the corpus callosum a particular pattern of disease progression is observed: first, the lesions appear centrally, then they become "diffuse" and later "curvilinear" [402]. As the disease progresses, demyelination spreads from the lobar and commissural white matter towards subcortical areas (U-fibers) with a parieto-occipital predominance.

At the advanced stages of the disease cerebral atrophy begins, first seen as enlargement of the inner ventricles and later as dilated outer CSF space [402, 406]. It seems that this atrophy is mainly due to the shrinkage of the white matter volume and only at the later stages slightly smaller cortical bands can be detected [406]. At this stage, demyelination of the projection fibers and of the cerebellar white matter, as well as cerebellar atrophy can also be observed [402, 404, 406].

Additionally, decreased signal intensity in the basal ganglia and the thalamus can be frequently seen on T2-weighted images in patients with advanced stages of MLD [402, 404], probably as the result of abnormal accumulation of breakdown products.

The common MRI manifestation of MLD include so-called tigroid or leopard-skin patterns (Fig. 8.1) [400–402]. The tigroid pattern is observed as numerous radiating linear structures in the periventricular region that have normal white matter signal intensity on the background of demyelinated white matter. The leopard-skin pattern is seen as numerous punctuate areas of normal-appearing white matter interspersed with demyelinated areas at the level of the centrum semiovale. Similar patterns were also described in other neurodegenerative processes, such as Pelizaeus-Merzbacher disease [392, 403, 404, 407, 408]. The areas ($\sim$1 mm thickness) of normal white matter signal intensities seen in the tigroid and leopard-skin patterns were shown to be residual islets of spared myelin, especially

around blood vessels [408, 409].

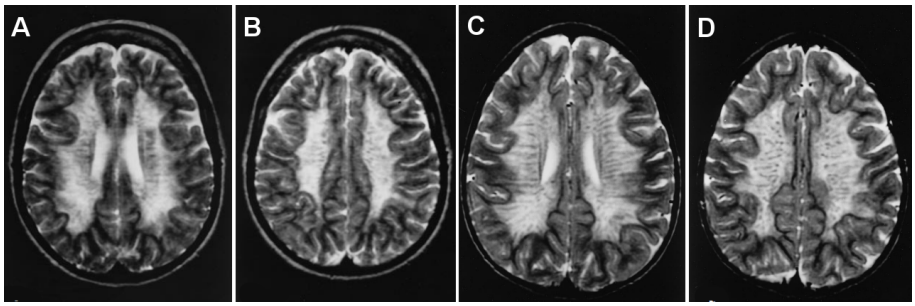

Figure 8.1: "Tigroid" and "leopard-skin" patterns in demyelinated centrum semiovale of a 2-year-old girl (A,B) and of a 5-year-old boy (C,D). Adapted from [400].

8.3.2 Diffusion imaging

Diffusion imaging studies in MLD are scarce and generally show cytotoxic edema-like patterns in the presumed zones of the disease progression [410–412]. Such patterns are likely to reflect restricted water diffusion within the affected white matter. The so-called "myelin edema" is thought to be due to small, fluid containing vacuoles developing within or under myelin layers, because of the loss of the myelin integrity. It is assumed that within such vacuoles water diffusion is restricted. However, this may not be the only explanation of what is referred to as "myelin edema". On the contrary, at the late stages of the disease, strongly demyelinated lesion areas show increased $\langle D \rangle$ values [411].

8.3.3 MRI spectroscopy

Within abnormal peri-ventricular white matter, MRI spectroscopy in MLD reveals elevated myoinositol(My)/creatine(Cr) and lactate(Lac)/creatine(Cr) ratios [402, 413–415]. Increased level of myoinositol, which is produced by astrocytes, is attributed to astrocytic gliosis, while the elevated level of lactate may be due to several reasons: 1) increased production due to astrocytic gliosis as a result of increased cell mass; 2) decreased lactate transport into axons due to oligodendrocyte injury; 3) decreased lactate uptake due to neuronal loss. A decreased N-acetyl aspartate(NAA)/creatine(Cr) ratio was also documented in MLD [402, 413, 414, 416]. This decrease is related to diffuse neuronal loss and was strongly correlated with motor function [416]. Additionally, elevated levels of choline (Cho)/creatine(Cr) ratio were observed in MLD patients compared to controls [402, 413], reflecting high myelin turnover.

8.4 Preliminary experimental work

8.4.1 Background and Objectives

The scoring method of Eichler et al. [404] provides a severity score (0–34) based on visual inspection of the location and extent of white matter involvement and the presence of global atrophy. This method allows defining 3 stages of the disease: mild (scores 1-6), moderate (scores 7-15) and severe disease (scores 16-34), with the severity scores highly correlated with gross motor deterioration assessed using the Gross Motor Function Classification system for MLD (GMFC-MLD) [417].

However application of this method for evaluation of mild and/or early-onset forms of MLD in infants is limited, probably because the terminal myelination zones seen in normal development overlap with early faint pathologic lesions. Indeed, several MRI features evaluated in this scoring system are associated with moderate and advanced, but not mild stages of the disease. The tigroid pattern is believed to be not just a diagnostic sign but an indication of advanced disease, associated with a severity score of ≥ 13 [402, 404]. The T2 hyperintensity of the corticospinal tract is also associated with an advanced disease [402]. Central hyperintensity in the genu of the corpus callosum and/or diffuse hyperintensity in the splenium are associated with moderate disease stages (mean score 13), while diffuse genu involvement and curvilinear splenium involvement may indicate advanced stages (mean score 17) [402]. The atrophy of the corpus callosum and cerebellar involvement (atrophy and T2 hyperintensity) are also characteristic to advanced disease (mean score > 18), while thalamic atrophy is associated with moderate disease (score > 14).

Another strong limitation of the scoring system is related to the longitudinal evaluation of the disease progression [404]. Although with a follow-up interval of 1 year it is possible to see the changes in the severity scores, this system may not be sensitive enough to reveal disease progression over shorter periods [404].

The preliminary work described below was performed as a part of a project initiated by Assistance Publique – Hôpitaux de Paris (project HCIT-MLD - P071232 - IDRCB 2009-A00094-5) with the goal of identifying new MRI biomarkers to evaluate the disease progression in relation to motor and cognitive functioning in children suffering from the late-infantile MLD and of estimating the efficacy of clinical treatments to come. Here, we describe preliminary results on microstructural changes within white matter bundles, assessed with MRI/DTI parameters in 5 LI-MLD patients.

8.4.2 Subjects and Data acquisition

Five pediatric patients (ages: 29-79 months) diagnosed with the late infantile form of MLD were recruited by neuropediatricians of Hôpital Bicêtre (Fig. 8.2 and Tab. 8.4.2). Three of these subjects were scanned twice at a $\sim$5 month interval. The diagnosis was confirmed by decreased activity of ARSA enzyme activity in leukocytes and abnormal urinary excretion of sulfatides.

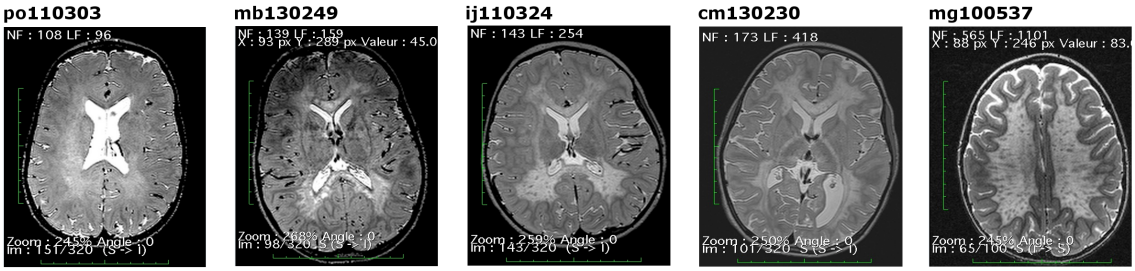

Figure 8.2: Clinical T2w images of the recruited MLD patients. Note pronounced T2 hyperintensity within white matter regions and a tigroid pattern in subject mg100537. Also note less pronounced white matter involvement in patient po110303.

Subject ID	Age at 1st acq.	Eichler score are 1st acq.	Age at 2nd acq.	Eichler score are 2nd acq.
po110303	2 years 4 months	12	2 years 9 months	15
mb130249	3 years 4 months	15		
ij110324	4 years 3 months	21	4 years 8 months	22
cm130230	4 years 7 months	23		
mg100537	6 years 1 month	17	6 years 6 months	20

Table 8.1: Details of MLD patients: ages and Eichler scores of disease severity at the 1st and 2nd (if applicable) acquisitions.

The severity of Eichler scores ranged from 12 to 23. All subjects showed involvement of periventricular and central regions of frontal, parieto-occipital and temporal white matter, while U-fibers were preserved (Tab. 8.2). The corpus callosum (both splenium and genu) was also affected in all subjects. Projection fibers were involved in subjects with scores >20 and in the 2nd acquisition for subject po110303 (score 15). Thalamus involvement was observed in subjects with scores $\geq$17 and cerebellum was involved in 2 subjects: po110303 (2nd acq., score 15) and ij110324 (1st acq., score 21).

Control group consisted of the 17 age-matched children with unilateral focal epilepsy described in previous chapters 6-7. This pseudo-control group was selected because at this age range it is almost impossible to acquire data in healthy unsedated children. Only unaffected hemispheres, which are expected to show normal or nearly normal values of MRI/DTI parameters, were considered for comparison with MLD children.

The acquisition protocol was described previously in chapter 6.

8.4.3 Data analysis

Quantitative MRI/DTI maps were generated for 7 parameters: qT1 and qT2; FA, $\langle D \rangle$, $\lambda_{\parallel}$ and $\lambda_{\perp}$ from DTI and MWF, computed as proposed in chapter 5.

Because motor deficits are among the first signs usually detected in MLD, these parameters were further quantified in each subject along the cortico-spinal tract

Brain region	po110303 (1st acq.)	po110303 (2nd acq.)	mb130249	ij110324 (1st acq.)	ij110324 (2nd acq.)	cm130230	mg100537 (1st acq.)	mg100537 (2nd acq.)
Frontal WM								
Periventricular	1	1	2	2	2	2	2	2
Central	1	2	2	2	2	2	2	2
U-fibers	0	0	0	0	0	0	0	0
Parieto-occipital WM								
Periventricular	2	2	2	2	2	2	2	2
Central	2	2	2	2	2	2	2	2
U-fibers	0	0	0	0	0	0	0	0
Temporal WM								
Periventricular	1	1	1	2	2	2	2	2
Central	1	1	2	2	2	2	2	2
U-fibers	0	0	0	0	0	0	0	0
Corpus callosum								
Genu	1	1	2	2	2	2	1	1
Splenium	2	2	2	2	2	2	1	1
Projection fibers								
Internal capsule posterior limb	0	1	0	1	2	2	0	1
Internal capsule anterior limb	0	0	0	0	0	1	0	1
Midline pons	0	0	0	2	2	2	0	1
Cerebral atrophy	1	1	0	0	0	1	1	1
Thalamus	0	0	0	1	1	1	1	1
Basal ganglia	0	0	0	0	0	0	1	1
Cerebellum								
WM	0	1	0	1	2	0	0	0
Atrophy	0	0	0	0	0	0	0	0
Total	**12**	**15**	**15**	**21**	**22**	**23**	**17**	**20**

Table 8.2: Details of the Eichler scores in MLD children.

(CST) and compared at each point along the tract to the corresponding mean values from the control group. For that, CST was reconstructed in each subject independently with regularized streamline tractography using Connectomist software [316] and manually placed regions of interest. Because in MLD patients it was not possible to perform reliable fiber tracking in highly demyelinated areas of the images coming from the 2nd acquisition (Fig. 8.3), CST reconstructed from the 1st acquisition was used for analysis in both acquisitions, after realignement.

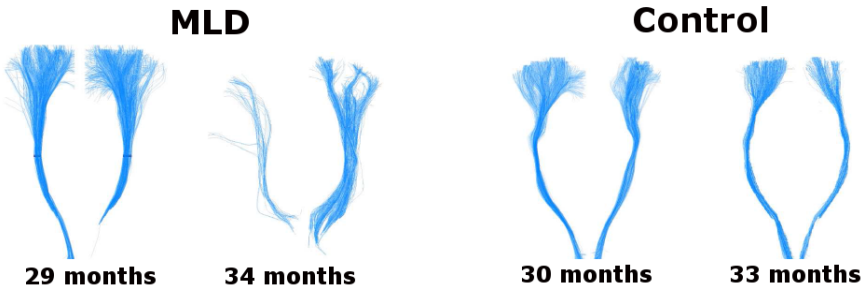

Figure 8.3: CST reconstructed in a typical MLD child of 29 months, and in the same child 5 months later (same child as in Fig. 8.4). On the right are CST reconstructed in age-matched control subjects.

Because of difficulties in bundle reconstruction in MLD patients, further comparison of the MRI/DTI parameters across other bundles was performed by projecting bundles from the connectivity atlas (see chapter 6) to the subjects data.

8.4.4 Results

Quantitative MRI maps showed dramatic differences of white matter characteristics between MLD subjects and their age-matched controls: global decrease in FA and MWF values and increase of other parameters (Fig. 8.4). As disease progressed, the maps also revealed the aggravation of these differences, with the most dramatic changes seen in the center of the parieto-occipital region: strong decrease on FA and MWF maps and increase on qT1, qT2 and $\lambda_\perp$ maps, while sub-cortical white matter was relatively preserved.

Analysis of the MRI parameters along the cortico-spinal tract demonstrated decreases of the anisotropy (down to -65%) and MWF (down to -70%), increases of the transverse diffusivity (up to +60%), qT1 and qT2 (up to +45% and +40% correspondingly) (Fig. 8.5).

Similarly to the observations in the cortico-spinal tract, comparison of the MRI parameters across other bundles projected from the connectivity atlas also revealed dramatic differences between MLD and control subjects (Fig. 8.6), with the most pronounced observed in the FA(decrease), MWF (decrease), qT1 (increase) and qT2 (increase). However, none of these changes, except in the fornix, showed correlation with disease severity as estimated by Eichler scores. In fornix, correlations with Eichler score were observed for FA ($R=-0.81$, $p<0.05$), $\lambda_\perp$ ($R=0.74$, $p<0.05$) and qT1 ($R=0.75$, $p<0.05$).

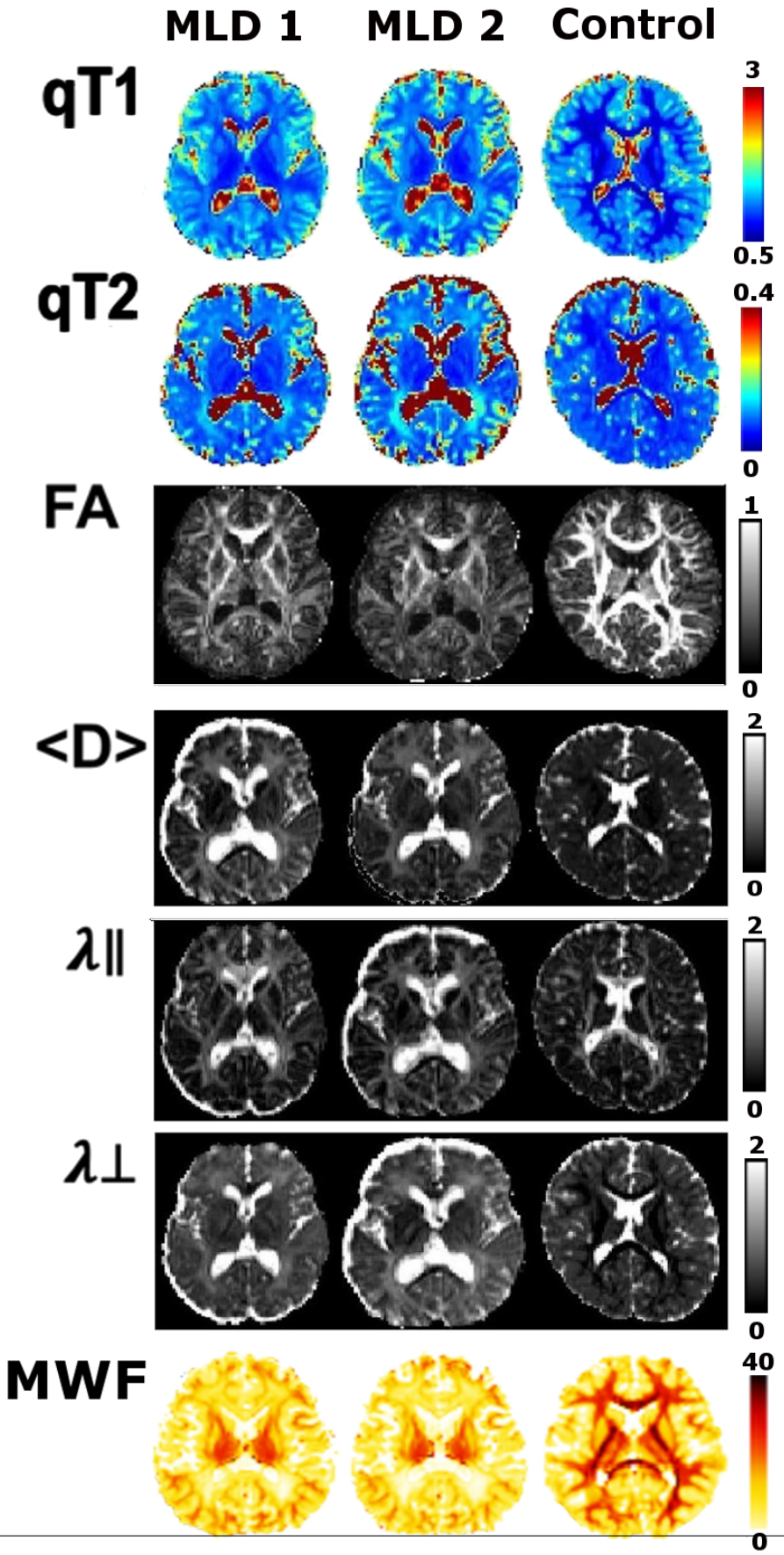

Figure 8.4: Quantitative MRI maps for a typical MLD child (MLD1, 29 months), same child 5 months later (MLD2) and an age-matched control child. qT1 and qT2 values are expressed in seconds, diffusivities ($\langle D \rangle$, $\lambda_{\parallel}$ and $\lambda_{\perp}$) are given in $10^{-3}\text{mm}^2/s$.

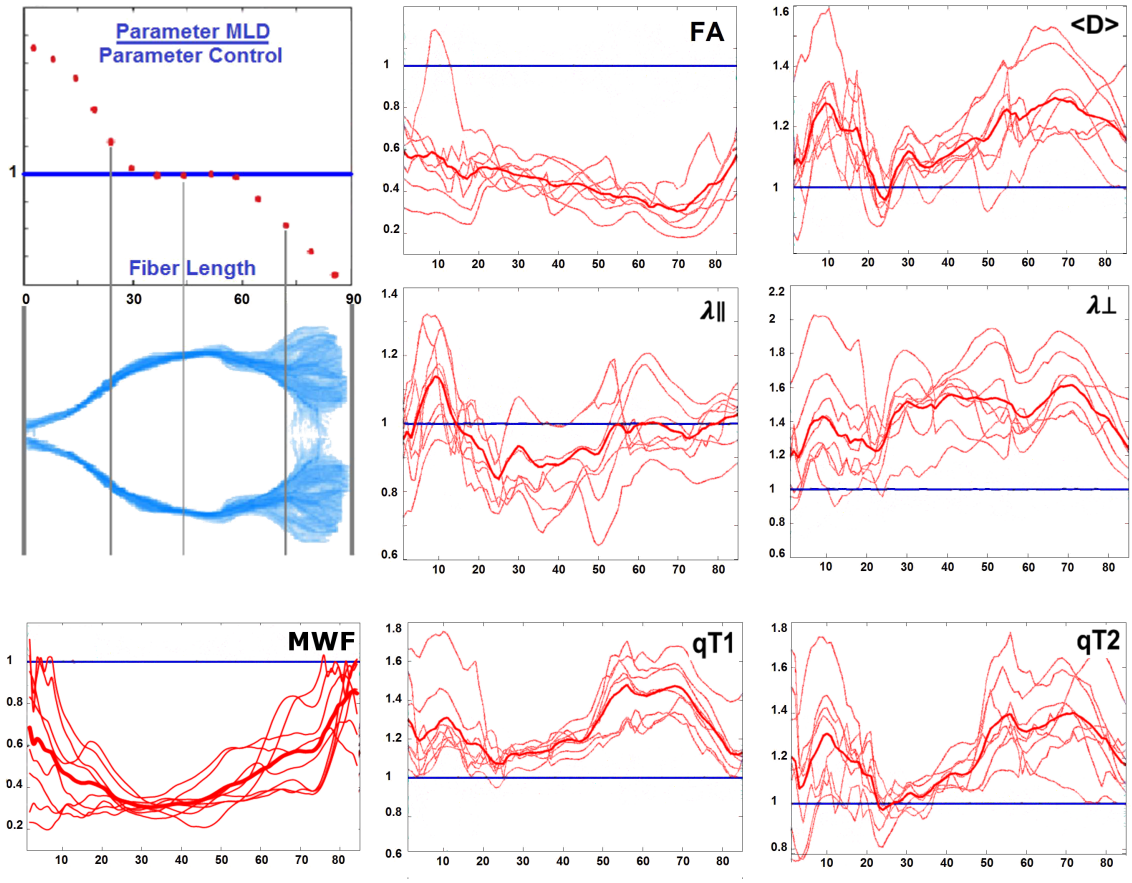

Figure 8.5: Quantitative comparison of the MRI parameters along the CST between 2 groups. The ratio between the MLD and control values is plotted at each point along the CST. Thick line presents group mean values, thin lines - values from MLD individuals.

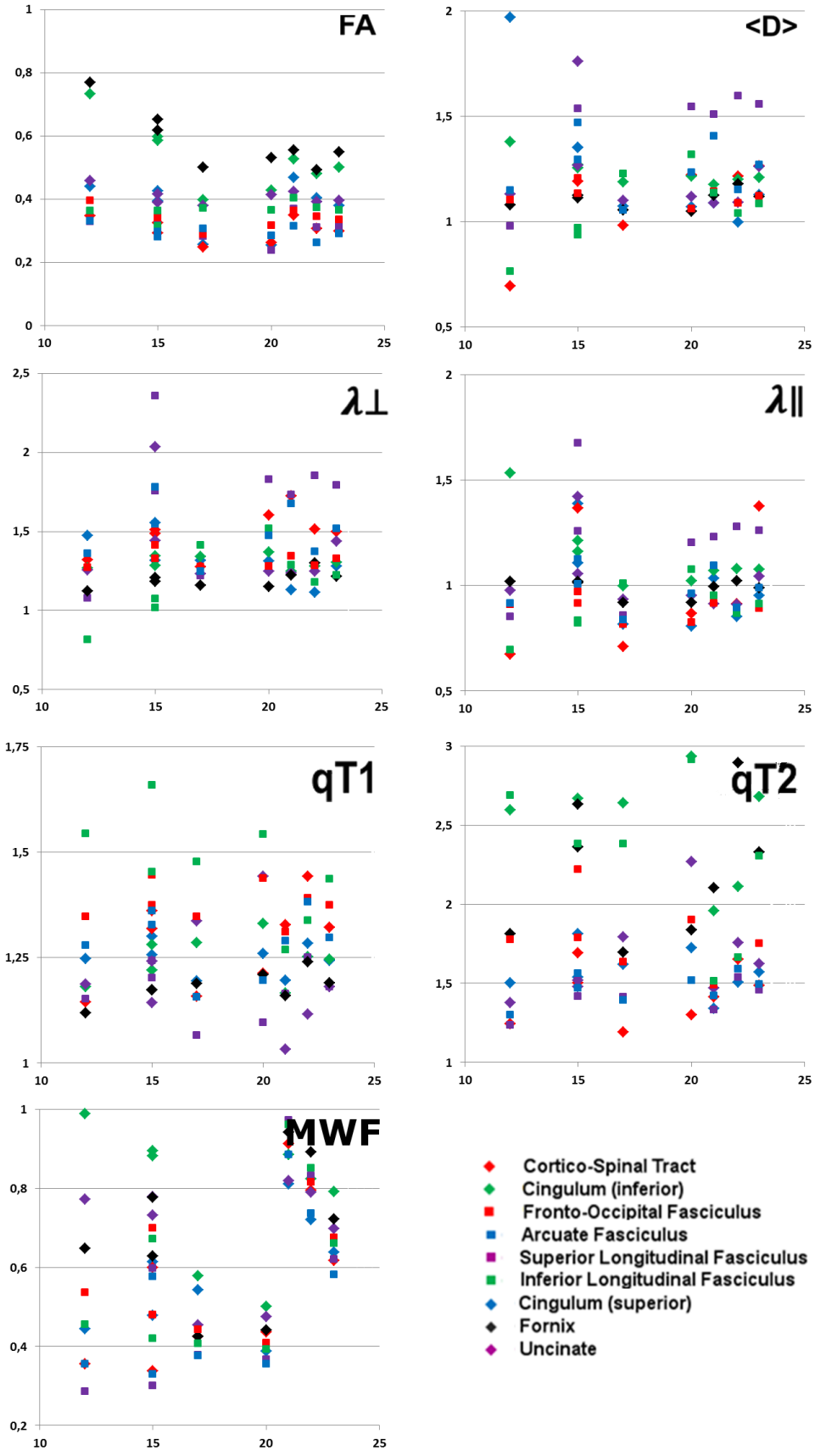

Figure 8.6: Ratios between MRI parameters in MLD patients and the corresponding normal control values in different white matter bundles vs. Eichler scores in MLD patients. In all MLD bundles FA and MWF values were lower than in control condition, while qT1 and qT2 values were higher. Diffusivities were generally higher in MLD children, but these differences were less consistent across the bundles. No correlation with Eichler scores were found, except in the fornix.

8.5 Discussion and Perspectives

In this preliminary work, the changes in MRI parameters of MLD patients reflect complex pathological changes that are not restricted to the white matter demyelination suggested by decreased MWF values in all bundles. In fact, almost none of these changes was correlated with disease severity as assessed by Eichler scores, maybe due to a small sample size, which is the main limitation of this work. Furthermore, according to Eichler scores, all subjects already showed moderate and advanced disease stages (scores >12), meaning that with this sample it may be difficult to reveal the first subtle signes of MLD. It should be noted that it was also hard to get longitudinal data because of a rapid disease progression and none of the subjects could be admitted to more than 2 examinations.

Thus, understanding of the relations between MRI changes and the demyelination process requires further investigation on more numerous cases. In the future, the spatio-temporal progression of MLD should be investigated by evaluating MRI parameters along different white matter bundles that can be projected to the subjects data from the connectivity atlas. The revealed changes should then be used to create a multi-parametric model of the disease progression, taking into account the age of onset, disease duration, degrees of functional and cognitive impairments, etc. This model could eventually be helpful to finely monitor new therapeutic approaches, such as enzyme replacement therapy or gene therapy that are currently being developed in phase I-II trials.

The results described in this chapter were partially presented as posters at the 23rd and 24th SFNP meetings (Nancy, 2013 and Reims, 2014), and at the 30ths ESMRMB meeting (Toulouse, 2013). The posters are included at the following pages.

IRM Multimodale quantitative à 3T dans la leucodystrophie métachromatique: données préliminaires.

S Kulikova [1,3], J Dubois*[2,3], C Sevin*[4], C Chiron[1,3], C Bellesme[4], N Chemaly[1], D Leunen[1], F Boumezbeur[3], C Poupon[3], P Aubourg[4], L Hertz-Pannier[1,3]

1 UMR 663 INSERM/CEA/Université Paris Descartes, Hopital Necker Paris; 2 UMR 992 INSERM/CEA/Université ParisSud, Neurospin, Saclay
3 Neurospin, Saclay; 4 INSERM U986, Service de neuropédiatrie, Hopital du Kremlin Bicêtre, France
* contributions équivalentes

Introduction et objectifs

La leucodystrophie métachromatique (MLD) est une maladie génétique entraînant une démyélinisation progressive de la substance blanche. L'imagerie conventionnelle à 1.5T est un mauvais prédicteur de l'évolution de la maladie.

L'objectif de cette étude en IRM 3T est de quantifier les changements microstructurels et métaboliques intervenant pendant la progression de la maladie.

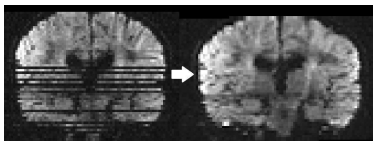

Fig.1 Correction des artéfacts de mouvements sur l'image pondérée en diffusion

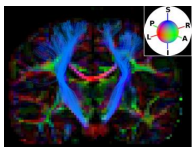

Fig.3 Le FCS identifié est superposé à la carte de FA codée en couleurs

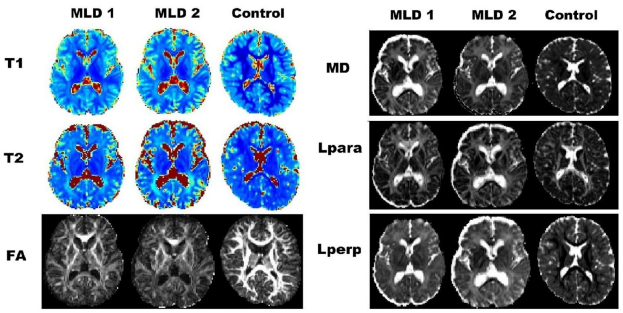

Fig.2 Cartes des paramètres IRM pour un enfant typique avec MLD (MLD1, 29 mois), pour le même enfant 5 mois plus tard (MLD2) et d'un enfant contrôle d'âge correspondant.

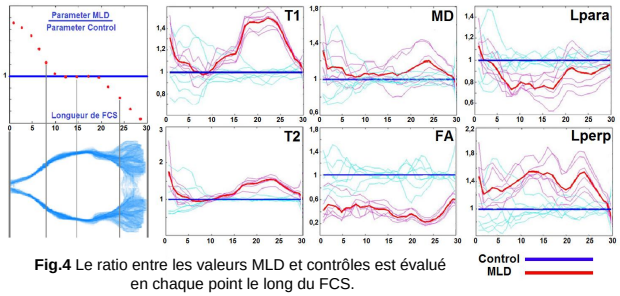

Fig.4 Le ratio entre les valeurs MLD et contrôles est évalué en chaque point le long du FCS.

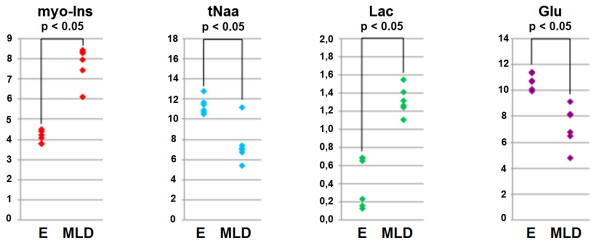

Fig.5 Concentrations des principaux métabolites: NAA, choline (Cho), glutamate (Glu), myoInositol (myo-Ins) et lactate (Lac), entre les contrôles (E) et MLD (t-tests p<0.05).

Méthodes

***Acquisition des données*:**

- 3 enfants avec forme infantile tardive de MLD (de 29 à 66 mois) ont été imagés deux fois à 5 mois d'intervalle
- comparés à 10 enfants contrôles (de 18 à 60 mois) avec épilepsie unilatérale et un bon développement fonctionnel (seul l'hémisphère contralésionnel a été considéré).
- À 3T, sous sédation
  - imagerie du tenseur de diffusion (DTI)
    - DW-SE-EPI, 55 coupes axiales 2 x 2 x 2 mm3, 60 orientations, b = 1500 s.mm-2 (+ b = 0): TE = 92ms, TR = 11s, imagerie parallèle facteur 2.
  - cartographie quantitative des temps de relaxation T1 et T2
    - EPI single-shot spin-écho SE, 55 coupes axiales 2 x 2 x 2 mm3
    - T2: 8 TE = 35 -> 280ms, chaque étape = 35ms, TR = 19s, imagerie parallèle facteur 2.
    - T1: SE-EPI avec inversion-récupération (IR) et 8 TI (TI = 250 -> 1500 ms, chaque étape = 250 ms, + TI = 2000, 2500ms): TE = 35 ms, TR = 16 s.
  - Imagerie spectroscopique, CSI
    - séquence CSI_SE (TE / TR = 30/1600ms) avec 6 OVS.

Post-traitement des données

• Correction des artéfacts (inhomogénéités de champ, courants de Foucault et mouvements (Fig.1).

• Calcul du tenseur de diffusion et création des cartes paramétriques: T1, T2, anisotropie fractionnelle (FA), diffusivités moyenne (MD), longitudinale (Lpara) et transversale (Lperp) (Fig.2).

• Reconstruction du Faisceau Cortico-Spinal (FCS) par tractographie déterministe avec régularisation, en utilisant le masque du cerveau généré à partir d'images T1 (Fig.3). Les faisceaux sont sélectionnés en définissant manuellement des régions d'intérêt.

Analyses des données

• Comparaison quantitative des paramètres IRM sur les FCSs entre les groupes contrôle et MLD (Fig.4, analyse *le long du faisceau* pour l'évaluation des différences spatiales). Compte tenu des difficulté de tractographie en cas de forte démyélinisation, l'analyse des 2èmes examens a été faite sur les FSCs reconstruits à partir des 1ères acquisitions.

• En CSI, comparaison quantitative des concentrations des principaux métabolites (NAA, choline, glutamate, myoInositol et lactate) entre les deux groupes (t-tests) dans une région d'intérêt englobant le FCS à la hauteur du centre semi-ovale (créatine en référence). (Fig.5)

Résultats et conclusions préliminaires

DTI et Quantification T1 et T2 (Fig 4)

Des changements massifs de tous les paramètres sont observés dans le FCS chez les enfants MLD par rapport aux contrôles:

- baisse significative de l'anisotropie (-68% en moyenne)
- hausse de la diffusivité transverse (jusqu'à +60%), et des temps T1 et T2 (jusqu'à +67% et +57%).
- Ces changements, fortement corrélés le long du faisceau, reflèteraient le processus de démyélinisation.

Spectroscopie

La spectroscopie confirme

- la perte neuronale (baisse de la concentration du NAA et du glutamate),
- la démyélinisation et l'astrogliose (élévation de la concentration de la choline et du myo-Inositol),
- et le stress métabolique (élévation de la concentration de lactate)(Fig.5).

La caractérisation de ces changements en longitudinal devrait permettre de mieux comprendre la dynamique de la démyélinisation, et de fournir des biomarqueurs sensibles pour tester l'efficacité de nouvelles thérapies.

Lectures supplémentaires

- Martin et al. (2012). Toward a better understanding of brain lesions during metachromatic leukodystrophy evolution.
- Groeschel et al. (2012). Cerebral gray and white matter changes and clinical course in metachromatic leukodystrophy.
- Groeschel et al. (2011). Metachromatic leukodystrophy: natural course of cerebral MRI changes in relation to clinical course.

La fraction d'eau liée à la myéline :
Un nouveau biomarqueur en imagerie de la myélinisation et de la démyélinisation ?

S Kulikova[1], L Hertz-Pannier[1], G Dehaene-Lambertz[2], C Sevin[3], C Chiron[1], C Bellesme[3], N Chemaly[1], D Leunen[1], R Nabbout[1], P Aubourg[3], C Poupon[4], J Dubois[2]

1) UMR 663 - UNIACT, INSERM/CEA/Université Paris Descartes, Paris; 2) UMR 992, INSERM/CEA/Université Paris Sud, NeuroSpin, Saclay;
3) UMR986, INSERM/Service de Neuropédiatrie, Hôpital du Kremlin Bicêtre; 4) UNIRS, CEA/Université Paris Sud, NeuroSpin, Saclay.

INTRODUCTION et OBJECTIFS

La fraction d'eau liée à la myéline, i.e. « Myelin Water Fraction » (MWF), est un nouveau paramètre IRM permettant de quantifier le contenu en myéline dans le cerveau *in vivo*. Elle est dérivée d'une analyse à plusieurs composants basée sur les signaux de relaxation T1 et T2 (**Fig. 1**) [1-2].

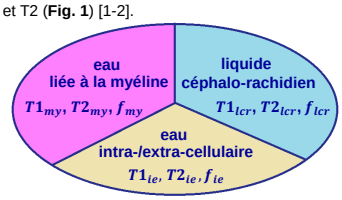

$$\begin{cases} f_{my} + f_{ie} + f_{lcr} = 1; \\ 1/T1 = {}^{f_{my}}/_{T1_{my}} + {}^{f_{ie}}/_{T1_{ie}} + {}^{f_{lcr}}/_{T1_{lcr}}; \\ S(T2) = f_{my}S(T2_{my}) + f_{ie}S(T2_{ie}) + f_{lcr}S(T2_{lcr}). \end{cases}$$

Fig. 1 Dans chaque voxel, les signaux de relaxation T1 et T2 peuvent être décomposés selon différents compartiments. Un modèle complexe relie les fractions *f* de ces composants (par rapport au volume d'eau total), et leurs valeurs respectives de *T1* et *T2*.

Les stratégies existantes pour la quantification de la MWF nécessitent des temps d'acquisition et / ou de post-traitement longs, ce qui limite son application pratique, en particulier chez les patients pédiatriques [2-3]. **Notre objectif est de mettre en place une nouvelle stratégie compatible avec sa utilisation en clinique.**

STRATÉGIE PROPOSÉE , MATÉRIELS ET MÉTHODES

Notre stratégie est basée sur un modèle qui s'appuie sur peu d'hypothèses *a priori* sur les différents composants, et comprend les deux étapes suivantes:

1) Calibration du modèle chez l'adulte à partir d'un protocole d'acquisition long

- 3 jeunes adultes sains
- IRM 3T TRIO Siemens, Neurospin, CEA
- Séquences EPI de relaxométrie: T1 séquence d'écho de spin avec inversion récupération et T2 séquence d'écho de spin avec un grand nombre (N = 30-60) de temps d'inversion TIs (entre 100 - 3100ms) pour la calibration des T1 de chaque compartiment, et de temps d'écho TEs (entre 30-310 ms) pour la calibration des T2.
- Une approche originale[4] de calcul a permis de caractériser chaque compartiment (**Fig.2**) :

  $T1_{my}$= 357±21ms; $T1_{ie}$= 1483±17ms; $T1_{lcr}$= 3441±36ms;
  $T2_{my}$= 18±5ms; $T2_{ie}$= 52±6ms; $T2_{lcr}$= 858±47ms.

2) Application chez les bébés ou patients avec un protocole court

Populations

- Nourrissons sains âgés de 1 à 5 mois (n=17),
- Enfants âgés de 18 à 66 mois
  - leucodystrophie métachromatique (MLD) à forme infantile tardive (n=5 dont 3 ont été vus 2 fois à 5 mois d'intervalle);
  - enfants avec épilepsie partielle unilatérale et un bon développement fonctionnel (n=10),
- Jeunes adultes (n=16).

Acquisition des données (<6 min par sujet)

- Pour T1: 8 valeurs de TI = 250 -> 1500 ms, chaque étape = 250 ms, + TI = 2000, 2500ms;
- Pour T2: 8 valeurs de TE= 35 -> 280ms, chaque étape = 35ms.

Cartographie quantitative de MWF

Après la calibration, les cartes MWF ont été calculées rapidement (<10min par sujet) en fixant les caractéristiques de chaque compartiment et en utilisant des algorithmes standards.

RESULTATS

Les cartes MWF montrent la progression précoce de la myélinisation chez les nourrissons, en accord avec les études précédentes (Fig.3) [3,5].

Dans la MLD, la diminution de la MWF est spectaculaire sur l'ensemble du cerveau (Fig.4). Des différences majeures sont observées dans les régions centrales, tandis que la substance blanche sous-corticale semble relativement préservée. L'évaluation longitudinale confirme la progression de la maladie sur une courte période de 5 mois.

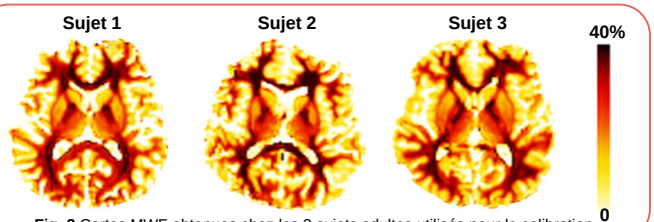

Fig. 2 Cartes MWF obtenues chez les 3 sujets adultes utilisés pour la calibration

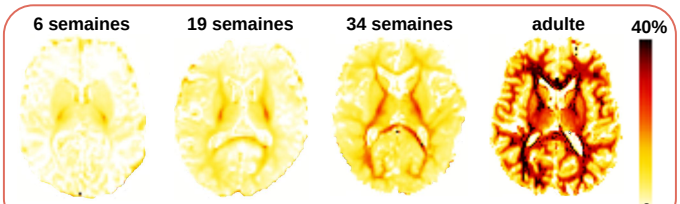

Fig. 3 Cartes MWF obtenues chez des nourrissons sains de différents âges.

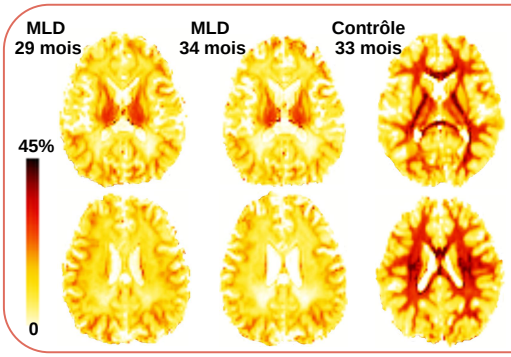

Fig. 4 Cartes MWF obtenues en longitudinal à 29 et 34 mois chez un enfant atteint de MLD, en comparaison d'un enfant contrôle de même âge.

CONCLUSIONS

- **L'imagerie MWF permet de quantifier les processus de myélinisation normale et de démyélinisation.**
- **Notre approche permet la quantification rapide et facile de la MWF, même chez des bébés et enfants.**
- **Elle sera prochainement implémentée dans le logiciel Relaxometrist de BrainVisa (http://brainvisa.info).**
- **Des études de comparaison et de corrélation avec les méthodes d'imagerie conventionnelle et d'histologie restent à mener.**

1) MacKay et al. (Magn Reson Med,1994); 2) Whittall et al. (Magn Reson Med, 1997); 3) Deoni et al.(NeuroImage, 2012); 4) Kulikova et al. (ISMRM 2014, soumis); 5) Deoni et al (Magn Reson Med, 2012)

3T multimodal quantitative longitudinal MRI study in metachromatic leukodystrophy : preliminary study

S Kulikova [1], J Dubois*[2], C Sevin*[3], C Chiron[4], C Bellesme[3], N Chemaly[4], D Leunen[4], F Boumezbeur[3], C Poupon[3], P Aubourg[3], L Hertz-Pannier[1]

1. CEA-Saclay, Neurospin/UNIACT/UMR663; 2. CEA-Saclay, Neurospin/UNICOG/UMR992; 3. Hopital du Kremlin Bicêtre, INSERM U986, Service de neuropédiatrie; 4. UMR663, Université Paris Descartes, Hopital Necker/enfants malades; 5. CEA-Saclay,Neurospin/UNIRS * equal contribution

Introduction and Objectives

Metachromatic leukodystrophy (MLD) is a rare devastating genetic disease accompanied by progressive demyelination of the brain white matter [1-3]. Conventional 1.5T MRI poorly predicts disease progression.

The objective of this longitudinal 3T MRI study is to quantify the microstructural et metabolic changes during the disease progression with the aim of finding sensitive and quantitative neuroimaging biomarkers to establish relevant criteria and endpoints for a gene therapy trial. In this preliminary presentation the developed methodologies were tested on the corticospinal tract (CST).

Methods

***Data acquisition*:**

- 5 infants with the late infantile form of MLD (29 - 66 months), 3 of whom were scanned twice with a 5 month interval.
- 10 control infants (18 - 60 months) with unilateral epilepsy showing good cognitive development (only unaffected hemisphere is considered). One child was scanned twice.
- At 3T, under sedation
  - diffusion tensor imaging (DTI)
    - DW-SE-EPI, 55 axial slices 2 x 2 x 2 mm3, 60 orientations, b = 1500 s.mm-2 (+ b = 0): TE = 92ms, TR = 11s, parallel factor 2.
  - quantitative mapping of the relaxation times T1 et T2
    - EPI single-shot spin-echo SE, 55 axial slices 2 x 2 x 2 mm3
    - T2: 8 TE = 35 -> 280ms, each step = 35ms, TR = 19s, parallel factor 2
    - T1: SE-EPI with inversion-recovery (IR) et 8 TI (TI = 250 -> 1500 ms , each step = 250 ms, + TI = 2000, 2500ms): TE = 35 ms, TR = 16 s.
  - spectroscopy
    - CSI_SE sequence (TE / TR = 30/1600ms) with 6 OVS.

Post-treatment of the data

• Correction of the artifacts (field inhomogeneities, Eddy currents and movements (Fig.1).

• Calculation of the diffusion tensor and creation of the quantitative maps for T1, T2, fractional anisotropy (FA), mean (MD), longitudinal (Lpara) and transverse (Lperp) diffusivities (Fig.2).

• Reconstruction of the CST with regularized streamline algorithm using Connectomist software [4] and regions of interest (ROIs) (Fig.3).

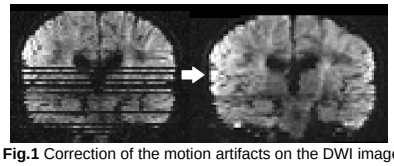

Fig.1 Correction of the motion artifacts on the DWI image

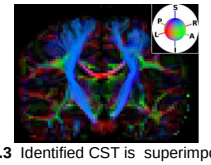

Fig.3 Identified CST is superimposed with the color-coded FA map.

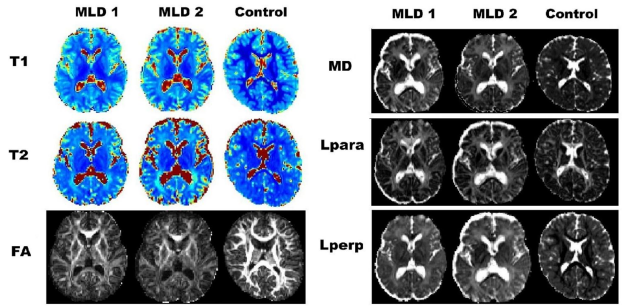

Fig.2 Quantitative MRI maps for a typical MLD infant (MLD1, 29 months), same infant 5 months later (MLD2) and an age-matched control infant.

Data analysis

•Quantitative comparison of the MRI parameters along the CST between 2 groups. The ratio between the MLD and control values is evaluated at each point along the CST (**Fig.4**).

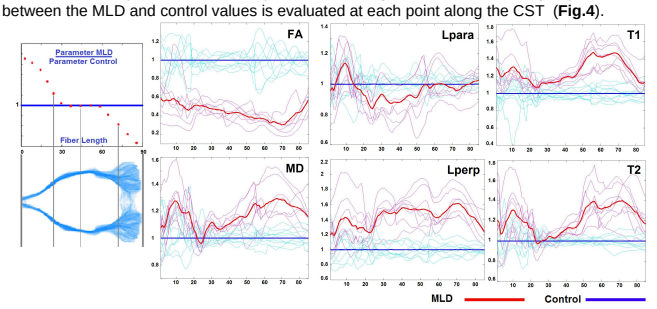

•Evaluation of the Myelin Water Fraction (MWF) in control and MLD infants using multicomponent analysis of the T1 and T2 relaxation times (Fig.5).

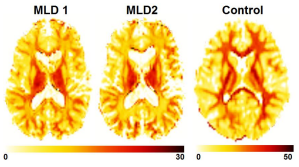

Fig.5 MWF maps for a typical MLD infant (MLD1, 29 months), same infant 5 months later (MLD2) and an age-matched control infant. Note the difference in the palette for MLD and control infants

•Quantitative comparison of the concentrations of the principal metabolites (NAA, choline (Cho), glutamate (Glu), myoInositol (myo-Ins) et lactate(Lac)) between control (E) and MLD groups (t-tests, p<0.05) in the region around the CST (creatine as a reference). (**Fig.6**)

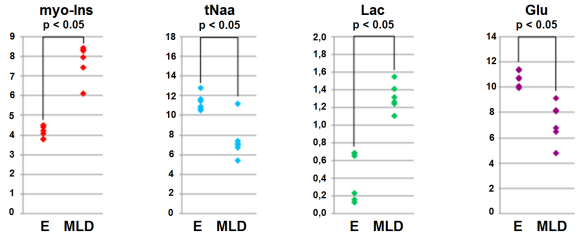

Results and preliminary conclusions

DTI , quantitative T1 and T2 times, MWF (Fig 4,5)

Dramatic changes of all the parameters were observed along the CST in MLD infants in comparison with controls:

- decrease of the anisotropy (up to -65%)
- increase of the transverse diffusivity (up to +60%), T1 and T2 (up to +45% and +40%).
- these changes, strongly correlated, but inhomogeneous, along the CST, likely reflected the demyelination process.
- MWF maps further detailed the spatial pattern of demyelination in MLD infants.

Spectroscopy confirms

- neuronal loss (decrease of the NAA and glutamate concentrations),
- demyelination and astrogliosis (increase of the choline and myo-Inositol concentrations),
- metabolic stress (increase of the lactate concentration)(Fig.6).

Further characterization of these changes longitudinally should allow better understanding of the demyelination dynamics and provide sensitive biomarkers for testing the efficacy of novel therapies.

Refs

1) Martin et al, AJNR 33:1731-1739.

2) Groeschel et al, Neurology 2012, 79:1662-1670

3)Groeschel et al, J Inherit Metab Dis 2011, 34:1095-1102.

4)Duclap et al, ESMRMB 2012, #842..

Conclusion

Investigating both normal and pathological white matter maturation in infants and children benefits from specially-adapted multiparametric approaches. In this work, we have demonstrated how such approaches can help to address specific neuroscience questions, namely:

1. evaluating of global maturational degree relative to the adult mature stage, using the Mahalanobis distance approach (chapter 4);

2. quantifying white matter myelination, using Myelin Water Fraction (MWF) (chapter 5);

3. investigating regional maturation across bundles, using a preliminary atlas of white matter structural connectivity in children (chapter 6).

Both Mahalanobis distance and MWF approaches were shown to be more advantageous for describing normal white matter maturation than conventional univariate MRI strategies thanks to complementary information from different MRI parameters. In the future, these approaches may be combined in one hybrid strategy: for example, by substituting qT1 and qT2 in the Mahalanobis distance approach by MWF, which might help to further understand the contribution of the white matter myelination assessed with MWF to the global ensemble of the maturational processes evaluated with the Mahalanobis distance.

Of importance, Mahalanobis distance approach suggested a general quantitative description of bundles global maturation and allowed estimating the relative maturational delays between bundles. In the future, this model might serve as a reference for evaluating pathological states in neurodevelopmental disorders, e.g. mental retardation. However, relationships between global white matter maturation, measured with Mahalanobis distance, and psychomotor development merits further studies. For example, one may question whether changes in Mahalanobis distance in language-related networks correlate with language acquisition. Similarly, Mahalanobis distance may be used to evaluate white matter changes in eldery people and investigate its relations to cognitive decline.

MWF may further highlight changes due to abnormal myelination and might present an important biomarker in demyelination pathologies. However, it should be kept in mind that MWF quantification relies on tissue modeling and only its future comparison with histological findings in *post-mortem* studies may reveal to which extent MWF calculated using the proposed strategy correlates with true myelin load.

In the future, application of these approaches to investigating regional white

matter maturation across bundles will further benefit from using age-specific atlases of white matter connectivity, like the preliminary atlas described in our work. Such connectivity atlases can speed up data analysis by automatic bundle extraction from tractography datasets and increase reproducibility across the studies. Furthermore, these atlases enable investigating white matter properties even when it is not possible to perform reliable tractography by projecting atlas bundles to the subject data.

The main limitation of the described approaches is that they are very sensitive to acquisition and post-processing settings, making it difficult to compare the obtained results with other studies, unless similar settings are used.

Despite this limitation, we believe that these approaches present powerful tools for further investigating white matter regional maturation in both normal and pathological white matter.

In this work, we have shown some preliminary observations obtained with multimodal MRI in two different pathologies: focal epilepsy and metachromatic leukodystrophy. Although we detected some changes in MRI parameters possibly reflecting pathological processes, our results remain insufficient to make any definite conclusions mainly due to small sizes of patients populations. It was also not possible to apply Mahalanobis distance approach to these populations because of the absence of an adult group acquired with the same acquisition protocol. Thus, our results need to be confirmed in further studies with larger samples that will also take into account multiple factors not included here into analysis: lesion localization (for focal epilepsy), disease onset, clinical scores, etc.

Bibliography

[1] T. M. Jessell and J. R. Sanes. "Development. The decade of the developing brain". eng. In: *Current Opinion in Neurobiology* 10.5 (Oct. 2000), pp. 599–611.

[2] C. S. Monk, S. J. Webb, and C. A. Nelson. "Prenatal neurobiological development: molecular mechanisms and anatomical change". eng. In: *Developmental Neuropsychology* 19.2 (2001), pp. 211–236. DOI: 10.1207/S15326942DN1902_5.

[3] J. Stiles and T. L. Jernigan. "The basics of brain development". eng. In: *Neuropsychology Review* 20.4 (Dec. 2010), pp. 327–348. DOI: 10.1007/s11065-010-9148-4.

[4] G. Z. Tau and B. S. Peterson. "Normal development of brain circuits". eng. In: *Neuropsychopharmacology: Official Publication of the American College of Neuropsychopharmacology* 35.1 (Jan. 2010), pp. 147–168. DOI: 10.1038/npp.2009.115.

[5] A. J. Copp, N. D. E. Greene, and J. N. Murdoch. "The genetic basis of mammalian neurulation". eng. In: *Nature Reviews. Genetics* 4.10 (Oct. 2003), pp. 784–793. DOI: 10.1038/nrg1181.

[6] M. Rhinn, A. Picker, and M. Brand. "Global and local mechanisms of forebrain and midbrain patterning". eng. In: *Current Opinion in Neurobiology* 16.1 (Feb. 2006), pp. 5–12. DOI: 10.1016/j.conb.2006.01.005.

[7] A. Wodarz and W. B. Huttner. "Asymmetric cell division during neurogenesis in Drosophila and vertebrates". eng. In: *Mechanisms of Development* 120.11 (Nov. 2003), pp. 1297–1309.

[8] K. Campbell. "Cortical Neuron Specification: It Has Its Time and Place". In: *Neuron* 46.3 (May 2005), pp. 373–376. DOI: 10.1016/j.neuron.2005.04.014.

[9] L. C. Greig, M. B. Woodworth, M. J. Galazo, H. Padmanabhan, and J. D. Macklis. "Molecular logic of neocortical projection neuron specification, development and diversity". en. In: *Nature Reviews Neuroscience* 14.11 (Nov. 2013), pp. 755–769. DOI: 10.1038/nrn3586.

[10] M. E. Hatten. “The role of migration in central nervous system neuronal development”. eng. In: *Current Opinion in Neurobiology* 3.1 (Feb. 1993), pp. 38–44.

[11] P. Rakic. “Specification of cerebral cortical areas”. eng. In: *Science (New York, N.Y.)* 241.4862 (July 1988), pp. 170–176.

[12] M. F. Casanova and J. Trippe II. “Regulatory mechanisms of cortical laminar development”. In: *Brain Research Reviews* 51.1 (June 2006), pp. 72–84. DOI: 10.1016/j.brainresrev.2005.10.002.

[13] A. R. Desai and S. K. McConnell. “Progressive restriction in fate potential by neural progenitors during cerebral cortical development”. eng. In: *Development (Cambridge, England)* 127.13 (July 2000), pp. 2863–2872.

[14] Z. Huang. “Molecular regulation of neuronal migration during neocortical development”. In: *Molecular and Cellular Neuroscience* 42.1 (Aug. 2009), pp. 11–22. DOI: 10.1016/j.mcn.2009.06.003.

[15] A. R. Kriegstein and S. C. Noctor. “Patterns of neuronal migration in the embryonic cortex”. In: *Trends in Neurosciences* 27.7 (July 2004), pp. 392–399. DOI: 10.1016/j.tins.2004.05.001.

[16] S. K. McConnell and C. E. Kaznowski. “Cell cycle dependence of laminar determination in developing neocortex”. eng. In: *Science (New York, N.Y.)* 254.5029 (Oct. 1991), pp. 282–285.

[17] B. J. Molyneaux, P. Arlotta, J. R. L. Menezes, and J. D. Macklis. “Neuronal subtype specification in the cerebral cortex”. eng. In: *Nature Reviews. Neuroscience* 8.6 (June 2007), pp. 427–437. DOI: 10.1038/nrn2151.

[18] T. Nomura, M. Takahashi, Y. Hara, and N. Osumi. “Patterns of neurogenesis and amplitude of Reelin expression are essential for making a mammalian-type cortex”. eng. In: *PloS One* 3.1 (2008), e1454. DOI: 10.1371/journal.pone.0001454.

[19] M. Rados, M. Judas, and I. Kostović. “In vitro MRI of brain development”. eng. In: *European Journal of Radiology* 57.2 (Feb. 2006), pp. 187–198. DOI: 10.1016/j.ejrad.2005.11.019.

[20] E. Takahashi, R. D. Folkerth, A. M. Galaburda, and P. E. Grant. “Emerging cerebral connectivity in the human fetal brain: an MR tractography study”. eng. In: *Cerebral Cortex (New York, N.Y.: 1991)* 22.2 (Feb. 2012), pp. 455–464. DOI: 10.1093/cercor/bhr126.

[21] S. A. Anderson, O. Marín, C. Horn, K. Jennings, and J. L. Rubenstein. “Distinct cortical migrations from the medial and lateral ganglionic eminences”. eng. In: *Development (Cambridge, England)* 128.3 (Feb. 2001), pp. 353–363.

[22] J. G. Corbin, S. Nery, and G. Fishell. “Telencephalic cells take a tangent: non-radial migration in the mammalian forebrain”. eng. In: *Nature Neuroscience* 4 Suppl (Nov. 2001), pp. 1177–1182. DOI: 10.1038/nn749.

[23] F. Encha-Razavi and P. Sonigo. “Features of the developing brain”. en. In: *Child’s Nervous System* 19.7-8 (June 2003), pp. 426–428. DOI: 10.1007/s00381-003-0765-6.

[24] S. Nery, G. Fishell, and J. G. Corbin. “The caudal ganglionic eminence is a source of distinct cortical and subcortical cell populations”. eng. In: *Nature Neuroscience* 5.12 (Dec. 2002), pp. 1279–1287. DOI: 10.1038/nn971.

[25] N. A. O’Rourke, M. E. Dailey, S. J. Smith, and S. K. McConnell. “Diverse migratory pathways in the developing cerebral cortex”. eng. In: *Science (New York, N.Y.)* 258.5080 (Oct. 1992), pp. 299–302.

[26] J. A. Cooper. “A mechanism for inside-out lamination in the neocortex”. eng. In: *Trends in Neurosciences* 31.3 (Mar. 2008), pp. 113–119. DOI: 10.1016/j.tins.2007.12.003.

[27] V. B. de Graaf-Peters and M. Hadders-Algra. “Ontogeny of the human central nervous system: what is happening when?” eng. In: *Early Human Development* 82.4 (Apr. 2006), pp. 257–266. DOI: 10.1016/j.earlhumdev.2005.10.013.

[28] E. C. Olson and C. A. Walsh. “Smooth, rough and upside-down neocortical development”. eng. In: *Current Opinion in Genetics & Development* 12.3 (June 2002), pp. 320–327.

[29] M. R. G. Emeritus, R. S. Julian, and H. W. Vicky. *Tuberous Sclerosis Complex*. en. Oxford University Press, July 1999.

[30] E. J. Uhlmann, M. Wong, R. L. Baldwin, M. L. Bajenaru, H. Onda, D. J. Kwiatkowski, K. Yamada, and D. H. Gutmann. “Astrocyte-specific TSC1 conditional knockout mice exhibit abnormal neuronal organization and seizures”. eng. In: *Annals of Neurology* 52.3 (Sept. 2002), pp. 285–296. DOI: 10.1002/ana.10283.

[31] M. Cayre, P. Canoll, and J. E. Goldman. “Cell migration in the normal and pathological postnatal mammalian brain”. eng. In: *Progress in Neurobiology* 88.1 (May 2009), pp. 41–63. DOI: 10.1016/j.pneurobio.2009.02.001.

[32] M. B. Luskin and K. McDermott. “Divergent lineages for oligodendrocytes and astrocytes originating in the neonatal forebrain subventricular zone”. eng. In: *Glia* 11.3 (July 1994), pp. 211–226. DOI: 10.1002/glia.440110302.

[33] I. Navarro-Quiroga, M. Hernandez-Valdes, S. L. Lin, and J. R. Naegele. “Postnatal cellular contributions of the hippocampus subventricular zone to the dentate gyrus, corpus callosum, fimbria, and cerebral cortex”. eng. In: *The Journal of Comparative Neurology* 497.5 (Aug. 2006), pp. 833–845. DOI: 10.1002/cne.21037.

[34] S. O. Suzuki and J. E. Goldman. “Multiple cell populations in the early postnatal subventricular zone take distinct migratory pathways: a dynamic study of glial and neuronal progenitor migration”. eng. In: *The Journal of Neuroscience: The Official Journal of the Society for Neuroscience* 23.10 (May 2003), pp. 4240–4250.

[35] W. Y. Chan, S. Kohsaka, and P. Rezaie. “The origin and cell lineage of microglia—New concepts”. In: *Brain Research Reviews* 53.2 (Feb. 2007), pp. 344–354. DOI: 10.1016/j.brainresrev.2006.11.002.

[36] M. A. Cuadros and J. Navascués. “The origin and differentiation of microglial cells during development”. eng. In: *Progress in Neurobiology* 56.2 (Oct. 1998), pp. 173–189.

[37] J. V. Browne. *Research on Early Developmental Care for Preterm Neonates*. en. John Libbey Eurotext, 2005.

[38] R. J. Martin, A. A. Fanaroff, and M. C. Walsh. *Fanaroff and Martin's Neonatal-Perinatal Medicine: Diseases of the Fetus and Infant*. en. Elsevier Health Sciences, Aug. 2014.

[39] I. Markiewicz and B. Lukomska. “The role of astrocytes in the physiology and pathology of the central nervous system”. eng. In: *Acta Neurobiologiae Experimentalis* 66.4 (2006), pp. 343–358.

[40] M. Nedergaard, B. Ransom, and S. A. Goldman. “New roles for astrocytes: redefining the functional architecture of the brain”. eng. In: *Trends in Neurosciences* 26.10 (Oct. 2003), pp. 523–530. DOI: 10.1016/j.tins.2003.08.008.

[41] E. A. Newman. “New roles for astrocytes: regulation of synaptic transmission”. eng. In: *Trends in Neurosciences* 26.10 (Oct. 2003), pp. 536–542. DOI: 10.1016/S0166-2236(03)00237-6.

[42] M. Slezak and F. W. Pfrieger. “New roles for astrocytes: Regulation of CNS synaptogenesis”. In: *Trends in Neurosciences* 26.10 (Oct. 2003), pp. 531–535. DOI: 10.1016/j.tins.2003.08.005.

[43] P. Tortori-Donati and A. Rossi. *Pediatric Neuroradiology: Brain. Head, Neck and Spine*. en. Springer Science & Business Media, Feb. 2010.

[44] S.-c. Lin and D. E. Bergles. “Synaptic signaling between GABAergic interneurons and oligodendrocyte precursor cells in the hippocampus”. eng. In: *Nature Neuroscience* 7.1 (Jan. 2004), pp. 24–32. DOI: 10.1038/nn1162.

[45] D. M. McTigue and R. B. Tripathi. “The life, death, and replacement of oligodendrocytes in the adult CNS”. eng. In: *Journal of Neurochemistry* 107.1 (Oct. 2008), pp. 1–19. DOI: 10.1111/j.1471-4159.2008.05570.x.

[46] G. M. Innocenti, S. Clarke, and H. Koppel. “Transitory macrophages in the white matter of the developing visual cortex. II. Development and relations with axonal pathways”. eng. In: *Brain Research* 313.1 (Dec. 1983), pp. 55–66.

[47] S. Elkabes, E. M. DiCicco-Bloom, and I. B. Black. “Brain microglia/macrophages express neurotrophins that selectively regulate microglial proliferation and function”. eng. In: *The Journal of Neuroscience: The Official Journal of the Society for Neuroscience* 16.8 (Apr. 1996), pp. 2508–2521.

[48] G. M. Jonakait, M. B. Luskin, R. Wei, X. F. Tian, and L. Ni. “Conditioned medium from activated microglia promotes cholinergic differentiation in the basal forebrain in vitro”. eng. In: *Developmental Biology* 177.1 (July 1996), pp. 85–95. DOI: 10.1006/dbio.1996.0147.

[49] Y. Ziv, N. Ron, O. Butovsky, G. Landa, E. Sudai, N. Greenberg, H. Cohen, J. Kipnis, and M. Schwartz. “Immune cells contribute to the maintenance of neurogenesis and spatial learning abilities in adulthood”. eng. In: *Nature Neuroscience* 9.2 (Feb. 2006), pp. 268–275. DOI: 10.1038/nn1629.

[50] S. P. Hamilton and L. H. Rome. “Stimulation of in vitro myelin synthesis by microglia”. eng. In: *Glia* 11.4 (Aug. 1994), pp. 326–335. DOI: 10.1002/glia.440110405.

[51] T. Andreas, U. Wedegärtner, M. Tchirikov, K. Hecher, and H. J. Schröder. “Fetal brain volume measurements by magnetic resonance imaging”. en. In: *Ultrasound in Obstetrics and Gynecology* 27.5 (May 2006), pp. 588–589. DOI: 10.1002/uog.2790.

[52] C. Clouchoux, N. Guizard, A. C. Evans, A. J. du Plessis, and C. Limperopoulos. “Normative fetal brain growth by quantitative in vivo magnetic resonance imaging”. eng. In: *American Journal of Obstetrics and Gynecology* 206.2 (Feb. 2012), 173.e1–8. DOI: 10.1016/j.ajog.2011.10.002.

[53] M. I. Levene and F. A. Chervenak. *Fetal and Neonatal Neurology and Neurosurgery*. en. Elsevier Health Sciences, 2009.

[54] T. Sakai, S. Hirata, K. Fuwa, K. Sugama, K. Kusunoki, H. Makishima, T. Eguchi, S. Yamada, N. Ogihara, and H. Takeshita. “Fetal brain development in chimpanzees versus humans”. In: *Current Biology* 22.18 (Sept. 2012), R791–R792. DOI: 10.1016/j.cub.2012.06.062.

[55] A. S. Dekaban. “Changes in brain weights during the span of human life: relation of brain weights to body heights and body weights”. eng. In: *Annals of Neurology* 4.4 (Oct. 1978), pp. 345–356. DOI: 10.1002/ana.410040410.

[56] R. C. Knickmeyer, S. Gouttard, C. Kang, D. Evans, K. Wilber, J. K. Smith, R. M. Hamer, W. Lin, G. Gerig, and J. H. Gilmore. “A structural MRI study of human brain development from birth to 2 years”. eng. In: *The Journal of Neuroscience: The Official Journal of the Society for Neuroscience* 28.47 (Nov. 2008), pp. 12176–12182. DOI: 10.1523/JNEUROSCI.3479-08.2008.

[57] *WHO | WHO Child Growth Standards: Methods and development*.

[58] W. R. Shankle, M. S. Rafii, B. H. Landing, and J. H. Fallon. "Approximate doubling of numbers of neurons in postnatal human cerebral cortex and in 35 specific cytoarchitectural areas from birth to 72 months". eng. In: *Pediatric and Developmental Pathology: The Official Journal of the Society for Pediatric Pathology and the Paediatric Pathology Society* 2.3 (June 1999), pp. 244–259.

[59] R. D. Bhardwaj, M. A. Curtis, K. L. Spalding, B. A. Buchholz, D. Fink, T. Björk-Eriksson, C. Nordborg, F. H. Gage, H. Druid, P. S. Eriksson, and J. Frisén. "Neocortical neurogenesis in humans is restricted to development". eng. In: *Proceedings of the National Academy of Sciences of the United States of America* 103.33 (Aug. 2006), pp. 12564–12568. DOI: 10.1073/pnas.0605177103.

[60] J. G. Chi, E. C. Dooling, and F. H. Gilles. "Gyral development of the human brain". en. In: *Annals of Neurology* 1.1 (Jan. 1977), pp. 86–93. DOI: 10.1002/ana.410010109.

[61] H. Huang, R. Xue, J. Zhang, T. Ren, L. J. Richards, P. Yarowsky, M. I. Miller, and S. Mori. "Anatomical characterization of human fetal brain development with diffusion tensor magnetic resonance imaging". eng. In: *The Journal of Neuroscience: The Official Journal of the Society for Neuroscience* 29.13 (Apr. 2009), pp. 4263–4273. DOI: 10.1523/JNEUROSCI.2769-08.2009.

[62] *Brain Mapping: An Encyclopedic Reference*. en. Academic Press, Feb. 2015.

[63] T. White, S. Su, M. Schmidt, C.-Y. Kao, and G. Sapiro. "The development of gyrification in childhood and adolescence". eng. In: *Brain and Cognition* 72.1 (Feb. 2010), pp. 36–45. DOI: 10.1016/j.bandc.2009.10.009.

[64] K. Zilles, A. Schleicher, C. Langemann, K. Amunts, P. Morosan, N. Palomero-Gallagher, T. Schormann, H. Mohlberg, U. Bürgel, H. Steinmetz, G. Schlaug, and P. E. Roland. "Quantitative analysis of sulci in the human cerebral cortex: development, regional heterogeneity, gender difference, asymmetry, intersubject variability and cortical architecture". eng. In: *Human Brain Mapping* 5.4 (1997), pp. 218–221. DOI: 10.1002/(SICI)1097-0193(1997)5:4<218::AID-HBM2>3.0.CO;2-6.

[65] G. López-Bendito, A. Cautinat, J. A. Sánchez, F. Bielle, N. Flames, A. N. Garratt, D. A. Talmage, L. W. Role, P. Charnay, O. Marín, and S. Garel. "Tangential neuronal migration controls axon guidance: a role for neuregulin-1 in thalamocortical axon navigation". eng. In: *Cell* 125.1 (Apr. 2006), pp. 127–142. DOI: 10.1016/j.cell.2006.01.042.

[66] P. Sonderegger and F. G. Rathjen. "Regulation of axonal growth in the vertebrate nervous system by interactions between glycoproteins belonging to two subgroups of the immunoglobulin superfamily". eng. In: *The Journal of Cell Biology* 119.6 (Dec. 1992), pp. 1387–1394.

[67] K. Thelen, V. Kedar, A. K. Panicker, R.-S. Schmid, B. R. Midkiff, and P. F. Maness. “The neural cell adhesion molecule L1 potentiates integrin-dependent cell migration to extracellular matrix proteins”. eng. In: *The Journal of Neuroscience: The Official Journal of the Society for Neuroscience* 22.12 (June 2002), pp. 4918–4931.

[68] S. S. Easter, J. Burrill, R. C. Marcus, L. S. Ross, J. S. Taylor, and S. W. Wilson. “Initial tract formation in the vertebrate brain”. eng. In: *Progress in Brain Research* 102 (1994), pp. 79–93. DOI: 10.1016/S0079-6123(08)60533-6.

[69] A. Chédotal and L. J. Richards. “Wiring the Brain: The Biology of Neuronal Guidance”. In: *Cold Spring Harbor Perspectives in Biology* 2.6 (June 2010). DOI: 10.1101/cshperspect.a001917.

[70] I. Kostovic and P. Rakic. “Developmental history of the transient subplate zone in the visual and somatosensory cortex of the macaque monkey and human brain”. en. In: *The Journal of Comparative Neurology* 297.3 (July 1990), pp. 441–470. DOI: 10.1002/cne.902970309.

[71] L. Mrzljak, H. B. Uylings, C. G. Van Eden, and M. Judás. “Neuronal development in human prefrontal cortex in prenatal and postnatal stages”. eng. In: *Progress in Brain Research* 85 (1990), pp. 185–222.

[72] H. Supèr, E. Soriano, and H. B. Uylings. “The functions of the preplate in development and evolution of the neocortex and hippocampus”. eng. In: *Brain Research. Brain Research Reviews* 27.1 (June 1998), pp. 40–64.

[73] K. L. Allendoerfer and C. J. Shatz. “The subplate, a transient neocortical structure: its role in the development of connections between thalamus and cortex”. eng. In: *Annual Review of Neuroscience* 17 (1994), pp. 185–218. DOI: 10.1146/annurev.ne.17.030194.001153.

[74] A. Ghosh, A. Antonini, S. K. McConnell, and C. J. Shatz. “Requirement for subplate neurons in the formation of thalamocortical connections”. eng. In: *Nature* 347.6289 (Sept. 1990), pp. 179–181. DOI: 10.1038/347179a0.

[75] A. Ghosh and C. J. Shatz. “Involvement of subplate neurons in the formation of ocular dominance columns”. eng. In: *Science (New York, N.Y.)* 255.5050 (Mar. 1992), pp. 1441–1443.

[76] P. O. Kanold. “Transient microcircuits formed by subplate neurons and their role in functional development of thalamocortical connections”. eng. In: *Neuroreport* 15.14 (Oct. 2004), pp. 2149–2153.

[77] I. Kostović and N. Jovanov-Milosević. “The development of cerebral connections during the first 20-45 weeks’ gestation”. eng. In: *Seminars in Fetal & Neonatal Medicine* 11.6 (Dec. 2006), pp. 415–422. DOI: 10.1016/j.siny.2006.07.001.

[78] A. Nobin and A. Björklund. “Topography of the monoamine neuron systems in the human brain as revealed in fetuses”. eng. In: *Acta Physiologica Scandinavica. Supplementum* 388 (1973), pp. 1–40.

[79] L. Olson, L. O. Boréus, and A. Seiger. “Histochemical demonstration and mapping of 5-hydroxytryptamine- and catecholamine-containing neuron systems in the human fetal brain”. eng. In: *Zeitschrift Für Anatomie Und Entwicklungsgeschichte* 139.3 (Apr. 1973), pp. 259–282.

[80] C. Verney. “Distribution of the catecholaminergic neurons in the central nervous system of human embryos and fetuses”. eng. In: *Microscopy Research and Technique* 46.1 (July 1999), pp. 24–47. DOI: 10.1002/(SICI)1097-0029(19990701)46:1<24::AID-JEMT3>3.0.CO;2-E.

[81] N. Zecevic and C. Verney. “Development of the catecholamine neurons in human embryos and fetuses, with special emphasis on the innervation of the cerebral cortex”. eng. In: *The Journal of Comparative Neurology* 351.4 (Jan. 1995), pp. 509–535. DOI: 10.1002/cne.903510404.

[82] L. Vasung, H. Huang, N. Jovanov-Milošević, M. Pletikos, S. Mori, and I. Kostović. “Development of axonal pathways in the human fetal fronto-limbic brain: histochemical characterization and diffusion tensor imaging”. eng. In: *Journal of Anatomy* 217.4 (Oct. 2010), pp. 400–417. DOI: 10.1111/j.1469-7580.2010.01260.x.

[83] I. Kostovic and M. Judas. “Prolonged coexistence of transient and permanent circuitry elements in the developing cerebral cortex of fetuses and preterm infants”. eng. In: *Developmental Medicine and Child Neurology* 48.5 (May 2006), pp. 388–393. DOI: 10.1017/S0012162206000831.

[84] I. Kostović and M. Judas. “Transient patterns of cortical lamination during prenatal life: do they have implications for treatment?” eng. In: *Neuroscience and Biobehavioral Reviews* 31.8 (2007), pp. 1157–1168. DOI: 10.1016/j.neubiorev.2007.04.018.

[85] I. Kostović and M. Judas. “The development of the subplate and thalamocortical connections in the human foetal brain”. eng. In: *Acta Paediatrica (Oslo, Norway: 1992)* 99.8 (Aug. 2010), pp. 1119–1127. DOI: 10.1111/j.1651-2227.2010.01811.x.

[86] T. Bui, J.-L. Daire, F. Chalard, I. Zaccaria, C. Alberti, M. Elmaleh, C. Garel, D. Luton, N. Blanc, and G. Sebag. “Microstructural development of human brain assessed in utero by diffusion tensor imaging”. eng. In: *Pediatric Radiology* 36.11 (Nov. 2006), pp. 1133–1140. DOI: 10.1007/s00247-006-0266-3.

[87] M. Judas, M. Rados, N. Jovanov-Milosevic, P. Hrabac, R. Stern-Padovan, and I. Kostovic. “Structural, immunocytochemical, and mr imaging properties of periventricular crossroads of growing cortical pathways in preterm infants”. eng. In: *AJNR. American journal of neuroradiology* 26.10 (Dec. 2005), pp. 2671–2684.

[88] G. Kasprian, P. C. Brugger, M. Weber, M. Krssák, E. Krampl, C. Herold, and D. Prayer. "In utero tractography of fetal white matter development". eng. In: *NeuroImage* 43.2 (Nov. 2008), pp. 213–224. DOI: 10.1016/j.neuroimage.2008.07.026.

[89] M. J. Burek and R. W. Oppenheim. "Programmed cell death in the developing nervous system". eng. In: *Brain Pathology (Zurich, Switzerland)* 6.4 (Oct. 1996), pp. 427–446.

[90] W. Y. Chan, D. E. Lorke, S. C. Tiu, and D. T. Yew. "Proliferation and apoptosis in the developing human neocortex". eng. In: *The Anatomical Record* 267.4 (Aug. 2002), pp. 261–276. DOI: 10.1002/ar.10100.

[91] J. M. Gohlke, W. C. Griffith, and E. M. Faustman. "Computational models of neocortical neuronogenesis and programmed cell death in the developing mouse, monkey, and human". eng. In: *Cerebral Cortex (New York, N.Y.: 1991)* 17.10 (Oct. 2007), pp. 2433–2442. DOI: 10.1093/cercor/bhl151.

[92] L. Lossi and A. Merighi. "In vivo cellular and molecular mechanisms of neuronal apoptosis in the mammalian CNS". eng. In: *Progress in Neurobiology* 69.5 (Apr. 2003), pp. 287–312.

[93] S. Rakic and N. Zecevic. "Programmed cell death in the developing human telencephalon". eng. In: *The European Journal of Neuroscience* 12.8 (Aug. 2000), pp. 2721–2734.

[94] M. E. Molliver, I. Kostović, and H. van der Loos. "The development of synapses in cerebral cortex of the human fetus". eng. In: *Brain Research* 50.2 (Feb. 1973), pp. 403–407.

[95] I. Kostovic and P. S. Goldman-Rakic. "Transient cholinesterase staining in the mediodorsal nucleus of the thalamus and its connections in the developing human and monkey brain". eng. In: *The Journal of Comparative Neurology* 219.4 (Oct. 1983), pp. 431–447. DOI: 10.1002/cne.902190405.

[96] A. Burkhalter. "Development of forward and feedback connections between areas V1 and V2 of human visual cortex". eng. In: *Cerebral Cortex (New York, N.Y.: 1991)* 3.5 (Oct. 1993), pp. 476–487.

[97] R. F. Hevner. "Development of connections in the human visual system during fetal mid-gestation: a DiI-tracing study". eng. In: *Journal of Neuropathology and Experimental Neurology* 59.5 (May 2000), pp. 385–392.

[98] I. Kostović, N. Jovanov-Milošević, M. Radoš, G. Sedmak, V. Benjak, M. Kostović-Srzentić, L. Vasung, M. Čuljat, M. Radoš, P. Hüppi, and M. Judaš. "Perinatal and early postnatal reorganization of the subplate and related cellular compartments in the human cerebral wall as revealed by histological and MRI approaches". eng. In: *Brain Structure & Function* 219.1 (Jan. 2014), pp. 231–253. DOI: 10.1007/s00429-012-0496-0.

[99] B. H. Landing, W. R. Shankle, J. Hara, J. Brannock, and J. H. Fallon. "The development of structure and function in the postnatal human cerebral cortex from birth to 72 months: changes in thickness of layers II and III co-relate to the onset of new age-specific behaviors". eng. In: *Pediatric Pathology & Molecular Medicine* 21.3 (June 2002), pp. 321–342. DOI: 10.1080/02770930290056541.

[100] H. Huang, J. Zhang, S. Wakana, W. Zhang, T. Ren, L. J. Richards, P. Yarowsky, P. Donohue, E. Graham, P. C. M. van Zijl, and S. Mori. "White and gray matter development in human fetal, newborn and pediatric brains". In: *NeuroImage* 33.1 (Oct. 2006), pp. 27–38. DOI: 10.1016/j.neuroimage.2006.06.009.

[101] S. G. Waxman and L. Bangalore. "Chapter 5 - Electrophysiologic Consequences of Myelination". In: *Myelin Biology and Disorders*. Ed. by R. A. Lazzarini, J. W. Griffin, H. Lassman, K.-A. Nave, R. Miller, and B. D. Trapp. San Diego: Academic Press, 2004, pp. 117–141.

[102] M. S. v. d. Knaap and J. Valk. "Myelin and White Matter". en. In: *Magnetic Resonance of Myelin, Myelination, and Myelin Disorders*. Springer Berlin Heidelberg, Jan. 1995, pp. 1–17.

[103] P. Morell and R. H. Quarles. "Myelin Formation, Structure and Biochemistry". en. In: (1999).

[104] R. E. Martenson. *Myelin*. en. CRC Press, Feb. 1992.

[105] Y. Min, K. Kristiansen, J. M. Boggs, C. Husted, J. A. Zasadzinski, and J. Israelachvili. "Interaction forces and adhesion of supported myelin lipid bilayers modulated by myelin basic protein". en. In: *Proceedings of the National Academy of Sciences* 106.9 (Mar. 2009), pp. 3154–3159. DOI: 10.1073/pnas.0813110106.

[106] N. Baumann and D. Pham-Dinh. "Biology of oligodendrocyte and myelin in the mammalian central nervous system." In: *Physiol Rev* 81 (2001), pp. 871–927.

[107] P. R. Lee, D. Fields, P. R. Lee, and R. D. Fields. "Regulation of myelin genes implicated in psychiatric disorders by functional activity in axons". In: *Frontiers in Neuroanatomy* 3 (2009), p. 4. DOI: 10.3389/neuro.05.004.2009.

[108] B. Stevens, S. Porta, L. L. Haak, V. Gallo, and R. D. Fields. "Adenosine: a neuron-glial transmitter promoting myelination in the CNS in response to action potentials". eng. In: *Neuron* 36.5 (Dec. 2002), pp. 855–868.

[109] J. Bernal. "Action of thyroid hormone in brain". eng. In: *Journal of Endocrinological Investigation* 25.3 (Mar. 2002), pp. 268–288.

[110] T. Noguchi. "Effects of growth hormone on cerebral development: morphological studies". eng. In: *Hormone Research* 45.1-2 (1996), pp. 5–17.

[111] C. A. Ghiani, X. Yuan, A. M. Eisen, P. L. Knutson, R. A. DePinho, C. J. McBain, and V. Gallo. "Voltage-activated K+ channels and membrane depolarization regulate accumulation of the cyclin-dependent kinase inhibitors p27(Kip1) and p21(CIP1) in glial progenitor cells". eng. In: *The Journal of Neuroscience: The Official Journal of the Society for Neuroscience* 19.13 (July 1999), pp. 5380–5392.

[112] G. Barbin, M. S. Aigrot, P. Charles, A. Foucher, M. Grumet, M. Schachner, B. Zalc, and C. Lubetzki. "Axonal cell-adhesion molecule L1 in CNS myelination". eng. In: *Neuron Glia Biology* 1.1 (Feb. 2004), pp. 65–72. DOI: doi:10.1017/S1740925X04000092.

[113] K. Itoh, M. Ozaki, B. Stevens, and R. D. Fields. "Activity-dependent regulation of N-cadherin in DRG neurons: differential regulation of N-cadherin, NCAM, and L1 by distinct patterns of action potentials". eng. In: *Journal of Neurobiology* 33.6 (Nov. 1997), pp. 735–748.

[114] K. Itoh, B. Stevens, M. Schachner, and R. D. Fields. "Regulated expression of the neural cell adhesion molecule L1 by specific patterns of neural impulses". eng. In: *Science (New York, N.Y.)* 270.5240 (Nov. 1995), pp. 1369–1372.

[115] M. Kukley, E. Capetillo-Zarate, and D. Dietrich. "Vesicular glutamate release from axons in white matter". eng. In: *Nature Neuroscience* 10.3 (Mar. 2007), pp. 311–320. DOI: 10.1038/nn1850.

[116] T. Ishibashi, K. A. Dakin, B. Stevens, P. R. Lee, S. V. Kozlov, C. L. Stewart, and R. D. Fields. "Astrocytes promote myelination in response to electrical impulses". eng. In: *Neuron* 49.6 (Mar. 2006), pp. 823–832. DOI: 10.1016/j.neuron.2006.02.006.

[117] B. A. Brody, H. C. Kinney, A. S. Kloman, and F. H. Gilles. "Sequence of central nervous system myelination in human infancy. I. An autopsy study of myelination". eng. In: *Journal of neuropathology and experimental neurology* 46.3 (May 1987), pp. 283–301.

[118] F. H. Gilles, A. Leviton, and E. C. Dooling. *The Developing Human Brain: Growth and Epidemiologic Neuropathology*. en. Butterworth-Heinemann, Oct. 2013.

[119] H. C. Kinney, B. A. Brody, A. S. Kloman, and F. H. Gilles. "Sequence of central nervous system myelination in human infancy. II. Patterns of myelination in autopsied infants". eng. In: *Journal of neuropathology and experimental neurology* 47.3 (May 1988), pp. 217–234.

[120] P. I. Yakovlev. "Morphological criteria of growth and maturation of the nervous system in man". eng. In: *Research Publications - Association for Research in Nervous and Mental Disease* 39 (1962), pp. 3–46.

[121] P. Yakovlev and A. Lecours. “The myelogenetic cycles of regional maturation of the brain”. In: *Regional Development of the Brain in Early Life*. Ed. by A. Minkowsky. Blackwell Scientific Publications, 1967, pp. 3–70.

[122] P. Flechsig. *Anatomie des menschlichen Gehirns und Rückenmarks auf myelogenetischer Grundlage*. Leipzig: G. Thieme, 1920.

[123] M. Iai, T. Yamamura, and S. Takashima. “Early expression of proteolipid protein in human fetal and infantile cerebri”. eng. In: *Pediatric Neurology* 17.3 (Oct. 1997), pp. 235–239.

[124] A. J. Barkovich, B. O. Kjos, D. E. Jackson Jr, and D. Norman. “Normal maturation of the neonatal and infant brain: MR imaging at 1.5 T”. eng. In: *Radiology* 166.1 Pt 1 (Jan. 1988), pp. 173–180. DOI: 10.1148/radiology.166.1.3336675.

[125] M. R. Asato, R. Terwilliger, J. Woo, and B. Luna. “White Matter Development in Adolescence: A DTI Study”. en. In: *Cerebral Cortex* 20.9 (Sept. 2010), pp. 2122–2131. DOI: 10.1093/cercor/bhp282.

[126] K. P. N. Forbes, J. G. Pipe, and C. R. Bird. “Changes in Brain Water Diffusion during the 1st Year of Life”. In: *Radiology* 222.2 (Feb. 2002), pp. 405–409. DOI: 10.1148/radiol.2222010179.

[127] X. Geng, S. Gouttard, A. Sharma, H. Gu, M. Styner, W. Lin, G. Gerig, and J. H. Gilmore. “Quantitative tract-based white matter development from birth to age 2 years”. In: *NeuroImage* 61.3 (July 2012), pp. 542–557. DOI: 10.1016/j.neuroimage.2012.03.057.

[128] L. Hermoye, C. Saint-Martin, G. Cosnard, S.-K. Lee, J. Kim, M.-C. Nassogne, R. Menten, P. Clapuyt, P. K. Donohue, K. Hua, S. Wakana, H. Jiang, P. C. M. van Zijl, and S. Mori. “Pediatric diffusion tensor imaging: Normal database and observation of the white matter maturation in early childhood”. In: *NeuroImage* 29.2 (Jan. 2006), pp. 493–504. DOI: 10.1016/j.neuroimage.2005.08.017.

[129] C. Lebel, L. Walker, A. Leemans, L. Phillips, and C. Beaulieu. “Microstructural maturation of the human brain from childhood to adulthood”. eng. In: *NeuroImage* 40.3 (Apr. 2008), pp. 1044–1055. DOI: 10.1016/j.neuroimage.2007.12.053.

[130] C. Lebel and C. Beaulieu. “Longitudinal development of human brain wiring continues from childhood into adulthood”. eng. In: *The Journal of Neuroscience: The Official Journal of the Society for Neuroscience* 31.30 (July 2011), pp. 10937–10947. DOI: 10.1523/JNEUROSCI.5302-10.2011.

[131] P. Mukherjee, J. H. Miller, J. S. Shimony, T. E. Conturo, B. C. P. Lee, C. R. Almli, and R. C. McKinstry. “Normal Brain Maturation during Childhood: Developmental Trends Characterized with Diffusion-Tensor MR Imaging”. In: *Radiology* 221.2 (Nov. 2001), pp. 349–358. DOI: 10.1148/radiol.2212001702.

[132] N. Sadeghi, M. Prastawa, P. T. Fletcher, J. Wolff, J. H. Gilmore, and G. Gerig. "Regional characterization of longitudinal DT-MRI to study white matter maturation of the early developing brain". In: *NeuroImage* 68 (Mar. 2013), pp. 236–247. DOI: 10.1016/j.neuroimage.2012.11.040.

[133] J. Dubois, G. Dehaene-Lambertz, S. Kulikova, C. Poupon, P. S. Hüppi, and L. Hertz-Pannier. "The early development of brain white matter: a review of imaging studies in fetuses, newborns and infants". eng. In: *Neuroscience* 276 (Sept. 2014), pp. 48–71. DOI: 10.1016/j.neuroscience.2013.12.044.

[134] S. C. L. Deoni, E. Mercure, A. Blasi, D. Gasston, A. Thomson, M. Johnson, S. C. R. Williams, and D. G. M. Murphy. "Mapping Infant Brain Myelination with Magnetic Resonance Imaging". In: *Journal of Neuroscience* 31.2 (Jan. 2011), pp. 784–791. DOI: 10.1523/JNEUROSCI.2106-10.2011.

[135] S. C. L. Deoni, D. C. Dean 3rd, J. O'Muircheartaigh, H. Dirks, and B. A. Jerskey. "Investigating white matter development in infancy and early childhood using myelin water faction and relaxation time mapping". eng. In: *NeuroImage* 63.3 (Nov. 2012), pp. 1038–1053. DOI: 10.1016/j.neuroimage.2012.07.037.

[136] T. P. L. Roberts and D. Mikulis. "Neuro MR: principles". eng. In: *Journal of magnetic resonance imaging: JMRI* 26.4 (Oct. 2007), pp. 823–837. DOI: 10.1002/jmri.21029.

[137] W. D. Rooney, G. Johnson, X. Li, E. R. Cohen, S.-G. Kim, K. Ugurbil, and C. S. Springer. "Magnetic field and tissue dependencies of human brain longitudinal 1H2O relaxation in vivo". eng. In: *Magnetic Resonance in Medicine* 57.2 (Feb. 2007), pp. 308–318. DOI: 10.1002/mrm.21122.

[138] G. J. Stanisz, E. E. Odrobina, J. Pun, M. Escaravage, S. J. Graham, M. J. Bronskill, and R. M. Henkelman. "T1, T2 relaxation and magnetization transfer in tissue at 3T". en. In: *Magnetic Resonance in Medicine* 54.3 (Sept. 2005), pp. 507–512. DOI: 10.1002/mrm.20605.

[139] M. Ditchfield. "3T MRI in paediatrics: challenges and clinical applications". eng. In: *European Journal of Radiology* 68.2 (Nov. 2008), pp. 309–319. DOI: 10.1016/j.ejrad.2008.05.019.

[140] B. J. MacIntosh and S. J. P. Graham. "Magnetic resonance imaging to visualize stroke and characterize stroke recovery: a review". In: *Stroke* 4 (2013), p. 60. DOI: 10.3389/fneur.2013.00060.

[141] J. P. Wansapura, S. K. Holland, R. S. Dunn, and W. S. Ball. "NMR relaxation times in the human brain at 3.0 tesla". eng. In: *Journal of magnetic resonance imaging: JMRI* 9.4 (Apr. 1999), pp. 531–538.

[142] W. L. Sibbitt, W. M. Brooks, L. J. Haseler, R. H. Griffey, L. M. Frank, B. L. Hart, and R. R. Sibbitt. "Spin-spin relaxation of brain tissues in systemic lupus erythematosus". en. In: *Arthritis & Rheumatism* 38.6 (June 1995), pp. 810–818. DOI: 10.1002/art.1780380615.

[143] S. Siemonsen, U. Löbel, J. Sedlacik, N. D. Forkert, K. Mouridsen, L. Østergaard, G. Thomalla, and J. Fiehler. "Elevated T2-values in MRI of stroke patients shortly after symptom onset do not predict irreversible tissue infarction". eng. In: *Brain: A Journal of Neurology* 135.Pt 6 (June 2012), pp. 1981–1989. DOI: 10.1093/brain/aws079.

[144] P. Tofts. *Quantitative MRI of the Brain: Measuring Changes Caused by Disease*. en. John Wiley & Sons, Aug. 2005.

[145] C. Poupon, J. Dubois, L. Marrakchi, V. Brion, J.-F. Mangin, and F. Poupon. "Real-time EPI T1, T2 and T2* mapping at 3T". In: *In proceedings of the 18th annual ISMRM meeting* (2010).

[146] P. A. Bottomley, T. H. Foster, R. E. Argersinger, and L. M. Pfeifer. "A review of normal tissue hydrogen NMR relaxation times and relaxation mechanisms from 1–100 MHz: Dependence on tissue type, NMR frequency, temperature, species, excision, and age". In: *Medical Physics* 11.4 (July 1984), pp. 425–448. DOI: 10.1118/1.595535.

[147] J.-P. Korb and R. G. Bryant. "Magnetic field dependence of proton spin-lattice relaxation times". eng. In: *Magnetic Resonance in Medicine* 48.1 (July 2002), pp. 21–26. DOI: 10.1002/mrm.10185.

[148] S. W. Atlas. *Magnetic Resonance Imaging of the Brain and Spine*. en. Lippincott Williams & Wilkins, 2009.

[149] P.-M. Robitaille and L. Berliner. *Ultra High Field Magnetic Resonance Imaging*. en. Springer Science & Business Media, Dec. 2007.

[150] T. Paus, D. L. Collins, A. C. Evans, G. Leonard, G. B. Pike, and A. Zijdenbos. "Maturation of white matter in the human brain: A review of magnetic resonance studies". In: *Brain Research Bulletin* 54.3 (2001), pp. 255–266.

[151] T. Autti, R. Raininko, S. L. Vanhanen, M. Kallio, and P. Santavuori. "MRI of the normal brain from early childhood to middle age. II. Age dependence of signal intensity changes on T2-weighted images". eng. In: *Neuroradiology* 36.8 (Nov. 1994), pp. 649–651.

[152] A. J. Barkovich. "Concepts of myelin and myelination in neuroradiology". eng. In: *AJNR. American journal of neuroradiology* 21.6 (July 2000), pp. 1099–1109.

[153] V. Engelbrecht, M. Rassek, S. Preiss, C. Wald, and U. Mödder. "Age-dependent changes in magnetization transfer contrast of white matter in the pediatric brain". eng. In: *AJNR. American journal of neuroradiology* 19.10 (Dec. 1998), pp. 1923–1929.

[154] C. B. McArdle, C. J. Richardson, D. A. Nicholas, M. Mirfakhraee, C. K. Hayden, and E. G. Amparo. "Developmental features of the neonatal brain: MR imaging. Part I. Gray-white matter differentiation and myelination". eng. In: *Radiology* 162.1 Pt 1 (Jan. 1987), pp. 223–229. DOI: 10.1148/radiology.162.1.3786767.

[155] N. Saito, O. Sakai, A. Ozonoff, and H. Jara. "Relaxo-volumetric multispectral quantitative magnetic resonance imaging of the brain over the human lifespan: global and regional aging patterns". English. In: *Magnetic Resonance Imaging* 27.7 (Sept. 2009), pp. 895–906. DOI: 10.1016/j.mri.2009.05.006.

[156] R. G. Steen, R. J. Ogg, W. E. Reddick, and P. B. Kingsley. "Age-related changes in the pediatric brain: quantitative MR evidence of maturational changes during adolescence". eng. In: *AJNR. American journal of neuroradiology* 18.5 (May 1997), pp. 819–828.

[157] A. Barkovich, B. Kjos, D. J. Jackson, and D. Norman. "Normal maturation of the neonatal and infant brain: MR imaging at 1.5 T." In: *Radiology* 166 (1988), pp. 173–180.

[158] J. Ono, R. Kodaka, K. Imai, Y. Itagaki, J. Tanaka, K. Inui, T. Nagai, K. Sakurai, K. Harada, and S. Okada. "Evaluation of myelination by means of the T2 value on magnetic resonance imaging". eng. In: *Brain & Development* 15.6 (Dec. 1993), pp. 433–438.

[159] M. S. van der Knaap and J. Valk. "MR imaging of the various stages of normal myelination during the first year of life". eng. In: *Neuroradiology* 31.6 (1990), pp. 459–470.

[160] A. Bizzi, R. A. Brooks, A. Brunetti, J. M. Hill, J. R. Alger, R. S. Miletich, T. L. Francavilla, and G. Di Chiro. "Role of iron and ferritin in MR imaging of the brain: a study in primates at different field strengths". eng. In: *Radiology* 177.1 (Oct. 1990), pp. 59–65. DOI: 10.1148/radiology.177.1.2399339.

[161] B. P. Drayer. "Basal ganglia: significance of signal hypointensity on T2-weighted MR images". eng. In: *Radiology* 173.2 (Nov. 1989), pp. 311–312. DOI: 10.1148/radiology.173.2.2798863.

[162] C. Schenker, D. Meier, W. Wichmann, P. Boesiger, and A. Valavanis. "Age distribution and iron dependency of the T2 relaxation time in the globus pallidus and putamen". eng. In: *Neuroradiology* 35.2 (1993), pp. 119–124.

[163] W. Kucharczyk, P. M. Macdonald, G. J. Stanisz, and R. M. Henkelman. "Relaxivity and magnetization transfer of white matter lipids at MR imaging: importance of cerebrosides and pH." In: *Radiology* 192.2 (Aug. 1994), pp. 521–529. DOI: 10.1148/radiology.192.2.8029426.

[164] M. Matsumae, D. Kurita, H. Atsumi, M. Haida, O. Sato, and R. Tsugane. "Sequential changes in MR water proton relaxation time detect the process of rat brain myelination during maturation". In: *Mechanisms of Ageing and Development* 122.12 (Sept. 2001), pp. 1281–1291. DOI: 10.1016/S0047-6374(01)00265-2.

[165] S. E. Poduslo and Y. Jang. “Myelin development in infant brain”. en. In: *Neurochemical Research* 9.11 (Nov. 1984), pp. 1615–1626. DOI: 10.1007/BF00964595.

[166] D. Le Bihan and E. Breton. “Imagerie de diffusion in vivo par résonance magnétique nucléaire”. fre. In: *Comptes rendus de l’Académie des sciences. Série 2, Mécanique, Physique, Chimie, Sciences de l’univers, Sciences de la Terre* 301.15 (1985), pp. 1109–1112.

[167] D. Le Bihan, E. Breton, D. Lallemand, P. Grenier, E. Cabanis, and M. Laval-Jeantet. “MR imaging of intravoxel incoherent motions: application to diffusion and perfusion in neurologic disorders”. eng. In: *Radiology* 161.2 (Nov. 1986), pp. 401–407. DOI: 10.1148/radiology.161.2.3763909.

[168] T. L. Chenevert, J. A. Brunberg, and J. G. Pipe. “Anisotropic diffusion in human white matter: demonstration with MR techniques in vivo”. eng. In: *Radiology* 177.2 (Nov. 1990), pp. 401–405. DOI: 10.1148/radiology.177.2.2217776.

[169] E. O. Stejskal and J. E. Tanner. “Spin Diffusion Measurements: Spin Echoes in the Presence of a Time Dependent Field Gradient”. In: *The Journal of Chemical Physics* 42.1 (Jan. 1965), pp. 288–292. DOI: 10.1063/1.1695690.

[170] P. Mukherjee, J. I. Berman, S. W. Chung, C. P. Hess, and R. G. Henry. “Diffusion Tensor MR Imaging and Fiber Tractography: Theoretic Underpinnings”. en. In: *American Journal of Neuroradiology* 29.4 (Apr. 2008), pp. 632–641. DOI: 10.3174/ajnr.A1051.

[171] S. Mori and J. Zhang. “Principles of Diffusion Tensor Imaging and Its Applications to Basic Neuroscience Research”. English. In: *Neuron* 51.5 (July 2006), pp. 527–539. DOI: 10.1016/j.neuron.2006.08.012.

[172] P. J. Basser, J. Mattiello, and D. LeBihan. “Estimation of the effective self-diffusion tensor from the NMR spin echo”. eng. In: *Journal of Magnetic Resonance. Series B* 103.3 (Mar. 1994), pp. 247–254.

[173] A. Drobyshevsky, S.-K. Song, G. Gamkrelidze, A. M. Wyrwicz, M. Derrick, F. Meng, L. Li, X. Ji, B. Trommer, D. J. Beardsley, N. L. Luo, S. A. Back, and S. Tan. “Developmental changes in diffusion anisotropy coincide with immature oligodendrocyte progression and maturation of compound action potential”. eng. In: *The Journal of Neuroscience: The Official Journal of the Society for Neuroscience* 25.25 (June 2005), pp. 5988–5997. DOI: 10.1523/JNEUROSCI.4983-04.2005.

[174] P. S. Hüppi, S. E. Maier, S. Peled, G. P. Zientara, P. D. Barnes, F. A. Jolesz, and J. J. Volpe. “Microstructural Development of Human Newborn Cerebral White Matter Assessed in Vivo by Diffusion Tensor Magnetic Resonance Imaging”. en. In: *Pediatric Research* 44.4 (Oct. 1998), pp. 584–590. DOI: 10.1203/00006450-199810000-00019.

[175] S. C. Partridge, P. Mukherjee, J. I. Berman, R. G. Henry, S. P. Miller, Y. Lu, O. A. Glenn, D. M. Ferriero, A. J. Barkovich, and D. B. Vigneron. "Tractography-based quantitation of diffusion tensor imaging parameters in white matter tracts of preterm newborns". eng. In: *Journal of magnetic resonance imaging: JMRI* 22.4 (Oct. 2005), pp. 467–474. DOI: 10.1002/jmri.20410.

[176] D. M. Wimberger, T. P. Roberts, A. J. Barkovich, L. M. Prayer, M. E. Moseley, and J. Kucharczyk. "Identification of "premyelination" by diffusion-weighted MRI". eng. In: *Journal of Computer Assisted Tomography* 19.1 (Feb. 1995), pp. 28–33.

[177] D. Prayer, A. J. Barkovich, D. A. Kirschner, L. M. Prayer, T. P. Roberts, J. Kucharczyk, and M. E. Moseley. "Visualization of nonstructural changes in early white matter development on diffusion-weighted MR images: evidence supporting premyelination anisotropy". eng. In: *AJNR. American journal of neuroradiology* 22.8 (Sept. 2001), pp. 1572–1576.

[178] R. Nossin-Manor, D. Card, D. Morris, S. Noormohamed, M. M. Shroff, H. E. Whyte, M. J. Taylor, and J. G. Sled. "Quantitative MRI in the very preterm brain: assessing tissue organization and myelination using magnetization transfer, diffusion tensor and T1 imaging". eng. In: *NeuroImage* 64 (Jan. 2013), pp. 505–516. DOI: 10.1016/j.neuroimage.2012.08.086.

[179] E. Zanin, J.-P. Ranjeva, S. Confort-Gouny, M. Guye, D. Denis, P. J. Cozzone, and N. Girard. "White matter maturation of normal human fetal brain. An in vivo diffusion tensor tractography study". en. In: *Brain and Behavior* 1.2 (Nov. 2011), pp. 95–108. DOI: 10.1002/brb3.17.

[180] C. Beaulieu. "The basis of anisotropic water diffusion in the nervous system - a technical review". eng. In: *NMR in biomedicine* 15.7-8 (Dec. 2002), pp. 435–455. DOI: 10.1002/nbm.782.

[181] M. S. v. d. Knaap. *Magnetic resonance of myelin, myelination, and myelin disorders*. 2nd ed. Berlin ; New York: Springer, 2005.

[182] J. Dubois, G. Dehaene-Lambertz, M. Perrin, J.-F. Mangin, Y. Cointepas, E. Duchesnay, D. Le Bihan, and L. Hertz-Pannier. "Asynchrony of the early maturation of white matter bundles in healthy infants: quantitative landmarks revealed noninvasively by diffusion tensor imaging". eng. In: *Human brain mapping* 29.1 (Jan. 2008), pp. 14–27. DOI: 10.1002/hbm.20363.

[183] S. Jiang, H. Xue, S. Counsell, M. Anjari, J. Allsop, M. Rutherford, D. Rueckert, and J. V. Hajnal. "Diffusion tensor imaging (DTI) of the brain in moving subjects: Application to in-utero fetal and ex-utero studies". en. In: *Magnetic Resonance in Medicine* 62.3 (Sept. 2009), pp. 645–655. DOI: 10.1002/mrm.22032.

[184] A. Aeby, Y. Liu, X. D. Tiège, V. Denolin, P. David, D. Balériaux, M. Kavec, T. Metens, and P. V. Bogaert. "Maturation of Thalamic Radiations between 34 and 41 Weeks' Gestation: A Combined Voxel-Based Study and Probabilistic Tractography with Diffusion Tensor Imaging". en. In: *American Journal of Neuroradiology* 30.9 (Oct. 2009), pp. 1780–1786. DOI: 10.3174/ajnr.A1660.

[185] A. Aeby, P. Van Bogaert, P. David, D. Balériaux, D. Vermeylen, T. Metens, and X. De Tiège. "Nonlinear microstructural changes in the right superior temporal sulcus and lateral occipitotemporal gyrus between 35 and 43 weeks in the preterm brain". In: *NeuroImage* 63.1 (Oct. 2012), pp. 104–110. DOI: 10.1016/j.neuroimage.2012.06.013.

[186] J. Dudink, M. Lequin, C. v. Pul, J. Buijs, N. Conneman, J. v. Goudoever, and P. Govaert. "Fractional anisotropy in white matter tracts of very-low-birth-weight infants". en. In: *Pediatric Radiology* 37.12 (Oct. 2007), pp. 1216–1223. DOI: 10.1007/s00247-007-0626-7.

[187] P. S. Hüppi, S. Warfield, R. Kikinis, P. D. Barnes, G. P. Zientara, F. A. Jolesz, M. K. Tsuji, and J. J. Volpe. "Quantitative magnetic resonance imaging of brain development in premature and mature newborns". en. In: *Annals of Neurology* 43.2 (Feb. 1998), pp. 224–235. DOI: 10.1002/ana.410430213.

[188] S. P. Miller, D. B. Vigneron, R. G. Henry, M. A. Bohland, C. Ceppi-Cozzio, C. Hoffman, N. Newton, J. C. Partridge, D. M. Ferriero, and A. J. Barkovich. "Serial quantitative diffusion tensor MRI of the premature brain: Development in newborns with and without injury". en. In: *Journal of Magnetic Resonance Imaging* 16.6 (Dec. 2002), pp. 621–632. DOI: 10.1002/jmri.10205.

[189] J. J. Neil, S. I. Shiran, R. C. McKinstry, G. L. Schefft, A. Z. Snyder, C. R. Almli, E. Akbudak, J. A. Aronovitz, J. P. Miller, B. C. Lee, and T. E. Conturo. "Normal brain in human newborns: apparent diffusion coefficient and diffusion anisotropy measured by using diffusion tensor MR imaging." In: *Radiology* 209.1 (Oct. 1998), pp. 57–66. DOI: 10.1148/radiology.209.1.9769812.

[190] W. Gao, W. Lin, Y. Chen, G. Gerig, J. K. Smith, V. Jewells, and J. H. Gilmore. "Temporal and spatial development of axonal maturation and myelination of white matter in the developing brain". eng. In: *AJNR. American journal of neuroradiology* 30.2 (Feb. 2009), pp. 290–296. DOI: 10.3174/ajnr.A1363.

[191] M. C. Morriss, R. A. Zimmerman, L. T. Bilaniuk, J. V. Hunter, and J. C. Haselgrove. "Changes in brain water diffusion during childhood". eng. In: *Neuroradiology* 41.12 (Dec. 1999), pp. 929–934.

[192] S. C. Partridge, P. Mukherjee, R. G. Henry, S. P. Miller, J. I. Berman, H. Jin, Y. Lu, O. A. Glenn, D. M. Ferriero, A. J. Barkovich, and D. B. Vigneron. "Diffusion tensor imaging: serial quantitation of white matter tract maturity in premature newborns". In: *NeuroImage* 22.3 (July 2004), pp. 1302–1314. DOI: 10.1016/j.neuroimage.2004.02.038.

[193] C. Lebel, M. Gee, R. Camicioli, M. Wieler, W. Martin, and C. Beaulieu. "Diffusion tensor imaging of white matter tract evolution over the lifespan". eng. In: *NeuroImage* 60.1 (Mar. 2012), pp. 340–352. DOI: 10.1016/j.neuroimage.2011.11.094.

[194] J. I. Berman, P. Mukherjee, S. C. Partridge, S. P. Miller, D. M. Ferriero, A. J. Barkovich, D. B. Vigneron, and R. G. Henry. "Quantitative diffusion tensor MRI fiber tractography of sensorimotor white matter development in premature infants". In: *NeuroImage* 27.4 (Oct. 2005), pp. 862–871. DOI: 10.1016/j.neuroimage.2005.05.018.

[195] J. B. Colby, L. Soderberg, C. Lebel, I. D. Dinov, P. M. Thompson, and E. R. Sowell. "Along-tract statistics allow for enhanced tractography analysis". In: *NeuroImage* 59.4 (Feb. 2012), pp. 3227–3242. DOI: 10.1016/j.neuroimage.2011.11.004.

[196] J. Dubois, G. Dehaene-Lambertz, C. Soarès, Y. Cointepas, D. Le Bihan, and L. Hertz-Pannier. "Microstructural correlates of infant functional development: example of the visual pathways". eng. In: *The Journal of Neuroscience: The Official Journal of the Society for Neuroscience* 28.8 (Feb. 2008), pp. 1943–1948. DOI: 10.1523/JNEUROSCI.5145-07.2008.

[197] F. Grinberg, E. Farrher, J. Kaffanke, A.-M. Oros-Peusquens, and N. J. Shah. "Non-Gaussian diffusion in human brain tissue at high b-factors as examined by a combined diffusion kurtosis and biexponential diffusion tensor analysis". In: *NeuroImage* 57.3 (Aug. 2011), pp. 1087–1102. DOI: 10.1016/j.neuroimage.2011.04.050.

[198] D. S. Tuch. "Diffusion MRI of complex tissue structure". eng. Thesis (Ph. D.)–Harvard–Massachusetts Institute of Technology Division of Health Sciences and Technology, 2002. Thesis. Massachusetts Institute of Technology, 2002.

[199] T. Niendorf, R. M. Dijkhuizen, D. G. Norris, M. van Lookeren Campagne, and K. Nicolay. "Biexponential diffusion attenuation in various states of brain tissue: implications for diffusion-weighted imaging". eng. In: *Magnetic Resonance in Medicine* 36.6 (Dec. 1996), pp. 847–857.

[200] C. A. Clark and D. Le Bihan. "Water diffusion compartmentation and anisotropy at high b values in the human brain". In: *Magnetic Resonance in Medicine* 44.6 (2000), pp. 852–859.

[201] S. Chabert and P. Scifo. "Diffusion Signal in Magnetic Resonance Imaging: Origin and Interpretation in Neurosciences". In: *Biological Research* 40.4 (Jan. 2007), pp. 385–400. DOI: 10.4067/S0716-97602007000500003.

[202] G. P. Winston. "The physical and biological basis of quantitative parameters derived from diffusion MRI". eng. In: *Quantitative Imaging in Medicine and Surgery* 2.4 (Dec. 2012), pp. 254–265. DOI: 10.3978/j.issn.2223-4292.2012.12.05.

[203] T. E. J. Behrens, M. W. Woolrich, M. Jenkinson, H. Johansen-Berg, R. G. Nunes, S. Clare, P. M. Matthews, J. M. Brady, and S. M. Smith. "Characterization and propagation of uncertainty in diffusion-weighted MR imaging". eng. In: *Magnetic Resonance in Medicine* 50.5 (Nov. 2003), pp. 1077–1088. DOI: 10.1002/mrm.10609.

[204] Y. Assaf, R. Z. Freidlin, G. K. Rohde, and P. J. Basser. "New modeling and experimental framework to characterize hindered and restricted water diffusion in brain white matter". eng. In: *Magnetic Resonance in Medicine* 52.5 (Nov. 2004), pp. 965–978. DOI: 10.1002/mrm.20274.

[205] Y. Assaf, T. Blumenfeld-Katzir, Y. Yovel, and P. J. Basser. "Axcaliber: A method for measuring axon diameter distribution from diffusion MRI". en. In: *Magnetic Resonance in Medicine* 59.6 (June 2008), pp. 1347–1354. DOI: 10.1002/mrm.21577.

[206] H. Zhang, T. Schneider, C. A. Wheeler-Kingshott, and D. C. Alexander. "NODDI: practical in vivo neurite orientation dispersion and density imaging of the human brain". eng. In: *NeuroImage* 61.4 (July 2012), pp. 1000–1016. DOI: 10.1016/j.neuroimage.2012.03.072.

[207] Z. Eaton-Rosen, A. Melbourne, E. Orasanu, M. J. Cardoso, M. Modat, A. Bainbridge, G. S. Kendall, N. J. Robertson, N. Marlow, and S. Ourselin. "Longitudinal measurement of the developing grey matter in preterm subjects using multi-modal MRI". In: *NeuroImage* 111 (). DOI: 10.1016/j.neuroimage.2015.02.010.

[208] I. O. Jelescu, J. Veraart, V. Adisetiyo, S. S. Milla, D. S. Novikov, and E. Fieremans. "One diffusion acquisition and different white matter models: How does microstructure change in human early development based on WMTI and NODDI?" In: *NeuroImage* 107 (Feb. 2015), pp. 242–256. DOI: 10.1016/j.neuroimage.2014.12.009.

[209] N. Kunz, H. Zhang, L. Vasung, K. R. O'Brien, Y. Assaf, F. Lazeyras, D. C. Alexander, and P. S. Huppi. "Assessing white matter microstructure of the newborn with multi-shell diffusion MRI and biophysical compartment models". In: *NeuroImage* 96 (Aug. 2014), pp. 288–299. DOI: 10.1016/j.neuroimage.2014.03.057.

[210] R. M. Henkelman, G. J. Stanisz, and S. J. Graham. "Magnetization transfer in MRI: a review". eng. In: *NMR in biomedicine* 14.2 (Apr. 2001), pp. 57–64.

[211] S. H. Koenig. "Cholesterol of myelin is the determinant of gray-white contrast in MRI of brain". eng. In: *Magnetic Resonance in Medicine* 20.2 (Aug. 1991), pp. 285–291.

[212] J. C. McGowan. “The physical basis of magnetization transfer imaging”. eng. In: *Neurology* 53.5 Suppl 3 (1999), S3–7.

[213] S. D. Wolff and R. S. Balaban. “Magnetization transfer imaging: practical aspects and clinical applications”. eng. In: *Radiology* 192.3 (Sept. 1994), pp. 593–599. DOI: 10.1148/radiology.192.3.8058919.

[214] R. C. Mehta, G. B. Pike, and D. R. Enzmann. “Magnetization transfer MR of the normal adult brain”. eng. In: *AJNR. American journal of neuroradiology* 16.10 (Dec. 1995), pp. 2085–2091.

[215] S. D. Wolff and R. S. Balaban. “Magnetization transfer contrast (MTC) and tissue water proton relaxation in vivo”. en. In: *Magnetic Resonance in Medicine* 10.1 (Apr. 1989), pp. 135–144. DOI: 10.1002/mrm.1910100113.

[216] M. A. van Buchem, S. C. Steens, H. A. Vrooman, A. H. Zwinderman, J. C. McGowan, M. Rassek, and V. Engelbrecht. “Global estimation of myelination in the developing brain on the basis of magnetization transfer imaging: a preliminary study”. eng. In: *AJNR. American journal of neuroradiology* 22.4 (Apr. 2001), pp. 762–766.

[217] J. Rademacher, V. Engelbrecht, U. Burgel, H. Freund, and K. Zilles. “Measuring in vivo myelination of human white matter fiber tracts with magnetization transfer MR”. eng. In: *NeuroImage* 9.4 (Apr. 1999), pp. 393–406.

[218] V. Xydis, L. Astrakas, A. Zikou, K. Pantou, S. Andronikou, and M. I. Argyropoulou. “Magnetization transfer ratio in the brain of preterm subjects: age-related changes during the first 2 years of life”. eng. In: *European Radiology* 16.1 (Jan. 2006), pp. 215–220. DOI: 10.1007/s00330-005-2796-8.

[219] C. L. Armstrong, E. Traipe, J. V. Hunter, J. C. Haselgrove, G. E. Ledakis, E. M. Tallent, D. Shera, and M. A. van Buchem. “Age-related, regional, hemispheric, and medial-lateral differences in myelin integrity in vivo in the normal adult brain”. eng. In: *AJNR. American journal of neuroradiology* 25.6 (July 2004), pp. 977–984.

[220] J. G. Sled and G. B. Pike. “Quantitative imaging of magnetization transfer exchange and relaxation properties in vivo using MRI”. en. In: *Magnetic Resonance in Medicine* 46.5 (Nov. 2001), pp. 923–931. DOI: 10.1002/mrm.1278.

[221] S. C. L. Deoni, L. Matthews, and S. H. Kolind. “One component? Two components? Three? The effect of including a nonexchanging ıfreeȷ water component in multicomponent driven equilibrium single pulse observation of T1 and T2”. In: *Magnetic Resonance in Medicine* (2012), pp. 147–154. DOI: 10.1002/mrm.24429.

[222] A. MacKay, K. Whittall, J. Adler, D. Li, D. Paty, and D. Graeb. “In vivo visualization of myelin water in brain by magnetic resonance”. eng. In: *Magnetic Resonance in Medicine* 31.6 (June 1994), pp. 673–677.

[223] K. P. Whittall, A. L. Mackay, D. A. Graeb, R. A. Nugent, D. K. Li, and D. W. Paty. "In vivo measurement of T2 distributions and water contents in normal human brain". In: *Magnetic Resonance in Medicine* 37.1 (1997), pp. 34–43.

[224] S. H. Kolind, B. Mädler, S. Fischer, D. K. Li, and A. L. MacKay. "Myelin water imaging: Implementation and development at 3.0T and comparison to 1.5T measurements". In: *Magnetic Resonance in Medicine* 62.1 (July 2009), pp. 106–115. DOI: 10.1002/mrm.21966.

[225] C. Laule, I. M. Vavasour, G. R. W. Moore, J. Oger, D. K. B. Li, D. W. Paty, and A. L. MacKay. "Water content and myelin water fraction in multiple sclerosis". In: *Journal of Neurology* 251.3 (Mar. 2004), pp. 284–293. DOI: 10.1007/s00415-004-0306-6.

[226] C. Laule, P. Kozlowski, E. Leung, D. K. Li, A. L. MacKay, and G. W. Moore. "Myelin water imaging of multiple sclerosis at 7 T: Correlations with histopathology". In: *NeuroImage* 40.4 (May 2008), pp. 1575–1580. DOI: 10.1016/j.neuroimage.2007.12.008.

[227] I. R. Levesque, C. L. Chia, and G. B. Pike. "Reproducibility of in vivo magnetic resonance imaging-based measurement of myelin water". In: *Journal of Magnetic Resonance Imaging* 32.1 (June 2010), pp. 60–68. DOI: 10.1002/jmri.22170.

[228] B. Mädler, S. A. Drabycz, S. H. Kolind, K. P. Whittall, and A. L. MacKay. "Is diffusion anisotropy an accurate monitor of myelination?" In: *Magnetic Resonance Imaging* 26.7 (Sept. 2008), pp. 874–888. DOI: 10.1016/j.mri.2008.01.047.

[229] J. Oh, E. T. Han, D. Pelletier, and S. J. Nelson. "Measurement of in vivo multi-component T2 relaxation times for brain tissue using multi-slice T2 prep at 1.5 and 3 T". In: *Magnetic Resonance Imaging* 24.1 (Jan. 2006), pp. 33–43. DOI: 10.1016/j.mri.2005.10.016.

[230] D. Hwang and Y. P. Du. "Improved myelin water quantification using spatially regularized non-negative least squares algorithm". In: *Journal of Magnetic Resonance Imaging* 30.1 (July 2009), pp. 203–208. DOI: 10.1002/jmri.21783.

[231] C. Labadie, J.-H. Lee, W. D. Rooney, S. Jarchow, M. Aubert-Frécon, C. S. Springer, and H. E. Möller. "Myelin water mapping by spatially regularized longitudinal relaxographic imaging at high magnetic fields". In: *Magnetic Resonance in Medicine* (Mar. 2013), n/a–n/a. DOI: 10.1002/mrm.24670.

[232] S. C. Deoni, B. K. Rutt, T. Arun, C. Pierpaoli, and D. K. Jones. "Gleaning multicomponent T_1 and T_2 information from steady-state imaging data". In: *Magnetic Resonance in Medicine* 60.6 (Dec. 2008), pp. 1372–1387. DOI: 10.1002/mrm.21704.

[233] J. L. Lancaster, T. Andrews, L. J. Hardies, S. Dodd, and P. T. Fox. "Three-pool model of white matter". In: *Journal of Magnetic Resonance Imaging* 17.1 (Jan. 2003), pp. 1–10. DOI: 10.1002/jmri.10230.

[234] A. MacKay, C. Laule, I. Vavasour, T. Bjarnason, S. Kolind, and B. Mädler. "Insights into brain microstructure from the T2 distribution". In: *Magnetic Resonance Imaging* 24.4 (May 2006), pp. 515–525. DOI: 10.1016/j.mri.2005.12.037.

[235] M. Prastawa, N. Sadeghi, J. H. Gilmore, W. Lin, and G. Gerig. "A new framework for analyzing white matter maturation in early brain development". ENG. In: *Proceedings / IEEE International Symposium on Biomedical Imaging: from nano to macro. IEEE International Symposium on Biomedical Imaging* (2010), pp. 97–100.

[236] A. Vardhan, M. Prastawa, S. Gouttard, J. Piven, and G. Gerig. "Quantifying regional growth patterns through longitudinal analysis of distances between multimodal MR intensity distributions". In: IEEE, May 2012, pp. 1156–1159. DOI: 10.1109/ISBI.2012.6235765.

[237] C. Beaulieu, C. Plewes, L. A. Paulson, D. Roy, L. Snook, L. Concha, and L. Phillips. "Imaging brain connectivity in children with diverse reading ability". eng. In: *NeuroImage* 25.4 (May 2005), pp. 1266–1271. DOI: 10.1016/j.neuroimage.2004.12.053.

[238] G. K. Deutsch, R. F. Dougherty, R. Bammer, W. T. Siok, J. D. E. Gabrieli, and B. Wandell. "Children's reading performance is correlated with white matter structure measured by diffusion tensor imaging". eng. In: *Cortex; a Journal Devoted to the Study of the Nervous System and Behavior* 41.3 (June 2005), pp. 354–363.

[239] K. S. Madsen, W. F. C. Baaré, M. Vestergaard, A. Skimminge, L. R. Ejersbo, T. Z. Ramsøy, C. Gerlach, P. Akeson, O. B. Paulson, and T. L. Jernigan. "Response inhibition is associated with white matter microstructure in children". eng. In: *Neuropsychologia* 48.4 (Mar. 2010), pp. 854–862. DOI: 10.1016/j.neuropsychologia.2009.11.001.

[240] Z. Nagy, H. Westerberg, and T. Klingberg. "Maturation of white matter is associated with the development of cognitive functions during childhood". eng. In: *Journal of Cognitive Neuroscience* 16.7 (Sept. 2004), pp. 1227–1233. DOI: 10.1162/0898929041920441.

[241] S. N. Niogi and B. D. McCandliss. "Left lateralized white matter microstructure accounts for individual differences in reading ability and disability". eng. In: *Neuropsychologia* 44.11 (2006), pp. 2178–2188. DOI: 10.1016/j.neuropsychologia.2006.01.011.

[242] J. O'Muircheartaigh, D. C. Dean, C. E. Ginestet, L. Walker, N. Waskiewicz, K. Lehman, H. Dirks, I. Piryatinsky, and S. C. L. Deoni. "White matter development and early cognition in babies and toddlers". eng. In: *Human Brain Mapping* 35.9 (Sept. 2014), pp. 4475–4487. DOI: 10.1002/hbm.22488.

[243] D. Prayer and L. Prayer. “Diffusion-weighted magnetic resonance imaging of cerebral white matter development”. English. In: *European Journal of Radiology* 45.3 (Mar. 2003), pp. 235–243. DOI: 10.1016/S0720-048X(02)00312-1.

[244] V. J. Schmithorst and W. Yuan. “White matter development during adolescence as shown by diffusion MRI”. eng. In: *Brain and Cognition* 72.1 (Feb. 2010), pp. 16–25. DOI: 10.1016/j.bandc.2009.06.005.

[245] S. J. Short, J. T. Elison, B. D. Goldman, M. Styner, H. Gu, M. Connelly, E. Maltbie, S. Woolson, W. Lin, G. Gerig, J. S. Reznick, and J. H. Gilmore. “Associations between white matter microstructure and infants’ working memory”. In: *NeuroImage* 64 (Jan. 2013), pp. 156–166. DOI: 10.1016/j.neuroimage.2012.09.021.

[246] C. K. Tamnes, Y. Østby, K. B. Walhovd, L. T. Westlye, P. Due-Tønnessen, and A. M. Fjell. “Intellectual abilities and white matter microstructure in development: a diffusion tensor imaging study”. eng. In: *Human Brain Mapping* 31.10 (Oct. 2010), pp. 1609–1625. DOI: 10.1002/hbm.20962.

[247] M. Vestergaard, K. S. Madsen, W. F. C. Baaré, A. Skimminge, L. R. Ejersbo, T. Z. Ramsøy, C. Gerlach, P. Akeson, O. B. Paulson, and T. L. Jernigan. “White matter microstructure in superior longitudinal fasciculus associated with spatial working memory performance in children”. eng. In: *Journal of Cognitive Neuroscience* 23.9 (Sept. 2011), pp. 2135–2146. DOI: 10.1162/jocn.2010.21592.

[248] J. Dubois, L. Hertz-Pannier, A. Cachia, J. F. Mangin, D. Le Bihan, and G. Dehaene-Lambertz. “Structural Asymmetries in the Infant Language and Sensori-Motor Networks”. In: *Cerebral Cortex* 19.2 (June 2008), pp. 414–423. DOI: 10.1093/cercor/bhn097.

[249] M. Mahmoudzadeh, G. Dehaene-Lambertz, M. Fournier, G. Kongolo, S. Goudjil, J. Dubois, R. Grebe, and F. Wallois. “Syllabic discrimination in premature human infants prior to complete formation of cortical layers”. en. In: *Proceedings of the National Academy of Sciences* 110.12 (Mar. 2013), pp. 4846–4851. DOI: 10.1073/pnas.1212220110.

[250] J. Pujol, C. Soriano-Mas, H. Ortiz, N. Sebastián-Gallés, J. M. Losilla, and J. Deus. “Myelination of language-related areas in the developing brain”. en. In: *Neurology* 66.3 (Feb. 2006), pp. 339–343. DOI: 10.1212/01.wnl.0000201049.66073.8d.

[251] P. Su, C.-C. Kuan, K. Kaga, M. Sano, and K. Mima. “Myelination progression in language-correlated regions in brain of normal children determined by quantitative MRI assessment”. English. In: *International Journal of Pediatric Otorhinolaryngology* 72.12 (Dec. 2008), pp. 1751–1763. DOI: 10.1016/j.ijporl.2008.05.017.

[252] J. Dubois, C. Poupon, B. Thirion, H. Simonnet, S. Kulikova, F. Leroy, L. Hertz-Pannier, and G. Dehaene-Lambertz. "Exploring the Early Organization and Maturation of Linguistic Pathways in the Human Infant Brain". en. In: *Cerebral Cortex* (Apr. 2015), bhv082. DOI: 10.1093/cercor/bhv082.

[253] D. López-Barroso, M. Catani, P. Ripollés, F. Dell'Acqua, A. Rodríguez-Fornells, and R. de Diego-Balaguer. "Word learning is mediated by the left arcuate fasciculus". In: *Proceedings of the National Academy of Sciences of the United States of America* 110.32 (Aug. 2013), pp. 13168–13173. DOI: 10.1073/pnas.1301696110.

[254] D. Antonenko, M. Meinzer, R. Lindenberg, A. V. Witte, and A. Flöel. "Grammar learning in older adults is linked to white matter microstructure and functional connectivity". In: *NeuroImage* 62.3 (Sept. 2012), pp. 1667–1674. DOI: 10.1016/j.neuroimage.2012.05.074.

[255] M. Vandermosten, B. Boets, H. Poelmans, S. Sunaert, J. Wouters, and P. Ghesquière. "A tractography study in dyslexia: neuroanatomic correlates of orthographic, phonological and speech processing". eng. In: *Brain: A Journal of Neurology* 135.Pt 3 (Mar. 2012), pp. 935–948. DOI: 10.1093/brain/awr363.

[256] D. Le Bihan and H. Johansen-Berg. "Diffusion MRI at 25: exploring brain tissue structure and function". eng. In: *NeuroImage* 61.2 (June 2012), pp. 324–341. DOI: 10.1016/j.neuroimage.2011.11.006.

[257] S. Pajevic and C. Pierpaoli. "Color schemes to represent the orientation of anisotropic tissues from diffusion tensor data: application to white matter fiber tract mapping in the human brain". eng. In: *Magnetic Resonance in Medicine* 42.3 (Sept. 1999), pp. 526–540.

[258] P. Fillard, M. Descoteaux, A. Goh, S. Gouttard, B. J. B, J. Malcolm, A. Ramirez-Manzanares, M. Reisert, K. Sakaie, F. Tensaouti, T. Y. T, J.-F. Mangin, and C. Poupon. "Quantitative evaluation of 10 tractography algorithms on a realistic diffusion MR phantom". In: *Neuroimage* 56.1 (2011), pp. 220–34.

[259] D. K. Jones, T. R. Knosche, and R. Turner. "White matter integrity, fiber count, and other fallacies: The do's and don'ts of diffusion MRI". In: *NeuroImage* 73 (June 2013), pp. 239–254. DOI: 10.1016/j.neuroimage.2012.06.081.

[260] M. Descoteaux, E. Angelino, S. Fitzgibbons, and R. Deriche. "Regularized, fast, and robust analytical Q-ball imaging". eng. In: *Magnetic Resonance in Medicine* 58.3 (Sept. 2007), pp. 497–510. DOI: 10.1002/mrm.21277.

[261] D. S. Tuch. "Q-ball imaging". eng. In: *Magnetic Resonance in Medicine* 52.6 (Dec. 2004), pp. 1358–1372. DOI: 10.1002/mrm.20279.

[262] J.-D. Tournier, F. Calamante, D. G. Gadian, and A. Connelly. "Direct estimation of the fiber orientation density function from diffusion-weighted MRI data using spherical deconvolution". eng. In: *NeuroImage* 23.3 (Nov. 2004), pp. 1176–1185. DOI: 10.1016/j.neuroimage.2004.07.037.

[263] J.-D. Tournier, F. Calamante, and A. Connelly. "Robust determination of the fibre orientation distribution in diffusion MRI: non-negativity constrained super-resolved spherical deconvolution". eng. In: *NeuroImage* 35.4 (May 2007), pp. 1459–1472. DOI: 10.1016/j.neuroimage.2007.02.016.

[264] M. Descoteaux, R. Deriche, T. R. Knösche, and A. Anwander. "Deterministic and probabilistic tractography based on complex fibre orientation distributions". eng. In: *IEEE transactions on medical imaging* 28.2 (Feb. 2009), pp. 269–286. DOI: 10.1109/TMI.2008.2004424.

[265] H.-W. Chung, M.-C. Chou, and C.-Y. Chen. "Principles and Limitations of Computational Algorithms in Clinical Diffusion Tensor MR Tractography". en. In: *American Journal of Neuroradiology* 32.1 (Jan. 2011), pp. 3–13. DOI: 10.3174/ajnr.A2041.

[266] J. Campbell, P. Savadjiev, K. Siddiqi, and G. Pike. "Validation and regularization in diffusion MRI tractography". In: *3rd IEEE International Symposium on Biomedical Imaging: Nano to Macro, 2006*. Apr. 2006, pp. 351–354. DOI: 10.1109/ISBI.2006.1624925.

[267] R. Deriche, D. Tschumperle, and C. Lenglet. "DT-MRI estimation, regularization and fiber tractography". In: *IEEE International Symposium on Biomedical Imaging: Nano to Macro, 2004*. Apr. 2004, 9–12 Vol. 1. DOI: 10.1109/ISBI.2004.1398461.

[268] X. Wu, Q. Xu, L. Xu, J. Zhou, A. W. Anderson, and Z. Ding. "Genetic white matter fiber tractography with global optimization". eng. In: *Journal of Neuroscience Methods* 184.2 (Nov. 2009), pp. 375–379. DOI: 10.1016/j.jneumeth.2009.07.032.

[269] H. Huang, J. Zhang, P. C. M. van Zijl, and S. Mori. "Analysis of noise effects on DTI-based tractography using the brute-force and multi-ROI approach". eng. In: *Magnetic Resonance in Medicine* 52.3 (Sept. 2004), pp. 559–565. DOI: 10.1002/mrm.20147.

[270] M. Catani, R. J. Howard, S. Pajevic, and D. K. Jones. "Virtual in vivo interactive dissection of white matter fasciculi in the human brain". eng. In: *NeuroImage* 17.1 (Sept. 2002), pp. 77–94.

[271] M. Catani and M. Thiebaut de Schotten. "A diffusion tensor imaging tractography atlas for virtual in vivo dissections". eng. In: *Cortex; a Journal Devoted to the Study of the Nervous System and Behavior* 44.8 (Sept. 2008), pp. 1105–1132. DOI: 10.1016/j.cortex.2008.05.004.

[272] S. Wakana, A. Caprihan, M. M. Panzenboeck, J. H. Fallon, M. Perry, R. L. Gollub, K. Hua, J. Zhang, H. Jiang, P. Dubey, A. Blitz, P. van Zijl, and S. Mori. "Reproducibility of quantitative tractography methods applied to cerebral white matter". eng. In: *NeuroImage* 36.3 (July 2007), pp. 630–644. DOI: 10.1016/j.neuroimage.2007.02.049.

[273] K. Oishi, K. Zilles, K. Amunts, A. Faria, H. Jiang, X. Li, K. Akhter, K. Hua, R. Woods, A. W. Toga, G. B. Pike, P. Rosa-Neto, A. Evans, J. Zhang, H. Huang, M. I. Miller, P. C. M. van Zijl, J. Mazziotta, and S. Mori. "Human brain white matter atlas: identification and assignment of common anatomical structures in superficial white matter". eng. In: *NeuroImage* 43.3 (Nov. 2008), pp. 447–457. DOI: 10.1016/j.neuroimage.2008.07.009.

[274] R. O. Suarez, O. Commowick, S. P. Prabhu, and S. K. Warfield. "Automated delineation of white matter fiber tracts with a multiple region-of-interest approach". eng. In: *NeuroImage* 59.4 (Feb. 2012), pp. 3690–3700. DOI: 10.1016/j.neuroimage.2011.11.043.

[275] Y. Zhang, J. Zhang, K. Oishi, A. V. Faria, H. Jiang, X. Li, K. Akhter, P. Rosa-Neto, G. B. Pike, A. Evans, A. W. Toga, R. Woods, J. C. Mazziotta, M. I. Miller, P. C. M. van Zijl, and S. Mori. "Atlas-Guided Tract Reconstruction for Automated and Comprehensive Examination of the White Matter Anatomy". In: *NeuroImage* 52.4 (Oct. 2010), pp. 1289–1301. DOI: 10.1016/j.neuroimage.2010.05.049.

[276] P. Guevara, C. Poupon, D. Rivière, Y. Cointepas, M. Descoteaux, B. Thirion, and J.-F. Mangin. "Robust clustering of massive tractography datasets". eng. In: *NeuroImage* 54.3 (Feb. 2011), pp. 1975–1993. DOI: 10.1016/j.neuroimage.2010.10.028.

[277] P. Guevara, D. Duclap, C. Poupon, L. Marrakchi-Kacem, P. Fillard, D. Le Bihan, M. Leboyer, J. Houenou, and J.-F. Mangin. "Automatic fiber bundle segmentation in massive tractography datasets using a multi-subject bundle atlas". eng. In: *NeuroImage* 61.4 (July 2012), pp. 1083–1099. DOI: 10.1016/j.neuroimage.2012.02.071.

[278] H. Li, Z. Xue, L. Guo, T. Liu, J. Hunter, and S. T. C. Wong. "A hybrid approach to automatic clustering of white matter fibers". eng. In: *NeuroImage* 49.2 (Jan. 2010), pp. 1249–1258. DOI: 10.1016/j.neuroimage.2009.08.017.

[279] M. Maddah, W. E. L. Grimson, S. K. Warfield, and W. M. Wells. "A unified framework for clustering and quantitative analysis of white matter fiber tracts". eng. In: *Medical Image Analysis* 12.2 (Apr. 2008), pp. 191–202. DOI: 10.1016/j.media.2007.10.003.

[280] L. J. O'Donnell, M. Kubicki, M. E. Shenton, M. H. Dreusicke, W. E. L. Grimson, and C. F. Westin. "A method for clustering white matter fiber tracts". eng. In: *AJNR. American journal of neuroradiology* 27.5 (May 2006), pp. 1032–1036.

[281] B. Tunç, W. A. Parker, M. Ingalhalikar, and R. Verma. "Automated tract extraction via atlas based Adaptive Clustering". eng. In: *NeuroImage* 102 Pt 2 (Nov. 2014), pp. 596–607. DOI: 10.1016/j.neuroimage.2014.08.021.

[282] D. Wassermann, L. Bloy, E. Kanterakis, R. Verma, and R. Deriche. "Unsupervised white matter fiber clustering and tract probability map generation: applications of a Gaussian process framework for white matter fibers". eng. In: *NeuroImage* 51.1 (May 2010), pp. 228–241. DOI: 10.1016/j.neuroimage.2010.01.004.

[283] E. Visser, E. H. J. Nijhuis, J. K. Buitelaar, and M. P. Zwiers. "Partition-based mass clustering of tractography streamlines". eng. In: *NeuroImage* 54.1 (Jan. 2011), pp. 303–312. DOI: 10.1016/j.neuroimage.2010.07.038.

[284] S. Zhang, S. Correia, and D. H. Laidlaw. "Identifying white-matter fiber bundles in DTI data using an automated proximity-based fiber-clustering method". eng. In: *IEEE transactions on visualization and computer graphics* 14.5 (Oct. 2008), pp. 1044–1053. DOI: 10.1109/TVCG.2008.52.

[285] L. J. O'Donnell and C.-F. Westin. "Automatic tractography segmentation using a high-dimensional white matter atlas". eng. In: *IEEE transactions on medical imaging* 26.11 (Nov. 2007), pp. 1562–1575. DOI: 10.1109/TMI.2007.906785.

[286] X. Wang, W. E. L. Grimson, and C.-F. Westin. "Tractography segmentation using a hierarchical Dirichlet processes mixture model". eng. In: *NeuroImage* 54.1 (Jan. 2011), pp. 290–302. DOI: 10.1016/j.neuroimage.2010.07.050.

[287] J. Zhang, A. Evans, L. Hermoye, S.-K. Lee, S. Wakana, W. Zhang, P. Donohue, M. I. Miller, H. Huang, X. Wang, P. C. M. van Zijl, and S. Mori. "Evidence of slow maturation of the superior longitudinal fasciculus in early childhood by diffusion tensor imaging". eng. In: *NeuroImage* 38.2 (Nov. 2007), pp. 239–247. DOI: 10.1016/j.neuroimage.2007.07.033.

[288] C. Mitter, D. Prayer, P. C. Brugger, M. Weber, and G. Kasprian. "In vivo tractography of fetal association fibers". eng. In: *PloS One* 10.3 (2015), e0119536. DOI: 10.1371/journal.pone.0119536.

[289] J. Pontabry, F. Rousseau, E. Oubel, C. Studholme, M. Koob, and J.-L. Dietemann. "Probabilistic tractography using Q-ball imaging and particle filtering: application to adult and in-utero fetal brain studies". eng. In: *Medical Image Analysis* 17.3 (Apr. 2013), pp. 297–310. DOI: 10.1016/j.media.2012.11.004.

[290] G. Kasprian, P. C. Brugger, V. Schopf, C. Mitter, M. Weber, J. A. Hainfellner, and D. Prayer. "Assessing prenatal white matter connectivity in commissural agenesis". eng. In: *Brain: A Journal of Neurology* 136.Pt 1 (Jan. 2013), pp. 168–179. DOI: 10.1093/brain/aws332.

[291] J. Dubois, L. Hertz-Pannier, G. Dehaene-Lambertz, Y. Cointepas, and D. Le Bihan. "Assessment of the early organization and maturation of infants' cerebral white matter fiber bundles: a feasibility study using quantitative diffusion tensor imaging and tractography". eng. In: *NeuroImage* 30.4 (May 2006), pp. 1121–1132. DOI: 10.1016/j.neuroimage.2005.11.022.

[292] N. Raschle, J. Zuk, S. Ortiz-Mantilla, D. D. Sliva, A. Franceschi, P. E. Grant, A. A. Benasich, and N. Gaab. "Pediatric neuroimaging in early childhood and infancy: challenges and practical guidelines". eng. In: *Annals of the New York Academy of Sciences* 1252 (Apr. 2012), pp. 43–50. DOI: 10.1111/j.1749-6632.2012.06457.x.

[293] B. Keil, V. Alagappan, A. Mareyam, J. A. McNab, K. Fujimoto, V. Tountcheva, C. Triantafyllou, D. D. Dilks, N. Kanwisher, W. Lin, P. E. Grant, and L. L. Wald. "Size-optimized 32-channel brain arrays for 3 T pediatric imaging". eng. In: *Magnetic Resonance in Medicine* 66.6 (Dec. 2011), pp. 1777–1787. DOI: 10.1002/mrm.22961.

[294] M. Perrin, C. Poupon, Y. Cointepas, B. Rieul, N. Golestani, C. Pallier, D. Rivière, A. Constantinesco, D. Le Bihan, and J. F. Mangin. "Fiber tracking in q-ball fields using regularized particle trajectories". eng. In: *Information processing in medical imaging: proceedings of the ... conference* 19 (2005), pp. 52–63.

[295] C. Poupon, A. Roche, J. Dubois, J.-F. Mangin, and F. Poupon. "Real-time MR diffusion tensor and Q-ball imaging using Kalman filtering". English. In: *Medical Image Analysis* 12.5 (Oct. 2008), pp. 527–534. DOI: 10.1016/j.media.2008.06.004.

[296] A. J. Barkovich, G. Lyon, and P. Evrard. "Formation, maturation, and disorders of white matter." en. In: *American Journal of Neuroradiology* 13.2 (Mar. 1992), pp. 447–461.

[297] M. S. v. d. Knaap and J. Valk. "MR imaging of the various stages of normal myelination during the first year of life". en. In: *Neuroradiology* 31.6 (Jan. 1990), pp. 459–470. DOI: 10.1007/BF00340123.

[298] M.-s. Choe, S. Ortiz-Mantilla, N. Makris, M. Gregas, J. Bacic, D. Haehn, D. Kennedy, R. Pienaar, V. S. Caviness, A. A. Benasich, and P. E. Grant. "Regional Infant Brain Development: An MRI-Based Morphometric Analysis in 3 to 13 Month Olds". en. In: *Cerebral Cortex* 23.9 (Sept. 2013), pp. 2100–2117. DOI: 10.1093/cercor/bhs197.

[299] J. Matsuzawa, M. Matsui, T. Konishi, K. Noguchi, R. C. Gur, W. Bilker, and T. Miyawaki. "Age-related volumetric changes of brain gray and white matter in healthy infants and children". eng. In: *Cerebral Cortex (New York, N.Y.: 1991)* 11.4 (Apr. 2001), pp. 335–342.

[300] M. Altaye, S. K. Holland, M. Wilke, and C. Gaser. "Infant brain probability templates for MRI segmentation and normalization". eng. In: *NeuroImage* 43.4 (Dec. 2008), pp. 721–730. DOI: 10.1016/j.neuroimage.2008.07.060.

[301] V. Fonov, A. C. Evans, K. Botteron, C. R. Almli, R. C. McKinstry, D. L. Collins, and Brain Development Cooperative Group. "Unbiased average age-appropriate atlases for pediatric studies". eng. In: *NeuroImage* 54.1 (Jan. 2011), pp. 313–327. DOI: 10.1016/j.neuroimage.2010.07.033.

[302] C. E. Sanchez, J. E. Richards, and C. R. Almli. "Neurodevelopmental MRI brain templates for children from 2 weeks to 4 years of age". eng. In: *Developmental Psychobiology* 54.1 (Jan. 2012), pp. 77–91. DOI: 10.1002/dev.20579.

[303] F. Shi, P.-T. Yap, G. Wu, H. Jia, J. H. Gilmore, W. Lin, and D. Shen. "Infant brain atlases from neonates to 1- and 2-year-olds". eng. In: *PloS One* 6.4 (2011), e18746. DOI: 10.1371/journal.pone.0018746.

[304] P. Mukherjee, J. H. Miller, J. S. Shimony, J. V. Philip, D. Nehra, A. Z. Snyder, T. E. Conturo, J. J. Neil, and R. C. McKinstry. "Diffusion-tensor MR imaging of gray and white matter development during normal human brain maturation". eng. In: *AJNR. American journal of neuroradiology* 23.9 (Oct. 2002), pp. 1445–1456.

[305] J. Dubois, C. Poupon, F. Lethimonnier, and D. L. Bihan. "Optimized diffusion gradient orientation schemes for corrupted clinical DTI data sets". en. In: *Magnetic Resonance Materials in Physics, Biology and Medicine* 19.3 (Aug. 2006), pp. 134–143. DOI: 10.1007/s10334-006-0036-0.

[306] L. R. Frank, Y. Jung, S. Inati, J. M. Tyszka, and E. C. Wong. "High efficiency, low distortion 3D diffusion tensor imaging with variable density spiral fast spin echoes (3D DW VDS RARE)". In: *NeuroImage* 49.2 (Jan. 2010), pp. 1510–1523. DOI: 10.1016/j.neuroimage.2009.09.010.

[307] M. Herbst, J. Maclaren, M. Weigel, J. Korvink, J. Hennig, and M. Zaitsev. "Prospective motion correction with continuous gradient updates in diffusion weighted imaging". en. In: *Magnetic Resonance in Medicine* 67.2 (2012), pp. 326–338. DOI: 10.1002/mrm.23230.

[308] X. Shi, E. G. Kholmovski, S.-E. Kim, D. L. Parker, and E.-K. Jeong. "Improvement of accuracy of diffusion MRI using real-time self-gated data acquisition". en. In: *NMR in Biomedicine* 22.5 (2009), pp. 545–550. DOI: 10.1002/nbm.1368.

[309] L.-C. Chang, D. K. Jones, and C. Pierpaoli. "RESTORE: robust estimation of tensors by outlier rejection". eng. In: *Magnetic Resonance in Medicine* 53.5 (May 2005), pp. 1088–1095. DOI: 10.1002/mrm.20426.

[310] J. Dubois, S. Kulikova, L. Hertz-Pannier, J.-F. Mangin, G. Dehaene-Lambertz, and C. Poupon. "Correction strategy for diffusion-weighted images corrupted with motion: application to the DTI evaluation of infants' white matter". eng. In: *Magnetic Resonance Imaging* 32.8 (Oct. 2014), pp. 981–992. DOI: 10.1016/j.mri.2014.05.007.

[311] S. J. Holdsworth, M. Aksoy, R. D. Newbould, K. Yeom, A. T. Van, M. B. Ooi, P. D. Barnes, R. Bammer, and S. Skare. "Diffusion tensor imaging (DTI) with retrospective motion correction for large-scale pediatric imaging". en. In: *Journal of Magnetic Resonance Imaging* 36.4 (2012), pp. 961–971. DOI: 10.1002/jmri.23710.

[312] D. Morris, R. Nossin-Manor, M. J. Taylor, and J. G. Sled. "Preterm neonatal diffusion processing using detection and replacement of outliers prior to resampling". en. In: *Magnetic Resonance in Medicine* 66.1 (2011), pp. 92–101. DOI: 10.1002/mrm.22786.

[313] M. Niethammer, S. Bouix, S. Aja-Fernández, C.-F. Westin, and M. E. Shenton. "Outlier Rejection for Diffusion Weighted Imaging". en. In: *Medical Image Computing and Computer-Assisted Intervention – MICCAI 2007*. Ed. by N. Ayache, S. Ourselin, and A. Maeder. Lecture Notes in Computer Science 4791. Springer Berlin Heidelberg, 2007, pp. 161–168.

[314] M. A. Sharman, J. Cohen-Adad, M. Descoteaux, A. Messé, H. Benali, and S. Lehericy. "Impact of outliers on diffusion tensor and Q-ball imaging: Clinical implications and correction strategies". en. In: *Journal of Magnetic Resonance Imaging* 33.6 (2011), pp. 1491–1502. DOI: 10.1002/jmri.22577.

[315] S. Kulikova, L. Hertz-Pannier, G. Dehaene-Lambertz, A. Buzmakov, C. Poupon, and J. Dubois. "Multi-parametric evaluation of the white matter maturation". ENG. In: *Brain Structure & Function* (Sept. 2014). DOI: 10.1007/s00429-014-0881-y.

[316] D. Duclap, Schmitt, Lebois, Riff, Guevara, Marrakchi-Kacem, Brion, Poupon, and Poupon. *Connectomist-2.0: a novel diffusion analysis toolbox for BrainVISA*. European Society for Magnetic Resonance in Medicine and Biology. Lisbon, Portugal: Springer, 2012.

[317] S. Kulikova, L. Hertz-Pannier, G. Dehaene-Lambertz, A. Buzmakov, C. Poupon, and J. Dubois. "Comparison of quantitative MRI parameters in the developing white matter bundles". In: *In Proc. of the 30th Annual ESMRMB Scientific Meeting* 26.S1 (Sept. 2013), p. 495. DOI: 10.1007/s10334-013-0384-5.

[318] P. Mahalanobis. "On the generalised distance in statistics". In: vol. 2. Apr. 1936, pp. 49–55.

[319] T. Takeshita, S. Nozawa, and F. Kimura. "On the bias of Mahalanobis distance due to limited sample size effect". In: *, Proceedings of the Second International Conference on Document Analysis and Recognition, 1993*. 1993, pp. 171–174. DOI: 10.1109/ICDAR.1993.395756.

[320] T. Paus, A. Zijdenbos, K. Worsley, D. L. Collins, J. Blumenthal, J. N. Giedd, J. L. Rapoport, and A. C. Evans. "Structural maturation of neural pathways in children and adolescents: in vivo study". eng. In: *Science (New York, N.Y.)* 283.5409 (Mar. 1999), pp. 1908–1911.

[321] D. C. Dean 3rd, J. O'Muircheartaigh, H. Dirks, N. Waskiewicz, K. Lehman, L. Walker, M. Han, and S. C. L. Deoni. "Modeling healthy male white matter and myelin development: 3 through 60months of age". eng. In: *NeuroImage* 84 (Jan. 2014), pp. 742–752. DOI: 10.1016/j.neuroimage.2013.09.058.

[322] S. C. L. Deoni, L. Matthews, and S. H. Kolind. "One component? Two components? Three? The effect of including a nonexchanging ıfreeȷ water component in multicomponent driven equilibrium single pulse observation of T1 and T2". en. In: *Magnetic Resonance in Medicine* 70.1 (2013), pp. 147–154. DOI: 10.1002/mrm.24429.

[323] Y. P. Du, R. Chu, D. Hwang, M. S. Brown, B. K. Kleinschmidt-DeMasters, D. Singel, and J. H. Simon. "Fast multislice mapping of the myelin water fraction using multicompartment analysis ofT2* decay at 3T: A preliminary postmortem study". In: *Magnetic Resonance in Medicine* 58.5 (Nov. 2007), pp. 865–870. DOI: 10.1002/mrm.21409.

[324] O. I. Kwon, E. J. Woo, Y. P. Du, and D. Hwang. "A tissue-relaxation-dependent neighboring method for robust mapping of the myelin water fraction". eng. In: *NeuroImage* 74 (July 2013), pp. 12–21. DOI: 10.1016/j.neuroimage.2013.01.064.

[325] J. L. Lancaster, J. D. Cody, T. Andrews, L. J. Hardies, D. E. Hale, and P. T. Fox. "Myelination in children with partial deletions of chromosome 18q". eng. In: *AJNR. American journal of neuroradiology* 26.3 (Mar. 2005), pp. 447–454.

[326] A. Raj, S. Pandya, X. Shen, E. LoCastro, T. D. Nguyen, and S. A. Gauthier. "Multi-Compartment T2 Relaxometry Using a Spatially Constrained Multi-Gaussian Model". In: *PLoS ONE* 9.6 (June 2014), e98391. DOI: 10.1371/journal.pone.0098391.

[327] M. A. Bernstein, K. F. King, and X. J. Zhou. *Handbook of MRI Pulse Sequences*. en. Elsevier, Sept. 2004.

[328] M. Berger and H. Silverman. "Microphone array optimization by stochastic region contraction". In: *IEEE Transactions on Signal Processing* 39.11 (Nov. 1991), pp. 2377–2386. DOI: 10.1109/78.97993.

[329] S. Kulikova, J. Dubois, P. Guevara, J.-F. Mangin, C. Chiron, N. Chemaly, S. Napuri, C. Poupon, and L. Hertz- Pannier. "Creating a child brain connectivity atlas for reliable bundle identification in developmental studies". In: *In proceedings of the 23rd annual ISMRM meeting* (2015).

[330] I. Corouge, S. Gouttard, and G. Gerig. "Towards a shape model of white matter fiber bundles using diffusion tensor MRI". In: *IEEE International Symposium on Biomedical Imaging: Nano to Macro, 2004.* Apr. 2004, 344–347 Vol. 1. DOI: 10.1109/ISBI.2004.1398545.

[331] A. T. Berg, S. F. Berkovic, M. J. Brodie, J. Buchhalter, J. H. Cross, W. Van Emde Boas, J. Engel, J. French, T. A. Glauser, G. W. Mathern, S. L. Moshé, D. Nordli, P. Plouin, and I. E. Scheffer. "Revised terminology and concepts for organization of seizures and epilepsies: Report of the ILAE Commission on Classification and Terminology, 2005–2009". en. In: *Epilepsia* 51.4 (Apr. 2010), pp. 676–685. DOI: 10.1111/j.1528-1167.2010.02522.x.

[332] D. C. Taylor, M. A. Falconer, C. J. Bruton, and J. A. N. Corsellis. "Focal dysplasia of the cerebral cortex in epilepsy". In: *Journal of Neurology, Neurosurgery, and Psychiatry* 34.4 (Aug. 1971), pp. 369–387.

[333] I. Blümcke, M. Thom, E. Aronica, D. D. Armstrong, H. V. Vinters, A. Palmini, T. S. Jacques, G. Avanzini, A. J. Barkovich, G. Battaglia, A. Becker, C. Cepeda, F. Cendes, N. Colombo, P. Crino, J. H. Cross, O. Delalande, F. Dubeau, J. Duncan, R. Guerrini, P. Kahane, G. Mathern, I. Najm, Ç. Özkara, C. Raybaud, A. Represa, S. N. Roper, N. Salamon, A. Schulze-Bonhage, L. Tassi, A. Vezzani, and R. Spreafico. "The clinico-pathological spectrum of Focal Cortical Dysplasias: a consensus classification proposed by an ad hoc Task Force of the ILAE Diagnostic Methods Commission". In: *Epilepsia* 52.1 (Jan. 2011), pp. 158–174. DOI: 10.1111/j.1528-1167.2010.02777.x.

[334] S. M. Sisodiya, S. Fauser, J. H. Cross, and M. Thom. "Focal cortical dysplasia type II: biological features and clinical perspectives". eng. In: *The Lancet. Neurology* 8.9 (Sept. 2009), pp. 830–843. DOI: 10.1016/S1474-4422(09)70201-7.

[335] P. Widdess-Walsh, C. Kellinghaus, L. Jeha, P. Kotagal, R. Prayson, W. Bingaman, and I. M. Najm. "Electro-clinical and imaging characteristics of focal cortical dysplasia: correlation with pathological subtypes". eng. In: *Epilepsy Research* 67.1-2 (Nov. 2005), pp. 25–33. DOI: 10.1016/j.eplepsyres.2005.07.013.

[336] A. Gambardella, A. Palmini, F. Andermann, F. Dubeau, J. C. Da Costa, L. Felipe Quesney, E. Andermann, and A. Olivier. "Usefulness of focal rhythmic discharges on scalp EEG of patients with focal cortical dysplasia and intractable epilepsy". In: *Electroencephalography and Clinical Neurophysiology* 98.4 (Apr. 1996), pp. 243–249. DOI: 10.1016/0013-4694(95)00266-9.

[337] F. Chassoux, B. Devaux, E. Landré, B. Turak, F. Nataf, P. Varlet, J.-P. Chodkiewicz, and C. Daumas-Duport. "Stereoelectroencephalography in focal cortical dysplasia". en. In: *Brain* 123.8 (Aug. 2000), pp. 1733–1751. DOI: 10.1093/brain/123.8.1733.

[338] A. Palmini, A. Gambardella, F. Andermann, F. Dubeau, J. C. da Costa, A. Olivier, D. Tampieri, P. Gloor, F. Quesney, and E. Andermann. "Intrinsic epileptogenicity of human dysplastic cortex as suggested by corticography and surgical results". eng. In: *Annals of Neurology* 37.4 (Apr. 1995), pp. 476–487. DOI: 10.1002/ana.410370410.

[339] S. Hirabayashi, C. D. Binnie, I. Janota, and C. E. Polkey. “Surgical treatment of epilepsy due to cortical dysplasia: clinical and EEG findings”. eng. In: *Journal of Neurology, Neurosurgery, and Psychiatry* 56.7 (July 1993), pp. 765–770.

[340] R. Kuzniecky and R. Powers. “Epilepsia partialis continua due to cortical dysplasia”. eng. In: *Journal of Child Neurology* 8.4 (Oct. 1993), pp. 386–388.

[341] A. Palmini, F. Andermann, A. Olivier, D. Tampieri, Y. Robitaille, E. Andermann, and G. Wright. “Focal neuronal migration disorders and intractable partial epilepsy: a study of 30 patients”. eng. In: *Annals of Neurology* 30.6 (Dec. 1991), pp. 741–749. DOI: 10.1002/ana.410300602.

[342] A. A. Raymond, D. R. Fish, S. M. Sisodiya, N. Alsanjari, J. M. Stevens, and S. D. Shorvon. “Abnormalities of gyration, heterotopias, tuberous sclerosis, focal cortical dysplasia, microdysgenesis, dysembryoplastic neuroepithelial tumour and dysgenesis of the archicortex in epilepsy. Clinical, EEG and neuroimaging features in 100 adult patients”. eng. In: *Brain: A Journal of Neurology* 118 (Pt 3) (June 1995), pp. 629–660.

[343] E. Wyllie, Y. G. Comair, P. Kotagal, J. Bulacio, W. Bingaman, and P. Ruggieri. “Seizure outcome after epilepsy surgery in children and adolescents”. eng. In: *Annals of Neurology* 44.5 (Nov. 1998), pp. 740–748. DOI: 10.1002/ana.410440507.

[344] A. Palmini, I. Najm, G. Avanzini, T. Babb, R. Guerrini, N. Foldvary-Schaefer, G. Jackson, H. O. Lüders, R. Prayson, R. Spreafico, and H. V. Vinters. “Terminology and classification of the cortical dysplasias”. eng. In: *Neurology* 62.6 Suppl 3 (Mar. 2004), S2–8.

[345] P. A. Schwartzkroin and C. A. Walsh. “Cortical malformations and epilepsy”. eng. In: *Mental Retardation and Developmental Disabilities Research Reviews* 6.4 (2000), pp. 268–280. DOI: 10.1002/1098-2779(2000)6:4<268::AID-MRDD6>3.0.CO;2-B.

[346] H. V. Vinters, R. S. Fisher, M. E. Cornford, V. Mah, D. L. Secor, M. J. De Rosa, Y. G. Comair, W. J. Peacock, and W. D. Shields. “Morphological substrates of infantile spasms: studies based on surgically resected cerebral tissue”. eng. In: *Child’s Nervous System: ChNS: Official Journal of the International Society for Pediatric Neurosurgery* 8.1 (Feb. 1992), pp. 8–17.

[347] D. R. Cotter, M. Honavar, and I. Everall. “Focal cortical dysplasia: a neuropathological and developmental perspective”. eng. In: *Epilepsy Research* 36.2-3 (Sept. 1999), pp. 155–164.

[348] C. Cepeda, V. M. André, M. S. Levine, N. Salamon, H. Miyata, H. V. Vinters, and G. W. Mathern. “Epileptogenesis in pediatric cortical dysplasia: The dysmature cerebral developmental hypothesis”. English. In: *Epilepsy & Behavior* 9.2 (Sept. 2006), pp. 219–235. DOI: 10.1016/j.yebeh.2006.05.012.

[349] P. B. Crino, J. Q. Trojanowski, and J. Eberwine. “Internexin, MAP1B, and nestin in cortical dysplasia as markers of developmental maturity”. eng. In: *Acta Neuropathologica* 93.6 (June 1997), pp. 619–627.

[350] E. A. Benardete and A. R. Kriegstein. “Increased excitability and decreased sensitivity to GABA in an animal model of dysplastic cortex”. eng. In: *Epilepsia* 43.9 (Sept. 2002), pp. 970–982.

[351] J. R. Smith, M. R. Lee, D. W. King, A. M. Murro, Y. D. Park, G. P. Lee, D. W. Loring, K. J. Meador, and R. Harp. “Results of lesional vs. nonlesional frontal lobe epilepsy surgery”. eng. In: *Stereotactic and Functional Neurosurgery* 69.1-4 Pt 2 (1997), pp. 202–209.

[352] A. J. Barkovich and R. I. Kuzniecky. “Neuroimaging of focal malformations of cortical development”. eng. In: *Journal of Clinical Neurophysiology: Official Publication of the American Electroencephalographic Society* 13.6 (Nov. 1996), pp. 481–494.

[353] N. Colombo, N. Salamon, C. Raybaud, C. Ozkara, and A. J. Barkovich. “Imaging of malformations of cortical development”. eng. In: *Epileptic Disorders: International Epilepsy Journal with Videotape* 11.3 (Sept. 2009), pp. 194–205. DOI: 10.1684/epd.2009.0262.

[354] P. Widdess-Walsh, B. Diehl, and I. Najm. “Neuroimaging of focal cortical dysplasia”. eng. In: *Journal of Neuroimaging: Official Journal of the American Society of Neuroimaging* 16.3 (July 2006), pp. 185–196. DOI: 10.1111/j.1552-6569.2006.00025.x.

[355] B. Gómez-Ansón, M. Thom, N. Moran, J. Stevens, and F. Scaravilli. “Imaging and radiological-pathological correlation in histologically proven cases of focal cortical dysplasia and other glial and neuronoglial malformative lesions in adults”. eng. In: *Neuroradiology* 42.3 (Mar. 2000), pp. 157–167.

[356] A. J. Barkovich, R. I. Kuzniecky, A. W. Bollen, and P. E. Grant. “Focal transmantle dysplasia: a specific malformation of cortical development”. eng. In: *Neurology* 49.4 (Oct. 1997), pp. 1148–1152.

[357] H. Urbach, B. Scheffler, T. Heinrichsmeier, J. Von Oertzen, T. Kral, J. Wellmer, J. Schramm, O. D. Wiestler, and I. Blümcke. “Focal Cortical Dysplasia of Taylor’s Balloon Cell Type: A Clinicopathological Entity with Characteristic Neuroimaging and Histopathological Features, and Favorable Postsurgical Outcome”. en. In: *Epilepsia* 43.1 (2002), pp. 33–40. DOI: 10.1046/j.1528-1157.2002.38201.x.

[358] J. T. Lerner, N. Salamon, J. S. Hauptman, T. R. Velasco, M. Hemb, J. Y. Wu, R. Sankar, W. Donald Shields, J. Engel, I. Fried, C. Cepeda, V. M. Andre, M. S. Levine, H. Miyata, W. H. Yong, H. V. Vinters, and G. W. Mathern. “Assessment and surgical outcomes for mild type I and severe type II cortical dysplasia: a critical review and the UCLA experience”. eng. In: *Epilepsia* 50.6 (June 2009), pp. 1310–1335. DOI: 10.1111/j.1528-1167.2008.01998.x.

[359] A. Dumas de la Roque, C. Oppenheim, F. Chassoux, S. Rodrigo, F. Beuvon, C. Daumas-Duport, B. Devaux, and J.-F. Meder. "Diffusion tensor imaging of partial intractable epilepsy". eng. In: *European Radiology* 15.2 (Feb. 2005), pp. 279–285. DOI: 10.1007/s00330-004-2578-8.

[360] S.-K. Lee, D. I. Kim, S. Mori, J. Kim, H. D. Kim, K. Heo, and B. I. Lee. "Diffusion tensor MRI visualizes decreased subcortical fiber connectivity in focal cortical dysplasia". eng. In: *NeuroImage* 22.4 (Aug. 2004), pp. 1826–1829. DOI: 10.1016/j.neuroimage.2004.04.028.

[361] E. Widjaja, S. Blaser, E. Miller, A. Kassner, P. Shannon, S. H. Chuang, O. C. Snead, and C. R. Raybaud. "Evaluation of subcortical white matter and deep white matter tracts in malformations of cortical development". eng. In: *Epilepsia* 48.8 (Aug. 2007), pp. 1460–1469. DOI: 10.1111/j.1528-1167.2007.01105.x.

[362] U. C. Wieshmann, C. A. Clark, M. R. Symms, F. Franconi, G. J. Barker, and S. D. Shorvon. "Reduced anisotropy of water diffusion in structural cerebral abnormalities demonstrated with diffusion tensor imaging". eng. In: *Magnetic Resonance Imaging* 17.9 (Nov. 1999), pp. 1269–1274.

[363] S. H. Eriksson, F. J. Rugg-Gunn, M. R. Symms, G. J. Barker, and J. S. Duncan. "Diffusion tensor imaging in patients with epilepsy and malformations of cortical development". eng. In: *Brain: A Journal of Neurology* 124.Pt 3 (Mar. 2001), pp. 617–626.

[364] G. P. Winston, C. Micallef, M. R. Symms, D. C. Alexander, J. S. Duncan, and H. Zhang. "Advanced diffusion imaging sequences could aid assessing patients with focal cortical dysplasia and epilepsy". eng. In: *Epilepsy Research* 108.2 (Feb. 2014), pp. 336–339. DOI: 10.1016/j.eplepsyres.2013.11.004.

[365] A. N. V. Moosa and E. Wyllie. "Chapter 53 - Focal epileptogenic lesions". In: *Handbook of Clinical Neurology*. Ed. by M. L. a. H. B. S. Olivier Dulac. Vol. 111. Pediatric Neurology Part I. Elsevier, 2013, pp. 493–510.

[366] S. E. Kim, J. H. Lee, H. K. Chung, S. M. Lim, and H. W. Lee. "Alterations in white matter microstructures and cognitive dysfunctions in benign childhood epilepsy with centrotemporal spikes". eng. In: *European Journal of Neurology: The Official Journal of the European Federation of Neurological Societies* 21.5 (May 2014), pp. 708–717. DOI: 10.1111/ene.12301.

[367] L. M. Lillywhite, M. M. Saling, A. S. Harvey, D. F. Abbott, J. S. Archer, D. F. Vears, I. E. Scheffer, and G. D. Jackson. "Neuropsychological and functional MRI studies provide converging evidence of anterior language dysfunction in BECTS". eng. In: *Epilepsia* 50.10 (Oct. 2009), pp. 2276–2284. DOI: 10.1111/j.1528-1167.2009.02065.x.

[368] G. M. Overvliet, R. M. H. Besseling, J. F. A. Jansen, S. J. M. van der Kruijs, J. S. H. Vles, P. A. M. Hofman, S. C. M. Ebus, A. de Louw, A. P. Aldenkamp, and W. H. Backes. "Early onset of cortical thinning in children with rolandic epilepsy". In: *NeuroImage: Clinical* 2 (2013), pp. 434–439. DOI: 10.1016/j.nicl.2013.03.008.

[369] M. Piccirilli, P. D'Alessandro, C. Tiacci, and A. Ferroni. "Language lateralization in children with benign partial epilepsy". eng. In: *Epilepsia* 29.1 (Feb. 1988), pp. 19–25.

[370] J. D. Riley, D. L. Franklin, V. Choi, R. C. Kim, D. K. Binder, S. C. Cramer, and J. J. Lin. "Altered white matter integrity in temporal lobe epilepsy: association with cognitive and clinical profiles". eng. In: *Epilepsia* 51.4 (Apr. 2010), pp. 536–545. DOI: 10.1111/j.1528-1167.2009.02508.x.

[371] L. Concha, H. Kim, A. Bernasconi, B. C. Bernhardt, and N. Bernasconi. "Spatial patterns of water diffusion along white matter tracts in temporal lobe epilepsy". eng. In: *Neurology* 79.5 (July 2012), pp. 455–462. DOI: 10.1212/WNL.0b013e31826170b6.

[372] H. Kim, A. Harrison, P. Kankirawatana, C. Rozzelle, J. Blount, C. Torgerson, and R. Knowlton. "Major white matter fiber changes in medically intractable neocortical epilepsy in children: a diffusion tensor imaging study". eng. In: *Epilepsy Research* 103.2-3 (Feb. 2013), pp. 211–220. DOI: 10.1016/j.eplepsyres.2012.07.017.

[373] B. M. Campos, A. C. Coan, G. C. Beltramini, M. Liu, C. L. Yassuda, E. Ghizoni, C. Beaulieu, D. W. Gross, and F. Cendes. "White matter abnormalities associate with type and localization of focal epileptogenic lesions". en. In: *Epilepsia* (2014), n/a–n/a. DOI: 10.1111/epi.12871.

[374] V. d. C. Fonseca, C. L. Yasuda, G. G. Tedeschi, L. E. Betting, and F. Cendes. "White matter abnormalities in patients with focal cortical dysplasia revealed by diffusion tensor imaging analysis in a voxelwise approach". eng. In: *Frontiers in Neurology* 3 (2012), p. 121. DOI: 10.3389/fneur.2012.00121.

[375] T. Duning, C. Kellinghaus, S. Mohammadi, H. Schiffbauer, S. Keller, E. B. Ringelstein, S. Knecht, and M. Deppe. "Individual white matter fractional anisotropy analysis on patients with MRI negative partial epilepsy". eng. In: *Journal of Neurology, Neurosurgery, and Psychiatry* 81.2 (Feb. 2010), pp. 136–139. DOI: 10.1136/jnnp.2008.160820.

[376] Q. Chen, S. Lui, C.-X. Li, L.-J. Jiang, L. Ou-Yang, H.-H. Tang, H.-F. Shang, X.-Q. Huang, Q.-Y. Gong, and D. Zhou. "MRI-negative refractory partial epilepsy: role for diffusion tensor imaging in high field MRI". eng. In: *Epilepsy Research* 80.1 (July 2008), pp. 83–89. DOI: 10.1016/j.eplepsyres.2008.03.009.

[377] L. Concha, C. Beaulieu, B. M. Wheatley, and D. W. Gross. "Bilateral white matter diffusion changes persist after epilepsy surgery". eng. In: *Epilepsia* 48.5 (May 2007), pp. 931–940. DOI: 10.1111/j.1528-1167.2007.01006.x.

[378] M. Seidenberg, K. G. Kelly, J. Parrish, E. Geary, C. Dow, P. Rutecki, and B. Hermann. "Ipsilateral and contralateral MRI volumetric abnormalities in chronic unilateral temporal lobe epilepsy and their clinical correlates". eng. In: *Epilepsia* 46.3 (Mar. 2005), pp. 420–430. DOI: 10.1111/j.0013-9580.2005.27004.x.

[379] V. Gieselmann and I. Krägeloh-Mann. "Metachromatic leukodystrophy–an update". eng. In: *Neuropediatrics* 41.1 (Feb. 2010), pp. 1–6. DOI: 10.1055/s-0030-1253412.

[380] P. Heim, M. Claussen, B. Hoffmann, E. Conzelmann, J. Gärtner, K. Harzer, D. H. Hunneman, W. Köhler, G. Kurlemann, and A. Kohlschütter. "Leukodystrophy incidence in Germany". en. In: *American Journal of Medical Genetics* 71.4 (Sept. 1997), pp. 475–478. DOI: 10.1002/(SICI)1096-8628(19970905)71:4<475::AID-AJMG20>3.0.CO;2-C.

[381] B. J. Poorthuis, R. A. Wevers, W. J. Kleijer, J. E. Groener, J. G. de Jong, S. van Weely, K. E. Niezen-Koning, and O. P. van Diggelen. "The frequency of lysosomal storage diseases in The Netherlands". eng. In: *Human genetics* 105.1-2 (Aug. 1999), pp. 151–156.

[382] S. Wolpert, M. Anderson, and E. Kaye. "Metabolic and degenerative disorders". In: *MRI in Pediatric Neuroradiology*. St Louis, Mo: Mosby. Wolpert SM, Barnes PD, 1992, pp. 121–150.

[383] J. Aicardi. *Disease of the Nervous System in Childhood*. Cambridge University Press. Cambridge, 1988.

[384] H. Holtschmidt, K. Sandhoff, H. Y. Kwon, K. Harzer, T. Nakano, and K. Suzuki. "Sulfatide activator protein. Alternative splicing that generates three mRNAs and a newly found mutation responsible for a clinical disease". eng. In: *The Journal of biological chemistry* 266.12 (Apr. 1991), pp. 7556–7560.

[385] K. Von Figura and J. Jaeken. "Metachromatic Leukodystrophy". In: *The Metabolic and Molecular Bases of Inherited Diseases*. Mac Graw-Hill: NewYork, NY. Scriver CR, Valle D, Sly WS, 2001, pp. 3695–3724.

[386] J. Austin. "Metachromatic leukodystrophy". In: *Merritt's Textbook of Neurology*. Philadelphia, Pa: Lea & Febiger. Rowland LP, 1989, pp. 527–530.

[387] C. Diebler and O. Dulac. *Pediatric Neurology and Neuroradiology*. en. Berlin, Heidelberg: Springer Berlin Heidelberg, 1987.

[388] V. Gieselmann. "Metachromatic leukodystrophy: genetics, pathogenesis and therapeutic options". eng. In: *Acta paediatrica (Oslo, Norway: 1992). Supplement* 97.457 (Apr. 2008), pp. 15–21. DOI: 10.1111/j.1651-2227.2008.00648.x.

[389] E. Kolodny and H. Moser. "Sulfatide lipidosis: metachromatic leukodystrophy". In: *The metabolic basis of inherited disease*. McGraw-Hill, NewYork. Stanbury JB, Wyngaarten JB, Frederickson DS, et al, pp. 881–905.

[390] M. Blomqvist, V. Gieselmann, and J.-E. Månsson. "Accumulation of lysosulfatide in the brain of arylsulfatase A-deficient mice". eng. In: *Lipids in Health and Disease* 10.1 (2011), p. 28. DOI: 10.1186/1476-511X-10-28.

[391] K. Toda, T. Kobayashi, I. Goto, K. Ohno, Y. Eto, K. Inui, and S. Okada. "Lysosulfatide (sulfogalactosylsphingosine) accumulation in tissues from patients with metachromatic leukodystrophy". eng. In: *Journal of Neurochemistry* 55.5 (Nov. 1990), pp. 1585–1591.

[392] L. E. Becker. "Lysosomes, peroxisomes and mitochondria: function and disorder". eng. In: *AJNR. American journal of neuroradiology* 13.2 (Apr. 1992), pp. 609–620.

[393] T. Haltia, J. Palo, M. Haltia, and A. Icén. "Juvenile metachromatic leukodystrophy. Clinical, biochemical, and neuropathologic studies in nine new cases". eng. In: *Archives of neurology* 37.1 (Jan. 1980), pp. 42–46.

[394] R. MacFaul, N. Cavanagh, B. D. Lake, R. Stephens, and A. E. Whitfield. "Metachromatic leucodystrophy: review of 38 cases". eng. In: *Archives of disease in childhood* 57.3 (Mar. 1982), pp. 168–175.

[395] A. K. Percy, M. M. Kaback, and R. M. Herndon. "Metachromatic leukodystrophy: comparison of early-and late-onset forms". eng. In: *Neurology* 27.10 (Oct. 1977), pp. 933–941.

[396] S. P. Batzios and D. I. Zafeiriou. "Developing treatment options for metachromatic leukodystrophy". eng. In: *Molecular Genetics and Metabolism* 105.1 (Jan. 2012), pp. 56–63. DOI: 10.1016/j.ymgme.2011.10.002.

[397] A. Biffi, G. Lucchini, A. Rovelli, and M. Sessa. "Metachromatic leukodystrophy: an overview of current and prospective treatments". eng. In: *Bone marrow transplantation* 42 Suppl 2 (Oct. 2008), S2–6. DOI: 10.1038/bmt.2008.275.

[398] S. A. Patil and G. H. B. Maegawa. "Developing therapeutic approaches for metachromatic leukodystrophy". eng. In: *Drug Design, Development and Therapy* 7 (2013), pp. 729–745. DOI: 10.2147/DDDT.S15467.

[399] C. Sevin, P. Aubourg, and N. Cartier. "Enzyme, cell and gene-based therapies for metachromatic leukodystrophy". eng. In: *Journal of Inherited Metabolic Disease* 30.2 (Apr. 2007), pp. 175–183. DOI: 10.1007/s10545-007-0540-z.

[400] E. N. Faerber, J. Melvin, and E. M. Smergel. "MRI appearances of metachromatic leukodystrophy". eng. In: *Pediatric radiology* 29.9 (Sept. 1999), pp. 669–672.

[401] T. S. Kim, I. O. Kim, W. S. Kim, Y. S. Choi, J. Y. Lee, O. W. Kim, K. M. Yeon, K. J. Kim, and Y. S. Hwang. "MR of childhood metachromatic leukodystrophy". eng. In: *AJNR. American journal of neuroradiology* 18.4 (Apr. 1997), pp. 733–738.

[402] A. Martin, C. Sevin, C. Lazarus, C. Bellesme, P. Aubourg, and C. Adamsbaum. "Toward a Better Understanding of Brain Lesions during Metachromatic Leukodystrophy Evolution". In: *American Journal of Neuroradiology* 33.9 (Apr. 2012), pp. 1731–1739. DOI: 10.3174/ajnr.A3038.

[403] A. G. Osborn. "Inherited metabolic, white matter, and degenerative diseases of the brain." In: *Diagnostic neuroradiology*. St. Louis: Mosby, 1994, pp. 717–747.

[404] F. Eichler, W. Grodd, E. Grant, M. Sessa, A. Biffi, A. Bley, A. Kohlschuetter, D. Loes, and I. Kraegeloh-Mann. "Metachromatic Leukodystrophy: A Scoring System for Brain MR Imaging Observations". en. In: *American Journal of Neuroradiology* 30.10 (Nov. 2009), pp. 1893–1897. DOI: 10.3174/ajnr.A1739.

[405] D. I. Zafeiriou, E. E. Kontopoulos, H. M. Michelakakis, A. L. Anastasiou, and N. P. Gombakis. "Neurophysiology and MRI in late-infantile metachromatic leukodystrophy". eng. In: *Pediatric neurology* 21.5 (Nov. 1999), pp. 843–846.

[406] S. Groeschel, C. Kehrer, C. Engel, C. í Dali, A. Bley, R. Steinfeld, W. Grodd, and I. Krägeloh-Mann. "Metachromatic leukodystrophy: natural course of cerebral MRI changes in relation to clinical course". en. In: *Journal of Inherited Metabolic Disease* 34.5 (Oct. 2011), pp. 1095–1102. DOI: 10.1007/s10545-011-9361-1.

[407] P. A. Caro and H. G. Marks. "Magnetic resonance imaging and computed tomography in Pelizaeus-Merzbacher disease". eng. In: *Magnetic resonance imaging* 8.6 (1990), pp. 791–796.

[408] I. E. Scheffer, M. Baraitser, J. Wilson, B. Harding, B. Kendall, and E. M. Brett. "Pelizaeus-Merzbacher disease: classical or connatal?" eng. In: *Neuropediatrics* 22.2 (May 1991), pp. 71–78. DOI: 10.1055/s-2008-1071420.

[409] J. P. van der Voorn, P. J. W. Pouwels, W. Kamphorst, J. M. Powers, M. Lammens, F. Barkhof, and M. S. van der Knaap. "Histopathologic correlates of radial stripes on MR images in lysosomal storage disorders". eng. In: *AJNR. American journal of neuroradiology* 26.3 (Mar. 2005), pp. 442–446.

[410] R. N. Sener. "Metachromatic leukodystrophy. Diffusion MR imaging and proton MR spectroscopy". eng. In: *Acta Radiologica (Stockholm, Sweden: 1987)* 44.4 (July 2003), pp. 440–443.

[411] Z. Patay. "Diffusion-weighted MR imaging in leukodystrophies". eng. In: *European Radiology* 15.11 (Nov. 2005), pp. 2284–2303. DOI: 10.1007/s00330-005-2846-2.

[412] V. Engelbrecht, A. Scherer, M. Rassek, H. J. Witsack, and U. Mödder. "Diffusion-weighted MR imaging in the brain in children: findings in the normal brain and in the brain with white matter diseases". eng. In: *Radiology* 222.2 (Feb. 2002), pp. 410–418. DOI: 10.1148/radiol.2222010492.

[413] M. Assadi, D.-J. Wang, Y. Velazquez-Rodriquez, and P. Leone. “Multi-Voxel 1H-MRS in Metachromatic Leukodystrophy”. eng. In: *Journal of Central Nervous System Disease* 5 (2013), pp. 25–30. DOI: 10.4137/JCNSD.S11861.

[414] B. Kruse, F. Hanefeld, H. J. Christen, H. Bruhn, T. Michaelis, W. Hänicke, and J. Frahm. “Alterations of brain metabolites in metachromatic leukodystrophy as detected by localized proton magnetic resonance spectroscopy in vivo”. eng. In: *Journal of Neurology* 241.2 (Dec. 1993), pp. 68–74.

[415] A. Bizzi, G. Castelli, M. Bugiani, P. B. Barker, E. H. Herskovits, U. Danesi, A. Erbetta, I. Moroni, L. Farina, and G. Uziel. “Classification of childhood white matter disorders using proton MR spectroscopic imaging”. eng. In: *AJNR. American journal of neuroradiology* 29.7 (Aug. 2008), pp. 1270–1275. DOI: 10.3174/ajnr.A1106.

[416] C. i Dali, L. G. Hanson, N. W. Barton, J. Fogh, N. Nair, and A. M. Lund. “Brain N-acetylaspartate levels correlate with motor function in metachromatic leukodystrophy”. eng. In: *Neurology* 75.21 (Nov. 2010), pp. 1896–1903. DOI: 10.1212/WNL.0b013e3181feb217.

[417] C. Kehrer, G. Blumenstock, C. Raabe, and I. Krägeloh-Mann. “Development and reliability of a classification system for gross motor function in children with metachromatic leucodystrophy”. eng. In: *Developmental medicine and child neurology* 53.2 (Feb. 2011), pp. 156–160. DOI: 10.1111/j.1469-8749.2010.03821.x.

CV

Kulikova Sofya

Education:

- **2011-2015: PhD in Neuroscience at ED3C, Université Paris-Descartes (France).**
- 2013, 25 August - 14 September: FENS-IBRO Imaging Summer School (Genève and Lausanne, Swiss).
- 2013, July: Biomedical Image Analysis Summer School (Paris)
- **2009-2011: Trinational Joint Master in Neuroscience Program (Université de Strasbourg, France). Diploma with Honors.**
- 2010, 27th September – 2nd October: Electrophysiological school of Strasbourg, France.
- **2005-2009: Bachelor diploma with Honors in Applied Mathematics and Physics at Moscow Institute of Physics and Technology (MIPT, Russia), department of automatized biotechnical systems.**

Professional experience:

- 2012-2015: CEA-Saclay/NEUROSPIN and INSERM 1129 (France). Project title: Integration of multimodal imaging data for investigation of brain development.
- 2014-2015: Teaching applied physics at Ecole Centrale Paris (Paris).
- 2014, 10-16 March: volunteer at the Brain Awareness Week. Popular science lectures at the "Palais de la Découverte" and at "Cité des Sciences et de l'Industrie" (Paris).
- 2013, 12-17 March: volunteer at the Brain Awareness Week. Popular science lectures at the Palais de la Découverte (Paris).
- 2009-2011: INSERM 666 (Strasbourg, France). Project title: dynamics and pathophysiology of cortico-thalamic systems in schizophrenia.
- 2008-2009: Institute of Higher Nervous Activity (Russian Academy of Science). Project title: Application of a modified Bayes method for recognition of different mental states in the development of brain-computer interface (BCI).
- 2008-2009: teacher of Math's and Physics in the correspondence school of the MIPT (Moscow).
- 2007-2009: technician at the Central Science Research Center of Chemistry and Mechanics (Moscow, Russia).

Title: Integration of multimodal imaging data for the investigation of brain development.

Discipline: Neuroscience

Abstract: Magnetic Resonance Imaging (MRI) is a fundamental tool for *in vivo* investigation of brain development in newborns, infants and children. It provides several quantitative parameters that reflect changes in tissue properties during development depending on different undergoing maturational processes. However, reliable evaluation of the white matter maturation is still an open question: on the one side, none of these parameters can describe the whole complexity of the undergoing changes; on the other side, neither of them is specific of any particular developmental process or tissue property.

Developing multiparametric approaches combining complementary information from different MRI parameters is expected to improve our understanding of brain development. In this PhD work, I present two examples of such approaches and demonstrate their relevance for investigating maturation across different white matter bundles. The first approach provides a global measure of maturation based on the Mahalanobis distance calculated from different MRI parameters (relaxation times T1 and T2, longitudinal and transverse diffusivities from Diffusion Tensor Imaging, DTI) in infants (3-21 weeks) and adults. This approach provides a better description of the asynchronous maturation across the bundles than univariate approaches. Furthermore, it allows estimating the relative maturational delays between bundles. The second approach aims at quantifying myelination of brain tissues by calculating Myelin Water Fraction (MWF) in each image voxel. This approach is based on a 3-component tissue model, with each model component having specific relaxation characteristics that were pre-calibrated in three healthy adult subjects. This approach allows fast computing of the MWF maps from infant data and could reveal progression of the brain myelination. The robustness of this approach was further investigated using computer simulations.

Another important issue for studying white matter development in children is bundles identification. In the last part of this work I describe creation of a preliminary atlas of white matter structural connectivity in children aged 17-81 months. This atlas allows automatic extraction of the bundles from tractography datasets. This approach demonstrated its relevance for evaluation of regional maturation of normal white matter in children. Finally, in the last part of the manuscript I describe potential future applications of the previously developed methods to investigate the white matter in cases of two specific pathologies: focal epilepsy and metachromatic leukodystrophy.

Key-words: White Matter, Development, Magnetic Resonance Imaging (MRI), Diffusion Tensor Imaging (DTI), Modeling, Mahalanobis Distance, Myelin, Structural Connectivity, Anatomical Atlas.

Laboratory: INSERM U1129, CEA/Neurospin/UNIACT, Gif-sur-Yvette, France

Titre: Intégration des données d'imagerie multimodale pour l'étude de développement cérébral.

Discipline: Neurosciences

Résumé: L'Imagerie par résonance magnétique (IRM) est un outil fondamental pour l'exploration *in vivo* du développement du cerveau chez le fœtus, le bébé et l'enfant. Elle fournit plusieurs paramètres quantitatifs qui reflètent les changements des propriétés tissulaires au cours du développement en fonction de différents processus de maturation. Cependant, l'évaluation fiable de la maturation de la substance blanche est encore une question ouverte: d'une part, aucun de ces paramètres ne peut décrire toute la complexité des changements sous-jacents; d'autre part, aucun d'eux n'est spécifique d'un processus de développement ou d'une propriété tissulaire particulière.

L'implémentation d'approches multiparamétriques combinant les informations complémentaires issues des différents paramètres IRM devrait permettre d'améliorer notre compréhension du développement du cerveau. Dans ce travail de thèse, je présente deux exemples de telles approches et montre leur pertinence pour l'étude de la maturation des faisceaux de substance blanche. La première approche fournit une mesure globale de la maturation basée sur la distance de Mahalanobis calculée à partir des différents paramètres IRM (temps de relaxation T1 et T2, diffusivités longitudinale et transverse du tenseur de diffusion DTI) chez des nourrissons (âgés de 3 à 21 semaines) et des adultes. Cette approche offre une meilleure description de l'asynchronisme de maturation à travers les différents faisceaux que les approches uniparamétriques. De plus, elle permet d'estimer les délais relatifs de maturation entre faisceaux. La seconde approche vise à quantifier la myélinisation des tissus cérébraux, en calculant la fraction de molécules d'eau liées à la myéline (MWF) en chaque voxel des images. Cette approche est basée sur un modèle tissulaire avec trois composantes ayant des caractéristiques de relaxation spécifiques, lesquelles ont été pré-calibrées sur trois jeunes adultes sains. Elle permet le calcul rapide des cartes MWF chez les nourrissons et semble bien révéler la progression de la myélinisation à l'échelle cérébrale. La robustesse de cette approche a également été étudiée en simulations.

Une autre question cruciale pour l'étude du développement de la substance blanche est l'identification des faisceaux dans le cerveau des enfants. Dans ce travail de thèse, je décris également la création d'un atlas préliminaire de connectivité structurelle chez des enfants âgés de 17 à 81 mois, permettant l'extraction automatique des faisceaux à partir des données de tractographie. Cette approche a démontré sa pertinence pour l'évaluation régionale de la maturation de la substance blanche normale chez l'enfant. Pour finir, j'envisage dans la dernière partie du manuscrit les applications potentielles des différentes méthodes précédemment décrites pour l'étude fine des réseaux de substance blanche dans le cadre de deux exemples spécifiques de pathologies : les épilepsies focales et la leucodystrophie métachromatique.

Mots-clés: substance blanche, développement, imagerie par résonance magnétique IRM, imagerie du tenseur de diffusion DTI, modélisation, distance de Mahalanobis, myéline, connectivité structurelle, atlas anatomique.

Laboratoire: INSERM U1129, CEA / Neurospin / UNIACT, Gif-sur-Yvette, France